JAERI-M
90-066

REVIEW OF JT-60 EXPERIMENTAL RESULTS FROM JANUARY TO OCTOBER, 1989

March 1990

JT-60 Team

日本原子力研究所
Japan Atomic Energy Research Institute

JAERI-Mレポートは，日本原子力研究所が不定期に公刊している研究報告書です。
入手の問合わせは，日本原子力研究所技術情報部情報資料課（〒319-11茨城県那珂郡東海村）あて，お申しこしください。なお，このほかに財団法人原子力弘済会資料センター（〒319-11 茨城県那珂郡東海村日本原子力研究所内）で複写による実費領布をおこなっております。

JAERI-M reports are issued irregularly.
Inquiries about availability of the reports should be addressed to Information Division Department of Technical Information, Japan Atomic Energy Research Institute, Tokai-mura, Naka-gun, Ibaraki-ken 319-11, Japan.

編集兼発行　日本原子力研究所
印　　刷　いばらき印刷㈱

JAERI-M 90-066

Review of JT-60 Experimental Results from January to October, 1989

JT-60 Team※
Department of Large Tokamak Research
Department of JT-60 Facility
Naka Fusion Research Establishment
Japan Atomic Energy Research Institute
Naka-machi, Naka-gun, Ibaraki-ken

(Received March 1, 1990)

Emphases in recent JT-60 experiments are placed on 1) improvements in plasma confinement with profile control and 2) steady state operation study. Two equipments were installed: a four-barrel pneumatic pellet injector with speed of 2.3 km/s and sizes of 3 mm and 4 mm, and a new multijunction-type lower hybrid launcher with sharp power spectra of $\Delta N_{||}$ ~0.5 and high directivity. Experiments have been carried out in the wide range of parameters: 0.5×10^{19} $m^{-3}< \bar{n}_e < 1.8\times10^{20}$ m^{-3}, 0.3 MA < Ip < 3.1 MA, B_T < 4.8 T, P_{NB} < 23 MW, P_{LH} < 7 MW and P_{IC} < 2.5 MW. Both limiter and lower X-point divertor configurations were employed. The operating gas was hydrogen and, in some cases, helium.

Improvements in confinement were demonstrated with pellet injection, LH current drive, high-Ti mode operation or ICRF. Peaked density profiles of $n_e(0)/\langle n_e\rangle$ < 4.5 were produced with successive three or four pellets injection. The sawtooth period was prolonged up to 1 sec by the pellet injection. Both density and pressure profiles were peaked inside the q=1 surface. The electron density and the total pressure at the plasma center reached 3×10^{20} m^{-3} and 2 atms, respectively. The energy confinement time was improved by 30-40 % relative to gas fuelled discharges for NB heating of 5-15 MW. The achieved $n_e(0)\tau_E Ti(0)$ is 1.2×10^{20} m^{-3}skeV at Ip=3.1 MA, which is twice that of gas fuelled discharges. The maximum value of the local pressure gradient inside q=1 surface and the onset condition of the fast crash are consistent with ideal MHD ballooning and low-n kink stability analysis.

Current profile controllability with energetic electrons has been improved by the new LH launcher. A broad hard X-ray profile was obtained with high $N_{||}$ injection. On the other hand, low $N_{||}$ injection was effective for suppression of sawtooth activities. Low-$N_{||}$ LH current driven discharges with high power NB heating showed centrally peaked hard X-ray and ion temperature profiles during the sawtooth free periods of up to 1.8 sec.

The H-mode was achieved in limiter discharges with LH current drive for the first time. Simultaneous application of RF powers at two different frequencies such as 1.74 + 2.23 GHz or 1.74 + 2.0 GHz appeared to be effective in the attainment of the H-mode. The threshold lower hybrid power was as low as ohmic heating power with hydrogen plasmas. Nearly steady-state ELM-free H-mode with durations up to 3.3 sec was established without significant impurity accumulation.

High-Ti and high-βp discharges were obtained in high field (B_T=4.5T) and low plasma current with JT-60's perpendicular injection. The discharge was realized with ~20 MW NB injection into low density (~0.5×10^{19} m^{-3}) lower X-point discharges. For the Ip regime of 0.5 - 0.7 MA (q_{eff} =8-13), the discharge showed no sawtooth activity. This resulted in an improved confinement, a peaked density profile of $n_e(0) \sim 6\times10^{19}$ m^{-3} and high Ti(0) of 12 keV.

Effective acceleration of high energy ions was observed in the H-minority He plasma by the combined heating of NB and ICRF with second to fourth harmonics of hydrogen cyclotron frequency. Giant sawteeth with a maximum period of 410 ms were observed. The energy confinement time was improved by a factor of 1.2 during the giant sawtooth period.

Major experimental issues for the steady-state operation research were non-inductive current drive and He-ash exhaust. LH current drive experiments were carried out for a wide range of $N_{||}$(1.0-3.4). The current drive efficienty η_{CD} was proportional to the product of $1/N_{||}^2$ and accessible power fraction, i.e. spectrum dependence of η_{CD} showed a good agreement with Fisch's theory. The maximum η_{CD} of 3.4×10^{19} $m^{-2}A/W$ has been achieved with LH injection of 2-4.5 MW for lower X-point discharges with $\bar{n}_e$ up to 3.0×10^{19} m^{-3} and Ip=1-1.75 MA. The achieved value is well approaching 5×10^{19} $m^{-2}A/W$, which is the efficiency necessary for the ITER steady-state operation.

The neoclassical bootstrap current was confirmed in the wide range of βp. The ratio of bootstrap current to the total current increased in

proportion to βp and reached 80% at $\beta p \sim 3.2$. The existence of the bootstrap current was also demonstrated by keeping the primary OH current constant and measuring the decay time of the total current. The result is encouraging for the design of high-Q(20-30) steady-state tokamak reactor.

To simulate the α-particle production in D-T plasmas, 30 keV helium NB was injected into NB heated lower X-point discharges, which produced centrally peaked birth profile of α-particles. Both the H_2 and helium pressure in the divertor region increased in propotion to $\bar{n}_e^3$. The helium pressure reached 0.02 Pa (10% of H_2 pressure) at $\bar{n}_e = 5\times10^{19}$ m^{-3}, in which α-particle density is 10% of the main proton density. A simple extension of the present result is promising for the helium exhaust in future device; pump speed of several tens m^3/s will be sufficient for 1000 MW fusion power reactor operating at $\bar{n}_e = 1\times10^{20}$ m^{-3}.

Keywords: Pellet, Sawtooth, LH Current Drive, H-mode, High-βp, H-minority ICRF, Bootstrap Current, He Exhaust

※
N.AKAOKA, H.AKASAKA, M.AKIBA, N.AKINO, T.ANDO, K.ANNOU, T.AOYAGI, T.ARAI, K.ARAKAWA, M.ARAKI, M.AZUMI, S.CHIBA, M.DAIRAKU, N.EBISAWA, T.FUJII, T.FUKUDA, A.FUNAHASHI, H.FURUKAWA, H.GUNJI, K.HAMAMATSU, M.HANADA, M.HARA, K.HARAGUCHI, H.HIRATSUKA, T.HIRAYAMA, S.HIROKI, K.HIRUTA, M.HONDA, M.HONDA, H.HORIIKE, N.HOSOGANE, Y.IIDA, T.IIJIMA, K.IKEDA, Y.IKEDA, T.IMAI, T.INOUE, N.ISAJI, M.ISAKA, N.ISEI, S.ISHIDA, K.ITAMI, N.ITIGE, T.ITO, T.KAKIZAKI, Y.KAMADA, A.KAMINAGA, T.KANEKO, M.KAWAI, M.KAWABE, Y.KAWAMATA, Y.KAWANO, K.KIKUCHI, M.KIKUCHI, H.KIMURA, T.KIMURA, H.KISHIMOTO, S.KITAMURA, K.KIYONO, K.KODAMA, Y.KOIDE, T.KOIKE, T.KOBAYASHI, M.KOMATA, I.KONDO, T.KONDO, S.KONOSHIMA, H.KUBO, S.KUNIEDA, K.KURIHARA, M.KURIYAMA, M.KUSAKA, Y.KUSAMA, T.KUSHIMA, M.MAENO, T.MATOBA, S.MATSUDA, M.MATSUKAWA, M.MATSUOKA, Y.MATSUZAKI, Y.MIURA, N.MIYA, K.MIYACHI, K.MIYAKE, Y.MIYO, M.MIZUNO, K.MOGAKI, S.MORIYAMA, Y.MURAKAMI, M.MUTO, M.NAGAMI, A.NAGASHIMA, K.NAGASHIMA, T.NAGASHIMA, S.NAGAYA, K.NAGAYAMA, O.NAITO, H.NAKAMURA, T.NAKAFUJI, H.NEMOTO, M.NEMOTO, Y.NEYATANI, H.NINOMIYA, N.NISHINO, T.NISHITANI, H.NOBUSAKA, H.NOMATA, A.OIKAWA, K.OBARA, K.ODAJIMA, N.OGIWARA, T.OHGA, Y.OHARA, H.OOHARA, T.OHSHIMA, K.OHTA, M.OHTA, S.OHUCHI, Y.OHUCHI, Y.OHUCHI, H.OKUMURA, K.OMORI, S.OMORI, Y.OMORI, T.OZEKI, M.SAEGUSA, N.SAITOH, A.SAKASAI, S.SAKATA, T.SAKUMA, T.SASAJIMA, K.SATOU, M.SATOU, M.SATOU, M.SAWAHATA, M.SEIMIYA, M.SEKI, M.SEKI, S.SEKI, K.SHIBANUMA, M.SHIMADA, K.SHIMIZU, M.SHIMIZU, Y.SHIMOMURA, S.SHINOZAKI, H.SHIRAI, H.SHIRAKATA, M.SHITOMI, K.SUGANUMA, T.SUGAWARA, T.SUGIE, H.SUNAOSHI, M.SUZUKI, N.SUZUKI, S.SUZUKI, H.TACHIBANA, M.TAKAHASHI, S.TAKAHASHI, T.TAKAHASHI, M.TAKASAKI, H.TAKATSU, H.TAKEUCHI, A.TAKESHITA, T.TAKIZUKA, S.TAMURA, S.TANAKA, T.TANAKA, Y.TANAKA, T.TANI, T.TANI, M.TERAKADO, T.TERAKADO, K.TOBITA, T.TOTSUKA, N.TOYOSHIMA, T.TSUGITA, S.TSUJI, Y.TSUKAHARA, M.TSUNEOKA, K.UEHARA, Y.URAMOTO, H.USAMI, K.USHIGUSA, K.USUI, J.YAGYU, K.YAMAGISHI, M.YAMAGIWA, M.YAMAMOTO, O.YAMASHITA, T.YAMAZAKI, K.YOKOKURA, K.YOKOYAMA, H.YOSHIDA, Z.YOSHIDA**, R.YOSHINO, Y.YOSHIOKA, I.YONEKAWA, K.WATANABE

* Contract Researcher
** Tokyo University

JTERI－M 90－066

JT－60　1989年1－10月期実験結果のレビュー

日本原子力研究所那珂研究所
臨界プラズマ研究部・JT－60試験部
JT－60チーム※

（1989年3月1日受理）

JT－60の最近の実験以下の2点に重点を置いて進めた：1）分布制御によるプラズマ閉じ込めの改善，2）定常運転の研究。この期間に次の2つの機器を導入した：ガス銃方式の速度 2.3 km／s，大きさ3 mm，4 mm の4ペレット入射装置，そしてシャープなパワー・スペクトルと強い方向性を有する新型マルチ・ジャンクションの低域混成（LH）波アンテナである。以下の広いパラメータ領域で実験を行った：電子密度＝ $0.5 \times 10^{19} - 1.8 \times 10^{20} m^{-3}$，プラズマ電流=0.3－3.1 MA，トロイダル磁場≦ 4.8 T，中性粒子（NB）入射パワー≦ 23 MW，LH パワー≦ 7MW そしてICRF パワー≦ 2.5 MW。リミター配位と下側X点ダイバータ配位の両方で実験を行い，放電には水素，場合によりヘリウムを用いた。

閉じ込めの改善を以下の手法により実現した：ペレット入射，LH電流駆動，高イオンモード運転，そしてICRF加熱である。連続した3個，あるいは4個のペレット入射で中心ピーク度最大 4.5 に達する密度分布を実現した。ペレット入射により鋸歯状振動の周期は，最大1秒まで増加する。電子密度及びプラズマ圧力は，q＝1磁気面の内側でピークする。中心での電子密度，プラズマ圧力はそれぞれ $3 \times 10^{20} m^{-3}$，2気圧に達する。5－15 MW のNB加熱でエネルギー閉じ込め時間は，ガス注入の放電に較べ30－40％増大する。プラズマ電流 3.1 MA における核融合積は，$1.2 \times 10^{20} m^{-3}$ skeVで，ガス注入の場合の2倍になる。q＝1磁気面内での圧力勾配上限値及び中心プラズマの内部崩壊の発生条件は，理想磁気流体安定性理論と良い一致を示す。

新しいLHアンテナの導入により，高速電子電流の分布制御性を大きく改善した。磁場方向屈折率の大きなLH波を入射すると，小半径方向に広い硬X線分布が得られる。一方，屈折率の小さいLH波入射の場合は，鋸歯状振動を安定化する。NB加熱プラズマに適用すると最大 1.8 秒間鋸歯状振動を安定化し，中心ピークした硬X線とイオン温度分布を形成する。

LH電流駆動を行うリミター放電で初めてHモードを実現した。1.74 ＋ 2.23 GHz，あるいは 1.74 ＋ 2.0 GHz の異なる周波数の組み合わせのLH波の入射がHモードの実現に有効である。水素プラズマにもかかわらずHモード発生に必要なパワーはジュール加熱パワーと同程度で，極

那珂研究所：〒311－01　茨城県那珂郡那珂町大字向山 801－1

めて小さい。不純物混入の増大を伴わない，準定常で安定なHモードを最大3.3秒間持続した。

高磁場，低プラズマ電流（0.5－0.7 MA；安全係数＝8－13）の運転で高イオン温度，高ポロイダルベータ値の放電モードを得た。このモードは下側X点の低密度プラズマに約20 MWのNB入射を行うことにより得られ，鋸歯状振動を安定化し，閉じ込めの改善，中心ピークした電子密度分布の形成，そして中心イオン温度12 keVを実現した。

水素イオンのICRF第2次－第4次共鳴とNBの複合加熱を行うとき，ヘリウムプラズマ中の少数水素イオンを効率良く加速する。このとき最大410 msecの間鋸歯状振動が安定化され，エネルギー閉じ込め時間は20％増大する。

定常化運転研究における主な実験テーマは，非誘導電流駆動とヘリウム灰の排気である。LH電流駆動の実験を入射波屈折率の広いパラメータ領域で行った。その結果，電流駆動効率のスペクトル依存性は，Fischの理論と良い一致を示すことを明らかにした。電流駆動効率の最大値は$3.4\times10^{19}m^{-2}A/W$であり，4.5 MWを入射する時電子密度$3\times10^{19}m^{-3}$のプラズマで1.75 MAの電流を駆動する。この結果は，国際熱核融合炉ITERの定常運転の駆動効率目標値$5.0\times10^{19}m^{-2}A/W$に近い値である。

流に対する割合は，ポロイダルベータ値に比例して増大し，ポロイダルベータ値3.2のとき80％に達する。更に，1次誘導コイルの電流を一定にした時のプラズマ電流の減衰速度を測定することにより自発電流の存在を一層明確にした。この実験結果は，高Q（20－30）の定常トカマク炉設計の重要なデータベースとなるものである。

DTプラズマにおけるアルファ粒子の発生を模擬するために，30 kVのヘリウム中性ビームを入射した。このときアルファ粒子は，中心ピークした発生分布を示す。ダイバータ領域の水素及びヘリウム中性ガス圧力は，主プラズマの電子密度の3乗に比例して増大する。主プラズマ中のアルファ粒子の密度がプロトンの10％の時，ダイバータでのヘリウム圧力は水素分子圧力の10％である。この実験結果を単純に将来の装置に適用すると，ヘリウム排気は容易であると予測できる。すなわち1000 MW核融合出力の炉において排気速度はおおよそ数十m^3/s程度で十分である。

※

青柳　哲雄・赤岡　伸雄・赤坂　博美・秋野　昇・秋場　真人・安積　正史・阿部　哲也
新井　貴・荒川喜代次・荒木　政則・安東　俊郎・安納　勝人・飯島　勉・飯田　一広
池田　幸治・池田　佳隆・井坂　正義・伊佐治信明・石田　真一・伊世井宣明・伊丹　潔
市毛　尚志・伊藤　孝雄・井上多加志・今井　剛・上原　和也・宇佐美広次・牛草　健吉
薄井　勝富・浦本　保幸・海老沢　昇・及川　晃・大内　章寿・大内　豊・大賀　徳道
大島　貴幸・太田　和也・太田　充・大原比呂志・大森憲一郎・大森　俊造・大森　栄和
荻原　徳男・奥村　義和・小関　隆久・小田島和男・小原建治郎・小原　祥裕・柿崎　禎之
鎌田　裕・神永　敦嗣・河合視己人・金子　高志・川崎　幸三・河野　康則・川辺　勝
川俣　陽一・菊池　勝美・菊池　満・岸本　浩・北村　繁・木村　豊秋・木村　晴行
清野　公広・日下　誠・草間　義紀・九嶋　孝憲・国枝　俊介・久保　博孝・栗原　研一
栗山　正明・軍司　秀穂・小池　常之・小出　芳彦・児玉　幸三・木島　滋・小林　輝明
小又　将夫・近藤　育郎・近藤　貴・斎藤　直之・三枝　幹雄・逆井　章・坂田　信也
佐久間　猛・笹島　唯之・佐藤　一也・佐藤　正泰・佐藤　稔・沢畠　正之・鄯　守正
篠崎　信一・柴沼　清・嶋田　道也・清水　勝宏・清水　正亜・下村　安夫・白井　浩
白形　弘文・菅原　忠義・菅沼　和明・杉江　達夫・鈴木　貞明・鈴木　紀男・鈴木　正信*
砂押　秀則・清宮　宗孝・関　正美・関　昌弘・関　省吾・高崎　學・高津　英幸
高橋　春次・高橋虎之助・高橋　実・滝塚　知典・竹内　浩・竹下　明・立花　英俊
田中　茂・田中竹次郎・田中　裕二・谷　啓二・谷　孝志・田村　早苗・大楽　正幸
千葉　真一・塚原　美光・次田　友宜・辻　俊二・恒岡まさき・寺門　恒久・寺門　正之
戸塚　俊之・飛田　健次・豊島　昇・内藤　磨・中藤　隆志・中村　博雄・長島　章
永島　圭介・永島　孝・永谷　進・永見　正幸・長山　清・西谷　健夫・西野　信博*
二宮　博正・根本　裕功・根本　正博・閨谷　譲・信坂　裕通・野亦　英幸・野本　弘樹
花田磨砂也・濱松　清隆・原　誠・原口　和三・平塚　一・平山　俊雄・蛭田　和治
廣木　成治・福田　武司・藤井　常幸・船橋　昭昌・古川　弘・細金　延幸・堀池　寛
本田　正男・本多　光輝・前野　勝樹・松岡　守・松川　誠・松田慎三郎・松崎　誼
的場　徹・間淵　幸雄・三浦　良和・水野　誠・宮　直之・三宅　一幸・宮地　謙吾
三代　康彦・武藤　貢・村上　義夫・藻垣　和彦・森山　伸一・柳生　純一・山岸耕二郎
山極　満・山崎　武・山下　修・山本　正弘・横倉　賢治・横山　堅二・吉岡　祐二*
吉田　善章**・吉田　英俊・芳野　隆治・米川　出・渡邊　和弘

＊　外来研究員

＊＊　東京大学

Contents

目　　次

1. PELLET INJECTION EXPERIMENT

1.1 Improvement of Energy Confinement in Pellet Fuelled Plasmas on JT-60

R.Yoshino, Y.Kamada, K.Shimizu, T.Hirayama,
T.Ozeki, T.Nishitani and M.Nagami

The experiments of pellet injection is expanded to high plasma current of 2.8 and 3.1MA in the limiter configuration and the improvement in energy confinement of ~30% is obtained with 10~15MW heating. Owing to the peaked density profile and the improved energy confinement, $n_e(0)\tau_E Ti(0)=12\times10^{19}m^{-3}sec keV$ is achieved with hydrogen plasmas.

1. Introduction

Pellet injection is the promising method to make a peaked density profile, and is useful to examine the performance of plasmas with the peaked pressure profile. In JT-60, high power heating of the pellet injected plasmas has been studied, and the improvement in energy confinement of 30~40% compared with gas fuelled plasmas is achieved with NB heating power of ~10MW at Ip≤2.1MA[1]. The plasma stored energy rises largely during the sawtooth-free phase just after the pellet injection and the increase in the stored energy is terminated by large sawtooth crashes or large m=1 internal mode. When the enhancement of the energy confinement is large, the well peaked profile of soft X-ray emission, that relates to the electron pressure profile, is always observed inside the q=1 rational surface in the pre-pellet phase. The numerical simulation of the plasma current profile suggests that q(0) is lower than 1.0 owing to the fast recovery of the electron temperature after the pellet injection[2]. These experimental observation and the numerical investigation clarify that the improvement in the energy confinement is due to the local improvement inside the q=1 rational surface. Then pellet injection experiments with the higher plasma current of 2.8 and 3.1MA with larger q=1 radius of ~0.4m (q(a)=~2.2, a~0.9m) are performed.

The pellet injector is improved to 4 hydrogen pellets with ~2.3km/s[3]. So the optimization of the pellet injection is performed again to get the optimum penetration depth[4] according to the experience of the last experimental period[5].

2. Improvement of the Energy Confinement

In Fig.1 the stored energy(W^{DIA}) measured by the diamagnetic loop of pellet injected limiter plasmas is shown by closed points versus the absorbed heating power(Pabs), and that of gas fuelled plasmas is presented by open points. The plasma current is scanned from 1.5MA to 3.1MA with NB heating power of <25MW, ICRF power of <3MW. The maximum increase in the stored energy compared with the gas fuelled plasma rises with the plasma current almost linearly. At Ip=2.8 and 3.1MA, the largest improvement in energy confinement of ~30% with the increased stored energy of ~0.6MJ from the gas fuelled plasmas is obtained at Pabs=10~15MW and the improvement in the energy confinement degrades with the increase in heating power at >15MW.

Fig.1

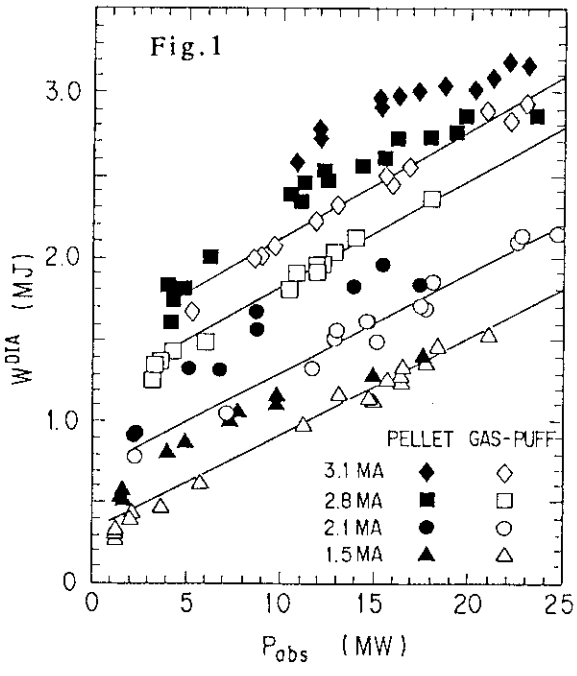

The relation between the energy confinement time and the density peaking factor defined by $n_e(0)/<n_e>_v$, where $<n_e>_v$ is the volume averaged density, is shown in Fig.2 at Ip=2.8MA and 10MW<Pabs<12MW. The stored energy is clearly improved with the peaked density profile. No clear relation is observed between the line averaged density and the stored energy.

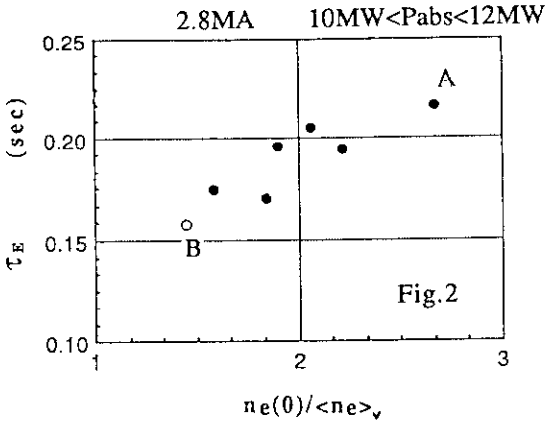

Fig.2

The local transport analysis is performed at the equilibrium state with the maximum stored energy as shown in Fig.3 for two cases labeled (A) and (B) in Fig.2(b). Where (A) is the pellet injected plasma with the highly peaked density profile, and (B) is the gas fuelled plasma with the flat density profile as shown in Fig.3(a). In the case of (B) plasma core is well heated by the NB heating. On the other hand the penetration of NB into the plasma is not enough in the case of (A) owing to the high density as shown in Fig.3(b). However heating of the plasma core is achieved a little for the sake of the tangential injection of NB. The effective heat diffusivity(χeff)[6] of the combined ion and electron is shown in Fig.3(c). χeff of case (A) is smaller than that of case(B) at r<~0.5m, that is almost same with the radius of q=1 rational surface of 0.4m. Furthermore χeff(0) of case (A) is ~0.2 of case (B).

For the sake of the improvement in the energy confinement and the peaked density profile, the fusion product defined by $ne(0)\tau_E Ti(0)$ reaches $12x10^{19}m^{-3}$seckeV with Ti(0)=3.4keV in 3.1MA limiter hydrogen discharges as shown in Fig.4. Where Ti(0) is measured by Doppler broadening of TiXXI Kα line. On the other hand the maximum value obtained by the gas fuelled plasmas is $6.6x10^{19}m^{-3}$seckeV in 3.15MA limiter discharge.

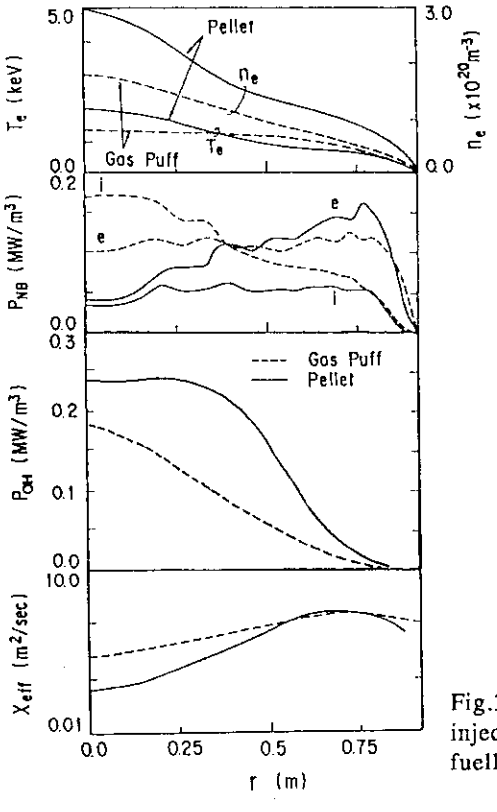

Fig.3 Transport analysis of pellet injected plasm(A in Fig.2) and gas fuelled plasma(B in Fig.2).

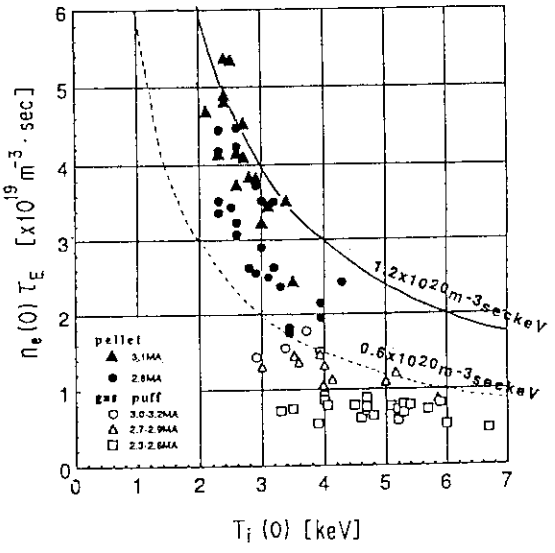

Fig.4 Lawson diagram

3. The effect of MHD Activity on the Energy Confinement

The density profile becomes peaked with the increase in the supply of particles inside the q=1 rational surface[4]. The characteristic length of the density gradient($Ln=(dn_e/n_e dr)^{-1}$) at q=1 surface, that is measured by Thomson scattering at 400~500 ms after the pellet injection, naturally decreases with the increase in the density peaking factor as shown in Fig.5.

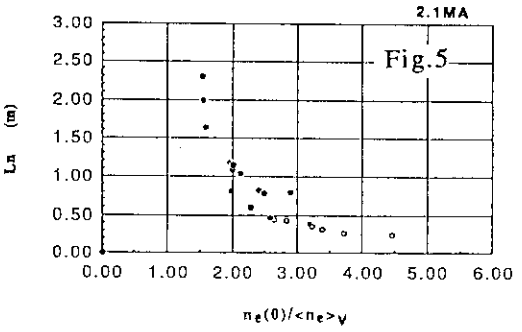

Fig.5

In the case of open points the sawtooth activity with the full reconnection is suppressed after the pellet injection until the time point of the Thomson scattering measurement. In that case the partially reconnected sawtooth crashes are sometimes observed, however that has no effect on the density profile and the energy confinement. In the case of the closed points the sawtooth activities with full reconnection are observed.

There are a few shots, in which no change is observed in the stored energy at the large sawtooth crash as shown in Fig.6. Four pellets are injected from 5.98 s to 6.02 s under 6MW NB heating. The stored energy rises just after the pellet injection with the abrupt increase in the oneturn loop voltage(V), and that subsequently rises from 2.05MJ to 2.8MJ within a short time period of 0.3 s (t=6.05s to 6.35s) due to the increase in the NB heating power from 6MW to 14MW. Then the stored energy gradually rises from 6.4 to 7.1sec. The sawtooth activities at t=6.85 s and 7.0 s have no effect on the stored energy. The investigations of soft X-ray array signals indicates that the plasma core behaves as a rigid body without the full reconnection at the sawtooth crashes[7]. The stored energy starts decreasing from 7.05s with the occurrence of m=1 internal mode, that is the another cause of the reduction in the energy confinement[1]. So that it is reconfirmed from Fig.5 and 6 that the stabilization of the sawtooth activity with full reconnection and the large m=1 internal mode are essential for getting the peaked density profile and improved energy confinement.

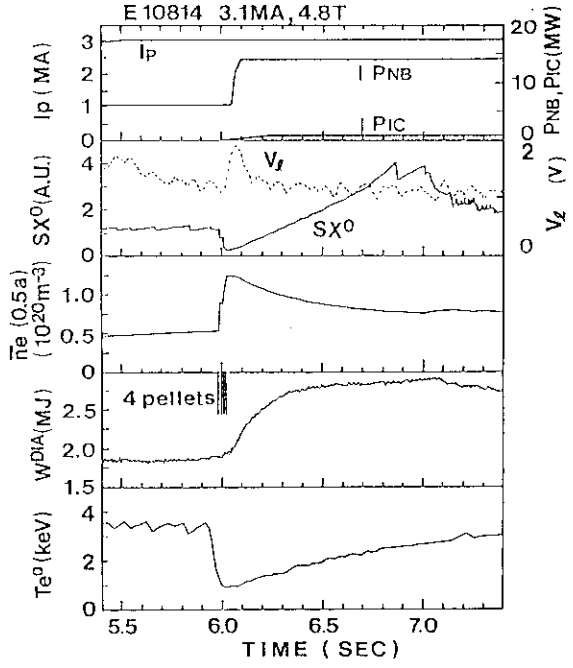

Fig. 6 Typical time evolution of the pellet injected plasma. SX^0 is the soft X-ray signal of the central cord. Te^0 is the central electron temperature measued by ECE.

The profiles of electron density and temperature during the rise of the stored energy are measured by Thomson scattering at 500 ms (t=6.5s) and 800 ms (t=6.8s) after the last pellet injection as shown in Fig.7. The peaked density profile is kept for about 1.0sec.

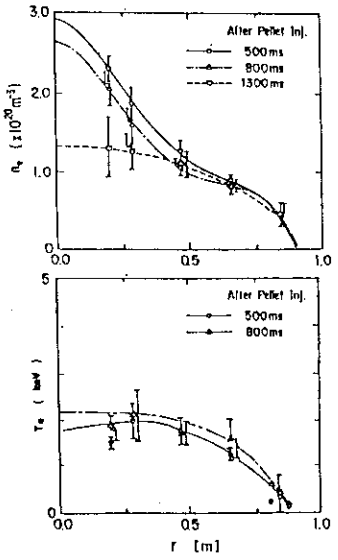

Fig.7 Profiles of electron density and temperature 500ms and 800ms after the pellet injection in Fig.6.

To investigate the effect of these MHD activities on the particle and energy confinement, numerical simulation of energy and particle transport has been performed to reproduce the case of Fig.6 and 7. Fully reconnected sawtooth is simulated by Kadomstev's model, and is suppressed after the pellet injection. The profiles of the particle diffusivity(D) is assumed to be a tailored step function with the lowered value inside the the q~1 radius(q=1 radius is 0.4m) as shown in Fig.8. The profile of electron thermal diffusivity χe is set to be flat within 0.9 of the minor radius, and is enlarged at the edge region. Absolute value of χe is assumed to be degraded with the increase in the additional heating power to fit the measured total stored energy. χi is assumed to be $\chi_i{}^{CH}+\chi_i{}^{an}$, and $\chi_i{}^{an}$ is set to be equal to χe. Particle inward pinch velocity is assumed to be zero, effect of that on the density profile will be discussed in elsewhere.

The time evolutions of the stored energy measured by a diamagnetic loop, line integrated density at a half radius measured by FIR and the central electron temperature measured by ECE are compared with the simulated result as shown in Fig.9, where solid lines are the measured values. Nice agreement is obtained in the case of sawtooth-free. The peaked density profile is also reproduced as shown in Fig.10. Both of improvement of the stored energy and peaked profile are not obtained in the case of sawtooth with 80ms interval. The same behavior is also simulated with a flat profile of D. Then three items are necessary to get the peaked density profile 1)the suppression of the fully reconnected sawtooth 2)the reduction of D inside q=1 radius 3)the supply of of many particles inside the q=1 radius[4]. The recovery of the electron temperature in the core region is almost reproduced as shown in Fig.9.

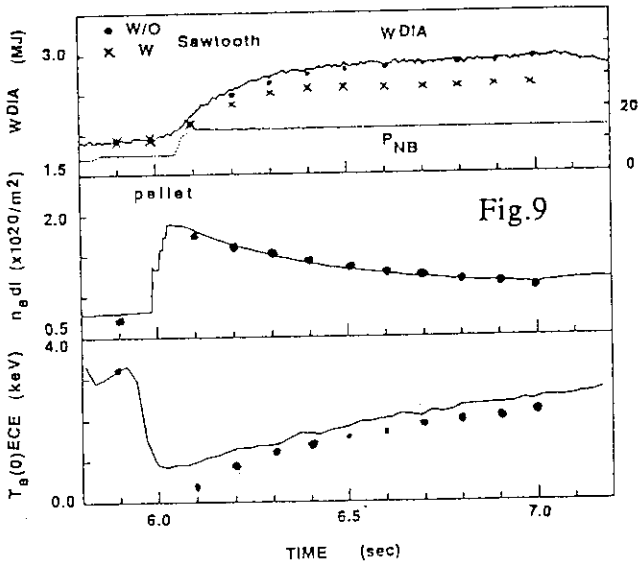

Fig.9

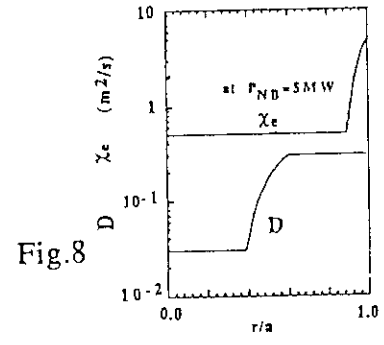

Fig.8

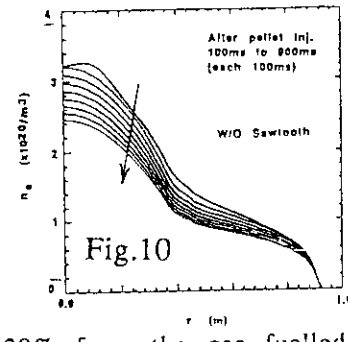

Fig.10

4. Conclusion

The improvement in the energy confinement of 30% from the gas fuelled plasmas is obtained at 2.8 and 3.1MA limiter plasmas with 10~15MW NB heating. The energy confinement is improved with the peaked density. The suppression of the sawtooth activity with full reconnection is essential to get this improvement, and the numerical simulation suggests that the improved particle diffusivity inside the q=1 radius is necessary to reproduce the experimental observations.

References

[1]KAMADA,Y., et al.., Nucl. Fusion 29 (1989) 1785 [2]YOSHINO,R., Nucl. Fusion 29 (1989) 2231 [3]HIRATSUKA,H., et al.., see section 1.8 and 1.9 [4]YOSHINO,R., et al.., see section 1.2 [5]YOSHINO,R., et al.., JAERI-M 88-246 (1988) [6]HIRAYAMA,T., et al., see section 8.6[7]KAMADA,Y.,et al.., see section 1.3

1.2 Optimization of the Pellet Injection

R.Yoshino, T.Hirayama, K.Shimizu, Y.Kamada , T.Nishitani,

The ablation of pellet measured by the Hα emission profile is compared with the numerical simulation result adopting the neutral gas shielding model, and reasonable agreement is obtained between them. The injection order of pellets in the multi-pellet injection is optimized according to the simulation results, and well peaked density profile is obtained by the suppression of sawtooth activities with full reconnection.

1. Pellet Injector and Diagnostics

Pellet injector is the pneumatic gan type with four hydrogen pellets of 3.0mmϕx3.0mm (two small pellets) and 4.0mmϕx4.0mm (two large pellet). Pellets are injected with an angle of 47 degree from the midplane as shown in Fig.1 of the ref.[1]. The velocity of pellets is ~2300m/sec[2]. The injection line is off-axis and the separation width between the pellet injection line and the plasma center is ~0.1m. Ablation profile of the pellet is monitored by the detector array of Hα emission as presented in Fig.1 of the ref.[1], where the set-up of the other diagnostics are also presented.

2. One Pellet Injection

In joule plasmas without runaway electrons, the electron temperature profile is essential to decide the penetration depth of the pellet into a plasma, and the optimum temperature profiles are strictly limited for getting the nice penetration of the pellet. Because the pellet cannot penetrate into the plasma core at high electron temperature, but passes through at low electron temperature. NB heating is adopted to avoid the disruption caused by the passing through of the pellet, that triggers the enhanced plasma-wall interaction[3].

The ablation profile of a pellet injected into a NB heated plasma is investigated to check the availability of the pellet ablation code[4], that equips Milora's neutral gas shield model[5] with self-limiting ablation model proposed by Houlberg et al[6]. Where in OH plasmas nice agreement is obtained between the measured profiles of the ablation and the simulated results by using the neutral gas shield model[7].

Figure1 shows an profile of the ablation of one large pellet injected into a 2.1MA limiter plasma under the condition of 5MW NB heating. The comparison of the measured Hα emission profile (solid line) and the calculated ablation profile (broken line) is shown in Fig.1(a).

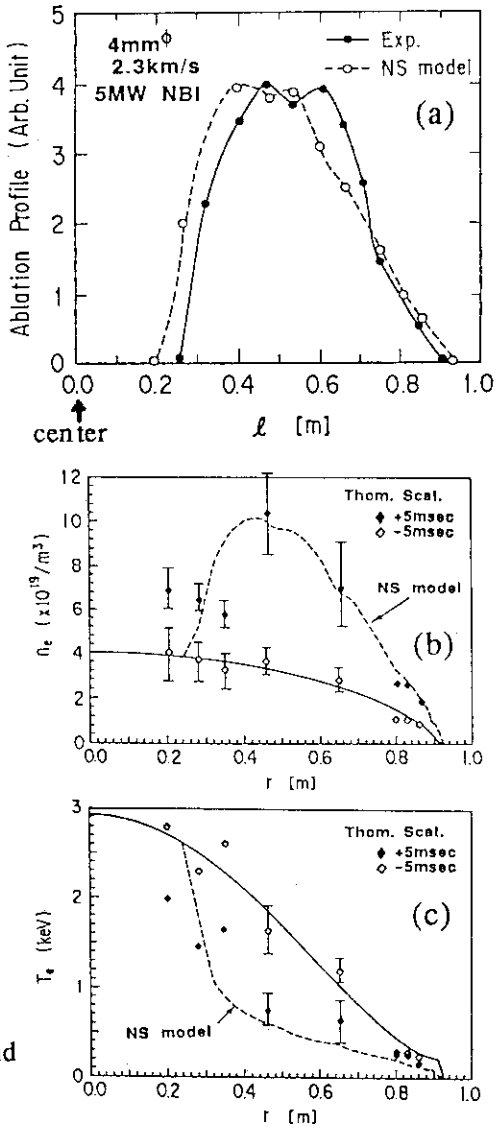

Fig.1 Ablation profile of a pellet and the modification of $n_e(r)$ and $Te(r)$

The profiles of electron density and temperature measured by Thomson scattering 5 ms before and after the pellet injection are shown in Fig.1(b)(c). The broken lines are the calculated profiles just after the pellet injection. Good agreement is obtained between the measured and simulated profiles. Figure1 suggests that the neutral gas shield model is reasonable to predict the operational scenario in the multi-pellet injection.

3. Simulation of Multi-Pellet Injection

To increase the supply of the particles in the plasma core, the pellet should penetrate to the another side of a plasma(beyond the plasma center) without the passing through. Furthermore many pellets should be injected in a short time period (e.g. ~50 ms). The constraint to this operation is the disruption mainly caused by the passing through of the pellet. NB heating is the powerful method to avoid the disruption. Where fast ions accelerate the ablation of the pellet, the control of which by adjusting the NB heating power makes it possible to control the penetration depth of the pellet.

The simulation study to decide the order of the pellet injection is performed with scanning NB heating power, where two cases of the injection order are compared;1)two small pellets are injected before two large pellets(SSLL), 2)two small pellets are injected after two large pellets(LLSS). The time interval of the injection of two large pellets is 20 ms, and the other time intervals are set 10 ms. The increase in the particle number inside the q=1 radius of 40cm (q(a)=2.2 with Ip=3.1MA) just after the last pellet from that just before the first pellet injection (ΔN) is shown in Fig.2. ΔN decreases with the increase in NB heating power, and ΔN of LLSS is almost same with that of SSLL at the same NB heating power. The deepest penetration-point of the last pellet (ℓp) is also presented in Fig.2. Where p=0.0m is the nearest point to the plasma center on the injection line, and pellet penetrates to the another side of plasma at $\ell p>0.0$m. ΔN rises with the deeper penetration of the pellet. However the pellet passes through the plasma,when ℓp is longer than 0.9m. Then ℓp~0.5m is considered to be the optimum penetration depth to get the large increase in the particle number inside the q=1 radius with keeping the operational margin to avoid the passing through of the pellet. 5MW of NB heating power is necessary in the case of LLSS, and 8MW is necessary in the case of SSLL. At these NB heating power, ΔN of LLSS is ~30% higher than that of SSLL. This suggests that LLSS is better than SSLL to raise the particle supply in the plasma core. This difference comes from the difference in the minimum central electron temperature to avoid the passing through. In the case of a large pellet Tc(0)=~1.5keV is necessary, on the order hand ~0.6keV is enough for a small pellet. Then two large pellets must be injected before two small pellets at low NB heating power of ~5MW. After the injection of two large pellets, small pellets can ablate near the plasma center.

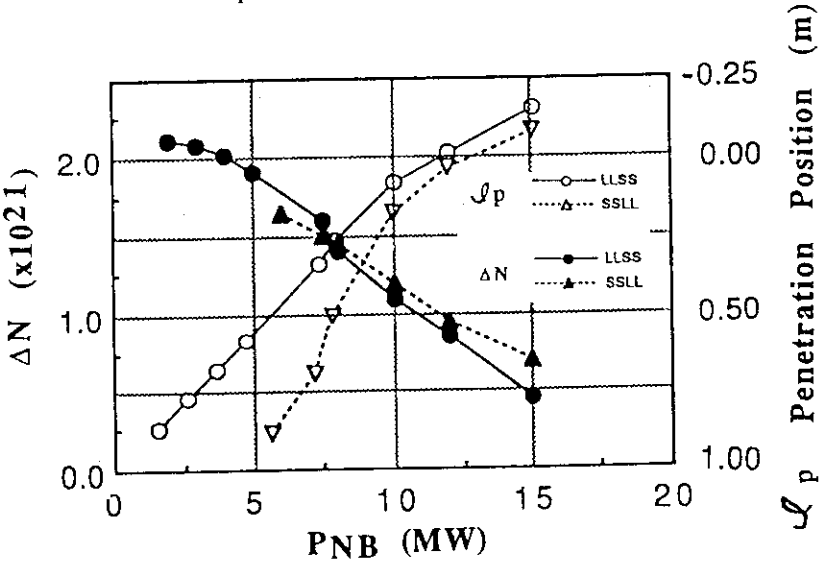

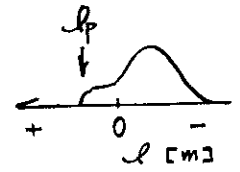

pellet ablation profile

Fig.2 ΔN and the deepest penetration position of the last pellet for each NB power

4.Optimization of the Multi-pellet Injection

Multi-pellet injection is optimized in the experiments according to the above simulation results, that suggest the narrow operational window of NB heating power(~±1 MW) to get the optimum penetration of the pellet. Moreover the fine adjustment of the electron temperature profile by gas puffing before the pellet injection and of the NB heating power level during the pellet injection are performed to get the optimum penetration depth of the pellets.

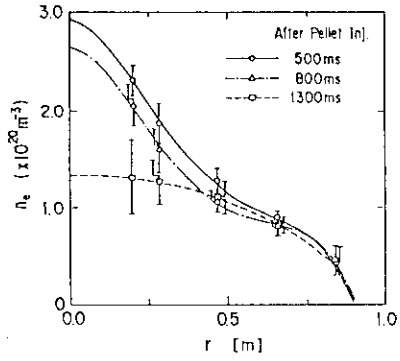

Fig.3 Density profile measured by Thomson scattering

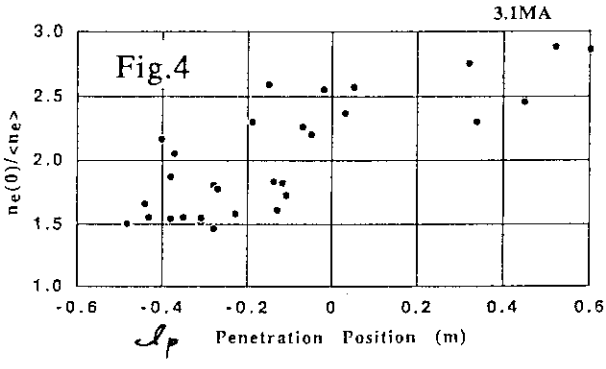

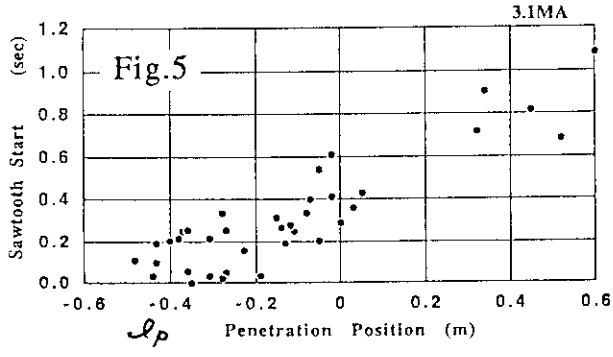

The following are confirmed in the experiments. In the case of SSLL, NB heating of >10MW is necessary to avoid the disruption, and no peaked density profile is obtained. In the case of LLSS with NB heating of 6MW, a peaked density profile of $n_e(0)/<n_e>_V$=~3.0 with $n_e(0)=3.0\times10^{21}$ /m^3 is obtained at 500 ms after the last pellet injection as shown in Fig.3. Where NB heating power is raised from 6MW to 14MW at 50 ms after the last pellet injection, and plasma current is 3.1MA. $n_e(0)$ is the central electron density and $<n_e>_V$ is the volume averaged electron density.

Figure 4 presents the density peaking factor at 400~500 ms after the pellet injection versus the deepest penetration depth of the last pellet(ℓ p) measured by the Hα emission profile in Ip=3.1MA. Peaked density profile of ~3.0 is obtained at ℓ p~0.5m. Where ℓ p is almost propotional to the particle number supplied in the plasma core as shown in Fig.2.

No sawtooth activity with full reconnection is observed during the ramp-up of the stored energy after the pellet injection, when a well peaked density profile is measured[8]. The start time of the full reconnected sawtooth after the pellet injection is shown in Fig.5. A long time period of the sawtooth-free phase is obtained only at ℓ p=0.3~0.6m. This suggests that the increase in the supply of particles inside the q=1 rational surface may be the cause of the suppression of the fully reconnected sawtooth. The suppression of the MHD activities is essential to improve the energy confinement[8], and the deep penetration of the pellet into a plasma is one of the method to study the mechanism of the sawtooth activity.

References

[1]KAMADA,Y., et al., Nucl. Fusion 29 (1989) 1785 [2]HIRATSUKA,H., et al., see section 1.8 and 1.9 [3]YOSHINO,R., et al., JAERI-M 88-246 (1988) [4]HIRAYAMA,T., et al., JAERI-M 86-170(1986) [5]MILORA,S.L., ORNL/TM-8616(1983) [6]HOULBERG,W.A., rt al., ORNL/TM-6549(1979) [7]NISITANI,T., et al., JAERI-M 89-033 120-123 [8]YOSHINO,R., see section 1.1 [9] KAMADA,Y., et al., see section 1.4

1.3 ROLE OF THE q=1 SURFACE FOR IMPROVED CONFINEMENT

Y.KAMADA, R.YOSHINO, M.NAGAMI and T.OZEKI

Improved energy confinement for the pellet fuelled plasmas on JT-60 is mainly due to the peaked density and pressure profiles inside the q=1 rational surface, where the confinement characteristics appear to be better than those in the outer (q>1) region. In the well-center-fuelled pellet injection discharges, the sawtooth activity can be suppressed completely during 0.4~1 sec or the frequency of sawteeth are reduced by up to one order of magnitude during 0.5~1.5 sec after the pellet injection. For high-current low-q (I_p=2.5~3.1MA; q(a)<3) discharges, reduction in the sawtooth frequency has a strong relationship with enhanced confinement and peakedness of the electron density profile. The contribution of the sawtooth activity to the global energy confinement increases systematically with decreasing q(a).

1. q=1 Surface

In JT-60, hydrogen pellets were injected into hydrogen discharges heated by OH, NB [1,2], LHRF [3] and/or ICRF. Energy confinement time (τ_E) was enhanced up to 40% relative to usual gas fuelled discharges at the medium NB or NB+ICRF heating power of ~10~15MW for which the strongly peaked pressure profile was sustained within 0.5~1.0 sec after a series of pellet injection [1,2]. One of the interesting characteristics for the improvement is its strong dependence on the central MHD behavior, namely the sawtooth activity. This section concentrates on the role of the q=1, q being the safety factor, rational surface for the improvement in NB heated, pellet fuelled limiter discharges. The pellet injector was up-graded to produce 4 pellets (3mmϕ×2 and 4mmϕ×2) with velocities approaching 2.3km/sec [2,4]. The basic scenario of pellet injection, the plasma equilibrium configuration and diagnostic systems were presented in ref [1] and the global confinement properties for high current (I_p~3.1MA) discharges was reported in Sec.1-1. In contrast to JET [5] where pellets were injected into sawtooth-free (q(0)>1) discharges, we injected the pellets into discharges with q(0)<1 and obtained the following characteristics.

Figure 1 shows electron pressure (electron density n_e × electron temperature T_e) profiles for pellet fuelled discharges (plasma current I_p=2.8, 2.1 and 1.5MA, safety factors at the plasma surface q(a)=2.3, 3.3 and 4.2), gas fuelled reference data (I_p=2.8 and 2.1MA) and positions of the q=1 rational surfaces (r_s) determined with the sawtooth inversion radii. About 50~70% of the enhancement in the stored energy measured with a diamagnetic loop (ΔW) is based on the peaked portion of the pressure profile inside r_s.The electron pressure profiles were constructed with combinations of Thomson scattering, ECE and soft-X ray emission (SX) data. The availability of SX measurements to evaluate the electron pressure profile was discussed in ref.[1].

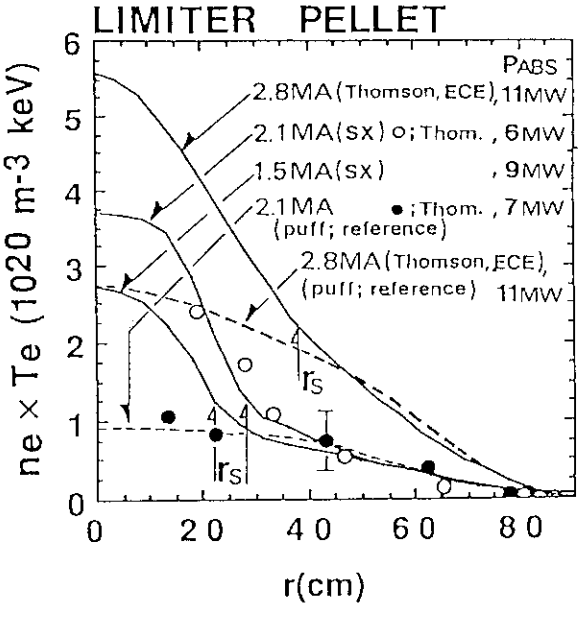

Fig. 1
Electron pressure (electron density n_e × electron temperature T_e) profiles for pellet fuelled discharges (I_p=2.8, 2.1 and 1.5MA; q(a)=2.3, 3.3 and 4.2), gas fuelled reference data (I_p=2.8 and 2.1MA) and positions of r_s. The electron pressure profiles were constructed with some combinations of Thomson scattering, ECE and soft-X ray emission (SX) data.

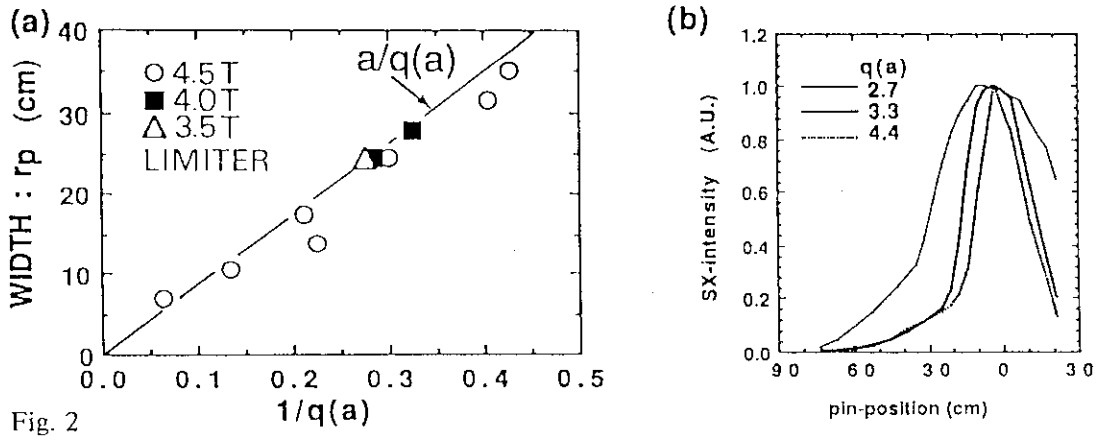

Fig. 2

Dependence of the width of the peaked portion of the electron pressure on q(a). The solid line in (a) indicating r_S for gas fuelled discharges is written by r_S=a/q(a). (b) shows relative profiles of SX intensity normalized by the central values for three cases with different q(a).

We scanned I_p (0.5~3.1MA)and the toroidal magnetic field B_t (3.5~4.8T) to survey the dependence of the width of the peaked portion of the electron pressure (r_p) on q(a) (Fig.2). The solid line in Fig.2(a) indicating r_S for gas fuelled discharges is written by r_S=a/q(a) (a is the plasma minor radius, ~0.9m in limiter discharges). The width (r_p) increases linearly with 1/q(a) and the values agree systematically with the q=1 surface (r_p=r_S). In the well-center-fuelled discharges, the sawtooth activity can be suppressed completely during 0.4~1 sec after the pellet injection and then a large sawtooth recovers or the frequency of sawteeth are reduced during 0.5~1.5 sec after the pellet injection. These sawteeth have the same inversion radii of r_S~a/q(a). Therefore it is concluded that the pressure profile produced by the pellet injection peaks inside the q=1 surface. Since the electron temperature in the central region is cooled adiabatically after the pellet injection, the central current density profile, therefore the magnetic shear, can be modified because of the ohmic dissipation and the penetration of the poloidal magnetic field. For the NB-heated JT-60 plasmas, a calculation of the current re-distribution shows that the safety factor at the plasma center dose not change drastically after the pellet injection because the re-heating time is short enough to keep the central q below unity [6].

After the injection for most of the discharges, the electron pressure rises gradually inside r_S until a sawtooth reappears. However, in well-center fuelled and NB heated discharges, the pressure gradient saturates at a certain value before the strong sawtooth reappears. Figure 3 gives the time evolution for the profile of electron pressure gradient estimated with SX signals for a 2.1MA limiter discharge heated by NB (P_{abs}=13MW). The pellets were injected at t=6.0sec. At first, the saturation occurs outer portion, then the pressure gradient reaches the limiting value in the whole region inside r_S. The saturated value scales roughly with B_t^2 and reaches the critical value determined by the high-n (n being the toroidal mode number) ideal ballooning instability [7]. In Figure 3, the calculated balloon-limits are drawn for two cases with assumed q(0) of 0.98 and 0.90. In the former case, the pressure gradient reaches the balloon-limit at r<23cm. When the sawtooth activity is not suppressed completely, the pressur gradient dose not reach the balloon limit and the central pressure is released gradually due to the sawteeth crashes. The upper limit of the poloidal β value for destabilization of the balloon and the internal kink modes is discussed in Sec 1.5 and the feature of sawtooth activity is stated in Sec. 1.4.

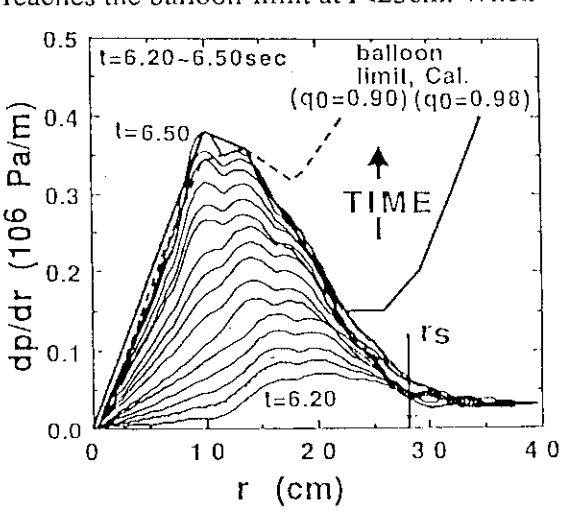

Fig. 3

Time evolution for the profile of electron pressure gradient estimated with SX signals for a 2.1MA limiter discharge heated by NB (P_{abs}=13MW). The solid and dashed bold lines indicate the calculated high-n ideal ballooning limits for assumed q(0) of 0.98 and 0.90, respectively.

The peaking of the pressure profile is due to the peaked electron density profile. Figure 4 shows the $n_e(r)$ for 0.02 and 0.4 sec after the pellet injection and that for the gas fuelling (before the injection). Since, after the injection, n_e in the outer ($r>r_s$) region decreases faster than that in the inner ($r<r_s$) region, the particle confinement inside r_s is better than that in the outer region. The figure also suggests the inward pinch of the plasma particle. The details for the transport characteristics will be discussed elsewhere [4]. Plasma equilibrium may be modified in the core regime of $r<r_s$ and the confinement property is improved. The evidence, however, has not been observed so far.

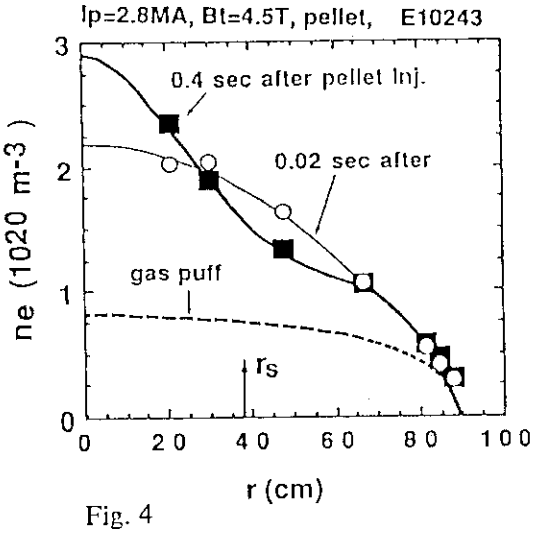

Fig. 4
$n_e(r)$ for 0.02 and 0.4 sec after the pellet injection and that for the gas fuelling (before the injection).

2.Sawtooth Frequency and Confinement

With the pellet injection, the frequency of sawteeth are reduced by up to one order of magnitude compared to gas fuelled discharges. Since the sawtooth activity flattens the peaked pressure profile, the occurrence of the mode has a direct influence on the global confinement especially for low-q ($q(a)<3$) discharges. Figure 5 shows the relationships among ΔW (improvement in the stored energy compared to the gas fuelled data), peaking factors of the n_e profiles and the sawteeth periods τ_{st} for 2.8MA limiter discharges. The peaking factor of n_e (F_{np}) is defined by the ratio of the off-axial (r=0.5m) line averaged n_e and n_e at r=0.2m (at the inner-most measurable position of the Thomson scattering system). Figure 5(a) indicates that ΔW increases linearly with F_{np}. Figure5(b) shows the relationship between F_{np} and the enhancement of the sawtooth period F_{st}; $F_{st}=(\tau_{st}$ for a pellet injected discharge) / (τ_{st} for a gas fuelled discharge having the same absorbed power with the pellet case). F_{np} (or ΔW) increases linearly with F_{st} for $F_{st}<3$ and saturates for $F_{st}>3$. The meaning of the saturation can be clarified when the sawtooth period t_{st} is normalized by τ_E. In Fig.6(a), the saturation occurs at $\tau_{st}\sim\tau_E$ and further improvement cannot be obtained for $\tau_{st}>\tau_E$. For these discharges (I_p=2.8MA), the pressure gradient dose not reach the ballooning limit.

Figure 6(b) corresponds to the data with I_p=2.1MA (q(a)=3.3). In this case, the saturation occurs at $\tau_{st}/\tau_E \sim 2$ and the level is limited by the ballooning instability. Figure 6(c) gives the relationship between q(a) and τ_{st}/τ_E at the saturation point, $(\tau_{st}/\tau_E)_{strt}$, obtained in some data sets with different I_p. The contribution of the sawtooth activity on the global confinement becomes larger for lower q(a) discharges. Basically, the saturation may occur at $\tau_{st} \sim \tau_E(q=1)$, the energy confinement time representing the transport property inside r_s. Therefore Fig.6(c) implies the relationship between the energy confinement at r=a and $r=r_s$. For the two cases of q(a)=2.35 and 2.8 in Fig.6(c), the plasma dose not reach the balloon-limit and the saturation is determined by the transport properties independent of the MHD modes considered so far. While, in the other cases of q(a)=3.3 and 4.1, the saturation occurs due to the balloon-limit. The values of $(\tau_{st}/\tau_E)_{strt}$ for the two cases could be higher than the obtained values, if the plasma had not reach the balloon-limit.

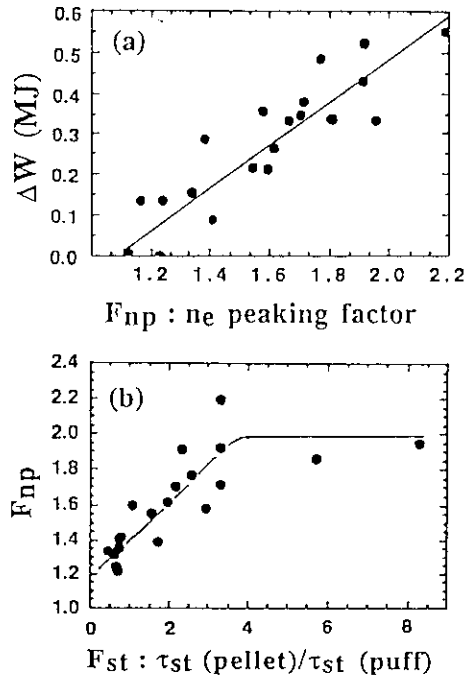

Fig. 5
The relationships among ΔW (improvement in the stored energy compared to the gas fuelled data), peaking factors of the n_e profile and the sawtooth periods τ_{st}.

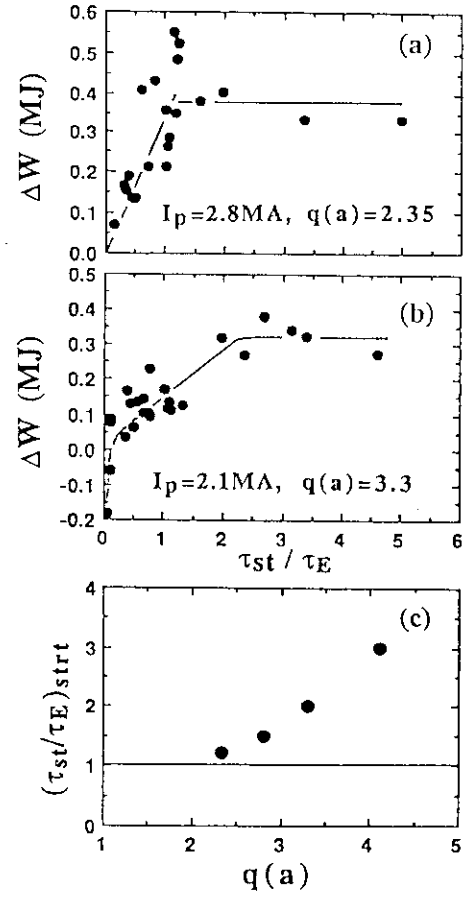

Fig. 6
Dependence of ΔW on τ_{St}/τ_E for 2.8MA(a) and 2.1MA(b) limiter discharges and relationship between q(a) and τ_{St}/τ_E at the saturation point obtained in some data sets with different I_p (c).

[1] KAMADA,Y., YOSHINO,R.,NAGAMI,M.,OZEKI,T., HIRAYAMA,T., et al. Nucl. Fusion **29** (1989) 1785

[2] JT-60 Team presented by NAGAMI,M., Plasma Phys. Control. Fusion **31,** (1989) 1597

[3] USHIGUSA, K., et al., 'Lower Hybrid Wave Heating in Peaked Density Plasmas Produced by Pellet Injections on JT-60', to be submitted to Nucl. Fusion

[4] YOSHINO, R., et al., to be submitted to Nucl. Fusion

[5] The JET Team presented by SCHMIDT,G.L., in *Plasma Physics and Controlled Nuclear Fusion Research* (Proc. 12th Int. Conf., Nice, 1988) IAEA-CN-50 / A-IV-1.

[6] YOSHINO, R. Nucl. Fusion **29** (1989) 2231.

[7] OZEKI, T., to be submitted to Nucl. Fusion

1.4 SAWTOOTH AND m=1 ACTIVITIES FOR PELLET FUELLED PLASMAS

Y.KAMADA, T.OZEKI, R.YOSHINO and M.AZUMI

In the well-center-fuelled pellet injection discharges, the sawtooth activity can be suppressed completely or the frequency of sawteeth are reduced. At the sawtooth emerging after the pellet injection, only small amount of the central kinetic energy is released and the sawtooth dose not follow the fully reconnecting style.

With deepening of the pellet penetration and peaking of the electron pressure profile, the following tendency of the central MHD behavior is observed;

i) Sawtooth frequency is reduced. Amplitude of the m=1 continuous oscillation and number of sawtooth with post-cursor oscillation increase.
ii) Sawtooth activity is suppressed for a long time (<1 sec) and the enhanced m=1 mode continues.
iii) Both sawteeth and m=1 modes are suppressed completely within ~1~1.5 sec.

Even in the case iii), the q(0) is considered to be below unity [1,2 and Sec. 1.3].

For the low-current (<2.1MA) discharges, the centrally peaked pressure profile was flattened and the total stored energy was reduced at the first large sawtooth emerging after the pellet injection [1,3]. For the high-current (Ip=2.5~3.1MA; q(a)<3) discharges, only small amount of the central kinetic energy is released at the sawtooth, and the sawtooth activity dose not follow the fully reconnecting style [4]. Figure 1 shows time evolutions of W^{DIA}, $n_e l$ (r~0.5m), soft-X ray intensity (central chord) for a pellet fuelled 3.1MA limiter discharge. Pellets were injected at t~6.0 sec. At the first and the second sawteeth at t=6,82 sec and 7.05 sec, the total stored energy is not affected by the sawteeth crashes. This observation suggests that the energy confined inside the q=1 surface is not released. This section discusses the behavior of sawteeth for the pellet fuelled high-current discharges.

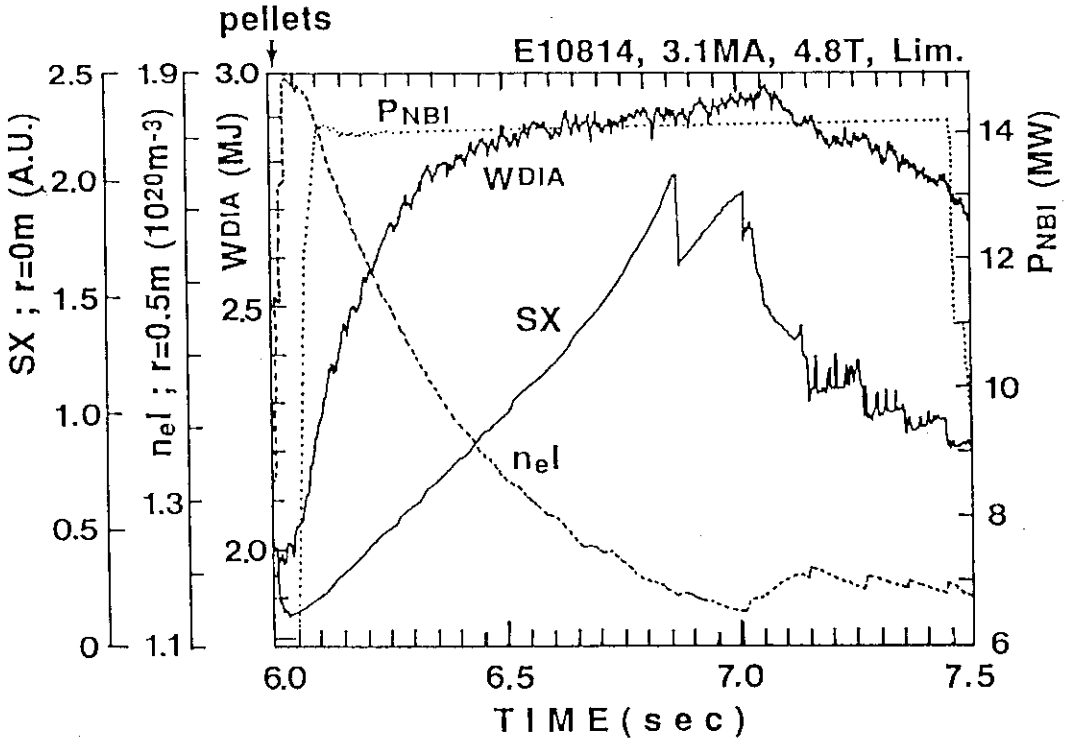

Fig. 1 Tme evolutions of W^{DIA}, $n_e l$ (r~0.5m), soft-X ray intensity (central chord) for a pellet fuelled 3.1MA limiter discharge.

Figure 2,3 and 4 give the behavior of SX emission for a 2.8MA (q(a)=2.34) discharge (E10324) where the sawtooth activity is not suppressed completely. The high frequency oscillation in Fig.2(b) is the (m,n)=(1,1) oscillation and the mode appears continuously before (precursor) and after (postcursor) the sawtooth crash. The similar behavior of the m=1 continuous mode was also observed on JET [5]. Figure 2(c) shows the evolution of the profile of $\widetilde{SX}/\overline{SX}$ (fluctuating part/averaged part) for the m=1 oscillation during the sawtooth period. The peak radius of the continuous mode, $r_{m=1}$, is small (~14cm) after the sawtooth crash, increases gradually and reaches 35cm (~a/q(a)) before the next crash. The time evolution of $r_{m=1}$ is given in Fig.2(d). After the crash at t=6.4115sec, $r_{m=1}$ moves inward with a time scale of ~10msec which is much slower the crash time (~400μsec). These observations give the fact that the q=1 rational surface survives during the sawtooth crash and the central kinetic energy is not released completely due to the crash. The SX-emission profiles just before and after the sawtooth at t=6.4115sec are shown in Fig.3. Figures 3(a) and (b) gives the profiles

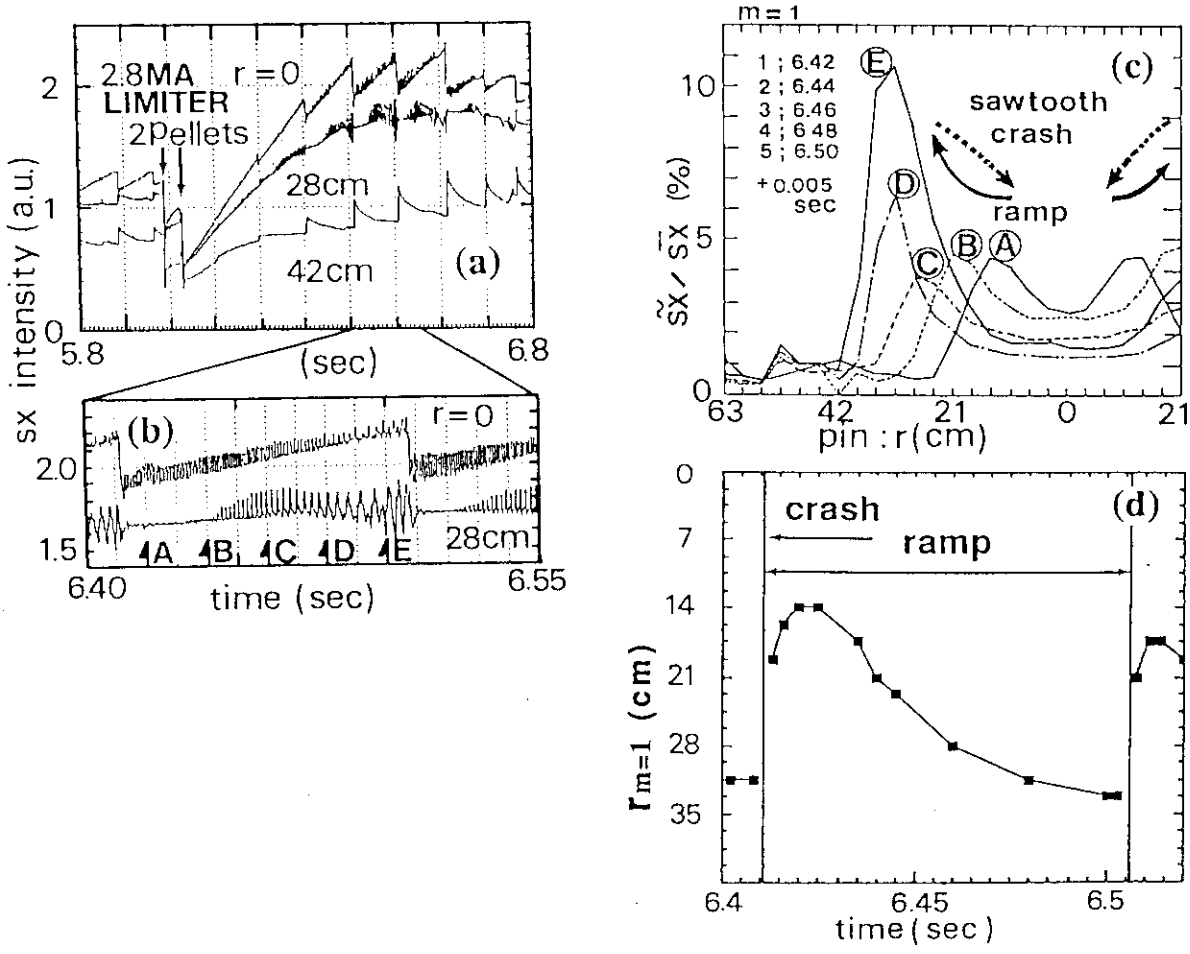

Fig. 2 Behavior of SX emission for a 2.8MA (q(a)=2.34) discharge. (c) and (d) show the evolution of the profile of $\widetilde{SX}/\overline{SX}$ for the m=1 oscillation and $r_{m=1}$during the sawteeth.

for the lower and upper PIN-diode arrays. The central core shifts (m=1 displacement) and is not flattened completely. The sawtooth crash time is typically about 300~600μsec, which is longer than that (~100 ~200 μsec) for gas fuelled discharges. Figure 4 indicates the time histories of crash times and the mixing radii. After the pellets injected at t=6.0sec, the crash time increases and the mixing radius dose not change. The latter observation means that the global current distribution after the pellet injection is similar to that in the gas fuelled portion of the discharge. The central electron density before (t=5.9sec) and after (t=6.4sec) the injection are 8 and $24\times10^{19}m^{-3}$ and, therefore, the Alfven transit time after the pellet injection is about 1.7 times longer than that for the gas fuelled portion. If the sawtooth crash is an ideal instability, the increased crash time may be explained by the change in the Alfven time. On the other hand, the magnetic Reynolds number (S) for pellet discharges is about 1/10 ~1/20 of that for gas fuelled shots. If the sawtooth is due to the m=1 resistive instability, the growth rate increases because of the reduction of S. Both the sawtooth crash time and the repetition time for pellet fuelled discharges increase, the observation may mean the sawtooth appeared after the injection is not the resistive mode. Conclusive results, however, cannot be presented because we do not have the measured data of local shear around the rational surface.

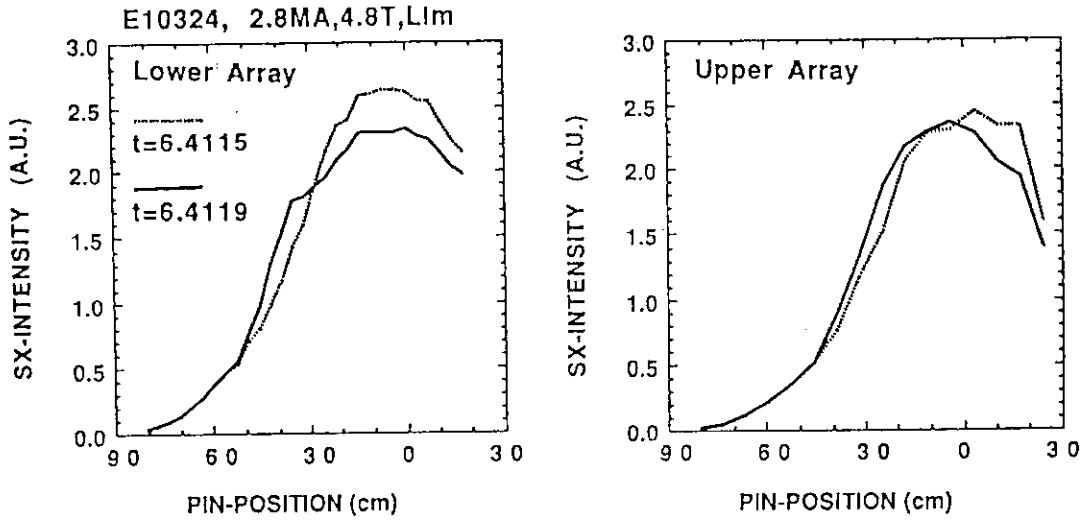

Fig. 3 a) and (b) gives the profiles for the lower and upper PIN-diode arrays, respectively.

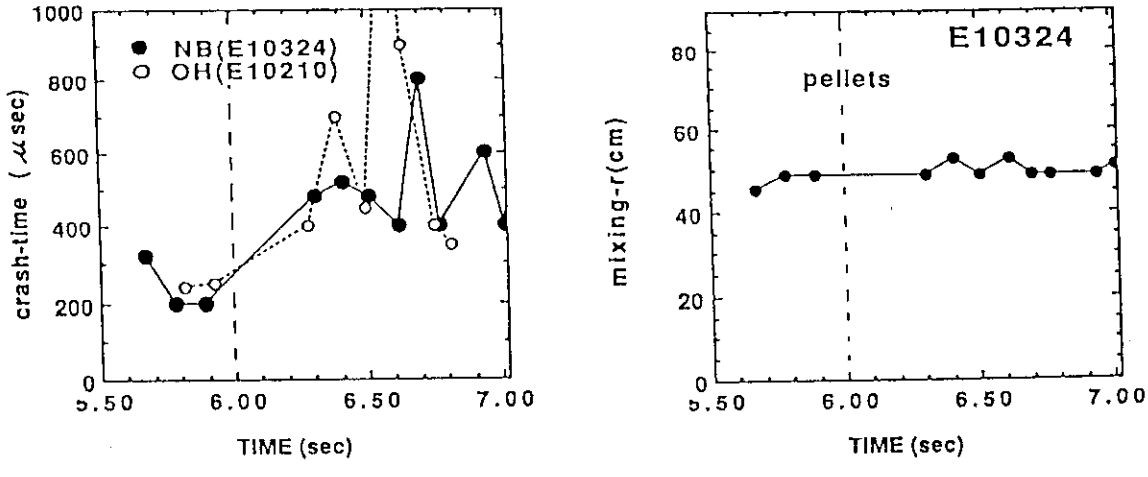

Fig. 4 Time histories of crash-times and the mixing-radii

Figure 5 shows an example where the sawtooth activity is suppressed within ~1sec after the pellet injection. The small oscillations observed at t=6.5~6.8sec are partial sawteeth originated at r~0.1m during which the central SX emission remains almost unchanged and the release of the central energy is small. The appearance of the partial crash implies the q-profile in the core region is flat. In this particular discharge, the plasma dose not rotate in the decay phase (t=7.2~7.7sec) of the central SX emission. Figure 5(b) indicates the time history for the contour lines of SX emission rate in the central region (r<50cm) from t=7.2 to 7.37 sec. The position of the q=1 surface is ~35cm. The hot and dense core shifts following the m=1 displacement, but behaves as a rigid body during the sawteeth (crash time~300μsec). The released kinetic energy is also small for the sawteeth. Figure 5(c) shows two profiles of the SX emission for t=7.3344sec (just before the crash) and 7.3347sec (just after the crash) and a plasma displacement in the radial direction estimated simply with the two SX-profiles. The shape of the displacement seems to be similar to that for the conventional ideal m=1 mode [6] rather than that for the quasi-interchange mode [7].

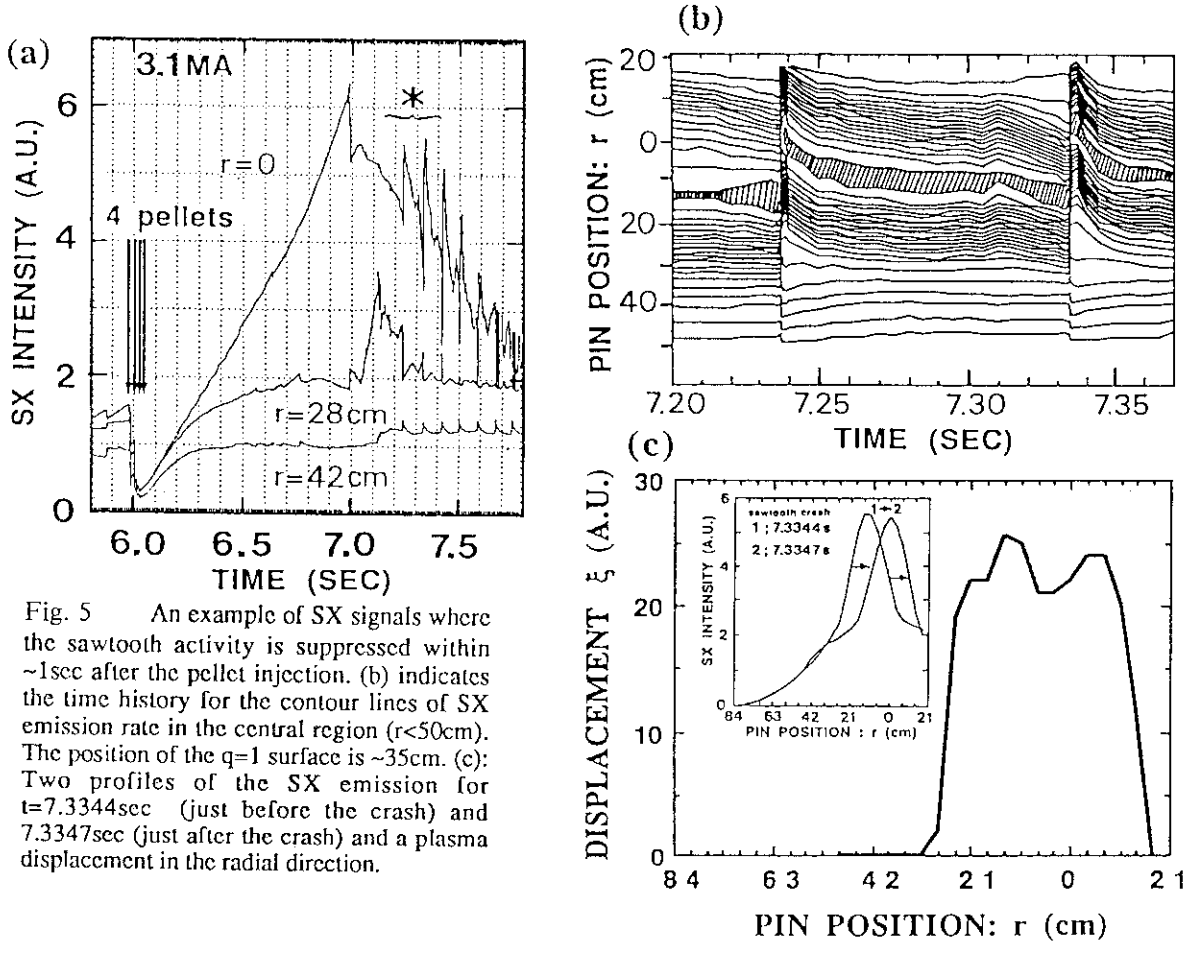

Fig. 5 An example of SX signals where the sawtooth activity is suppressed within ~1sec after the pellet injection. (b) indicates the time history for the contour lines of SX emission rate in the central region (r<50cm). The position of the q=1 surface is ~35cm. (c): Two profiles of the SX emission for t=7.3344sec (just before the crash) and 7.3347sec (just after the crash) and a plasma displacement in the radial direction.

[1] KAMADA,Y., YOSHINO,R.,NAGAMI,M., et al. Nucl. Fusion **29** (1989) 1785.
[2] YOSHINO, R. Nucl. Fusion **29** (1989) 2231.
[3] JT-60 Team presented by NAGAMI,M., Plasma Phys. Control. Fusion **31,** (1989) 1597
[4] KADOMTSEV, B.B., Fiz. Plazmy **1**, (1975) 710 or Sov. J. Plasma Phys. **1**, (1975) 389
[5] WELLER, A., CHEETHAM, A.D., EDWARDS, A.W., GILL, R.D., GONDHALEKAR,A., et al., in *Control. Nucl. Fusion and Plasma Physics* (Proc. 14th Europ. Conf., Madrid, 1987), Vol. 11D, part I, EPS (1987) 25.
[6] BUSSAC, M.N., PELLAT,R., EDERY, Q. , et al., Phys. Rev. Lett. **15** (1975) 1638
[7] WESSON, J.A., KIRBY,P., NAVE,M.F.F, in *Plasma Physics and Controlled Nuclear Fusion Research* (Proc. 11th Int. Conf., Kyoto, 1986) Vol.II, (IAEA, Vienna, 1987) 3.

1.5 IDEAL MHD STABILITY IN PELLET FUELLED PLASMAS

T. Ozeki, M. Azumi, Y. Kamada, R. Yoshino, S. Tokuda
T. Tsunematsu, K. Nagashima, H. Yoshida and M. Nagami

1. INTRODUCTION

Pellet injections are useful method to produce the center peaked profile plasma, which provide us the enhanced central values, T_{i0}, n_{e0}, and τ_E. In pellet fuelled experiments in JT-60 [1], the energy confinement time was enhanced up to 40% relative to usual gas fuelled discharges with NB heating. A strongly peaked pressure profile was produced in the area inside a inversion radius of m=1 sawteeth activity, when the pellets well penetrated near the plasma center. However, the stored energy inside the q=1 surface could not increase over a certain values even though the NB input power increased. The high pressure gradients (dP/dr is about $5 \times 10^5 Pa/m$) formed in a low shear region near the q=1 surface, so that the confinement within the q=1 surface may be restricted by the ideal infinite n ballooning or low n kink modes (where n is a toroidal mode number). Therefore, it is important to investigate the MHD stabilities of these modes for peaked profile plasmas in the JT-60 operation regime, and discuss the restriction of the peakedness within the q=1 surface.

2. FEATURE OF PELLET FUELLED PLASMA IN JT-60 AND RECONSTRUCTION OF EQUILIBRIUM

Strongly peaked pressure profiles were obtained in all operation regimes, when the pellets penetrated to the plasma center. However, β_p inside the $q = 1$ surface, which well reflects to the pressure peakedness, was saturated even though the input NB power increased. Here, β_{p1} is defined as

$$\beta_{p1} = \frac{2\mu_0}{B_p^2(r_1)} \int_0^{r_1} (\frac{r}{r_1})^2 (-\frac{dP}{dr}) dr, \tag{1}$$

where r_1 is the minor radius of the q=1 surface [2]. To analyse this phenomena, first, we summarize the characteristics of the pellet fuelled plasmas in JT-60, as follows; 1) the high pressure gradient exists inside of the inversion radius of sawteeth, being q=1 surface, 2) the electron temperature profile is broad, so that q-profile is seems to be flat, and 3) the center q is probably under unity.

The MHD equilibria used in the following stability calculations are reconstructed by solving the Grad-Shafranov equation iteratively using all characteristics described previously. The two free functions, the plasma pressure $dP/d\psi$ and the toroidal field function $F(\psi)$, are obtained by the kinetic data and the surface averaged parallel current $< J_\parallel >$ $(=< J_\parallel \cdot B > / < B >)$, respectively.

The pressure profile is determined by the n_e, T_e data from Thomson scattering measurements and the SX emission rate. As shown in Fig. 1, the SX emission rate is roughly proportional to $n_e^2 T_e^{1.3-2.0}$ in the pellet fuelled plasma in JT-60. The ion pressure profile is assumed to equal to the electron pressure profile because of the high density, and the total pressure is adjusted by the stored energy from a diamagnetic measurement. The surface averaged parallel current is assumed as a following function in this study,

$$< J_\parallel \cdot B > \propto \frac{1}{1+\sigma} \{(1 - \tilde{\psi}^{\alpha 1})^{\alpha 2} + \sigma\}, \tag{2}$$

Parameters, $\alpha 1$, $\alpha 2$ and σ, are defined from the $q = 1$ surface, the internal inductance ℓ_i and the central q value, where $\tilde{\psi}$ is a normalized poloidal flux defined as $\tilde{\psi} = (\psi - \psi_{axi})/(\psi_{bun} - \psi_{axi})$. ψ_{axi} and ψ_{bun} are the poloidal flux at the plasma axis and the boundary, respectively. Because the center q is not measured, we have scanned the profiles with q_0 from 0.9 to 0.98. Figure 2 shows three type q-profile, where the q=1 surface is defined by the observed inversion radius and the surface q are the same value (=3.4).

3. BALLOONING STABILITY ANALYSIS

Ballooning stability analysis was carried out by solving the ordinary infinite n ballooning equation [3]. The flux function shape and the pressure and current profiles, which have been reconstructed by the equilibrium code, are used for stability analysis. The marginal pressure gradient dP/dr_m is determined on each flux surface by demanding that the growth rate be zero. Figure 3 shows the measured pressure gradient and the marginal value against ideal ballooning mode, when the pressure profile becomes mostly peaked. The measured pressure gradient just inside the $q = 1$ surface violates the ideal ballooning stability limit for $q_0 = 0.95, 0.98$. Also for $q_0 = 0.90$ it is very close to the marginal value. Here, we note that the observed pressure gradient from the Thomson scattering measurements (Fig. 1) has a about 20%-30% error. Therefore, the region of the highest pressure gradient is considered to be almost marginal value for the ideal ballooning stability. The difference of marginal ballooning pressure gradient limits by scanning of q_0 (from 0.9 to 0.98) is small especially in the region around the highest pressure gradients, so that the marginal value does not depend on q_0 very much.

It is of interest to examine the temporal development of events of the highly peaked plasma. As shown in Fig. 4, after two pellets were injected at 6.0 sec, the density rapidly rose and decayed slowly. The temperature transiently decreased and recovered relatively fast. The SX intensity, which is nearly proportional to P^2, significantly increased near the plasma center, while the value at the peripheral point ($0.4r_p$) remained the same value. Consequently, the pressure profile became peaked. As the time of discharge proceeded, the maximum pressure gradient against the minor radius increased and reached the marginal value of the ballooning mode stability, which is denoted by a shaded region. The upper limit of the shaded region corresponds to $q_0 = 0.9$ and the lower does to $q_0 = 0.98$. However, as the pressure gradient increases, we can see that the marginal values also increase due to the effect of magnetic well stabilization and the difference due to the effect of the q_0 becomes small. From the discharge time of 6.3 sec, the observed pressure gradient overtook the marginal pressure gradient and around 6.4 sec the observed pressure gradient was close to a marginal value, and the increase of the pressure gradients became suppressed.

B_T-scan experiments were carried out for about same q_{eff} values in the limiter plasma with a circular cross section. The observed pressure gradient for the minor radius, dP/dr, is almost proportional to the square of the toroidal field ${B_T}^2$, as shown in Fig. 5. In the infinite n ballooning analysis, the normalized pressure gradient, α , is usually used, where $\alpha = -2\mu_0(Rq^2/{B_T}^2)(dP/dr)$. From this definition, dP/dr is proportional to ${B_T}^2$ for the same α value because $q \approx 1.0$ and R is constant. The marginal ballooning pressure gradient limits for the given q profile with q_0=0.9-0.98 lie within the hatched region. Therefore, the maximum pressure gradients are close to the ideal ballooning limit for various toroidal fields. The high toroidal field is preferable to obtain the high pressure gradient for the same q-profile.

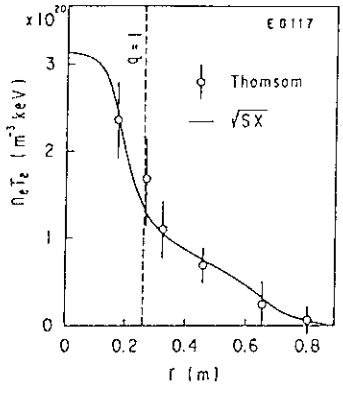

Fig. 1 The electron pressure profile n_eT_e from the thomson scattering and the SX.

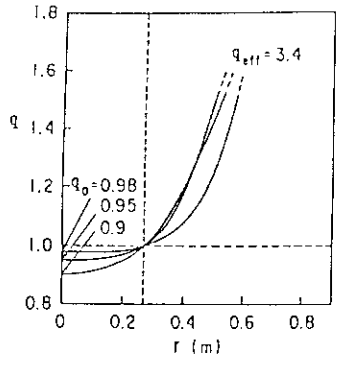

Fig. 2 q-profiles for three central q_0 of 0.9, 0.95, and 0.98 with the fixed q_{eff}.

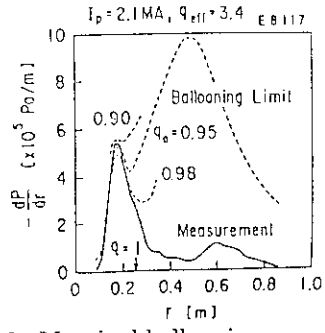

Fig. 3 Marginal ballooning pressure gradient (broken line) and the experimental pressure gradient (solid line) for a minor radius r(m).

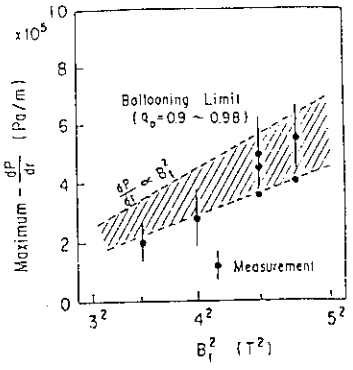

Fig. 5 Marginal (hatched region) and measured (closed circle) pressure gradients against B_t^2.

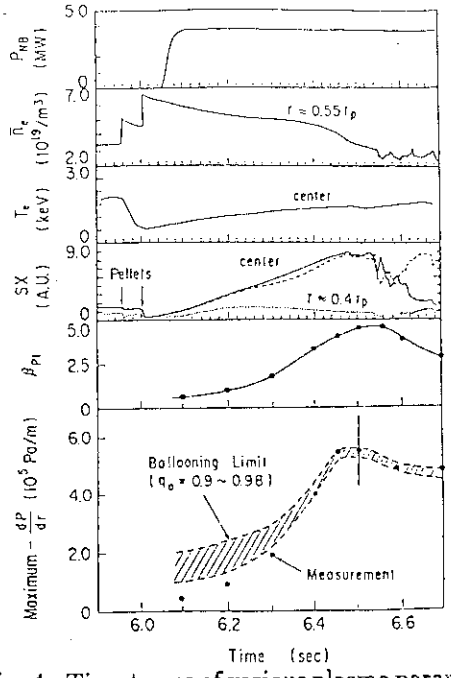

Fig. 4 Time traces of various plasma parameters for a strongly peaked plasma, $I_p = 2.1MA$, $B_T = 4.8T$.

4. KINK STABILITY ANALYSIS

The MHD stability against the low n ideal kink modes is computed using the ERATO-J code [4,5], which solves the linearized ideal MHD equations in variational form using a finite hybrid element approach. As in the analysis of the ballooning mode, the current profile is chosen to obey the eq.(2) and the center q_0 value was scanned from 0.9 to 0.98. The q=1 surface was also adjusted in r_p/q_{eff} [6]. The pressure profile is chosen to have the form

$$P \propto exp\{-(\frac{\bar{\psi}}{\delta})^{\nu}\} + \kappa(1-\bar{\psi}), \tag{3}$$

which provides a fair description of the pressure profile in the pellet fuelled plasma of JT-60, as shown in Fig. 6.

The n=1 internal kink mode is considered to be most restrictive against the strongly peaked plasma with low q_0 (< 1.0) in JT-60 pellet fuelled plasmas. Figure 7 shows the critical beta limit against q_0 for the fixed q_{eff}, where we use the pressure profile parameter, $\nu = 4$, $\delta = 0.1$, $\kappa = 0.6$ with q_{eff}=3.55. For the q_0 of 0.9-0.95, the change of the stability boundary against the q_0 is small. As to be pointed out by Nave and Wesson [7], the boundary of critical beta reduces in the degree of ~20% as the q_0 goes up to 0.98, due to the decrease of the global shear. Here, the unstable condition is defined by $\hat{\gamma}^2 \geq 5 \times 10^{-5}$. The boundary of the critical β_{p1} with a locally high pressure gradient just inside the q=1 surface is higher than that with a parabolic pressure profile. This results means that the strongly peaked profile plasma is rather stable against n=1 internal

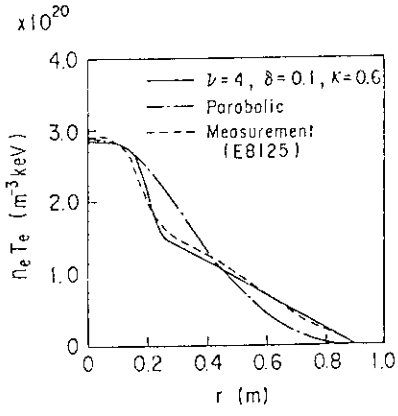

Fig. 6 Electron pressure profile n_eT_e defined by the Eq. (3) and the parabolic profile, and comparison with the measured pressure profile from the SX intensity.

kink mode than the weekly peaked profile plasma.

Dependence of the critical beta boundary on the q_{eff} is examined for the fixed q_0 of 0.95 and the pressure profile parameter ν of 4.0. Figure 8 shows the theoretically predicted beta limit against the q_{eff} for the fixed q_0 and the experimentally attained values for various q_{eff}. The boundary of critical β_{p1} for ν of 4.0 (the solid line) decreases as the q_{eff} reduces because of the decrease of the shear. The boundary of the critical β_{p1} reduces in the degree of ~20% by the flattening of the pressure profile. Fast crashes due to the m=1 mode, which behaves as a rigid body (crash time $\approx 300\mu sec$), were observed after the peaked profile obtained in JT-60 [6]. The experimentally attained β_{p1} with the fast crash (the open circle) lie in the critical beta limit within the difference due to the pressure profile. The results of this experimental observation together with the numerical analysis suggests that the strongly peaked profile is limited by the ideal n=1 internal kink mode.

Next the $n \geq 2$ kink modes are investigated for the fixed boundary plasma in order to evaluate the kink-ballooning effects due to the high β_{p1}. The critical β_{p1} for n=2 mode is higher than that for n=1 mode, and the ideal n=3, 5, 10 and 20 modes are more stable than the n=2 mode.

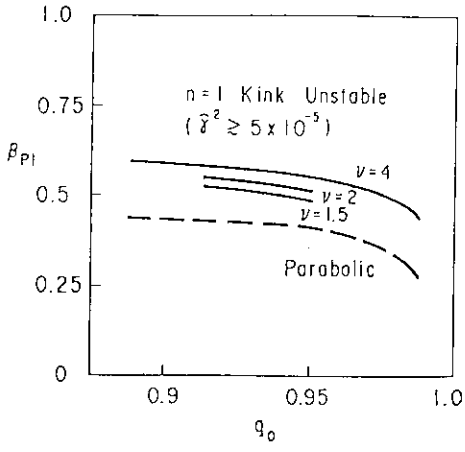

Fig. 7 Dependency of critical β_{p1} and the central pressure profile as a function of the q_0 with fixed q_{eff} of 3.55 and the pressure profile.

5. CONCLUSION

The ideal MHD stability for the plasma with strongly peaked pressure profile within the q=1 surface is investigated. The results of the study show that the plasma locally reaches the limit of the ideal ballooning mode just inside the q=1 surface. After reaching the marginal value in a magnetic flux surface, the increase of the pressure gradient is suppressed and the marginally stable region spreads. The achieved β_{p1} values is lower than the beta limit imposed by the ballooning mode. However, the achieved β_{p1} values are close to the beta limit of the ideal n=1 internal kink mode and these attained beta are saturated with the fast crashes of the m=1 mode.

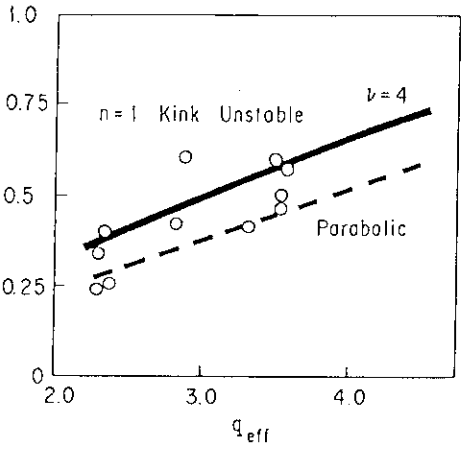

Fig. 8 Comparison of critical β_{p1} against n=1 internal kink with experimentally obtained values with the fast crash (open circles) as a function of q_{eff} with fixed q_0 of 0.95. The solid line is the boundary for the plasma with $\nu = 4.0$, $\delta = 0.1$ and $\kappa = 0.6$. The broken line is that for the parabolic pressure profile.

REFERENCES

[1] KAMADA,Y., YOSHINO,R., NAGAMI,M., et al., Nucl. Fusion 29 (1989) 1785.
[2] BUSSAC,M.N., PELLAT,R., EDERY,D., SOULE,J.L., Phys. Rev. Lett. 35 (1975) 1638.
[3] CONNOR,J.W., HASTIE,R.J., TAYLOR,J.B. Phys. Rev. Lett. 40 (1978) 396.
[4] TANAKA,Y., MATSUURA,T., TAKEDA,T., et al., MHD Stability Analysis Code ERATO-J, Rep. JAERI-M 9040, Japan Atomic Energy Research Institute, Ibaraki (1980).
[5] TOKUDA, S., TSUNEMATSU, T., AZUMI, M., TAKIZUKA, T., NARAOKA, K., TAKEDA, T., MHD Stability Analysis by Revised Version of ERATO-J, Rep. JAERI-M 9899, Japan Atomic Energy Research Institute, Ibaraki (1982).
[6] KAMADA,Y., YOSHINO,R., NAGAMI,M., OZEKI,T., submitted for Nucl. Fusion.
[7] NAVE,M.F.F., WESSON,J., Nucl. Fusion 28 (1988) 297.

1.6 Sawtooth Effect on the energy confinement

K. Shimizu, R. Yoshino, Y. Kamada and T. Hirayama

The sawtooth effect on the energy confinement has been investigated with the predictive transport code. The good particle confinement within the q=1 surface yields the improved energy confinement under the certain condition, i.e. the strong particle source in the core region and the sawtooth suppression.

1. Introduction

Improved energy confinement for additional heating plasma has been obtained by hydrogen pellet injection. The plasma stored energy is increased up to ~ 0.5 MJ compared with the gas fuelled plasma at Ip = 2.8 ~ 3.1 MA plasmas with 10 ~ 15 MW NB heating. It is considered that the enhanced confinement has been yielded as a result of the suppression of sawtooth activity during 0.4 ~ 1 sec after the pellet injection [1]. The sawtooth effect on the energy confinement has been investigated numerically by using the 1-1/2 D transport code. It is often said that the peaked density profile stabilizes the ion gradient drift instability and improves the plasma confinement. But the enhancement of the stored energy in the pellet injected plasma can be explained by the good particle confinement within the q=1 surface, without the improvement due to the peaked density profile.

2. Simulation model

Pellet ablation model : The ablation profile of the pellet is calculated by the neutral-gas shielding model [2]. The comparison of this model with the experimental data of ablation monitor shows that the ablation effect from first ions seems to be more weak than the neutral-gas shielding model. In our simulations, the charge exchange loss of fast ions at the plasma peripheral is enhanced so as to agree with the experimental penetration depth.

Sawtooth model : In this model, the minor disruption occurs repeatedly with the fixed period (i.e. 60 msec for OH plasma, 90 msec for NB heated plasma). When the minor disruption occurs, the profiles of the density, the electron and ion temperature and the plasma current density within the region $0 \leq r \leq r_0$ are mixed based on the conservational laws of the particle, the energy and the magnetic flux, respectively. The mixing radius r_0 is given by $\sim 1.2\, r_s = 1.2\, a / q(a)$, where r_s is the singular surface of q = 1 and the q(a) is the safety factor at the plasma surface.

Diffusion coefficient : The steady state transport analysis [3] shows that the effective heat diffusivity χ_{eff} for OH plasma decreases with q(r) while χ_{eff} for NB heated plasma increases with q(r). Taking this analysis result into the consideration, the parameter survey of the diffusion coefficient has been carried out extensively. The power degradation of the energy confinement and the improvement with the plasma current can be well reproduced by the simulation with the following diffusion coefficients.

$$D_e(r) = (0.2 + 0.015\ P_{NB}) \times q(r) \quad (m^2/s)$$
$$\chi_e(r) = (0.6 / q(a) + 0.045\ P_{NB}) \times q(r) \quad (m^2/s)$$
$$\chi_i(r) = \chi_i^{CH} + \chi_e$$

where P_{NB} is the absorption power of Neutral Beam heating in MW unit, and χ_i^{CH} is the neoclassical diffusivity derived by Chang-Hinton. The anomalous inward velocity is not included in our simulations because there is no experimental data which indicates the pinch effect obviously. The impurity accumulation inside the q = 1 surface observed in DIII experiment suggests the good particle confinement in this region [4]. The diffusion coefficient in this region is assumed to be

$$D_e(r) = 0.05 \ (m^2/s) \qquad (q(r) \leq 1)$$

Figure 1 shows the relation between the plasma stored energy and the absorbed power for 3.1 MA (closed circles) and 2.1 MA (closed triangles) plasma with Bt = 4.8 T. The line-averaged density $\bar{n}_e$ are fixed at the value of 5.7×10^{19} m^{-3}. The simulation results are in good agreement with the experimental data shown by the solid lines. The density and the electron temperature profiles calculated also agrees with the experimental data within the error bars. (The electron temperature has somewhat peaked profile compared with that of the Thomson scattering measurement .)

3. Simulation result

The purpose of the simulation is to clarify the contribution of the sawtooth activity to the energy confinement. For the shot E10814 , where the peaked density profile with $n_e(0) \approx 2.7 \times 10^{20}$ m^{-3} was sustained for about 0.8 sec after the pellet injection, the simulation analysis has been carried out. (see Fig. 6 and 7 in section 1.1) The expression for the electron diffusivity used here is $\chi_e(r) = (0.2 + 0.04\ P_{NB}) \times q(r)$.

Figure 2 shows the time evolution of the plasma stored energy and the central electron temperature. The recovery of the central electron temperature is somewhat slower than that of the ECE measurement. The broken line shows the stored energy of the plasma with the sawtooth oscillation. The stored energy is saturated immediately and the reduction in the stored energy is about 0.5 MJ. This value corresponds to the enhancement stored energy for the pellet fuelled plasma obtained experimentally. In case that the particle diffusion within the q=1 surface does not reduce significantly, the suppression of the sawtooth activity makes no difference in the stored energy. The evolution of the density profile and the total plasma pressure profile are shown in Fig. 3. The peaked density profile observed is well reproduced. The pressure profile peaks strongly inside the q = 1 surface. This is consistent with the data of soft X-ray signal [1]. Figure 4 shows the electron density and temperature profile and the diffusion coefficient at t = 6.8 sec. The agreement with the Thomson data is fairly good. The relation between the enhancement stored energy, the penetration length and the absorbed power are now under investigation.

4. Conclusion

The long temporal relaxation of the density and temperature after the pellet injection can be well reproduced by the simulation with the same diffusion coefficient of the L-mode plasma. The simulation result shows that the good particle confinement within the q= 1 surface yields the improved energy confinement under the certain condition, i.e. the strong particle source in the core region and the sawtooth suppression.

References

[1] KAMADA, Y., et al., Nucl. Fusion **29** (1989) 1785.

[2] MILORA,S.,L., ORNL/TM-8616 (1983).

[3] HIRAYAMA., et al., see section 8.6.

[4] Doublet III Group, J. Nucl. Mater **93 & 94** (1980) 259.

Figure captions

Fig. 1 The relation between the plasma stored energy Wst and the absorbed power Pabs for 3.1 MA (closed circles) and 2.1 MA (closed triangles) plasma with Bt = 4.8 T. The experimental data is shown by the solid lines.

Fig. 2 The evolution of the plasma stored energy and the electron temperature at the center. The broken lines shows the stored energy of the plasma with the sawtooth oscillation.

Fig. 3 The evolution of the density profile (a) and the total plasma pressure (b). The pressure profiles peaks strongly within the q = 1 surface.

Fig. 4 The electron temperature and density profile at t = 6.8 sec (a) and the diffusion coefficient (b). The Thomson data is also plotted.

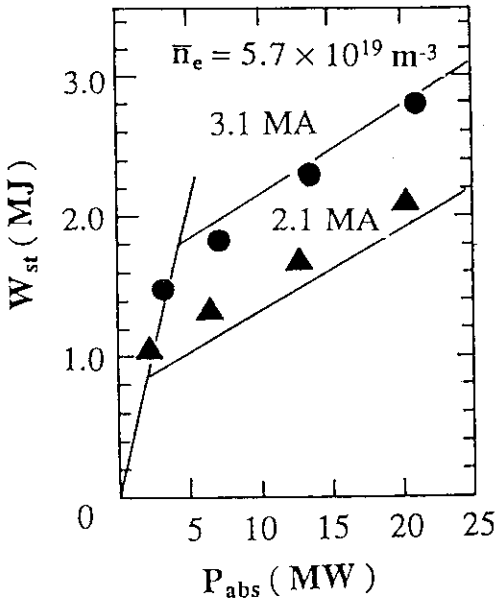

Fig. 1

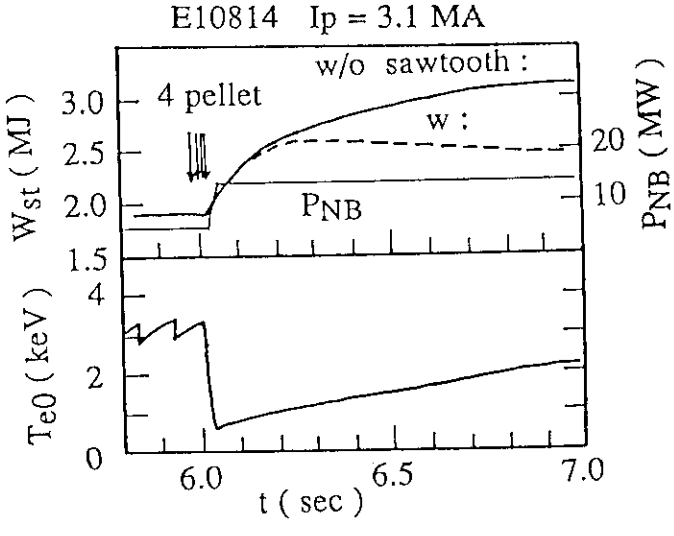

Fig. 2

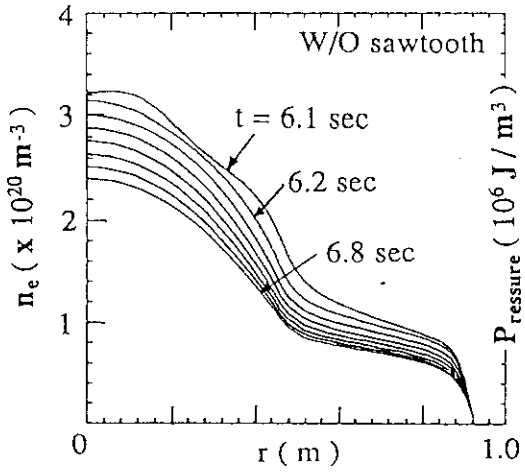

Fig. 3 (a)

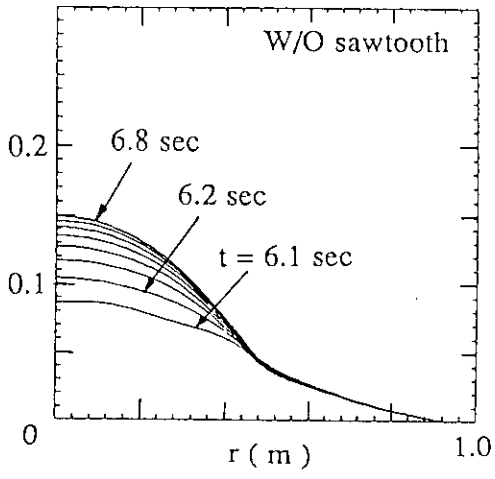

Fig. 3(b)

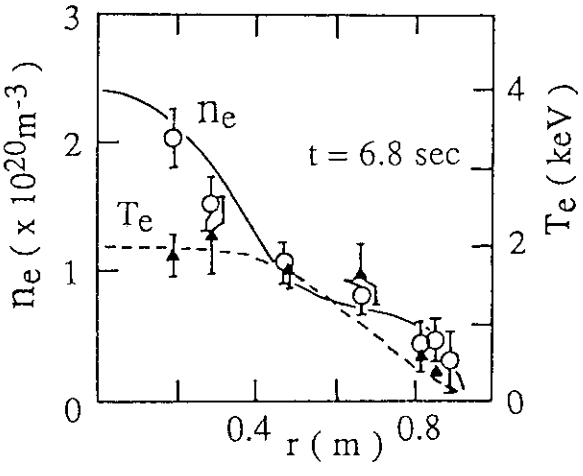

Fig. 4 (a)

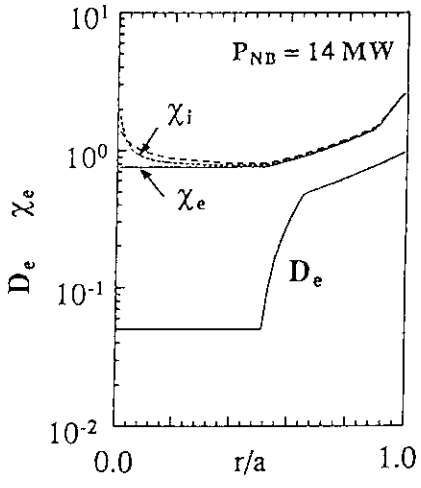

Fig. 4 (b)

1.7 Impurity Behavior in Pellet Fuelled Plasmas

T.Sugie, H.Kubo, A.Sakasai, K.Nagashima, Y.Kawano, H.Yoshida,
Y.Koide, N.Nishino, T.Nishitani, N.Akaoka and H.Takeuchi

Impurity behaviors in pellet fuelled plasmas were investigated mainly with spectroscopic method. Z_{eff} values measured by visible bremsstrahlung decreased from 2.5 to 1.5 just after the pellet injection. Carbon concentration decreased from 3.5% to 1% and oxygen one also decreased from 1% to 0.5%. Measured time evolution of soft X-ray signal was consistent with the calculated one assuming that only carbon was contained for the impurity. For metallic impurities, it has been still analyzing using a impurity transport code whether impurity ions accumulate to the plasma center.

1. Measurements

For the plasma and impurity transport study, time evolutions of electron temperature and density distribution were measured, shot by shot, by Thomson scattering method during the pellet injection with the several repeat shots. In these repeat shots, Z_{eff} values, impurity lines and soft X-ray signal were measured by visible monochromator, grazing incidence spectrometers and PIN photo diode array.

2. Experimental results and discussion

(a) Hydrogen pellet injections to hydrogen limited plasmas

Time evolutions of central soft X-ray signal PIN_{center} and TiXXI (2.6Å), TiXX (259.3lÅ), TiXII (460.7Å), CVI (33.7Å) and OVIII (18.97Å) lines were measured under the condition of B_T =4.5T and Ip=2.1MA. Those results are shown in Fig.1 (a)-(d), with line integrated electron density along the U6 line (r/a=0.6) $n_e l_6$ and injected NB power P_{NBI}. In these figures, central soft X-ray signal decreased just after the pellets injection and increased with no sawtooth oscillation. Intensity of the TiXXI line measured by crystal spectrometer also decreased just after the pellets injection because the electron temperature decreased to 500eV , and after that the intensity increased with the electron temperature. Closed circles show soft X-ray signals which were calculated by measured Z_{eff} and distributions of electron temperature and density, assuming only carbon impurity. These values were consistent with the measured one, as shown in Fig.1(a). This consistency shows that the titanium concentration was so small that the contribution to the soft X-ray signal was very small. But this result do not indicate that the impurity ions do not accumulate to the plasma center. It is necessary to analyze the time evolutions of impurity lines by impurity transport code.

Figure 2 (a) shows the time evolution of Z_{eff} value along the U6 cord measured by visible bremsstrahlung. The Z_{eff} value was decreased from 2.5 to 1.5 just after the pellets injection and increased to 2.3 after one second. Carbon and oxygen cocentrations were calculated by Z_{eff} values and intensity ratio of CVI (33.7Å) and OVIII (18.97Å) lines [1], as shown in Fig.2(b). In this

figure, closed squares and open squares indicate carbon and oxygen concentrations respectivly. Carbon concentration Nc/ne decreased from 3.5% of the electron density to 1% just after the pellets injection and oxygen one No/ne also decreased from 1% to 0.5%.

(b) Hydrogen pellet injection to helium limited plasmas (after Ti-gettering)

Time evolutions of central soft X-ray signal PIN_{center} and TiXXI (2.6Å), TiXX (259.31Å), TiXIX (169.6Å), CVI (33.7Å) and OVIII (18.97Å) lines were measured under the condition of B_T =4.8T and Ip=3.0MA. Those results are shown in Fig.3 (a)-(d) with line integrated electron density $n_e l_6$ and injected NB power P_{NBI}. In these figures, time evolutions of the central soft X-ray signal and TiXXI line had similar behaviors. In these shots, titanium concentration was larger than that of the plasmas before titanium gettering. Therefore, it seems that titanium radiation contribute to the soft X-ray signal. It is necessary to analyze whether the titanium ions accumulate to the plasma center or not.

3. Summary

Impurity behaviors of pellet fuelled plasmas were investigated on the repeat shots, when time evolutions of temperature and density distributions were measured by Thomson scattering. Z_{eff} values and impurity concentrations were decreased just after the pellet injection. Measured time evolution of soft X-ray signal was consistent with the calculated one. For metallic impurities, it has been still analyzing using a impurity transport code whether impurity ions accumulate to the plasma center. But,no large increase of the radiation loss was observed in this experiment.

Reference

[1] KUBO, H., SUGIE, T., SAKASAI, A., et al., Nucl. Fusion 29 (1989) 571.

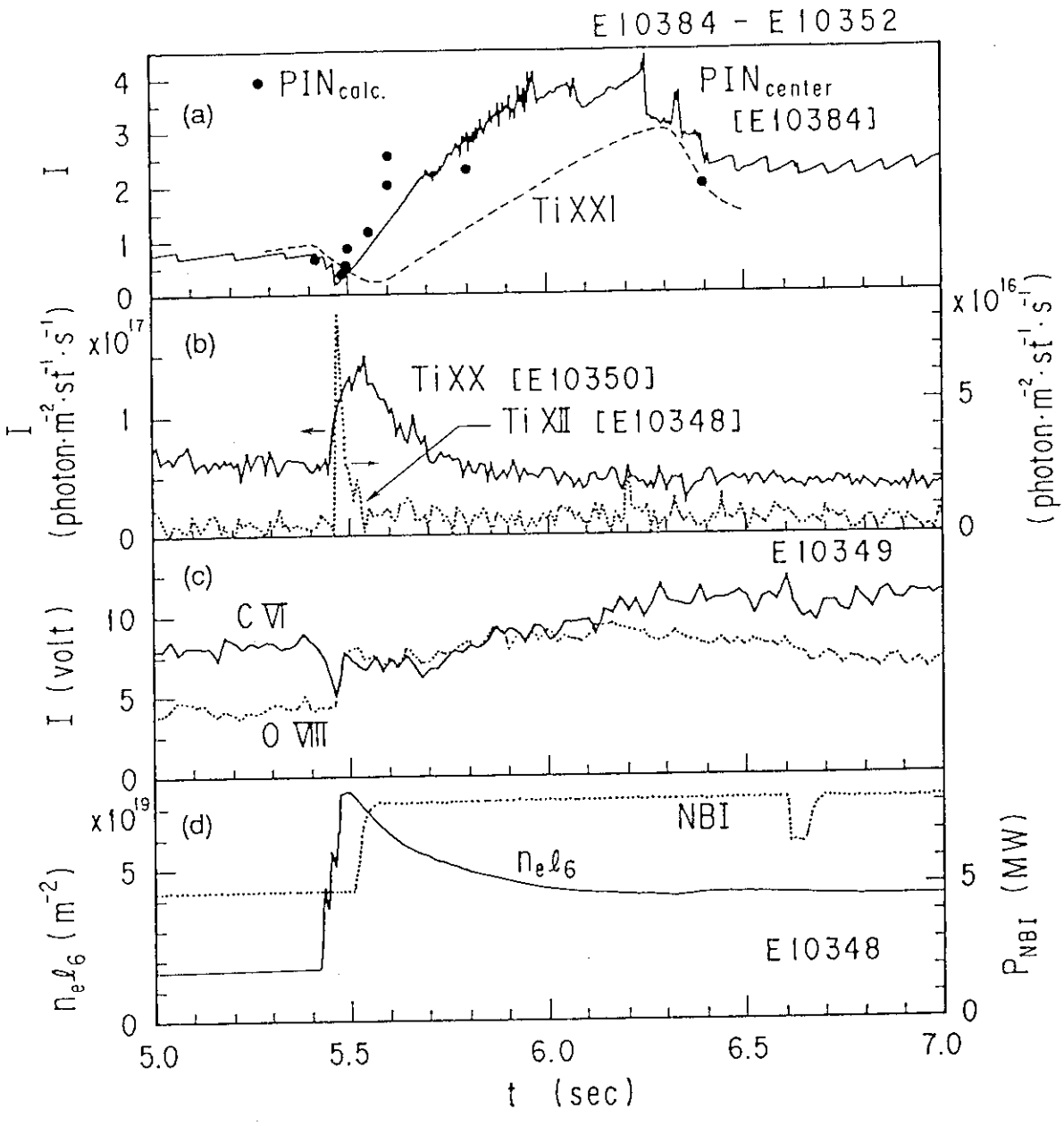

Fig.1 For the hydrogen pellets injection to the hydrogen plasmas under the condition of B_T =4.5T and Ip=2.1MA.

(a)Time evolutions of central soft X-ray signal P_{center} and TiXXI(2.6Å) line. Closed circles indicate calculated soft X-ray signal $P_{calc.}$.
(b)Time evolutions of TiXX(259.31Å) and TiXII (460.7Å) lines.
(c)Time evolutions of CVI (33.7Å) and OVIII (18.97Å) lines.
(d)Time evolutions of line integrated electron density along the U6 line (r/a=0.6) $n_e l_6$ and injected NB power P_{NBI}.

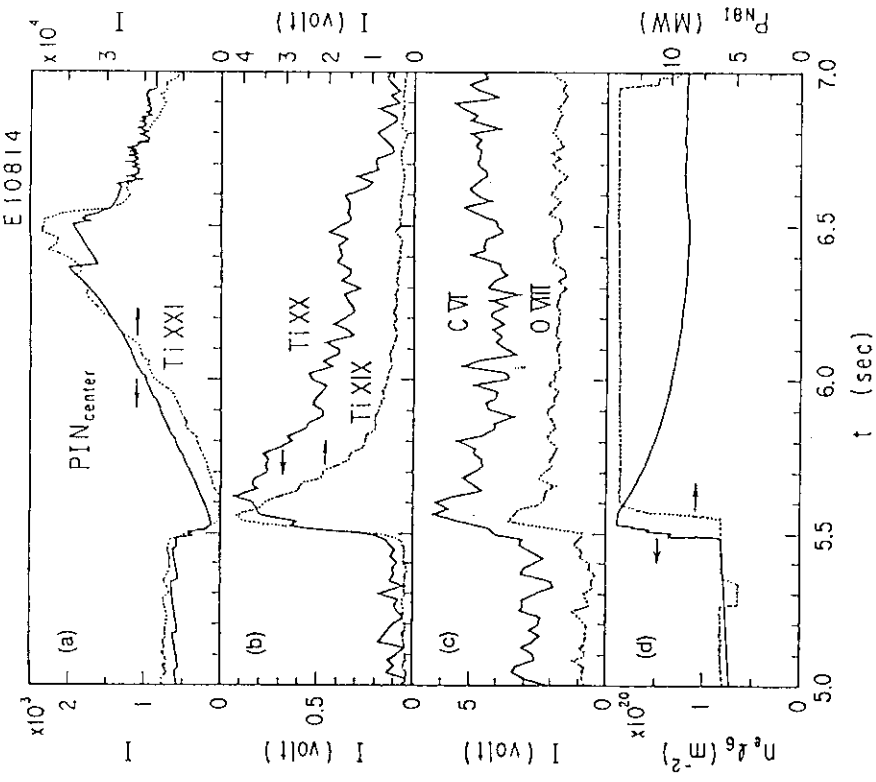

Fig.3 For the hydrogen pellets injection to the helium plasmas under the condition of B_T=4.8T and Ip=3.0MA.

(a)Time evolutions of central soft X-ray signal P_{center} and TiXXI(2.6Å) line.
(b)Time evolutions of TiXX(259.3iÅ) and TiXIX (169.6Å) lines.
(c)Time evolutions of CVI (33.7Å) and OVIII (18.97Å) lines.
(d)Time evolutions of line integrated electron density along the U6 line (r/a=0.6) $n_e l_6$ and injected NB power P_{NBI}.

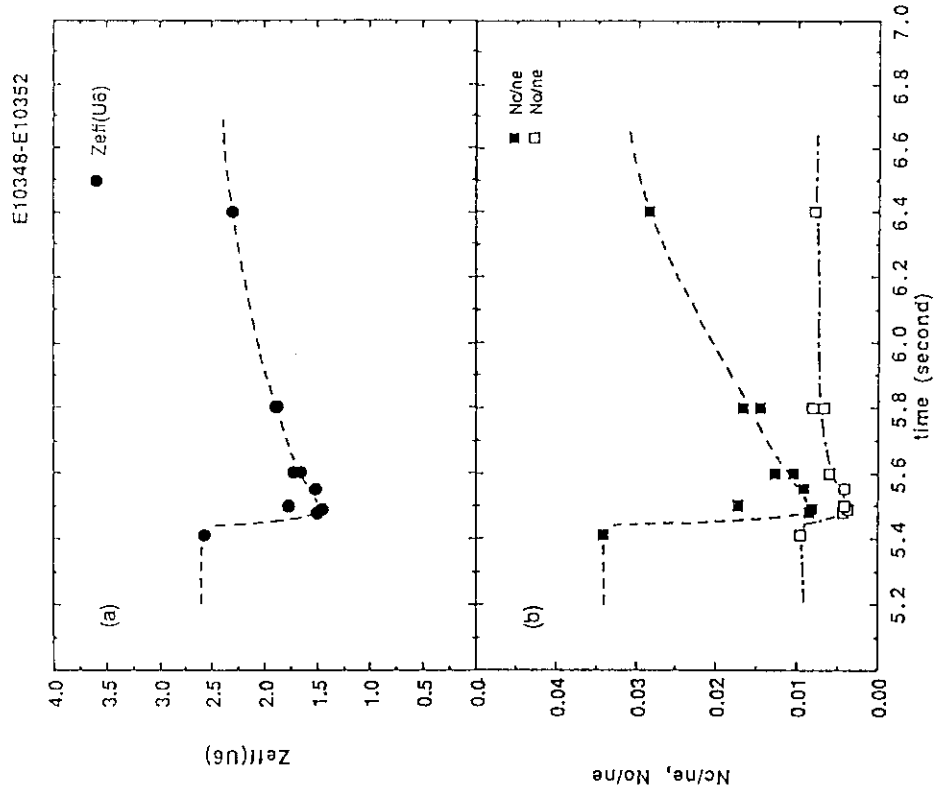

Fig.2 For the hydrogen pellets injection to the hydrogen plasmas under the condition of B_T =4.5T and Ip=2.1MA.

(a)Time evolution of Z_{eff} value along the U6 cord measured by visible bremsstrahlung.
(b)Time evolutions of carbon and oxygen cocentrations, Nc/ne and No/ne, calculated by Z_{eff} values and intensity ratio of CVI (33.7Å) and OVIII (18.97Å) lines.

1.8 Upgrade of JT-60 Pellet Injector for Higher Velocity of 2.3 km/s (I)

Hajime HIRATSUKA, Kouzo KAWASAKI+, Yasuhiko MIYO,
Yuji YOSHIOKA and Kengo MIYACHI

1. DESIGN

1.1 Description of JT-60 pellet injector[1]

The JT-60 pellet injector consists of a gun assembly, a gas feed line, a cryogenic feed line, a pellet injection line and a control system composed of a mini-computer, a programable logic controller and CAMAC modules. The schematic diagram of the JT-60 pellet injector is shown in Fig.1.

(1) Gun assembly

The gun assembly is a main component which produces four ice pellets and injects them into the JT-60 vacuum vessel. The schematic drawing of the gun assembly is shown in Fig.2. The gun assembly consists of four heat exchangers and four barrel housings containing pellet carries, driving shafts and gun barrels. The barrel housing is connected to the heat exchanger which reserves liquid helium provided for cooling the barrel housing up to an operating temperature of 14-10°K.

The gun barrel made of stainless steel is connected to each barrel housing made of OFHC copper. The pellet carriers with two gun barrel diameters of 3.0 mm and 4.0 mm can slide up and down between OFHC copper washers in the barrel housing.

After frozen pellets are formed in the condensating well located at a lower position named pellet making position in the barrel housing, the pellet carrier is slided up to a higher position named pellet injection position to chamber each pellet in the corresponding gun barrel. Then the pellets are injected into plasmas.

The pellet carrier is driven at a constant speed by a stepping motor with an angular velocity of 0.72deg/6μs and a torque of 11.8 kg-cm and travels about 10 mm from the pellet making position to the pellet injection position. The position of pellet carrier is monitored by an encorder in order to control it accurately.

The pellet is propelled by a fast magnetic valve working by pressurized hydrogen gas up to 100 bar. This valve is opened quickly by discharging electricity released from a 2000 μF capacitor charged to 150 V. The temperature of this valve is necessary to maintain over a room temperature by an electrical heater because it is afraid that the valve does not open due to adhesion between a nozzle and a seal material at a cryogenic temperature. Also this valve is usable under 473 °K maintained by the electrical heater. A reservoir which stores the propellant gas is connected to the FMV and is heated up to 473 °K in order to improve pellet acceleration capability.

(2) Injection line

The injection line is composed of three diagnostic stations, two sets of vacuum isolation shutter valves and guide tubes. A pellet is transported to the plasma through this injection line. After leaving the gun nozzle, the pellet passes through the vacuum isolation shutter valves. The valves are opened to allow passage of the pellet and are immediately closed to limit the propellant gas flow entering the plasma.

The first and second diagnostic stations are connected to a low vacuum tank (1.2 m^3) and a high vacuum tank (1.0 m^3), respectively. These large

+ Department of HTTR Project, Oarai Research Establishmnet

expansion tanks, vacuum isolation shutters valves and guide tubes are designed to minimize the propellant gas flow into the plasma.

The light sensors for pellet velocity measurement are located at the first and second diagnostic stations and the microwave cavity measurement for measuring pellet fueling efficiency is located at the first diagnostic station.

(3) Refrigerant and gas supplies

Various refrigerant and gas suppliers are provided for cooling down, and supplying fuel and propellent gases. Liquid helium is transfered from 2000 ℓ He dewar to each heat exchanger in the gun assembly. The exhausted gas of refrigerant is heated up to room temperatures. The propellant gas (hydrogen) and the fuel gas (hydrogen or deuterium) are transfered to the gun assembly through liquid nitrogen traps and filters to remove impurities contained in the gases.

(4) Control system

The control system enables us local and remote operations such as injection, vacuum pumping and baking for de-gassing of the nearest vacuum pipes. The major components of this system are a programable logic controller (PLC) and a mini-computer (M-70 made by Mitsubishi Electric, Co.) including a CAMAC serial highway interface and a MODEM interface.

The PLC performs all control functions for injection, vacuum pumping, baking and gas supplying. The mini-computer has two CRT displays for operation, the CAMAC serial highway interface for data acquisition and communication of the pellet experiment condition between the JT-60 master controller named ZENKEI and the JT-60 pellet injector, and the optical MODEM interface for communication between the PLC and the mini-computer.

The CAMAC interface also allows interconnection to the timing system in the ZENKEI for triggering of the pellet injection. The transient information containing the pellet velocity and pellet fueling efficiency is transfered to the ZENKEI through the CAMAC serial highway.

1.2 Improvements and developed components [2]

Improvement was made to cool down the housing effectively by using (1) the silver contained formed-copper to transfer the heat from the surrounding to the heat exchanger and (2) silver joints at connection surfaces. The gun assembly is housed in a vacuum chamber to provide thermal insulation.

Each heat exchangers is also thermally isolated independently against the heat load of the gun barrel generated by pellet injection. The temperature of the barrel is controlled within about ±2°K by making use of temperature controller (Chino C.O: Type D.A.) and Au-Fe Constantan thermo-couples.

Main effort for construction of the JT-60 pellet injector was to develop FMV which should open against the high propellant gas pressure. It was an important component for providing a burst of high pressurized hydrogen gas for acceleration of pellets. Requirements of the fast acting magnetic valve for the JT-60 pellet injector were to work under higher propellant gas pressure up to 100 bar and to obtain higher pressure rise rate up to 200 bar/ms because the pellet velocity greater than 1900 m/s was required.

The improvements of the new FMV compared to the commercial were brought in (1) selection of a seal material, (2) short time constant of a magnetic coil, (3) increase of a nozzle diameter and (4) increase of the velocity of the seal material. The first improvement was useful to protect the seal leakage against a high working temperature for a long period and other improvements were useful to increase the pressure rise rate. Cross-sectional view of the developed FMV is shown in Fig.3. The seal material

made of polimide is pushed to the end of 4.5 mmϕ nozzle by a spring force. The plunger, which is separated from the seal, begins to move as soon as the magnetic coil is energized, and hits the seal just after the plunger travels in 2 mm. The stroke of the plunger is designed to be 4 mm. As a results, quick open/close movement was ensured and the valve satisfied the specified requirement.

The obtained results using the developed FMV are summarized as follows: pressure rise time of 0.2 ms, pressure rise rate of 474 bar/ms and vacuum leak rate less than 1.0×10^{-6} Pam^3/s were obtained under a pressure of 100 bar and the reliability was confirmed by the repetition test of $1.0\times10^{+4}$ cycles [3].

The JT-60 pellet injector has been operated reliably without any serious troubles under the strong magnetic field.

2. OPERATION PROCEDURE

Operation of the pellet injection system began with complete evacuation of the gas feed lines using the vacuum pumps. We describes the operation procedure of the pellet injection.

The barrel housings are cooled down by liquid helium supplied from the 2000 ℓ He Dewar. It takes about 2-4 hours with a liquid helium flow of 9 ℓ/hr to cool down from a room temperature to 30-40°K. The pellet carriers are placed at the pellet making position and the fuel gas is introduced into the barrel housings from the fuel gas line. Temperature of the gun barrel is cooled down from 30-40°K to 10-50°K for 4-5 minutes. The time behavior of the gun barrel temperature and the pressure rise of the fuel gas are shown in Fig.4.

The gun barrel temperature and the pressure rise of the fuel gas become in steady state because the hydrogen fuel gas changes into a frozen hydrogen isotope pellet. The pellet carriers drive the pellet to the pellet injection position. Then the FMVs are opened independently, providing high pressureized propellant gas burst to accelerate the pellets in the gun barrel and the pellets are injected into the plasma through this injection line. After pellet injection, barrel housings are heated up to 30-40°K by electrical heaters mounted on them.

Operation of the pellet experiment with plasma discharges are as follows. The operational conditions including the number of injected pellets and injection timing parameters are transfered from the ZENKEI to this system through the CAMAC serial highway. These conditions are sent to the PLC and the pellet injection pulser. A firing signal of t=0 is transfered from the JT-60 timing system of the ZENKEI to the pellet injection pulser through the CAMAC timing modules of this system. A counted clock pulse of the pellet injection pulser reaches the setted timing parameter and a triggering signal is sent to the FMV.

The pellet injection operation is interrupted by the interlock system on some occations such as no plasma build-up, plasma disruption and leakage of hydrogen gases around the machine. The reasons of the interruption are to protect contamination of the first walls and to protect hydrogen gas explosion.

References

[1] H. Hiratsuka, et al., JAERI-M 88-214 (1988).
[2] K. Kawasaki, et al., To be published in Proc. 15th Symp. on Fusion Technology, Utrecht, 1988.
[3] H. Hiratsuka, et al., To be published in Proc. 15th Symp. on Fusion Technology, Utrecht, 1988.

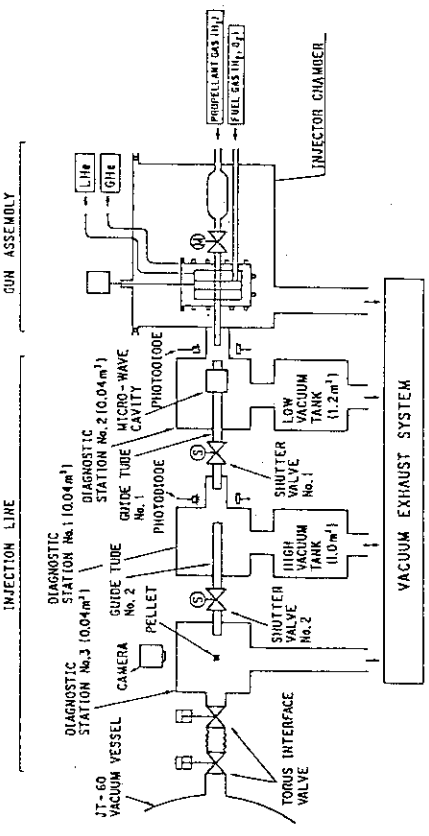

Fig. 1 SCHEMATIC OF 4-SHOT PELLET INJECTOR

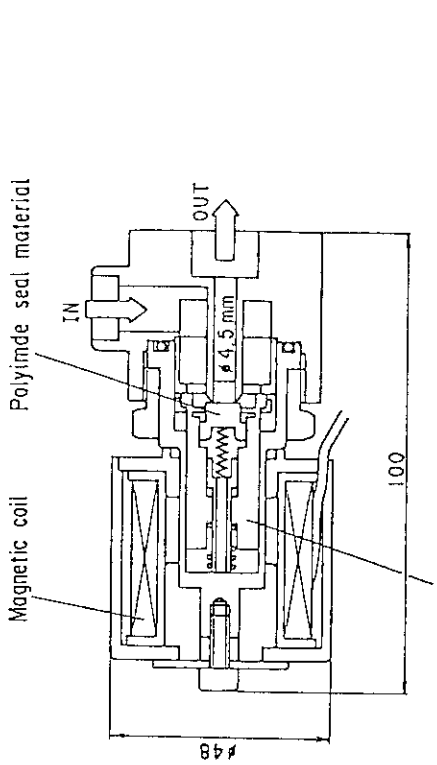

Fig. 3 FAST-ACTING MAGNETIC VALVE (FMV)

Fig. 2 SCHEMATIC DRAWING OF GUN ASSEMBLY

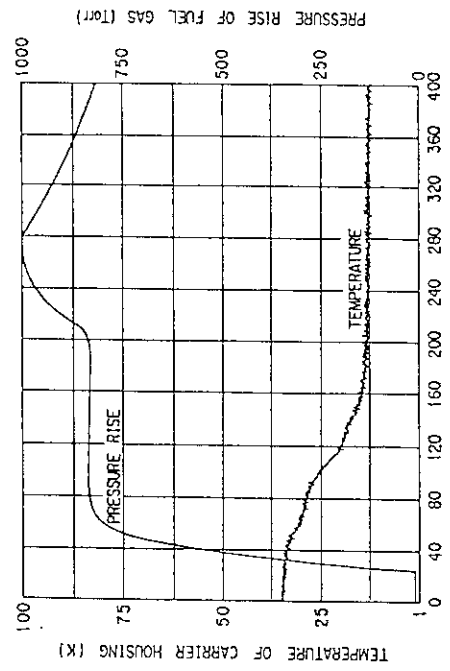

Fig. 4 TIME BEHAVIOR OF THE GUN BARREL TEMPERATURE AND THE PERSSURE OF THE FUEL GAS

1.9 Upgrade of JT-60 Pellet Injector for Higher Velocity of 2.3 km/s (II)

Hajime HIRATSUKA, Kouzo KAWASAKI+, Yasuhiko MIYO,
Yuji YOSHIOKA and Kengo MIYACHI

1. TEST RESULTS

The pellet fueling efficiency and the pellet velocity were measured by the change of the resonance frequency in the microwave cavity and the time of flight between fixed distance at the pellet injection line. The dispersion of the pellets was measured at the third diagnostic station using soft aluminum targets to intercept the flight line of the pellets. All pellets hit the aluminum target within 2 cm circle located at 400 cm away from the FMVs. Typical test results are summarized as follows.

(1) Characteristics of vacuum and cooling

Three diagnostic stations were exhausted to about 10^{-4} Pa from an atmospheric pressure within 30 minutes. After 120°C baking, the ultimate pressure at the third diagnostic station was less than 2.0×10^{-5} Pa. The amount of the propellant gas flow entering the third diagnostic station was dependent on the open holding time of the vacuum isolation shutter valve. The vacuum isolation shutter valve must close within 50 msec after the FMV has worked because the amount of the gas due to propellant gas flow is afraid to become over 10 % of the pressure rise due to the hydrogen pellets. This value satisfied sufficiently the specification value.

The cooling time from a room temperature to 30-40°K at the gun barrel was about 150 minutes with 9 ℓ/hr liquid helium flow. The barrel housings were cooled down to a low temperature (8.3°K) enough to make the frozen hydrogen pellet. Obtained temperature distribution at the gun barrel agreed with the calculated.

(2) Determination of pellet fueling efficiency

A microwave cavity measurement is to measure an amount of reflected power which is induced by mistuning the resonance frequency. By mistuning the resonance frequency during the introudction of the pellet, a linear relation-ship between an output voltage and a frequency shift in the cavity is obtained for changes in the frequency that are small compared with the resonance frequency.

Results from characteristics of the pellet fueling efficency by the microwave measurement are shown in Fig.1. The pressure rise at the third diagnostic station was measured as a function of the output voltage corresponding the shift in resonance frequency. The fueling efficiency was defined the ratio between the injected fuel gas particles and an amount of the ideal fuel gas particles with the theoretical dencity and the same sized of the pellet carrier. The results shown in this figure indicate a fairly linear relationships between the pressure rise and the output voltage with ±10 % variation. Obtained pellet fueling efficency was up to 60-65 % for both dimensions of pellets. Measured fueling efficiency by this method is agree with the other experimental results of plasma density [1].

(3) Injection performance

Velocities measured by the time-of-flight method are shown in Fig.2. Theoretical curves based on the ideal gun theory are shown in the same figure [2]. The horizontal axis in this figure designates the propellant

---

+ Department of HTTR Project, Oarai Research Establishment

gas pressure. The pellet velocity was ranged from 1700 m/s to 2200 m/s, where the propellant gas pressure was in the range 50 bar to 100 bar and the temperature of the propellant gas was 313°K. Experimental data were lower than those calculated from the gun theory. The difference resulted from the fact that the pellet residence time in the gun barrel was less than the FMV full opening time. The incremental pellet velocity is about 12 % against the propellant gas pressure up to 100 bar from 50 bar. The tendencies of the measured velocity on the pressure was similar to the ideal curve. Improvement of the propellant gas temperature against the pellet velocity is shown in Fig.3. About 16 % for the pellet velocity was improved at a propellant gas temperature ranged from 313°K to 473°K. The incremental pellet velocity against the pressure rise and temperature of the propellant gas was calculated 16-17 % and 4-5 %. The experimental and computational results are in good agreement. The highest velocity over 2300 m/s was obtained for two dimensions of pellets. When operated conditions were 100 bar and 413°K in the propellant gas pressure and temperature, obtained velocity and fueling efficiency were 2323 m/s and 53.7 %, respectively.

Detailed pellet velocity analysis was carried out using the developed computer program based on Navier-Stokes equations for the fluid driver in an eqivallent one dimensional formula. Comparison of the experimental and computational results are shown in Table 1. This table shows that the pellet velocity of the small size pellet is greater than that of the large size pellet and the experimental and computational results are in good agreement.

In this table, the velocity of the small size pellet is greater than that of the larger one because the accelleration of the pellet is in proportion to the pellet mass and the obtained velocity is faster than that of the calculated one because the open-closed time of the FMV in which the calculation is about 2~2.5 times as much as the actual FMV. Especilly the velocity of pellet is stronglly depend on the open-close time of the FMV. The obtained velocity used the old typed FMV which the open-close time was about 1.1 ms is about 60-65 % and the developed FMV which the open-closed time is about 0.4-0.5 ms, the obtained is about 80-90 % from the theoritical value based on the ideal gun theory, respectively. This experimental results shows that the FMV must be opened quickly to increase the pellet velocity.

2. CONCLUSION

The JT-60 pellet injector was constructed successfully and the obtained pellet velocity was ranged from 1700 to 2300 m/s. The maximum pellet fueling efficiency was 60-65 % for two dimensions of pellets. The dispersion of pellets has been determined at the third diagnostic station corresponding to the entrance of the JT-60 vacuum vessel using soft aluminum targets to intercept the pellets. All pellets hit within 2 cm circle as indicated by the impact craters. This system has been in use for the JT-60 since February in 1989.

References

[1] Y. Kamada, et al., JAERI-M 89-050 (1989).
[2] C.A. Foster, et al., IAEA Technical Committee Meeting on Pellet Injection and Toroidal Confinement. Gut Ising, Upper Bavaria, FRG October 24-26, 1988.

Table 1 Comparison between the obtained and the calculated pellet velocity

Pellet dimension	Calculated		Measured	
	Temp(k)	Velocity(m/s)	Temp(k)	Velocity(m/s)
4.0mm × 4.0mm	300	1698	313	2100
	473	1906	473	2200
3.0mm × 3.0mm	300	1884	313	2150
	473	2090	473	2280

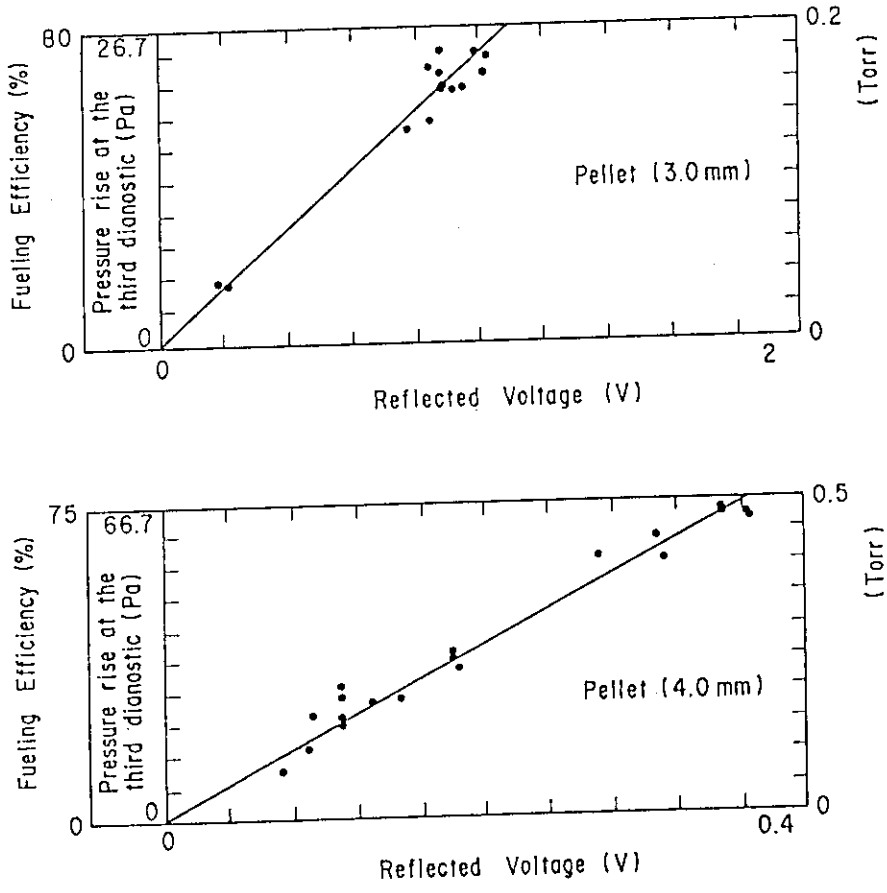

Fig. 1 CHARACTERISTICS OF THE PELLET FUELING EFFICIENCY BY THE MICROWAVE MEASUREMENT

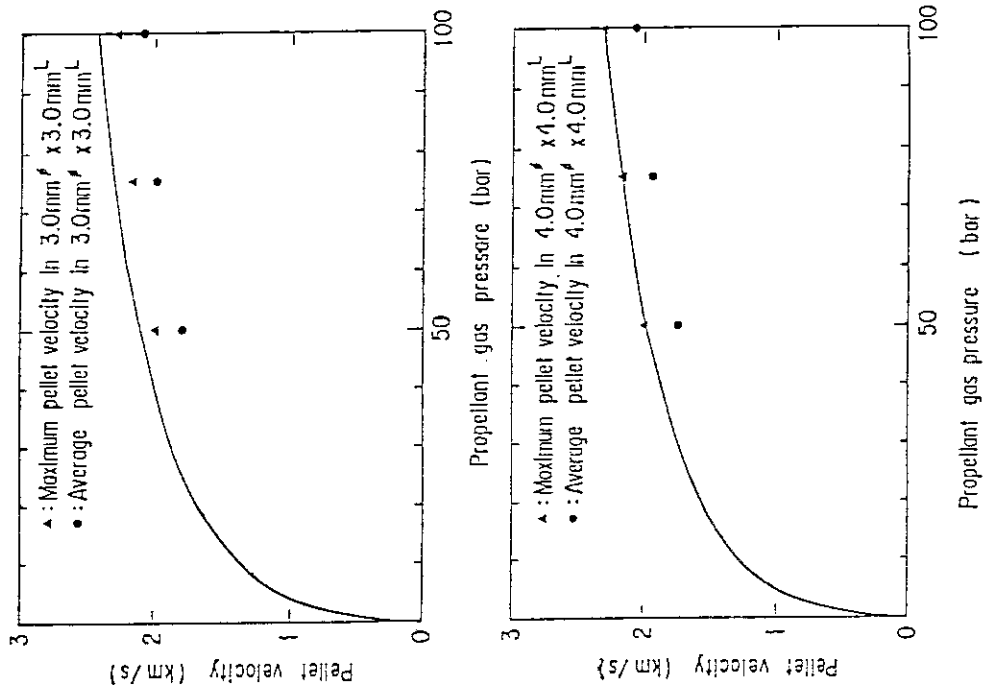

Fig. 2 PELLET VELOCITY DEPEND ON PROPELLANT GAS PRESSURE COMPARED CALCULATED ONES

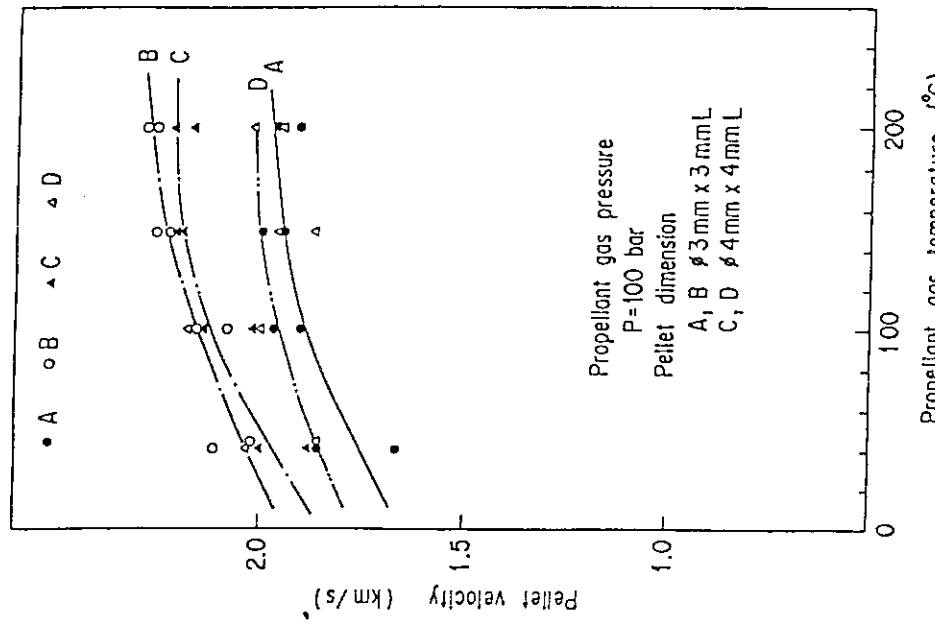

Fig. 3 PELLET VELOCITY DEPEND ON PROPELLANT GAS TEMPERATURE

2. LHRF Experiments

2.1 First Operation of Multijunction LHCD Launcher

Y.IKEDA, T.IMAI, K.USHIGUSA, M.SEKI, K.KONISHI, O.NAITO, M.HONDA, K.KIYONO, S.MAEBARA, T.NAGASHIMA, M.SAWAHATA, K.SUGANUMA, K.UEHARA, K.YOKOKURA and JT-60 team

1. Introduction

The development of steady-state current drive would considerably enhance the prospects for a tokamak fusion reactor. Lower hybrid current drive is one of the most promising method to achieve a steady-state tokamak. Another application of lower hybrid current drive is the control of the plasma current profile to improve MHD stability and confinement in tokamaks. So the main objective of LHRF experiment is to optimize the wave spectrum for each item. Recent experimental results have shown that the current drive efficiency was improved by sharpening wave spectrum on PLT[1] and that a good qualitative agreement exists between the Fisch's theory[2] and the experimental data. The theoretical current drive efficiency is given by $\eta_{CD}^{th} = K \cdot G$, where $K = (42.45 + 1.954 \cdot Z_{eff})/(5 + Z_{eff})$ and G is defined as follow[3],

$$G = \frac{1}{(N_{//}min)^2} \cdot \frac{1-(N_{//}min/N_{//}max)^2}{\ln(N_{//}max/N_{//}min)} \cdot \frac{P_{acc}}{P_{LH}}$$

$N_{//}min$, $N_{//}max$ are the minimum and maximum of the effective part of the parallel refractive index spectrum, respectively, and P_{acc}/P_{LH} is the directivity and the accessible power ratio of the launched waves. So a large number of waveguides in toroidal direction are required to launch a narrow wave spectrum ($(N_{//}max/N_{//}min) \rightarrow 1$).

A multijunction launcher was proposed in order to increase the number of the waveguide with simplified modification of the launching system[4]. The JT-60 has three LHRF launching systems and has achieved a current drive efficiency of 2.65 $\times 10^{19} m^{-2} A/W$ and $2.9 \times 10^{19} m^{-2} A/W$ without and with NBI at $N_{//}$peak of 1.0 - 1.7[5]. And improvement of confinement has been observed at broad plasma current profile by launching the wave spectrum of 1.7 through the conventional launchers, which are composed of a phased waveguides array of 8 columns in the toroidal direction by 4 rows in poloidal direction[6]. We aimed at improving the current drive efficiency and confinement by launching a narrow and highly unidirectional spectrum through a new multijunction type launcher.

We report the overview of this multijunction launcher and the first results of experiments on the JT-60 using this launcher.

2. Overview of Launcher

From experimental view points, the launching system needs a high controllability of $N_{//}$ to optimize the spectrum. So a large number of waveguides in toroidal direction are required for a launching system. The launching system of the JT-60 features to be separable at 3 m far from the launcher mouth to make it easy to modify the grill part. We modified the grill part from the conventional grill to the multijunction one. The divided number of three in the transmitted waveguide was adopted to sharpen the wave spectrum, and the pitch of the

waveguide was constrained by the requirement to connect the conventional launching element. The $N_{//}$peak is given by $30/(f\cdot\delta)\cdot\theta/2\pi$, where f is the frequency(GHz), δ pitch (cm) and θ the phase angle. Since We have already had a conventional launcher of $N_{//}$peak of 1.7 for current drive experiment, we selected $N_{//}$peak of 2.2 to obtain more flatten plasma current profile by LHCD. A geometric phase angle θ of 70° was adopted to launch the $N_{//}$peak = 2.24, when the phase difference between adjacent module was 70° . Since the launching system has 8 modules in the toroidal direction, the wave spectrum can be controllable to select the best value for current drive experiment from 1 to 3.5 with a high directivity as shown in Fig. 1. The multijunction module was manufactured by welding 3 secondary waveguides with geometric phase shifter. A taper waveguide was adopted to match at the geometric phase shifter in each secondary waveguide. The length of the module and the width of the waveguide were limited by the technical requirement of copper plating and welding. The resulting module is shown in Fig. 2. Manufacturing tolerances were $\pm$0.2mm and $\pm$ 0.2mm on height and width of the waveguide at grill mouth, respectively. The phase shift and power balance were measured on every module and were about 70$\pm$ 10° and 1/3 $\pm$ 1/15, respectively. These discrepancies may be due to the deformation at the welding point in the waveguide. Since the the number of waveguide of 24 in the toroidal direction is much enough to average these discrepancies, the Fourier analysis of the manufactued launcher's spectrum shows that the deformation of the spectrum is little compared with designed spectrum.

3. Experiment

Before the experiment, the launcher was conditioned by only high power RF injection into the vacuum vessel of the JT-60 without plasma, and with Tayor Discharge Cleaning (TDC) plasmas for two days. In the case of without adequate density plasma (vacuum or TDC plasma), the temperature rise of about 4.5℃/MW·s at the geometric phase shifter was observed due to a high Voltage Standing Wave Ratio (VSWR) at the secondary waveguides without plasma loading. So the conditioning in this case was performed under high RF field at the secondary waveguides. Following these procedures, a current drive experiment up to 2 MW was carried out after only 30 plasma shots. This conditioning time up to 2 MW was about one-fifth shorter than that of conventional current drive one. We suppose the RF conditioning without adequate plasma is much effective on the multijunction launcher due to high VSWR at secondary waveguides. At present, the maximum injected power reached at 2.75MW.

The measured coupling agreed fairly well with the theoretical one as shown in Fig.3(a). The theory curve assumes an edge density of 5×10^{18} m^{-3}, a density gradient of 5×10^{19} m^{-4} and a vacuum gap of 2×10^{-3} m. The temperature rise at the geometric phase shifter shows that a high VSWR stands at high reflection condition in Fig.3(b). This data indicates that a good coupling should be necessary from the view point of not only injection of a high power and designed spectrum into plasmas but also decreasing the rf loss on the grill part in the multijunction launcher.

The current drive efficiency with the multijunction launcher was studied by means of $N_{//}$peak scans from 1 to 2.5. As the plasma current is usually maintained by the feedback system in the JT-60, we determine the current drive efficiency from the data of one-turn loop voltage of approximately zero. Figure 4 shows the

current drive efficiency dependent on the $N_{//}$peak at I_p = 1 MA. The closed and open data show the experimental η_{CD} for the multijunction and the conventional launchers in the same target plasma, respectively. A maximum η_{CD} of 2.8 was obtained for the multijunction launcher with the spectrum of $N_{//}$peak = 1.3 at n_e = 0.8×10^{19} m^{-3} and the η_{CD} for the multijunction launcher is about 1.4 time larger than that of the conventional one at $N_{//}$peak = 1.7. This data shows the LH wave with narrow and high directivity spectrum gives a improvement in the current drive efficiency. The reason of the drop in η_{CD} at $N_{//}$peak = 1.1 is that wave accessibility limits the minimum spectrum. The solid line in this figure shows the theoretical current drive efficiency of the multijunction launcher calculated from Fisch's theory on the assumption of Z_{eff} = 2 and $N_{//}$acc = 1.3. We also obtained a higher efficiency of 3.4 at a higher plasma current of 1.74 MA at $N_{//}$peak = 1.3. The experimental data qualitatively agreed with the theoretical one. These results clearly show that the fastest wave spectrum with a high directivity, which is accessible into the plasma, is optimum for current drive and also that the launched waves from the multijunction launcher have the calculated spectra as shown in Fig. 1.

4. Conclusion

A high efficiency current drive of η_{CD} = 3.4 have been obtained by using a multijunction launcher. A good agreement between the Fisch's theory and the data from the grill phasing shows that a narrow wavenumber spectrum at the lowest possible $N_{//}$ which can access to the plasma core is the best value to drive a plasma current efficiently. Moreover the multijunction launcher leads to the improved grill conditioning. High availability of the multijunction launcher for current drive have been validated on the JT-60, and therefore such a launcher may be considered for use in the steady-state tokamaks.

REFERENCES

[1] STEVEN,J.,BELL,R.,BERNABEI, S.,et al., Nucl.Fusion 28(1988)217.
[2] FISCH,N.,Phys.Rev.Lett.41(1978)873.
[3] TONON,G.,Plasma Phys. Controll. Fusion 26(1984)145.
[4] NGUYEN,T.K.,MOREAU,D.,Fusion Tech.,2(1982)1381.
[5] USHIGUSA.K.,IMAI,T.,IKEDA.Y., et al. in Plasma Physics and Controlled Nuclear Fusion Research 1988(Proc. 12th Int. Conf. Nice,1988)IAEA, Paper IAEA-CN-50/E-3-1
[6] IMAI,T.,USHIGUSA.K.,SAKAMOTO,K., et al., Nucl.Fusion 28(1988)1341.

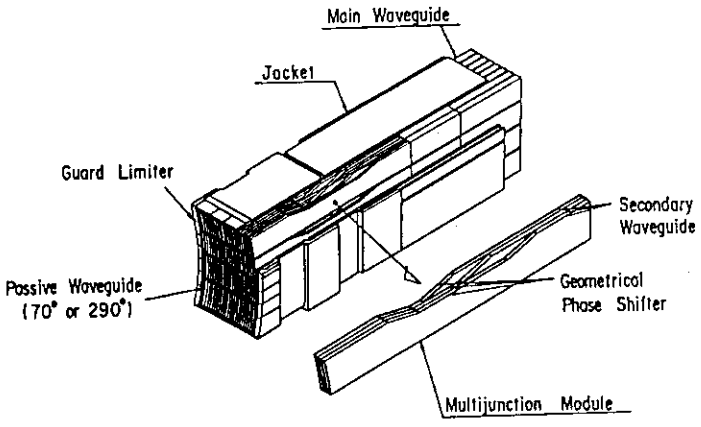

Fig. 1 Structure of LHRF multijunction launcher for JT-60.

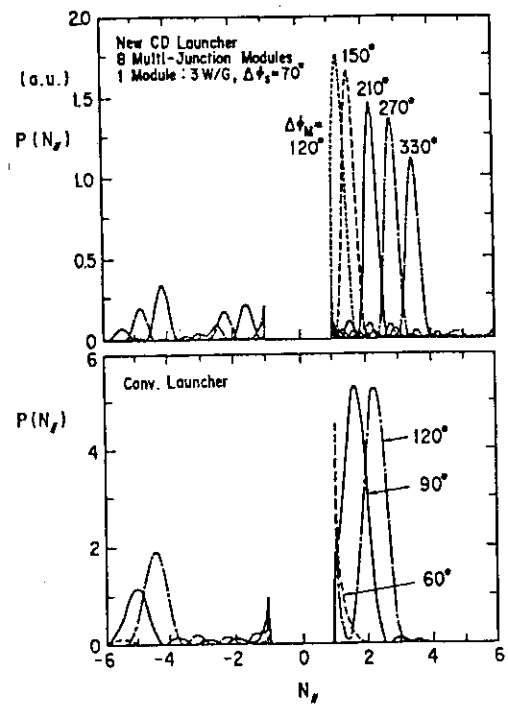

Fig. 2 $N_{//}$ spectra of a multijunction launcher and of a conventional current drive launcher.

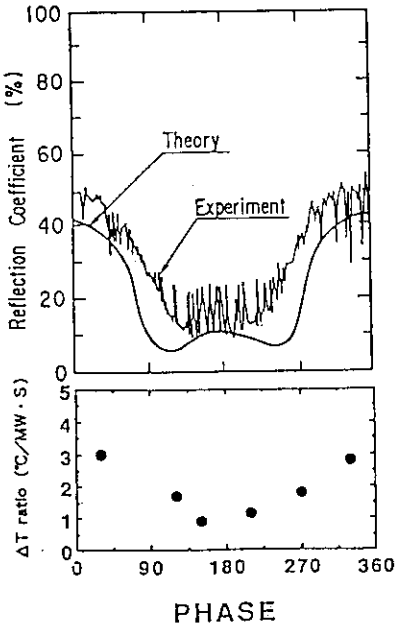

Fig. 3 Total reflection coefficiency and temperature rise ratio versus phase difference between adjacent module.

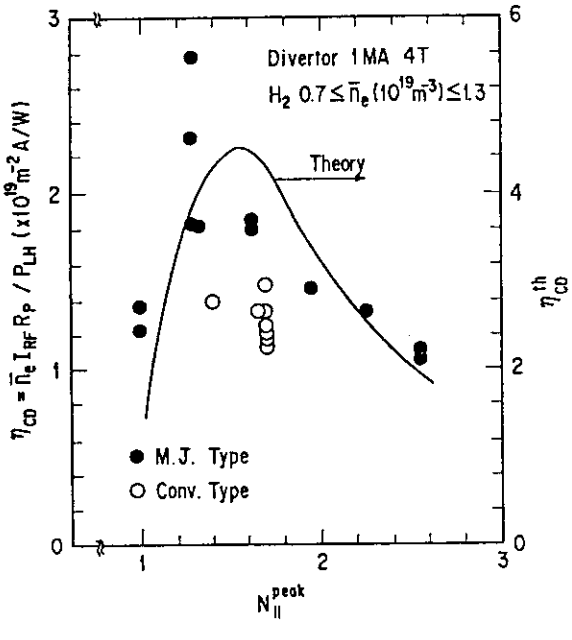

Fig. 4 Current drive efficiency versus $N_{//}^{peak}$

2.2 Improvement of Current Drive Efficiency and Enlargement of Current Drive Product

T. Imai, K. Ushigusa, Y. Ikeda, O. Naitoh, M. Seki, K. Uehara, H. Yoshida, M. Nagami and JT-60 Team

1. Introduction

Key issues for the development of steady state tokamak reactor are to get high current drive efficiency above $5\times10^{19}m^{-2}A/W$ and large current drive product up to 500 $\times10^{19}m^{-2}MA$. There are several current drive schemes in tokamaks, like Lower Hybrid (LHCD), Fast Wave (FWCD), Electron Cyclotron Wave (ECCD), NBI (NBCD) and etc.. Among them, LHCD is now the most sophisticated to produce the steady state current. Since the success of the LHCD in JFT-2 tokamak, progress of the LHCD is the most impressive, as seen in the recent JT-60 LHCD results [1-8]. This progress of the LHCD, however, also reveals the problems in it like hot spot, surface current and α particle absorption in a reactor grade plasma. But the LHCD is still the most reliable and powerful current drive scheme and will be in the near future reactor grade tokamaks like FER and ITER in the limited usage. The report provides the recent progress of the current drive efficiency and large current drive product in JT-60, using two current drive launchers including a multi-junction one, with a power of up to 4.5 MW.

2. Improvement of Current Drive Efficiency

Previous experiment of the LHCD in the outer and lower X-point and limiter discharge in JT-60 and other small tokamaks clarified the scaling of the current drive efficiency ($\eta_{CD}=\bar{n}_e R_p I_{RF}/P_{LH}$) on plasma parameters as

$$\eta_{CD} \propto \langle T_e \rangle/(5+Z_{eff}) \qquad (1)$$

where $\langle T_e \rangle$ is the volume average electron temperature and Z_{eff} is the effective ionic charge. This scaling gives us very promising prospect for the future non-inductive current drive. On the other hand, the theoretical current drive efficiency is given by

$$\eta_{CD} \cong \frac{46}{Z_{eff}+5}\frac{1}{N_1^2}\frac{1-N_1^2/N_2^2}{\ln(N_2/N_1)}\frac{P_{ACC}}{P_{LH}} \qquad (2)$$

where N_1 and N_2 are the minimum and maximum values of the $N_{\parallel}$ and P_{ACC}/P_{LH} is the effective uni-directional power fraction.The equation (2) implies that sharp and lower $N_{\parallel}$ spectrum and highly directive wave could have better efficiency. Large number of waveguides are required to get such a spectrum, so as to complicate the RF system. To

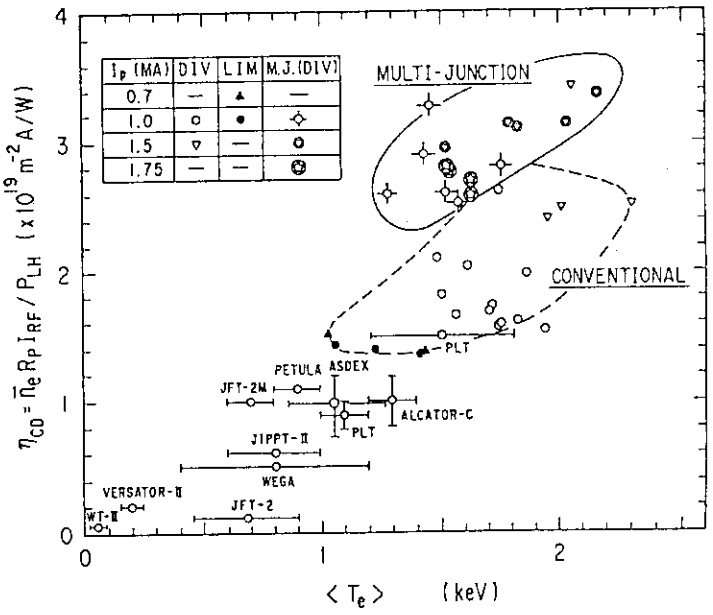

Fig. 1 Dependence of η_{CD} on <Te> and its comparison between the conventional and multi-junction launchers. Results in other tokamaks are also shown.

avoid such complication, multi-junction type launcher was introduced in JT-60 as described in the section 2.1. Improvement of directivity and sharpness of $N_{\parallel}$ spectrum predicts higher current drive efficiency by a factor of 1.3~1.5 from Eq. (2). The results of the experiment in JT-60 are shown in Fig 1, where current drive efficiency η_{CD} VS $<T_e>$ is shown with results of other previous experiments. Progress of the current drive efficiency due to the higher performance of plasma parameters based on the scaling of Eq.(1) and further development of the efficiency by the introduction of the multi-junction launcher are clearly seen in the figure. The maximum value of $3.4\times10^{19}m^{-2}A/W$ is achieved and is almost 2 times higher than the results of other machines. It is said that the value approaches significantly to the required one in the reactor.

New scaling for the current dive efficiency with the combination of Eq.(1) and recent experimental results corresponding to Eq.(2) is written as

$$\eta_{CD} \approx \frac{12}{Z_{eff}+5} <T_e> \frac{1}{N_1^2} \frac{1-N_1^2/N_2^2}{\ln(N_2/N_1)} \frac{P_{ACC}}{P_{LH}} \quad . \qquad (3)$$

We must be careful in the usage of Eq. (3) in higher $<T_e>$ than 5 keV, since Eq. (2) predicts the theoretical maximum of LHCD efficiency is $7\sim10\times10^{19}m^{-2}A/W$. So the η_{CD} saturates at high temperature. But Eq. (3) predicts hope to achieve the required value ($>5\times10^{19}m^{-2}A/W$) in the steady state tokamak reactor.

3. Enlargement of the Current Drive Product

Large current drive is another key for the steady state tokamak reactor. Resistive force against the non-inductive current in tokamaks is collision of current carriers along the

distance of the torus ($2\pi R$). Therefore, the index to measure the quantity of the non-inductive current drive is identified by

$$CDP \equiv \bar{n}_e R_p I_{RF} \tag{4}$$

which we call " current dive product "(*CDP*). The next generation tokamaks of FER and ITER require the value of ~$500\times10^{19}m^{-2}MA$, while the values were ~$1\times10^{19}m^{-2}MA$ in the maximum in the previous non-inductive current drive experiments. In JT-60, early experiment with the conventional LHCD launcher with ~1.5MW achieved the value of $1.5\times10^{19}m^{-2}MA$. In the lower X-point divertor plasma, up to $5\times10^{19}m^{-2}MA$ was obtained by the power up and improvement of efficiency. In the recent experiment, two LHCD launchers were available because of the introduction of the multi-junction launcher. The maximum LHCD power of 4.5MW with improved $N_{\parallel}$ spectrum was injected into JT-60 plasma and produced the maximum value of $12.5\times10^{19}m^{-2}MA$ as seen in Fig.2. The enlargement of the *CDP* by a factor of ~10 compared with those in other LHCD experiments have been achieved. This value is also larger than those of recent NBCD experiments in large tokamaks like DIII-D, TFTR and JET as seen in the figure. It must be noted the value of NBCD include the effect of bootstrap current and therefore the net *CDP* due to NBCD is far lower than that in the figure.

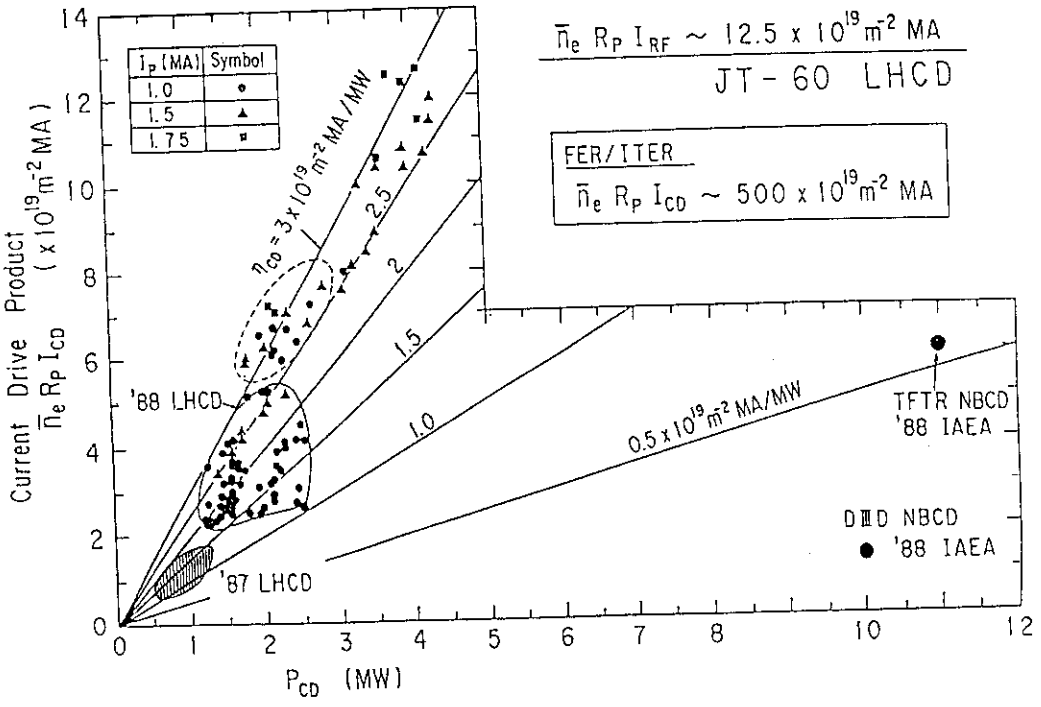

Fig. 2 Development of the current drive product *CDP* in JT-60.

One of the problems in the large current drive is hot spot caused by the intense high energy electrons which carry the large amount of currents. The key factor of successful enlargement of the current drive product in JT-60 is an employment of the divertor configuration in the current drive experiments. A carbon bloom due to the hot spot easily occur in the limiter discharge and the current drive efficiency is low. The details of the impurities during the LHCD is described in the section 2.14. The success of divertor configuration in LHCD experiments suggests that the control of the high energy electron is very important to reduce the hot spot. Presence of the high energy electrons plays a key role in causing the hot spot, since the threshold power of the carbon boom (hot spot) in the LHCD experiments is around 5 MW for 1sec., which is far lower than that in NBI heating. Study of the plasma -wall interaction under the presence of the high energy electrons as well as the enlargement of the *CDP* and the improvement of η_{CD} are extremely important to apply the LHCD in large scale like FER and ITER.

4. Conclusion

Remarkable improvement of the current drive efficiency by the improved performance of plasma parameters and the optimization of the $N_{\parallel}$ spectrum with the introduction of the multi-junction launcher was obtained and the maximum value of current drive efficiency reached up to $3.4 \times 10^{19} m^{-2} A/W$, which is 2 times larger than previous results in other tokamaks. High power LHCD with two LHCD launchers in the divertor discharge enabled the maximum current drive product of $12.5 \times 10^{19} m^{-2} A/W$, which is 10 times larger than those of other experiments. Experimentally obtained scaling for current drive predicts hopeful prospects to achieve the required values of both current drive efficiency and current drive product. But careful treatment will be required to avoid the hot spot in the next generation tokamaks.

References

[1] T. Yamamoto, T. Imai, M. Shimada, et al., Phys. Rev. Lett. **45** (1980) 716.
[2] S. Bernabei, C. Daughney, P. Efithimion et al., Phys. Rev. Lett. **49** (1982) 1255.
[3] T. Maekawa, T. Saito, M. Nakamura, et al., Phys. Letts. **85A** (1981) 339.
[4] M. Porkolab, J. J. Schuss, B. Lloyd, et al., Phys. Rev. Lett. **53** (1984) 450.
[5] F. Leuterer, F. X. Soldner, et al., Plasma Phys. and Controlled Fusion **27** (1985) 1399.
[6] T. Imai, K. Ushigusa, K. Sakamoto, et al., Nuclear Fusion **28** (1988) 1341.
[7] K. Ushigusa, T. Imai, Y. Ikeda, et al., Nuclear Fusion **29** (1989) 1052.
[8] Y. Ikeda, T. Imai, K. Ushigusa, et al., Nuclear Fusion **29** (1989) 1815.

2.3 Suppression of Sawtooth by Lower Hybrid Current Drive

O. Naito, K. Ushigusa, Y. Ikeda, T. Imai, K. Nagashima, Y. Koide

Introduction

The sawtooth oscillations commonly observed in tokamak discharges are considered harmless as long as power levels are low. In nowadays high power experiments, however, the sawtooth oscillations sometimes greatly modulate central electron temperature/core energy contents. Therefore suppression of sawtooth is an important issue in a core ignition regime. Experiments of suppressing sawtooth oscillation by lower hybrid wave have been carried out in several devices. The results can be classified into two groups; namely by flattening a current profile so that q(0) be above unity; or by some other mechanism involving such effect as of high energy particles with q(0) being less or equal than unity. In the ASDEX tokamak, a detailed measurement of current density profile j(r) has revealed that the sawtooth oscillations in Ohmic and NB heated discharges are suppressed by a global current flattening with the application of LHCD, although the sawtooth period increases with decreasing $N_{\parallel}$. In the PLT tokamak, continuous m=1 oscillations have been observed during sawtooth suppression by LHCD, suggesting an existence of q = 1 surface.

Experimental results

The effect of LH on sawtooth activity is shown in Fig. 1, where 4.6 MW of NB power is injected into a divertor discharge with q_{eff} = 3.2. In a discharge without LH (E8866), sawtooth already exists before the NB injection. Whereas in a discharge with LH (E8879), sawtooth is suppressed for 1.7 seconds by 2 MW of LH injection. The total radiation power and Z_{eff} value are nearly the same level in both cases, therefore an effect of impurity is not a cause of the difference in sawtooth activity. Figure 2 shows time evolutions of inversion radius for the above two cases. For comparison, Ohmic (E10103) and low LH power (E8873) cases are also shown. For Ohmic and NB only cases, inversion radius evolves almost the same way and begins less than 10 % of the minor radius. For the case with P_{LH} = 1 MW, the sawtooth starts at around 15 % of the minor radius, 0.75 seconds after the NB injection. The case with P_{LH} = 2 MW has even larger inversion radius ($r_s/a \sim 0.2$) at the beginning of sawtooth. This result implies that the central safety factor q(0) may be less than or equal to unity during sawtooth suppression by LHCD. Alternatively we have applied LHCD to a NB heated plasma as in Fig. 3. By an injection of LH, inversion radius shrinks and suddenly disappears around $r_s/a \sim 0.18$. After LH has turned off, sawtooth reappears near the disappeared point. Suppression of sawtooth by LHCD is also effective in a high

power NB heated discharge as is shown in Fig. 4, where sawtooth is suppressed for a second with P_{NB} = 18 MW. During the sawtooth free period, soft X-ray signal and ion temperature (Fig. 5) have peaked profiles. Therefore it is expected that a confinement in the central portion is improved during sawtooth free phase. Also peakedness of hard X-ray profile persists during sawtooth suppression as is seen in Fig. 6. The length of sawtooth suppression period Δt_{ST}, defined as the lag of the first sawtooth appearance behind the NB onset, increases with injected LH power as in Fig. 7. If the sawtooth is suppressed by a global current flattening, it is expected that a wave with higher $N_{\parallel}^{peak}$ is more effective in sawtooth suppression. Whereas the results shown in Fig. 8 exhibit an opposite tendency; the sawtooth suppression time Δt_{ST} has a maximum around $N_{\parallel}^{peak} \sim 1.3$ which corresponds to the maximum current drive efficiency. For even larger $N_{\parallel}$'s ($N_{\parallel}^{peak} > 1.9$), Δt_{ST} is no longer different from the case without LHCD. Which indicates that driving current in outer region is not effective in suppressing the sawtooth. In some discharges, noticeable fluctuations localized near the inversion radius are observed before the sawtooth crash as in Fig. 9. Most of these fluctuations consist of m =1 oscillations. There are also discharges with m = 1 oscillation during sawtooth free period. So there is a possibility of q(0) being less than or equal to unity. An indication of the effect of high energy electron (E > 200 keV) on the sawtooth activity is shown in Fig. 10, where Δt_{ST} is plotted against the central hard X-ray intensity $I_{HX}(0)$ before the NB injection. The plasma internal inductance before NB is constrained to l_i = 0.88 - 0.9. Those longest Δt_{ST} points are from low P_{NB} therefore low density discharges. As can be seen, Δt_{ST} is longer for larger $I_{HX}(0)$.

To summarize, the appearance of sawtooth at a finite minor radius and the existence of m = 1 oscillation suggest that q(0) may be less than or equal to unity during sawtooth suppression period. A better suppression efficiency for lower $N_{\parallel}$ also supports that sawtooth suppression mechanism in JT-60 is not likely to be by a global current flattening. From the correlation between Δt_{ST} and $I_{HX}(0)$, it is expected that local current profile modification by LHCD or existence of high energy electron may be possible keys to the sawtooth suppression mechanism.

References

[1] F.X. Söldner, K. McCormick, D. Eckhartt, et al., Phys. Rev. Lett. **57** (1986) 1137.

[2] T.K. Chu, R. Bell, S. Bernabei, et al., Nucl. Fusion **26** (1986) 666.

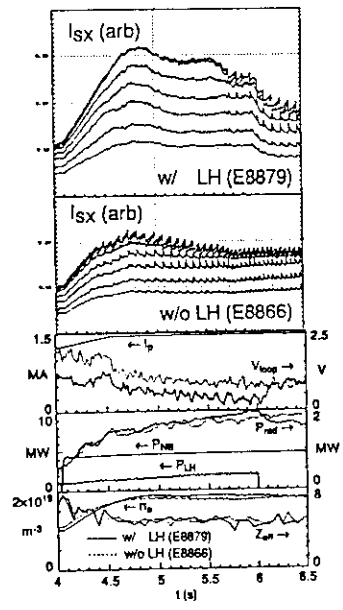

Fig. 1 Typical waveforms for sawtooth suppression by LH.

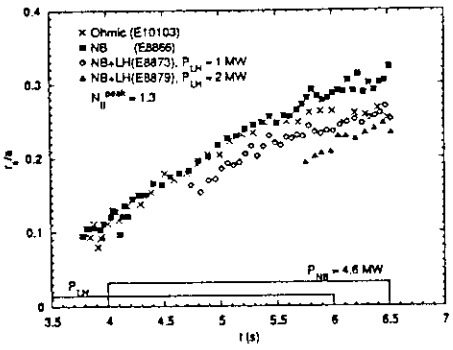

Fig. 2 Evolution of inversion radius for shots in Fig. 1.

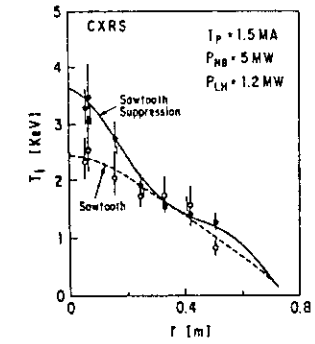

Fig. 5 Ion temperature profile peaks during sawtooth free period.

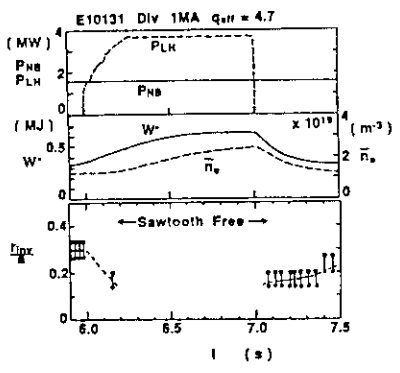

Fig. 3 A decrease in inversion radius is seen before the sawtooth is suppressed by LH.

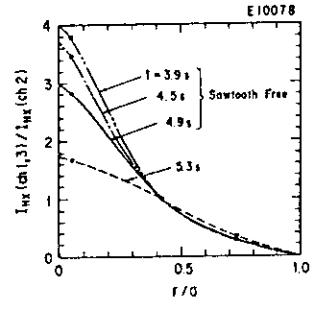

Fig. 6 Centrally peaked hard X-ray profile is observed during sawtooth free period.

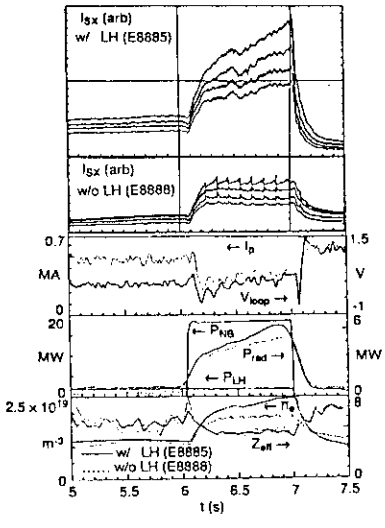

Fig. 4 Sawtooth in high power NB heated discharge can be suppressed with LH.

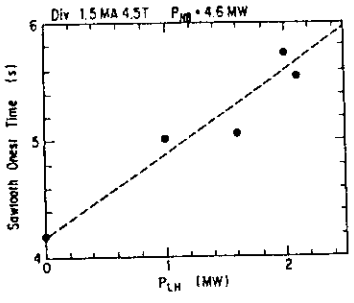

Fig. 7 Sawtooth suppression period as a function of LH power.

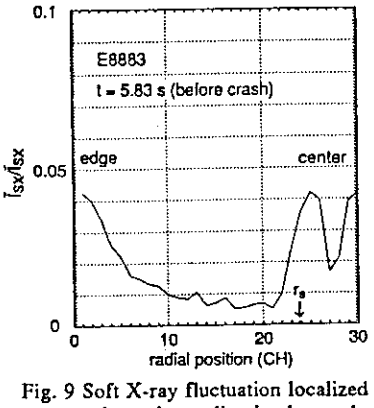

Fig. 9 Soft X-ray fluctuation localized near inversion radius is observed before sawtooth crash.

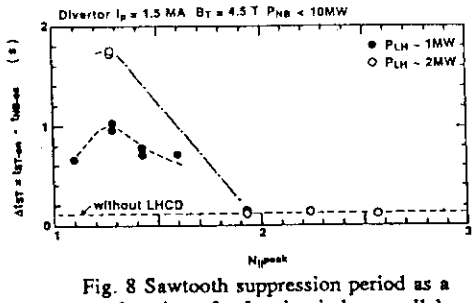

Fig. 8 Sawtooth suppression period as a function of refractive index parallel to the static field.

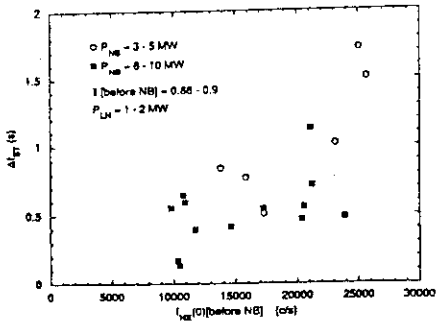

Fig. 10 Sawtooth suppression period as a function of central hard X-ray intensity before NB injection.

2.4 Hard X-ray Measurement during Current Profile Control Experiment by LHCD

K. Nagashima, T. Imai, K. Ushigusa, O. Naito and JT-60 team

In a series of lower hybrid current drive experiments, the injected power spectra of LHRF was scanned using the newly installed multi-junction launcher [1] ($N_{//}$ scan experiment). In the experiment, the plasma parameters were I_p=1.0 MA, B_t=4.0 T, n_e=0.8-1.0x10^{19} m^{-3}, P_{LH}=1.4-1.9 MW, hydrogen working gas and divertor configuration. The hard X-ray(HX) in the energy range of 50 keV to 1 MeV generated by the RF induced high energy electrons was measured by the 4 channel NaI(Tl) scintillation detectors in a perpendicular direction to the electron current. The measured HX energy spectrum was characterized by its intensity and declination, in which the latter corresponds to a temperature in a maxwellian distribution.

In the $N_{//}$ scan experiment, increasing $N_{//}$ of the injected RF spectrum the central HX intensity decreased and its spatial profile became broader. This indicates that the RF power was absorbed in the more peripheral region with increasing $N_{//}$ and that the current profile became broader with $N_{//}$, which was confirmed by the decreasing of plasma internal inductance l_i with $N_{//}$. The relation between the broadening of HX profile and the decreasing of l_i is shown in Fig.1. In a case of low $N_{//}$, plasma current was almost fully driven by the RF-induced electrons and the hard x-ray intensity I_{HX} was consistent with the relation of $I_{HX}(r) \propto j(r)\, n_e(r)$.

In addition to the HX intensity profile, the declination of the energy spectrum featured the RF-induced high energy electrons in the $N_{//}$ scan experiment as shown in Fig.2. It can be seen in Fig.3 that the declination becomes steeper with increasing $N_{//}$, and it corresponds to that the phase velocity of injected RF spectrum decreases with $N_{//}$. However, in LHCD the resonant electrons are driven in a parallel direction and the measured HX spectrum is in a perpendicular direction, so the declination of the energy spectrum does not reflect the RF-induced high energy tail directly [2]. To

estimate the relation between the measured energy spectrum(in a perpendicular direction) and the RF-induced diffusion in a electron velocity space, we used the 2-dimensinal fokker-planck analysis as follows [3],

$$\frac{\partial f}{\partial t} = D_{RF}\frac{\partial^2 f}{\partial v_{//}^2} + C(f,f) + \delta f_{other} \qquad (1)$$

where D_{RF}, $C(f,f)$ and δf_{other} represent the RF-induced diffusion coefficient, collision operator and the other source and sink term, respectively. In the analysis the last term in eq.(1) was neglected because in our simple estimation we considered that electrons were driven in a parallel directon by LHRF and the collision spreads them over in a velocity space. And the measured HX energy spectrum is written approximately by

$$\left(\frac{dS}{dk}\right)_{det} \approx \varepsilon_d \int dl\ Z_{eff} n_e^2 k \frac{d\langle\sigma v\rangle}{dk} \qquad (2)$$

where ε_d, Z_{eff} and n_e are detector efficiency, effective ionic charge and electron density, respectively. $d<\sigma v>/dk$ represents the differential cross section averaged over the calculated distribution function. The calculated declination of energy spectrum in the energy range of 100 to 300 keV are also shown in Fig.3, which is sensitive only to the injected RF spectrum. The dependence on $N_{//}$ is in agreement between the measured and calculated values. However, the latters are larger than the formers both in the two calculated cases, perhaps because of the inaccuracy of RF-induced diffusion coefficient or the considerable sink term(the last term in eq.(1)) in the large pitch angle space.

References

[1] IKEDA, Y., et al., Nucl. Fusion 29 (1989) 1815

[2] Von GOELER, S., et al., Rev. Sci. Instrum. 57 (1986) 2130
[3] FISCH, N. J., Reviews of Modern Physics 59 (1987) 175

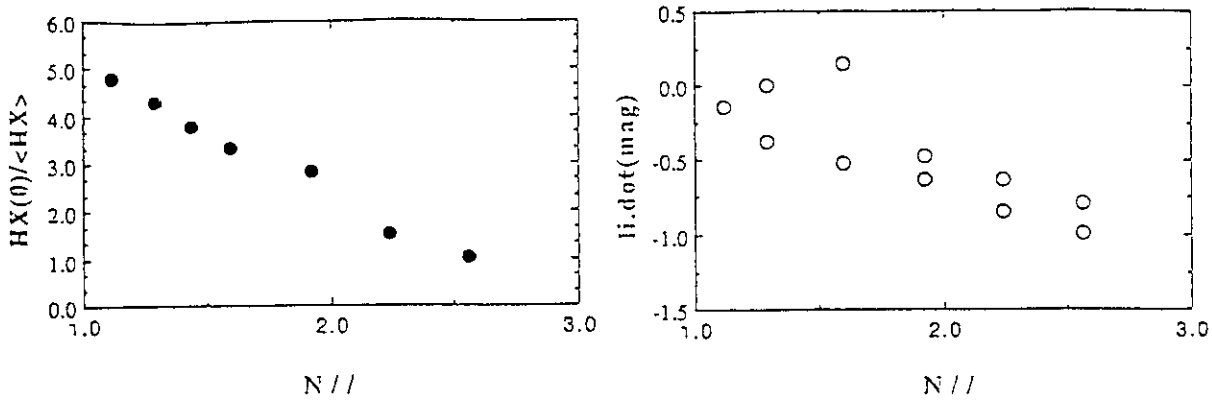

Fig.1 $N_{//}$ dependences of the hard x-ray profile peaking factor $I_{HX}(r=0)/<I_{HX}>$ and the time derivative of plasma internal inductance l_i.

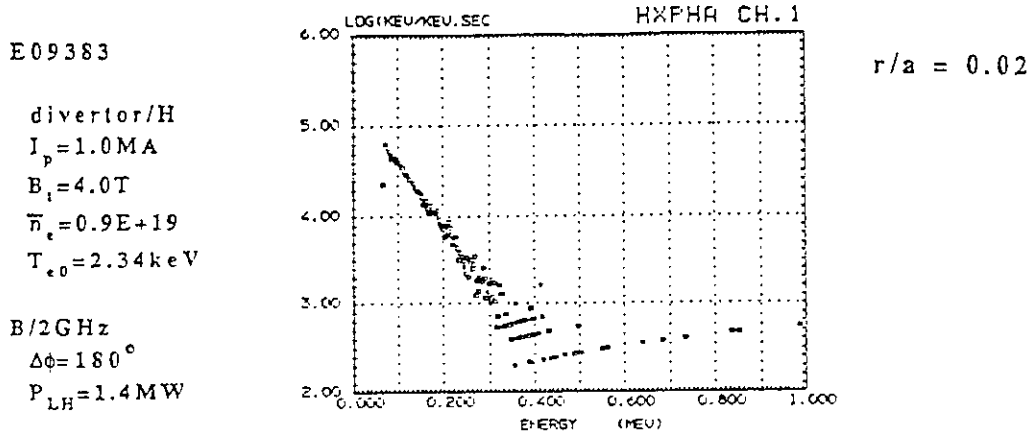

Fig.2 Typical hard x-ray energy spectra measured in the lower hybrid current drive discharge.

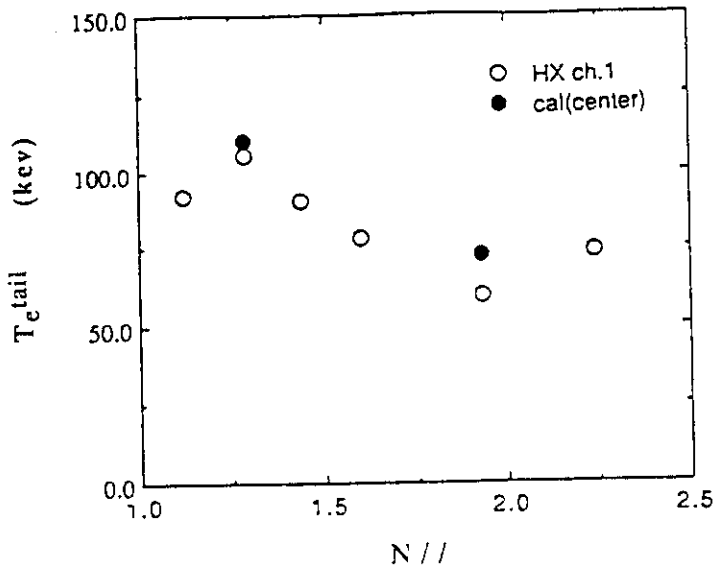

Fig.3 The measured and calculated declinations of hard x-ray energy spectrum(T_e^{tail}) in the energy range of 100 to 300 keV.

2.5 Energy Confinement in Lower Hybrid Current Drive Plasmas

K. Ushigusa, T. Imai, O. Naito, Y. Ikeda and the JT-60 Team

1. Introduction

A study of energy confinement property in non-inductively current driven (CD) tokamak is very important because a steady state operation of tokamak reactor requires the non-inductive current drivers. The lower hybrid current drive (LHCD) is one of the most promising method to drive plasma current non-inductively. Therefore, the energy confinement in LHCD plasmas should be studied to estimate the energy confinement property of future steady state tokamak reactor.

The energy confinement in LHCD plasmas has been studied in small and medium size tokamaks. In ASDEX [1], the diamagnetically deduced confinement time was improved with respect to Ohmic discharges. In ALCATOR-C, the thermal energy confinement time of LHCD plasmas did not depend on the electron density[2], and a deterioration of the total energy confinement time, which includes the contribution of the electron tail energy, relative to the Ohmic confinement time was observed[3] This deterioration was similar in magnitude to that predicted by Kaye-Goldston scaling.

This paper presents the energy confinement study of high power LHCD plasmas in JT-60 divertor configuration ($R_p \sim 3.16$ m, $a_p \sim 0.7$ m) with the parameter range $\bar{n}_e = (0.8 - 3.2) \times 10^{19}$ m^{-3}, $I_p = 1.0 - 1.75$ MA, $B_T = 4.0 - 4.5$ T, $P_{LH} < 4.5$ MW, f = 2.0 GHz. For the high power LHCD experiments, two launchers were employed. One of the two launchers consists of 8x4 waveguides array (the conventional launcher) and excites waves of the parallel wave refractive index $N_{\|}^{peak} \sim 1.7$ with the adjacent phase difference of $\Delta\phi = 90°$ at 2GHz. Another launcher is a multijunction type and excites waves of typically $N_{\|}^{peak} \sim 1.45$ with the high directivity and the sharp spectrum.

2. Results

Typical example of LHCD discharge is shown in Fig.1(a), where the RF input power of ~ 2.2MW and ~ 1.2MW are injected by the multijunction and the conventional launchers, respectively. The total power of ~ 3.4MW gives the current drive product of ~9.4 x 10^{19} m^{-2}MA with a correction of the change in the plasma internal inductance. At t = 6.5s, where almost all plasma current is driven by the LH power, the diamagnetic energy content is $W^* \sim 0.55$MJ with the line averaged density $\bar{n}_e \sim 2.1 \times 10^{19}$ m^{-3}. The electron temperature and the density profiles measured with Thomson scattering at t = 6.5s are shown in Fig. 1(b). At this time, the visible Bremsstrahlung signal and the Doppler broadening of titanium have indicated that $Z_{eff} \sim 4$ and $T_i(0) \sim 3.5 \pm 1.0$ keV, respectively. These data indicates that the thermal electron energy content is $W_e \sim 0.41$MJ and the ion energy is $W_i \sim 0.13$MJ, where we assume that the ion pressure has the same profile as the electron pressure. The estimated kinetic energy

content agrees with the diamagnetically measured energy in this case. However, the kinetic energy content has a large error bar (typically ± 20%) and this error is mainly due to the error of the Thomson scattering.The energy confinement time at LHCD phase (at t = 6.9 s) is $\tau_E \sim 0.17$ s with $\bar{n}_e \sim 2.5 \times 10^{19}$ m^{-3}, while the OH confinement time at the same density is ~ 0.4 s.

Figure 2(a) shows the density dependence of the diamagnetically estimated confinement time τ_E^{dia} for 1MA divertor discharges, where open and solid circles show OH plasmas and LHCD plasmas, respectively. The confinement time of LHCD plasmas is roughly constant against the electron density, while the OH confinement time increases with the density. The energy confinement time of 1MA LHCD plasmas is almost the same as that of the OH plasmas at the low density regime ($\bar{n}_e \sim 1 \times 10^{19}$ m^{-3}). The multijunction launcher excites low $N_\parallel$ waves with a narrow spectrum ($N_\parallel$ = 1-1.9). Therefore, the wave power excited by the multijunction launcher tends to be affected by the accessibility condition at the high density regime. At $\bar{n}_e \sim 3 \times 10^{19}$ m^{-3}, the accessibility condition is $N_\parallel^{acc} \sim 1.35$ with f = 2.0GHz and B_T = 4T and ~70% of the wave power excited by the multijunction launcher satisfy the accessibility condition. If we use the accessible power as the absorption power, the energy confinement time at $\bar{n}_e \sim 3 \times 10^{19}$ m^{-3} is almost the same as that at $\bar{n}_e \sim 0.8 \times 10^{19}$ m^{-3}. Figure 2(b) shows the density dependence of the ratio of the increase in β_p^{equ} and β_p^{dia} at the first 0.3s of onset of LHCD power, where we assume that the internal inductance does not change for a first 0.3 s. At $\bar{n}_e \sim 1 \times 10^{19}$m^{-3}, a significant pressure anisotropy ($\Delta\beta_p^{equ} / \Delta\beta_p^{dia} > 2.0$) is observed. In these low density regime, the total energy confinement time $\tau_E^{tot} = (W_{OH} + 2\,(\Delta W^{equ} + \Delta W^*/2\,)\,/\,3\,)\,/\,P_{LH}$ becomes $\tau_E^{tot} = (1.1\text{-}1.2)\,\tau_E^{dia}$.

The power dependence of W* is shown in Fig. 3 for several plasma currents where closed and open symbols are the LHCD cases and the neutral beam (NB) heating cases, respectively. In the heating power $P_{abs} = P_{OH} + P_{LH} + P_{NB}^{abs}$, we use the torus input power P_{LH} for the LH power and the absorbed NB power P_{NB}^{abs} in which the shine through and the reionization losses are subtracted from the input power. For the LHCD cases, the Ohmic power is almost negligible ($P_{OH}/P_{abs} \ll 1$). The operating density is almost the same regime for both NB heating cases ($\bar{n}_e \sim 1.5 - 4.0 \times 10^{19}$ m^{-3}) and LHCD cases ($\bar{n}_e \sim 0.8 - 3.2 \times 10^{19}$ m^{-3}) and increases with the heating power. It is found that the confinement time of 1MA LHCD plasmas is higher than that of the NB heated plasmas at the same power level. At I_p = 1.5MA, the LHCD plasma has almost the same confinement time as NB heated plasma with P_{abs} < 5MW. In the NB heated plasmas, the energy content increases offset linearly with the absorption power and the incremental confinement time is around 55-60 ms independently of the plasma current . The current dependence of the energy content in NB heated plasmas comes from the difference of the offset stored energy and it is originally the OH confinement

characteristics. The diamagnetic energy content in LHCD plasmas does not depend on the plasma current as shown in Fig.4 and depends only on the CD power (or, equivalently, the density). This seems to be a quite different aspect from the usual L-mode scaling. The effect of the offset stored energy, which is the OH confinement characteristics, and the dependence of the plasma current on the energy content disappear in the non-inductively current driven plasmas because of no Ohmic heating power. In Fig. 3, the confinement time decreases with the LHCD power ($\tau_E^{dia} \propto P_{abs}^{-0.32}$). The LHCD power is not independent of the density and the current in LHCD plasma; $P_{abs} = P_{LH} \propto \bar{n}_e I_p$. Therefore, this power dependence of the confinement time is roughly equivalent to the density dependence of the confinement time. In Fig. 2, $\tau_E^{dia} \propto \bar{n}_e^{-0.19}$ for 1MA LHCD plasmas. For LHCD data of all current, the experimentally observed confinement time can be fitted as $\tau_E^{dia} \propto \bar{n}_e^{-0.3}$. When we write the confinement time as $\tau_E \propto P^{\alpha} \bar{n}_e^{\beta}$ in LHCD plasmas, observed data indicate $\alpha + \beta \sim -0.3$. If the power degradation of energy confinement time is similar to the Goldston scaling ($\alpha = -0.5$), observed data suggest that the density dependence of τ_E is weak ($\alpha \sim 0.2$). The incremental confinement time of LHCD plasmas, here we define $\tau_E^{INC}(LHCD) \equiv dW^*/dP_{abs}$, is around 0.1 s, and this value is almost twice of that for NB heating and does no depend on the plasma current.

Figure 4 shows the comparison of the electron temperature and the density profiles for the LHCD plasmas at I_p = 1MA ($\bar{n}_e \sim 2 \times 10^{19}$ m^{-3}) and 1.5MA ($\bar{n}_e \sim 1.5 \times 10^{19}$ m^{-3}) with the same LHCD power (P_{LH} = 2MW). The diamagnetic stored energy is W* ~ 0.48MJ and 0.45MJ for 1 MA case and 1.5MA case, respectively. The electron temperature for the 1.5MA case has a peaked profile compared with the 1MA case, while the density for both cases is almost the same profile. The electron thermal energy is We ~ 0.23MJ and 0.24MJ for 1 MA case and 1.5MA case, respectively, and they are almost the same value. The electron thermal energy for LHCD plasmas depends only on the power or the density and does not depend on the plasma current similarly to the diamagnetically measured energy.

3. Summary

In conclusion, it is shown that the confinement property of the LHCD plasmas has a different aspect from usual L-mode scaling. The low current LHCD plasma has a longer confinement time than the NB heated plasma. The confinement time depends on the LHCD power and the density, however, it is independent of the plasma current.

References

[1] SÖLDNER,F.X., et al., in Controlled Fusion and Plasma Physics (Proc. 12th Europ. Conf., Budapest, 1985), Vol.9F, Part II, (1985) 244.

[2] KNOWLTON, S., et al., Phys. Review Letters 57 (1986) 587.

[3] TAKASE, Y., et al., Nucl. Fusion 27(1987)53.

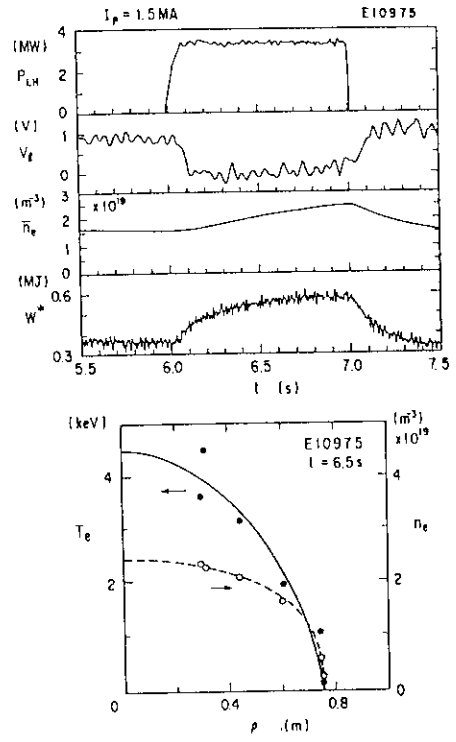

Fig.1 (a); Typical example of LHCD discharge with B_T = 4.5T.
(b); The electron temperature and the density profile at t = 6.5 s.

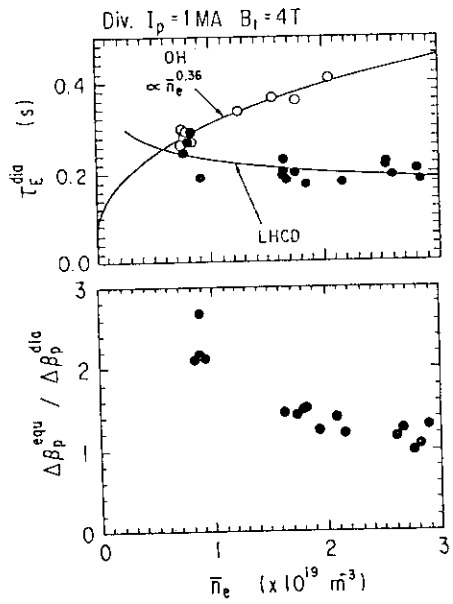

Fig.2 The density dependence of τ_E^{dia} and the pressure anisotropy $\Delta\beta_p^{equ} / \Delta\beta_p^{dia}$. The LH power is injected by the multijunction launcher alone.

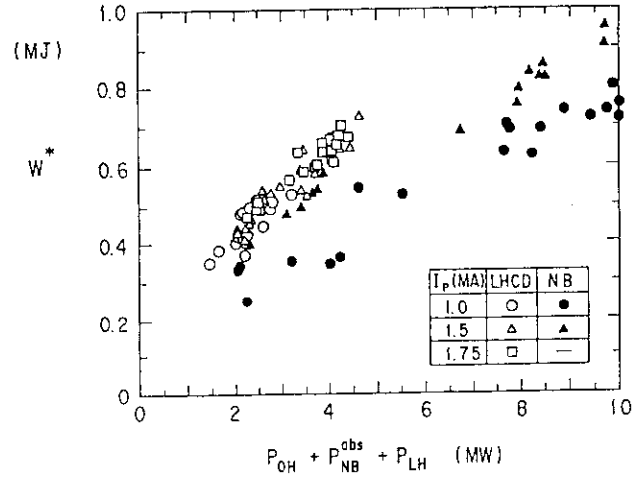

Fig.3 Diamagnetic Energy W* as a function of the heating power P_{abs}.

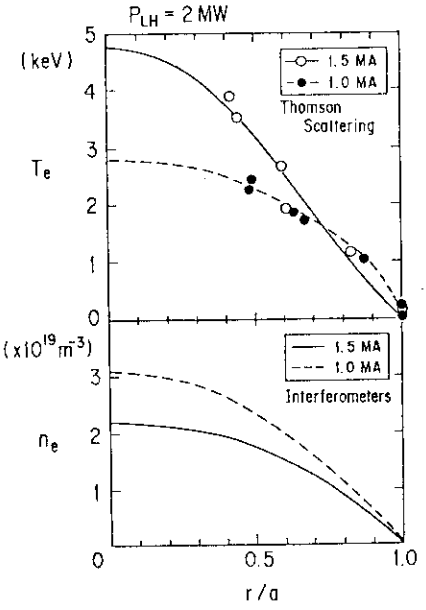

Fig. 4 The electron temperature and density profile for LHCD plasmas with $N_{//}^{peak} \sim 1.45$.
Solid line; 1.5MA, 4.5 T and $\bar{n}_e = 1.5 \times 10^{19}$ m^{-3}.
Broken line ; 1MA, 4.0 T and $\bar{n}_e = 2 \times 10^{19}$ m^{-3}.

2.6 Volt-Second Saving by Lower Hybrid Current Drive

O. Naito, K. Ushigusa, Y. Ikeda, T. Imai, H. Kimura

Abstract

The volt-second consumption of the Ohmic primary circuit is reduced by lower hybrid (LH) current drive (CD) during the current rise phase. Most of the LH power is consumed in compensating the resistive voltage typically 0.8 V. Up to 2.5 V·s of flux is saved by 2 MW × 2.5 s of LH injection which could be projected to several tens of volt-seconds in ITER class reactors. In most cases, LH assisted current ramp-up can safely passes through $q_a = 3$ without causing any disastrous MHD instabilities leading to major disruption.

The estimation of volt-second consumption and the means of its saving is a crucial issue in designing the poloidal field system in a large tokamak. In the Ohmic discharges, the volt-seconds are generally saved by the optimization of the current ramp-up rate and density. Besides these operational means, the volt-seconds can be saved either by current drive or auxiliary heating with external tools. These, at the same time, may reduce the complexity of the poloidal field system and widen the operational margin. The volt-second analyses of the Ohmic discharges are performed either with the axial method [1] or the Poynting method [2]. Here we follow basically the Poynting formalism. The JT-60 tokamak has three LH launchers; two of which are designed for current drive and used in the volt-second saving experiments [3,4]. In divertor discharges, up to 2.5 V·s of volt-seconds are saved with 2 MW × 2.5 s of LH injection during current rise phase.

Typical waveforms of one turn voltage, Ohmic primary coil current I_F, plasma current I_p and LH power P_{LH} are shown in Fig. 1. The plasma current is raised from 0.7 to 1.4 MA in 2 seconds where 1.6 MW of LH is injected with parallel refractive index of $N_{||}^{peak} = 1.45$. The one turn voltage is reduced from 1.8 to 0.9 V and the ramping rate of the primary coil current necessary for rising plasma current is reduced by $\delta I_F = 6.36$ kA/s which corresponds to 1.76 V·s of flux saving during two seconds of LH injection. This could be extrapolated to more than 40 V·s of volt-second saving in ITER operation scenario where 20 MA of plasma current is raised in ~ 50 seconds [5].

Using the plasma internal inductance L_i , the inductive voltage is estimated as $I_p^{-1} \cdot d/dt(L_i I_p^2/2)$. Then the resistive voltage is evaluated as the difference between the surface voltage and the inductive voltage. For discharge without LH, the resistive voltage is typically 0.8 V and is roughly constant during current rise phase. With LH injection, the resistive voltage drops to ~ 0 V while the inductive portion being almost unchanged. Which means that the LH power is consumed mainly for compensating the resistive voltage. Time evolutions of the plasma surface flux change $\Delta\phi_{sur}$ and the inductive component $\Delta\phi_{ind}$ relative to the values at t = 2 s are shown in Fig. 2 for Ohmic and LH assisted cases. The inductive portion is almost the same in both cases except that $\Delta\phi_{ind}$ tends to be a little lower for the LH assisted case in the later phase of current ramp-up, which is probably due to the slight broadening of the current profile by LHCD. Thus we can expect that the difference in the surface flux change ($\Delta\phi_{sur}^{OH} - \Delta\phi_{sur}^{LH}$) mainly comes from the resistive volt-seconds saved by LH waves.

On applying LH, a certain portion of the Ohmic induced current $\delta I_{OH} = M_{pF} \delta I_F / r_p$ is replaced by RF driven current $\delta I_{RF} = \eta_{CD} P_{LH} / n_e R_p$ where M_{pF}, r_p, η_{CD}, n_e

and R_p are respectively the plasma-Ohmic-primary-coil mutual inductance, plasma resistance, current drive efficiency, electron density and major radius. Equating these currents and integrating over the LH injection period gives a rough estimate of volt-seconds saved by LH:

$$\Delta\phi_F \approx \frac{r_p \eta_{CD}}{R_p} \int \frac{P_{LH}}{n_e} dt \equiv 2\pi\rho_p \eta_{CD} \int \frac{P_{LH}}{n_e} dt$$

where $\Delta\phi_F = \int M_{pF} \delta\dot{I}_F \, dt$ is the saved volt-seconds and $\rho_p \equiv r_p / 2\pi R_p$ is the plasma resistance for unit length. And it is assumed that the product $\rho_p \eta_{CD}$ is a weak function of electron temperature, since previous results show that $\eta_{CD} \propto T_e$ [6] and $\rho_p \propto T_e^{-3/2}$. Figure 3 shows $\Delta\phi_F$ as a function of $\int P_{LH} / n_e \, dt$ for some current ramp-up rates where most of the discharges are performed with $N_{\parallel}^{peak} = 1.3$ or 1.45. The saved volt-seconds increase linearly with the time integral of LH power density: $\Delta\phi_F = 0.55 \times 10^{19} \int P_{LH} / n_e \, dt$. And the efficiency of flux saving varies not so much with current ramp-up rates. Employing typical values of the parameters $r_p \lesssim 2\ \mu\Omega$, $\eta_{CD} \gtrsim 1.5 \times 10^{19}$ A W^{-1} m^{-2} and $R_p \sim 3$ m, the coefficient $\rho_p \eta_{CD}$ has a value around 10^{19} V·s m^{-3} / MJ which is roughly consistent with the experimental results.

Another point in applying LH to volt-second saving is the stability of discharge to the MHD modes. The stabilization of m=2 tearing mode in LH current driven discharges has been previously reported on the Petula-B tokamak, where the current density profile has been flattened within q=1 surface by LHCD [7]. In high current shots of JT-60, discharges are often terminated with major disruption caused by the large m=3 locked mode when the safety factor passes through three [8], although this locked mode can be avoided by a certain amount of neutral beam heating power. The relative amplitude of m=3 poloidal magnetic field component $\delta B_\theta / B_\theta$ in discharges with $q_a = 2.8$ - 3.2 and $\dot{I}_p = 0.32$ - 0.44 MA/s is 1.44±0.54 % for the case without LH whereas 0.97±0.77 % for LH assisted case. Thus the assistance of LH does no harm to the MHD stability, at least to m=3 locked mode. In fact, in a series of high current limiter discharges, LH assisted shots suffer less disruption caused by m=3 locked mode than Ohmic shots.

To summarize, up to 2.5 V·s of flux is saved by the assistance of LH in current rise phase. The saved volt-second increases linearly with $\int P_{LH} / n_e \, dt$ where the LH power is mainly consumed in compensating the resistive volt-seconds. In most cases LH assisted discharge can safely pass through q_a=3 without causing any harmful MHD instabilities.

REFERENCES

[1] R.J. HAWRYLUK, K. BOL, D. JOHNSON, Nucl. Fusion **19** (1979) 1519.

[2] S. EJIMA, R.W. CALLIS, J.L. LUXON, et al., Nucl. Fusion **22** (1982) 1313.

[3] T. IMAI, K. USHIGUSA, K. SAKAMOTO, et al., Nucl. Fusion **28** (1988) 1341.

[4] Y. IKEDA, T. IMAI, K. USHIGUSA, et al., Nucl. Fusion **29** (1989) 1815.

[5] ITER CONCEPT DEFINITION, Vol. 2, IAEA, Vienna (1989) 31.
O. NAITO, K. USHIGUSA, Y. IKEDA,. et al., submitted to Nucl. Fusion.

[6] K. USHIGUSA, T. IMAI, Y. IKEDA, et al., Nucl. Fusion **29** (1989) 1052.

[7] D. VAN HOUTTE, G. BRIFFOD, P. CHABERT, et al., Nucl. Fusion **24** (1984) 1485.

[8] H. NINOMIYA, K. ITAMI, Y. NEYATANI, et al., Nucl. Fusion **28** (1988) 1275.

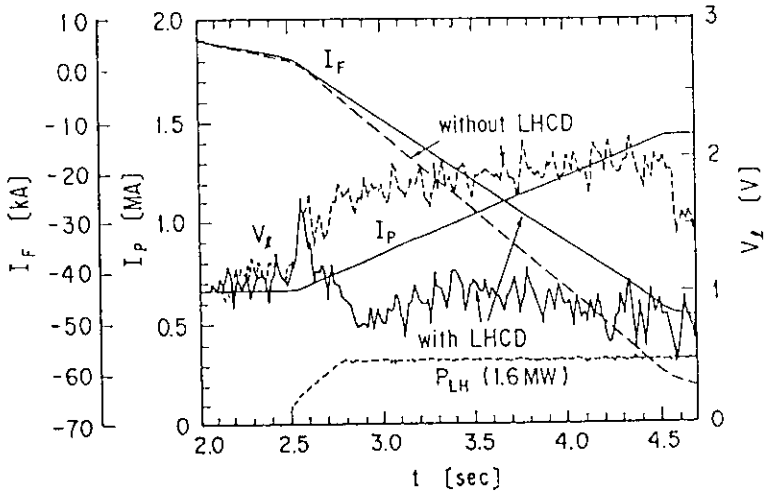

Fig. 1 Typical waveforms of Ohmic primary coil current I_F, one turn voltage V_l, plasma current I_p and LH power P_{LH} in LH assisted current rise.

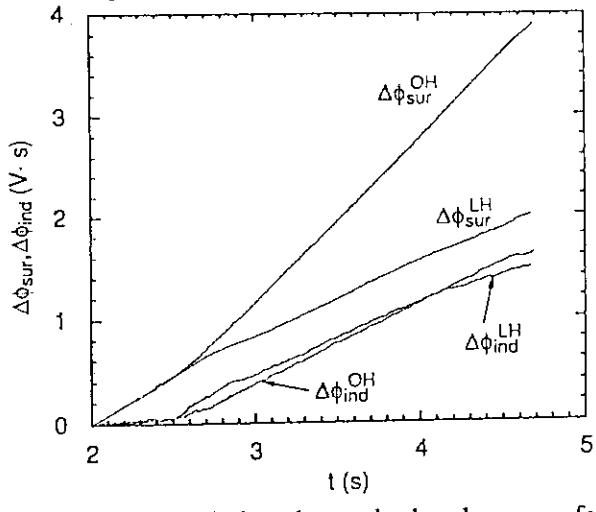

Fig. 2 Time evolution of the relative change in the plasma surface flux $\Delta\phi_{sur}$ and the inductive component $\Delta\phi_{ind}$ for Ohmic and LH assisted cases.

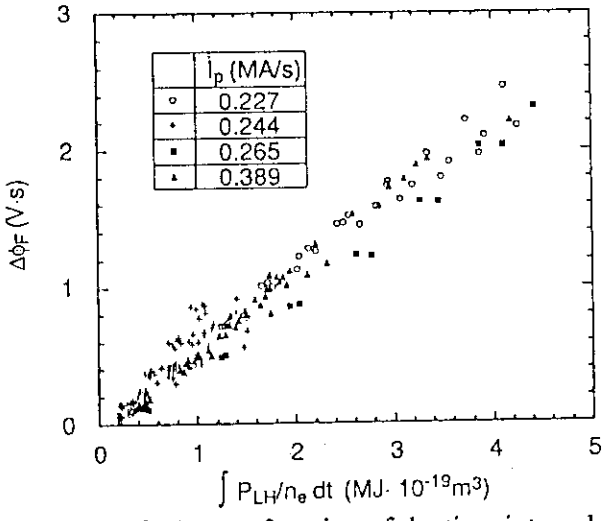

Fig. 3 Saved volt-second $\Delta\phi_F$ as a function of the time integral of LH power density $\int P_{LH} / n_e\, dt$.

2.7 Current Ramp-up by Lower Hybrid Wave

O. Naito, K. Ushigusa, T. Imai, Y. Ikeda

Driving noninductive current with some means is essential to the achievement of steady state tokamak reactor. Even though the complete elimination of Ohmic circuit requires sufficiently high current ramp-up and current drive efficiencies, it is still useful in reducing the volt-second requirement for Ohmic circuit. Experiments of ramping up plasma current with the assistance of lower hybrid wave has been reported in PLT [1] and Alcator C [2]. A demonstration of ramp-up in a large tokamak is presented here.

In this experiment, the plasma current is initiated by the Ohmic circuit. After initiation, the Ohmic primary coil current has been kept at a constant value so that no inductive power is supplied by the Ohmic circuit. Then the lower hybrid waves are injected with various relative waveguide phasings ($\Delta\phi$) using mainly the multijunction launcher. Typical ramp-up discharges for different phasings are shown in Fig. 1. In the case without LH injection, the plasma current decays with a constant rate after the Ohmic circuit is decoupled. For the case with $\Delta\phi = 210°$ ($N_{||}^{peak}$=2.2), although the absolute rate is much smaller than the former, I_p still decays. As the $\Delta\phi$ is lowered, however, the plasma current starts to ramp up.

Figure 2 shows the current ramp-up efficiency as a function of $N_{||}^{peak}$. The current ramp-up efficiency η_{ramp} is defined as the ratio of the power input to poloidal field (subtracting the external inductive power input from equilibrium field circuit) to the injected LH power [2]. As is seen, LH-to-poloidal-field energy conversion is most efficient around $N_{||}^{peak}$ = 1.3 - 1.5, which coincides the $N_{||}^{peak}$-value for the best current drive efficiency η_{CD}. The ramp-up experiment has been also carried out after the titanium gettering experiment. After gettering, the density during current ramp-up has been reduced and the current ramp-up rate has slightly increased. However, the resultant ramp-up efficiency has roughly the same value as that before Ti gettering.

The dependence of η_{ramp} on a line average density is shown in Fig. 3. For fixed phasing angle, η_{ramp} is a decreasing function of density. Although the current ramp-up is still effective at $n_e = 1.3 \times 10^{19}$ m^{-3}, low density regime with $n_e < 0.5 \times 10^{19}$ m^{-3} is most efficient.

Figure 4 shows the conversion efficiency of LH to electromagnetic energy as a function of normalized phase velocity v_{ph}/v_r where v_r is the runaway velocity and P_{el} is the total electromagnetic input from LH (including resistive loss and subtracting external input from equilibrium field circuit). The solid curve is the value of Fisch-Karney theory [3]. The data in $v_{ph}/v_r > 1$ are those obtained after Ti gettering. The experimental results and the theory are roughly consistent, although the conversion efficiencies in $0 < v_{ph}/v_r < 1$ are slightly higher than the theoretical prediction.

In some shots, the current ramp-up rate suddenly decreases when the stored energy begins to increase. In this case, an electron collides with and gives its energy to the background plasma rather than decelerated by and giving energy to the field. A definite condition for these phenomena to occur is, however, not yet clear.

Current ramp-up by lower hybrid (LH) current drive has been carried out in the JT-60 tokamak. Up to ~ 120 kA of plasma current is ramped up in 7 seconds with ~ 1.5 MW of LH injection. The efficiency of converting the lower hybrid energy to the poloidal field energy is typically 5 - 10 % depending on the wave refractive index $N_{||}^{peak}$ and density. The efficiency is better for smaller wave refractive index $N_{||}^{peak}$ and for lower density. The results are consistent with the theory of Fisch and Karney.

References

[1] F.C. Jobes, S. Bernabei, T.K. Chu, et al., Phys. Rev. Lett. **55** (1985) 1295.
[2] Y. Takase, S. Knowlton and M. Porkolab Phys. Fluids **30** (1987) 1169.
[3] N.J. Fisch and C.F.F. Karney, Phys. Rev. Lett. **54** (1985) 897.

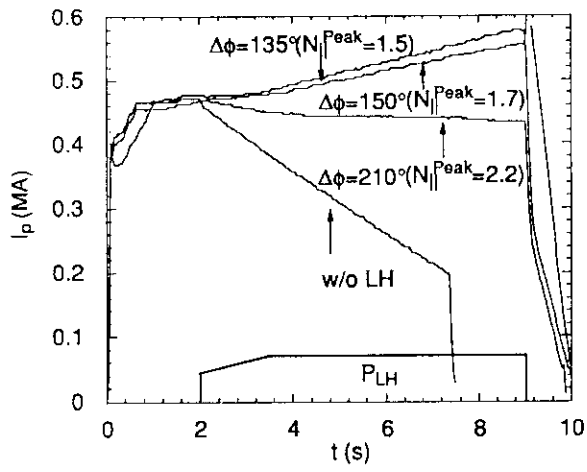

Fig. 1 Time evolution of plasma current for different phasings.

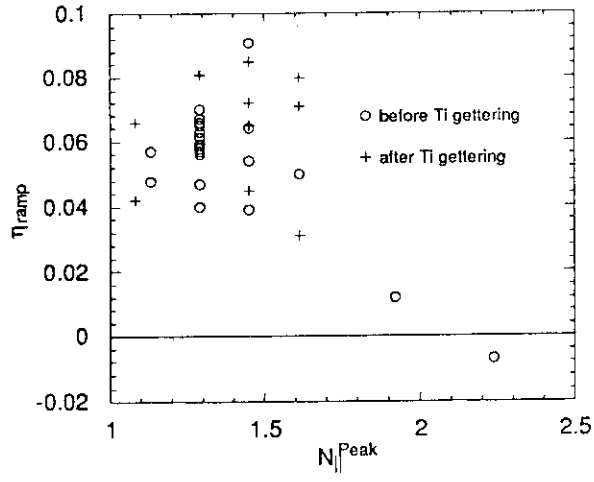

Fig. 2 Ramp-up efficiency as a function of wave refractive index.

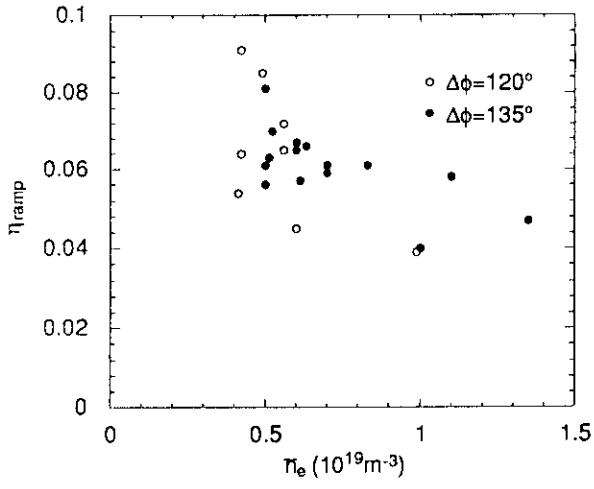

Fig.3 Ramp-up efficiency as a function of density.

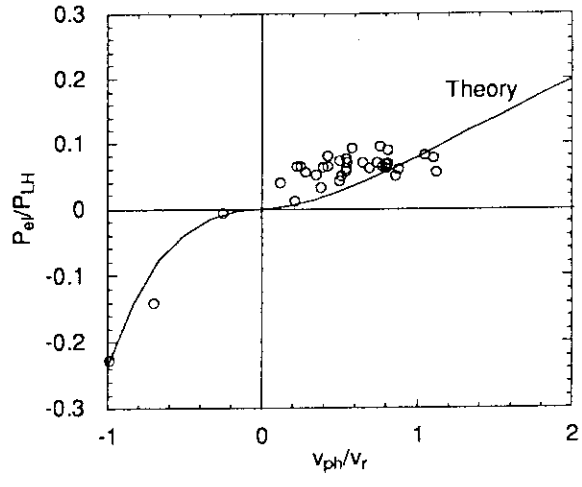

Fig. 4 Conversion efficiency of LH to electromagnetic energy as a function of normalized wave phase velocity.

2.8 Limiter H-Mode with Lower Hybrid Current Drive

S. Tsuji, K. Ushigusa, Y. Ikeda, T. Imai, K. Itami, M. Nemoto,
K. Nagashima, Y. Koide, Y. Kawano, T. Fukuda, T. Kondoh, M. Shimada,
H. Nakamura, O. Naito, H. Yoshida, T. Nishitani, H. Kubo, K. Tobita,
Y. Kusama, S. Ishida, M. Sato, N. Isei, T. Sugie, K. Uehara

1. Introduction

Since the discovery of a phase of improved confinement during neutral beam injection (NBI) heating, known as H mode, in the poloidal divertor configuration of ASDEX,[1] the H mode has been obtained with several heating schemes such as ion cyclotron resonance heating (ICRH),[2-4] a combination of NBI and electron cyclotron heating (ECH),[5] ECH,[6,7] and ohmic heating alone.[8] The H mode has also been realized in limiter discharges.[3,10,11] This paper reports the first observation of the H mode in limiter discharges with lower hybrid current drive (LHCD). The threshold LH power for the H-mode transition was about 1.2 MW with hydrogen plasmas.

In JT-60, the H mode was obtained in the outer or lower divertor configuration with NBI heating and combined heating with NBI + ICRH or NBI+LH.[12] The threshold heating power was about 16 MW. In contrast to the beam heated H mode with frequent edge localized modes (ELM) in the divertor configuration, the limiter H mode with LHCD produced ELM-free H phases longer than 3 sec.

2. Experimental observations

Typical plasmas of the present experiments had R = 3.04 m, a = 0.89 m, and nearly circular cross section which contacted inner bumper-type limiters. The gap between the outermost flux surface and the outside limiters was about 5 cm. Graphite first walls were conditioned by Taylor-type discharge cleaning. The plasma was developed from hydrogen gas at B_t = 4.5 T, and the plasma current was 1.5 MA resulting in $q_{sur} \sim 4.7$. The LH power was applied from two launchers; a conventional grill of 8(toroidal)×4(poloidal) and a multi-junction type of 24×4 phased array waveguides.[13,14] The launchers were located at the outer (low field) side of torus at a upward angle of 40° from the midplane. Most of the experiments were conducted with LH waves at two different frequencies of 1.74 GHz and 2.23 GHz from the multi-junction and conventional launchers, respectively. The phase differences between adjacent waveguides were 180° and 90°, the phasing of which provides high directivity for current drive. The peaks of the refractive index parallel to the magnetic field were about 2.1 and 1.5, respectively.

Typical traces of an H-mode discharge with LHCD are shown in Fig. 1. The LH power of about 1.4 MW was launched for three seconds. The gas feed was turned off just before the application of the LH pulse. The L-mode plasma of this discharge lasted for 0.7 sec before the first H transition was triggered at 5.76 sec. After repeated short H phases, the discharge entered a quiescent H phase at 6.2 sec. A sharp drop in H_α emission below the ohmic level was accompanied by increases in the plasma stored energy and in the line-averaged electron density. All H_α signals fell almost the same way as the H_α trace in the figure along a view chord just above the plasma-limiter interaction points. The low energy neutral flux levels decreased substantially as well. This behavior indicates a sudden improvement in the global particle confinement. On rough estimation, the improvement is by an order of magnitude since the electron density was nearly doubled with reduced particle recycling by a factor of about 5. The loop voltage increased gradually since the fraction of current driven by the LH waves was reduced due to the rise of the electron density. The impurity accumulation, which is often observed during ELM-free H phases, were so modest that the discharge reached a quasi-steady state. Although the dominant impurity ions were carbon, the carbon influx behaved almost the same way as hydrogen. The giant ELMs were accompanied by carbon influx as seen in the CVI^{edge} trace.

The formation of electron temperature pedestal was confirmed by filtering of soft x-ray emission near the edge with Be foils of 250-μm and 25-μm thickness; sharp rises in the ratio of the two signals were detected at the H transitions as shown in the second box from bottom of Fig. 1. The T_e profile measured by a 8-point Thomson scattering system remained almost the same both in magnitude and in shape despite the increasing density. Temperature changes at the

edge were not clear within error bars. The peakedness parameter of electron density profile, $n_e(0)/<n_e>$, calculated from Thomson data changed from about 1.9 during the L-mode phase to about 1.5 just after the H transition. Then it increased slightly during the H-mode phase to around 1.7. A preliminary measurement by a millimeter-wave reflectometer suggested steepening of the edge density profile at the H transitions. These observations agree with the characteristic signatures of the H mode.

It should be noted that the LH power could be coupled to the H-mode plasma. The sudden variation of the edge plasma parameters, however, modified the RF coupling to the plasma. The reflection coefficient of the power from the conventional launcher increased by about 0.1 at the H transitions as shown in Fig.1, whereas it changed only a few percent for the multi-junction type.

The operational region where the H mode was observed is illustrated in Fig. 2 in terms of the line averaged electron density and LH power for the combination of 1.74 GHz and 2.23 GHz. The lines indicate the electron density intervals which evolved during each LH pulse. The closed and open lines indicate that the discharge stayed in the L phase and in the quiescent H phase, respectively. The broken lines correspond to the marginal intervals where short H phases were repeated as in the period from 5.8 sec to 6.1 sec in Fig. 1. Figure 2 tells us that the threshold LH power is around 1.2 MW and that there is a lower limit for the electron density of about 2×10^{19} m^{-3} to achieve the H mode. The H mode was reproducible as long as the LH power and the electron density exceeded the thresholds.

The open lines in Fig. 2 represent the increment in the electron density with the H mode without gas feed. Then the electron density stayed nearly constant presumably because the LH power does not provide particle fueling like NBI. A gas puff of 2 Pam^3/sec for 0.5-sec duration into an H-mode phase did not destroy the H mode despite inducing frequent ELMs. The volume-averaged electron density increased later on by about 6×10^{18} m^{-3} which corresponds to twice the usual fueling efficiency of about 0.3. When the gas feed was kept during the LH pulse, however, the H transition tended to be delayed until the gas was turned off.

By feedback controlling the electron density at the LH initiation to be above the threshold density, we could lengthen the H-mode phase up to 4.6 sec. Figure 3 shows a discharge where the ELM-free H-mode phase lasted for 3.3 sec. The gap between the outermost flux surface and the outside limiters was controlled to be about 6 cm since only short H phases were triggered when it was less than 4 cm. This sensitive gap dependence on the H-mode quality is common to the beam heated H mode in diverted plasmas.[9]

The Z_{eff} value estimated from visible bremsstrahlung emission and the n_e and T_e profiles from Thomson scattering measurements increased slightly from about four during the L phase to around five at the later phase of the H mode. The soft x-ray emission profile became slightly peaked with time, which suggested impurity accumulation at the center. Nevertheless the radiation power measured by bolometer arrays remained about 40 % of the total input power as shown in Fig 3. The attainment of the modest impurity accumulation even in the ELM-free phase may be due to the relatively low input power.

The properties of energy confinement are summarized in Fig. 4. The plasma stored energy increases almost linearly with the total input power as shown in Fig. 4 (a). Here we assumed that the injected LH power was completely absorbed by the plasma. The scatter of the data points is mainly due to the variation of the electron density. The energy confinement is enhanced by up to 30 % by the H mode. The increment in the plasma stored energy, however, is primarily gained by the increase in the electron density as plotted in Fig. 4(b). The L-mode plasmas with LHCD have almost the same electron density dependence as the ohmic stored energy[15] of $W_{OH} \propto n_e^{0.62}$ presumably because the total input power does not greatly exceed the ohmic input. The H-mode data points appear to have a little stronger n_e dependence than ohmic.

3. Discussion

The critical factor in obtaining the H mode with LHCD is not yet established. The effect of the current profile modification by LHCD on the H transition is not clear since the change in the internal inductance was small. Other heating schemes such as NBI or ICRH using the second harmonic resonance with powers up to 20 MW and 2 MW, respectively, never produced the limiter H mode in JT-60. The application of LH power at two different frequencies, however, appeared to be favorable in the attainment of the H mode. When the frequencies from the two

launcher were both set at 1.74 GHz, no H mode was observed within applied powers up to 1.5 MW. Although the combined LH power at 2.0 GHz of higher than 2.0 MW produced the H mode, the H phase did not last long due to abruptly enhanced carbon influx.

The beat frequency of 1.74 + 2.23GHz is 490 MHz, for which the 7th harmonic ion cyclotron resonance occurs at the plasma center and 9th at the outer edge when B_t = 4.5 T. The H transition became obscure with lowering B_t down to 3.5 T. In the combination of 1.74 + 2.0 GHz, sharp H transitions were triggered in the range of B_t from 2.8 T to 4.3 T; the beat frequency corresponds to from 3rd to 8th harmonics in the plasma column. The waves at the beat frequencies, however, were not detected by a RF probe. Thus it is not clear whether the presence of the ion cyclotron harmonic resonances is connected with the H transition.

NBI heating was combined to examine the effect of wave-particle interactions. Figure 5 shows an example where an NB power of 1.2 MW was injected into an H-mode phase. The beam pulse interrupted the H phase as seen in the concurrent rise in the H_α emission and fall in the electron density. Note that the trace of the electron cyclotron emission at $1.5\omega_{ce}$ multiplied by n_e, which is a measure of LH coupling to fast electrons,[16] dropped at the same time. Hard x-ray emission behaved similarly to $I_{ECE}(1.5\omega_{ce}) \times n_e$. During the L phase with NBI, beam acceleration by the LH waves[17] was observed in the neutral flux as shown in Fig. 5(b). These facts suggest that the H mode could not be sustained when the LH power was absorbed by beam ions. Such ion tails were not observed in the H phase with LH alone. No parametric decay instabilities were observed neither. Non-thermal ECE spectra suggest a favorable effect of fast electrons on the H transition. In fact, ECH has been reported to be more efficient than NBI in producing the H mode.[6-8] The presence of fast electrons may be relevant to the low threshold power.

It is a puzzling question that the H mode with LHCD has never been obtained in the lower X-point divertor configuration. One of the possible causes is that gas feed must be maintained to keep the electron density above the threshold against the divertor pumping. The favorable effect of the application of LH powers at two different frequencies is left for future work. Resolving these issues should shed light on the H-mode physics.

4. Summary

The H mode with LHCD was demonstrated in the limiter discharges of JT-60. These discharges exhibited the characteristics of the H mode. The improvement in particle confinement was prominent. The ELM-free H phase with durations up to 3.3 sec was attained without significant impurity accumulation.

References

[1]F. Wagner *et al.*, Phys. Rev. Lett. **49**, 1408 (1982).
[2]K. Steinmetz *et al.*, Phys. Rev. Lett. **58**, 124 (1987).
[3]H. Matsumoto *et al.*, Nucl. Fusion **27**, 1181 (1987).
[4]B.J.D. Tubbing *et al.*, Nucl. Fusion **29**, 1953 (1989).
[5]K. Hoshino *et al.*, Nucl. Fusion **28**, 301 (1988).
[6]J. Lohr *et al.*, Phys. Rev. Lett. **60**, 2630 (1988).
[7]K. Hoshino *et al.*, Phys. Rev. Lett. **63**, 770 (1989).
[8]K.H. Burrel *et al*, *Plasma Physics and Controlled Nuclear Fusion Research 1988* (Proc. 12th Int. Conf. Nice, 1988), IAEA, Vienna **Vol. 1,** 193.
[9]M. Keilhacker *et al*, *ibid.*, **Vol. 1,** 159.
[10]J. Manickam *et al*, *ibid.*, **Vol. 1,** 395.
[11]K. Toi *et al.*, submitted to Phys. Rev. Lett.
[12]S.C. Luckhardt *et al.*, Phys. Fluids **29**, 1985 (1986).
[13]H. Nakamura *et al.*, Nucl. Fusion **30,** 235 (1990).
[13]T. Imai *et al.*, Nucl. Fusion **28**, 1341 (1988).
[14]Y. Ikeda *et al.*, Nucl. Fusion **29**, 1815 (1989).
[15]M. Kikuchi *et al.*, Nucl. Fusion **27**, 1239 (1987).
[16]K. Ushigusa *et al.*, Nucl. Fusion **29**, 265 (1989).
[17]T. Imai *et al.*, Nucl. Fusion **30**, 161 (1990).

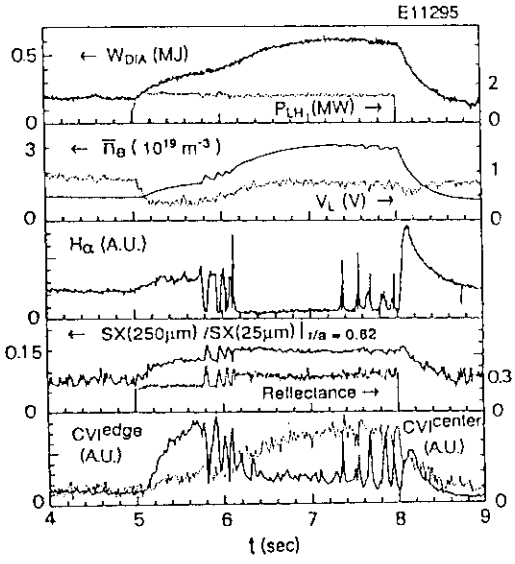

Fig. 1 Time evolution of an H-mode shot with LHCD. The reflection coefficient is from the conventional launcher. The edge CVI signal is along a chord with a tangential radius of r/a~0.9.

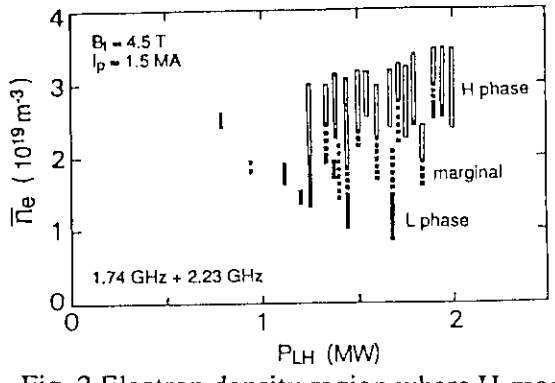

Fig. 2 Electron density region where H-mode phase was observed as a function of LH power.

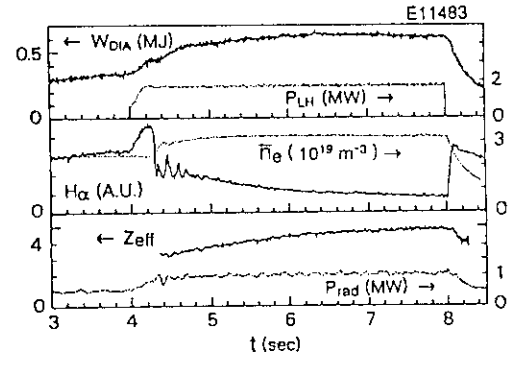

Fig. 3 Time histories from a discharge with ELM-free phase of 3.3 sec. The effective ionic charge from visible bremsstrahlung emission and total radiation power are shown in the third box.

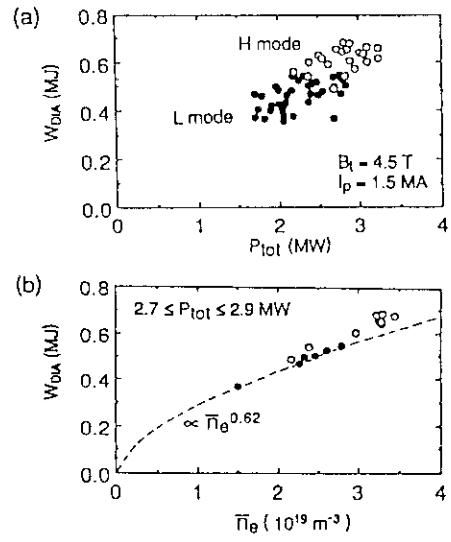

Fig. 4 (a)Plasma stored energy as a function of $P_{tot} = P_{OH} + P_{LH}$. Open and closed circles represent data from the H and L mode, respectively. (b)Electron density dependence of plasma stored energy when the total power is restricted.

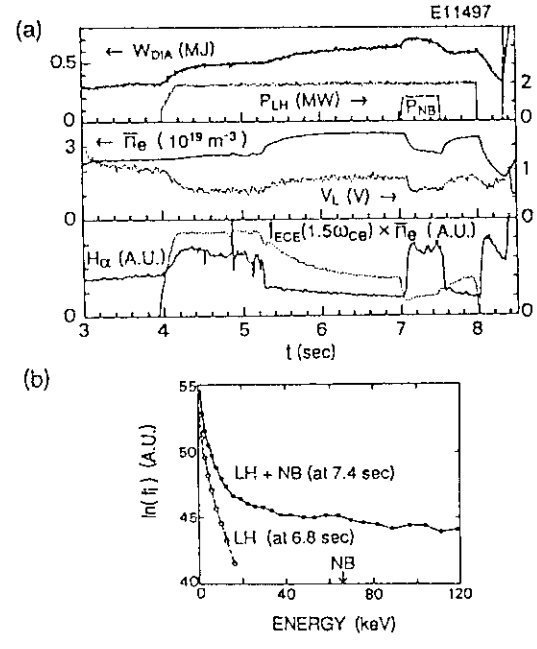

Fig. 5 (a)Time evolution of a discharge where the H mode with LHCD was destroyed by NBI. (b)Neutral particle spectra from a charge exchange analyzer whose chord normal to the magnetic field crosses the NB line at the plasma center. NB injection energy is indicated by an arrow.

2.9 Edge Plasma Behavior in Limiter H-mode with Lower Hybrid Current Drive

Y. Kawano, H. Kubo, T. Sugie, S. Tsuji, T. Imai, K. Itami, A. Nagashima, T. Matoba and JT-60 team.

1. Introduction

At the transition from L to H-phase of limiter discharges with Lower Hybrid current drive, the increase in carbon impurity and the Zeff value were observed. From the Zeff value and the spectroscopic measurement of carbon and oxygen impurities, concentrations of carbon and oxygen were evaluated. The result indicates that the increase in carbon raises the electron density.

Increases of the Visible Bremsstrahlung (Vis.Brems.) emissivity and the line spectrum of CV were observed before and after the H-transition. The Vis.Brems. profile shows that the increase in its emissivity starts at the plasma edge region. Subsequently, the emissivity begins to rise at the more inside of the plasma. It is estimated that the increase in the Vis.Brems. emissivity at the plasma edge region for the beginning of the H-phase is caused by increases in the electron density and the Zeff value due to the increase of the carbon influx under some assumptions.

2. Concentrations of impurities

Figure 1 shows the time evolution of the limiter H-mode experiment by Lower Hybrid (LH) waves. [1] Here, LH waves at different frequencies, 1.74GHz and 2.00GHz, were injected into the hydrogen discharge from t= 4.0sec to t=8.0sec. Plasma current; Ip=1.5MA, toroidal magnetic field; Bt=4.3T, plasma major radius; Rp=3.05m and plasma minor radius; ap=0.9m, respectively. Applied RF powers were 0.8MW for 1.74GHz wave and 0.95MW for 2.00GHz wave, respectively. In fig.1, the H-transition occurred at t=4.9sec. At the H-transition, the sudden increase in line averaged electron density (fig.1(a)) and the sudden decrease of $H\alpha$ intensity (fig.1(b)) were observed. Line spectra of CVI(1s-2p) and OVIII(1s-2p) are shown in the fig.1(c). These spectra were observed using the VUV multi-chordal spectrometer. [2] In fig.1(c), the intensity of CVI increases steeply at the H-transition, and begins to rise by factors up to 2. Here, it is supposed that the ELM-like perturbation shown in fig.1(b) as the large $H\alpha$ spike raises the carbon influx. On the other hand the intensity of OVIII tends to decrease during RF power is applied. This tendency seems to be pronounced at the H-transition. In this discharge, spectra of metallic impurities, such as titanium and nickel, did not show large changes. Figure 1(d) shows time evolutions of the Vis.Brems. intensity (I_{VB}) observed at the chord of R=3.55m (see fig.2) and $I_{VB} / \overline{n_e}^2$ which is almost proportional to the Zeff value. Chord averaged Zeff values evaluated from I_{VB} and profiles of n_e and T_e measured by the Thomson scattering are also shown in fig.1(d). It is noted that the Zeff value rises steeply just after the H-transition and is increasing during the H-phase. From the Zeff value and the intensity ratio of the CVI to the OVIII, we can estimate concentrations of carbon and oxygen [2] of the L and the H-phase plasma at the each steady state.

Here it is assumed that the major impurities of the plasma are carbon (ionic charge number;Z=6) and oxygen (Z=8). Table 1 shows the result of this estimation. In table 1, the concentration of carbon rises from 4% for the L-phase plasma to 11% for the H-phase plasma. While the oxygen concentration decreases from 1% to 0.5%. The concentration of hydrogen decreases from 68% to 30%, which means that the dilution of hydrogen is occurred and that the proton density decrease by about 40% presumably because gas puffing was turned off. Consequently, it is indicated that the increase in electron density is mainly attributed to the increase in the carbon density.

3. Behavior of the Vis.Brems. profile at the plasma edge

Behaviors of profiles of the Vis.Brems. emissivity and the spectrum of CV (2s-2p) were observed by the multi-chordal spectrometer.[3] Viewing chords of the spectrometer are shown in Fig.2. Figure 3 shows profiles of the Vis.Brems. emissivity before and after the H-transition. And fig.4 shows profiles of the CV emissivity. These profiles were evaluated by the Abel inversion with a Wiener filter.[4] In fig.3 and 4, their horizontal axes are flux co-ordinate along plasma minor radius. Since viewing chords of the spectrometer did not observe up to the plasma exterior as shown in fig.2, there is the possibility that accuracies of the Abel inversion are slightly insufficient. It is examined, however, that intensity profiles integrated along viewing chords for Abel inverted emissivities are in agreement with raw profiles. In fig.4, after the H-transition, CV emissivities become negative around ρ = 0.65(m). This fact may indicate that profiles of the CV emissivity have some poloidal asymmetries after the H-transition. In fig.3, after the H-transition, the Vis.Brems. seems to begin rising at the edge region ($\rho \geqq \sim 0.8$(m)) at first. Then Vis.Brems. emissivities increased at more inside of the plasma. In fig.4, the CV emissivity increases with almost the same shapes from L to H-phases keeping those peaks around $\rho \sim 0.86$(m). We consider the influence of the increase in carbon density just after the H-transition to the Vis.Brems. emissivities under some assumptions as follows;

(1)Zeff value is constant along the ρ-direction before the transition,
(2)electron temperature changes a little and does not influence the Vis.Brems. emissivities,
(3)only the carbon density varies,
(4)CV emissivity is proportional to the carbon influx to the plasma and is proportional to the carbon density for the case of steady state.

Since the increase in the CV emissivity seems to be almost saturated at t=5.25sec in fig.4, the rate of the increase in carbon density from t=4.85sec to t=5.25sec is regarded as a factor of 2.6 at the maximum of CV profile. This rate corresponds to increase rates in the electron density of factor 1.4 and the Zeff value of factor 1.6, respectively. As the Vis.Brems. emissivity is proportional to $Zeff \cdot n_e^2 / T_e^{1/2}$, the increase rate of Vis.Brems. emissivity is estimated to be factor 3.1. This value is close to the factor 3 obtained from t=4.9sec to t=5.4sec at $\rho \sim 0.85$(m) in fig.3. Thus the increase in the carbon can cause the increase in the Vis.Brems. emissivity at the plasma edge just

after the H-transition under some assumptions mentioned above. And this result allows us to conclude for the case of this discharge that the electron density and the Zeff value increased at the plasma edge region at the beginning of the H-phase due to the increase in the carbon influx.

4. Summary

In the discharge of H-mode experiment by LH waves, concentrations of carbon and oxygen are estimated for the L-phase and the H-phase plasmas at their steady state. The carbon concentration rises from 4% to 11%, while the oxygen concentration decreases from 1% to 0.5%. As a result, the dilution of hydrogen occurred, and its concentration decreases from 68% to 30%.

Time evolutions of profiles of Vis.Brems. and CV emissivities were observed. The Vis.Brems. emissivity rises at the edge region at first after the H-transition, then the increase at the more inside region starts. This increase in the Vis.Brems. emissivity at the edge region is explained by increases in the electron density and the Zeff value due to the increase in the carbon influx under some assumptions.

References

[1] S.Tsuji et al., this report, Section 2.8.
[2] H.Kubo et al., Nucl.Fusion 29(1989)571.
[3] Y.Kawano et al., JAERI-M 89-033, Section 4.9.
[4] Y.Yamashita, JAERI-M 87-206.

Table 1 Zeff values and concentrations of impurities and hydrogen for the L and H-phase plasmas.

SN11489	L－phase(t=4.8sec)	H－phase(t=6.5sec)
$\overline{n_e}^{us}$	1.6×10^{19} m^{-3}	2.2×10^{19} m^{-3}
$\overline{Z_{eff}}^{us}$	2.7	4.5
n_C / n_e	4%	11%
n_O / n_e	1%	0.5%
n_H / n_e	68%	30%

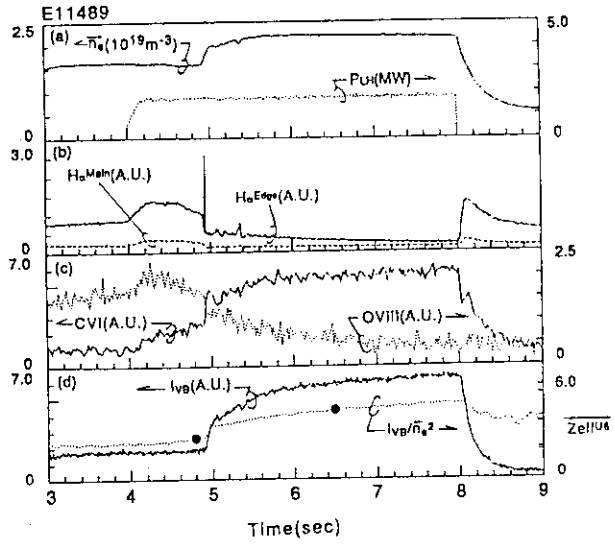

Fig. 1 Time evolutions of the H-phase plasma by LH waves.
(a) line averaged electron density at U6 chord and total applied power of LH waves.
(b) Intensities of Hα at edge and center chords.
(c) intensities of CVI (1s-2p) and OVIII (1s-2p).
(d) intensity of Vis. Brems. at U6 chord (I_{VB}), I_{VB}/n_e^2 and chord averaged Zeff values at timings of Thomson scattering (●).

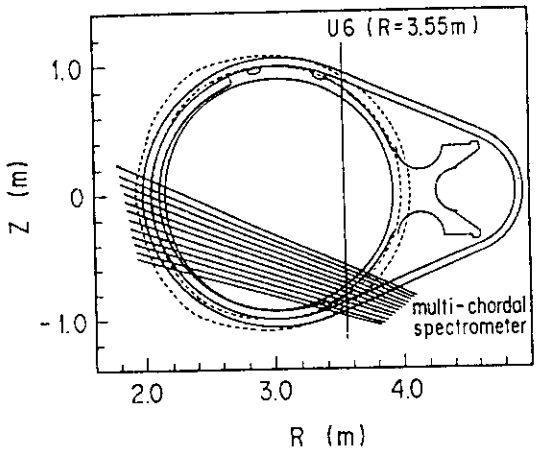

Fig. 2 Viewing chords of the multi-chordal spectrometer and U6 chords.

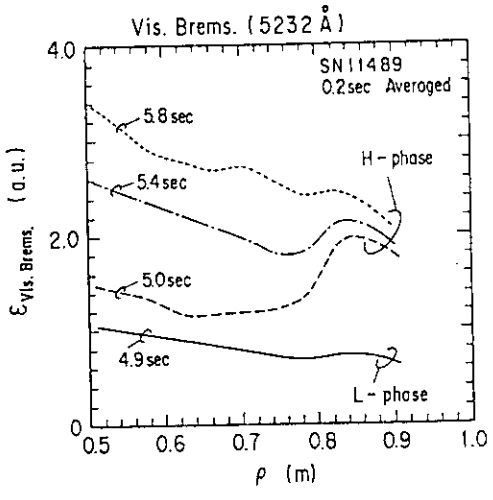

Fig. 3 Abel inverted profiles of the Vis. Brems. emissivity before and after the H-transition.

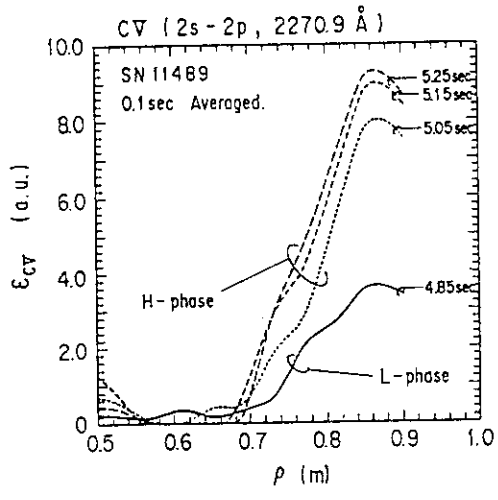

Fig. 4 Abel inverted profiles of the CV emissivity before and after the H-transition.

2.10 Lower Hybrid Wave Heating in Peaked Density Plasmas produced by Pellet Injections

K.Ushigusa, T. Imai, O. Naito, Y. Ikeda, R. Yoshino, Y. Kamada, H. Hiratsuka and the JT-60 Team

1. Introduction

The appearance of parametric instabilities and a high energy ion tail near the plasma surface has been commonly observed in lower hybrid (LH) wave heating at ion heating regime. It is thought that parametric instabilities may prevent the central core heating by LH waves. Previous studies on JT-60 has indicated the possibility of effective heating by LH waves in ion heating regime with peaked density plasmas produced by pellet injections[1]. Unfortunately, a lack of the density and the temperature profile data in previous studies prevented a clear understanding of central core heating by LH waves.

This paper presents a clear central heating by LH waves in peaked density plasmas produced by pellet injections on JT-60. Experiments were carried out in limiter discharges with I_p = 2.1 MA, B_T = 4.5 T, R_p ~ 3.07m, a_p ~ 0.91m. Two hydrogen pellets were injected with injection speed of around 2.0km/sec at 20msec intervals into a helium plasma at typically $\overline{n_e}$ ~ 3.5 x $10^{19}m^{-3}$. Lower hybrid waves at a frequency of 2GHz were injected by two launchers ($N_{||}^{peak}$ ~ ± 3.4 with $\Delta N_{||}$ ~ 1.0 and $N_{||}^{peak}$ ~ 1.9 with $\Delta N_{||}$ ~ 0.5).

2. Results

Figure 1 shows a comparison of pellet fuelled discharges with and without LH heating. Compared with the pellet alone shot, about 2MW of LH power increases the diamagnetic energy content by ~150kJ and decreases the loop voltage by 0.25V. The incremental energy confinement time of the LH power in this discharge corresponds to $\tau_E^{INC} = \Delta W^*/(P_{LH} - I_p \Delta V_l)$ ~ 100 ms. The hard X-ray signal is quite small during the LH pulse. The line averaged density at around the half radius $\overline{n_e}|_{0.5a}$ tends to decrease rapidly after the onset of LH pulse compared with the pellet alone shot. This tendency were observed in all pellet injected discharge with LH heating. The ratio of the visible bremsstrahlung signals viewing the plasma radius at r ~ 0 and r ~ 0.5a has suggested that the peaked density profile is kept by LH power.

The electron density and the temperature profiles measured with the Thomson scattering for the same shot as Fig.1 are shown in Fig. 2(a) and (b), respectively. A

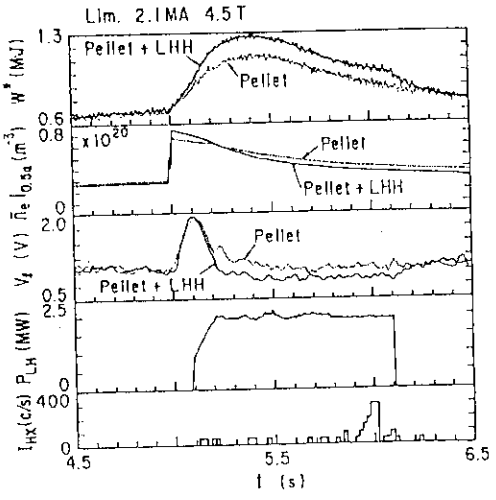

Fig.1 Typical example of pellet fuelled discharges with and without LH heating.

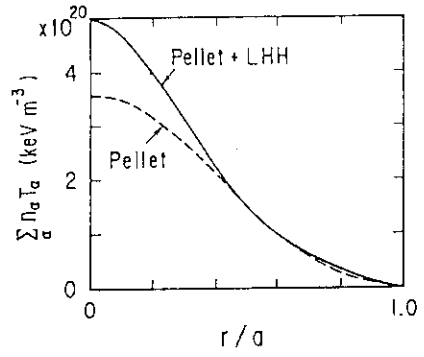

Fig.3 The total pressure profiles for pellet injected shots with and without LH heating for the same shot as Fig.2.

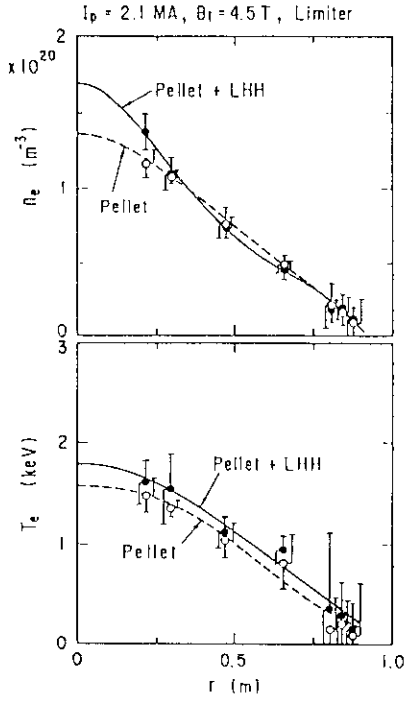

Fig.2 Electron density and temperature profiles at t = 5.4s for the shots shown in Fig. 1.

more peaked density profile is formed in LH heated case. The LH heated plasma has the central electron density $n_{eo} \sim 1.7 \times 10^{20}$ m^{-3}, the line averaged density $\overline{n_e} \sim 0.85 \times 10^{20}$ m^{-3} and the density peaking factor $n_{eo}/\langle n_e \rangle \sim 3.1$, while $n_{eo} \sim 1.4 \times 10^{20}$ m^{-3}, $\overline{n_e} \sim 0.75 \times 10^{20}$ m^{-3} and $n_{eo}/\langle n_e \rangle \sim 2.6$ for the pellet alone case. The electron temperature for the LH heated case is slightly higher than that for the pellet alone case. The central ion temperature measured with the forward scattering of the 200keV helium beam and the Doppler broadening of the titanium agrees with the central electron temperature with the scattering of ± 20% for both cases. The effective ion charge Z_{eff} measured with the visible bremsstrahlung is around 1.6 for both cases. If we assume that the plasma contains hydrogen and helium ions only and the ion pressure profile is the same as the electron pressure, the total energy content W_{kin} estimated from the electron thermal energy and Z_{eff} becomes ~ 1.32MJ and ~ 1.07MJ with and without LH heating, respectively. These value agree with the diamagnetically measured energy content within the error of ± 5%.

Figure 3 shows the total pressure profile which is estimated from the electron pressure profile and the diamagentically measured energy, where we multiply the factor to the electron pressure so that the total energy coincides with the diamagnetic energy. The observed density and temperature at the plasma center for the pellet fuelled plasma shown in Fig. 2 show $f / f_{LH} \sim 1.19$ where f_{LH} is the lower hybrid resonance frequency and it is assumed that $Z_{eff} = 1.6$ (hydrogen and helium ions), $n_e = 1.7 \times 10^{20}$ m^{-3}, $B_T = 4.5$ T, $T_i = T_e = 1.8$keV and f = 2GHz. The linear turning point to thermal mode from slow mode exists near the plasma center in these condition for excited wave spectra. This suggests that the increase in the central pressure shown in Fig. 3 is due to the central ion heating by the LH waves.

Fig.4 (a);Comparison of LH heated plasma with pellet injected plasma (solid line) and with gas fuelled plasma (dotted line).
(b) and (c);The electron density and temperature profiles for the shots shown in (a) at t = 5.4 s for the pellet+LH shot and at t = 7.4 s for the gas puff shot.

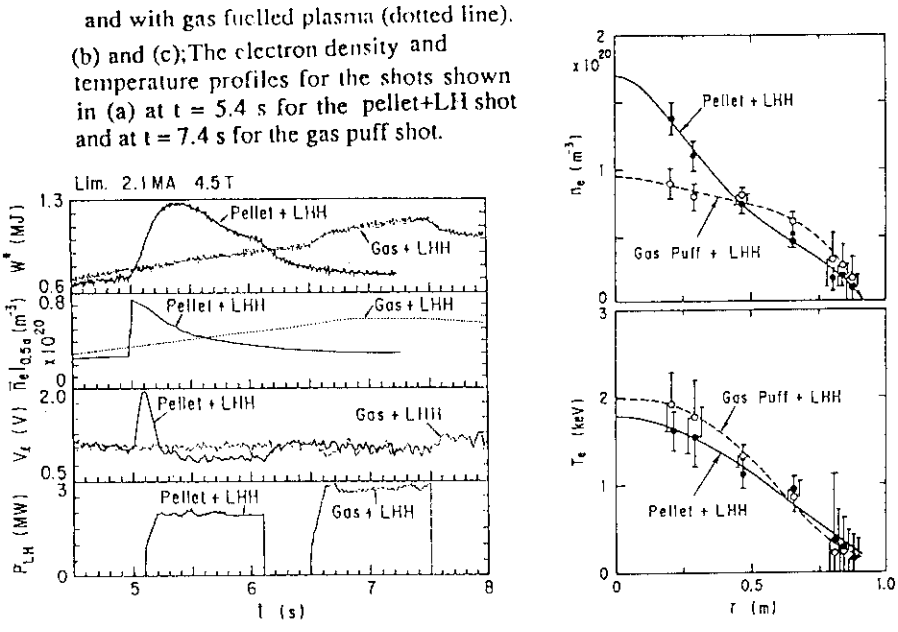

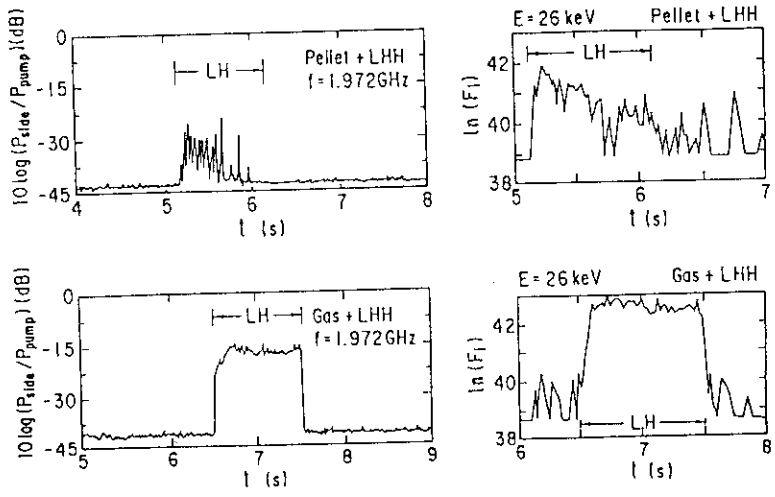

Fig.5 Time evolutions of the parametric decay wave at the frequency of 1.972GHz and the high energy ion nuetral flux with the energy of 26keV for the same shots as shown in Fig. 4. The pump frequency is 2GHz.

A comparison of the LH heating into the pellet fuelled plasma and the gas fuelled plasma is shown in Fig. 4. Figure 4(a) shows time evolution of plasma parameters, where the solid and dotted lines show the pellet fuelled case and the helium gas fuelled case, respectively. The electron density and the temperature profiles at t = 5.4 s for the pellet fuelled case and at t = 7.4 s for the gas fuelled case are shown in Fig.4(b) and (c). In gas fuelled case, the electron density has a broad profile; $n_{eo} \sim 0.94 \times 10^{20}$ m^{-3}, $\overline{n_e} \sim 0.69 \times 10^{20}$ m^{-3} and $n_{eo}/\langle n_e \rangle \sim 1.68$. The incremental confinement time for the gas fuelled case is $\tau_E^{INC} \sim 35$ ms and this is about half of the incremental confinement time of the pellet fuelled case.

High power LH electron heating experiments on JT-60 have shown that the degradation of the incremental confinement time correlates to the occurrence of parametric instabilities and this can be avoided by increasing the plasma current. Figure 5 shows time evolutions of the intensity of parametric decay wave at a frequency of 1.972GHz normalized by the pump wave intensity and the high energy ion tail flux with the energy of 26keV for the pellet and the gas fuelled plasmas. A strong parametric decay wave and the high energy ion tail are observed in the gas fuelled plasma during the LH pulse. The decay wave intensity in the pellet fuelled plasma is ~ -35dB against the pump wave and decreases during the LH pulse. Corresponding to the time evolution of decay wave, the high energy ion flux decreases during the LH pulse. These time evolutions may correlate to the behavior of the edge density and temperature in pellet fuelled plasma. Observed results indicates that, at least, parametric instabilities at the plasma edge are suppressed in the LH heating into peaked density plasma produced by pellet injections.

3. Summary

Lower hybrid(LH) waves at a frequency of 2 GHz has increased the plasma central pressure in pellet fuelled plasma at the central electron density of ~ 1.7×10^{20} m^{-3}. In peaked density profile produced by the pellet injections, parametric instabilities were significantly suppressed and the efficient central heating by LH waves was possible at the ion heating regime ($f \sim f_{LH}(0)$).

References

[1] K. Ushigusa, et al., in Proc.12th Int. Conf. on Plasma Phys. Controlled Nucl. Fusion Res. (Nice, France) Paper IAEA-CN-50/E-3-1, (1988).

2.11 High Power Lower Hybrid Electron Heating in High Density Plasmas with High Plasma Current

T. IMAI, K. USHIGUSA, O. NAITO, Y. IKEDA, S. TSUJI, M. NEMOTO, H. YOSHIDA

LHRF waves have many varieties of applications to control a tokamak plasma, Lower Hybrid Current Drive (LHCD) ,electron heating (LHEH) and ion Heating (LHIH) including beam ion heating. In addition, the profile control of plasma current by LHCD becomes to get a great attention. In spite of these attractive features, LHRF is sometimes accused that physics of wave penetration and absorption is complicated. Spectrum gap, density limit and power balance at high power experiments are problems to be solved. There are some theoretical proposals on them[1-3]. Interaction with ions, accessibility and parametric instabilities seem to be the major processes to paralyze the LHCD, LHEH and LHIH effects. The dominant process differs among machines and depends on the plasma parameters. Among these, the investigation of the parametric instabilities are most important, since the parametric instabilities always appear in high power and high density LHRF experiments and they correlate with the degradation of the heating and current drive efficiency[4]. The suppression of the parametric instabilities is one of keys to understand the LHRF physics. High plasma current could suppress the parametric instabilities in FT tokamak[5]. High energy ion flux was enhanced by the suppression of them but the effect to the main plasma parameters like stored energy or temperature increase was not observed. Details of the parametric instabilities are described in the section 2.13. In this paper, it will be shown that the suppression of the parametric instabilities by the high plasma current recovers the heating and current dive effects.

JT-60 is one of the large present tokamaks. The major radius and the minor radius are 3.1 and 0.85 m. The maximum plasma current and toroidal field are 3.2 MA and 4.8 T. The line averaged electron density range of the present experiments is 2.0-7.0 x $10^{19}m^{-3}$ in He plasma with hydrogen minority. LHRF system is composed of three subsystems, each of which has 8 klystrons feeding 4x8 conventional or 4x24 multi-junction waveguide array[6,7]. The center frequency is 2.0 GHz.

The efficient electron heating was obtained in relatively low density plasma of $\bar{n}_e$= $1.7x10^{19}m^{-3}$ with low power heating, where the electron temperature of 6 keV was measured by Thomson scattering. Electron heating efficiency η_e^{LH}= 2~3 eV $10^{19}m^{-3}$/kW of the LHEH is notably higher than those of NBI heating and close to the ohmic heating. The high performance of the LHEH was not maintained in the higher density and higher power experiments. Stored energy became to saturate. Instead parametric instabilities and

fast ions of short life time appeared. Typical example of the density dependence of the various observed quantities are shown in Fig.1, where plasma current I_P = 1.5 MA in limiter discharges. Intensity of the hard X-ray decreased against the density increase, while the intensity of the fast ion flux of 30 keV increased. The critical density to disappear the coupling to electron was $\bar{n}_e = 3.5 \times 10^{19} m^{-3}$. Parametric instabilities became to grow around the critical density and incremental confinement time τ_E^{INC} decreased, which is defined as,

$$\tau_E^{INC} = \frac{\Delta W}{\Delta P_{LH} + \Delta P_{OH}} \quad . \qquad (1)$$

Similar density dependence was obtained in the discharges of 2 MA plasma current, but the critical density of electron coupling of LH waves apparently increased. Threshold power of the onset of the parametric instabilities seemed to increase in accordance with the increase of the plasma current. Similar observation was already reported in the FT tokamak[5]. In contrast to

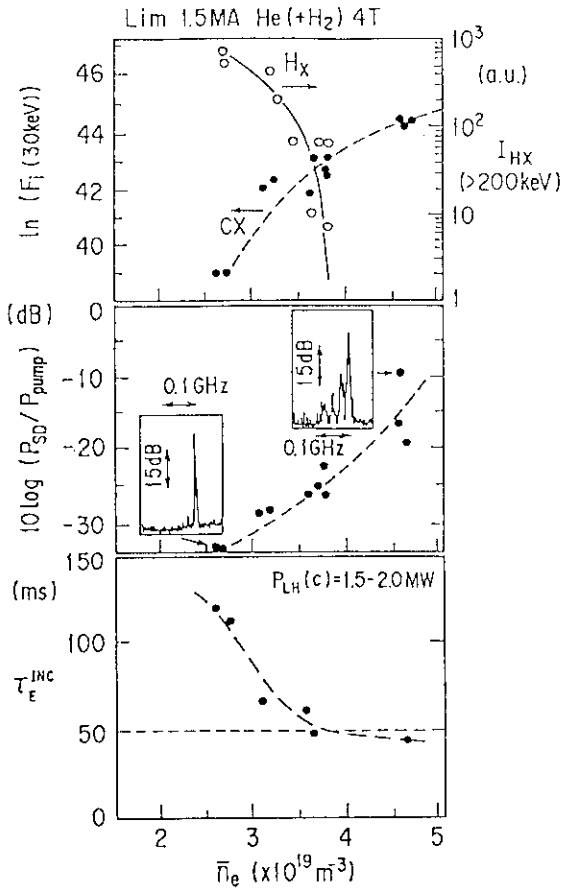

Fig. 1 Dependence of fast ion flux, Hard Xray signal, parametric instabilities and incremental energy confinement time on density.

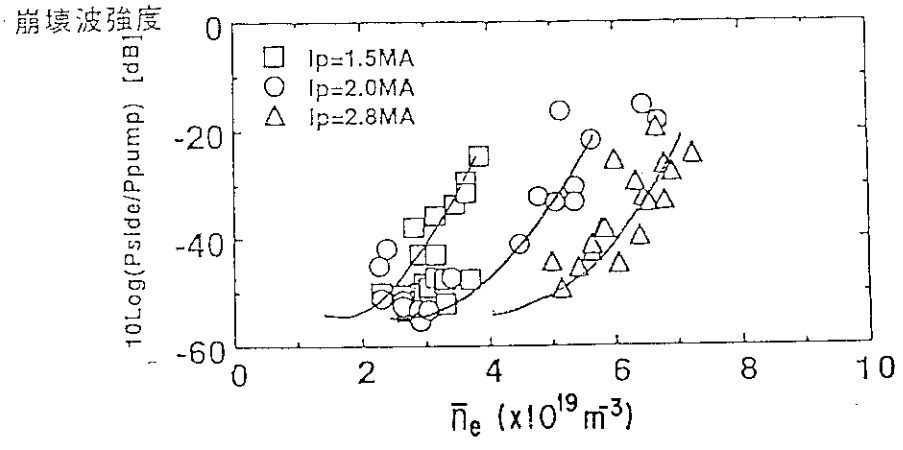

Fig. 2 Intensity of Parametric instabilities in terms of density in cases of various plasma currents.

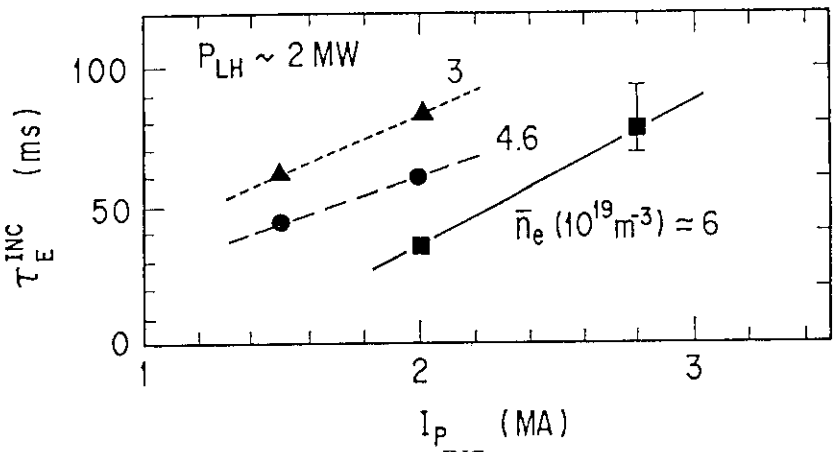

Fig. 3 Improvement of the τ_E^{INC} as a function of plasma current.

the their observation, the behavior of the fast ion was opposite. The fast hydrogen ion flux and intensity of the parametric instabilities increased at the same time. Dependence of the relative intensity of parametric instabilities on the density with various plasma currents is shown in Fig. 2. It is clear that high plasma current reduces the parametric instabilities. Since the plasma current is very effective to reduce the parametric instabilities, we further increased the plasma current up to 2.75 MA. The results are shown in Fig 3. The improvement of the heating performance corresponding to the reduction of parametric instabilities were obtained as expected. It is found that the τ_E^{INC}decreases with density in the same plasma current but it is recovered by the increase in the plasma current. Higher density and higher power cause the parametric instabilities but higher plasma current reduces them.

Typical example of LHRF heating in high density and high plasma current discharge (I_P= 2.75 MA, B_t=4.5T and $\bar{n}_e$=

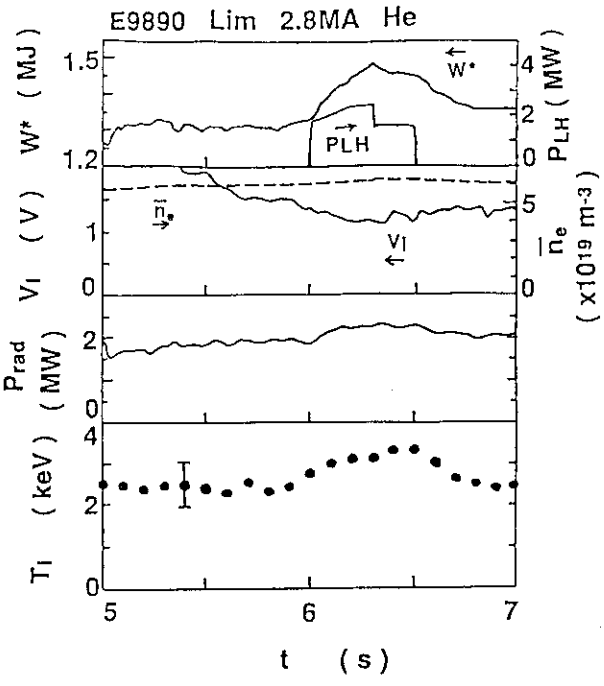

Fig. 4 Typical waveforms of LHEH in high plasma current of 2.75 MA.

~$7x10^{19}m^{-3}$) is shown in Fig. 4. Stored energy increased about 200 kJ with about 2MW LHRF power. No appreciable increase in both $\bar{n}_e$ and radiation power were observed. The slight decrease in loop voltage indicates the increase in electron temperature due to Lower Hybrid heating. Hard Xray signal perpendicular to the magnetic field is weak but some enhancement of $2f_{ce}$ signal during LH pulse indicate electron heating by Lower Hybrid wave. It is natural that the hard X-ray intensity radiated from energetic electrons more than 70keVwas small, since the accessibility condition in the present condition is $N_{\parallel acc}$=1.7~2.0 which corresponds to the resonant electron energy of 60~100 keV. No fast ions were observed, while ion temperature measured by the Doppler broadening of TiXXI line increased by about 500eV as seen from the bottom of Fig. 4, due to the increase in the power transfer from electrons heated by the Lower Hybrid wave.The stored energy increased linearly against absorbed power defined by $P_{abs}=P_{OH}+P_{LH}$ up to about 10 MW in the case of high plasma current of 2.75 MA, where $\bar{n}_e$= 6~$7x10^{19}m^{-3}$ with He. Both LHEH and NBI heating have almost same τ_E^{INC}. The saturation of the stored energy is not seen up to 10MW, which is in contrast to the results with I_p=1.5MA.

In conclusion, high power and/or high density degrades the heating or current drive efficiency of the Lower Hybrid wave, since the parametric instabilities excited near the surface absorbed the LH power and lost their energy rapidly through surface fast ions. High plasma current, however, reduced parametric instabilities and recovered the heating performance up to P_{abs}~ 10MW and $\bar{n}_e=7x10^{19}m^{-3}$ with the same 2GHz frequency. High plasma current as well as high frequency of lower hybrid wave extend the electron heating region, which is favorable for future tokamk.

REFERENCES

[1] P. T. Bonoli and R. C. Englade, Phys. Fluids **29** (1986) 2937.
[2] J. B. Wegrow, 5th Topical Conference on RF heating, Madison (1983).
[3] L. H. Stverdrup and P. M. Bellan, Phys. Rev. Lett. **59** (1987) 1197.
[4] T. Imai, et al., Phys. Rev. Lett., **43** (1979) 586.
[5] R. Cesario, P. Ridolfini, Nucl. Fusion **27** (1987)435.
[6] T. Nagashima et al., Fusion Engineering and Design **5** (1987) 101.
[7] Y. Ikeda et al., Nuclear Fusion **29** (1989) 1815.

2.12 Acceleration of beam ions in simultaneous injection of NB and LH wave

M.Nemoto, O.Naito, K.Ushigusa, T.Imai, Y.Ikeda, Y.Kusama, K.Tobita, H.Takeuchi and JT-60 Team

For a future tokamak like ITER or FER, it is very important to predict the absorption of LH power by high energy α-particles leading to decrease of the heating and current-drive efficiencies. Coupling characteristics of LH wave for beam ion of NB have been investigated by simultaneously injecting NB and LH wave into the JT-60 plasmas.

Experiments were carried out in hydrogen plasmas with near-circular limiter configurations and following parameters; plasma current I_P=1.5MA, the toroidal magnetic field B_T=4.5T, major radius R=3.04m and minor radius a_P=0.89m. We investigated a frequency dependence of coupling characteristics, by varing the wave frequency from 1.74GHz to 2.23GHz with fixed $N_{//}$ of 2.2, in order to clarify a critical density of the beam acceleration resulted from interact LH waves and hydrogen beam ions.

Figure1(a) shows waveforms of simultaneous injections of LH and NB when frequensies of LH were 1.74, 2.0 and 2.23GHz and beam energy was 65keV. High power NB injection would raise plasma density and makes the accurate measurement of the acceleration phenomena difficult. Therefore, we injected lower NB powerfrom a beam-line which was viewed by a CX analyzer for an increase of signal to noise ratio of CX measurement. The top column shows time evolutions of line-integrated electron density and NB power P_{NBI}. The electron density was raised with a constant rate by a feedback control system. The second column shows the evolution of CX flux intensities lnFi of 150keV for three LH frequencies. The flux intensities show clear differences for critical densities of the acceleration. Accompaning with the increase of accelerated ions by LH, LH power absorbed by electrons were steeply decreasing, as shown in the third column. Vertical axis in the column is a product of the intensity of non-thermal electron cyclotron emission (ECE) at $1.5\omega_{ce}$ and the line-integrated density. Here, data for 2.23GHz case was absent because of the ECE system error. Differences in injected LH powers shown in the bottom column for three cases did not influence the essential characteristics. Typical ion energy distributions at $\overline{n_e}=1.8\times10^{19}m^{-3}$ for those three cases are shown in Fig.1(b). In the case of 1.74GHz, shown with closed circles, the most

enhanced beam acceleration up to 200keV occurred. On the other hand, the tail slope of 2.23GHz case shown with closed triangles was similar to the case of NB only. The ion acceleration was due to the absorption of LH wave because electricstatic probes did not detect parametric decay waves in these discharges.

In an electro-static cold plasma, approximation LH wave satisfies the following dispersion relation

$$\left(\frac{k_{//}}{k_{\perp}}\right)^2 = \left(\frac{N_{//}}{N_{\perp}}\right)^2 = \left(\frac{f}{f_{pe}}\right)^2 + \left(\frac{f}{f_{ce}}\right)^2 - \left(\frac{f_{pi}}{f_{pe}}\right)^2 , \qquad (1)$$

where $k_{//}$ and $k_{\perp}$ are wave numbers parallel and perpendicular to the magnetic field, and f, f_{pe}, f_{ce} and f_{pi} are pump-frequency, electron plasma-, electron gyro- and ion plasma-frequency, respectively. Here, we define two parameters, which indicate absorption rates of LH power by electrons δ_e and ions δ_i, as

$$\delta_e \equiv \left(F_\delta \frac{v_e}{v_{//}}\right)^2$$

$$\delta_i \equiv \left(\frac{v_B}{v_{\perp}}\right)^2 ,$$

where v_e and v_B are electron and beam ion velocities, and $v_{//}$ and $v_{\perp}$ are LH phase velocities parallel and perpendicular to the magnetic field. These parameters mean that if they are close to unity, each species is easy to absorb LH wave power. Also, we define a ratio $\delta = \delta_i/\delta_e$ which gives a critical density between electron and ion heating when $\delta=1$. Using beam energy E_B and the electron temperature T_e, we can re-write Eq.(1) as

$$\left(\frac{f}{f_{pe}}\right)^2 = \frac{m_e E_B}{F_\delta^2 m_p T_e \delta} - \left(\frac{f}{f_{ce}}\right)^2 + \left(\frac{f_{pi}}{f_{pe}}\right)^2 , \qquad (2)$$

where m_e and m_p are masses of electron and proton as beam species. The critical electron density n_e^c in units of $10^{19}m^{-3}$ when $\delta=1$ are given as follows

$$n_e^c = \frac{2.28 f_G^2}{\dfrac{E_B}{F_\delta^2 A_B T_e} + \gamma - 2.34\left(\dfrac{f_G}{B_T}\right)^2} , \qquad (3)$$

where f_G is LH wave frequency in GHz, E_B and T_e are in eV, B_T is in Tesla, A_B is atomic number of injected beam species and γ is defined as

$$\gamma \equiv \frac{1}{\overline{n_e}} \sum_i \frac{Z_i^2 \overline{n_i}}{A_i}$$

$\overline{n_e}$ and $\overline{n_i}$ are densities of electron and ion expressed in units of $10^{19}m^{-3}$, the suffix "i" in γ is ion species with charge state Z_i and atomic number A_i.

We calculated a dependence of the critical electron density on LH frequency with typical JT-60 experiment parameters of E_B=65keV, T_e=3keV, B_T=4.5T and γ~1.2 on Z_{eff}=3 assuming carbon as a dominant impurity. A satisfactory result was obtained at F_δ=2.75. Figure2 shows the calculation result with a solid line and the experiment data with closed circles. They were in good agreement. Here, we converted critical density into averaged one $\overline{n_e}^c$ with a coefficient which was based on a parabolic density profile.

Next, in order to investigate the dependence on beam energy, we carried out an experiment with NB of E_B=40keV, LH wave of f=2.0GHz and $N_{//}$=2.2 and the same B_T and configuration as previous experiment. The electron density when accelerated ions of 120keV were detected was $2.35\times10^{19}m^{-3}$ as shown in Fig.2 with open circle. The correlation between the generation of high energy ions and the production of the ECE wave intensity and the electron density was same as that in the case of 65keV injection. The dependence of the critical density on beam energy , which was caluculated from Eq.(3) using the previous parameters and shown with a broken line in Fig.2, were also consistent with the experimental data.

Equation(3) predicted that the critical density did not depend on $N_{//}$, therefore, we verificated that experimentally. The plasma parameters were the same as the first experiment, except that LH frequency is fixed to 2.0GHz. $N_{//}$ was varied from 1.3 to 2.8, by changing the phase differences from120° to 270°. No significant differences in the critical density for the generation of high energy ions are seen among three $N_{//}$ cases as the prediction. We characterized an enhancement of high energy ion flux by the tail temperature T_i^{tail} which was derived from a slope steepness over injected beam energy of an ion energy distribution measured by the CX analyzer. Figure3 shows the dependence of the tail temperature on the density for three $N_{//}$ cases with 2.0GHz. The dependence is same as Fig.2 in spite of the variation of $N_{//}$.

In summary, the beam acceleration by LH wave was studied with the limiter plasmas on JT-60. It was evidenced that critical density to couple to beam ions was in good agreement with the prediction from the simple LH wave dispesion relation. The results can clearly predict the interaction of the α-particles with LH wave in the future tokamak.

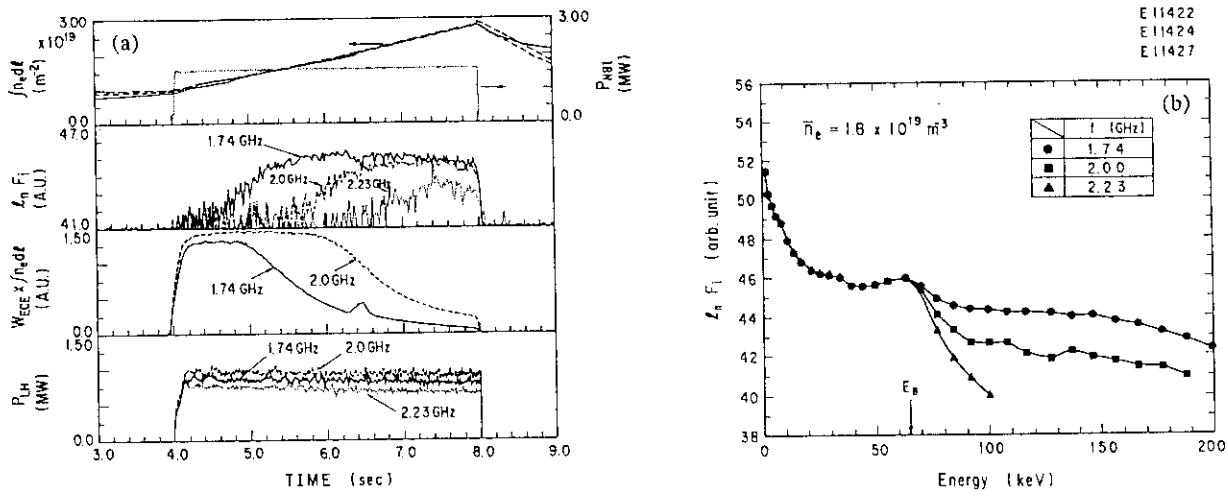

Fig.1 (a) Time evolutions of line density, injected neutral beam power, CX flux intensity, product of 1.5ω_{ce} wave and line density and injected LH wave power.
(b) Typical ion energy distributions measured from CX analyzer

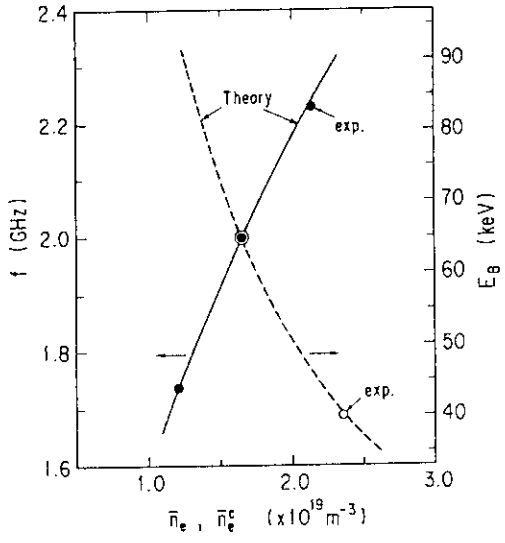

Fig.2 Comparison with experimental data and calculation with respect to the critical density of the beam acceleration. Solid line and closed circles are a calculation result and experimental data for frequency dependence, respectively. Broken line and open circles are a calculation result and experimental data for beam energy dependence, respectively.

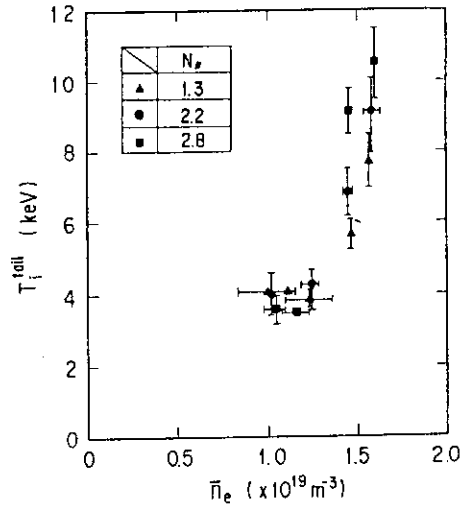

Fig.3 Density dependence of the tail temperature derived from a slope steepness over injected beam energy of an ion energy distribution.

2.13 Parametric Decay in the Lower Hybrid Frequency Range

Y. Ikeda, T. Imai, K. Ushigusa, M. Naito, M. Seki, M. Nemoto and K. Uehara

1. Introduction

Recently, lower-hybrid experiments have demonstrated the ability of steady state currents without an Ohmic transformer in addition to heat electrons. The rf-driven currents are generated by the enhancement of a fast tail in the electron distribution function. This interaction between the electrons and the lower hybrid wave is due to Landau damping in the toroidal direction. However, most current drive and electron heating experiments in the medium-size tokamaks have encountered a density threshold above which the electron absorption can not occur. In the high-density operation, a parametric decay into the harmonics of ion-cyclotron frequency below the frequency of the pump is seen, and the parametric decay is seemed to be one of the reason for the density limit.

This paper presents experimental data of the parametric decay in the operation regime near the density limit for the electron interaction in the JT-60 LHRF experiments. The experiments were carried out on various plasma parameters (limiter with/without pellet, divertor) to investigate the profile dependency of the parametric decay.

2. Experimental Conditions

The JT-60 LHRF heating system is composed of three launching units. Each unit has capability to inject 2 - 4 MW at the frequency of 2 GHz. Two are conventional type launcher designed for heating (A-unit) and current drive (C-unit), respectively. The other (B-unit) is multijunction type in order to control current profile and to drive RF current efficiently. The A-unit and B,C-units are installed in the downward and upward ports of the JT-60 vacuum vessel. Because the distance between the plasma edge and the grill of the A-unit launcher is too far to obtain a good coupling in the lower X-point divertor operation, only B and C units are available in this operation.

The experiments of the parametric decay were performed mainly in the parameter range Ip = 1.5 - 2.8 MA, Bt = 4.0 - 4.8 T, $\bar{n}e$ = (2.0 - 7.0) X 10^{19} m^{-3} for the limiter gas puffing He plasma, Ip = 2 MA, Bt = 4.5 T, $\bar{n}e$ = 8 X 10^{19} m^{-3} for pellet H plasma, and Ip = 1.5 MA, Bt = 4.5 T, ne = (2.0 - 6.0) X 10^{19} m^{-3} for divertor He plasma. The RF probes are equipped on the launchers side behind 10 mm from the grill mouth. The RF spectra are collected every 400 ms at the frequency range from 10MHz to 2.9GHz during a plasma shot. So we can confirm the decay wave is actually determined by the interaction of the injected wave and the plasma.

3. Experimental Results

A large level of the parametric decay signal was observed when the density was increased over the $3x10^{19}$ m^{-3} in the He plasma, Ip=1.5MA. The typical spectra near the pump frequency f_0=2 GHz are shown in Fig. 1. This signal was detected at the RF probe on the C-unit launcher for injected RF power of the C-unit around 1.5 MW at the average density $\bar{n}e$ = $2X10^{19}$ and $4X10^{19}$ m^{-3}, respectively. The

several satellite shifted from the pump by multiples of the ion cyclotron frequency at the grill mouth is observed at high density operation.

Then, we studied the plasma current dependence of the parametric decay on limiter He plasma. Figure 2 shows the density dependence of the amplitude of the first satellite signal, flux of the ion tail and radiation loss normalized by injection RF power. The data of Ip =1.5 MA is presented at the injection RF power from C-unit 2 MW, and the data at Ip=2 MA, 2.8 MA are plotted at the injection power from C-unit 2 MW combined with A, B-units at the total injecting power around 3 - 5 MW. The parametric decay was detected by the RF probe on the C-unit launcher. The parametric decay grows in proportion to the density and the fast ion and the radiation loss were observed in accordance with the growth of parametric decay. The effect of multiplied total RF power from launchers on the decay wave was not clear in this experiment, because the data set at the same density was a rather limited due to increasing plasma density during RF injection into a limiter discharge. However, it was obviously shown that the parametric decay was suppressed by increasing the plasma current at high density and high RF power.

The density and temperature profile during RF injection were measured by Thomson scattering in order to investigate the plasma current effect on the parametric decay. We studied the plasma parameter at a point r/a =0.8 during RF injection. Figure 3 (a), (b) shows the density and temperature at r/a = 0.8 for total injection power PLH = 1 - 6 MW the plasma current Ip = 1.5, 2 and 2.8 MA, respectively. The temperature at r/a = 0.8 clearly depend on the plasma current.

A high plasma current leads the high temperature at the same average density. If the edge parameter, where the parametric decay occurs, are in proportion to these measured values at r/a = 0.8, the effect of the plasma current on the parametric decay is related to increasing the edge temperature.

We study the profile influence of the parametric decay on peaked density plasma by using a pellet injection. As reported in Section 2.10, a peaked density plasma with a lower edge density was obtained by pellet injection at high density operation $\bar{n}e$ = 7-8x10^{19} m^{-3}. The signal of the sideband was very small and was about -35dB compared with the pump signal in the pellet injecting plasma, while that of the gas puffing discharge was about -15dB. The center density of the pellet injecting plasma was more than 1.5X$10^{20}m^{-3}$, where the turning point to thermal mode exists, and no heating degradation was observed in such high density plasma as reported in Section 2.10.

Therefore, the parametric decay can be suppressed by controlling the edge density and temperature.

4. Discussion

The study of the parametric decay has been performed on FT LHRF experiment on the basis of the non-linear ion-cyclotron damping theory [1][2]. We discussed our experimental results on the same interpretation as FT group have done. In this theory, the amplification factor for the parametric decay is approximately in proportion to the $n\,e^{1.5}/(T\,e \cdot B\,t)^{-1}$. Because the measured space points of Thomson scattering existed around out side on limiter plasma configuration, we can obtained density and temperature profile from r/a = 0.2 to r/a = 0.8, where a is minor radius. Figure 4 shows the amplitude of the first satellites of the parametric decay normalized the $n\,e(r/a=0.8)^{1.5}/(T\,e(r/a=0.8) \cdot B\,t)^{-1}$, where ne

and T_e is measured by Thomson scattering and B_t corresponds to the ion cyclotron field of the first satellites. It seemed that the dependency of the parametric decay agrees fairly well with the theoretical dependency. And the influence of plasma current on the parametric decay seemed to closely related to the edge temperature. These results show that the density limit for interaction between wave and electron does not depends on the accessbility but on the parametric decay on the plasma parameter of the JT-60 in the case of ohmic target plasma.

5. Conclusion

The parametric decay plays the dominant role to limit the interaction between electron and LH wave at high density plasma on JT-60 tokamak LH experiment. The effect of plasma current on the parametric decay seemed to be increasing of the edge temperature, and the edge density can be sustained at low level by pellet injector so the parametric decay does not occur at high average density. The control of the edge density and temperature may delieve the desgade of the interaction between wave and electrons at high density regime.

REFFERNCES

[1] CESARIO,R.,PERICOLI-RIDOLFINI,V., Nucl.Fusion 27(1987)435.
[2] LIU,C.S.,TRIPATHI,V.K.,CHAN,V.S.,STEFAN,V., Phys. Fluids 27(1984)1709.

Figure captions

Fig.1 phenomena at high density.
Fig.2 effect of plasma current on the decay wave.
Fig.3 (a);effect of the plasma current on edge density,
(b);effect of the plasma current on edge temperature.
Fig.4 intensity of the decay wave as a function of $n_{e_{edge}}^{1.5}/T_{e_{edge}}$.

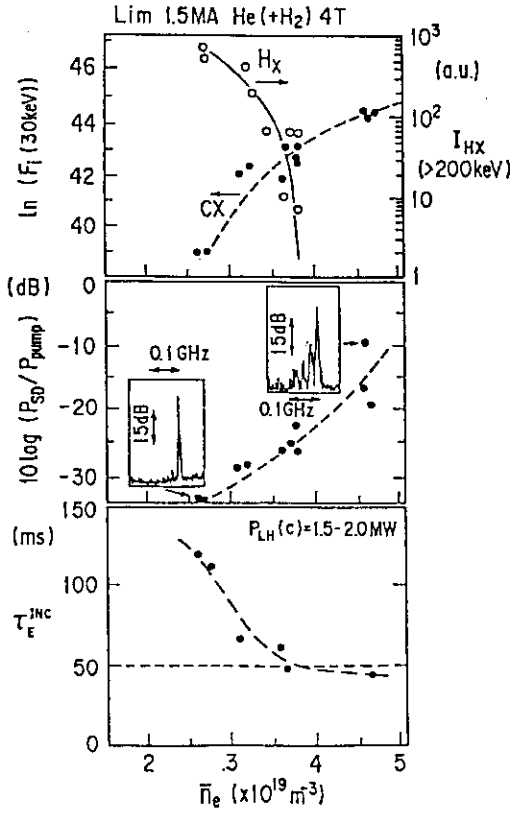

Fig. 1 Phenomena at high density.

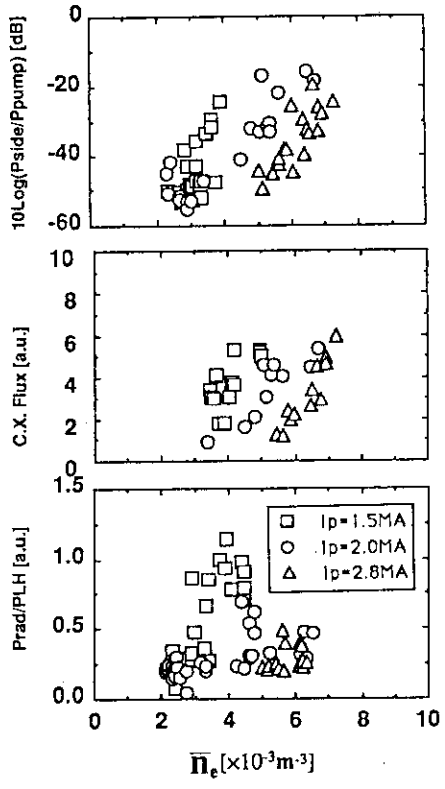

Fig. 2 Effect of the plasma current on the parametric decay wave.

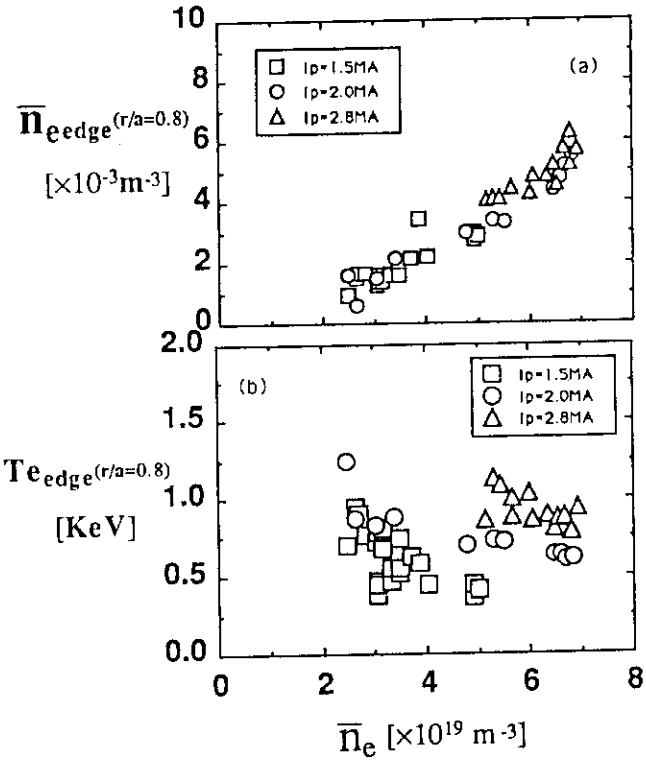

Fig. 3 (a); Effect of the plasma current on edge density.
(b); Effect of the plasma current on the edge temperature.

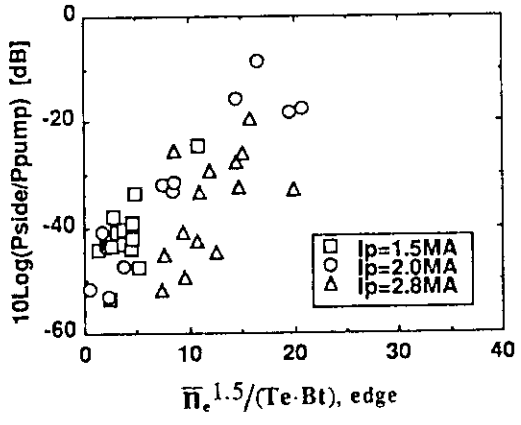

Fig. 4 Intensity of the decay wave as a function of $\bar{n}_e/(Te \cdot Bt)_{edge}$

2.14 IRTV measurement in LHRF current driven plasmas

K.Itami and T.Nishitani

From the view points to reduce the plasma wall interactions and to keep the divertor safe, it is necessary to estimate the heat flux. Impurity production at the divertor plate is a major impurity source in diverted plasmas. The heat flux and particle flux relate on the impurity production and the impurity influx to the main plasma in various ways. The thermal stress cause the fragment of the ceramic come off the surface of carbon tile and go into the plasma. The sublimation and sputtering yield at the carbon surface strongly depend on the surface temperature. The characteristics of divertor plasma with the intense LHRF heating has been not been studied. This paper presents one of the first studies in the large tokamak devices. which emphasize on the behavior of heat flux at the divertor plates using IRTV camera.

The scrape-off layer may not be so clearly defined in LHRF heated plasmas as in beam heated discharges. In order to couple RF power effectively the launcher must be close to the plasma. The gap from the launchers to the separatrix is controlled 0.5cm to 3cm in JT-60 divertor discharges.

In a discharges with small gap, it is expected that the scrape off layer behaves as a intermediate between that in limiter discharges and that in divertor discharges. The energy balance is also different from the discharges with a larger gap. We found that a smaller gap causes larger radiation loss in the main plasma and smaller heat load at the divertor. Figure 1 shows the ratio of the total divertor heat load to the LHRF power as a function of δ_{30} for discharges with small gaps. In the discharges with $\delta_{30} < 1$ cm, 25% of input power is deposited to the divertor as shown in the figure. From the bolometric measurement, 75% of the input power is lost by the radiation loss. The power deposited at the launcher and the walls is small. In LHRF heated discharges, it is found that the sum of the radiation loss power estimated by the bolometric measurement and the divertor heat load from the IRTV measurement agree with LHRF input power quite well.

Figure 2 plots the ratio of heat load to the total RF power as a function of total RF power. The data base points is sampled every 100msec from each discharges during LHRF heating to chase the time evolution. As shown in this figure, up to 45% of input power is deposited at the divertor. After Ti flush, we found completely different behavior of the energy balance. Due to the reduction of oxygen, the radiation loss from the main plasma is reduced

significantly[1]. As shown in Fig.3, more than 70% of input LHRF power is deposited to the divertor plate in the discharges with large LHRF power. Only 30% of the LHRF power is lost by the radiation from the main plasma.

The FWHM of heat flux (the half width) measures the heat flux density. In order to design the fusion device with larger input power, the establishment of scaling of the half width is needed. This value is also useful to estimate the width of the scrape-off layer.

In low electron density discharges, we found the half width depends on the electron density . In current ramp up experiment, the plasm density is as low as $10^{13}\,cm^{-3}$. In these discharges, the plasma current is almost kept constant or slightly increasing while the plasma density increases twice at the end of the discharge. Figure 4 shows typical current ramp up discharges shown with the half width of the heat flux. As the plasma density increases, the half width increases while LHRF power is kept at 2MW. Although the equilibrium calculation shows that the gap between the separatrix and the launcher is increasing during the discharge, this change doesn't affect the heat flux because the scrape-off width is estimated to be a half of the gap. This consideration is supported by the density dependence given by the time evolution of same type discharges. Figure 5 plots the half width against the plasma density from the database of July 24th. Three discharges plotted in this figure reached different density and different gap width, while the LHRF power is about 2MW in the all discharges.

We found the half width is insensitive to the evolution of the electron density during the discharges as shown in the figure 6 in high elctron density discharges. In this figure the data base points of the half width are plotted against the electron density. Only in the discharges with the large gap($\delta_{30} > 2$ cm), the half width depends on the LHRF power. The figure 7 shows the data points of the half width plotted against the LHRF power. Although data points are scattered, the half width decreases as the LHRF power increases.

So called the " hot spot " phenomenon cause the carbon influx and the major disruption of the discharge. Although the phenomenon is referred as the carbon burst caused by high temperature, no significant temperature rise (the temperature of divertor plates go to 400 °C during discharges with 4MW of LHRF power.) has been observed before the onset of the disruption.

References

[1] M.Shimada et al. In this review

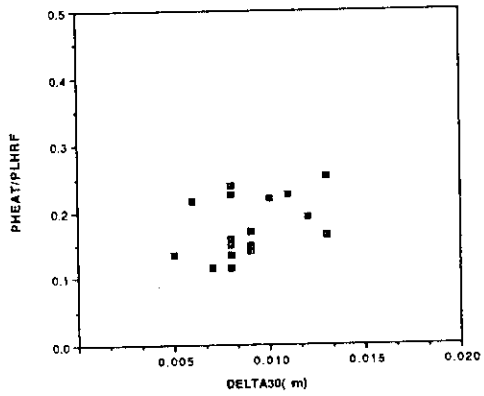

Fig.1 PHEAT/PLHRF vs delta30 in small gap discharges

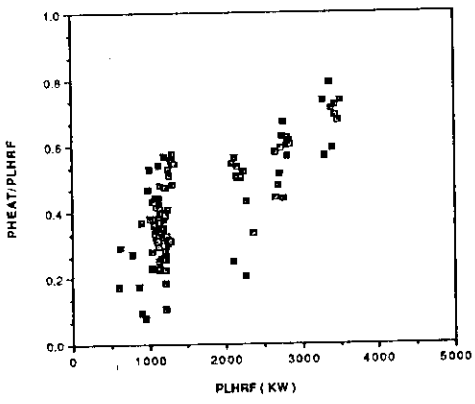

Fig. 3 PHEAT/PLHRF vs PLHRF after TI flush

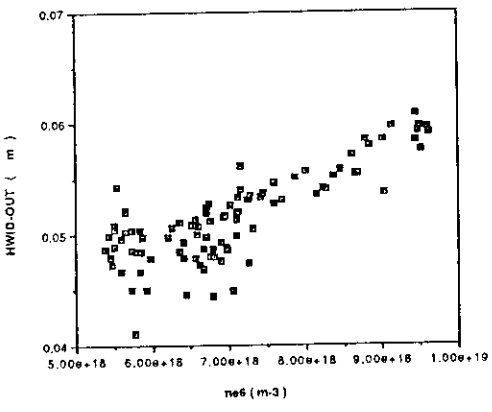

Fig.5 Density dependense of Half Width of heat flux in LHCD plasmas

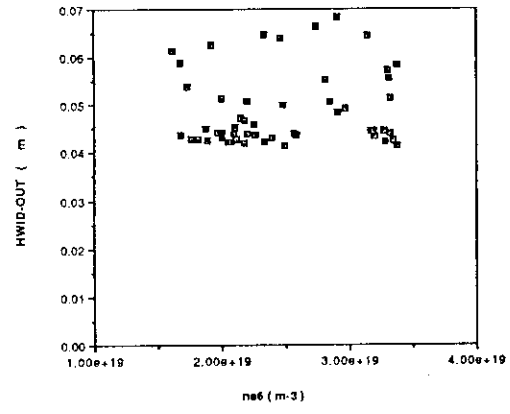

Fig.6 Half Width vs ne6 (elctron density)

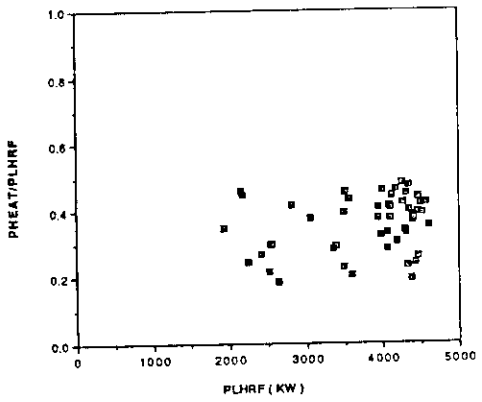

Fig.2 PHEAT/PLHRF vs PLHRF before TI flush

Fig.4 Typical LHCD ramp up discharge

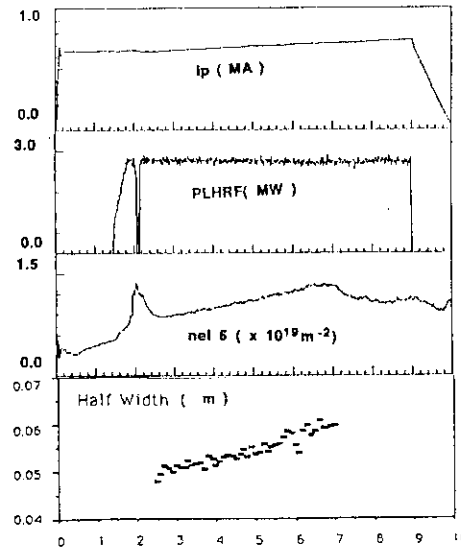

Fig.4 Typical LHCD ramp up discharge

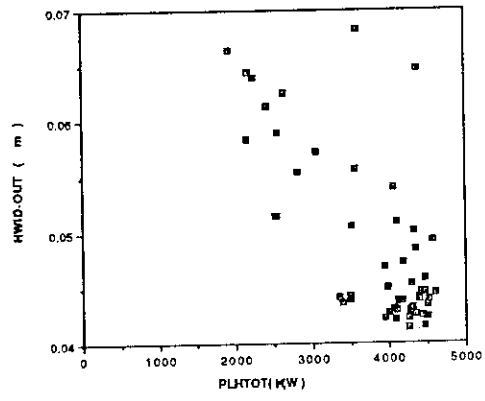

Fig.7 LHRF power dependence of Half Width

2.15 Impurities and Carbon Bloom in LHCD Plasmas

H. Kubo, K. Ushigusa, K. Itami, Y. Kawano, T. Imai, A. Sakasai, Y. Koide, N. Nishino, M. Naito, N. Akaoka, and T. Sugie

The impurity concentrations and the carbon bloom in LHCD discharges are discussed. The concentration of carbon in LHCD discharges was approximately 1.3 times higher than the concentration in OH discharges, and other impurity concentrations were not significantly affected by LHRF injection. The carbon bloom tented to occur in the region of high LHRF power and low electron density. And the amount of the integrated LHRF power added to the plasma to bring about the carbon bloom was 2.2 MW•sec.

1. Impurity Concentrations

Fig. 1 shows temporal behaviors of signals in a LHCD discharge. During the LHCD, the electron density and the intensity of the C VI line ($\propto n_C$) increased. And the increase of the intensity of the O VIII line ($\propto n_O$), the intensity of bremsstrahlung divided by the square of the electron density ($\propto Z_{eff}$), and intensity of the Ti XX line divided by the square of the electron density ($\propto nTi/ne$) were relatively small.

Fig. 2 shows the electron density dependence of Z_{eff} in LHCD discharges (PLH = 1.75-4.44MW) and in OH discharges. Z_{eff} in LHCD discharges was higher than that in OH heated discharges, and Z_{eff} in LHCD discharges was 4 at $\bar{n}_e = 3 \times 10^{19}$ m^{-3}. We should note that the electron density increased with LHRF power in these discharges. Fig. 3 shows the electron density dependence of the concentrations of light impurities in LHCD discharges. In the analysis, the concentration was derived by the same method described in Ref. 1 assuming $n_C/n_O = 0.5\times$ I(C VI)/I(O VIII). The carbon concentration in LHCD discharges is about 1.2 times higher than the concentration in OH discharges, and the oxygen concentration in LHCD discharges is as high as the concentration in OH discharges. And the titanium concentration was estimated to be about 10^{-4} - 10^{-5} from the intensity of Ti XX divided by the square of the electron density. As a results, The dominant impurity in LHCD discharge was carbon, and the increase of oxygen and metal with LHCD was not significantly.

2. Carbon bloom

The duration of the LHCD discharges was sometimes limited by the event which produce a large influx of carbon into the

plasma. The events caused minor disruptions, and sometimes major disruptions followed the events. Fig. 4 shows an example of temporal behaviors of signals in such a LHCD discharge. At t = 6.63 sec, the loop voltage, line intensity of C VI (proportional to the influx of carbon to the main plasma), and the electron density increased suddenly. After that, the discharge was disturbed and disrupted. When the influx of carbon increased, the increase of the intensities of O VIII line (proportional to the influx of oxygen to the main plasma) and other metal lines were not observed. In the divertor region, only the intensity of C II line increased while the intensities of O II line and H_γ line did not increase. Therefore, the event was one of the carbon bloom.

Fig.5 shows the regime of the carbon bloom. As shown in the upper figure, the carbon boom tended to occur in the region of high LHRF power and low electron density. As shown in the lower figure, the energy injected to the plasma did not directly limit the onset of the carbon bloom. Fig. 6 shows the LHRF power dependence of the onset time. The fact that the data fall along a straight line suggests that the amount of the integrated LHRF power to bring about the carbon bloom is constant (2.2 MW•sec) for a given plasma, while a simple local 1-D heat transfer analysis for a tile would give a result of the form, $T_{WALL} \propto P\sqrt{T_{PULSE}}$. This characteristic was also observed in carbon bloom in NB heated discharge in JET[2]. However, the integrated power in JT-60 was much smaller than the power in JET (8 MW•sec). Moreover, the threshold temperature at the surface of the tile in NB heated discharges in TFTR[3] and JET (1900-2000 K) was much higher than the surface temperature of divertor plates observed by an IRTV camera in JT-60.

Because there is no observation of spectra of low ionized carbon ion covering the wide region of the plasma in JT-60, it is difficult to identify where the bloom occurred. It is necessary to install visible TV cameras observing wide area of the first wall surface, and further analysis of the present data should be continued.

3. Summary

The impurity concentrations and the carbon bloom in LHCD discharges are discussed. The carbon concentration in LHCD discharges was approximately 1.3 times higher than the concentration in OH discharges. The carbon bloom tented to occur in the region of high LHRF power and low electron density. And the amount of the integrated LHRF power added to the plasma to bring about the carbon bloom is constant, and this character is similar to the onset condition of carbon bloom in JET. However, the

integrated power in JT-60 was much smaller than the power in JET and the observed surface temperature of divertor plates was much lower than the threshold temperature at the surface of the tile in NB heated discharges in TFTR and JET. It is necessary to observe the wide area of the first wall surface by visible TV cameras, and further analysis of the present data should be continued.

References

1) H. Kubo, T. Sugie, A. Sakasai, et al., Nucl. Fusion, **29** (1989) 571.
2) D. Pasini, Contributed paper in Topical Meeting on High Temperature Erosion of Graphite in Plasmas, Pcinceton Plasma Physics Laboratory, (1989).
3) A Ramsey, Contributed paper in Topical Meeting on High Temperature Erosion of Graphite in Plasmas, Pcinceton Plasma Physics Laboratory, (1989).

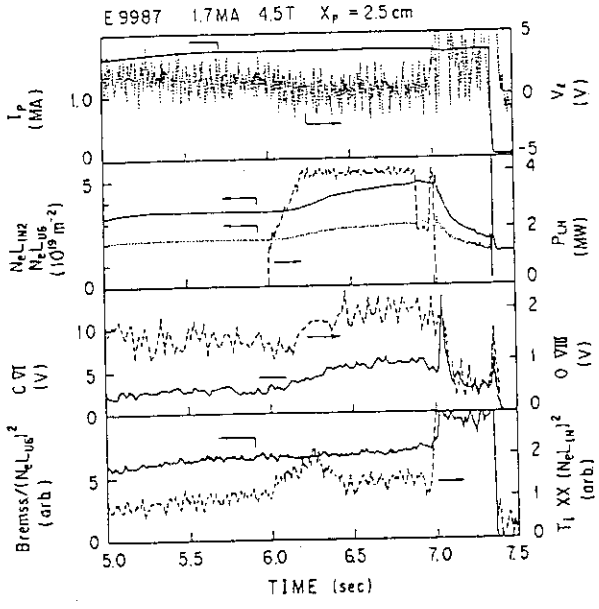

Fig. 1 Temporal behaviors of plasma current, loop voltage, electron density, LHRF power, intensity of C VI 33.7, intensity of O VIII 18.9, intensity of visible bremsstrahlung divided by the square of the line integrated electron density (U6), and intensity of Ti XX 259.3 divided by the square of the line integrated electron density (IN2).

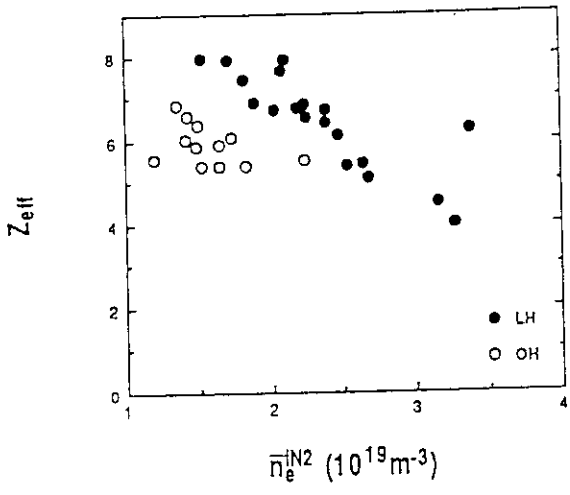

Fig.2 Z_{eff} (U6) versus electron density.

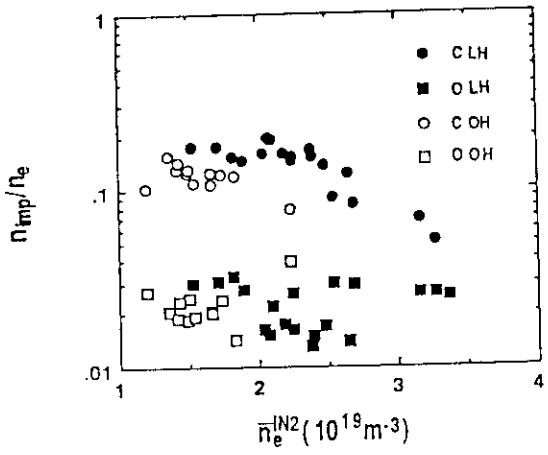

Fig.3 Concentrations of light impurities versus electron density.

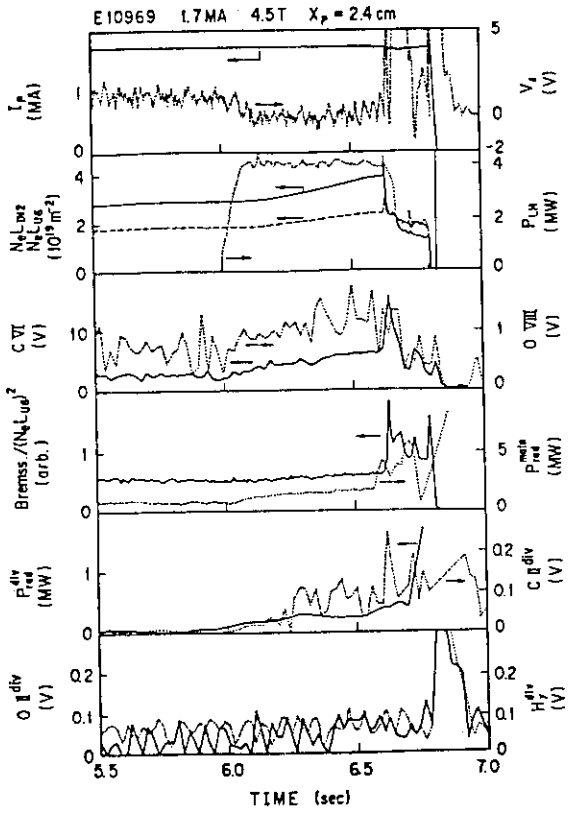

Fig.4 Temporal behaviors of signals in the LHCD discharge with the carbon bloom. C II^{div} (4267), O II^{div} (4190), and H_γ^{div} were observed by a visible spectrometer. The signals have discrepancies of time due to different intervals of their data sampling.

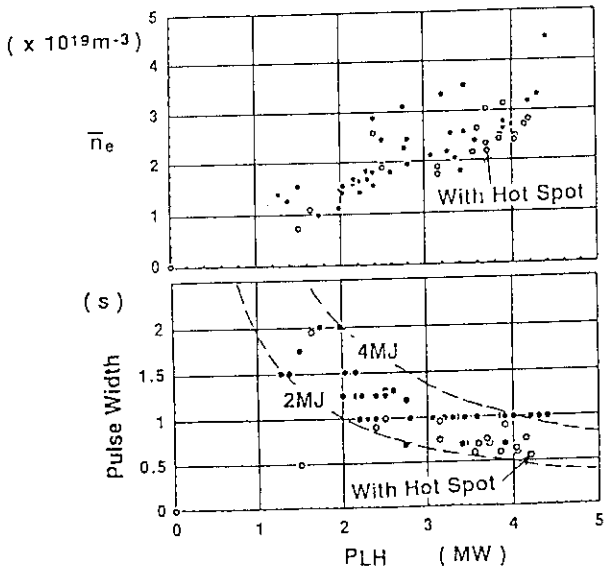

Fig.5 Regime of the carbon bloom.

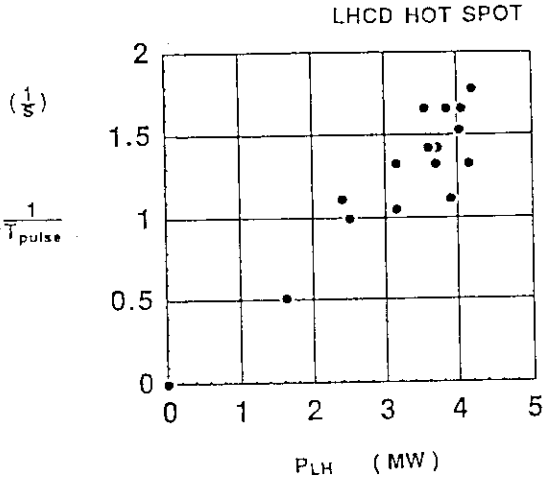

Fig. 6 Onset time of the carbon bloom versus LHRF power.

3. ICRF EXPERIMENT

3.1 Antenna-plasma Coupling and Power-up

S. Moriyama, T. Fujii, H. Kimura M. Saigusa,
K. Annoh, Y. Ogawa, S. Kogure, S. Shinozaki, M. Terakado

1. Introduction

The second and the third harmonic ion cyclotron range of frequency heating to the H-minority and H-majority plasma has been investigated in JT-60 at the frequency of 131MHz. The antenna-plasma coupling properties have been investigated during the ICRF experiment. The coupling resistance is one of the most important factor to limit the injection power. This paper reports the antenna-plasma coupling properties and how to inject ICRF power as high as possible on the coupling and other conditions. The antenna performances till the end of the JT-60 ICRF experiments are also reported.

2. Coupling properties in (π,0) phasing injection

Coupling properties of the ICRF antenna have been investigated in limiter discharge in $B_T \sim 3T$ for $3\omega_{cH}$ heating and 4,3T for $2\omega_{cH}$ heating. The antenna coupling resistance, Rc, versus line averaged electron density are shown in Fig. 1. The launcher-plasma distances i.e. distances between the top of the antenna guard limiter and the outermost magnetic surface are 15 ~ 25mm in these data. Rc seems almost proportional to averaged electron density in 4.0 ~ 4.5T case. In 3.0 ~ 3.3T case, Rc is larger than in 4.0 ~ 4.5T case. It probably comes from steeper decay of the edge plasma profile in higher toroidal field case. The relationship of coupling resistance and the edge plasma profile is discussed in [1].

Figure 2 shows the antenna coupling resistances versus launcher-plasma distance. Rc decreases with increasing the distance and in the case of 85mm distance it reduces to 30% of that of 15mm case. To inject 3MW ICRF power into the plasma, Rc should be larger than 3Ω. Therefor, averaged electron density of 4×10^{19} m^{-3} was needed at the optimum distance, ~ 20mm, in the 4T case.

3. Antenna Performance

At the end of the JT-60 ICRF experiment, achievements of the ICRF launcher are shown in table 1.

In (π,0).phasing, the coupling power has reached the limit determined by the coupling resistance and the limitation of the voltage stand-off at the antenna. The voltage limit once reached 47kV by RF aging of the antenna to vacuum load, but lower voltage limit setting of the protection was chosen to protect the damaged 1st feed through. In (0,0) phasing, more aging shots and enough optimization of the launcher-plasma distance were required to get more coupled power. Because the coupling resistance was relatively high, ~5Ω, and the method of impedance matching was improved [2], 4MW injection could be realized at least with more injection chances.

The power density through the launcher cross section is the highest value among ICRH system, in the world.

PLASMA COUPLING POWER :	2.9 MW in (π,0) phasing 3.1 MW in (0,0) phasing
POWER DENSITY :	16 MW / m^2
VOLTAGE STAND-OFF :	35 kV in plasma 47 kV in vacuum
INJECTION ENERGY :	6.7 MJ

Table 1 Achievement of JT-60 ICRF Launcher

4. Power-up Properties

The coupled power to the plasma of the JT-60 ICRF system is limited by two main reasons. One is the voltage stand-off at the antenna determined by antenna coupling resistances, Rc, and the other is reflected power toward the generator by mismatching of the impedance between the antenna and the transmission line [3]. The problem of the impedance matching discussed in [2].

The voltage stand-off at the antenna and coupled power in the same shots versus launcher-plasma distance are shown in Fig. 3 and Fig. 4 respectively. These data indicate the difference of power-up property between (π,0) phasing and (0,0) phasing. In (π,0) case most of the data reach the voltage limit i.e. the injected power is as high as possible with the coupling resistance of the shot, except some low power shots in more than 40mm region to get coupling property data. In (0,0) phasing larger distance

is required than (π,0) phasing. In the region of less than 40mm, immediately increase of the reflected power probably by breakdown at the antenna was often observed. This limit the injection power in this region. It seems that limit of the voltage stand-off in (0,0) phasing goes down in short distance case. The coupling resistance decreases with increasing distance so the optimum distance exist around 80mm, but enough shots for distance optimization and also for launcher aging were not able to perform in this period of the experiment.

5. Summary

The antenna-plasma coupling property in JT-60 ICRF experiment on the condition of B_T, toroidal field, ~ 3T for $3\omega_{cH}$ heating and 4.3T for $2\omega_{cH}$ heating was investigated. The coupling resistance was larger in 3T case than 4.3T case. It probably comes from steeper decay of the edge plasma profile in higher toroidal field case. Power up property in (π,0) and (0,0) phasing were also investigated. Achieved coupled power is 2.9MW in (π,0) phasing, and 3.1MW in (0,0) phasing respectively. In (π,0) case the power is limited mainly by the voltage stand-off determined by the coupling resistance, and in (0,0) case it is limited by launcher aging and launcher-plasma distance optimization.

References

[1] M. Saigusa, et al., Nuclear Fusion Vol.29, No.1 (1989), pp.73-77.

[2] S. Moriyama, et al., Section 3.2 of this report.

[3] JT-60 Team, Japan Atomic Energy Research Institute Report JAERI-M, 89-033 (1989), pp.173-176.

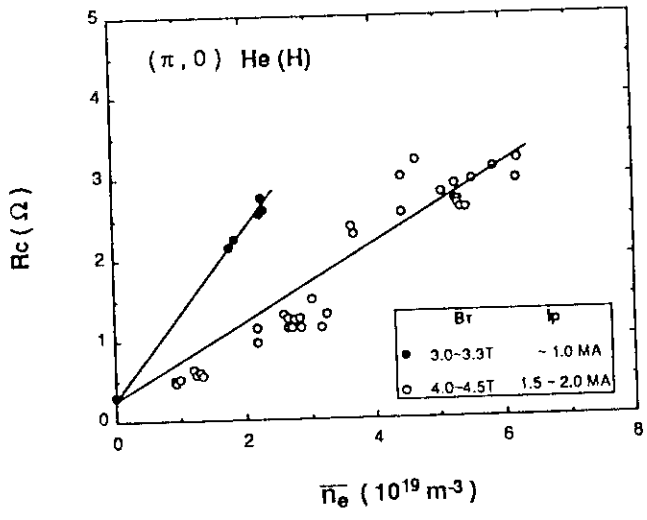

Fig. 1 Coupling registance versus line averaged electron density in (π,0) phasing. Launcher-plasma distance are 15 ~ 30 mm. The coupling resistances (Rc) were averaged value for four antennae.

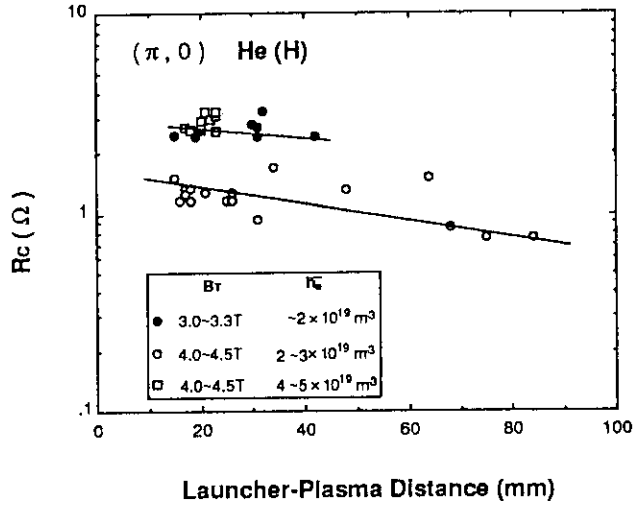

Fig. 2 Coupling resistance versus launcher-plasma distance in (π,0) phasing.

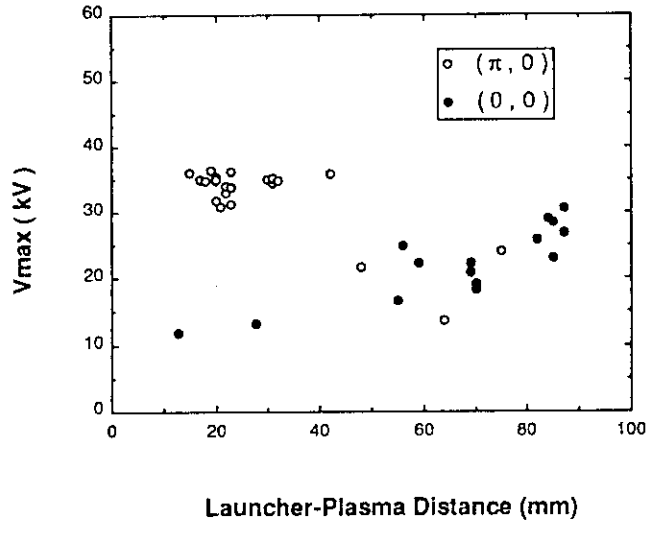

Fig. 3 Voltage stand-off at the antenna versus launcher-plasma distance in (π,0) and (0,0) phasing. Line averaged electron density are 2.0 ~ 5.0 $\times 10^{19}$ m^{-3} for (π,0), and 1.0 ~3.0 $\times 10^{19}$ m^{-3} for (0,0).

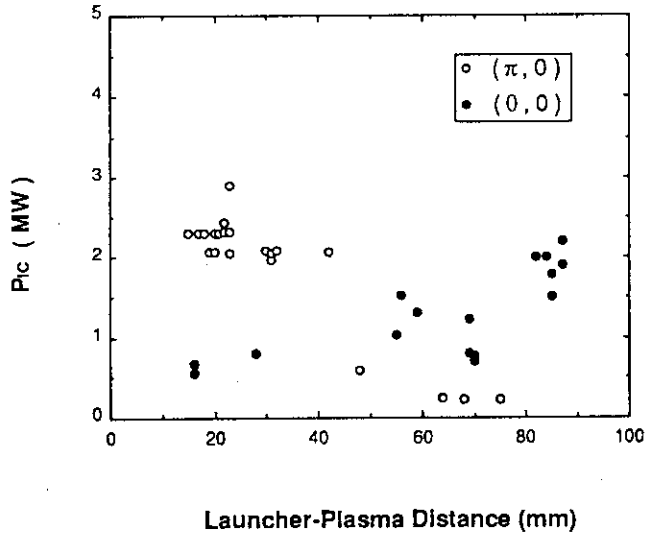

Fig. 4 ICRF power coupled to plasma versus launcher-plasma distance. Points in more than 40 cm region are lowpower shots to get coupling property data.

3.2 Improvement of Impedance Matching by Frequency Feed-back Control

S. Moriyama, H. Kimura T. Fujii, M. Saigusa,
K. Annoh, Y. Ogawa, S. Kogure, S. Shinozaki, M. Terakado

1. Introduction

Frequency feed-back control (FFC) was introduced to JT-60 ICRF experiment to improve antenna-transmission line impedance matching. Impedance matching is important to reduce reflected power toward the generator and enable high power injection. FFC is effective to improve the matching rapidly when the setting position of the stub tuner comes inappropriate for the matching when the antenna impedance changes with plasma parameters. This paper reports the principle of the frequency feed-back control, typical result in the JT-60 ICRF experiment and analyses of the effect of FFC.

2. Necessity of precise impedance matching for the ICRH system

In general, the antenna impedance is different from transmission line impedance in the ICRF heating system. In the case of JT-60 ICRF system, these are 0.3 ~ 6Ω and 50Ω respectively, and double stub tuners are used for matching.[1] If the matching is insufficient, reflected power toward the generator decreases the gain of the amplifier and increases the voltage at the output port of the cavity and in the tube of the final stage amplifier. Figure 1 shows relation between injection power and upper limit of allowable power reflection coefficient. Curves indicate the levels of the protection circuit for the amplifier or for the tube, if the reflection coefficient comes over these lines out put power of the generator will be reduced or cut off.[2] Reflection coefficient less than 15 % enables 3 MW injection and to get 4 ~ 5 MW reflection coefficient must be less than 5 %.

3. Principle of frequency feed-back control

Precise matching can be easily got with the steady load, but the antenna impedance with the plasma load changes shot by shot or also during a shot. The stub tuners must be set at the position predicted from the impedance data of previous similar shots, and it was impossible to keep the precise matching during the shot if large impedance change happens. The frequency feed back control is useful for these problem.

Figure 2 shows the reflection coefficient versus frequency calculated from certain stub positions and a impedance, and shows the principle of frequency feed-back control. The reflection coefficient varies with frequency and the minimum point exists. From the original frequency (point No.0), FFC changes frequency up (No.1) and down (No.2) automatically and compare the reflection coefficient. Then the frequency is changed step by step toward the minimum reflection coefficient point. For rapid search, the step size increases so long as the gradient is same sign. And the reflection coefficient, Γ, becomes smaller than set value the frequency is fixed. If it becomes larger with change of the load, then the search will begin again.

The frequency step is 2kHz, band width is ± 400kHz (± 200kHz for full power) and averaged time for one step is about 500μsec in this system.

4. Typical Results

Figure 3a and 3b shows time evolution of the frequency, reflection coefficient, and forward and reflected power in the JT-60 ICRF heating experiment. These shots are almost same plasma parameter, antena-plasma distance or line averaged electron density etc., Fig. 3a without FFC and Fig. 3b with FFC. In Fig. 3a, reflected power limiter [2] reduced the power to protect amplifier, then the reflection coefficient indicate the effect of FFC. The reflection coefficient exceeded 10 % without FFC and it was kept around 5 % with FFC. (Power cutting off for short period in fig. 3b was caused by breakdown at the antenna.) The result shows that FFC can keep better matching even if the stub position is not best.

FFC is also effective for suddenly impedance change in a shot. Figure 4 shows time evolution of some plasma parameters, forward and reflected power, antenna coupling resistance, and frequency. In spite of rapid change of the coupling resistance caused, FFC kept low reflected power without power cutting off with reflected power limiter.

Figure 5 also shows that FFC kept good matching against difference of coupling resistance with and without NBI in one plasma shot. Thus FFC can enable various experiment scenarios shot by shot, and save time and labor for precise impedance matching.

5. Analysis

Figure 6a shows improvement of matching by FFC on the impedance plane. The point 3 and 4 are the measured impedance of antenna No. 3 and No. 4 in the antenna array of the JT-60 ICRF launcher. The contours indicate the transmission coefficient i.e. $1-\Gamma$, which is calculated from stub positions and frequency. In this shot, frequency shift by FFC is +55kHz. In Fig. 6b, the contours are calculated with fixed frequency and the point 1 and 2 is plotted same positions as in Fig. 6a. We can see that the transmission coefficient of antenna No.4 is increased 75% to 85% with 55kHz of frequency shift. This result shows the matching improvement with enlargement of better matching region on the impedance plane, by FFC.

6. Summery

Frequency feed back control (FFC) was introduced in JT-60 ICRF heating system. FFC enabled better impedance matching between antenna and transmission line, even if the stub position is not best. For suddenly impedance change in a shot, FFC can keep reflected power low. Much time and labor for precise impedance matching are saved by the effect of FFC. To realize fully automatic impedance matching, feed back control of the stub tuners is under consideration..

References

[1] JT-60 Team, Japan Atomic Energy Research Institute Report JAERI-M, 87-009 (1989), pp.196-201.
[2] JT-60 Team, Japan Atomic Energy Research Institute Report JAERI-M, 89-033 (1989), pp.173-176.

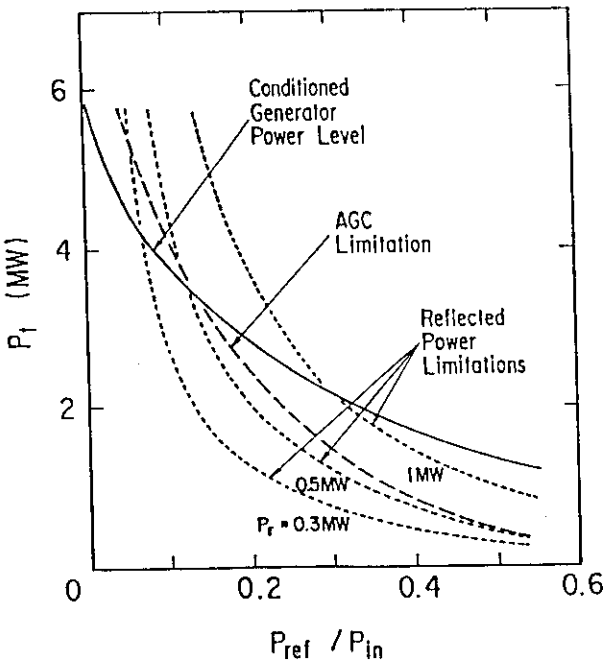

Fig. 1 Relation between injection power and upper limit of allowable power reflection coefficient. Curves indicate the levels of the protection circuit for the amplifier or for the tube.

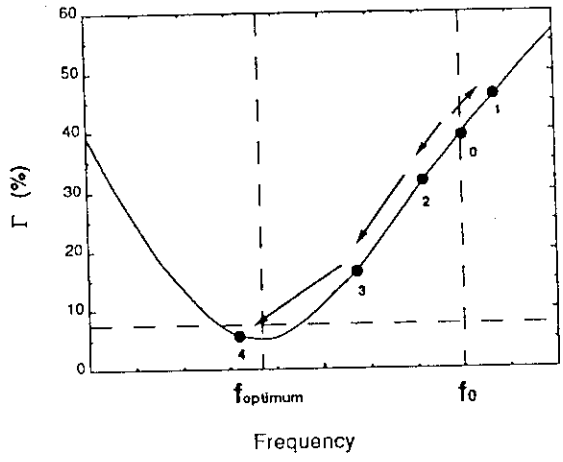

Fig. 2 The reflection coefficient versus frequency calculated from certain stub positions and a impedance. Frequency is changed step by step toward the minimum reflection coefficient point by FFC.

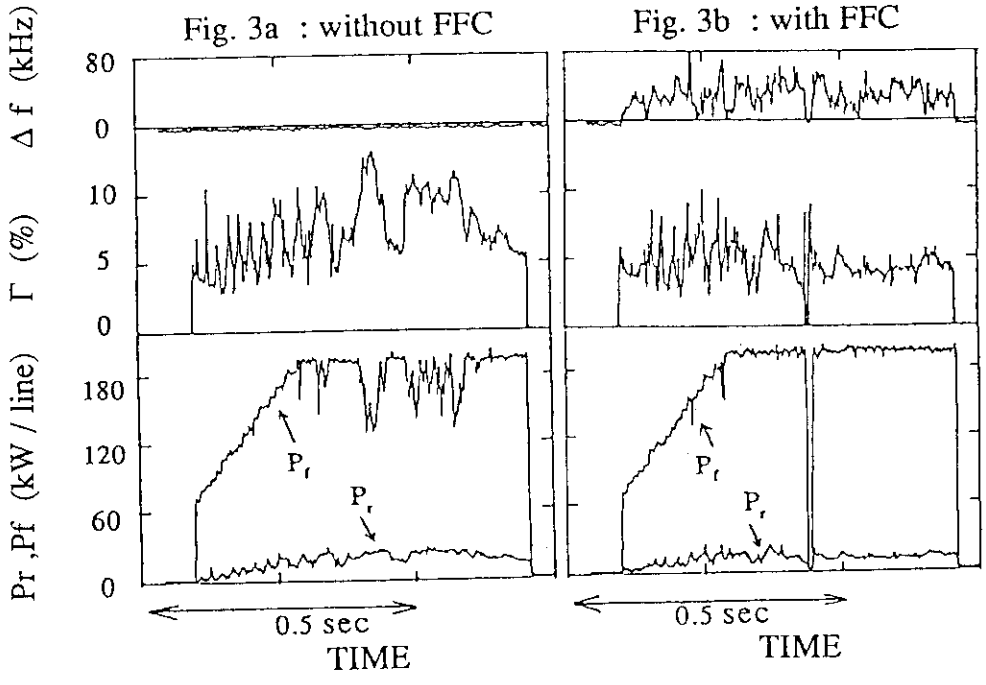

Fig. 3 Time evolution of the frequency, reflection coefficient, and forward and reflected power in the JT-60 ICRF heating experiment. These shots are almost same plasma parameter, antena-plasma distance or line averaged electron density etc., Fig. 3a without FFC and Fig. 3b with FFC.

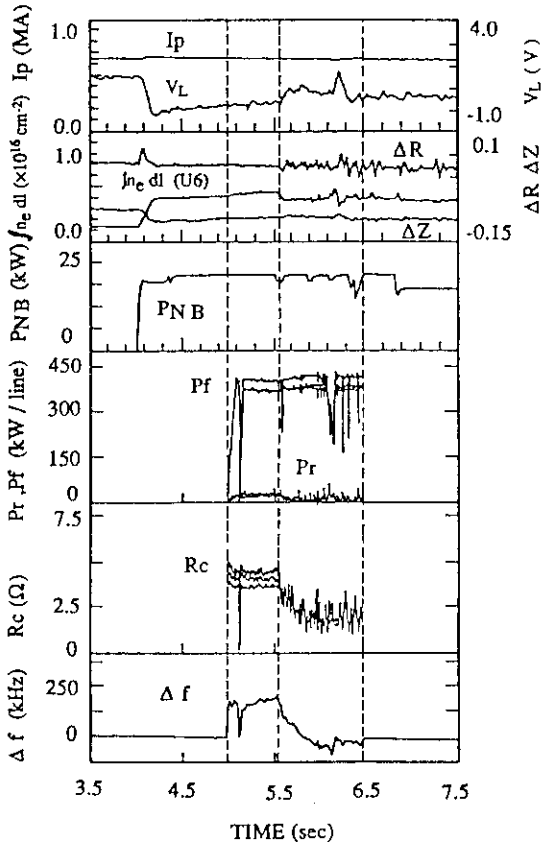

Fig. 4 Time evolution of some plasma parameters, forward and reflected power, antenna coupling resistance, and frequency. In spite of rapid change of the coupling resistance caused, FFC kept low reflected power without power cutting off with reflected power limiter.

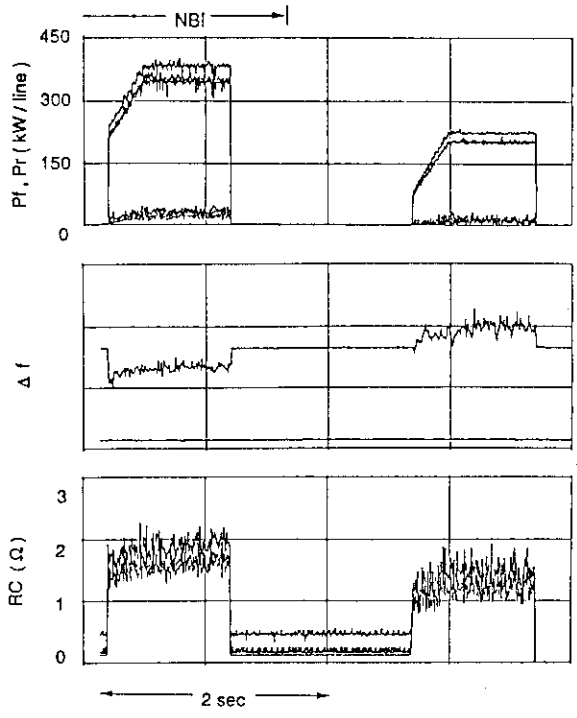

Fig. 5 FFC kept good matching against difference of coupling resistance with and without NBI in one plasma shot.

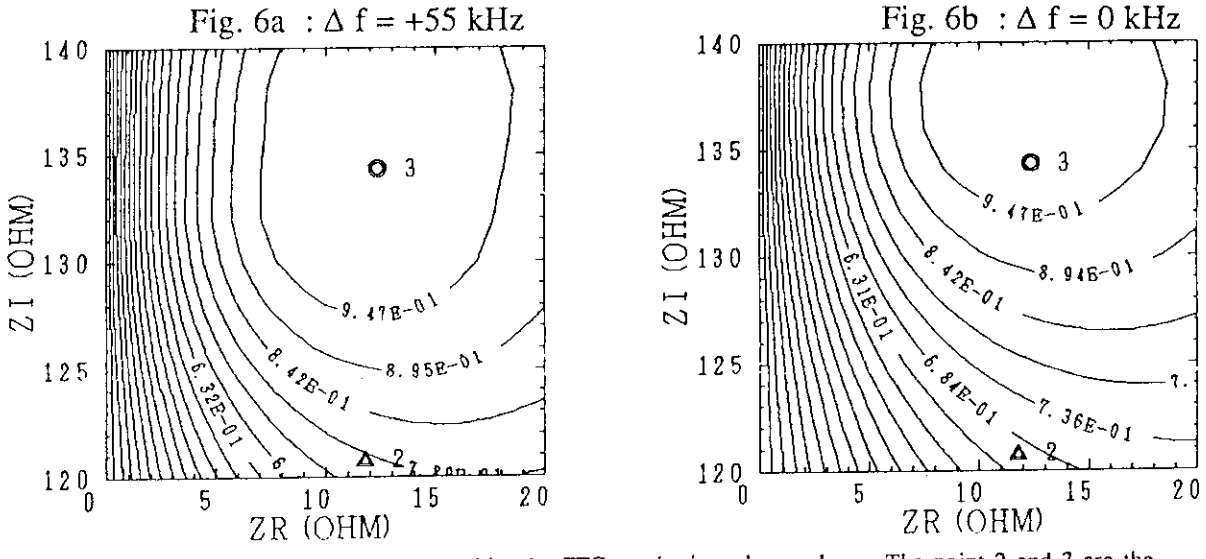

Fig. 6 Improvement of matching by FFC on the impedance plane. The point 2 and 3 are the measured impedance of two antennae in the antenna array of the JT-60 ICRF launcher. The contours indicate the transmission coefficient i.e. 1-Γ, which is calculated from stub positions and frequency. In this shot, Fig. 6, frequency shift by FFC is +55kHz. In Fig. 6b, the contours are calculated with fixed frequency and the point 2 and 3 are plotted same positions as in Fig. 6a

3.3 Hydrogen Minority Second Harmonic Heating in Helium Discharge

T. FUJII, H. KIMURA, M. SAIGUSA, K. HAMAMATSU, S. MORIYAMA, T. FUKUDA, S. ISHIDA, Y. KOIDE, H. KUBO, Y. KUSAMA, K. NAGASHIMA, M. NEMOTO, A. SAKASAI, K. TOBITA

1. Introduction

The second harmonic heating is one of attractive heating schemes of ion cyclotron range of frequencies (ICRF) in a large tokamak because the ICRF power is expected to be sufficiently absorbed in hot and dense plasmas from theoretical predictions [1]. The second harmonic heating also is insensitive to ion species mix [2] which can not be easily controlled in a reactor grade tokamak. Furthermore, from a view-point of antenna technology, it is possible to use a compact phased array or a waveguide antenna because the higher frequency is applied. Therefore, the investigation of the second harmonic ICRF heating on JT-60 is substantially significant in order to optimize the plasma heating in a reactor grade tokamak. This paper presents the heating characteristics of the hydrogen minority second harmonic (H-minority 2 ω_{cH}) scheme in two phasing modes, in-phase and out-of-phase of antenna currents in the toroidal direction, compared with those of the hydrogen majority second harmonic (H-majority 2 ω_{cH}) scheme.

2. Experimental Results and Discussion

2. 1 Heating Characteristics

The H-minority second harmonic ICRF heating experiments in helium plasmas ($n_H/n_{He} \approx 0.1$) has been performed with a phased 2 x 2 loop antenna in wide parameters of the ohmically heated target plasmas, $\bar{n}_e = 1.3 - 6.6 \times 10^{19}$ m^{-3}, $I_P = 1 - 2.4$ MA $q_{eff} = 6.4 - 2.6$ and $T_{e0} = 1.5 - 3.0$ keV in limiter configuration on JT-60. The applied frequency is 131 MHz which corresponds to the hydrogen second (helium fourth) harmonic cyclotron frequency at $B_T = 4.3$ T. The phase difference between the antenna currents can be controlled in the toroidal and poloidal directions. We denote a phasing mode as ($\Delta\phi$, $\Delta\theta$), where $\Delta\phi$ is the toroidal phase difference and $\Delta\theta$ the poloidal one. The ICRF power has been injected into plasmas up to 2.9 MW in the (π,0) phasing.

Figure 1 (a) shows a set of time evolution of W^{DIA}, $\bar{n}_e$, T_{e0}^{ECE} and P_{IC} in a typical result of H-minority 2 ω_{cH} heating at $I_P = 2.4$ MA, $\bar{n}_e = 5.9 \times 10^{19}$ m^{-3} and $P_{IC} = 2.1$ MW. The stored energy increases by about 260 kJ during the ICRF heating. The large sawtooth oscillations in the central electron temperature are observed such as the giant sawteeth observed in JET [3]. The changes in the stored energy coincident with the sawtooth oscillations are found. The oscillation period is approximately 0.25 s which is twice longer than that of H-majority 2 ω_{cH} heating in the (π,0) phasing at $I_P = 1.5$ MA. Further, the electron temperature tends to saturate during the sawtooth period. The electron temperature profile as a function of the effective minor radius estimated by the ECE measurements are given in Fig. 1 (b). The electron temperature shows a centrally-peaked profile during the ICRF heating. The sawtooth inversion radius is about 0.4 m which roughly corresponds to a_p/q_{eff}.

Power absorption profiles are calculated from the modified 1-dimensional kinetic code which takes the ion tail formation into account but does not the absorption by the fourth harmonic cyclotron resonance of helium [4]. The radial profile of the absorbed power partition after the collisions is given in Fig. 2 (a). The plasma parameters, $T_{e0} = 3.0$ keV, $n_{e0} = 6.5 \times 10^{19}$ m^{-3} and $n_H/n_{He} = 0.1$ in the shot shown in Fig. 1 (b), $P_a = 1.4$ MW and $\rho_w = 10^{-4}$ Ωm are used in the calculation. First, the ICRF power is strongly absorbed by the minority ion tail of hydrogen in the narrow region near the plasma center. The absorbed power by the minority ion tail, P_H^{tail}

reaches 0.99 of the total absorbed power P_a. Next, the absorbed power is distributed to bulk helium and hydrogen ions and electrons through coulomb collisions. Electrons gain the large fraction of the absorbed power, namely about 0.73. The bulk helium and hydrogen ions obtain 0.24 and 0.03 of the absorbed power, respectively. Then, the calculated result explains the centrally-peaked profile of the measured electron temperature. Figure 2 (b) shows the distribution function for the minority hydrogen ions at $r < 0.2$ m as a function of the ion energy, which reveals that the minority ion tail can be generated even in high density for H-minority 2 ω_{cH} heating. On the other hand, in the experiments, the fast hydrogen ions with their energy of more than 50 keV are not observed in high densities with the cx neutral analyzer although the intensive non-Maxwellian tails are observed in the low densities ($\bar{n}_e < 3\times10^{19}$ m^{-3}). But even if the fast hydrogen ions are generated near the plasma center, the fast ions can not be observed because the hydrogen density near the plasma center are reduced due to high density helium discharge and further the cx neutrals are reionized within the plasma. The electron heating efficiency ($\eta_e = \bar{n}_e \Delta T_{e0} R / P_{IC}$) indicates a relative high value of about 6.1 keV10^{19}m^{-2} / MW, which corresponds to a half level of that of fundamental minority ICRF heating in JET [5]. Therefore, significant electron heating, even in high density is caused by the ion tail formation.

2. 2 Incremental Energy Confinement

The incremental energy confinement time can be regarded as the total heating efficiency and is defined as

$$\tau_E^{inc} = (\Delta W^{DIA} - \Delta W_s(\Delta \bar{n}_e)) / (P_{IC} + I_P \Delta V_L),$$

where $\Delta W_s(\Delta \bar{n}_e)$ is increment in the ohmic stored energy due to the increase in $\bar{n}_e$ and ΔV_L the change in one turn loop voltage during the ICRF heating. Figure 3 shows the $\bar{n}_e$ dependence of τ_E^{inc} in different heating regimes at I_P = 1.5 MA. Excellent values of $\tau_E^{inc} \approx$ 90 - 120 ms are achieved by H-minority $2\omega_{cH}$ heating in the (π,0) phasing, which are approximately constant in the density range of $\bar{n}_e$ = 2.5 - 5.6 x 10^{19} m^{-3}. The (π, 0) phasing heating shows larger τ_E^{inc} than the (0,0) phasing one in both H-minority and H-majority heating schemes. The parametric decay instabilities are observed only in the (0,0) phasing for both heating schemes as described in Section 3.8, which may dissipate the ICRF power in the edge plasma. Therefore, the parametric decay instability is one of the possibilities that degrade τ_E^{inc} in the (0,0) phasing.

Figure 4 shows the I_P dependence of τ_E^{inc} for various heating regimes in the range of I_P = 1-2.4 MA which corresponds to $q_{eff} \approx$ 6.4 - 2.6. The (π,0) phasing data in H-minority 2 ω_{cH} heating increase from 1 MA to 1.5 MA and are approximately constant at $\tau_E^{inc} \approx$ 90 - 120 ms from 1.5 MA up to 2.4 MA in low and high densities. The degradation of τ_E^{inc} is not clearly observed at $q_{eff} < 3$ ($I_P > 2.1$ MA). The ion tail formation is one of mechanisms that enhance the power absorption. The non-Maxwellian ion tails are observed in each heating regime. The remarkable ion tails are observed at I_P = 1. 5, 1.9 MA in low density, indicating that the maximum ion energy reaches 80 - 130 keV. However, the intense ion tails are not observed at I_P = 1 MA. Accordingly, the ion tail is one of the causes that bring the enhancement of the power absorption and the resulting improvement of τ_E^{inc} at $I_P \geq$ 1.5 MA. Furthermore, these weak I_P and $\bar{n}_e$ dependences of τ_E^{inc} in H-minority $2\omega_{cH}$ heating support Shimomura-Odajima scaling of τ_E^{inc} [6] given by

$$\tau_E^{inc} \text{ (ms)} = 85\ \kappa\ a_p^2\ M_{eff}^{1/2},$$

where κ is the ellipticity and M_{eff} the effective ion mass in AMU and a_p the minor radius in m. But the data are larger by a factor of about 1.5 than Shimomura-Odajima scaling if $M_{eff} = 1$. Consequently, the helium mass effect is one of the possibilities that improve τ_E^{inc}, which is clearly observed in combined NBI and ICRF heating as described in Section 3.4.

In order to find the relation between the power absorption efficiency P_a/P_{IC} and τ_E^{inc}, the absorbed power is estimated from the time evolution of W^{DIA} after the ICRF pulse. One estimation of P_a is done by a time differential of W^{DIA} at the end of the ICRF pulse ($P_a = -dW^{DIA}/dt$). Another estimation is done by fitting the measured time evolution of W^{DIA} with that calculated from the model where the stored energy is contained in the bulk electrons and ions and the fast ions. Figure 5 shows τ_E^{inc} versus P_a/P_{IC} for the various heating regimes, electron densities and plasma currents. The value of τ_E^{inc} increases roughly with P_a/P_{IC}. The ratio of τ_E^{inc} to P_a/P_{IC} is found to be approximately constant at 180 ms irrespective of $\bar{n}_e$, I_P and the heating schemes.

3. Conclusions

Heating characteristics of H-minority $2\omega_{cH}$ ICRF scheme in helium plasmas ($n_H / n_{He} \approx 0.1$) have been examined on JT-60 with the ohmically heated target plasmas of $\bar{n}_e$ = 1.3 - 6.6 x 10^{19} m^{-3}, I_P = 1 - 2.4 MA in limiter configuration. Effective electron heating are obtained even in high density. This result is explained with the minority ion tail formation which is predicted by the modified 1-dimensional kinetic code. The sawtooth oscillations with enhanced period such as the giant sawteeth are observed during the ICRF heating. H-minority $2\omega_{cH}$ heating indicates better heating efficiency than H-majority $2\omega_{cH}$ heating. The (π,0) phasing heating shows better heating efficiency (excellent τ_E^{inc} of about 90 -120 ms) than the (0,0) phasing one. The parametric decay instability is one of the possibilities that degrade τ_E^{inc} in the (0,0) phasing. The (π,0) phasing data of τ_E^{inc} are almost constant with $\bar{n}_e$ and I_P except 1 MA, which support Shimomura-Odajima scaling of τ_E^{inc}. But the data are larger by a factor of about 1.5 than Shimomura-Odajima scaling if $M_{eff} = 1$. Consequently, the helium mass effect is one of the possibilities that improve τ_E^{inc}. Further, the observed non-Maxwellian ions enhance the power absorption and may explain the improvement of τ_E^{inc} at $I_P \geq 1.5$ MA. The value of τ_E^{inc} increases roughly with the power absorption efficiency P_a/P_{IC} irrespective of $\bar{n}_e$, I_P and the heating schemes.

References

[1] A. Fukuyama, S.-I. Itoh, K. Itoh, Research Report HIFT-86 (Hiroshima Univ. 1983).
[2] K. Steinmetz, F. X. Soldner, D. Eckhartt, et al., in Plasma Physics and Controlled Nuclear Fusion Research 1986 (Proc. 11th Int. Conf. Kyoto, 1986), Vol. 1, IAEA, Vienna (1987) 461.
[3] D. J. Campbell, P. A. Duperrex, A. W. Edwards, et al., in Plasma Physics and Controlled Nuclear Fusion Research 1986 (Proc. 11th Int. Conf. Kyoto, 1986), Vol. 1, IAEA, Vienna (1987) 433.
[4] K. Hamamatsu, M. Azumi, Y. Kishimoto et al., Nucl. Fusion **29** (1989) 147.
[5] JET Team, Plasma Phys. Controll. Fusion **30** (1988) 1467.
[6] Y. Shimomura, K. Odajima, Comments Plasma Phys. Controlled Fusion **10** (1987) 207.

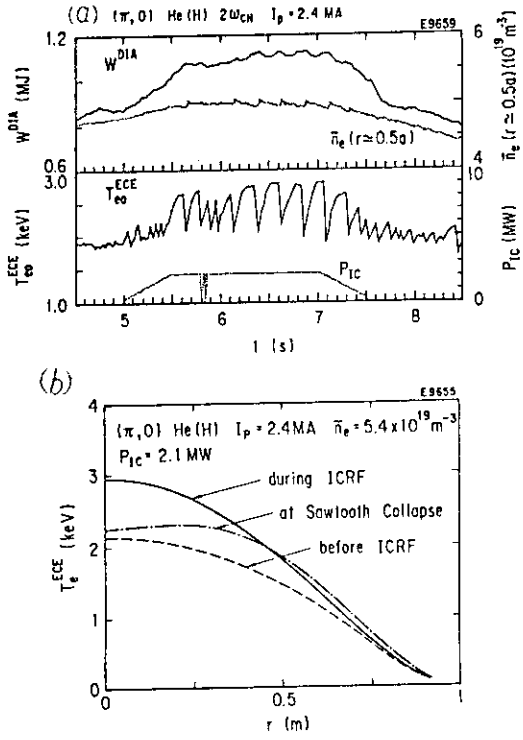

Fig. 1 (a) A set of time evolution of W^{DIA}, $\bar{n}_e$, T_{e0}^{ECE} and P_{IC} in H-minority 2 ω_{cH} heating at I_P = 2.4 MA, $\bar{n}_e$ = 5.9 x 10^{19} m^{-3} and P_{IC} = 2.1 MW. (b) The electron temperature profiles estimated by the ECE measurements as a function of the effective minor radius.

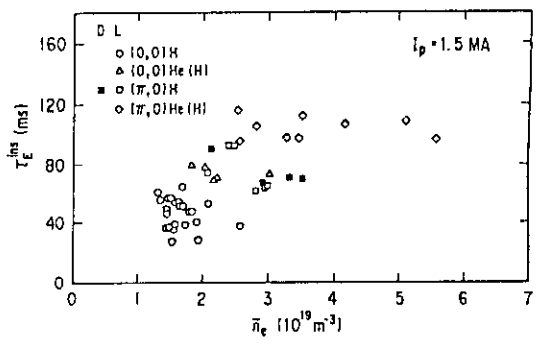

Fig. 3 Dependence of τ_E^{inc} on $\bar{n}_e$ for different heating regimes at I_P = 1.5 MA.

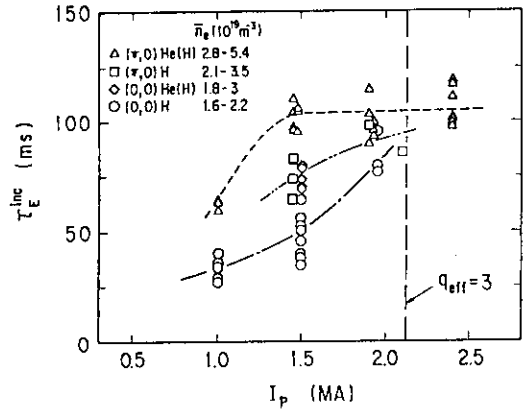

Fig. 4 I_P dependence of τ_E^{inc} for different heating regimes in the range of I_P = 1- 2.4 MA.

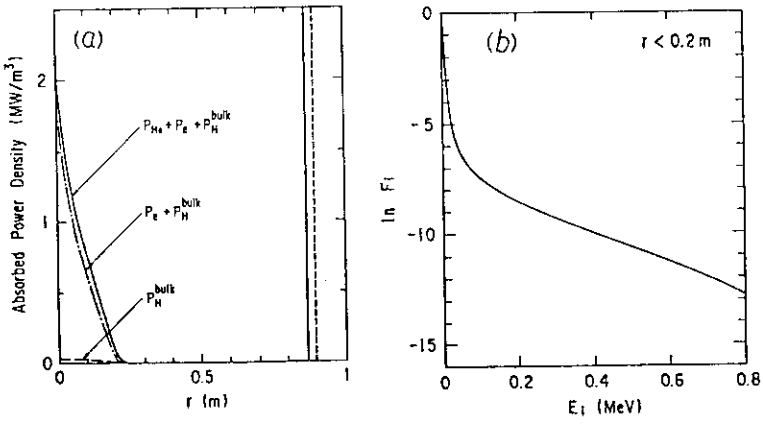

Fig. 2. The calculated results for the plasma parameters shown in Fig. 1 from the modified 1-dimensional kinetic code. (a) Radial profile of the power partition due to collisions with bulk helium and hydrogen ions and electrons for the absorbed power. (b) Distribution function for the minority hydrogen ions at r < 0.2 m as a function of the ion energy.

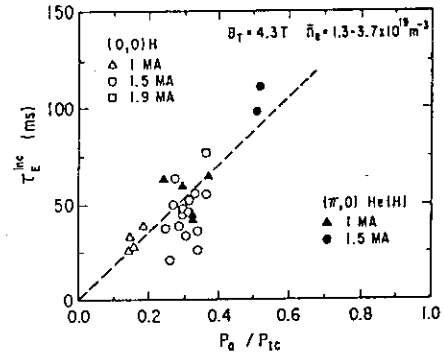

Fig. 5 Dependence of τ_E^{inc} on P_a/P_{IC} for different heating regimes, electron densities and plasma currents.

3.4 Higher Harmonic ICRF Heating in Combination with NBI Heating

H. KIMURA, T. FUJII, K. HAMAMATSU,
K. TOBITA, M. NEMOTO, S. MORIYAMA, M. SAIGUSA

1. Introduction

ICRF heating accompanied with beam acceleration in higher harmonic regime was investigated in JT-60. In this section, experimental results on third harmonic heating in hydrogen or helium discharges and hydrogen minority second harmonic heating in helium discharges, in combination with NBI heating are presented. These results will extend applicability of ICRF heating in a fusion reactor, e.g., selective heating of α particles in the plasma core for heating to ignition and burn control by the third harmonic heating. Related sections to this section are as follows. In Sec. 3.3, results on hydrogen minority second harmonic heating with ohmic target plasmas are described. In Sec. 3.5, beam acceleration during the higher harmonic heating in combination with NBI heating is presented. Analysis of the beam acceleration with higher harmonic ICRF waves is given in Sec. 3.6.

In all cases of the present experiments, hydrogen is resonant species for ICRF heating and hydrogen neutral beam is employed. A frequency of ICRF heating is 131MHz and a toroidal field is selected in order to place the pertinent resonance layer near the plasma center, i. e. 4.3T for the second harmonic heating and 3T for the third harmonic heating. Antenna phasing mode is chosen at $(\pi,0)$, which was found to be efficient in bulk plasma heating and beam acceleration [1].

2. Third Harmonic Heating

Experiments on the third harmonic heating was carried out with following discharge conditions; B_T =3T, I_P=0.7~1.4MA, q_{eff}=7~3.2, $\bar{n}_e$=1.7~4$\times10^{19}$m^{-3}. Both hydrogen and helium discharges were employed. Ohmic target plasmas are found to be insufficient for absorption of the third harmonic waves even with $(\pi,0)$ mode. Therefore we added neutral beam power in order to increase absorption. A range of the NBI power in the present experiment is 2~18MW. Mixture gas (He;90%, H2:5%) was used for helium discharges. However, because the electron density of ohmic target plasmas is relatively low ($\bar{n}_e$=1~1.5$\times10^{19}$m^{-3}), the proton concentration ratio to the electron amounts to as much as 60% with hydrogen neutral beam injection of ~10MW.

Typical time evolution of the third harmonic heating at I_P=1MA and q_{eff}=5 is shown in Fig. 1(a). In order to check the effects of NBI power on the third harmonic heating, NBI power was varied during the shot (i. e., absorbed NBI power 5.4MW $\rightarrow$ 10.3MW). ICRF power was also varied according to the change of NBI power (i. e., coupled ICRF power 1.9MW $\rightarrow$ 2.3MW). The plasma stored energy increases step by step according to the change of the heating power. Central electron temperature increases significantly and giant sawtooth oscillation is observed at combined ICRF and higher power NBI heating phase. A period of the sawteeth reaches 410msec, which is about 6 time as long as the energy confinement time of this discharge (73msec). The sawtooth period, however, decreases with increasing electron density in the course of the discharge. The plasma stored energy also oscillates with giant sawtoothing. Figure 1(b) shows a detail of the oscillation of the stored energy. The stored energy does not decay immediately after the sawtooth crash, but

it decays with a time constant of ~40msec, which is about half of the global energy confinement time. Profiles of the soft X-ray signal at the bottom (t=5.43sec) and the top (t=5.83sec) of the sawtooth and the bottom of the stored energy (t=5.5sec) are indicated in Fig. 2. The internal disruption does not directly lose energy from entire volume of the plasma column. One can see from the change of the soft X-ray profiles from 5.43sec to 5.5sec that a certain amount of the stored energy (~50kJ) is lost from outside of q=1 surface. A broad profile formed just after the sawtooth crash may make confinement degrade, since decay time of the stored energy after sawtooth crash is shorter than the global energy confinement time. From the bottom of the oscillation of the stored energy, the profile becomes peaked due to the ICRF central heating. The confinement is improved significantly with the peaked profile, which is understood from much longer time constant of the growing phase of the stored energy.

Figure 3 shows the plasma stored energy against the absorbed power. The data of combined heating and NBI heating only for both helium and hydrogen discharges as well as those of ohmic plasmas are plotted. A ratio of ICRF power to NBI power ranges from 0.1 to 0.7. The maximum ICRF power is 2.3MW. There is no big difference between helium and hydrogen discharges, and combined heating and NBI heating only, except the data around the absorbed power of ~13MW, where combined heating shows better results, especially with helium discharges. The NBI data show degradation above the absorbed power of around 8MW. However, it seems that the stored energy of the combined heating shots increases with the same rate as below ~8MW. As mentioned above, giant sawteeth appears in the power range where combined heating shows good confinement. Energy confinement time of the third harmonic heating in combination with NBI heating is about 20% higher than those of NBI heating alone with same discharge conditions.

A period of the sawtooth oscillation during combined heating tends to increase in proportion to $P_{NB}/\bar{n}_e$ with fixed ICRF power, as indicated in Fig. 4. A sawtooth period during NBI heating alone seems to saturate with increasing $P_{NB}/\bar{n}_e$. Therefore, substantial difference in the sawtooth periods is seen between combined heating and NBI heating alone in large $P_{NB}/\bar{n}_e$-value region. Difference between helium and hydrogen discharges is small because of high proton concentration ratio in helium discharges.

3. Hydrogen Minority Second Harmonic Heating in Combination with NBI

With hydrogen minority second harmonic heating in helium discharge, a good incremental energy confinement time (~110msec) is obtained for the ohmic target plasmas in a wide range of the electron density [2]. This value is considerably better than the one of the incremental confinement time of the pure hydrogen second harmonic heating (~80msec). In this subsection, we present results on the combined second harmonic ICRF and NBI heating in helium discharges. Figure 5 shows the plasma stored energy with the combined heating and the NBI heating alone in helium discharges (B_T=4.3T and I_P=2MA) as a function of the absorbed power. In this experimental run, high electron density ($\bar{n}_e \sim 6\times10^{19}m^{-3}$) is chosen in order to keep low proton-to-electron concentration ratio. For a typical case ($\bar{n}_e \sim 5.8\times10^{19}m^{-3}$, P_{IC}~2.3MW, P_{NB}~2MW and P_{abs}~5.9MW), the proton-to-electron concentration ratio is estimated to be ~24% from the change of the electron density associated with neutral beam and ICRF injection. The plasma stored energy increases with same incremental energy confinement time τ_E^{inc} for both heating schemes. A range of the data of NBI heating in the hydrogen discharges [3] is also indicated in Fig. 5. τ_E^{inc} of the helium discharges is about 90ms and the one of the hydrogen discharges is about 55 ms.

Thus enhancement of the incremental energy confinement time due to mass effects is clearly demonstrated by producing helium-dominated discharges with the total heating power up to 10MW.

Giant sawteeth appear during the minority second harmonic heating of ohmic plasmas even in high density and low q regimes ($\bar{n}_e$ up to $6.5\times10^{19}m^{-3}$ and q_{eff} up to 2.6). A threshold ICRF power (~2MW) exists for producing giant sawteeth. It is found that the largest sawteeth appear with ohmic target plasmas. A small additional power of NBI (less than 1MW) during giant sawtooth oscillation reduces sawtooth period substantially as shown in Fig. 6, especially for high density case. This tendency is in contrast with that of the third harmonic heating mentioned above. The reason may be explained with the different dependence of the stored energy of the energetic ions, which is produced by ICRF waves, on NBI power between the two cases. However, it has not yet been understood sufficiently.

4. Conclusions

Encouraging results on the third harmonic ICRF heating in combination with NBI heating has been obtained. Strong central heating accompanied with giant sawteeth is observed. The energy confinement time is enhanced by about 20% with the combined heating (P_{IC}~2.3MW, P_{NB}~10.3MW and $\bar{n}_e$~$2.8\times10^{19}m^{-3}$) from the one of the NBI heating alone with similar total heating power and electron density. The sawtooth period increases in proportion to $P_{NB}/\bar{n}_e$ with fixed ICRF power. The incremental energy confinement times of the combined second harmonic ICRF and NBI heating and NBI heating alone in helium discharges are ~90ms, which is considerably better than those of the NBI heating in hydrogen discharges (~55ms). The improvement may be due to the mass effects. Giant sawteeth produced by the second harmonic ICRF heating of the ohmic plasmas disappear with small additional NBI power less than 1MW.

REFERENCES

[1] UEHARA, K., KIMURA, H., Radio Frequency Power in Plasma (Proc. 8th Top. Conf. Irvine, CA, 1989), American Institute of Physics, New York (1989).
[2] FUJII, T., et al., Sec. 3.3 of this report.
[3] NAITO, O., JAERI-M 89-033 (1989) p.89-91.

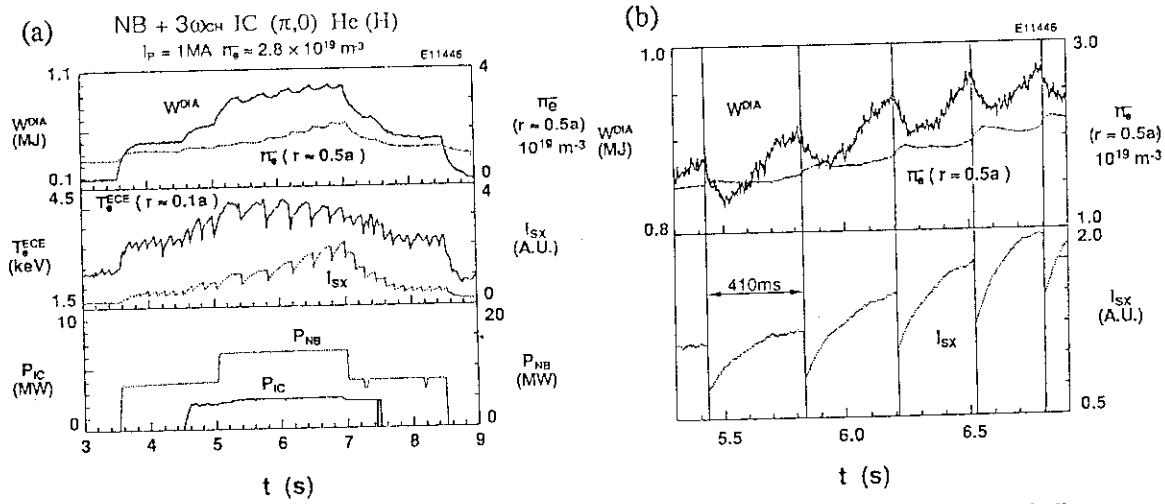

Fig. 1(a) Time evolutions of the combined third harmonic ICRF and NBI heating. Each trace indicates, from the top, the plasma stored energy, the line-averaged electron density at a half radius, the electron temperature near the center, soft X-ray signal of the central chord, NBI power (torus input) and ICRF power. (b) Time evolutions from 5.3sec to 6.9sec of the same shot as in (a).

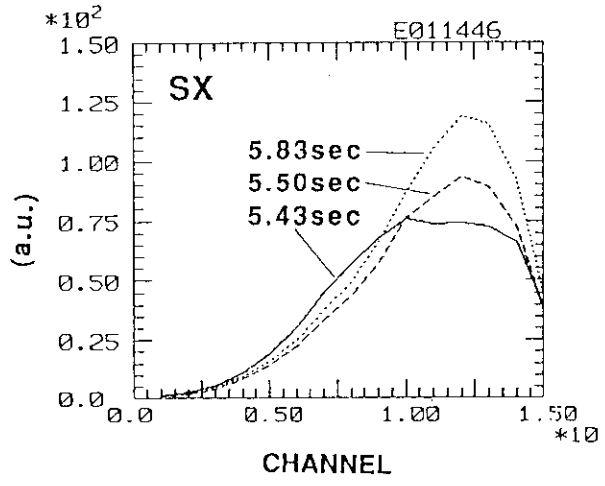

Fig. 2 Evolution of spatial profile of the soft X-ray intensity during a giant sawtooth of the same shot as in Fig. 1.

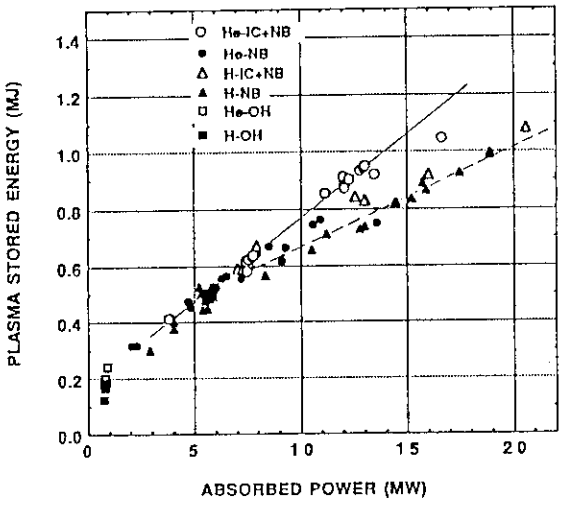

Fig. 3 Plasma stored energy against absorbed power for combined third harmonic ICRF and NBI heating and NBI heating only. I_p=1MA, B_T=3T and $\bar{n}_e$=1.4~4.3×10^{19}m^{-3}

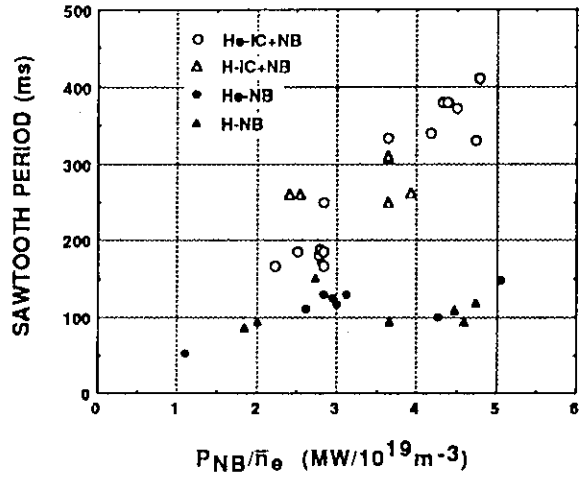

Fig. 4 Sawtooth period as a function of $P_{NB}/\bar{n}_e$ for combined third harmonic ICRF and NBI heating and NBI heating only. I_p=1MA, B_T=3T, $\bar{n}_e$=1.4~3.8×10^{19}m^{-3}, P_{IC}=1.7~2.3MW and P_{NB}=1.5~14MW.

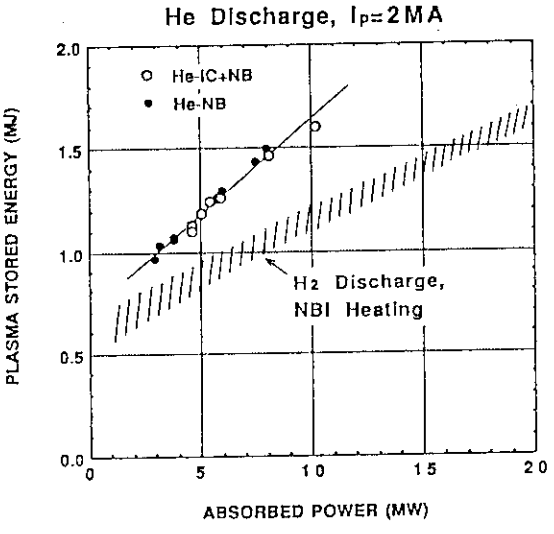

Fig. 5 Plasma stored energy against absorbed power for combined second harmonic ICRF and NBI heating and NBI heating only in helium discharges. I_p=2MA, B_T=4.3T and $\bar{n}_e$=5.0~6.2×10^{19}m^{-3}. A range of the data of hydrogen discharges with NBI heating is indicated by the shaded region.

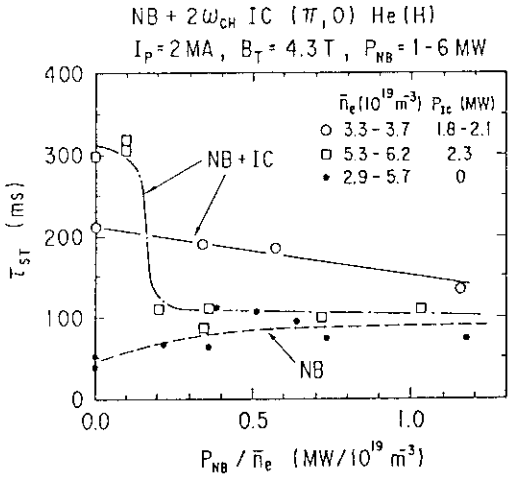

Fig. 6 Sawtooth period as a function of $P_{NB}/\bar{n}_e$ for combined second harmonic ICRF and NBI heating and NBI heating only, in helium discharges.

3.5 Behavior of fast ions in combined higher harmonics ICRF and NBI heating

K. Tobita, M. Nemoto, Y. Kusama, H. Kimura, T. Fujii, S. Moriyama,
M. Saigusa and H. Takeuchi

1. Introduction

In previous combined $2\omega_{CH}$ ICRF and NBI heating experiments on JT-60, it is found that the tail temperature T_{tail}, which is defined by the inverse gradient of $\ln(E^{-1/2}F(E))$ vs. E plot above the injection beam energy, is independent of the injected neutral beam power P_{NB} and proportional to the ICRF power P_{IC}. In this report, we describe the behavior of fast ions in NBI-combined higher harmonics ICRF heating in hydrogen and helium discharges.

The fast ion behavior is investigated using two analyzers: one (CX-A) is oriented near-perpendicular to the plasma (r = 0.3 m), and the other (CX-B) vertically views the plasma center (r = 0 m). The ICRF wave is launched at a frequency of 131 MHz with $(\pi,0)$ phasing.

2. Higher harmonics heating

Changing the toroidal field B_T, we formed resonance layers for $2\omega_{CH}$, $3\omega_{CH}$ and $4\omega_{CH}$ near the plasma center (R = 3.04 m). In experiments presented here, the behavior of fast ions is investigated by the vertically viewing neutral particle analyzer which detects the trapped ions whose turning points are located at R = 3.03-3.05 m. Since the line-of-sight of the analyzer crosses a heating beam in the core, the charge exchange (CX) spectrum measured by the analyzer mainly reflects the energy distribution of the central fast ions. Figure 1 shows energy spectra of ions during NBI-combined $2\omega_{CH}$, $3\omega_{CH}$ and $4\omega_{CH}$ ICRF heating for H_2 plasmas. In Fig.1, acceleration of fast ions by these harmonics is seen above the injection energy (65 keV). Reason why T_{tail} for $3\omega_{CH}$ and $4\omega_{CH}$ heating is lower than that for $2\omega_{CH}$ is that the resonance layer and the line-of-sight of the analyzer do not overlap because of restriction in adjusting B_T and that the analyzer detects the ions diffused from the resonance regions.

3. Comparison between H_2 and He discharges

Comparison of T_{tail} during $3\omega_{CH}$ heating for H_2 and He discharges is shown in Fig.2. Here, note that He discharges does not mean pure helium plasma: He discharges are performed by using mixed gas of 90% He and 5% H_2 and hydrogen beam injection. T_{tail} is estimated from the gradient of $\ln(E^{-1/2}f_H(E))$ in the energy range of 60-110 keV. We can see from this figure that T_{tail} is independent of P_{NB} and there is not a large difference of T_{tail} in both discharges. T_{tail} in He discharges with low P_{NB} (~5 MW) is somewhat higher. There may be a large difference in T_{tail} between H_2 and He discharges at higher densities. Because the energy confinement time τ_E for the $3\omega_{CH}$ IC+NBI heating of He plasma is longer than that of H_2 plasma at equally absorbed power[2] at $\bar{n}_e \geq 4\times10^{19}$ m^{-3} although there is little difference in τ_E at low $\bar{n}_e(\leq 2\times10^{19}$ $m^{-3})$. Possible reason for little difference in T_{tail} and τ_E in both discharges at low $\bar{n}_e$ is that proton concentration in low $\bar{n}_e$ He discharges is as high as that in H_2 discharges because of hydrogen NBI and recycling of H_2 gas. The low P_{NB} data for He discharges in Fig. 2 can be also explained by the proton concentration because the proton concentration at low P_{NB} is thought to be lower than that at high P_{NB} owing to decrease in the number of injected particles.

4. Fast ion behavior during giant sawtooth oscillation

In the $3\omega_{CH}$ ICRF+NBI heating, giant sawtooth oscillations are observed in soft x-ray, T_e and diamagnetic probe signals, and the sawtooth period increases with P_{NB}. Figure 3 shows typical waveforms in a giant sawtooth shot. The fast neutral fluxes decrease with $n_e l$ because the transmission of the CX neutrals in the plasma and halo neutral density in the core decreases with $n_e l$. In the data by CX-B, the CX fluxes with 25 keV and 68 keV plumet at the time of sawtooth crashes. In contrary to these data, the bottom data measured by CX-A exhibit spikes in the CX flux near the injection energy (65 keV) at the time of sawtooth crashes. This behavior of the CX flux indicates that fast ions near the injection energy are transported across the sight of CX-A. Time evolutions of CX fluxes of CX-A and CX-B provide an indirect evidence for outward transport of fast trapped ions at the sawtooth event.

5. Summary

Prominent acceleration of beam ions was observed in $2\omega_{CH}$, $3\omega_{CH}$ and $4\omega_{CH}$ ICRF heating in combination with NBI heating. Tail temperatures of protons during $3\omega_{CH}$ heating in the H_2 and He discharges were determined from CX spectra. The proton tail temperature in the He discharges rised with decreasing P_{NB}. Time evolutions of CX fluxes indicated the outward transport of fast ions at the giant sawtooth event.

References

[1] JT-60 Team, JAERI-M 87-113 (1987) p. 293 (in Japanese).

[2] H. Kimura et al., in this report (Section 3.4).

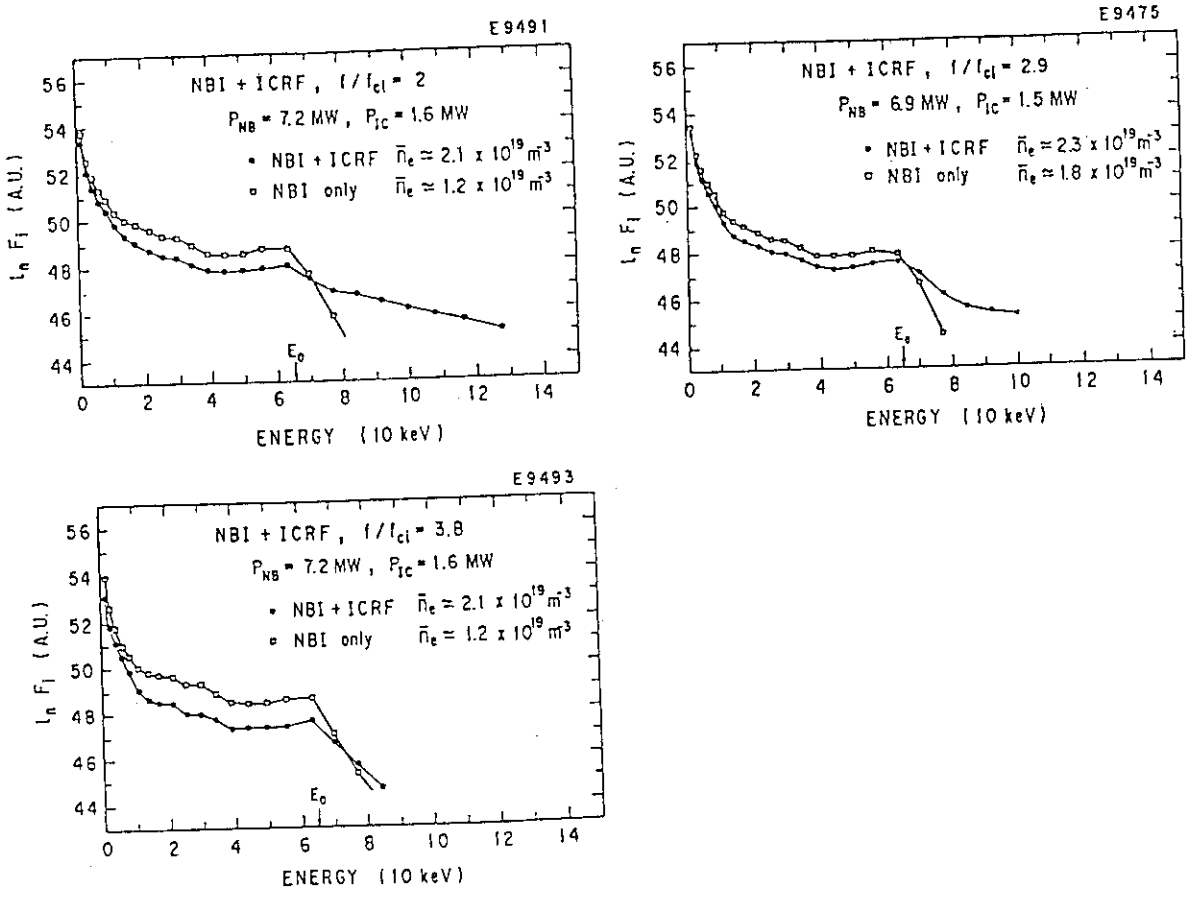

Fig.1 Acceleration of fast ions by ICRF waves of 2nd, 3rd and 4th harmonics.

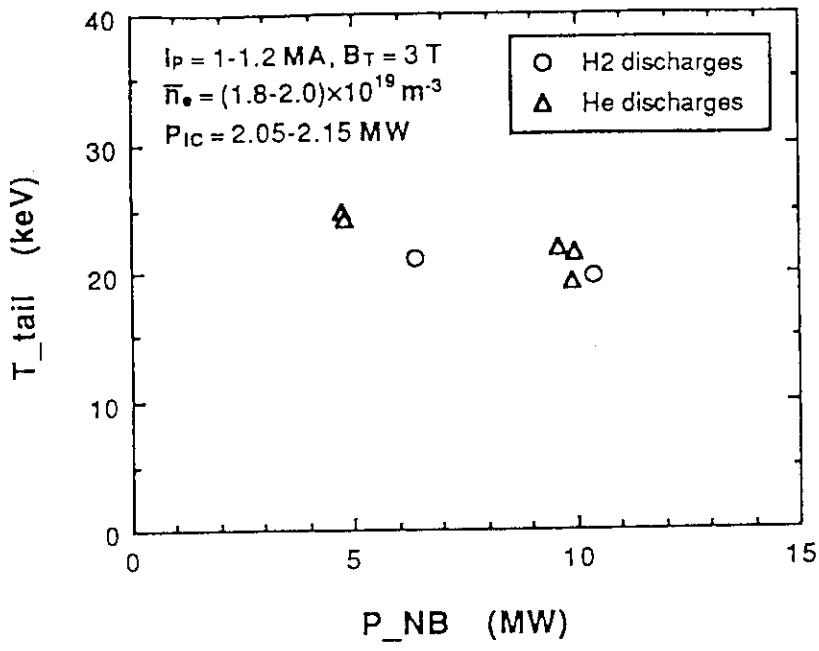

Fig.2 Tail temperature during $3\omega_{CH}$ ICRF heating in H_2 and He discharges.

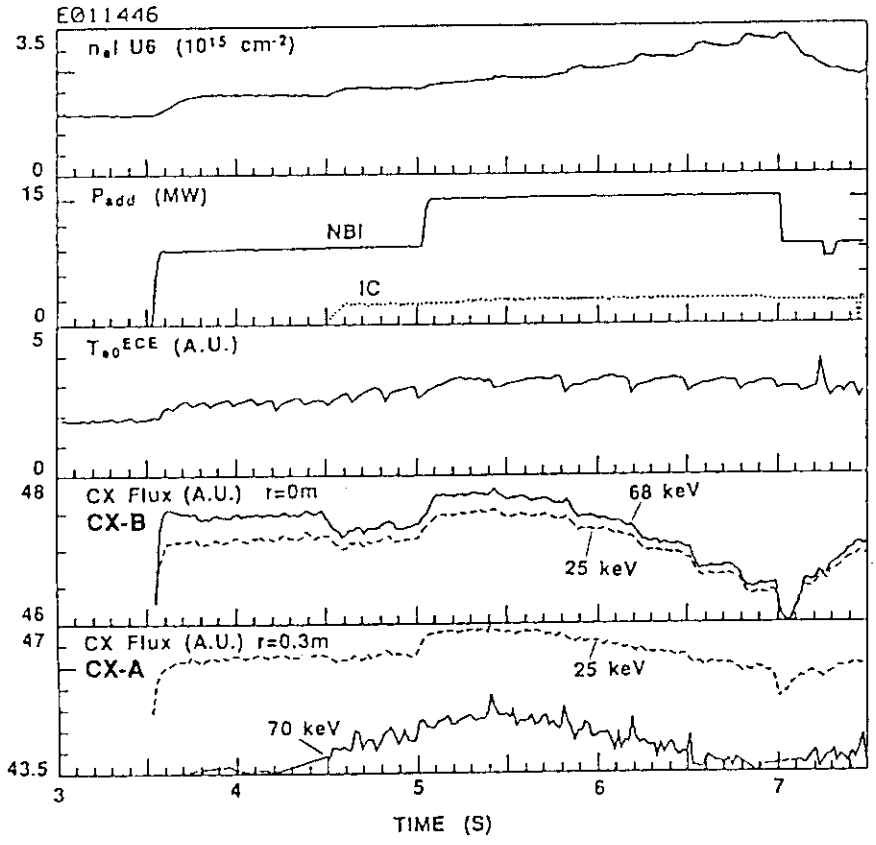

Fig.3 Time evolutions of $n_e l$, P_{add}, T_{e0}^{ECE} and fast neutral effluxes in a giant sawtooth event.

3.6 Analysis of Fast Ion Production by Higher Harmonic ICRF Waves

K.HAMAMATSU, H.KIMURA, T.FUJII and M.AZUMI

I. Introduction

The second and third harmonic ICRF heating experiments have been carried out with neutral beam injection on JT-60. The plasma is composed of helium and hydrogen. The rf-frequency is chosen to be the second or third cyclotron resonance of hydrogen. The hydrogen neutral beam is injected into the plasma ($H^0 \rightarrow H^+$). Fast ions are observed in the charge exchange neutral spectrum in the both case of second and third harmonic resonance heating. The giant sawtooth oscillation is also observed in the soft X-ray signal.

As for the second harmonic heating combined with NBI, the theoretical model has been developed[1] and applied to the experimental results[2]. We extend this model into the higher harmonic cyclotron resonance heating. The global wave structure and the acceleration of high-energy particles are analyzed in a self-consistent manner.

II. Theoretical Model

Our model consists of two parts. The first part is the description of wave propagation and absorption in a real space. The second part is the description of the deformation of the velocity distribution caused by NBI and ICRF heating. In the analys of the ICRF wave propagation and absorption, a one-dimensional slab model[3] is employed. We assume that the distributions of electron and helium are unaffected and take into account the deformation of the velocity distribution of hydrogen. Furthermore, the problem is restricted in the steady state.

The wave field structure is solved in the one-dimensional model geometry in which the inhomogeneities in the direction of the major radius(x-direction) are kept. The density and temperature are given as $n_j(x) = (n_{j0} - n_{js})(1 - x^2/a^2) + n_{js}$,($j$=e, He, H) and $T_j(x) = (T_{j0} - T_{js})(1 - x^2/a^2) + T_{js}$,($j$=e,He). The conductive wall is located at $x = \pm b$. The wave field in the plasma is described by the Maxwell equation

$$\nabla \times \nabla \times \mathbf{E} - \frac{\omega^2}{c^2} = \mathrm{i}\omega\mu_0(\sum_j \mathbf{J}_j + \mathbf{J}^A), \tag{1}$$

whrer ω is the rf angular frequency, $\mathbf{J}_j$ is the induced current by the j-th species and $\mathbf{J}^A$ is the antenna current. The induced current $\mathbf{J}_j$ is culculated by the nonlocal cunductivity tensor[4]. In the calculation of the conductivity tensor, the velocity distribution of hydrogen is assumed to be bi-Maxwellian. These temperatures are determined by the velocity moment of distribution function obtained from the Fokker-Planck equation.

The velocity distribution function of hydrogen is obtain by solving the Fokker-Planck equation. On each magnetic surface, we take the 0th order moment of the Legendre expansion of velocity distribution function, f, and obtain

$$\frac{\partial f}{\partial t} = C(f) + S_{\mathrm{NBI}} + Q_{\mathrm{rf}}(f) + L_{\mathrm{p}}(f), \tag{2}$$

where C is the Coulomb collision term, $S_{\rm NBI}$ is a source term of NBI, $Q_{\rm rf}$ is an rf heating term, $L_{\rm p}$ is a particle loss term. The NBI source term is obtained by the pencil beam model and the particle loss term is determined by the NBI source term to keep a steady state, i.e., $\partial f/\partial t = 0$. The rf heating term includes the $(\ell-1)$-th order Bessel function $J_{\ell-1}(k_\perp v_\perp)$, where ℓ is the harmonic number, $k_\perp$ is a perpendicular wave number and $v_\perp$ is the velocity perpendicular to the magnetic field. The rf heating term also contains an unknown factor which is associated with the absorbed wave power density. The unknown factor is determined by solving self-consistently Eqs.(1) and (2), i.e., $< \mathbf{E}^* \cdot \mathbf{J}_{\rm H} >= 4\pi \int dv v^2 \frac{1}{2} m v^2 Q_{\rm rf}(f)$. In order to combine the solution of the ICRF wave equation in a slab geometry and the solution of Fokker-Planck equation on each magnetic surface, we must calculate the power deposition of the ICRF wave averaged on each magnetic surface and solve Eq.(2) on each magnetic surface. However, to save a CPU time, the Fokker-Planck equation is solved at the cyclotron resonance point($x=0$) where the magnetic axis($r=0$) locates. We assume that the power deposition of the ICRF wave is parabolic around the magnetic axis: $P_{\rm rf}(r) \propto (1-(r/L_{\rm A})^2)$, $L_{\rm A} = 0.2$m. The temperature and density of high-energy tail component are assumed to be similar distributions.

III. Wave Propagation

We apply this theoretical model to the regime of JT-60 plasma. Plasma parameters are $R = 3.07$m, $a = .9$m, $n_{\rm e0} = 5. \times 10^{19}$, $n_{\rm He} = 2.25 \times 10^{19}$, $n_{\rm H} = .5 \times 10^{19}$, $T_0 = T_{\rm e0} = T_{\rm He} = T_{\rm H} = 3$keV, $\omega/\pi = 131$MHz. A toroidal magnetic field is chosen in order to place the resonance layer at the magnetic axis, i.e., $B_{\rm T} = 4.3$T for the second harmonic resonance heating and $B_{\rm T} = 2.9$T for the third one. Two antennas, which have the phase difference with 180° in the toroidal direction, is arranged in the low field side of the torus. The launched rf-power is 2MW and the applied NBI power is about 5MW and beam energy is 65keV.

In both case of the second and third resonance, the rf-wave power is mainly absorbed by hydrogen. Figure 1 (a) shows the radial profiles of electric field, E_y, and (b) shows the power deposition profile and power flux in the case of the third harmonic resonance. The rf-wave propagates in the high-field side ($x<0$) and reflected at the plasma boundary. In this case, the main part of rf-power absorbed by hydrogen is due to the contribution of the high energy component. The absorbed power by bulk hydrogen is negligibly small. As the plasma density and/or temperature increases, the absorbed power by hydrogen tail decreases according to the increase of electron absorbed power due to the Landau damping. On the other hand, in the second resonance heating case, the absorbed power by hydrogen is not affected so much by the plasma parameters. Because, the wave damping rate is larger than that of third harmonic resonance. The absorption due to the bulk hydrogen is about several percents of total absorbed power.

IV. Tail Acceleration

In order to discuss the heating efficiency, it is an important issue to evaluate the quantities associated with high energy particles. We define the velocity distribution function of tail component as $f_{\rm t}(v) = f_{\rm FP}(v) - f_{\rm FP}(0)\exp\{-mv^2/2T_{\rm b}\}$, where the bulk temperature is determined by the gradient of velocity distribution function at

$v = 0$. In the followings, the stored energy, temperature and density of tail component is calculated by the velocity moment of f_t.

Figure 2 shows the NBI power dependences of the high-energy component for the various population of hydrogen, $\delta = n_H/n_e$ =0.14, 0.3 and 0.5. Plasma density is $n_{e0} = 7. \times 10^{19}$ and other parameters are the same as in Fig.1. Figure 2(a) is the NBI power dependence of the tail stored energy. The production of fast ions by the third resonance heating is greater than that by the second resonance. This is caused by the difference of the quasi-linear diffusion coefficient. In the case of the third resonance heating, the changes of the hydrogen population and/or NBI power cause a slight change in the stored energy. This means that the fast ions are accelerated enough to exceed the drag force due to electron in this ICRF power range. The tail stored energy heated by the second harmonic resonance increases with increasing of the power density according to the decrease of hydrogen population. It also increases with the increase of NBI power. Figure 2(b) and (c) show the temperature and density of high-energy tail. In the contrast with ICRF heating, the NBI heating is regarded as the low energy particle source. Therefore, in the third resonance heating case, the tail temperature decreases with the increase of the NBI power. On the other hand, in the second resonance heating case, the tail temperature is not affected by the NBI power. Because, the Coulomb collision between tail component and electron is dominant process in the power level up to 2MW of second harmonic resonance heating.

V. Conclusion and Discussion

In both case of the second and third harmonic resonance heating with NBI, the wave propagation, power absorption and production of fast ions are numerically analyzed using the self-consistent model. Although the damping rate of the third harmonic resonance is weak, the wave power is mainly absorbed by hydrogen due to the acceleration of fast ions. The incremental tail energy of third resonance heating is greater than that of second resonance heating.

The characteristics of ICRF heating is that the resonance particle is accelerated in the perpendicular direction to the magnetic field. This causes the increasing of high-energy trapped particles. Our model, however, assumes that the velocity distribution function is isotropic. In the rarely collisional regime, i.e., low density and/or high-temperature plasma, the velocity distribution will be anisotropic. If the giant sawtooth is caused by the stabilization of the internal kink mode due to the high-energy trapped particles, the two dimensional analysis in the velocity space will be necessary. The problems in connection with trapped particles will have to be further investigated.

REFERENCES

[1] K.HAMAMATSU, et al., Nucl. Fusion **29** (1989) 147.
[2] T.FUJII, et al., Proc. of 15th Europ. Conf. on Cont. Fusion and Plasma Physics. Dubrovnik (1988) Vol.12B, Pt.2, p.766.
[3] A.FUKUYAMA, et al., Nucl. Fusion **23** (1983) 1005.
[4] S.-I.ITOH, et al., J.Phys.Soc.Jpn. **54** (1985) 1808.

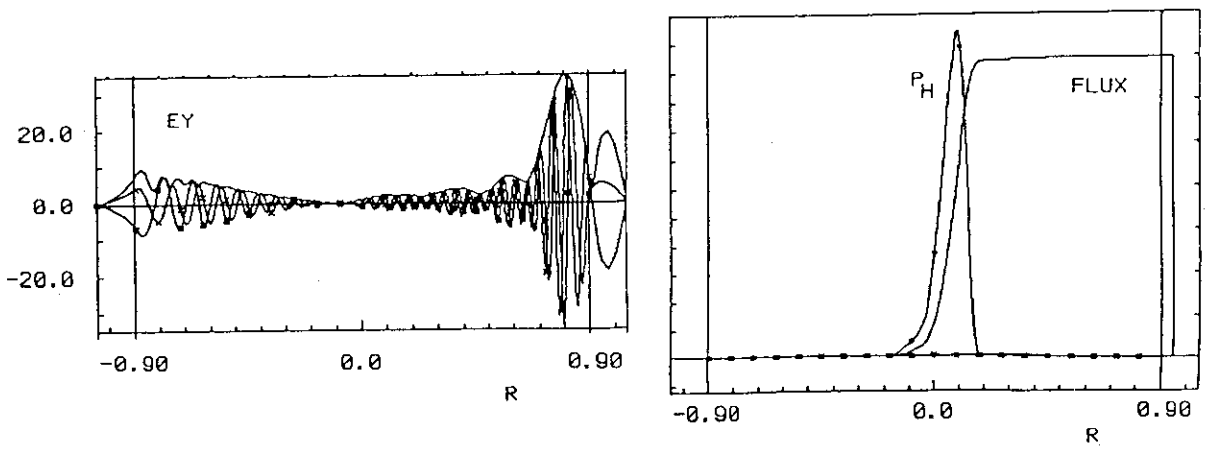

(a) (b)

Fig.1 The radial profiles of electric field, E_y, power deposition and power flux.

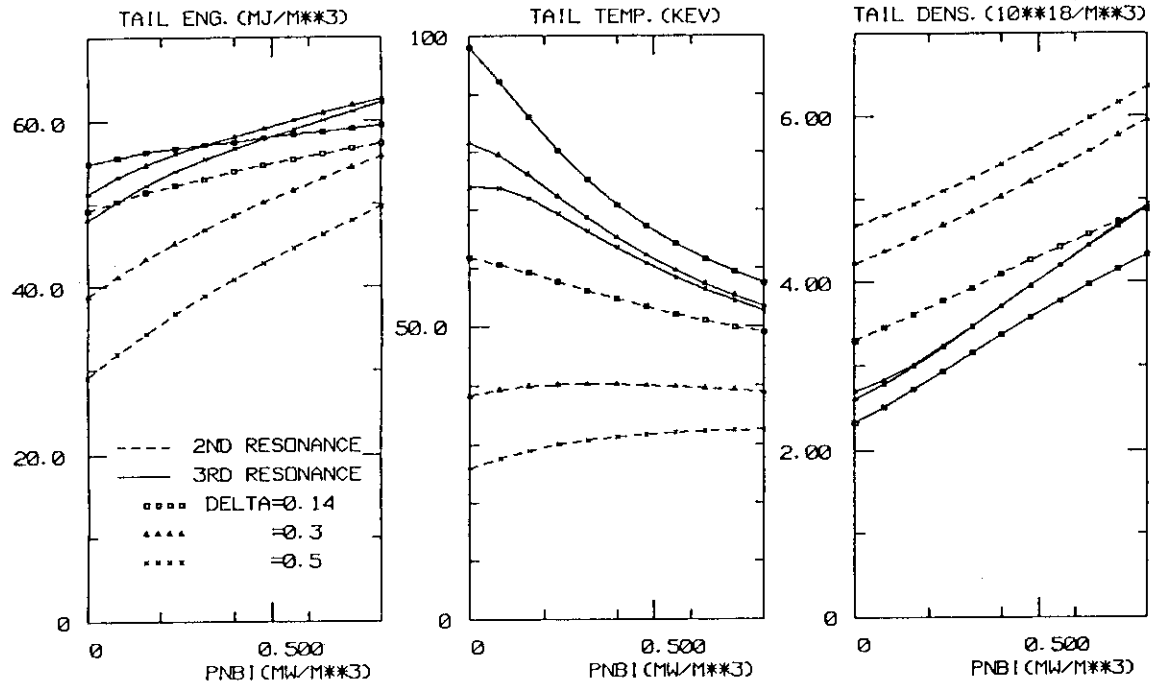

(a) (b) (c)

Fig.2 The NBI power dependences of tail stored energy, tail temperature and tail density.

3. 7 Direct Electron Heating by ICRF Fast Wave

T. FUJII, H. KIMURA, M. SAIGUSA, K. NAGASHIMA, Y. KISHIMOTO, M. SATO, H. YOSHIDA, S. MORIYAMA, K. ANNOH

1. Introduction

Recently, the current drive experiments using fast waves from the ion cyclotron range of frequencies (ICRF) to LHRF are intensively carried out in small and medium size toroidal devices [1]-[3]. Current drive by slow waves in the lower hybrid range of frequencies (LHRF) have been established in present tokamaks. But, there is a problem that the current may not be driven in the plasma central region by the LHRF slow wave because the LHRF power is absorbed by α particles or deposited in the edge plasma due to high temperature in a reactor grade tokamak. Then the current drive by the fast waves is expected as one of current drive means in a reactor grade tokamak because the fast wave power is more absorbed by electrons via Landau damping and transit time magnetic pumping (TTMP) in the plasma central region as the plasma is hotter and denser. However, the power absorption of the fast wave is small in the present tokamak since the plasma temperature is relatively low. The demonstration of the current drive by the fast wave is crucially difficult. Accordingly the experimental estimation of the direct electron heating via Landau damping and TTMP experiments has been performed assisted with the electron cyclotron resonance (ECR) heating or the LHRF slow wave heating [4]. The direct electron heating by the fast wave in the second harmonic ICRF has been investigated on JT-60 with a phased 2 x 2 loop antenna which can control the $k_{//}$ spectrum of the radiated power. This paper presents enhanced electron heating in the combination with LHRF heating and the estimation of electron absorption power via Landau damping in the ICRF fast wave heating alone.

2. Enhanced Electron Heating in combination with LHRF Heating

We examined the direct electron heating in off-axis ICRF heating alone and in combination with the low power LHRF heating at B_T = 3.3 T and f = 131 MHz where the second and third harmonic resonance layers were at r = - 0.7, 0.5 m , respectively, expecting a small power absorption by ions from the previous experimental results in Ref. [5]. Figure 1 shows a set of time evolution of plasma current I_p, one turn loop voltage V_L, the stored energy W^{DIA}, line-averaged electron density $\bar{n}_e$, ICRF power P_{IC} and LHRF power P_{LH} for the (π,0) phasing in the ICRF heating alone and combined ICRF and LHRF heating in a shot. In both heating, the electron density increases as well as the stored energy. Then we should estimate the electron absorption power P_e with the consideration of the changes in V_L and the ohmic stored energy due to the increase in electron density. So that we estimate the quantity $P_e = dW^{DIA} / dt - I_p \Delta V_L - dW_{OH}(\Delta n_e) / dt$. Here, dW^{DIA} / dt and $d\bar{n}_e / dt$ are the slopes of W^{DIA} and $\bar{n}_e$ at the beginning of the shots, respectively and $dW_{OH}(\Delta n_e) / dt$ is calculated from the stored energy scaling for the ohmically heated plasmas [6] with the measured $d\bar{n}_e / dt$. Further, we assume the direct ion heating power is negligible as mentioned above and the ion-electron equi-partition

relaxation is neglected because of the relatively low densities. The dependence of P_e/P_{IC} on P_{LH} is given in Fig. 2. The electron power absorption is enhanced with increasing P_{LH} for each phasing mode. Figure 3 (a) and (b) show the electron temperature profiles measured by Thomson scattering method for (0,0) and (π, 0) phasing. In the case of (0,0) phasing, no difference in the temperature profiles is observed between the ICRF alone and combined ICRF and LHRF. On the other hand, the electron temperature rise is obtained in the whole plasma region for the (π,0) phasing as expected because of higher $k_{//}$ spectrum. However, the electron power absorption efficiency is a small value of about 0.1 even in the (π, 0) phasing. The enhancement of the electron power absorption by the LHRF heating seems to be due to the high energy electron generation by the LHRF or due to the temperature rise because the electron power absorption efficiency is enhanced sensitively by the electron temperature in the range of 3 - 5 keV according to the calculation results shown in next Section.

3. Numerical Estimations of Electron Absorption Power and Driven Current

Figure 4 shows the dependence of P^*_e / P_{IC} on the toroidal phase difference $\Delta\phi$ between the antenna currents at $n_{e0} \sim 1 \times 10^{19}$ m^{-3}, $T_{e0} \sim 3$ keV, $T_{i0} \sim 1.8$ keV and $B_T = 3.3$. Experimental data of the electron absorption power are cross-checked by integrating time differential of the electron temperature estimated by the ECE measurements over the plasma volume. The lines indicate the calculated electron power absorption efficiency as a parameter of the wall resistivity ρ_w for $n_{e0} = 1 \times 10^{19}$ m^{-3}, $T_{e0} = 3$ keV, $T_{i0} = 1.8$ keV and $B_T = 3.3$ T from the 1-dimensional kinetic code [7]. The calculated results for the assumed wall resistivity $\rho_w = 10^{-2}$ - 10^{-3} Ωm are close to the experimental ones although the graphite wall resistivity is about 5×10^{-6} Ωm. The $\Delta\phi$ dependence of P^*_e / P_{IC} is well explained with the calculated results. Figure 5 shows the calculated electron power absorption efficiency versus the central electron temperature for $n_{e0} = 1 \times 10^{19}$ m^{-3}, $\Delta\phi = 90°$ and $B_T = 3.3$ T with the simulated $k_{//}$ spectrum of the 2 x 2 loop antenna. The efficiency increases strongly with the electron temperature in the range of 3 - 5 keV and almost saturates in the range of 6 - 10 keV irrespective of the wall resistivity. Accordingly, the appropriate electron absorption of the fast wave power is expected with the electron temperature of about 6 keV. The dependence of the driven current by the fast wave on the central electron temperature calculated for $n_{e0} = 1 \times 10^{19}$ m^{-3}, $\Delta\phi = 90°$, $B_T = 3.3$ T and $P_{IC} = 1$ MW is shown in Fig. 6. The driven current also shows the similar T_{e0} dependence to that of the electron power absorption. The driven current is expected to be only about 10 kA at $T_{e0} = 3$ keV although it is expected to be about 200 kA with $P_{IC} = 1$ MW at $T_{e0} = 6$ keV which is detectable amount. However, the current dive efficiency η_{CD} is about 0.4×10^{19} Am^2/W at $T_{e0} = 6$ keV and smaller than that obtained by the LHRF slow wave by a factor of about 5. This reduced efficiency is caused by small directivity of the excited wave and the broad spectrum (the fast waves with $n_{//} > \sim 4$ hardly penetrate into the plasma and the fast wave with $n_{//} > \sim 1$ are slightly absorbed in the plasma) because of 2 loop antennas in the toroidal direction. Then the higher current drive efficiency of ~ 1 is expected for the same plasma parameters if the antenna is designed so that the $n_{//}$ spectrum of the excited wave has a peak of $n_{//} = 2$ - 3.

4. Conclusion

The direct electron heating in the ICRF alone and in combination with the low power LHRF heating is examined at B_T = 3.3 T and f = 131 MHz where the second and third harmonic resonance layers were at r = - 0.7, 0.5 m , respectively. The weak direct electron heating is observed in the ICRF heating alone. Enhanced electron heating by the combination of low power LHRF heating is obtained for various phasing modes. However, the electron power absorption efficiency is a small value of about 0.1 even in the (π, 0) phasing which shows the best results. Further the numerical studies of the direct electron heating is performed. The calculated electron power absorption efficiency for the assumed wall resistivity $\rho_w = 10^{-2} - 10^{-3}$ Ωm are close to the experimental ones although the graphite wall resistivity is about 5×10^{-6} Ωm. The $\Delta\phi$ dependence of P^*_e / P_{IC} is well explained with the calculated results. The calculated results reveal that the absorption efficiency and the driven current by the fast wave increase strongly with the electron temperature in the range of 3 - 5 keV and almost saturates in the range of 6-10 keV. Moreover, it is predicted that the detectable current drive is expected for $T_{e0} \sim 6$ keV.

References

[1] J. Goree, et al., Phys. Rev. Lett. **55** (1985) 1669.

[2] R. McWilliams, R. Platt, Phys. Rev. Lett. **56** (1986) 835.

[3] Y. Uesugi, et al., in Proc.14th Europ. Conf. on Controlled Fusion and Plasma Physics, Madrid (1987) Vol 11D, Part III, p 942.

[4] T. Yamamoto, Y. Uesugi, H. Kawashima, et al., Phys. Rev. Lett. **63** (1989) 1148.

[5] T. Fujii, H. Kimura, M. Saigusa, et al., in Section 6.6 of JAERI - M 89 - 033 (1989).

[6] M. Kikuchi, T. Hirayama, K. Shimizu, et al., Nucl. Fusion **27** (1987) 1239.

[7] Y. Kishimoto, et al., Nucl. Fusion **27** (1987) 549.

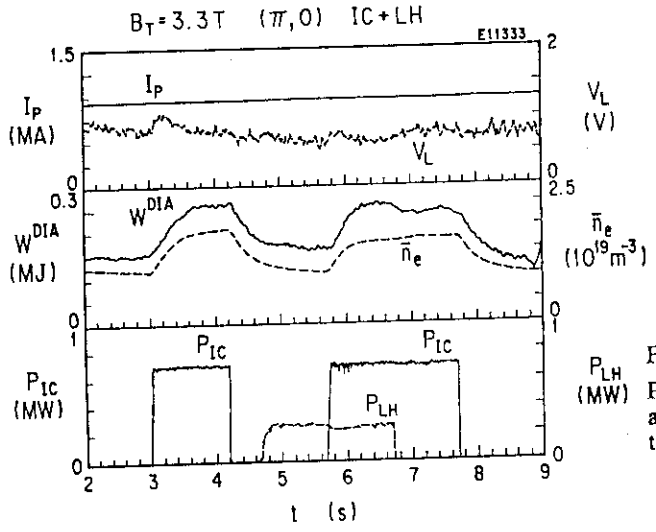

Fig.1 A set of time evolution of I_p, V_L, W^{DIA}, $\bar{n}_e$, P_{IC} and P_{LH} for the (π,0) phasing in the ICRF heating alone and combined ICRF and LHRF heating in a typical shot.

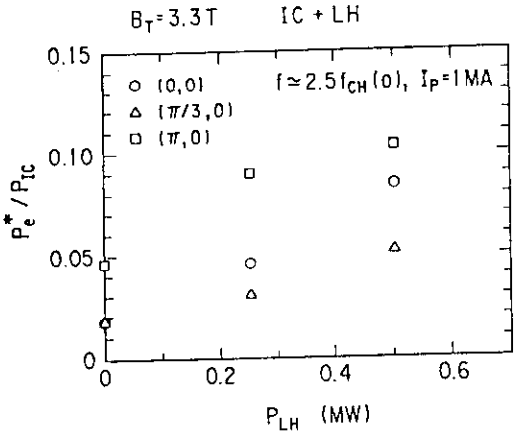

Fig. 2 Dependence of the electron power absorption efficiency P_e/P_{IC} on P_{LH} for the various phasing modes.

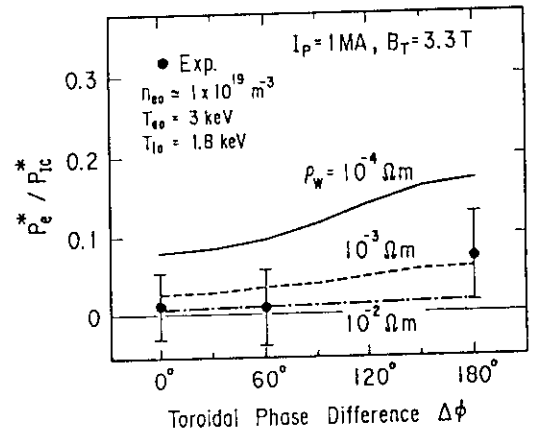

Fig. 4 Dependence of ratio P_e^*/P_{IC} on the toroidal phase difference $\Delta\phi$ between the antenna currents. The lines indicate calculated results with the 1-dimensional kinetic cord for the measured plasma parameters

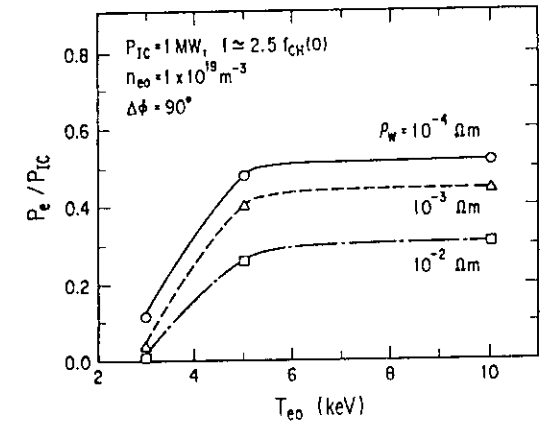

Fig. 5 Calculated electron power absorption efficiency versus the central electron temperature for n_{e0} = 1 x 10^{19} m^{-3}, $\Delta\phi$ = 90° and B_T = 3.3 T.

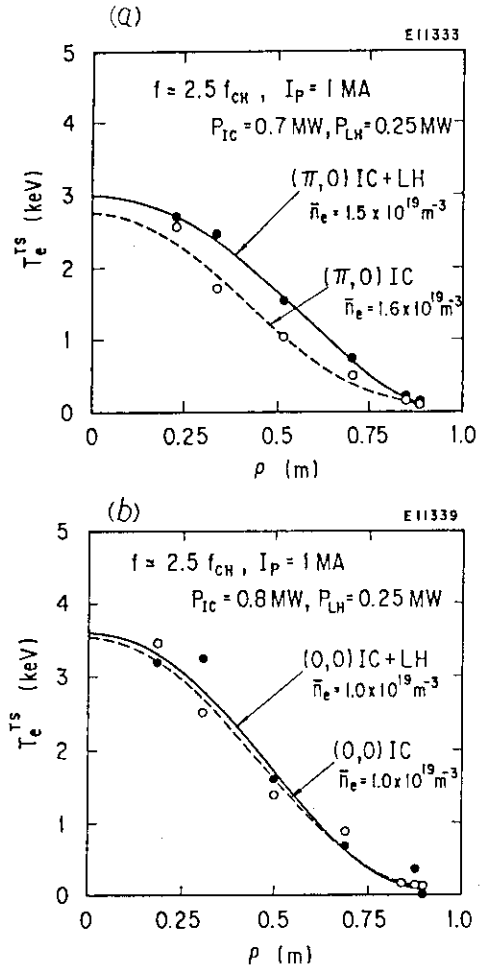

Fig. 3 Electron temperature profiles measured by Thomson scattering method (a) for the (0,0) phasing and (b) for the (π, 0) phasing.

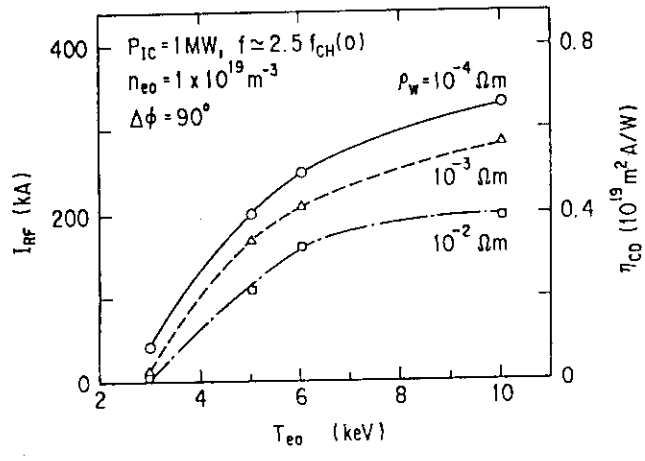

Fig. 6 Dependence of the driven current by the fast wave on the central electron temperature calculated for n_{e0} = 1 x 10^{19} m^{-3}, $\Delta\phi$ = 90°, B_T = 3.3 T and P_{IC} = 1 MW.

3.8 Parametric Decay Excitation during Second Harmonic ICRF Heating

T. FUJII, M. SAIGUSA, H. KIMURA, M. ONO, S. MORIYAMA, K.TOBITA, M. NEMOTO, Y. KUSAMA, M. SEKI, T. NISHITANI, K. ANNOH

1. Introduction

Recently, interesting experimental results on parametric decay instability in the ion cyclotron frequency range are reported in several tokamaks [1-3]. The investigation of these phenomena is required from a view-point of impurity generation during ICRF heating at high power level. Moreover, the parametric decay instabilities have a possibility to affect the heating properties of the bulk plasma as well as the interaction of the edge plasma. Then it is significantly important to understand the phenomena induced by the parametric decay instabilities. Two types of parametric decay instabilities near the plasma edge are observed during the second harmonic ICRF heating with a phased array of 2 x 2 loop antennas on JT-60. In this paper, the properties of the parametric decay instability are presented.

2. Experimental Results and Discussion

The second harmonic ICRF heating has been carried out with a phased 2 x 2 loop antenna on JT-60. The peak value of the toroidal wave number $k_{//}$ spectrum of the antenna currents changes from 0 to 18 m^{-1} by phasing from the (0, 0) to the (π, 0), where the former in the parentheses is the toroidal phase difference between the antenna currents and the latter the poloidal. The applied frequency is 131 MHz, which has the hydrogen second harmonic cyclotron resonance near the plasma center at $B_T = 4.3$ T. Parametric decay instabilities occur in both pure hydrogen plasmas (H-majority second harmonic heating) and helium plasmas with hydrogen concentration of $n_H/n_{He} \approx 0.1$ (H-minority second harmonic heating) but only in the case of the (0, 0) phasing. Two types of parametric decay instabilities are identified. One type is decay into an ion Bernstein wave (IBW) and an ion cyclotron quasimode (IQM) and the other into an IBW and a cold electrostatic ion cyclotron wave (CESICW) or an electron quasimode (EQM). The selection rules in the parametric decay process are

$$\omega_0 = \omega_1 + \omega_2, \qquad \mathbf{k}_0 = \mathbf{k}_1 + \mathbf{k}_2$$

where (ω_0, $\mathbf{k}_0$) denotes pump fast wave (FW), (ω_1, $\mathbf{k}_1$) low frequency (LF) and (ω_2, $\mathbf{k}_2$) lower side band (LSB). Two pairs of Langmuir probes are employed to detect waves induced by the ICRF injection and to measure scrape-off plasma parameters. One is located near the antenna as shown in Fig. 1 and the other at the toroidal angle of 140° from the antenna. Figure 2 (a) shows a typical frequency spectrum of the probe signal at $B_T = 3.8$ T in H-majority second harmonic heating with the (0, 0) phasing. Here, all the probe signals shown in this paper are detected by the probe placed near the antenna. From the figure, two decay processes are recognized as the following expressions, which are verified later.

$$\text{FW } (f_0) \rightarrow \text{IQM } (f_1) + \text{IBW } (f_2), \quad \text{FW } (f_0) \rightarrow \text{CESICW or EQM } (f'_1) + \text{IBW } (f'_2).$$

The IQM was hardly detected directly by the probe which is placed behind the first wall presumably due to the expected strong damping of the IQM in the edge plasma. The presence of IQM can be easily determined from the $\omega \cong \Omega_i$ relationship, where Ω_i is the ion cyclotron frequency. Then $f_1 = \Omega_H/2\pi$ and $f_2 = 1.8\ \Omega_H/2\pi$ for the magnetic field near the antenna (R = 3.8 m) in Fig. 2 (a). The LF wave with $f'_1 = 22.5$ MHz is CESICW or EQM and satisfies the frequency selection rule $f_0 = f'_1 + f'_2$ together with IBW (f'_2). Only a slight sign of the decay is detected by the probe which is placed at 140° apart from the antenna in the toroidal direction, indicating that the decay processes take place mainly in the antenna near field region. An example of frequency spectrum of the probe signal at $B_T = 4.3$ T with the (π, 0) phasing is given in Fig. 2 (b). No parametric decay instability is found in this case.

The dispersion relations of the decay waves of IBW [4] and CESICW [5] are given by

$$\text{IBW}: \quad 1 + \left[\sum_{\sigma} \frac{\omega_{p\sigma}^2}{b_\sigma} \exp(-b_\sigma) \sum_{n=1}^{\infty} I_n(b_\sigma) \frac{2n^2}{n^2\Omega_\sigma^2 - \omega^2} \right] \frac{k_\perp^2}{k_0^2} - \frac{\omega_{pe}^2}{\omega^2} \frac{k_{//}^2}{k_0^2} = 0 \tag{1}$$

$$\text{CESICW}: \quad 1 + \frac{\omega_{pi}^2}{\Omega_i^2 - \omega^2} \frac{k_\perp^2}{k^2} - \frac{\omega_{pe}^2}{\omega^2} \frac{k_{//}^2}{k^2} = 0 \tag{2}$$

where $b_\sigma = (k_\perp \rho_\sigma)^2$ and $\omega_{p\sigma}$ is the plasma frequency, ρ_σ ($\rho_\sigma^2 = T_\sigma / m_\sigma \Omega_\sigma^2$) the Larmor radius of species σ and I_n a modified Bessel function of order n. Figure 3 shows the calculated dispersion relations from eqs. (1) and (2) at B_T = 4.3 T for the assumed edge plasma parameters $n_{eb} = 2 \times 10^{18}$ m^{-3} and $T_{eb} = T_{ib} = 100$ eV. Since the IQM is a non-resonant mode, its frequency is constant at $\Omega_i/2\pi$ irrespective of $k_\perp$, which is indicated by the broken line. From this figure, it is shown that two types of decay processes, FW into IBW and IQM and FW into IBW and CESICW which satisfy the frequency and wave number selection rules are possible. The dependence of the frequency of LF decay waves on B_T in H-majority second harmonic heating is given in Fig. 4. The frequency of IQM is inferred from the LSB frequency, i.e. $f_1 = f_0 - f_2$. The solid line shows the hydrogen cyclotron frequency for the magnetic field at the antenna (R = 3.8 m). The broken line shows the frequency of CESICW estimated from eqs. (1) and (2) and the wave number selection rule for the edge plasma parameters of $n_{eb} = 2 \times 10^{18}$ m^{-3} and $T_{eb} = T_{ib} = 100$ eV on the assumption of uniform pump field ($\mathbf{k}_0 = \mathbf{0}$) as indicated in Fig. 3. The EQM is a non-resonant mode and its frequency is given by $f'_1 \sim 0.1 k_{//} v_{Te}$, where $v_{Te} = (2T_e/m_e)^{1/2}$. Then its frequency is estimated as ~ 25 MHz for $T_{eb} = 100$ eV and $k_{//} = 40$ m^{-1} irrespective of B_T. The observed frequencies in both decay processes are consistent with theoretical ones. Therefore, two decay processes are identified as the ones described above. Figure 5 shows the detected intensities of LSB waves (IBW) by the probe near the antenna versus B_T in H-majority second harmonic heating. The intensity of IBW $P_d(f_2)$ for the decay into IBW and IQM increases with reduction in the magnetic field for the range of 3.8 - 4.5 T. However, the intensity of IBW $P_d(f'_2)$ for the decay into IBW and CESICW or EQM is almost constant with B_T.

Here, we briefly discuss the B_T dependence of the intensity of IBW for the decay into IBW and IQM. The damping for the IQM is determined by the electron Landau damping. The damping for the IBW is also determined primarily by the electron Landau damping and the convective loss and further the electron Landau damping is substantially dominant. Accordingly, the growth rate for this parametric decay instability [6] is given by

$$\gamma \approx 2\sqrt{\pi}\, \omega_{pe}^2 \frac{-\frac{y_2^3}{\omega_2^2} \exp(-y_2^2) + \frac{1}{4} |\mu_e - \mu_i|^2 \frac{y_1^3}{\omega_1^2} \exp(-y_1^2)}{\left| \partial\varepsilon / \partial\omega_2 \right|} \tag{3}$$

with

$$\mu_\sigma = \left(\frac{q_\sigma}{m_\sigma}\right) \left[\left(\frac{E_{0//} k_{//}}{\omega_0^2} + \frac{E_{0\perp} k_\perp}{\omega_0^2 - \Omega_\sigma^2} \right)^2 + \frac{(E_{0x} k_y - E_{0y} k_x)^2 \Omega_\sigma^2}{(\omega_0^2 - \Omega_\sigma^2)^2 \omega_0^2} \right]^{\frac{1}{2}} \tag{4}$$

where $y_j = \omega_j / k_{j//} v_{Te}$ and μ_σ is the ratio of drift excursion of species σ for a plane-polarized pump wave $\mathbf{E}_0$ to the wavelength of the decay wave. The subscripts 0, 1, 2 refer to pump (FW),

LF (IQM), LSB (IBW), respectively. The IQM occurs for $y_1 \approx O(1)$ which tends to maximize the electron interaction. Then, as y_2 increases, the first term of the numerator which is the damping rate of the IBW decreases making the growth rate larger. When the magnetic field is reduced for the fixed pump frequency, ω_2 and y_2 increase while ω_1 decreases. Therefore, one may understand the behavior of the increasing intensity of the IBW with the reduction in the magnetic field.

Next, we estimate the threshold pump electric field. At the threshold, $\gamma = 0$ and from eq. (3), we have

$$|\mu_e - \mu_i|^2_{th} = 4 \frac{\omega_2 k_{1//}^3}{\omega_1 k_{2//}^3} \exp\left\{ - \left[\left(\frac{\omega_2 k_{1//}}{\omega_1 k_{2//}} \right)^2 - 1 \right] y_1^2 \right\}. \quad (5)$$

From eqs. (4) and (5), the threshold pump electric field is given by

$$E_{0\perp th} \approx B_T \frac{\omega_2}{k_\perp} \frac{\left(\omega_0^2 - \Omega_i^2\right)}{\omega_2 \Omega_i} |\mu_e - \mu_i|_{th}. \quad (6)$$

As $k_{0//} \approx 0$ m^{-1} in the case of the (0,0) phasing, $k_{1//} \approx k_{2//}$. Then $E_{0\perp th}$ is estimated as about 380 V/cm for the observed value of $f_2/f_1 = 1.84$ at $B_T = 3.8$ T assuming $k_{1//} = 25$ m^{-1}. Here, $k_\perp$ is calculated from eq. (1) for the assumed edge plasma parameters of $n_{eb} = 2 \times 10^{18}$ m^{-3} and $T_{eb} = T_{ib} = 100$ eV. The estimated antenna electric field is about 1 kV/cm, which is much larger than the calculated threshold value. In the case of the (π, 0) phasing, $k_{0//} \approx 20$ m^{-1}. Since the pump field is finitely extended, $k_{1//}$ and $k_{2//}$ must be lager than $k_{0//}$. If $k_{1//} = 25$ m^{-1}, then $k_{2//} = 45$ m^{-1} from the wave number selection rule. The threshold pump power for the (π, 0) phasing is estimated to be two order of magnitude larger than that of the (0, 0) phasing for the same edge plasma parameters, which may explain relative lack of parametric activities for the (π, 0) phasing.

3. Conclusions

Two types of parametric decay instabilities near the plasma edge are observed during the second harmonic ICRF heating on JT-60. One type is the decay into an ion Bernstein wave (IBW) and an ion cyclotron quasimode (IQM) and the other into an IBW and a cold electrostatic ion cyclotron wave (CESICW) or an electron quasimode (EQM). The decay processes are observed in both pure hydrogen plasmas (H-majority second harmonic heating) and helium plasmas with hydrogen concentration of $n_H/n_{He} \approx 0.1$ (H-minority second harmonic heating) but only in the (0, 0) phasing. The intensity of IBW detected by the probe placed near the antenna in the decay into IBW and IQM increases with reduction of B_T. The B_T dependence and the relative lack for the (π, 0) phasing of the parametric decay activity are well consistent with the theoretical predictions. On the other hand, the intensity of IBW in the decay into IBW and CESICW or EQM is constant with B_T.

References

[1] J.-M. Noterdaeme,et al., in Controlled Fusion and Plasma Heating (Proc. 15th Eur. Conf. Dubrovnik, 1988) Vol. 12B, Part II, European Physics Society (1988) 762.
[2] R. Van Nieuwenhove, G. Van Oost, J.-M. Beuken, et al., , ibid., p.778.
[3] M. Saigusa, et al., in Radio-Frequency Power in Plasmas (Proc. 8th Top. Conf. Irvine, 1989), American Institute of Physics, New York (1989) 326.
[4] D. G. Swanson, Phys. Fluids **10** (1967) 1531.
[5] M. Ono, Phys. Rev. Lett. 42 (1979) 1267.
[6] M. Ono, M. Porkolab, R. P. H. Chang, Phys. Fluids. **23** (1980) 1656.

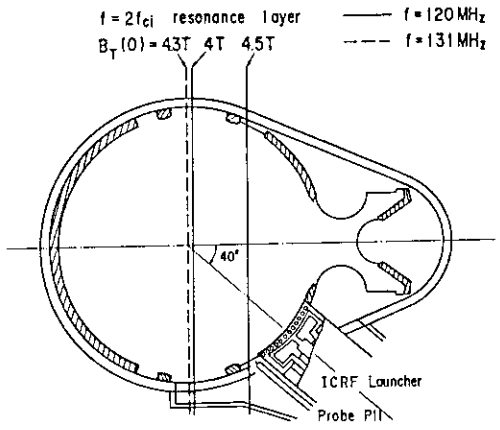

Fig. 1 Poloidal cross-section of JT-60 with the ICRF antenna.

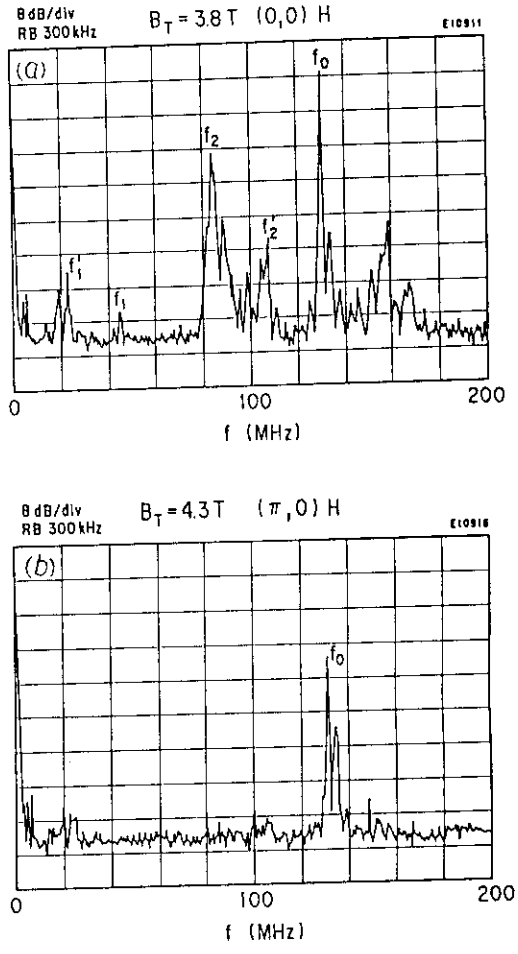

Fig. 2 Typical frequency spectra detected by the probe near the antenna. (a) For the (0,0) phasing at B_T = 3.8 T in H-majority second harmonic heating, where f_0 is the pump frequency, f_1 the IQM, f'_1 the CESICW or EQM, f_2 and f'_2 the IBW. (b) For the (π, 0) phasing at B_T = 4.3 T in H-majority second harmonic heating.

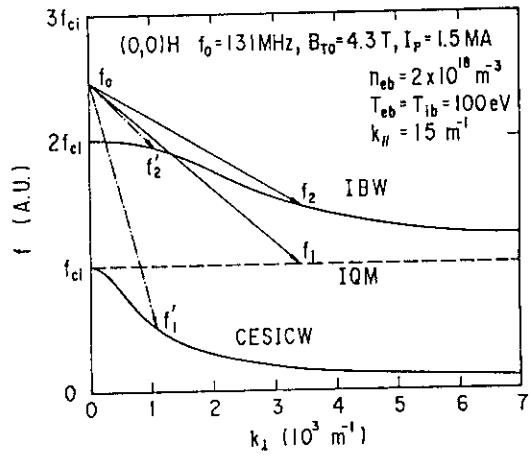

Fig. 3 Calculated dispersion relations at B_T = 4.3 T for the (0,0) phasing in H-majority second harmonic heating.

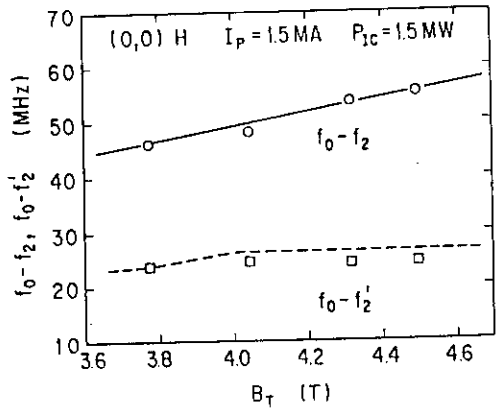

Fig. 4 Dependence of the frequency of LF decay wave on B_T in H-majority second harmonic heating with the (0, 0) phasing. The solid line shows the hydrogen cyclotron frequency for the magnetic field at the antenna (R=3.8 m) and the broken line the frequency of CESICW estimated from the uniform pump theory.

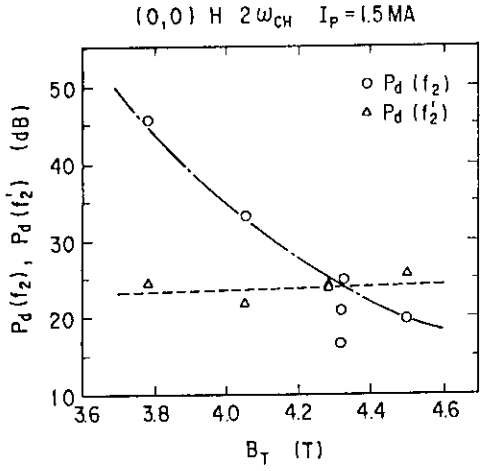

Fig. 5 The intensity of LSB waves (IBW) detected by the probe near the antenna versus B_T in H-majority second harmonic heating with the (0, 0) phasing.

4. H-mode Experiments

4.1 Comparison of H-mode with outer and lower X-point

H. Nakamura, S. Tsuji, T. Ozeki, S. Ishida, M. Nagami, M. Azumi

1. Introduction

Until the end of 1987, JT-60 had a single null poloidal divertor at the outer midplane of the torus. From June 1988, lower divertor experiment has been started to compare H-mode characteristics between the outer divertor (FY1987) and the lower one (FY1988) without Ti-gettering. Experimental arrangements are shown in Fig. 1. In this paper, the H-mode characteristics of the both divertors without titanium gettering will be compared[1].

2. Results of Outer Divertor (FY 1987)

Figure 2 summarizes the operational diagrams of n_e vs. P_{ABS} in the H-mode experiments with the outer divertor. Threshold values of ne and P_{ABS} are 1.8×10^{19} m^{-3} and 16MW. Upper threshold value of n_e increases with P_{ABS} . In the H-mode, the L- mode energy confinement times are improved at most by 10 %. This small improvement of the energy confinement time is due to the very short period of the H-mode phase. In electron temperature measurement by ECE, the maximum radius reliable enough is around 0.73 a. The H-mode transition is strongly dependent on the edge electron temperature. Threshold electron temperature at r=0.73 a is 1 to 1.1 keV while the edge electron density must be higher than 1.5×10^{19} m^{-3}. Magnetic fluctuations near the X-point measured with a magnetic probe shows reduction in $|\widetilde{B_P}/B_P|$ by a factor of about 6 down to the base level is observed during the L-phase to the H-phase transitions. Figure 3 shows the soft X-ray signals, which includes periods of the L-mode (t=5.83 to 5.85 s) and the H-mode (t=5.85 to 5.87 s). The outermost channel is correspond to $r \fallingdotseq 0.9$ a. At the L to H transition (t=5.853 s), the H α signals drop and the soft X-ray signals begin to increase. Although relatively clear change is observed in the channel two ($\fallingdotseq$ 0.8 a), the soft X-ray signals of the other channels change in the same manner. Therefore, clear localization of the fluctuation is not observed in the outer divertor.

An ideal MHD ballooning stability analysis has been done using highly accurate numerical equilibria of JT-60. Threshold of pressure gradient parameter, α $(=-\frac{2r^2}{RB_p^2}\frac{dP}{dr})$ increases as global shear parameter $S(=\frac{r}{q}\frac{dq}{dr})$ becomes higher, where r minor radius, R major radius, Bp poloidal field, p plasma pressur and q safety factor. This shows that the ballooning/interchange mode is stable even in the outer X-point.

3. Results of Lower Divertor(FY1988)

Figure 4 shows operational diagram of absorbed power (P_{ABS}) vs. n_e for the H-mode transitions and the ELMs. In the hydrogen discharges with a plasma current of 1 MA and a toroidal magnetic field of 3~3.3 T, threshold electron density is 1.7×10^{19} m^{-3} for the H-mode transitions. The threshold absorbed power is 14.5 MW for the H-mode transitions. At the H-mode transition, reduction in magnetic fluctuations is observed. Improvements in the confinement in the H-mode are around 10 % in $P_{ABS} \fallingdotseq 15$ MW. Degree of the improvement is small in $P_{ABS} \geqq 20$ MW. At the L-H transition, Te^{ECE} (r= 0.8a) and ne (r=0.6a) reach 1.6 keV and 1.3×10^{19} m^{-3}, respectively. However, in the L-mode shot, Te^{ECE} is less than 1.5 keV during the NB heating. Te^{ECE} (r=0.8a) necessary for the L-H transition is about 1.6 keV. Occurrence of the ELM is observed in Hα signals around the main plasma and the divertor region. Spacial location of the ELM can be measured by the soft X-ray array. Figure 5 shows soft X-ray signals measured by PIN diode array with viewing angles from separatrix surface to plasma center. An edge localized fluctuation is observed in $r \geqq 0.7a$ and an inversion radius of the soft X-ray signals is located around $r \fallingdotseq 0.95a$.

Ballooning/interchange stability has been analysed with the similar method as in the outer divertor. The critical pressure gradient of the these modes increase as increases of the shear parameter S same as in the outer divertor. In the ballooning mode, critical pressure gradient parameter is almost the same value as in the outer divertor. The interchange mode is more stable than one in the outer divertor. This difference in the interchange boundary arises from magnetic well effect.

4. Discussion

Comparison of the JT-60 H-mode characteristics between the outer divertor and the lower one shows that the H-mode is realized even in the outer divertor, which has similar features as the H-mode in the lower divertor. As shown in section 3, the ballooning/interchange modes are not unstable in the outer divertor in contradiction to Bishop's result with semi-analytic model. This shows that the ballooning/interchange mode near the separatrix are sensitive to the magnetic configuration near the separatrix. Therefore, to discuss the possibility of the H-mode transition from the view point of MHD stability, calculation with precise equilibria of divertor configuration is necessary. Moreovere, the H-mode theory on mirror trapping is not applicable to JT-60 outer divertor results, since banana-trapped ions escape to the outer X-point. These results shows that location of the separatrix is not necessary condition for realization of the H-mode. These results show the existence of the separatrix is not always necessary for the occurrence of the H-mode. In the H-mode with the outer divertor of

JT-60, the threshold power (P_{TH}) is about 16 MW. One of the reason of the high threshold power in the outer divertor is $H^0 \rightarrow H^+$ or $H^0 \rightarrow He^{++}$ operation. Another reason is location of the X-point of JT-60.

Finally, in the JT-60 lower divertor, the threshold power of 15 MW is almost same as the one in the outer divertor. Although reason of this high threshold power is not clarified, there are two possibilities of the reason. One of the reason might be effect of impurity contamination. At present, value of Z_{EFF} is estimated to be 3 to 5 in the JT-60 lower divertor. Another reason is considered to be effect the specific vacuum chamber with large volume (V_0) between the plasma surface and the vacuum vessel. The ratio of V_0 to the plasma volume(V_{PL}) in JT-60 outer divertor is 0.7 although V_0 / V_{PL} is about 0.1 to 0.2 in DIII-D and JET. Large amount of neutral particle is expected around the main plasma of JT-60 lower divertor configuration and threshold power to increase edge temperature to critical value for the H-mode transition tends to increase.

5. Summary

In the JT-60 H-mode experiments with outer divertor and lower one; the results are summarized as follows;

Outer Divertor

- H-mode discharges similar to the ones in the lower/upper divertor are observed in contradiction to the previous H-mode theories.
- The threshold absorbed power and electron density are 16 MW and 1.8 $\times 10^{19}$ m^{-3}, respectively.
- Improvement in the energy confinement time is limited to less than 10 %.
- Ballooning/interchange stability calculations with JT-60 equiribria show that there are enough stable region in the outer divertor experiment.

Lower Divertor

- The threshold absorbed power and electron density are 14.5 MW and 1.7 $\times 10^{19}$ m^{-3}, respectively.
- Improvement in the energy confinement time is less than 10 % limited by the grassy ELMs.
- From the soft X-ray signals, edge fluctuations are localized in $r \geqq 0.8$.
- Calculated value of critical pressure gradient for ballooning mode is the same as one in the outer divertor.

Reference

[1] H. Nakamura, et al., JAERI-M 89-106(1989) and to be published in Nucl. Fusion Vol. 30, No. 2(1990).

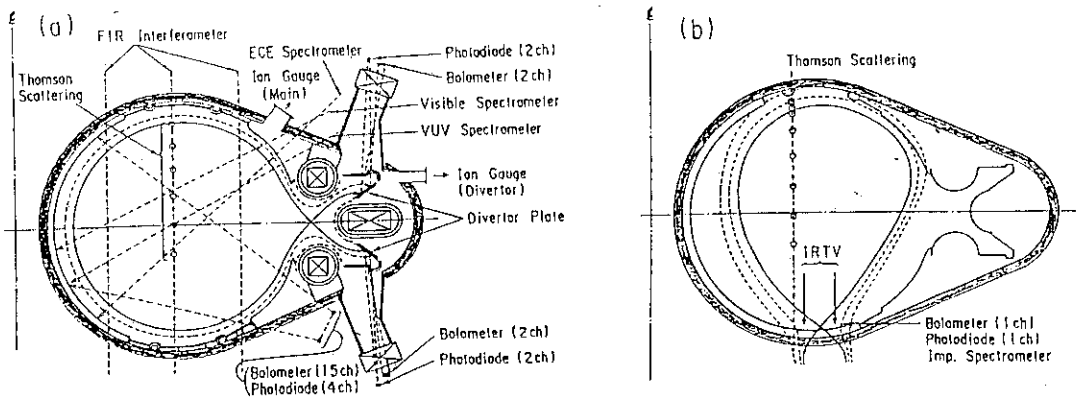

Fig. 1 Cross sectional view of JT-60 showing diagnostics (a) Outer divertor, (b) Lower Divertor

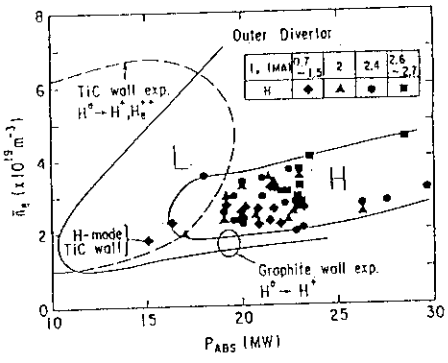

Fig. 2 H-mode thresholds of Pabs and ne in outer divertor.

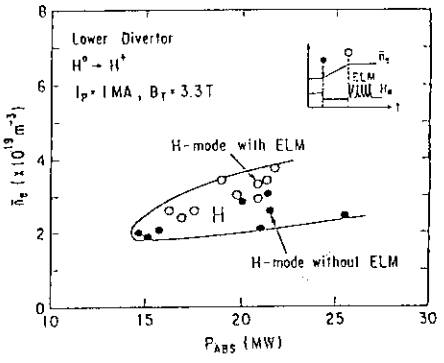

Fig. 4 H-mode thresholds of Pabs and ne in lower divertor.

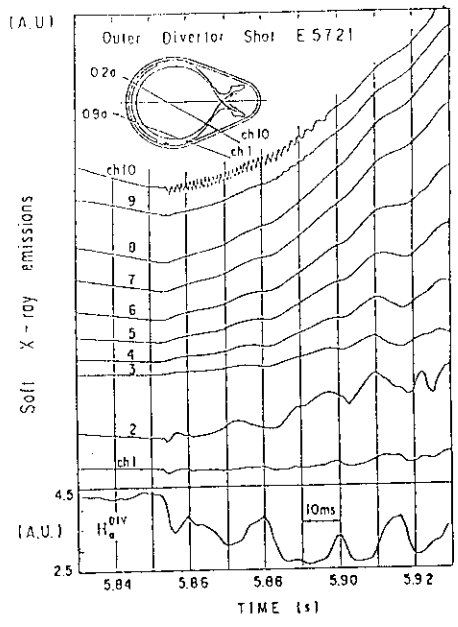

Fig. 3 Soft X-ray and Hα signals in outer divertor.

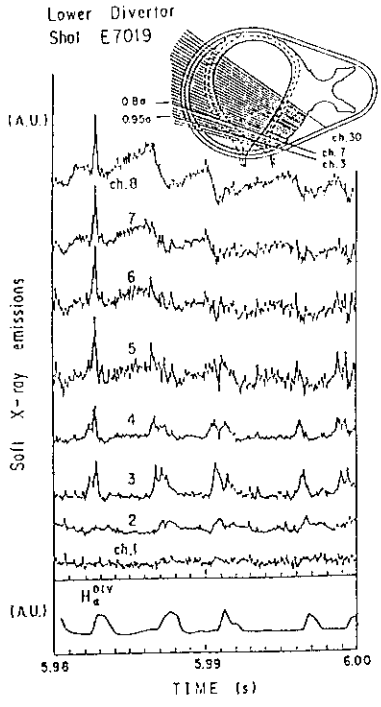

Fig. 5 Soft X-ray and Hα signals in lower divertor.

4.2 H-mode Experiments with Titanium Gettering

Michiya Shimada, Norio Suzuki and Hiroo Nakamura

1. Introduction

H-mode was investigated with JT-60 hydrogen and helium discharges with hydrogen beams. Previous work[1] described H-mode discharges with a null at the outer midplane or bottom side of the discharge. For the case of a divertor at the outer midplane, TiC-coated molybdenum and graphite were used as the divertor plate material. For the case of a single-null divertor on the bottom, graphite tiles were used. In these investigations, H-mode period was short, the threshold power was higher than 14.5 MW, and improvement of confinement was modest(<10%). This paper describes an H-mode investigation with walls and graphite divertor plates gettered with titanium. This investigation was motivated by JFT-2M result[2], which shows that with titanium gettering, the threshold power was reduced by a factor of two.

2. Results of Titanium Gettering

Two sets of titanium gettering system were installed on JT-60, spaced 180 degrees apart toroidally[3,4]. Each system is equipped with four titanium/tungsten filaments of 45 cm in length, and 3.5 mm in outer diameter. Usually, titanium was flashed once a day before the start of tokamak operation by using either one of the systems or both. The amount of titanium flashed each day was 5-10 g, which corresponds to 50-100 monolayers. Titanium gettering reduced the amount of oxygen by a factor of 3

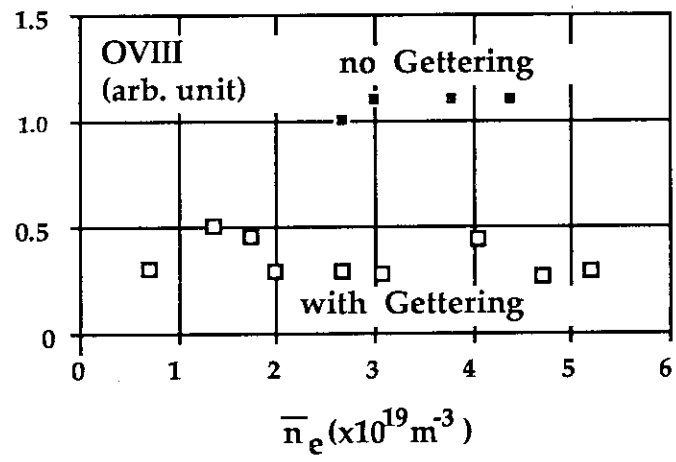

Fig. 1 Reduction of Oxygen by Titanium Gettering

in both ohmic and neutral-beam heated discharges. Particle recycling coefficient, as inferred by the global particle confinement time τ_p^*, was also reduced by a factor of two. However, little change was observed in carbon impurity content. Z_{eff} values were about 2 at relatively low density discharges(line-average density of $2x10^{19}$ m^{-3}) at modest power levels(10MW).

3. Results of H-mode Experiments

PARAMETER	range of scan
Bt	2.08-4.5 T
outer gap	37->18.7 cm
Ebeam	65 kV->40 kV
gas	H, He
Ip	0.7-1.4 MA
Ip ramp down	1.0->0.7 MA
ne	2.3-4.2 E19m-3
Xp	0-13.7 cm
Xp ramp up	4->13cm, 2->9cm

Table I. Parameter Ranges Scanned

After titanium gettering each day, we did parameter scans of wide ranges as listed in the table I to search for the best condition to obtain H-mode transition.

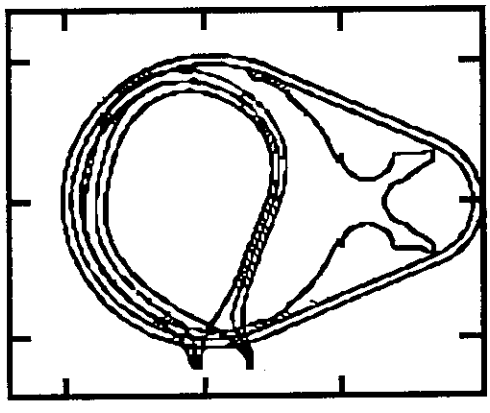

Fig. 2 The configuration in which a clear LH transition was observed

A clear LH transition was observed with 9.5 MW beam power, which is a significant reduction from the previous results without titanium. The toroidal field was 3.3 T, the plasma current was 1 MA, q^* was 3.8, and the line-average density prior to the transition was 2.3 x $10^{19}m^{-3}$. This LH transition was associated with a drop in H_α signals, a drop in neutral particle pressure, increase in density by a factor of two, and stored energy increase by 49%. Taking into account the increase of absorbed power due to density increase, we estimate the improvement of energy confinement to be about 30%. However, this transition was also associated with a significant increase in carbon impurity, Z_{eff} increase from 2.0 to 2.6, and radiation power increase up to 70% of input power, which terminated the H-mode phase. Attempts were made to reproduce a similar LH transition. However, reproducibility of this kind of a clear LH transition was very poor.

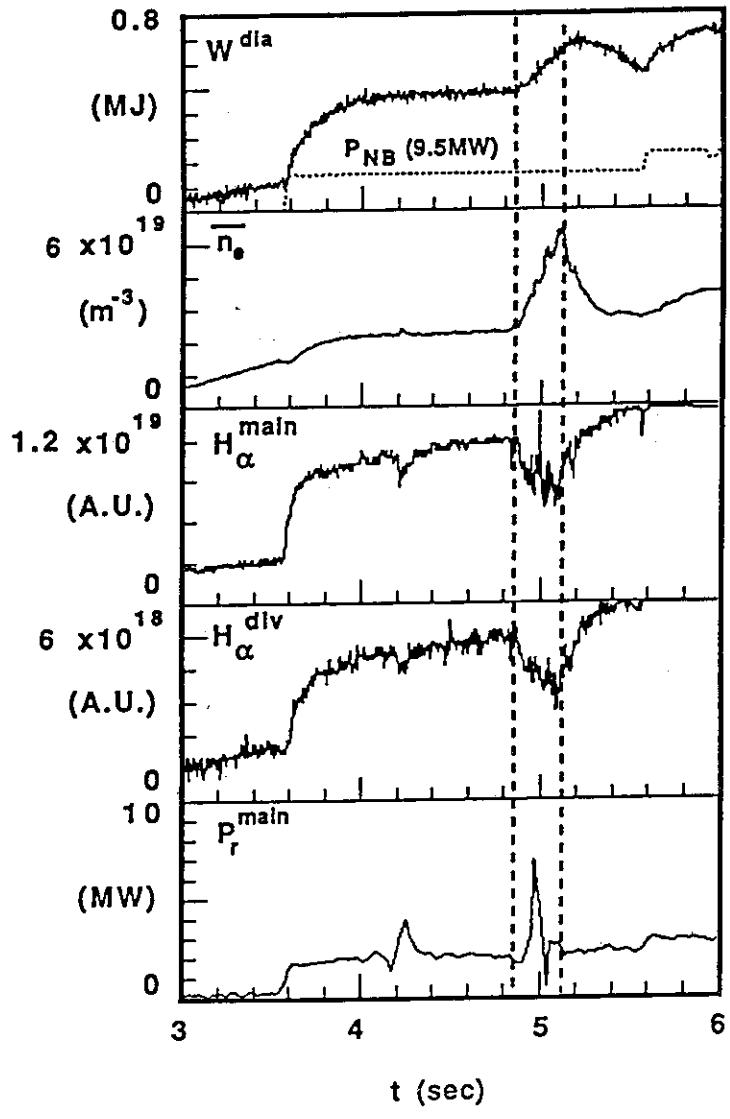

Fig. 3 A Discharge with A Clear LH Transition

4. Discussions

We would like to discuss here possible reasons why it is very difficult to obtain H-mode with neutral beam injection in JT-60.

(1) Working gas

It is a well established fact that the threshold power with hydrogen gas is about factor of two higher than with deuterium.

(2) Injection Power, Impurity

It was suspected that because the threshold power is high due to the hydrogen working gas, enhancement in impurity made the accessibility to the H-mode difficult. This may be the case without gettering and with high power; Z_{eff} values of the target plasma was 3-5. As Z_{eff} of the target plasma was about 2 with titanium gettering and beam power of 10 MW, the impurity does not seem to be the major cause of the difficulty to obtain H-mode with gettering.

(3) Configuration

Neutral particles may affect the accessibility to the H-mode if the divertor configuration is too much open to allow the neutral particles to flow back to the main plasma. We tested the configuration with outer or inner gaps similar to DIII-D. However, we could not test a configuration with small gaps at both outer and inner side of the plasma surface. Therefore, this cannot be excluded as a possible cause of the difficulty.

(4) Error Field

Due to the presence of a virtual loop at the feeder of the divertor coil, a toroidally localized error field of 200-300 G is created near the separatrix. This effect was investigated by making puncture plots of electrons orbiting near the separatrix. This calculation shows little particle orbit distortion inside the separatrix.

(5) Injection Angle

The injection angles of JT-60 neutral beams are 12-14 degrees as measured from the top view of the machine. However, as JT-60 neutral beams are not injected from the outer midplane, the effective injection angle should be determined from the pitch angle of the fast particles when they reach at the outer midplane. Neutral beam orbit calculation shows that the effective injection angles are about 22 degrees, which is not very much different from those of DIII and DIII-D perpendicular beams(27 degrees).

(6) Shear

In case of small divertor coil current and divertor coils close to the discharge, the magnetic shear is smaller than otherwise. However, the existence of H-mode with limiter configuration is a fact against this argument.

To summarize, the major cause of the difficulty to access H-mode seems to be the working gas. The configuration remains to be a possible candidate. The impurity may be a possible cause particularly in the case of no gettering and high power.

5. Conclusions

Following results were obtained in H-mode experiments with walls and divertor plates gettered by titanium.

(1) Oxygen was reduced by a factor of 3 by titanium gettering, but no significant reduction was seen in carbon.

(2) Particle recycling coefficient was reduced by a factor of two by titanium gettering.

(3) A clear H-mode transition was observed with heating power of 10 MW. The line-averaged density increased by a factor of two, and the energy confinement improved by 30%.

(4) Reproducibility of this kind of a clear LH transition was very poor.

References

[1] H. Nakamura et al., JAERI-M 89-106 (1989).

[2] N. Suzuki et al., in Plasma Phys. and Controlled Nucl. Fusion. Res. (Proc. 12th IAEA Conf., Nice) Vol. 1 (1989) 207.

[3] Kenjiro Obara et al., JAERI-M 87-143 (1987) (in Japanese)

[4] Kenjiro Obara et al., JAERI-M 88-117 (1988) (in Japanese)

5. IMPROVED DIVERTOR CONFINEMENT EXPERIMENTS

5.1 Oxygen Impurity Reduction and Energy Confinement Improvement with Ion ∇B Drift toward X-point

S. Tsuji, N. Hosogane, K. Itami, H. Kubo, M. Shimada, T. Sugie,
T. Nishitani, K. Nagashima Y. Kawano, O. Naito, N. Miya

1. Introduction

The improved divertor confinement (IDC) was observed in the lower X-point configuration of JT-60. The IDC regime was characterized as high particle recycling and remote radiative cooling in the divertor region [1-3]. The particle recycling, however, was found not to have been enhanced appreciably during IDC since H_α signals through interference filters had been contaminated by C II line emission.

We operated JT-60 in four combinations of I_p and B_t polarities to examine the effects of ion ∇B drift direction on IDC and to check the symmetry of the device. As a result, we found that IDC develops only when the ion ∇B drift is toward the X-point. Reversal of B_t direction changed light impurity behavior significantly. Reduction in oxygen impurities were observed when the ion ∇B drift was toward the X-point and the heating power exceeded a threshold power of about 10 MW. Reversal of I_p direction did not affect the confinement properties and impurity behavior so much.

2. B_t Reversal Experiments

Discharge waveforms with nearly the same NB power and line averaged electron density are compared in Fig. 1 to illustrate the distinct time evolution with B_t reversal. The plasma current (1 MA) and toroidal magnetic field (4.5 T) were reversed at the same time to keep the helical magnetic field structure and, in particular, the field lines impinging the divertor plates. A dramatic difference is seen in the OVIII line evolution. Oxygen impurities in the main plasma decreased with time when the ion ∇B drift was toward the X-point (solid traces), while it increased with electron density when the ion ∇B drift was away from the X-point (broken traces). Carbon impurities behaved oppositely. When the O VIII trace was reduced, carbon influx from divertor was enhanced as seen from the C II trace. As is always the case, the IDC regime was preceded by an abrupt rise and fall of the O III signal along a vertical chord staring the inside leg of divertor. The radiation power from the divertor region is well correlated with the C II signal. And most of the radiated power is accounted by carbon and hydrogen emissions [4]. Note that the radiation power from the main plasma is higher and that from the divertor region is suppressed at lower levels with reversed B_t. Heating power dependences of those powers are plotted in Fig. 2(a). The radiation power from main plasma is 40 to 50 % of heating power and the divertor radiation remains at low levels around 20 %. These fractions are exchanged during IDC. The high radiation from the main plasma agrees with higher Z_{eff} as shown in Fig. 2(b).

The characteristics of particle recycling are examined in Fig. 3. Both divertor H_α emission and neutral pressure around the main plasma increase parabolically with line averaged electron density of the main plasma. Those levels, however, are different with B_t polarities. Whereas particle recycling in the divertor is higher with the ion ∇B drift toward the X-point, the neutral pressure is lower. These observations imply that the particle confinement is better and the particle recycling is more localized in the divertor with the ion ∇B drift toward the X-point. The particle confinement is improved further during IDC since the both strengths are reduced. Note that linear dependences of the divertor H_α emission normalized to the neutral pressure on electron density are clearly separated depending on the ion ∇B drift directions and that the IDC data points obey the same dependence as the non-IDC data as shown in Fig. 4 (a). The ordinate is a measure of

hydrogen ionization in the divertor. Thus divertor effects are concluded to be enhanced with the ion ∇B drift toward the X-point. Figure 4(b) shows that the carbon contents in the main plasma is lower when normalized to the carbon influx from the divertor, which suggests that shielding effects on carbon impurities by the divertor is enhanced as well.

3. Energy Confinement Improvement

The carbon influxes and resulting divertor radiation power in beam heated plasmas in later 1989 were not enhanced so much as before. Yet we observed the improvement in energy confinement during IDC. To find mechanism for the improvement, we examined correlations of the energy confinement time with several parameters. Some of the correlations are shown in Fig. 5. Here the energy confinement time is normalized to an absorbed power of 20 MW assuming an Goldston scaling-like inverse-square dependence to cancel the power dependence of data from 14 MW to 22 MW. The improvement is best correlated with reduction in oxygen contents in the main plasma (a). The enhanced divertor radiation power appears to be a sufficient condition for the improvement rather than a necessary one (c). There is no correlation with carbon contents (d). Although the neutral pressure data for the best improved data points are missing, the energy confinement improvement appears to be correlated with reduction in neutral pressure (b), namely improvement in particle confinement.

4. Discussion

IDC is characterized as an improved particle confinement regime, which may be explained by the Hinton & Staebler's theory [5,6]. Whereas the reduction of oxygen is correlated with the improvement in energy confinement, it is unlikely to be the direct cause. A clear correlation has been observed between oxygen contents and neutral pressure around the main plasma. The oxygen impurities seem to originate from the first walls due to charge exchanged particles, which is supposed from similar time evolution of oxygen line emissions and low-energy charge exchange neutral fluxes.

From the experimental observations, the time evolution of IDC may be described as follows; i)the particle confinement improves in discharges with the ion ∇B drift toward the X-point when electron density reaches a threshold which depends on heating power and the connection length between the X-point and the divertor plates, ii)oxygen impurities in the main plasma decrease owing to the reduced charge exchange particles, iii)carbon influx increases with increased power to the divertor due to the reduced main plasma radiation, iv)carbon impurities are accumulated near the X-point by the enhanced divertor shielding effect, v)the discharge reaches a quasi-steady state with the improved confinement and the enhanced divertor radiation, the latter of which alleviate heat load on the divertor plates. The first step appears not to occur when the ion ∇B drift is away from the X-point.

5. Summary

Spectacular changes in light impurity behavior with B_t reversal were observed in the beam heated lower X-point configuration of JT-60. The IDC regime develops only when the ion ∇B drift is toward the X-point. The improvement in energy confinement during IDC by up to 20 % is correlated with the improved particle confinement and with resulting reduced oxygen impurities.

References

[1] S. Tsuji, et al., *Plasma Physics and Controlled Nuclear Fusion Research 1988* (Proc. 12th Int. Conf. Nice, 1988), IAEA, Vienna Vol. **1**, p. 265.
[2] S. Tsuji, et al., JAERI-M 89-033, Section 2.2.
[3] N. Hosogane, et al., JAERI-M 89-033, Section 2.7.
[4] H. Kubo et al., this report, Section 5.3.
[5] F.L. Hinton and G.M. Staebler, Nucl. Fusion **29** (1989) 405.
[6] K. Itami et al., this report, Section 5.2.

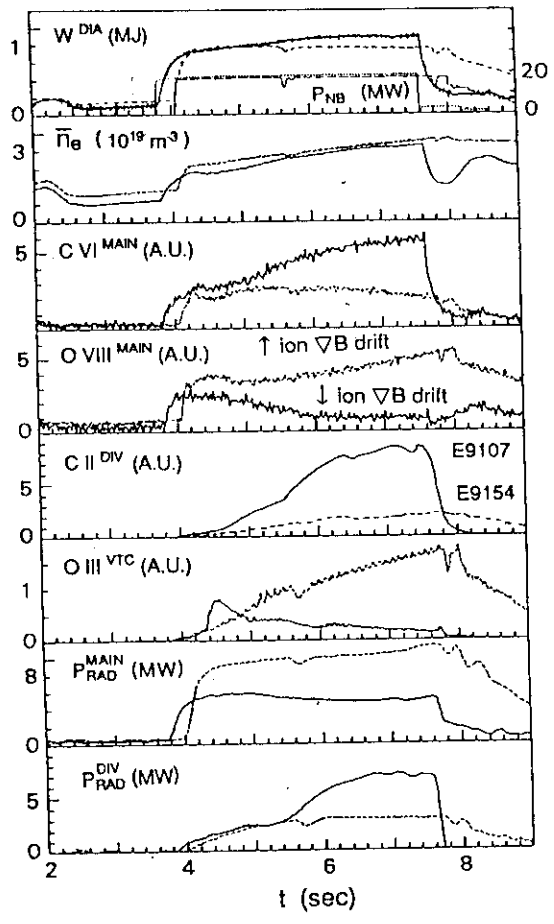

Fig. 1 Comparison of two discharges with nearly identical operational parameters except B_t and I_p polarities.

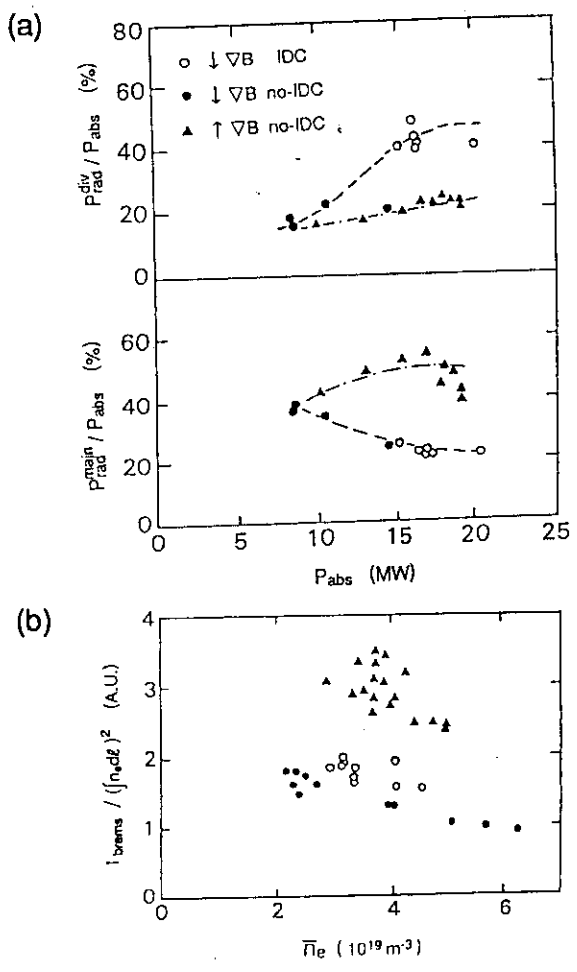

Fig. 2 Higher radiation loss from the main plasma and no enhanced divertor radiation (a) and higher Z_{eff} (b) with the ion ∇B drift away from the X-point.

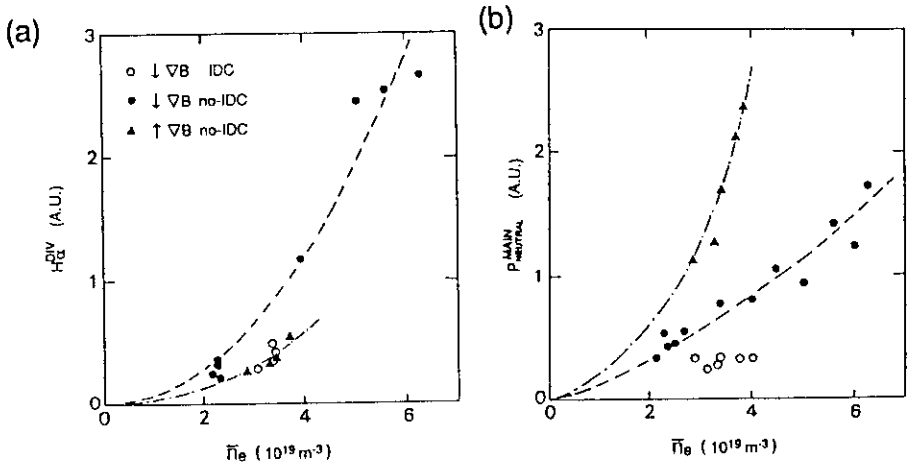

Fig. 3 Changes in particle recycling in the divertor region (a) and in neutral pressure around the main plasma (b) with B_t reversal.

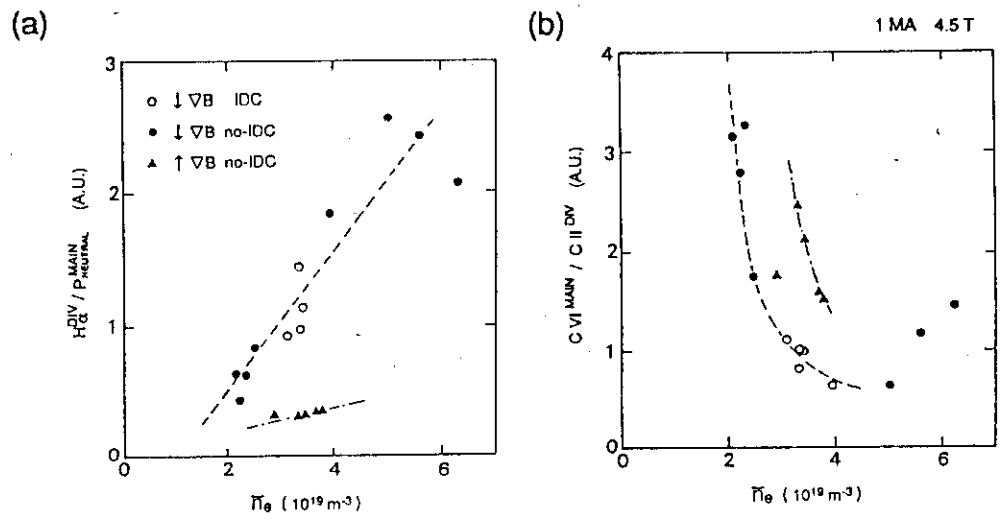

Fig. 4 Reduction in hydrogen ionization rate in the divertor region (a) and weaker shielding effect on carbon impurities (b) with the ion ∇B drift away from the X-point.

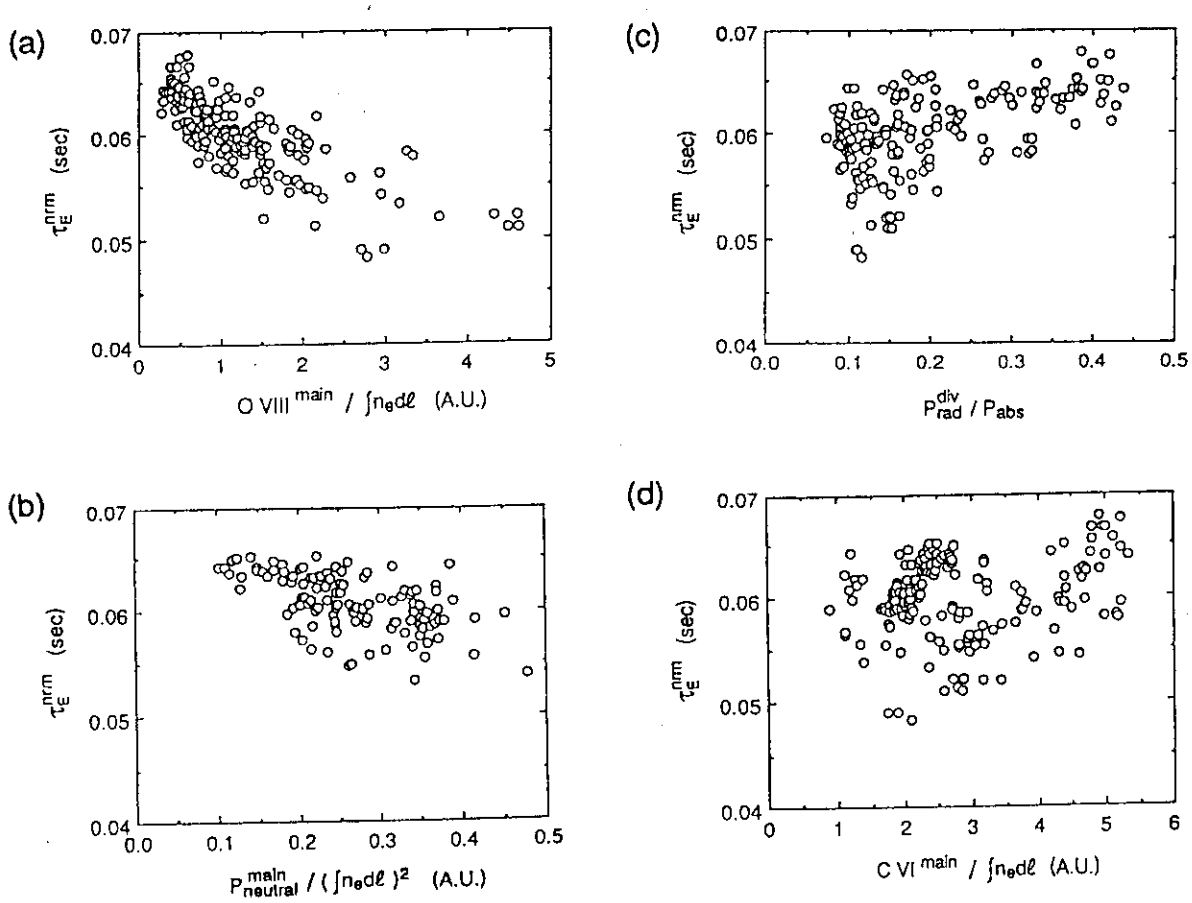

Fig. 5 Parameter dependences of the normalized energy confinement time. The absorbed powers from 14 MW to 22 MW are normalized 20 MW.

5.2 Measurement of Particle and Heat Flux in the collisional Scrape-off Layer in Divertor Discharges

K.Itami

It is recently recognized that the collisional transport of ions and electrons driven by temperature gradient along the magnetic field in the scrape-off layer is important process to affect the energy and particle confinement in the core plasma [1]. In beam heated discharges, the asymmetry in particle recycling between inner divertor and outer divertor is found to be enhanced. This asymmetry is reversed if the ion grad-B drift direction is reversed as shown in Fig.1. And this asymmetry in particle recycling is consistent with the enhanced particle flux due to collisional fluxes across the magnetic field. It is also found that the heat flux to the divertor shows the reversed asymmetry which also depends on the direction of ion grad-B drift.[2]

The characteristics of IDC (Improved Divertor Confinement) has been extensively studied. The characteristics of IDC discharges are summarized, 1) increase in plasma density and stored energy correlates with the increase in radiation around the X-point with a slow rise time about 1 sec, 2) there exist minimum beam input power and density requirement, 3) replacement of oxygen by carbon in the plasma causes the radiation in the core radiation, 4) it has only been obtained when ion grad-B drift is toward the X-point. The peripheral spectroscopy measurement has shown the accumulation of carbon and the pump out of oxygen. IRTV measurement has shown the drastic change in the heat flux at the inner divertor during IDC. After the IDC onset, the heat flux to the inner divertor decreases in a time scale of the increase in the radiation in the divertor region, while the change in the heat flux to the outer divertor is smaller [2]. Hα TV measurement shows the recycling at the inner divertor is decreasing during the IDC at the inner divertor as shown in Fig.2. It is consistent with the improvement of the particle confinement.

In order to explain these behaviors, a positive feedback mechanism driven by the carbon radiation and increase of inward pinch due to collisional particle transport is proposed [3]. When ion grad-B drift is toward X-point, the collisional transport across the separatrix driven by temperature gradient along the field line have net inward flow. This flux is large enough to modify the particle transport near the X-point and become large by increase in the asymmetry in heat flux to toward X-point. The growth rate of IDC

is given by

$$\gamma = \frac{\mathrm{Area}}{\mathrm{Vol}} \frac{Z_c \alpha}{Z_{eff} n_e \chi_e eB} \frac{q_\psi}{\varepsilon} \delta Q$$

Here, δQ denotes a change in the asymmetry in heat flux density to the divertor, **Area** denotes the surface area of the separatrix and **Vol** denotes the volume of the plasma. For typical discharge parameters, the growth rate is about 1 sec and is consistent with the observed value.

Since the Staebler's model assumes the temperature at the inner divertor and the outer divertor is same, the model doesn't explain the asymmetries between the inner divertor and the outer divertor driven by IDC. For example, the model doesn't explain the particle recycling at the inner divertor during the IDC phenomena. If the radiation simply decreased the temperature of the plasma at the inner divertor, the particle confinement deteriorates due to the enhanced particle outflux by increased temperature gradient. This phenomenon should be observed as the increase in Hα signal. But the experimental result is the reverse. More precise treatment is needed to explain the all phenomena consistently.

References

[1] S. Tsuji et al. , in Plasma Physics and Controlled Nuclear Fusion Research 1988 (Proc. 12th Int. Conf. Nice, 1988), Vol. 1, IAEA, Vienna(1989) 265.

[2] JAERI-M 89-033, section 2.5.

[3] G. M. Staebler GA-A19796.

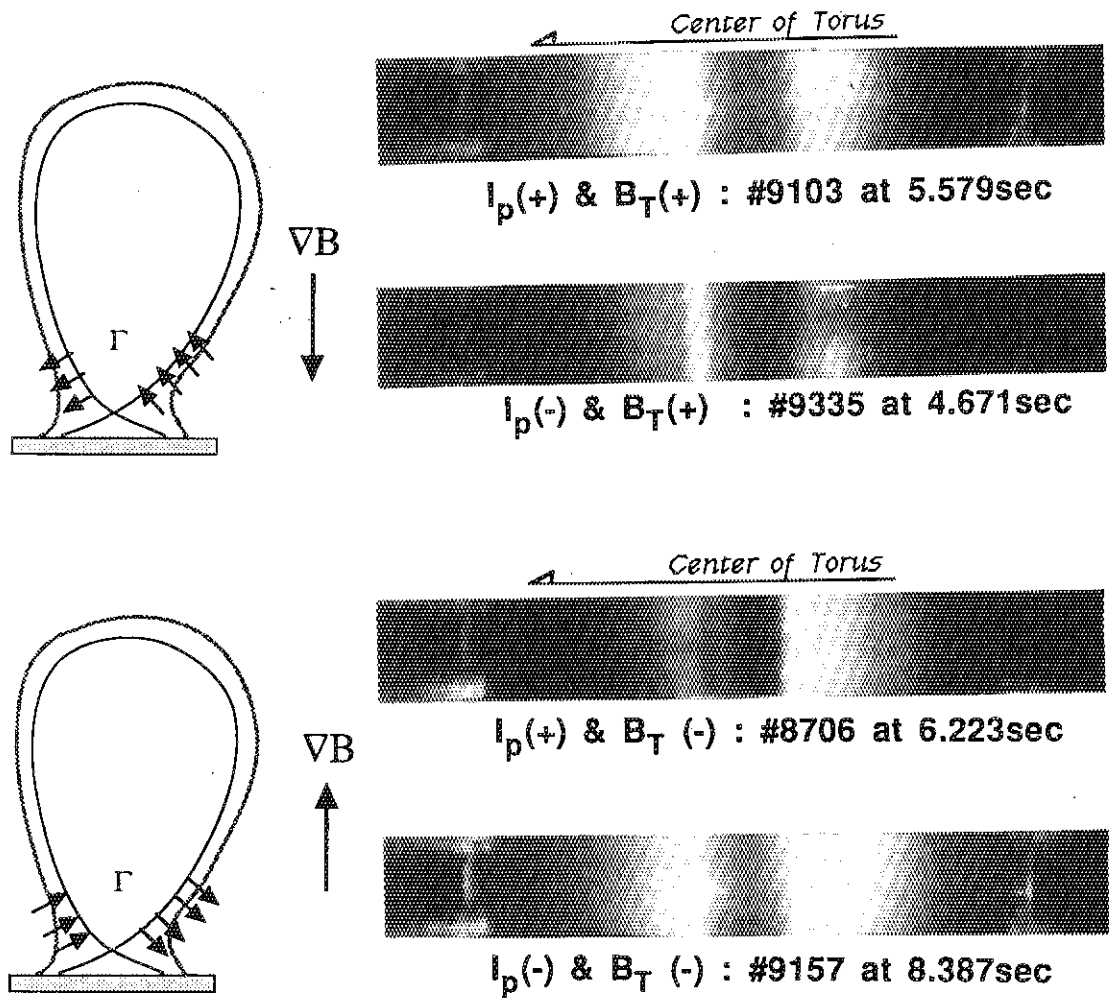

Fig.1
As is expected from the figure which shows the direction of the classical flux due to the collisional transport, the asymmetry of Hα intensity (particle recycling) is observed

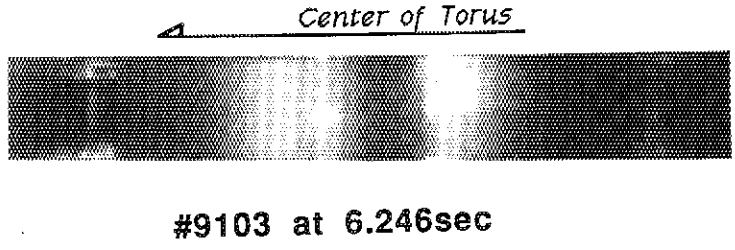

Fig.2
Hα TV measurement shows the recycling at the inner divertor is decreasing during the IDC at the inner divertor .

5.3 Spectroscopic Studies of Remote Radiative Cooling in JT-60

H. Kubo, K. Itami, M. Shimada, T. Nishitani, A. Sakasai, Y. Koide,
N. Nishino, N. Akaoka, S. Tsuji, N. Hosogane, and T.Sugie

Spectroscopic measurements in vacuum-ultraviolet and visible regions were carried out to investigate the source of radiation power from the JT-60 divertor. The analysis shows that the bolometrically-measured divertor radiation can be nearly accounted for by hydrogen radiation, low-ionized carbon impurity radiation, and charge-exchange loss. The electron density and temperature estimated by using the heat flux density and H_α intensity at the divertor plate are 26 eV and 2.4 x $10^{20}m^{-3}$. This result suggests that dense, cold and radiative divertor plasma is formed with strong neutral beam heating of up to 20 MW.

1. Diagnostic System and Temporal Behaviors of Signals

Figure 1 presents a schematic diagram of the experimental set-up of the diagnostics for divertor plasma. Through a horizontal port, a photo-diode with Hα filter, a bolometer and a visible spectrometer observed Hα intensity, radiated loss, and line intensities of light impurities and hydrogen, respectively. Because the band width of the Hα filter was not enough narrow, the signal of the photo-diode included the signal of a carbon line. Therefore, the intensity of the Hα line refereed in this paper is the photo-diode signal corrected by using the intensity ratio of the carbon line and Hα line measured by the visible spectrometer, whose sensitivity was calibrated only relatively. The heat flux to the divertor plates were derived from the surface temperature of the divertor plates measured by an IRTV camera. And a VUV monochromator measured line intensities of light impurities in the divertor region around the inner separatrix.

The temporal behaviors of the signals in the discharges to be discussed in the following sections are shown in Fig.2. The discharges were repeated with same the condition; I_p = 1 MA, B_T = 4.5 T, X_p =3.5 cm, P_{NB} = 23 MW, etc. They were the IDC (Improved Divertor Confinement) discharges, while the radiated power in the divertor region was not so large. The line intensities of the carbon ions were measured by the monochromator on shot to shot bases. In the following sections, we present the analysis of the data at t = 6.25sec.

2. Estimation of Electron Temperature and Density

The electron temperature and the electron density in the divertor plasma were estimated from the heat flux and the intensity of Hα line.

If we assume that the recycling rate of the hydrogen is unity and all of the recycling hydrogen is ionized in the divertor region, the particle flux to the divertor plate: Γ is expressed as

$$\Gamma = \alpha(n_e, T_e) I(H\alpha), \qquad (1)$$

where α is the ratio of the ionization rate to the emission rate of Hα. If we assume that the particle flows to the divertor plates at the sound velocity and $n_e = n_{H^+}$, the particle flow is expressed as

$$\Gamma/\theta = n_e C_s, \qquad (2)$$

where C_S is the sound velocity and θ is the pitch of the plasma. The heat flow: ϕ and the particle flow has the relation given as

$$\phi = \gamma_s T_e \Gamma, \qquad (3)$$

where γ_s is the heat transmission coefficient at the sheath and we use $\gamma_s \fallingdotseq 7$. From Eqs. (1)-(3), we obtain

$$\theta = \gamma_s T_e \alpha(T_e, n_e) I(H_\alpha) \qquad (4)$$

$$\left(\frac{2kT_e}{m}\right)^{1/2} n_e = \alpha(T_e n_e) I(H_\alpha) / \theta \qquad (5)$$

In this paper, we assumed that the divertor plasma was uniform with the dimensions of X_p $\times$ the full half width of the heat flow: 3.5 cm (H) $\times$ 6 cm (W). $\theta = 0.013$ at the divertor plate was derived from magnetic probes measurements. And we used α presented in Ref.1 with the assumption that the plasma was optically thin, while the assumption is not valid for Lyman α line. As a result, we obtain $n_e = 2.4 \times 10^{20}$ m^{-3} and $T_e = 26$ eV at t = 6.25sec in the discharges shown in Fig.2.

The assumption that all of the recycling hydrogen is ionized in the divertor region may not be valid, and the real particle flux may be larger than the estimated flux. However, because the analysis tends to overestimate the electron temperature and underestimate the electron density, we can conclude that the divertor plasma is dense and cold.

3. Investigation of Radiative Source

The radiative source in the divertor region was investigated from spectroscopic measurements.

The radiated power due to the carbon was estimated from the VUV lines: C II ($2s^2 2p\ ^2P$ - $2s 2p^2\ ^2P$, 904Å), C III ($2s^2\ ^1S$ - $2s 2p\ ^1P$, 977Å), and C IV($2p\ ^2P$ - $3d\ ^2D$, 384Å), observed by the monochromator. The recycling carbon may not be ionized up to C^{+3} in the divertor region, because the confinement time is much shorter than the time for them to reach the equilibrium and the electron temperature is low. The higher ionized carbon ions are produced in the scrape-off layer of the main plasma and flow to the divertor region without recombination, Therefore, they can be in the recombining phase. However, generally speaking, the emission rate attributed to the recombination flow is much smaller than the rate attributed to the excitation flow. Therefore, we calculated the cooling rate from the excitation cross section presented in Ref.2 assuming the coronal equilibrium for the population density of excited levels. Fig. 3 shows the ratio of the total radiation power of the carbon ion to the observed line radiation power. Using the figure and assuming the symmetry with respect to the inner and outer layer, the radiated power due to the carbon ions were estimated.

Fig.4 shows the ratio of the total radiation power due to hydrogen to the radiation power from n = 3 level, which is calculated from the line intensity ratios presented in Ref.3 assuming optically thin.

Charge exchange loss was also estimated from Hα line intensity assuming the uniformity and the dimensions of the plasma described in the previous section. Because the solid angle of the bolometer was very little, the charge exchange loss power observed by the bolometer is expressed as

$$P_{CX} = 2\pi R l_v \frac{3}{2} k T_i n_H n_{H^+} \sigma_{CX} v \int_0^{l_p} e^{-n_H \sigma_{CX} v (x - l_p)} dx \qquad (6)$$

where the dimensions of the divertor plasma are expressed as l_p width and l_v height. Fig. 5 shows the ratio of the charge exchange loss power to the radiation power from n = 3 level,

where the population density ratio n(n = 3) / n(n = 1) presented in Ref.3 was used by assuming optically thin.

Table 1 shows the estimation of the radiated power at t = 6.25 in the discharges shown in Fig. 2 using the plasma parameters estimated in the previous section; T_e = 26 eV and $n_e = 2.4 \times 10^{20}$ m^{-3}. About a half of the radiated power is accounted for the radiation of hydrogen, and the power due to oxygen is very small. As a result, regardless of some assumptions in the analysis, the estimated radiated power can nearly account for the power observed by the bolometer. However, the estimation is very rough because of many assumptions. The radiated power due to the carbon depends on temperature, because the observed line of C IV is the radiation from n = 3 level. Moreover, the radiated power due to hydrogen depends on the density, and the CXR loss depends on the temperature. Therefore, further observation of spectra and more precise measurement of the plasma parameter is needed.

4. Summary

Spectroscopic measurements in vacuum-ultraviolet and visible regions were carried out to investigate the source of radiation power from the JT-60 divertor. The analysis shows that the bolometrically-measured divertor radiation can be nearly accounted for by hydrogen radiation, low-ionized carbon impurity radiation, and charge-exchange loss. However, the analysis is very rough because of many assumptions. Therefore, further observation of spectra and more precise measurement of the plasma parameter is needed. The electron density and temperature estimated by using the heat flux density and H_α intensity. This result suggests that dense, cold and radiative divertor plasma is formed.

References

1) L. C. Johnson and E. Hinnov, J. Quant. Spectrosc. Radiat. Transfer **13** (1973) 333.
2) Y. Itikawa, S. Hara, T. Kato et al., ADNDT **33** (1985) 149.
3) T. Fujimoto, S. Miyachi, and K. Sawada, Nucl. Fusion **28** (1988) 1255.
4) P. G. Carolan and V. A. Piotrowicz, Plasma Physics, **25** (1983) 1065.

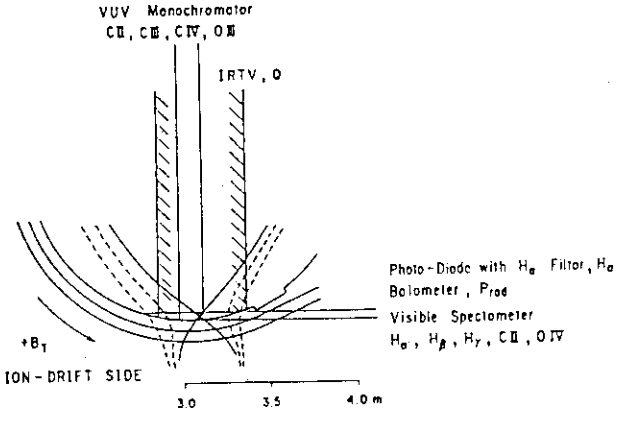

Fig.1 Schematic diagram of the experimental set-up of the diagnostics for divertor plasma.

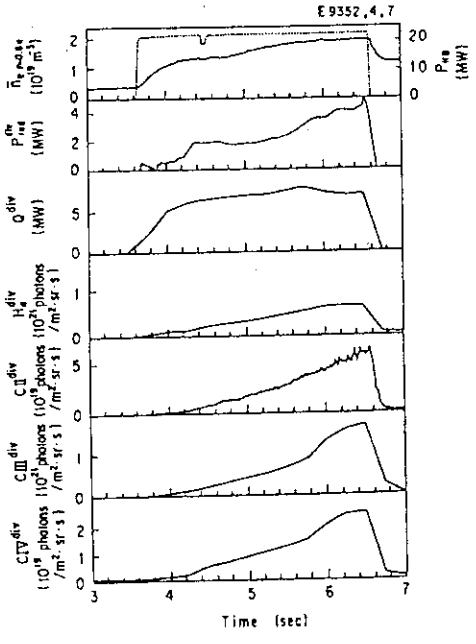

Fig.2 The temporal behaviors of line averaged electron density, NB power, radiated loss in the divertor plasma, heat flux to the divertor plates, and line intensities of Hα, C II 904, C III 977, and C IV 384 in the divertor plasma.

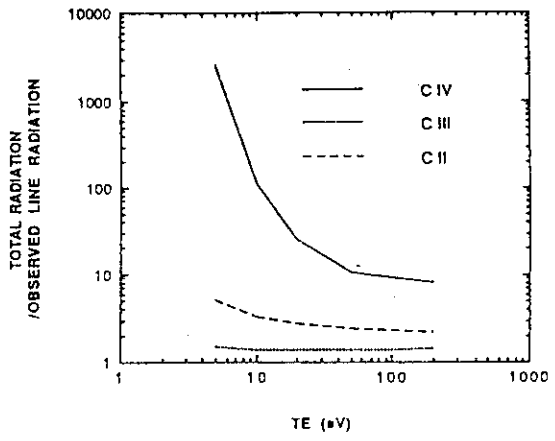

Fig. 3 Ratios of the total radiation powers due to carbon ions to the observed line radiation powers.

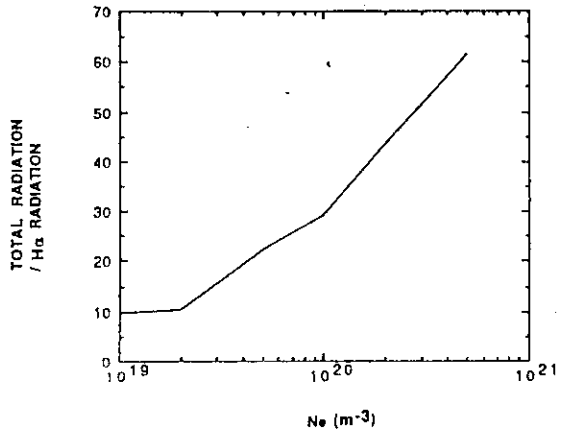

Fig. 4 Ratios of the total radiation powers due to hydrogen to the radiation power from n = 3 level of hydrogen atom.

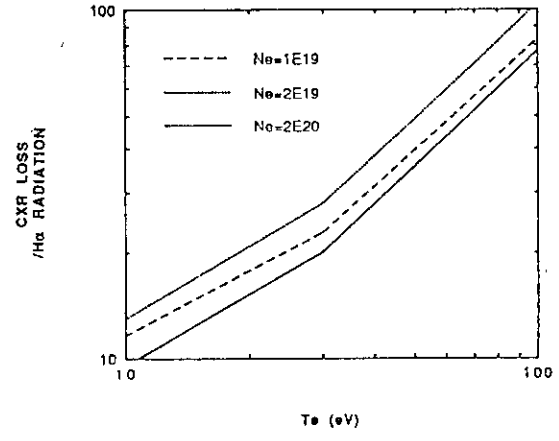

Fig. 5 Ratio of the charge exchange loss power to the radiation power from n = 3 level.

Table 1 Estimation of the radiated power. a) The intensity of O III $2s^22p^2\ ^3P_2$ - $2s2p^3\ ^3P_{1,2}$ 704Å was observed in the other discharge (E9107, t = 6.25sec). b) Radiation power from n= 3 level. c) The value was estimated by comparing the radiation power of O III 703Å and the total cooling rate of oxygen presented in Ref. 4.

LOSS SOURCE	OBSERVATION	OBSERVED LOSS	ESTIMATED TOTAL LOSS
C II	904Å	0.0074MW	0.019MW
C III	977Å	0.22MW	0.30MW
C IV	384Å	0.011MW	0.20MW
O	704Å a)	0.00057MW	<0.020MW c)
H I	6563Å(Hα)	0.0383MW b)	1.8MW
CXR	Hα	–	0.67MW
TOTAL RADIATION	BOLOMETER	4.0MW	3.0MW

5.4 PARAMETER DEPENDENCE OF DIVERTOR HEAT LOAD IN JT-60 SINGLE NULL LOWER DIVERTOR

H.NAKAMURA, K. ITAMI and JT-60 Team

1. Introduction

To establish scalings of divertor heat load on peak heat flux and half width is important for design of divertor in next fusion device Therefore, in JT-60 single null lower divertor experiments, the divertor heat load has been measured by infra-red camera. All discharges were L-mode plasmas. Schematic view of the IRTV camera system in this study is shown in Fig.1[1].

2. Results

(1) Typical Spatial Profile

Figure 2 shows typical result of spatial profile of the divertor heat load. Heat load was calculated by one dimensional inverse heat conduction code. In this shot, experimental conditions are Pabs=14 MW, ne=2E19 m-3 and Xp= 5 cm where Xp is distance between X-point and divertor plate. In this data base, parameter ranges are Pabs=7 to 12 MW , ne=(2-4)E19m-3 and Xp=4-5 cm.

(2) Half Width

In the conditions of ne=(2 - 4)E19 m-3 and Pabs=5-12 MW, no clear dependence of the half width on ne and Pabs is observed. Figure 3 shows dependence of the half width of the heat flux on ne/Pabs. The half widths are almost constant and have no dependence on ne/Pabs. The half widths in the inner and outer divertor plates are 2.5 to 3 cm and 4 to 5 cm, respectively. Half width on the divertor plate strongly depends on magnetic equilibrium parameters such as Xp. In case of Xp=4-5 cm, magnetic surface near the mid plane spreads by a factor 3 on the divertor plate. Therefore,the half widths near the mid plane are expected to be 0.8-1 cm in the inner mid plane and 1.3-1.7 cm in the outer one.The above dependence of the half width on ne and Pabs is in contradiction to result of ref[2] assuming a constant value of heat conductivity coefficient perpendicular to magnetic field. According to this result, the half width is in proportion to $ne^{7/9}/Q^{5/9}$,where Q is divertor heat load. To explain the JT-60 results, calculation of the divertor heat load considering dependence of the perpendicular heat conduction on plasma parameters is necessary.

(3) Peak Heat Flux

Figure 4 shows dependence of peak heat flux on total absorbed power. This result shows that the peak heat flux in the inner and outer divertor plates increase with the total absorbed power. In this density range, the peak heat flux on the inner divertor plate is by a factor 2-3 larger than the one on the inner divertor one. But, this in the higher density region above ne=4E19m-3, the outer heat flux becomes larger than the inner one. This tendency is shown in Fig.5.In the inner divertor plate, the heat flux decreases with the electron density. On the other hand, in the outer divertor plate, the heat flux increases with the electron density. To clarify this characteristics, further study in the condition of the higher absorbed power is now in progress.

3. Summary

In JT-60 single null lower divertor with Pabs=5-12 MW and ne=(2-4)E19m-3, the results are summarized as follows;

a. Half width of the divertor heat flux has not clear dependence on ne and Pabs. Half widths are 2.5-3 cm in the inner divertor plate and 4-5 cm in the outer one.

b. Peak heat flux increases with the absorbed power. Peak heat flux in the inner divertor plate decreases with ne. But, in the outer divertor plate, the heat flux increases with ne.

To obtain scaling of the half width and the peak heat flux, data analysis of the divertor heat load is now in progress.

References

[1] K.Itami, T.Nishitani, N.Hosogane, T.Matoba and JT-60 Team, Proc. of IAEA Technical Committee Meeting on Impurity Control, Feb 13-15,1989, Naka Fusion Research Establishment, JAERI,Japan.

[2] M.Harrison,ITER -IL-PH-13-9-E12,Sep. 1989.

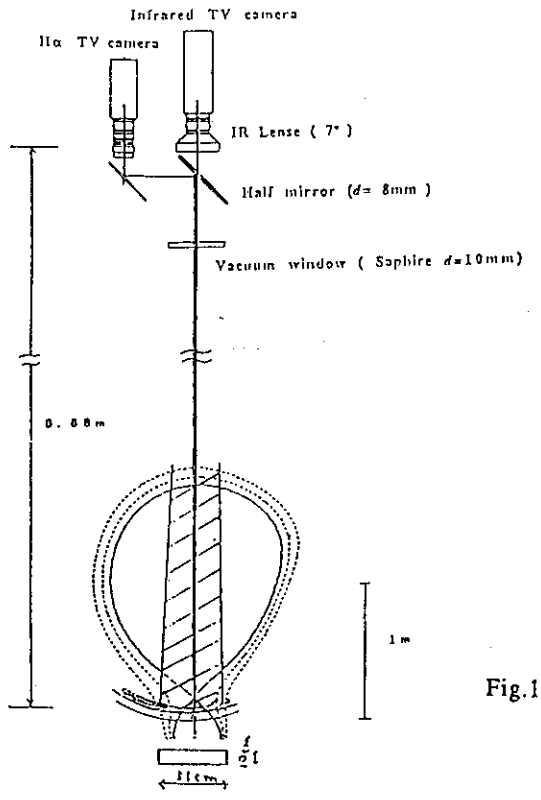

Fig.1 Schematic view of IRTV system.

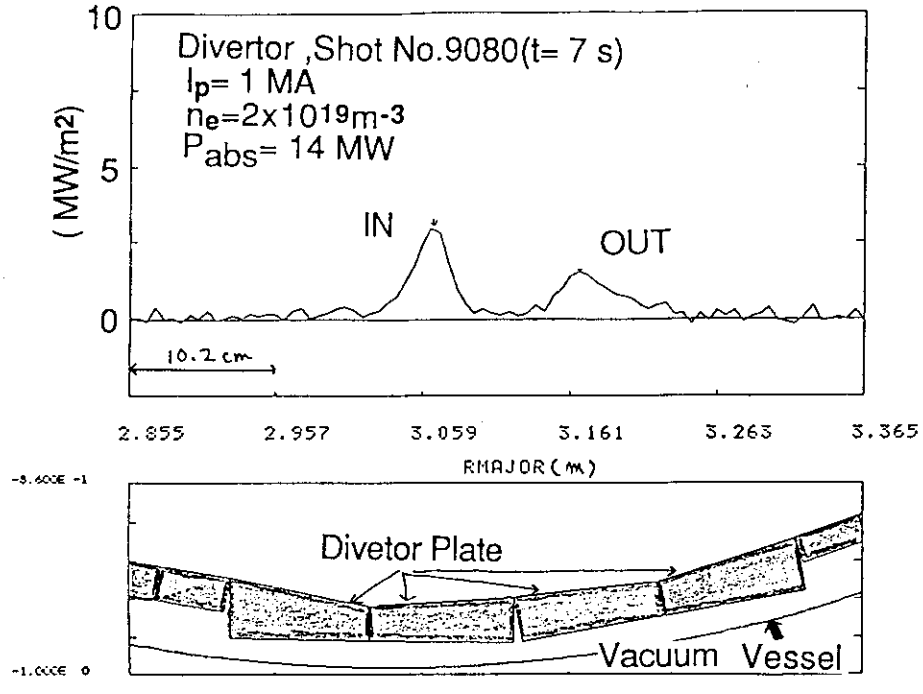

Fig.2 Typical result of spatial profile of the divertor heat load in Pabs=14 MW,ne=2E19m-3 and Xp= 5 cm.

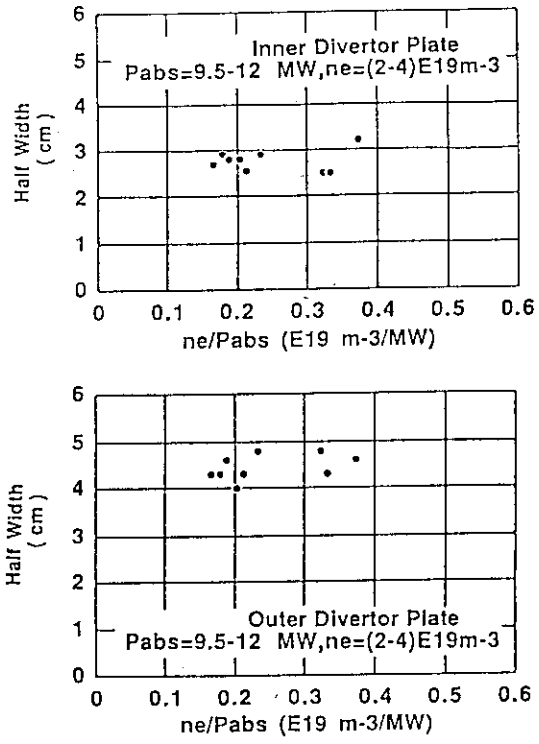

Fig.3 Half width vs ne/Pabs in Pabs=9.5-12 MW and ne=(2-4)E19 m-3.

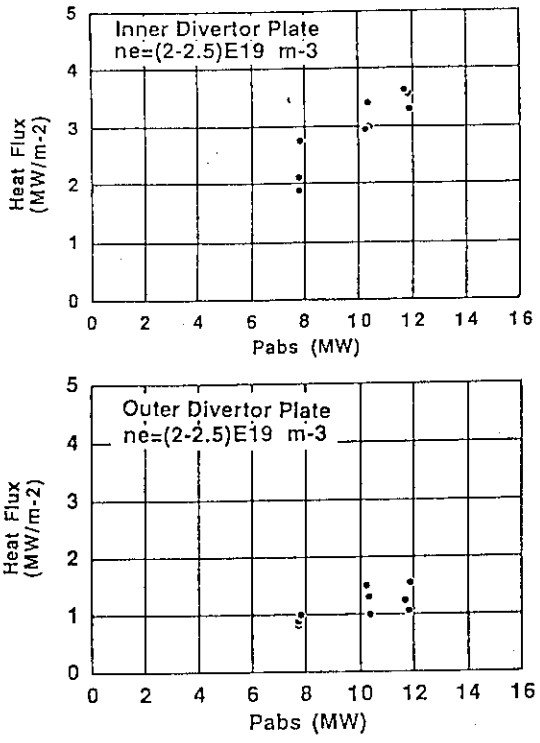

Fig.4 Dependence of peak heat flux on absorbed power in ne=(2-4)E19m-3.

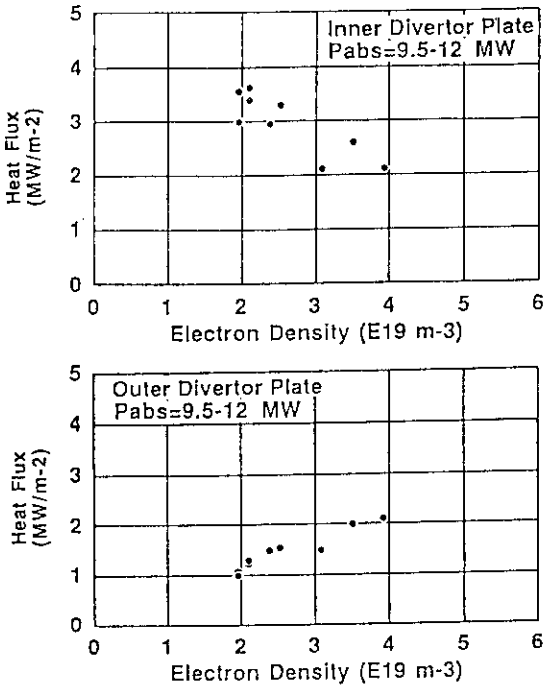

Fig.5 Dependence of peak heat flux on electron density in Pabs=9.5-12 MW.

6. High-Poloidal-Beta Experiments with Hot Ion Regime

6.1 Optimization and Sustainment of High-Poloidal-Beta High-Ion-Temperature Plasmas

S. Ishida, Y. Koide, T. Hirayama, T. Ozeki, H. Shirai, M. Kikuchi, O. Naito, S. Tsuji and M. Nagami

In tokamak research, improvement of energy confinement and its sustainment in steady state for auxiliary heated plasmas remain the critical issues for a forthcoming tokamak reactor. High-temperature enhanced confinement regime, which was originally attained in TFTR ("supershot"), may provide an attractive way for tokamak experiments to approach the breakeven condition in nuclear fusion research because of the high fusion product gain[1]. However, operation in the supershot regime required sufficient recycling suppression and led to a relatively high-poloidal-beta discharge. In TFTR, the attainable stored energy content was limited by disruptions at high poloidal-beta up to β_p~2[2]. Thus, it is necessary for a scenario of steady-state tokamak operation to demonstrate that the supershot discharges is stably sustained in the high poloidal-beta operation. While a hot ion regime similar to the TFTR supershot has been subsequently obtained in JET[3], both regimes have been so far explored only with tangential neutral beam injection (NBI) for limiter configurations. This paper presents major results from high-poloidal-beta experiments in a hot-ion enhanced confinement regime with high-power long-pulse neutral beam heating in JT-60. Objectives of the experiments in JT-60 are; 1) production of hot-ion plasma and its sustainment, 2) optimization of confinement (that is realization of the supershot by means of near-perpendicular NBI), 3) investigation of poloidal beta limits, and 4) demonstration of discharges dominated by bootstrap currents.

After changing the divertor geometry to the lower X-point configuration, the hot-ion enhanced confinement regime has been attained in 1989 by means of centrally-oriented near-perpendicular NBI with ~21 MW for 3-5 s into hydrogen plasmas with a small volume. The target Ohmic plasma was produced to have low density ($\overline{n_e}$~0.5×10^{19} m^{-3}) without gas puffing utilizing helium TDC, and the density was increased by beam fueling, typically, up to $\overline{n_e}$~4×10^{19} m^{-3}. We have carried out I_p scan in detail in the range of $0.3\le I_p(MA)\le1.2$. The experiments have been conducted for the lower X-point divertor configuration with the major radius of R=2.9 m, the minor radius of a=0.70-0.72 m, the triangularity of κ=1.4 at the toroidal fields of B_t=4.0 T and 4.5 T, as shown in Fig. 1. This configuration was slightly shifted inward from nominal major radii of the JT-60 plasma at R~3.1 m, so that the neutral beams are centrally deposited and the profile measurements are made focussing on the central region of the plasma.

As shown in Fig. 2, the best performance of this regime was achieved in a narrow range of I_p~0.5-0.7 MA, where high temperatures were obtained up to T_i~12 keV and T_e~6 keV. The L-mode enhancement factor of ~1.7 was maximized up to τ_E/τ_E^L~1.7 against the Goldston L-mode scaling. The ion temperature of ~12 keV is a record value in hydrogen tokamak experiments; waveforms for a typical 12 keV discharge are shown in Fig. 3. Although the energy confinement is significantly degraded at lower I_p than ~0.5 MA, the discharges have not been disrupted with stronger pressure anisotropy up to $\beta_p^{dia}/\beta_p^{equ}$~1.5 due to perpendicular injection.

This regime with high q_{cyl} (up to ~13) was free from sawtoothing modulation of local transport in the core plasma. Similar to the supershots in TFTR, highly peaked profiles of $T_i(r)$ and $n_e(r)$ were observed, showing that their peaking parameters are strongly correlated up to $T_{i0}/\langle T_i\rangle$~4.2 and $n_{e0}/\langle n_e\rangle$~2.7 as shown in Fig. 4. Decoupling of energy balances for electrons and ions as T_i~2T_e was a characteristic feature in the core region, where the convection losses exceed the conduction losses. Peaking parameters of $T_e(r)$ are found to be mostly independent on q_{cyl}, indicating a large divergence from prediction of the q-dependent profile consistency assuming Spitzer resistivity and q(0)=1.

Nearly-isotropic high-β_p values around 3 ($\varepsilon\beta_p$~0.8) have been achieved with low collisionality (ν_e^*~0.2) and moderate Z_{eff} (~3), so that a conclusive investigation on neoclassical bootstrap current has been accomplished showing demonstration of a steady-state bootstrap-current discharge up to 80 % to the total plasma current under negligibly small beam currents. These discharges also reach the stability boundary for high-n ideal ballooning modes. As shown in Fig. 5, the poloidal beta of β_p^{dia}=3.2 was sustained in quasi-steady state for ~1 s. and the toroidal rotation velocity, V_ϕ, was also highly peaked up to ~1x10^5 m/s with high rotational shear. The ion and electron temperature profiles with T_{i0}~8 keV and T_{e0}~4 keV are shown in Fig. 6 for the same discharge as in Fig. 5. After t=6.1 s, as the values of W_{dia}, T_i and V_ϕ are decreased, substantial confinement degradation was observed to be clearly correlated with large continuous m=2 modes located at r/a~0.3 on soft X-rays.

In order to investigate whether the plasma configuration can result in the enhancement of the β_p limit, we have carried out small-volume inner-limiter experiments with R=2.8 m and a=0.69 m comparable with the divertor configuration. As a result, the attainable β_p value reached ~3 for 0.4 MA discharges, so that it is not plausible that a stabilization effect of magnetic shear with the divertor configuration on external kink modes directly leads to the result of obtaining higher β_p values in JT-60.

In conclusion, we have obtained and sustained "supershot" discharges by means of near-perpendicular NBI into hydrogen plasmas on JT-60. Although a variety of MHD activities give rise to significant confinement degradation, no

disruptive β_p limit has been observed up to β_p^{dia}~5. Nearly-isotropic β_p value reaches 3, leading to a demonstration of 80 % bootstrap current discharge. The hot-ion enhanced confinement regime carrying a large fraction of intrinsic bootstrap currents in JT-60 may have some impact on a steady-state operation scenario for a future tokamak reactor. More detailed discussions about the experiments will be presented in the following sections.

[1] J.D. Strachan et al., Phys. Rev. Letter 58, 1004(1987).
[2] K.M. McGuire et al., Plasma Phys. Controlled Fusion 26, 87(1984).
[3] The JET Team (presented by P.R. Thomas), in Proceeding of the Twelfth International Conference on Plasma Physics and Controlled Nuclear Fusion Research, 12-19 October 1988, Nice, France, paper IAEA-CN-50/A-4-4 (to be published).

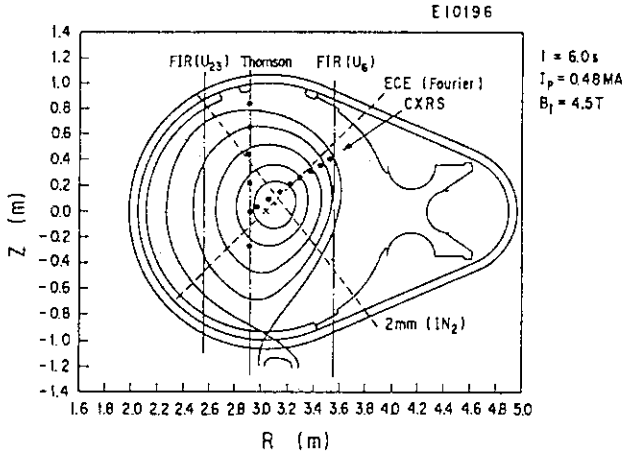

Fig. 1 Plasma configuration in high β_p experiments and the diagnostic sightlines.

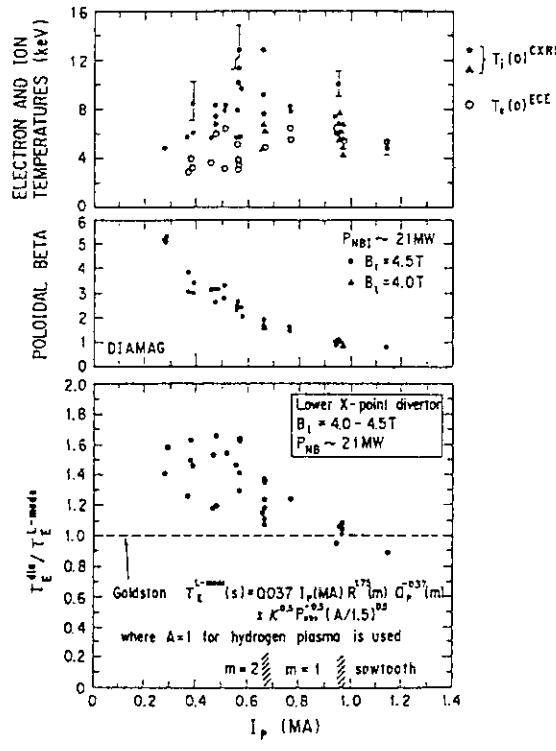

Fig. 2 Temperatures, β_p values and L-mode enhancement factors as a function of I_p in the I_p scan experiments.

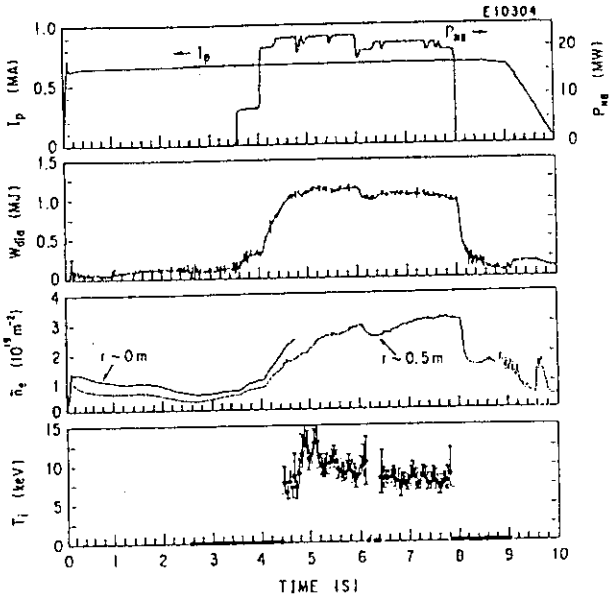

Fig. 3 Waveforms for a typical discharge with the highest ion temperature, ~12 keV.

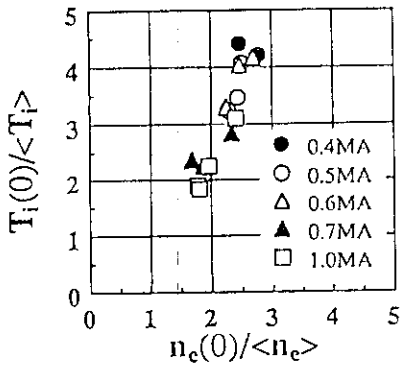

Fig. 4 Correlation of the peaking parameter between ion temperature and electron density profiles.

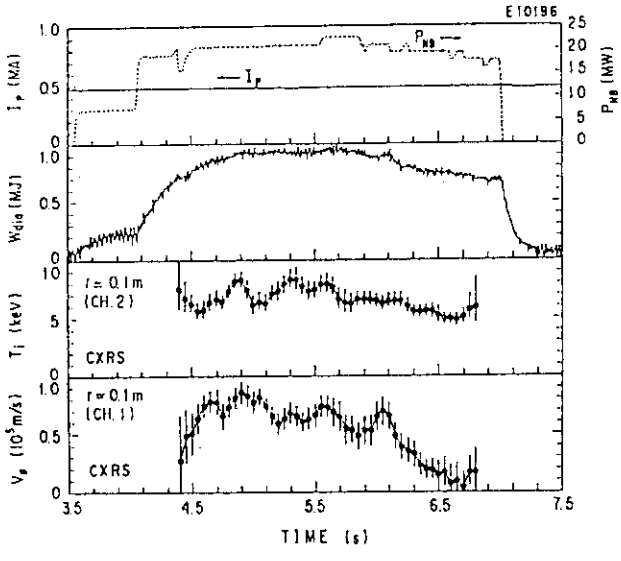

Fig. 5 Waveforms for a typical discharge with β_p^{dia}=3.2.

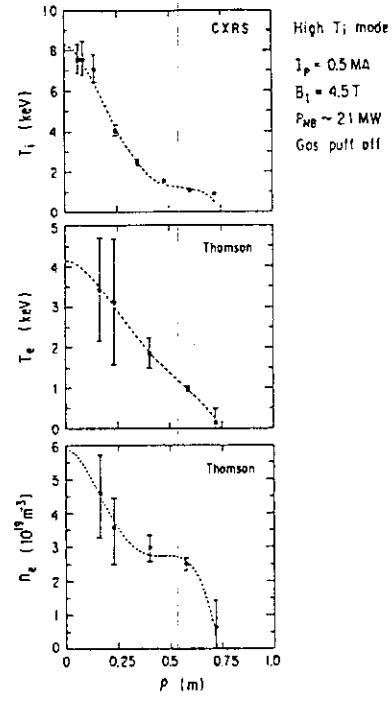

Fig. 6 Profiles of T_i, T_e and n_e at t=5.5 s for the discharge with β_p^{dia}=3.2 same as in Fig.6.1-5.

6.2 Energy confinement characteristics compared with L-mode scalings

O. Naito, S. Tsuji

Global energy confinement characteristics in high poloidal beta experiments are presented. The total energy contents are estimated from diamagnetic measurements described in Section 6.3 along with their validity. The enhancement in energy confinement depends on which scaling law is employed, therefore a definite conclusion could not be drawn whether a high β_p discharge has better confinement than usual L-mode or not. At least obtained data do not contradict the previous JT-60 L-mode scaling for plasma current as low as 0.5 MA.

Parameter ranges of the data base

The mean value of line average density increases with plasma current. Its dependence on I_p is, however, stronger for limiter discharges than for divertor discharges. In fact, for data set collected here, limited discharges have a dependence of density on plasma current as $n_e \propto I_p^{0.72}$ while diverted discharges have $n_e \propto I_p^{0.41}$. In most shots, the toroidal magnetic field has been fixed to 4.5 tesla and the plasma current is varied (I_p = 0.3–1.2 MA). Figure 1 shows a line average density as a function of safety factor. The density decreases monotonically with q_a due to a decrease in plasma current. For lower β_p case, limited discharges have about 50 % higher density than diverted discharges. Most of the divertor discharges are carried out in $n_e = (2–3) \times 10^{19}$ m^{-3}. The high β_p experiments are concentrated on high power discharges with 19.2±1.0 MW.

Comparison between Divertor and Limiter experiments

Figure 2 shows the global confinement time τ_E as a function of plasma current. For fixed current, τ_E for divertor discharges is about 20 % larger than that for limiter discharges. The ellipticities for divertor and limiter discharges are respectively 1.39±0.04 and 1.04±0.03. However the plasma volumes for both configurations have roughly the same value; V = 28.4±1.3 m^3. Accounting for its lower density, divertor discharge is expected to have higher electron/ion temperature than limiter discharge. This will be discussed in Sections 6.7 and 6.8.

Enhancement factor with different L-mode scalings

Since the data set consists of shots with low plasma currents that are not available in the previous L-mode data base, the global confinement enhancement factor is defined with respect to standard L-mode scaling laws. Figure 3 shows the experimental confinement time normalized by Goldston scaling [1], Shimomura-Odajima scaling [2] and a JT-60 L-mode scaling [3], as a function of plasma current. For Goldston scaling $\tau_E^{exp}/\tau_E^{scale}$ is around unity for $I_p \geq 0.8$ MA. Whereas for $I_p <$ 0.8 MA, $\tau_E^{exp}/\tau_E^{scale}$ increases with decreasing current. It has been found that the global confinement time in JT-60 L-mode discharge fits well to the Goldston scaling around I_p = 1 MA and has weaker I_p-dependence than that in high current cases. Thus the enhancement with respect to the Goldston scaling in low I_p regime could rather be regarded as a manifestation of weak I_p-dependence of JT-60 discharges. For Shimomura-Odajima and JT-60 L-mode scalings $\tau_E^{exp}/\tau_E^{scale}$ has constant values down to I_p = 0.5 MA, although the Shimomura-Odajima scaling predicts somewhat higher τ_E^{scale}. For even lower current, $\tau_E^{exp}/\tau_E^{scale}$ has lower values than those for $I_p \geq 0.5$ MA. The difference between divertor and limiter cases can be resolved into κ-dependence both in the case of power law and offset linear scalings. For instance, the Goldston scaling that has a κ-dependence in the form $\tau_E^{Goldston} \propto \kappa^{0.5}$ predicts 20 % better confinement for divertor discharges whose ellipticity is typically 1.4.

References

[1] GOLDSTON, R.J., Plasma Phys. Controll. Fusion **26** (1984) 87.

[2] SHIMOMURA, Y., ODAJIMA, K., Comments Plasma Phys. Controll. Fusion **10** (1987) 207.
ODAJIMA, K., SHIMOMURA, Y., Energy Confinement Scaling based on Offset Linear Characteristic, JAERI-M 88-068 (1988).

[3] NAITO, O., HOSOGANE, N., TSUJI, S., et al., Nucl. Fusion **30** (1990).

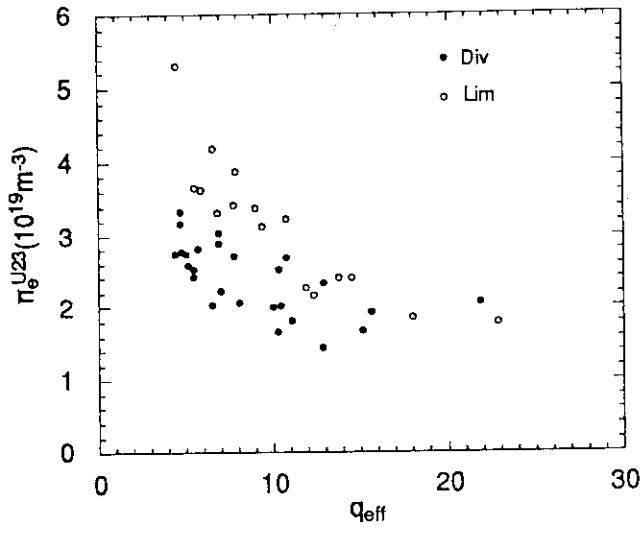

Fig. 1 Operation diagram of high poloidal beta experiments

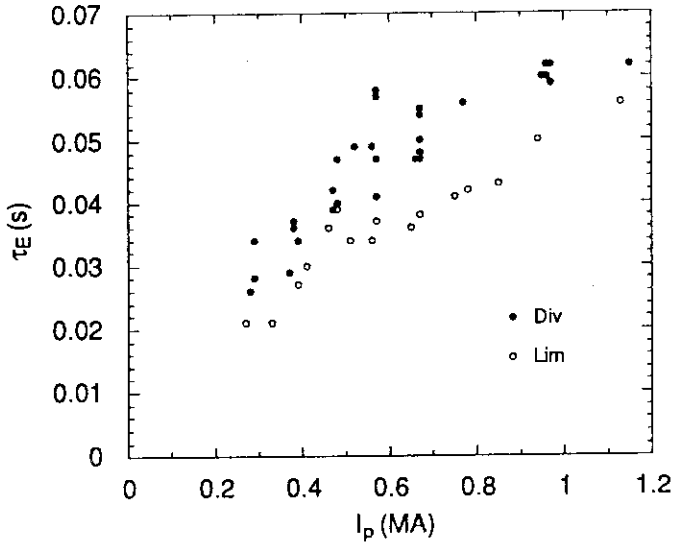

Fig. 2 Confinement time as a function of plasma current

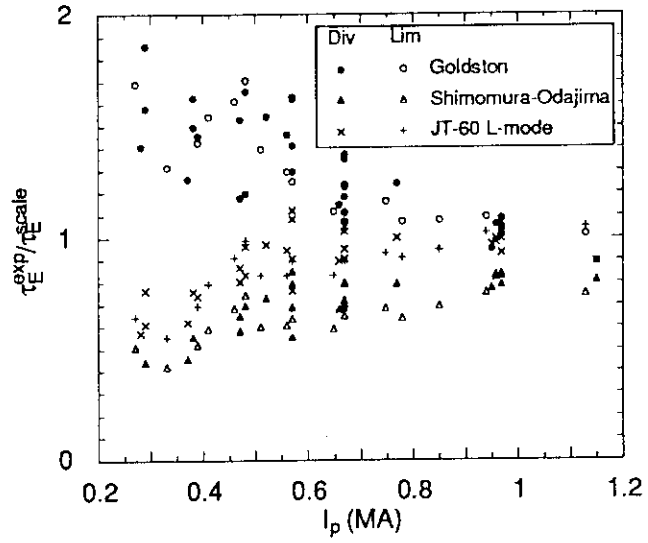

Fig. 3 Enhancement factor with respect to different scalings

6.3 Diamagnetic and MHD Equilibrium Analysis of β_p Values and Pressure Anisotropy

S. Tsuji, N. Hosogane, O. Naito, M. Kikuchi, S. Ishida

1. Introduction

The hot-ion and high-β_p regime has been established by means of nearly perpendicular beam injection on JT-60 [1]. It is important to evaluate poloidal beta values accurately to investigate confinement properties and to correlate with MHD activities [2] and bootstrap currents [3]. The β_p evaluation, however, is not so easy because of relatively low SN ratios of magnetic data due to low I_p operation and of plasma pressure anisotropy due to low n_e operation. This paper describes diamagnetic measurements and MHD equilibrium analysis on JT-60. The plasma pressure anisotropy will be discussed from the data analysis.

2. Diamagnetic Measurement

Figure 1 illustrates the arrangement for the diamagnetic measurement on JT-60. A diamagnetic loop is located inside the vacuum vessel. A Rogowski coil was wound around a toroidal coil case to measure an effective coil current which includes eddy currents flowing along the case. Differential integration is made by an analogue circuit. Compensation of the dominant eddy current with the longest time constant flowing on the vacuum vessel is implemented in the circuit [4]. Error fluxes due to poloidal coil currents are numerically subtracted basing on the measured fluxes from individual coil discharges.

Since the diamagnetic loop plane makes an angle of about 5° with the symmetric plane which contains the torus axis as shown in Fig. 1 (b), the loop picks up horizontal fluxes, which results in coupling to the plasma current. Thus the diamagnetic measurement is very sensitive to the plasma vertical shift. The plasma stored energy evaluated from diamagnetics must be corrected with the plasma current and the vertical position of the current centroid by rates around 40 kJ/MA/cm, which weakly depend on plasma horizontal shifts. The correction coefficients were determined experimentally by sweeping the plasma column vertically or horizontally during low density discharges and by calculating those plasma stored energies not to be greatly deviate from an ohmic scaling on JT-60.

3. MHD Equilibrium Analysis

A MHD equilibrium code on JT-60 [5] is organized by two steps: a fast boundary identification (FBI) code which approximates the plasma current as six filaments [6] and a full equilibrium identification (FEI) code based on the fast Buneman solver. The results from FBI are fed into FEI to save the computational time. Three points at the plasma edge (top, bottom and inner points for the lower X-point configuration) are used as the fixed boundary for the solution to the Grad-Shafranov equation. The plasma cross-sections calculated by FBI are sometimes misleadingly distorted in the cases of high β_p discharges. Thus the locations and measuring angles of pick-up probes are re-evaluated from the designed values so that the calculated shapes from FBI and FEI agree well.

The β_p value is calculated in FBI by the following equations [7,8];

$$\beta_p^{\perp} = s_1 + \mu \tag{1}$$

$$(\beta_p^{\parallel} + \beta_p^{\perp}) / 2 + \ell_i / 2 = s_1 / 2 + s_2 \tag{2}$$

$$s_1 = \pi / (V \bar{B}_p^2) \oint R B_p^2 (R e_R + Z e_Z - R_p e_R) \cdot \mathbf{n} \, d\ell \quad (3)$$

$$s_2 = \pi R_p / (V \bar{B}_p^2) \oint B_p^2 \, R e_R \cdot \mathbf{n} \, d\ell \quad (4)$$

$$\mu = 1 / (V \bar{B}_p^2) \int (B_{tv}^2 - B_t^2) \, dV \approx 4 \pi R_p B_{t0} \phi^{dia} / (V \bar{B}_p^2) \quad (5)$$

$$\bar{B}_p = \oint B_p \, d\ell / \oint d\ell = \mu_0 I_p / \oint d\ell \quad (6)$$

where the line integral is carried out along the plasma surface, V and ϕ^{dia} are the plasma volume and the diamagnetic flux, respectively, and $\mathbf{e}_R$, $\mathbf{e}_Z$ and $\mathbf{n}$ are unit vectors. The mean radius R_T is approximated to be the plasma major radius R_p. For the average poloidal magnetic field energy we use $\bar{B}_p^2$ instead of the usual definition of

$$< B_p^2 > = \oint B_p \, d\ell \; / \; \oint 1 / B_p \, d\ell \quad (7)$$

since $1/B_p$ diverges at the separatrix in the case of divertor configurations.

As Eqs.(1) and (2) show, we get the perpendicular and average components of β_p from the diamagnetic measurement and equilibrium analysis, respectively. The internal inductance ℓ_i on the right-hand side of Eq. (2) can be separated for elongated plasmas by least-squares minimization techniques to reproduce magnetic data measured outside the plasma [9,10].

The plasma current density profile is assumed as

$$j (\psi) = j_0 \{ \beta_p^* R / R_p + (1 - \beta_p^*) R_p / R \} f (\tilde{\psi}) \quad (8)$$

$$f (\tilde{\psi}) = 1 + \alpha \tilde{\psi} + \gamma \tilde{\psi}^2 - (1 + \alpha + \gamma) \tilde{\psi}^3 \quad (9)$$

$$\tilde{\psi} = (\psi - \psi_{axis}) / (\psi_{sur} - \psi_{axis}) \quad (10)$$

The functional form of $f (\tilde{\psi})$ adopted by the Doublet III group [11] is well modelled in JT-60, too. Two of the unknown parameters, j_0 and α, are determined by specifying I_p and q_{axis}. The rest two parameters, β_p^* and γ, and resulting $\beta_p^{eq} = (\beta_p^{\parallel} + \beta_p^{\perp}) / 2$ and ℓ_i are scanned to minimize deviations of the calculated magnetic fields at 12 magnetic pick-up probes on JT-60;

$$\sigma = \sigma_b + \sigma_v = \Sigma \, w_{pi} (B_{pi}^{cal} - B_{pi}^{exp})^2 + w_v (I_v^{cal} - I_v^{exp})^2 \quad (11)$$

where w_{pi} and w_v are weights. The weights for the magnetic fields normal to the limiter surfaces are assumed to be one-order heavier than those for tangential ones. The second term is added since the vertical coil current is one of three unknown external coil currents to solve the Grad-Shafranov equation as a fixed boundary problem. The other unknown currents are chosen to be the primary ohmic current and a virtual coil current which produces uniformly horizontal magnetic field.

An example of the minimization for a time slice of a high β_p discharge is shown in Fig. 2. The minimized σ in terms of γ and resulting ℓ_i are plotted as a function of β_p^{eq} on the assumption of $q_0 = 1.0$. The overall minimum is achieved around $\beta_p^{eq} = 2.72$. The minimum is mainly determined by the σ_v term with the assumed weights. The variations in σ_b are relatively small presumably because the actual locations and angles of the pick-up probes are not well specified. Below $\beta_p^{eq} = 2.6$, the minimized $\beta_p^{eq} + \ell_i / 2$ disagrees with that obtained from Eq. (2) by FBI.

Around the overall minimum, β_p^{eq} and ℓ_i are well separated in the lower X-point configurations of JT-60 with $\kappa \approx 1.3$. In the cases of limiter configurations with nearly circular cross-sections, β_p^{eq} and ℓ_i can not be separated experimentally although it was possible for numerical test data owing to toroidal effects [5].

4. Discussion

The true poloidal beta is expressed as $\beta_p = (\beta_p^{//} + 2 \beta_p^{\perp}) / 3 = (\beta_p^{dia} + 2 \beta_p^{eq}) / 3$ taking into account the pressure anisotropy [8]. Figure 3(a) shows the resulted β_p values of high β_p discharges as a function of the plasma current. The β_p values are calculated to exceed 3 when $I_p < 0.4$ MA. The data point of $\beta_p \approx 5$, however, is questionable because of relatively large errors in magnetics. From β_p^{dia} and β_p^{eq}, the plasma pressure anisotropy is evaluated by a measure defined as $(\beta_p^{\perp} - \beta_p^{//}) / (\beta_p^{\perp} + \beta_p^{//}) = (\beta_p^{dia} - \beta_p^{eq}) / \beta_p^{eq}$, parameter dependences of which are plotted in Figs. 3 (b) - (d). The plasma pressure becomes anisotropic in plasmas of low I_p and low n_e operations. The high β_p values were achieved in highly anisotropic plasmas, and hence beam dominated plasmas. Accordingly energy confinement analyses based only on diamagnetics such as Ref. [12] should be made with reservations.

When the information on beam anisotropy is provided from calculation with an orbit following Monte Carlo code, we can evaluate thermal and beam components of β_p. In the case of the data of Fig.1, $\beta_p^{dia} = 3.14$, $\beta_p^{eq} = 2.72$ and calculated $f_b^{//} = 3\beta_{pb}^{//} / (2 \beta_{pb}^{\perp} + \beta_{pb}^{//}) = 0.64$. From simple mathematics, we get $\beta_{pb}^{//} = 1.10$, $\beta_{pb}^{\perp} = 1.85$, $\beta_p^{b} = 1.57$ and $\beta_p^{th} = 1.29$. If we assume $q_0 = 2.0$, which may be a better approximation than $q_0 = 1.0$ from MHD activities, the results differ slightly as $\beta_p^{eq} = 2.77$, $f_b^{//} = 0.66$, $\beta_{pb}^{//} = 1.05$, $\beta_{pb}^{\perp} = 1.85$, $\beta_p^{b} = 1.58$ and $\beta_p^{th} = 1.31$. The present FEI code can not resolve q_0 by less than a factor of two [5]. The use of the toroidal flux value measured by the diamagnetic loop as an additional constraint to the MHD equilibrium problem was reported to provide a more precise evaluation of q_0 [13]. Improvements in the code along this line are left for future work.

5. Summary

The poloidal beta values of high β_p discharges are evaluated from the diamagnetic measurement and MHD equilibrium analysis on JT-60. β_p^{eq} and ℓ_i are well separated with $\kappa \approx 1.3$. The β_p values are calculated to exceed 3 when $I_p < 0.4$ MA. The high β_p plasmas achieved in JT-60 are highly anisotropic.

References

[1] S. Ishida, et al., this report, Section 6.1.
[2] S. Ishida, et al., this report, Sections 6.4 - 6.6.
[3] M. Kikuchi, et al., to be published in Nucl. Fusion and this report, Section 7.
[4] S. Tsuji, et al., JAERI-M 88-063, Section 10.1. (in Japanese)
[5] S. Tsuji, et al., JAERI-M 86-006. (in Japanese)
[6] D.W. Swain and G.H. Neilson, Nucl. Fusion **22** (1982) 1015.
[7] V.D. Shafranov, Plasma Phys. **13** (1971) 757.
[8] W.A. Cooper and A.J. Wootton, Plasma Phys. **24** (1982) 1183.
[9] J.L. Luxon and B.B. Brown, Nucl. Fusion **22** (1982) 1015.
[10] L.L. Lao, et al., Nucl. Fusion **25** (1985) 1421.
[11] L.L. Lao, et al., Nucl. Fusion **25** (1985) 1611.
[12] O. Naito and S. Tsuji, this report, Section 6.2.
[13] E. Lazzaro and P. Mantica, Plasma Phys. Controll. Fusion **30** (1988) 1735.

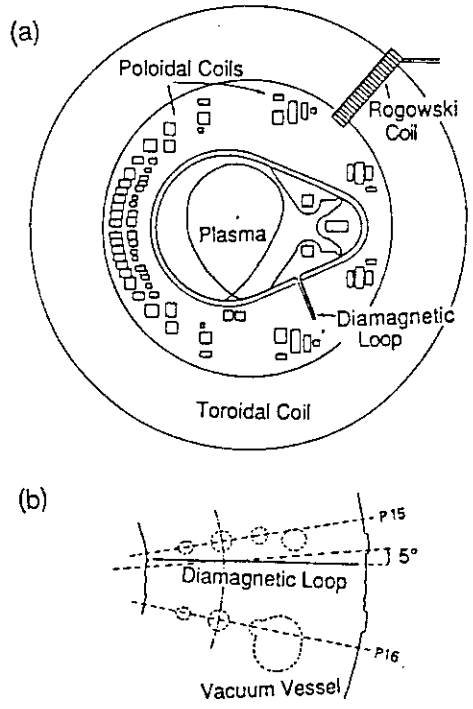

Fig. 1 Arrangement for the diamagnetic measurement on JT-60. A cross-sectional view (a) and a plane view (b) of the vessel.

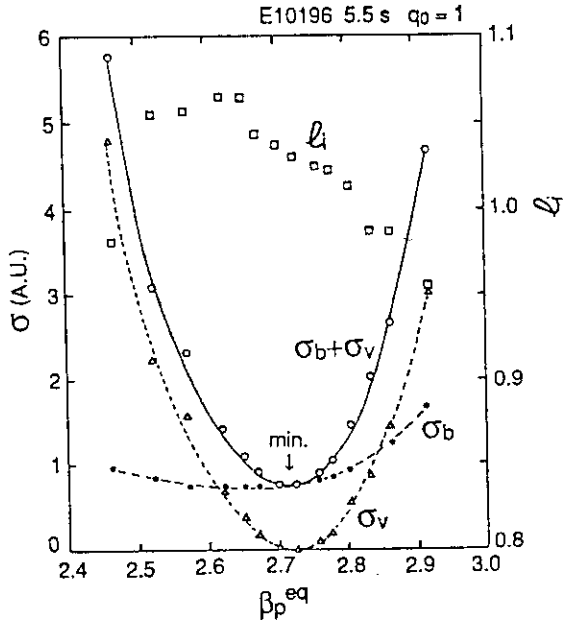

Fig. 2 Poloidal β dependences of deviations of calculated magnetic fields from measured values σ_b and those for the vertical coil current σ_v with the minimized internal inductance ℓ_i.

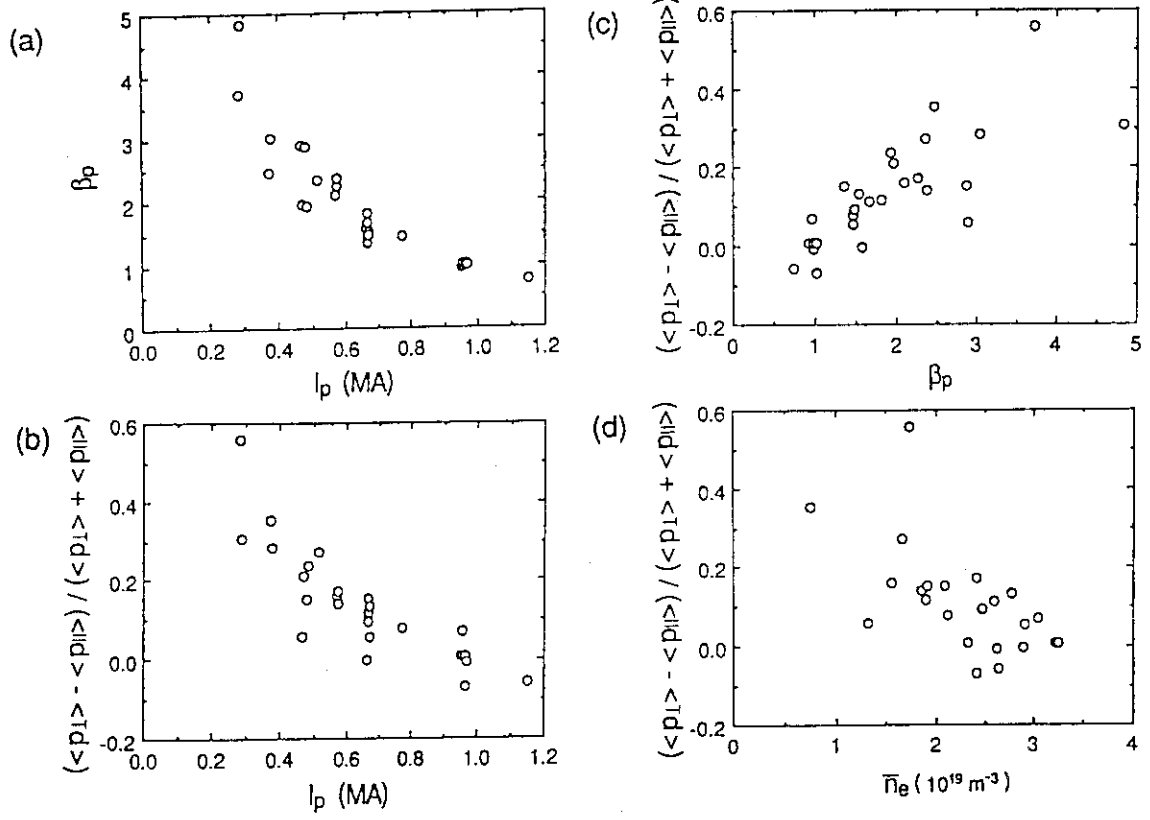

Fig. 3 Plasma current dependences of $\beta_p = (\beta_p^{\parallel} + 2\,\beta_p^{\perp}) / 3$ (a) and plasma pressure anisotropy $(\beta_p^{dia} - \beta_p^{eq}) / \beta_p^{eq}$ (b). The plasma pressure anisotropy is plotted as functions of β_p (c) and of electron density (d).

6.4 MHD Activity and β_p Limits

S. Ishida, T. Ozeki, Y. Koide amd H. Shirai

In this paper, the observations of MHD activities in high-β_p experiments with the hot-ion enhanced confinement regime in JT-60 are presented.

(1) Classification of MHD activities

In the high-β_p experiments on JT-60, coherent MHD activities substantially deteriorate the confinement properties of the plasma. We have carried out detailed scan-experiments over a wide range of parameter spaces with respect to I_p, P_{NB} and B_t for the fixed configurations of divertor and limiter. A variety of MHD activities in these experiments are characterized by two categories; 1) continuous low-m modes such as m=1, m=2 and m=3 modes, which give rise to gradual enhancement of transport; 2) occasional (not periodical) partial-collapses such as β_p collapses and mini-partial collapses, which cause the flattening of local pressure around a rational surface of the plasma leading to a rapid decrease of the stored energy. Although the toroidal mode number, n, is not directly measured, the n is inferred to be unity from the observations such as the location of islands and the mode frequency. It should be noted that no sawtooth oscillations have been observed in the high-β_p high-T_i regime in JT-60.

(2) Transition of MHD-mode features with I_p scan:

A clear correlation has been observed between the confinement properties and the MHD activities according to the plasma current (see Fig. 2 in [1]); sawteeth in $I_p \geq 1.0$ MA, continuous m=1 modes in $0.7 \leq I_p(MA) \leq 1.0$, continuous m=2 modes (sometimes, m=3 modes) in $I_p(MA) \leq 0.7$. As sawtooth oscillations were suppressed, the profiles of T_i and n_e become peaked. The confinement properties were improved with decreasing the current up to $I_p \sim 0.5$ MA. However, in lower current range than ~0.5 MA, the confinement tends to be significantly deteriorated due to the m=2 modes and additional mini partial-collapses, while the ion temperature and the density remains a peaked profile.

(3) Overall MHD observations for I_p, P_{NB} and B_t scan experiments

Figure 1 shows the characteristic MHD observations such as sawteeth, m=1 and m=2 modes together with β_p^{dia} values and the threshold q_{eff} value bounding the regions of sawtooth suppression. fishbone-like m=1 mode bursts are in some occasions clearly observed in the sawtoothing discharges at B_t=2.5 T. In high-β_p discharges ($\beta_p > 2$), continuous m=2/n=1 modes were most often observed probably because of calculated q(0) above ~1.5 due to large bootstrap current fraction. Soft X-ray measurements manifest that the enhanced confinement zone was limited within the q=2 surface with m=2 islands, while the energy confinement is most enhanced without coherent MHD activity. Using tomografic reconstruction technique from soft X-ray emissions, it is shown that the m=2 islands with a full width of ~10 cm are located at r~25 cm near the q=2 surface, consistent with equilibrium calculation including bootstrap currents.

(4) Ideal high-n ballooning modes

The BETA code analysis shows that the discharges near $\beta_p \sim 3$ reach the stability boundary of ideal high-n ballooning modes, based on the measured pressure profile and

the calculated q profile indicating the effect of bootstrap currents[2]. However, no signatures of ballooning modes have been found yet. As low-m modes and β_p collapses are localized around the rational surfaces such as q=2 and q=3, the observations rather suggest that the pressure driven kink/tearing modes with n=1 are regarded as the most likely candidates of theoretical approachs.

(5) Examination of disruptive β_p limit

Although the discharges in JT-60 are similar to the TFTR supreshots, a remarkable difference is the fact that no disruptive β_p limit has been observed up to β_p^{dia}~5 in JT-60 in contrast with the clear limit at β_p^{dia}~2 in TFTR[3]. In order to compare the results of JT-60 with those of TFTR in view of disruptive β_p limit, we plot the normalized beta as a function of the cylindrical q in Fig. 2, the normalized beta is defined as the toroidal beta values (β_t^{dia}) normalized by $I_p/(\mu_0 a B_t)$. As shown in this figure, the discharges of JT-60 have explored a new region without disruption substantially exceeding the boundary of $\varepsilon\beta_p$~0.7 limiting the TFTR operation.

(6) β_p collapse phenomena

Although the spontaneous increase of energy confinement time was sometimes observed, this enhanced confinement was limited by the β_p collapse as the discharge exceeds β_p~3. Figure 3 shows the waveforms for two discharges with and without β_p collapses; it is evident that the attainable β_p value is obviously limited up to ~3 by the repetitive β_p collapses. After the reached β_p value is maintained at β_p^{dia}=3.2 for ~1 s up to t~6.1 s without β_p collapse, the confinement is deteriorated due to the m=2 activity. By comparing these discharges, it should be noticed that both β_p collapse and m=2 activity cause a confinement deterioration with the same order of magnitude, leading to ~20 % decrease of the stored energy.

Soft X-ray waveforms: The detailed MHD features for the β_p collapse has been revealed from soft X-ray measurements with 30 channels and a fast sampling of 80 μs, designating the process of β_p collapse as shown in Fig. 4. As shown in this figure, mini partial collapses with the inversion radius near q=2 surface precede the β_p collapse.

Soft X-ray, T_i and V_ϕ profiles: The soft X-ray profiles just before and after a β_p collapse is shown in Fig. 5, noted that there is a pedestal at r~25 cm near q=2 surface just after the collapse. In general, the β_p collapse can be described as a large-amplitude partial collapse localized around q=2 surface without precursor and successor oscillations, which falls within ~100 μs. The observations suggest that the β_p collapse appears to be caused by pressure-driven modes due to increased pressure gradient at q=2 surface. Figure 6 shows T_i and V_ϕ (toroidal rotation velocity) profiles at t=7.3 s just before β_p collapse. It is found that the central plasma toroidally rotates up to ~1.0×10^5 m/s with high rotational shear, though the beam momentum input remains stationary. From neoclassical theory. it is inferred that a strong negative radial electric field is induced with a large poloidal rotation in the vicinity of the large radial gradient of $T_i(r)$.

Temporal evolution of soft X-ray profile: We have investigated the process leading to the β_p collapse in detail. Temporal evolution of the soft X-ray profile is shown in Fig. 7, where the process is separated into two characteristic phases as follows; 1) 6.1≤t[s]≤6.6: m=2 modes are unstable. The profiles indicate a pedestal due to m=2 islands; 2) 6.7≤t[s]≤7.3:

m=2 modes are stabilized and m=3 modes are destabilized, when the peaking of profile is extended up to the location of m=3 modes. Before the β_p collapse occurs at t=6.34 s, the m=3 modes come to be stabilized, while the pressure gradient at q=2 surface become so high that the β_p collapse could occur.

Causality in W_{dia}, $T_i(r)$, $V_\phi(r)$ and MHD modes: As mentioned above, the mechanism with improvement of energy confinement appears to be associated with location of magnetic islands, toroidal rotation profile and the resulting radial electric field. Figure 8 shows a causality of these phenomena such as improved confinement, peaking of profiles and MHD modes as follows; The increase of stored energy is initiated by the transition of MHD instability from m=2 modes to m=3 modes leading to the expansion of enhanced confinement boundary from q=2 to q=3 surface. Simultaneously, the toroidal rotation velocity gradually increases up to ~1×10^5 m/s in the co-direction inside r~a/3 accompanied with a negative radial electric field of ~400 V/cm inferred from equations of neoclassical relation and force balance. Following the increased toroidal rotation, the central ion temperature begins to increase, which gives rise to the increase of stored energy.

REFERENCES:

[1] S. Ishida et al. in Section 6.1 of this review.

[2] T. Ozeki et al. in Section 6.5 of this review.

[3] K.M. McGuire et al., Plasma Phys. Controlled Fusion 26, 87(1984).

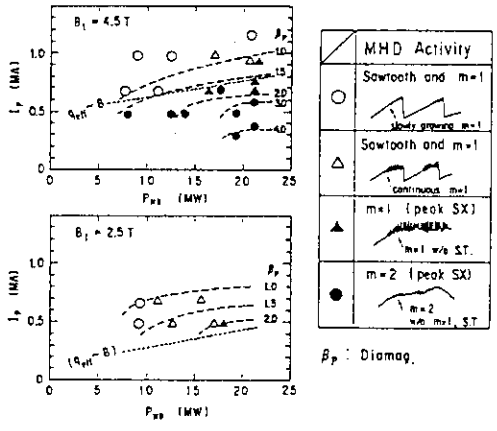

Fig. 1

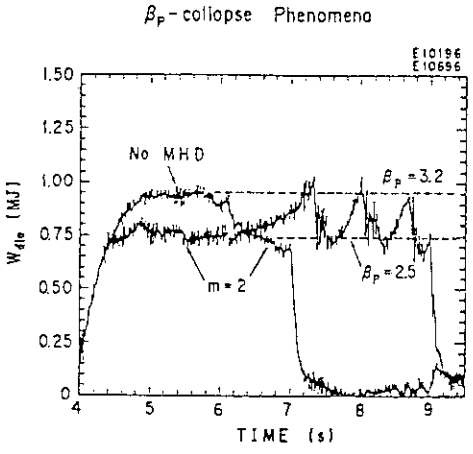

Fig. 3

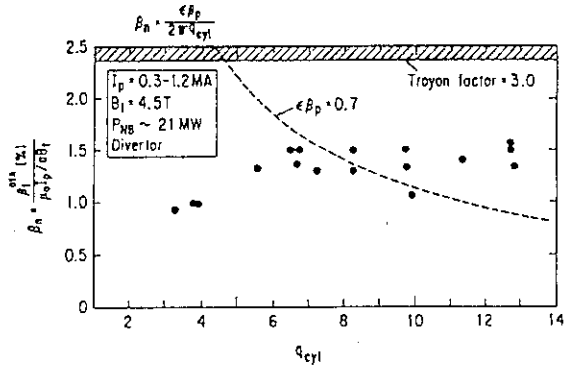

Fig. 2

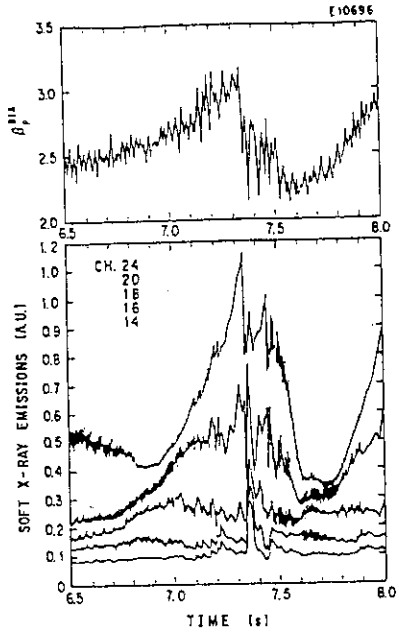

Fig. 4

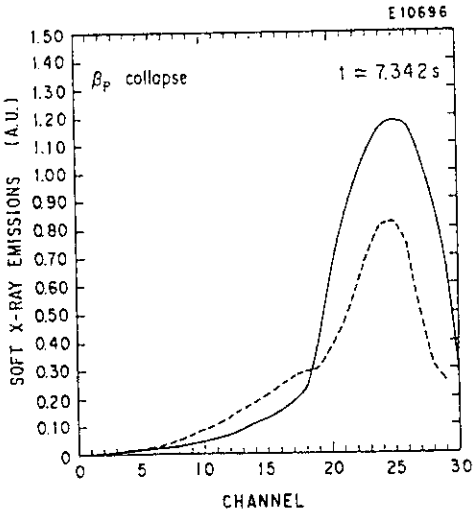

Fig. 5

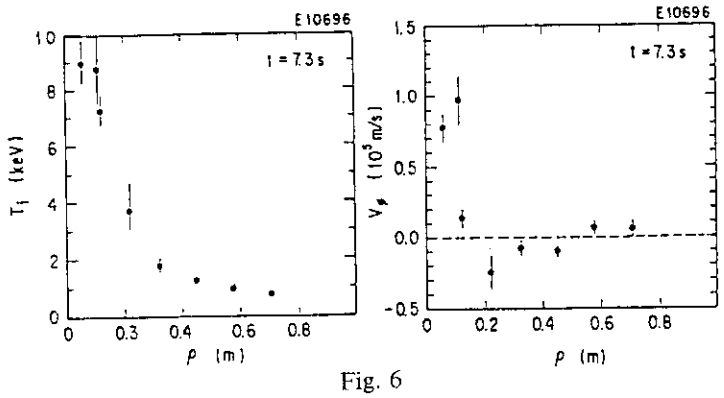

Fig. 6

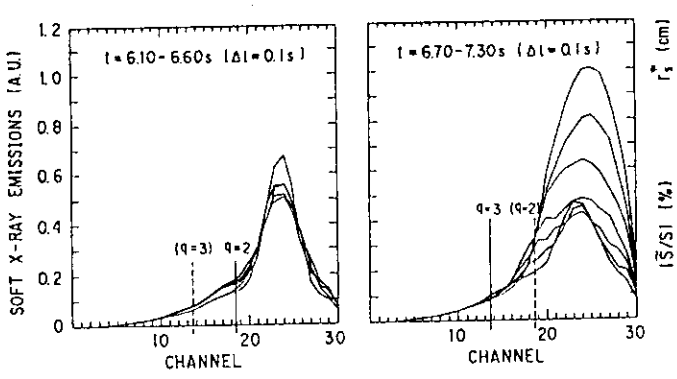

Fig. 7

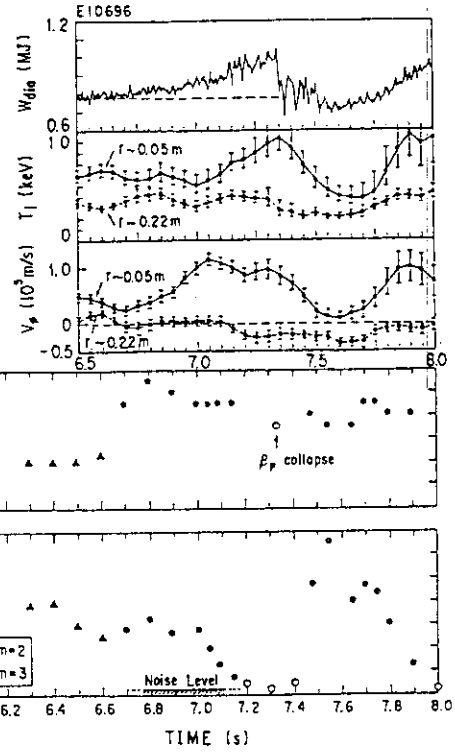

Fig. 8

6.5 IDEAL BALLOONING AND KINK LIMITS RELATED TO BETA COLLAPSE

T. Ozeki, M. Azumi, S. Ishida, Y. Koide, S. Tokuda and T. Tsunematsu

1. INTRODUCTION

High beta poloidal plasmas provide us the interesting features, which are the enhanced confinement and the sustain in the plasma current by the bootstrap current [1,2]. However, in high β plasmas, beta limit becomes a serious problem. The limit of beta was theoretically explained by the ideal infinite n ballooning and low n kink modes. (where n is a toroidal mode number) [3]. In this report, therefore, we investigate the ballooning and kink modes stabilities of high β_p plasmas in JT-60 related to beta collapse, and consider the effect of the hollow current profile by the bootstrap current.

2. FEATURE OF HIGH β_p PLASMA IN JT-60

The high beta poloidal plasmas were produced by the low plasma current (0.5MA< I_p <1.0MA) with high toroidal field (4.5T) so that the safety factor is high (q_a >6). In high poloidal beta regime (β_p=2-3), the strongly peaked profile of the ion temperature were obtained. Figure 1 shows that the profile of ion temperature, electron temperature and electron density. The plasma current is dominated by the bootstrap current, so that the current is broad or hollow. These current profiles are seems to be not preferable against low n kink modes because of the low shear. As the poloidal beta increase over 3.0, beta collapse phenomena were observed. By this collapse, the stored energy rapidly 30% decrease with a fast time scale ($\geq 100\mu s$). Although no precursor oscillation are observed just before the β_p collapse, m=2 mode activity is seems to be correlated with the collapse [1]. From this phenomena, we summarize the characteristics of the high β_p plasmas in JT-60, as follows; 1) the centrally peaked pressure profile exists inside of the q=2 surface, which is estimated by the SX inversion radius, 2) the q-profile is seems to be broad or hollow due to the bootstrap current, 3) the safety factor is high.

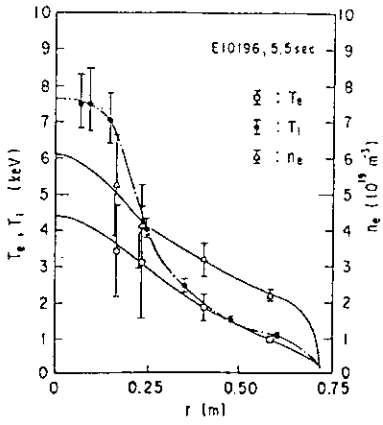

Fig. 1 The n_e, T_e from the thomson scattering and the T_i from CXR.

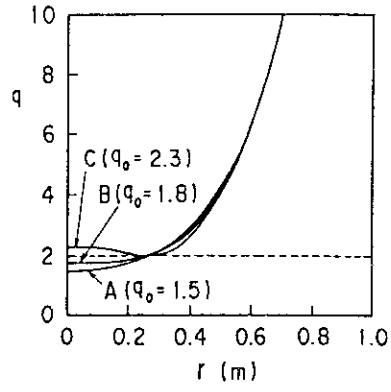

Fig. 2 q-profiles for three types with the fixed q_{eff}. Case C is a hollow profile.

3. RECONSTRUCTION OF EQUILIBRIUM

The MHD equilibria used in the following stability calculations are reconstructed by solving the following Grad-Shafranov equation iteratively using all characteristics described previously.

$$\Delta^*\psi = \mu_0 R J_\varphi, \tag{1}$$

$$J_\varphi = -R\frac{dP}{d\psi} - \frac{1}{\mu_0 R}F\frac{dF}{d\psi}, \tag{2}$$

where ψ is the poloidal flux function and J_φ is a toroidal current density. The two free functions, i.e., the plasma pressure $dP/d\psi$ and the toroidal field function $F(\psi)$, are obtained by the kinetic data and the surface averaged parallel current $< J_\parallel >$ ($=< J_\parallel \cdot B > / < B >$), respectively.

The pressure profile is determined by the n_e, T_e data from Thomson scattering measurements and the T_i data from CXR, as shown in Fig. 1. The ion density profile is assumed to equal to the electron density profile, and the total pressure is adjusted by the stored energy from a diamagnetic measurement. In the ERATO-J code analysis, the sufficiently smoothing pressure profile is required because of the numerical accuracy. Thus, in stead of the experimental data, the pressure profile is chosen to have the form

$$P \propto exp\{-(\frac{\tilde{\psi}}{\delta})^\nu\} + \kappa(1-\tilde{\psi}), \tag{3}$$

which provides a fair description of the pressure profile in the high β_p plasma of JT-60. In this calculation, we use ν of 1.02, δ of 0.15 and κ of 0.4 for the pressure profile of E10196. The surface averaged parallel current is assumed as a following function in this study,

$$< J_\parallel \cdot B > \propto \{(1-\tilde{\psi}^{\alpha_1})^{\alpha_2}\}\{1+\alpha_3 exp(-\frac{\psi}{\alpha_4})^2\}. \tag{4}$$

Parameters, α_1,..,α_4 and σ, are defined from the $q=1$ surface and the central q value, where $\tilde{\psi}$ is a normalized poloidal flux defined as $\tilde{\psi} = (\psi - \psi_{axi})/(\psi_{bun} - \psi_{axi})$. ψ_{axi} and ψ_{bun} are the poloidal flux at the plasma axis and the boundary, respectively. Because the center q is not measured, we have scanned the profiles for three type, as shown in Fig.2, where the q=2 surface is defined by the observed inversion radius and the surface q are the same value.

4. BALLOONING AND KINK STABILITY ANALYSIS

Ballooning stability analysis was carried out by solving the ordinary infinite n ballooning equation [4]. The flux function shape and the pressure and current profiles, which have been reconstructed by the equilibrium code, are used for stability analysis. The marginal pressure gradient dP/dr_m is determined on each flux surface by demanding that the growth rate be zero. Figure 3 shows the measured pressure gradient and the marginal value against ideal ballooning mode for the three type q-profiles. The measured pressure gradient near the plasma center are close to the marginal value for the case A,B. For the hollow q-profile cases (the C case), the global shear is smaller

than the case A profile, so that the marginal pressure gradient is expected to be small near the plasma center. However, the negative local shear is produced near the plasma center, as shown in Fig.4, and the marginal value is rather higher than the high shear case (case A). This result shows that the hollow current profile, produced by the large bootstrap current, has no bad effect on the ideal ballooning mode stability.

Next, the MHD stability against the low n ideal kink modes is computed using the ERATO-J code [5], which solves the linearized ideal MHD equations in variational form using a finite hybrid element approach. Because the low m MHD activities were observed in the experiments, first, we consider the n=1 internal mode and the fixed boundary plasma. We choose the pressure profile of the value of E10196, which is the typical high beta discharge. Beta-scan was carried out by fixing this pressure profile function. Figure 5 shows the squared growth rate of the n=1 kink mode against the poloidal beta for three q-profiles in Fig. 2. The plasma with the hollow current profile (case C) is most unstable than that of other profiles. The dominant mode of the unstable plasma in β_p of 5.0 are m/n=2/1 for three q-profiles, as shown in Fig. 6, which is mixed by the higher m modes due to the pressure driven. However, the β_p value (~3.2) in which the beta collapse were observed is lower the beta limit of the m/n=2/1 internal kink mode. We need the further analysis of the stability window of low n mode.

5. DISCUSSION

The ideal ballooning and kink mode stabilities are investigated. The hollow current profile, produced by the large bootstrap current, provides us the possibility of the access to the second stability regime of the infinite n ballooning mode near the plasma center, because the low or negative global shear and the high q_0 produce the negative local shear. However, the hollow current is not preferable for the low n-kink mode than the normal q-profile. The observed beta collapse is lower than the beta limit of the n=1 mode. Therefore, we must consider the following problem; 1) The stability window against q_0 fixing the q-profile function, 2) The internal inductance in this calculation (1.2-1.5) is higher than the experimentally observed internal inductance (0.9), 3) The stability window of the medium n mode (n≥2), 4) The effect of the resistive modes, i.e., the resistive ballooning mode and the tearing mode. Also, we used the up-down symmetry code, so that this code is not enough accuracy to interpret the single-null divertor discharges in JT-60. Therefore, the further investigations are necessary.

REFERENCES

[1] ISHIDA,S., et al., (in this paper, section 6.1,6.4).

[2] KIKUCHI,M., et al., to be published Nucl. Fusion (1990).

[3] TROYON,F., et al., Plasma Physics and Controlled Fusion 26 No.1A (1984) 209.

[4] CONNOR,J.W., HASTIE,R.J., TAYLOR,J.B. Phys. Rev. Lett. 40 (1978) 396.

[5] TOKUDA, S., TSUNEMATSU, T., AZUMI, M., TAKIZUKA, T., NARAOKA, K., TAKEDA, T., MHD Stability Analysis by Revised Version of ERATO-J, Rep. JAERI-M 9899, Japan Atomic Energy Research Institute, Ibaraki (1982).

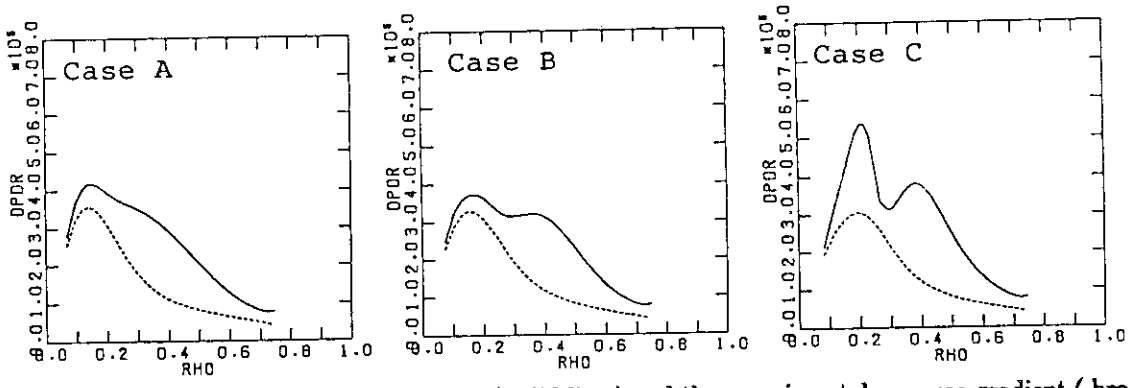

Fig. 3 Marginal ballooning pressure gradient (solid line) and the experimental pressure gradient (broken line) for a minor radius r(m).

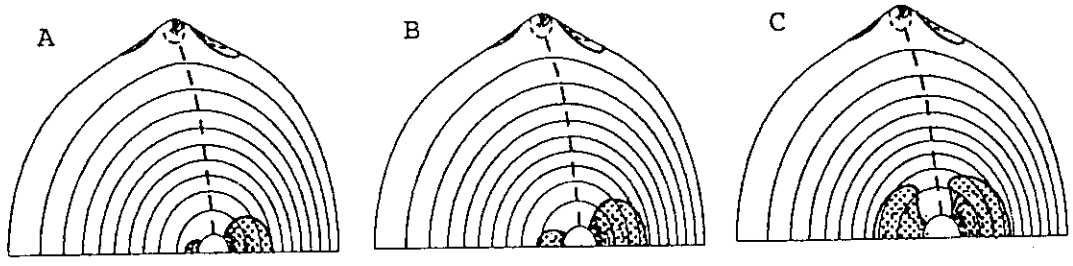

Fig. 4 Contour of local shear (shaded region)

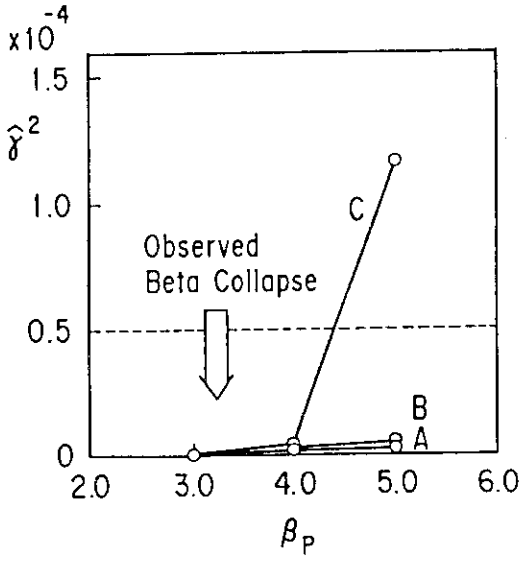

Fig. 5 The squared growth rate of n=1 internal kink as a function of β_p.

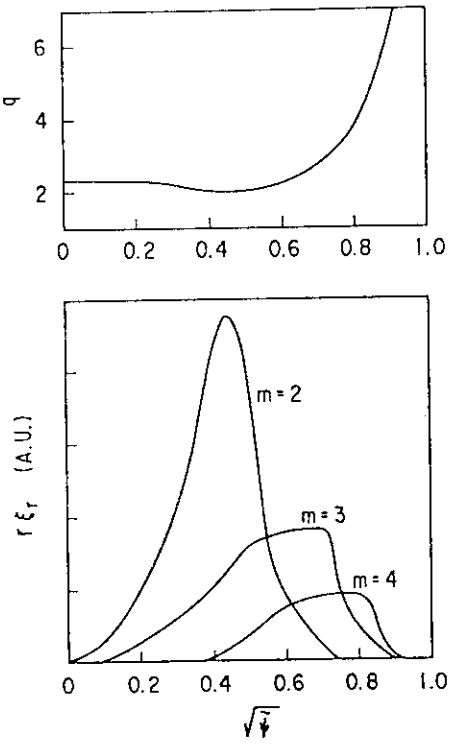

Fig. 6 Eigenfunction of m=2-4 for the n=1 unstable plasma of β_p=5.0 in the case C.

6.6 MHD Mode Analysis by Soft X-Ray Signals

Hiroshi SHIRAI, Shinichi ISHIDA, Keisuke NAGASHIMA
Masafumi AZUMI

Abstract

The profile of the line integrated soft X-ray intensity emitted from plasmas which have magnetic island structure is calculated. The profile of soft X-ray intensity, poloidal mode number, rational surface, island width are given in the calculation. The most outer phase inversion position of the soft X-ray intensity exists near the rational surface regardless of poloidal mode number, magnetic island width and the profile of soft X-ray intensity. The number of phase inversion in the plasma depends on the profile of soft X-ray intensity outside the magnetic island.

Soft X-ray signal detected by 32 channels of bolometer array installed in JT-60 gives us useful information about MHD mode structure inside the plasma. Because we get the line integrated values of soft X-ray signal, Abel conversion method is adopted to know the radial profile of soft X-ray intensity. However, since the interval between each viewing chord is about 3.5 centimeter, small magnetic island structure whose width is less than this interval may be overlooked. Still more, island structure with different helicity is difficult to analyze if they locate close to each other.

At present, we are developing the two dimensional tearing mode analysis code which can calculate realistic magnetic island structure in the up-down asymmetry plasma. It will enable us to know the line integrated value of soft X-ray intensity when plasma current, electron density and temperature profiles are given. Before that, it is instructive to know the rough estimation of how the line integrated soft X-ray signal is detected when there are magnetic island structures in the plasma. In this section, we calculate the soft X-ray intensity profile when the poloidal mode number, the radius of rational surface and the magnetic island width is given and integrate it along the viewing chord in the circular cross section plasma.

The profile of initial soft X-ray intensity without magnetic island structure is assumed as follows;

$$I^0_{SX}(r) = I^0_{SX}(0) \exp\left[- \left(\frac{r}{C1} \right)^{C2} \right] \quad (1)$$

where $I^0_{SX}(0)$ is the initial soft X-ray intensity at the plasma center. Coefficients C1 and C2 is given so as to reproduce the profile of line integrated value of soft X-ray signal measured in the experiment. We consider the peaked soft X-ray profile (C1=0.3, C2=1.5 ; we call it case I) and the broad soft X-ray profile (C1=0.6, C2=1.5 ; we call it case II). Figure 1 shows the soft X-ray profile (solid line) and its line integrated profile (broken line) of case I and II. Figure 2 is the contour of the same soft X-ray intensity with (a) m=2 island and (b) m=4 island with the radius of rational surface; r_s =0.3 and island width, W=0.1 for case I. The intensity of soft X-ray is assumed to be constant within the magnetic island. The intensity of soft X-ray is given as;

$$I_{SX}(r,\theta) = I^0_{SX}(r) + \Delta I_{SX}(r,\theta) \quad (2)$$

where the variation from the initial soft X-ray intensity, ΔI_{SX} ,inside the magnetic island is;

$$\Delta I_{SX}(r,\theta) = I^0_{SX}(r_s) - I^0_{SX}(r) \tag{3}$$

and outside the island is

$$\Delta I_{SX}(r,\theta) = \Delta I_{SX}(r^\theta_{s-},\theta) \exp\left[\frac{2(r - r^\theta_{s-})}{C3*W^\theta}\right] \tag{4}$$

for the plasma central side and

$$\Delta I_{SX}(r,\theta) = \Delta I_{SX}(r^\theta_{s+},\theta) \exp\left[\frac{2(r^\theta_{s+} - r)}{C4*W^\theta}\right] \tag{5}$$

for the plasma edge side. Other parameters are defined as follows;

$$W^\theta = W\left|\sin\left(\frac{m\theta}{2}\right)\right| \tag{6}$$

$$r^\theta_{s\pm} = r_s \pm 0.5\, W^\theta \tag{7}$$

$$\Delta I_{SX}(r^\theta_{s\pm},\theta) = I^0_{SX}(r_s) - I^0_{SX}(r^\theta_{S\pm}) \tag{8}$$

Coefficients C3 and C4 represents the degree of influences by the magnetic island structure on the soft X-ray intensity profile outside the magnetic island. In this case, we set C3=0.5 and C4=0.1.

The profile change of line integrated soft X-ray signal with m=2 island structure when plasma rotates 90 degree in the poloidal direction is shown in Fig. 3 (a). The solid line and the broken line cross each other twice (at r=0.136 and r=0.294). At this point, we can see the phase inversion in the time evolution of soft X-ray intensity.

As for the m=4 island case, the profile change of line integrated soft X-ray signal when plasma rotates 45 degree in the poloidal direction is shown in Fig. 3 (b). In this case, the solid line and the broken line cross each other three times (at r=0.068, r=0.211 and r=0.307). There are three phase inversion points in this case.

We calculate the radius of phase inversion point of the soft X-ray intensity as the function of the magnetic island width in case I and II with m=2, m=3 and m=4 island structure in the plasma. The results of calculation is shown in Fig.4. Three kinds of line indicates the different C3 and C4 value. The solid line, the broken line and the dotted line represent the case of (C3,C4) = (0.2,0.2), (0.5,0.5) and (0.5,0.1) respectively. In the m=2 case, there are two inversion point in the plasma in case I. The inner inversion radius gradually decreases with island width, W, and the outer one is almost independent of W and exists near the rational surface. In the case II, the number of inversion point (one or two) depends on the soft X-ray profile outside the magnetic island (depends on coefficients C3 and C4). Also in this case, the outer inversion radius locates near the rational surface. In the m=3 case, there are two inversion points in every case. The radius of inner one decreases and the outer one increases as W increases. But since their changes are rather weak, it is hard to know the island width from the two inversion radii. In the m=4 case, there are three inversion points in the plasma in case I. Their location weakly depend on W. In the case II, the number of inversion radius (two or three) depends on C3 and C4. Only, the most outer radius locates near the rational surface.

We also calculate the case of r_s =0.5 with m=2, 3,and 4 island structure. To summarize the results of calculation, the most outer soft X-ray inversion radius locates near the rational surface for every case and it is independent of the soft X-ray profile. The number of soft X-ray inversion radius and their location except for the most outer one, however, depends on the soft X-ray intensity profile outside the magnetic island. It is very difficult to know the island width from the inversion point even if the poloidal mode number is recognized.

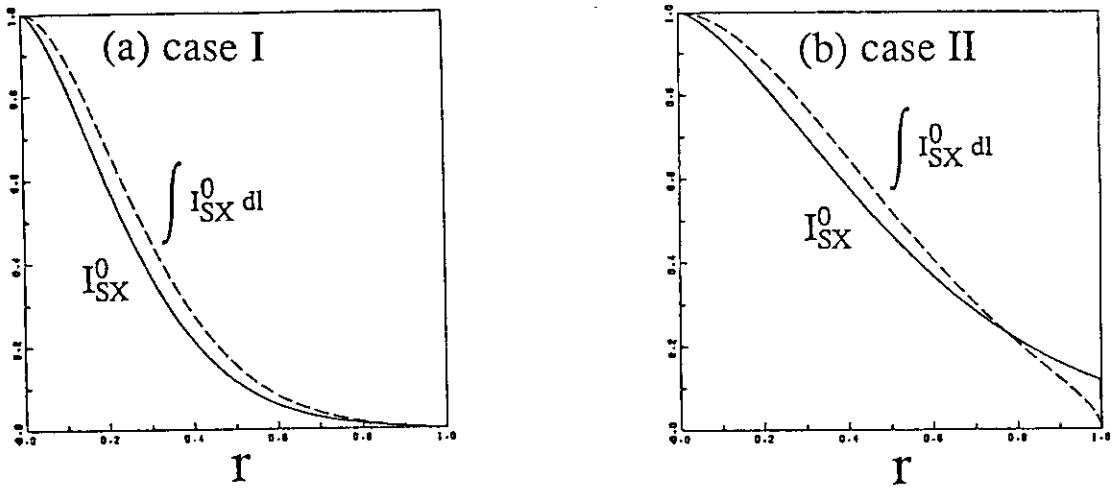

Fig.1 The profile of soft X-ray intensity and its line integrated value for (a) case I (peaked profile) and (b) case II (broad profile)

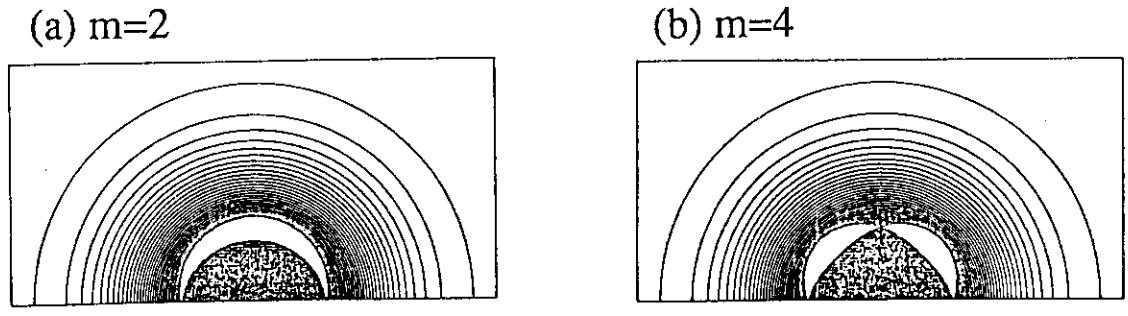

Fig.2 The contour of soft X-ray intensity in the poloidal cross section with (a) m=2 and (b) m=4 islands. Coefficients are C1=0.3, C2=1.5, C3=0.5 and C4=0.1.

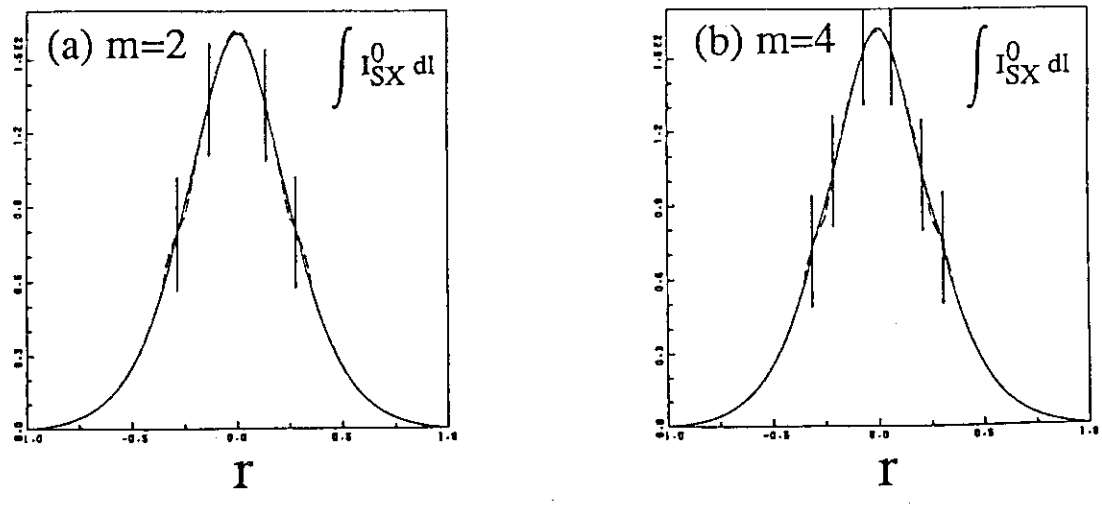

Fig.3 The profile of line integrated soft X-ray intensity. There are phase differences in the poloidal direction between the solid line and the broken line. They are 90 degree for m=2 case and 45 degree for m=4 case. The vertical lines indicate the phase inversion point of soft X-ray intensity.

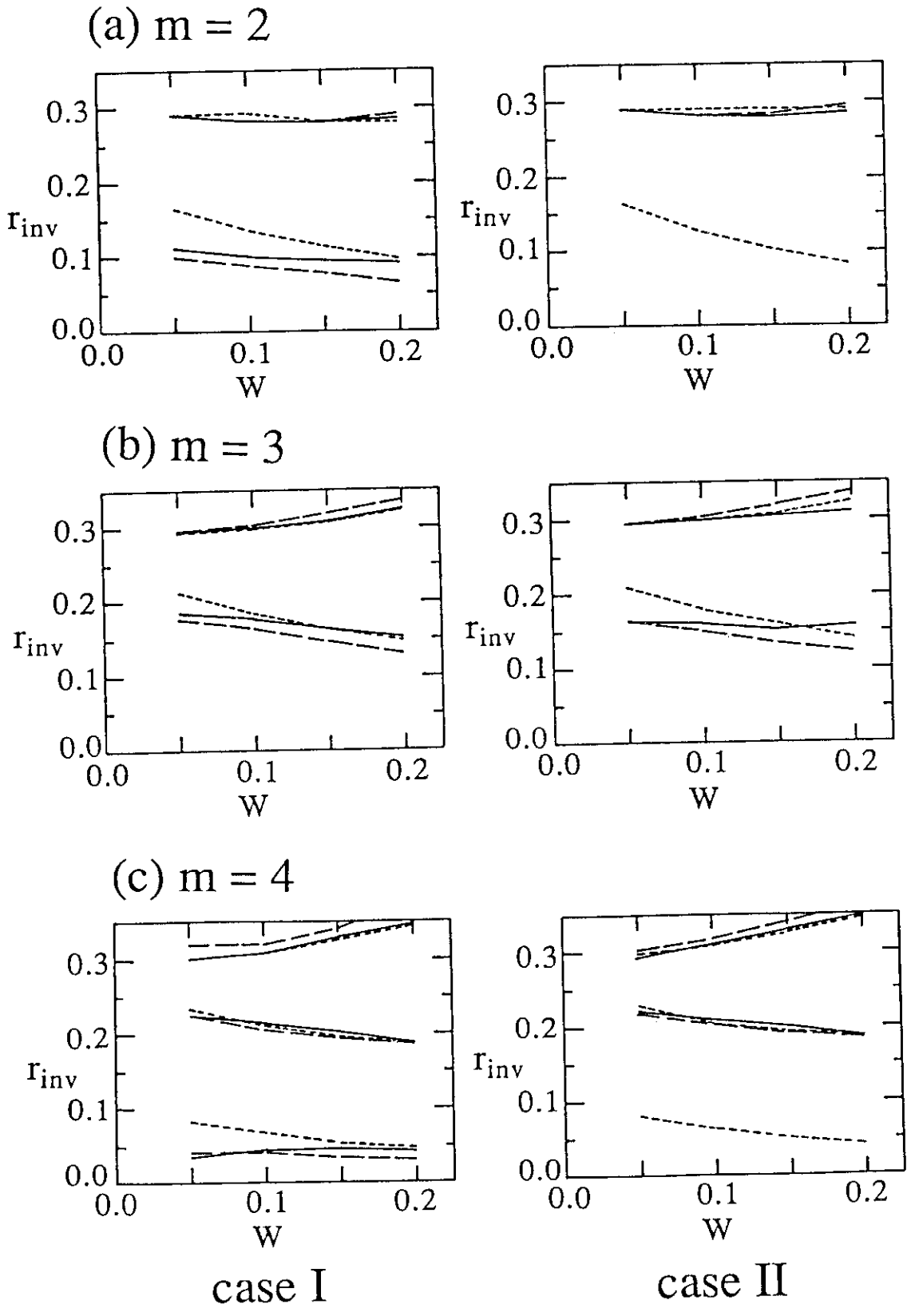

Fig.4 The phase inversion position of soft X-ray intensity as the function of magnetic island width. The solid line, the broken line and the dotted line represent the case of (C3,C4) = (0.2,0.2), (0.5,0.5) and (0.5,0.1) respectively.

6.7 Ion Temperature and Toroidal Rotation

Y. Koide, S. Ishida, A. Sakasai

1. Introduction

One of the characteristic features of high-T_i mode is its peaked ion-temperature profile as well as the attained high temperature itself. The flat $T_i(r)$ accompanied by sawtooth (I_p ~ 1 MA) changes to peaked one as discharge goes into high βp regime ($I_p \leq 0.7$ MA). Because the incremental confinement in the peaking region contributes to the global improved confinement, peaking radius is one of the key parameters for high-T_i mode study. In section 2, the width of peaking region is discussed from the viewpoint of its relation with the rational surfaces. Toroidal rotation velocity, which peak sometimes takes its maximum before $T_i(0)$ reaches at maximum, is also discussed.

2. Experimental results

First, we show that peaking region of ion temperature is closely related to the locations of rational surfaces inferred from the poloidal mode number of MHD oscillations.

Figure 1(a) shows the radial profile of soft X-ray emission (I_p=0.5MA, B_T=4.5 T, q_{eff}=12.4. The time point is t=7.2 sec in Fig. 4 which will be discussed later.). The amplitude of m=3 oscillation is also plotted with a broken line in the same figure. From this fluctuation pattern, q=3 surface is inferred to be located between chs.15 and 16. Then the radius of q=3 surface is ~ 31 cm. Figure 1(b) shows the radial profiles of ion temperature (broken line) and toroidal rotation velocity (solid line) measured

with charge exchange recombination spectroscopy (CXRS . See paper 8.1) at the same time point. Central T_i is high as 10 keV and the peaking is remarkable within the q=3 surface mentioned above. Peaking inside q=2 surface, the location of which is inferred from m=2 oscillation, is also recognized under almost the same controllable parameters. Narrow peaking inside q=1 surface inferred from m=1 oscillation appears under lower q_{eff} =5~10. From these results, the peaking region of $T_i(r)$ seems to be closely related to the rational surfaces. We note, in Fig.1(a), that soft X-ray profile also peaks, the radius of which seems to be a little narrower than q=3 surface by the island width. Here spatial resolution of PIN diode array is ~3.6 cm, which is ~3 times better than that of present CXRS measurement. So we shall regard the peaking radius of soft X-ray as the representative of peaking region, which is roughly equal to rational surfaces. Figure 2 show the q_{eff} dependence of peaking region (I_p=0.4~1MA, B_T=4.5T). Data with identified poloidal mode number as a measure of rational-surface radius, are principally selected. In this figure, abscissa is $1/q_{eff}$ and ordinate is the normalized peaking radius defined as peaking radius divided by minor radius. Sawtooth inversion radius is also plotted (shown with +). After all, this figure shows the q_{eff} dependence of peaking region fixed by rational surfaces. In the range of $q_{eff} \leq 5$, sawtooth oscillation appears, where no peaking in T_i and soft X-ray is observed. As q_{eff} is increased above 5, peaking inside q=1 surface appears. In the range of $q_{eff} > 10$, m=1 oscillation (shown with circles) changes to m=2 one (triangles) and peaking radius can reach at 30 % of minor radius. In some discharges, m=2 oscillation changes to m=3 oscillation, which is accompanied by

the broadened peaking radius up to 40 % of minor radius. As mentioned in paper 6.2, the improvement in energy confinement seems to be crucially related to q_{eff} and the best confinement is obtained when no clear MHD oscillations is observed. So there is no measure of peaking radius relevant to safety factor in this case. However, such broad peaking radii seems to lie in the region of q=3 surface. As seen in this figure, mode number and peaking radius can be roughly classified by a product of q_{eff} and normalized peaking radius.

As shown in Fig.1(b), co-directed sheared toroidal-rotation is observed, where $V_t(0)$ reaches at $\sim 1\times10^5$ m/s. In usual full injection experiments, toroidal rotation velocity is small as a few times 10^4 m/s because of almost balanced injection. Figure 3 shows the time evolutions of (a) NBI power, stored energy, (b) central ion temperature and (c) central toroidal rotation velocity (T_i and V_t are measured with CXRS. See paper 8.1). Accompanying β_p collapses at t ~ 7.3 and 8 sec, growth and crush in $T_i(0)$ and W_{dia} is observed. Although $V_t(0)$ is also modulated up to ~ $1X10^5$ m/s, it is often observed that it takes its maximum before $T_i(0)$ takes its maximum as seen in the first β_p collapse at t=7.3.

3. Conclusions

In high T_i/β_p experiments, characteristic peakings in $T_i(r)$ and $V_t(r)$ are observed. Peaking region seems to be closely related to the rational surfaces such as q=1, 2 or 3 surfaces. The co-directed sheared rotation often grows before ion temperature is maximized. The study of the role of induced electric field is in progress from the viewpoint of transport.

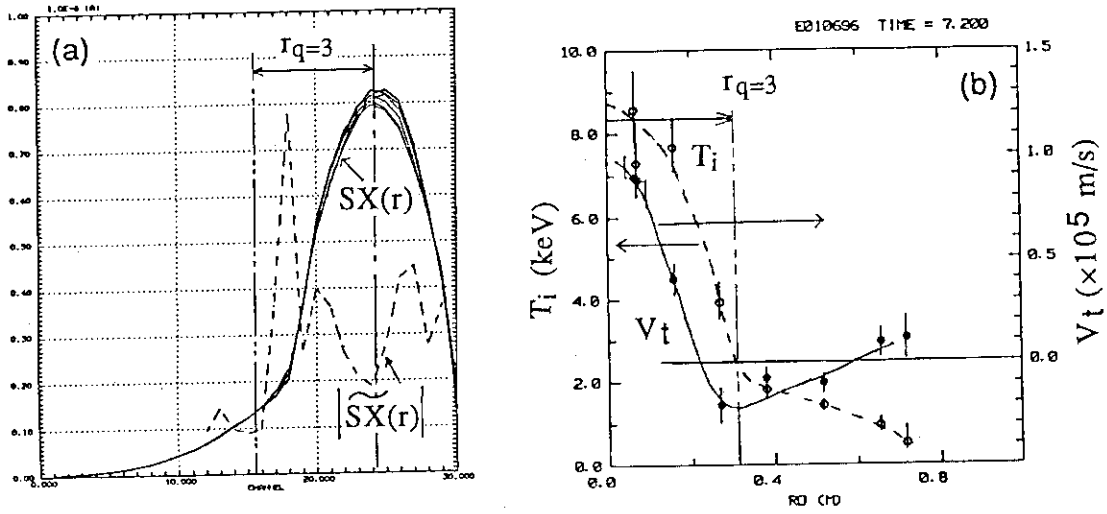

Fig.1(a) Soft X-ray profile and amplitude of m=3 oscillation. The location of q=3 surace, indicated by '$r_{q=3}$', is inferred from the fluctuation pattern, . (b) Profiles of ion temperature and toroidal rotation velocity. Inside q=3 surface, Ti peaks and sheared rotation in co-direction appears. I_p=0.5MA. B_T=4.5T. q_{eff}=12.4.

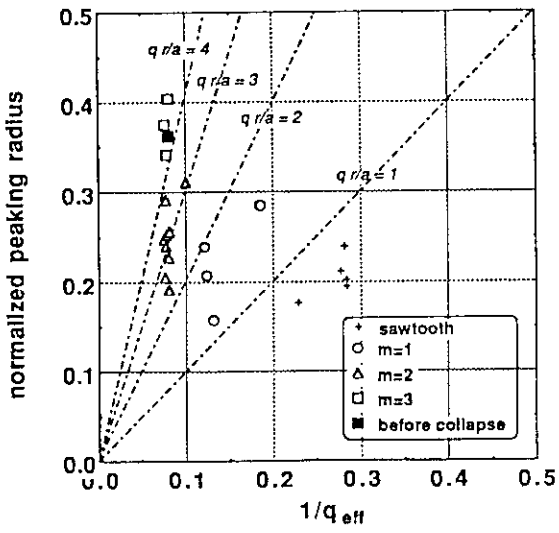

Fig.2 qeff dependence of peaking region of soft X-ray profile. The poloidal mode number of simultaneous MHD oscillations are distinguished by different symbols. The peaking radius just before β_p collapse,where best confinement is obtained, is shown with closed square.

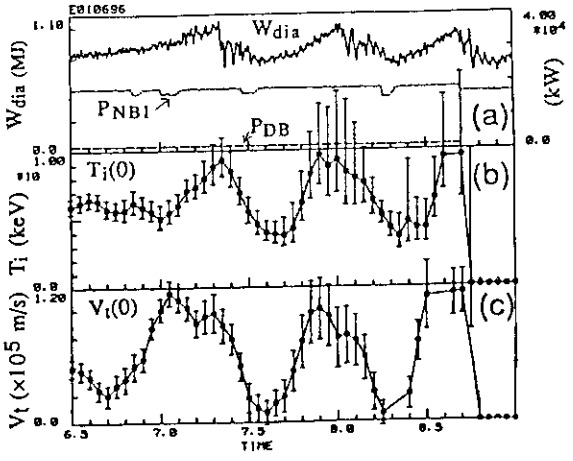

Fig.3 Evolutions of (a) NBI power, stored energy, (b) central ion temperature, (c) central toroidal rotation velocity. β_p collapse is observed at t = 7.3 and 8.

6.8 Electron Temperature Profiles and Profile Consistency

S. Ishida, N. Isei and M. Sato

Characteristics of electron temperature profiles for high-β_p high-T_i plasmas in JT-60 have been investigated using the data on ECE measurements by Fourier transform spectroscopy. The procedures of obtaining the electron temperature profiles are described by Isei et al. in Section 11.2 of this review[1].

Waltz et al. show that the profile peaking parameter of electron temperature is quantified between q(a) and $q(a)^{2/3}$ assuming Spitzer conductivity and q(0)=1; the peaking parameter is defined as the peak electron temperature value normalized by the volume-averaged value, usually written as $T_e(0)/\langle T_e\rangle$[2]. In order to characterize the profile shapes and compare the experimental results with the picture of the q-dependent profile consistency, we have obtained the peaking parameters over a wide range of q(a) values. As discussed in Section 6.1[3], this regime with high q discharges does not involve sawtoothing modulation of the central transport of the plasma.

Figure 1 shows the peaking parameter of the electron temperature profile as a function of the q_a value (the same as the cylindrical q value at the edge) for the I_p scan experiments in JT-60, together with the observed MHD activities[3]. The values of the peaking parameter indicate those at a peaked electron temperature during neutral beam heating. It is found from this result that the peaking parameter is quite insensitive to the q values over the wide range of q_a~3-10 in spite of these sawtooth-free discharges. The similar observations have been also obtained for the TFTR supershot discharges[4].

The strong dependence of the peaking parameter on q_a was believed to suggest that $T_e(r)$ and J(r) profiles are strongly coupled together through the plasma conductivity, while sawtooth oscillations vary the scaling in terms of the peaking parameter to some degree. However, even in the absence of sawteeth, the $T_e(r)$ shapes tend to be invariable to the q_a values in the high-q regime. It is apparent that the following experimental results in JT-60 contradict the assumptions of the q-dependent profile consistency; 1) the plasma conductivity can be predicted by neoclassical theory including bootstrap currents[5]. 2) the central q-values are above unity[3]. The experimental result in JT-60 also confirms the stronger statement of $T_e(r)$ profile consistency, so that the old picture of profile consistency remains forced to be reconsidered.

REFERENCES:

[1] N. Isei et al., Section 11.2, in this review.
[2] R.E. Waltz et al., Nucl. Fusion 26(1986)1729.
[3] S. Ishida et al., Section 6.1 in this review.
[4] G. Taylor et al., Nucl. Fusion 29(1983)3.
[5] M. Kikuchi et al., Section 7.5, in this review.

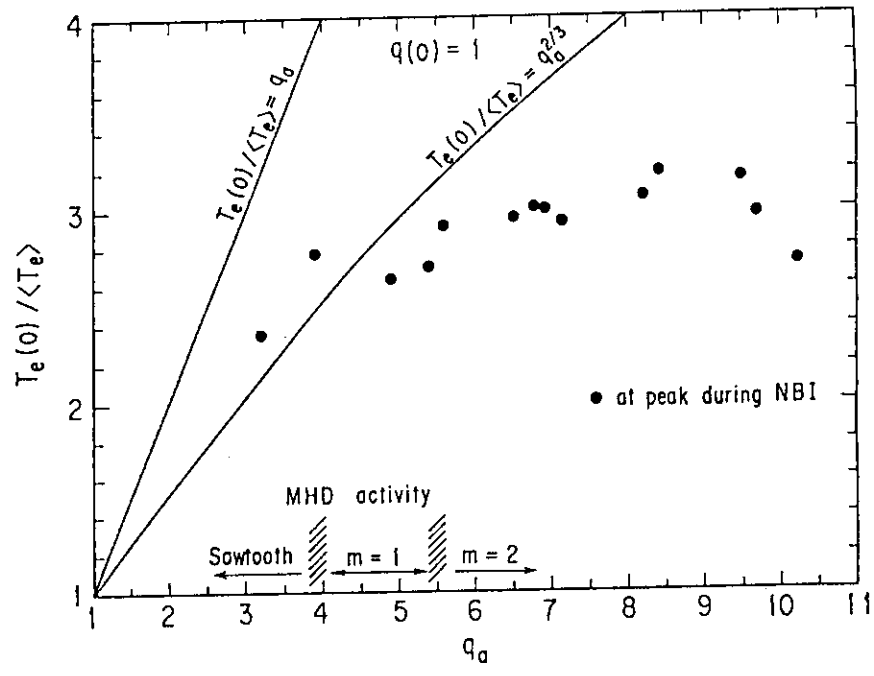

Fig.1 Peaking parameter of the electron temperature profile as a function of q_a, together with the observed MHD activities, as compared with the scaling of the peaking parameter predicted by the q-dependent profile consistency[2].

6.9 Effects of Zeff Values on High-Ion-Temperature Plasmas

Y. Kawano, H. Kubo, K. Itami, T. Sugie, S. Ishida, Y. Koide,
A. Nagashima, T. Matoba and JT-60 team

1. Introduction

Variations of Zeff values for lower divertor plasmas in high ion temperature experiments are discussed. In a series of scanning of the plasma current (Ip) before titanium(Ti)-flash for gettering, the Zeff value increased from 3.0 at Ip=0.4MA to 5.3 at Ip=1.2MA. This is caused by the increase in the carbon concentration. After Ti-flash, stable and low Zeff discharges were achieved at Ip=0.5MA. In these experiments, no obvious correlation was observed between the Zeff value and the ion temperature.

2. Ip dependences of the Zeff value and light impurity concentrations

Figure 1 shows viewing chords to measure the Zeff profile for high ion temperature experiments. [1] Zeff values were deduced from Visible Bremsstrahlung (Vis.Brems.) intensities along viewing chords. [2] Figure 2 shows chord averaged Zeff ($\overline{Zeff}$) profiles before and after Ti-flash evaluated at timings of Thomson scattering. Before Ti-flash, the Zeff value along the IN2 chord ($\overline{Zeff}^{IN2}$) is a little smaller than Zeff values at $\rho \sim 0.4$m, but it is basically supposed that Zeff values have almost flat profiles at $\rho \leqq 0.5$m (here, causes for steep increases in Zeff profiles at $\rho \geqq 0.5$m are suggested in ref.[2].) In fig.2, Zeff values after Ti-flash are about 30%～50% smaller than those before Ti-flash at $\rho = 0 \sim 0.5$m. Figure 3 shows the correlation between Zeff values and Ip before Ti-flash, discharge conditions are as follows; Ip= 0.4～1.2MA, Bt=4.5T, P_{NBI} = 19～22MW, $\overline{n_e}^{U23}$ =1.6～3.2 $\times 10^{19}$ m^{-3} and they are evaluated at 1.5sec after the beginning of NBI. In fig.3, it can be recognized that the $\overline{Zeff}^{IN2}$ increases with Ip. Figure 4 shows Ip dependence of light impurity concentrations such as carbon and oxygen. These values are evaluated by $\overline{Zeff}^{IN2}$ values and intensity ratios of CVI and OVIII [3] neglecting contributions of other impurities. In fig.4, the carbon concentration (n_c/n_e) increases from about 4% at Ip=0.5MA to 12% at Ip=1.2MA, while the oxygen concentration (n_o/n_e) has small values about 1～2% and does not show a clear dependence on Ip. Therefore the increase in the $\overline{Zeff}^{IN2}$ value is mainly caused by the increase in the carbon concentration with Ip. Here, the maximum temperature of the divertor plate measured by the IRTV system [4] tends to increase with Ip as shown in fig.5. Since the divertor plate is made of the carbon graphite, we can suppose that the carbon impurity mainly comes from the divertor plate.

3. Effect of Ti-flash

Figure 6 shows the $\overline{Zeff}^{IN2}$ values for a series of the experiment before Ti-flash, and discharges shown in fig.6 are same as already shown in fig.3. Figure 7 shows the $\overline{Zeff}^{IN2}$ values for a series after about 150 discharges from the last operation of Ti-flash, and discharge conditions are as follows; Ip=0.5MA, Bt=4.5T, P_{NBI} = 17～19MW, $\overline{n_e}^{U23}$ =

$1.6\sim2.4\times10^{19}$ m^{-3} and evaluated at 0.6sec and 3.0 sec after the start of NBI. The vacuum vessel was baked up to about 300℃ at the inner wall for both series of experiments. In fig.6, $\overline{Zeff}^{IN2}$ have a variance from about 3.0 to about 5.3. It is supposed that this variance is caused by the Ip dependence of the Zeff value as discussed in section 2. From disruption timings noted beneath symbols in fig.6, we have 7 diruptions out of a series of 13 discharges before Ti-flash. On the other hand, in fig.7, no disruption was observed for a series of discharges after Ti-flash. Here, average values of $Zeff^{IN2}$ are 3.2 in fig.6 (Ip=0.4$\sim$0.6MA, $\overline{n_e}^{U23} = 1.6\sim2.1\times10^{19}$ m^{-3}) and 2.6 in fig.7 (Ip=0.5MA, $\overline{n_e}^{U23} = 1.6\sim2.4\times10^{19}$ m^{-3}). Though there are some differences of discharge conditions between in fig.6 and in fig.7, we note that $\overline{Zeff}^{IN2}$ values after Ti-flash are about 20% smaller than those before Ti-flash. Thus, stable and low Zeff discharges are achieved after Ti-flash.

4. Correlation between the Zeff value and the ion temperature

Figure 8 shows the correlation between the $\overline{Zeff}^{IN2}$ values and the ion temperature of discharges shown in fig.6 and fig.7. In fig.8, the ion temperature denotes the maximum value near the plasma center, which was measured by CXRS.[5] And they were evaluated at same timings in fig.6 and fig.7. High ion temperatures up to about 10KeV are observed at $\overline{Zeff}^{IN2}$ values of 3.0 and 5.3 as shown in fig.8. Since plotted data in fig.8, however, are scattered considerably, we have no clear correlation between the $\overline{Zeff}^{IN2}$ value and the ion temperature in these series of experiments.

5. Summary

We discussed the Zeff value and light impurity concentrations of lower divertor plasmas in high ion temperature experiments. Results are summarized as follows;

(1) The Zeff value and the carbon concentration tended to increase with Ip, while the oxygen concentration does not vary significantly.
(2) Discharges after Ti-flash were more stable and have lower Zeff values compared with those before Ti-flash.
(3) No obvious correlation was observed between the Zeff value and the ion temperature.

References

[1] S.Ishida et al., this report, Section 6.1.
[2] Y.Kawano et al., this report, Section 8.2.
[3] H.Kubo et al., Nucl.Fusion 29(1989)671.
[4] K.Itami et al., JAERI-M 89-033(1989)251.
[5] Y.Koide et al., JAERI-M 89-033(1989)243.

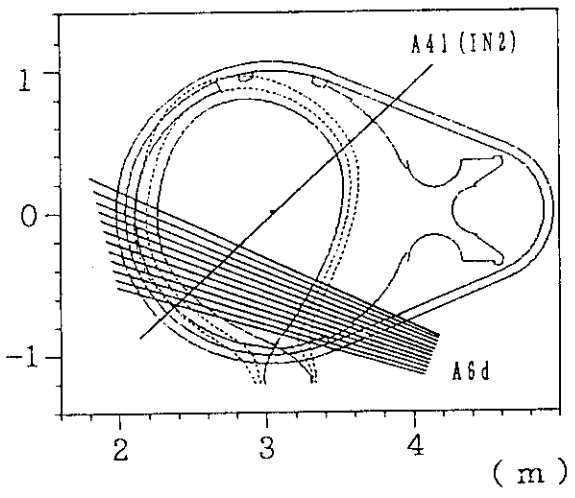

Fig. 1 *Viewing chords for the observation of Vis. Brems. intensities of lower divertor plasmas in high ion temperature experiments.*

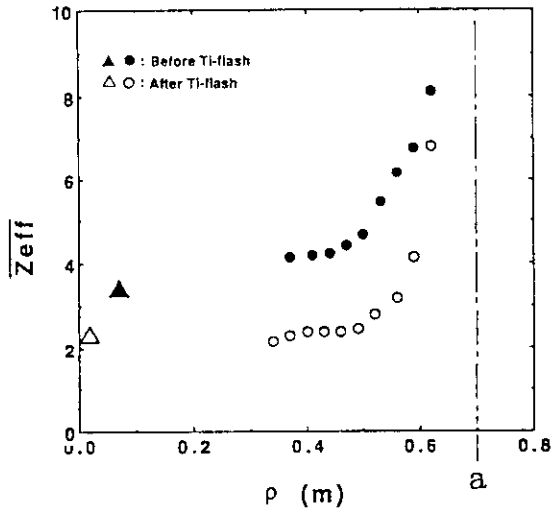

Fig. 2 *Chord averaged Zeff profiles before and after Ti-flash.*
▲●: *Before Ti-flash (Ip=0.6MA, Bt=4.5T, P_{NBI} =21MW, $\overline{ne}^{VIS}$ =1.9×10^{-19} m^{-3}, at 1.5sec after the beginning of NBI).*
△○: *After Ti-flash (Ip=0.5MA, Bt=4.5T, P_{NBI} =17MW, $\overline{ne}^{VIS}$ =1.6×10^{-19} m^{-3}, at 0.6sec after the beginning of NBI).*
(a) *denotes the plasma minor radius.*

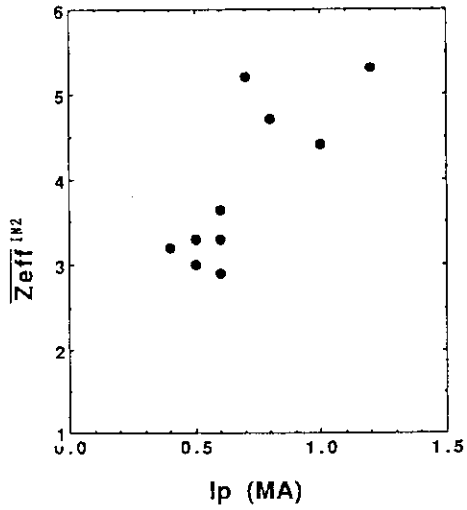

Fig. 3 *Ip dependence of the $\overline{Zeff}^{IN2}$ value before Ti-flash. Ip=0.4~1.2MA, Bt=4.5T, P_{NBI} = 19~22MW, $\overline{ne}^{VIS}$ =1.6~3.2 ×10^{19} m^{-3}, evaluated at 1.5sec after the beginning of NBI.*

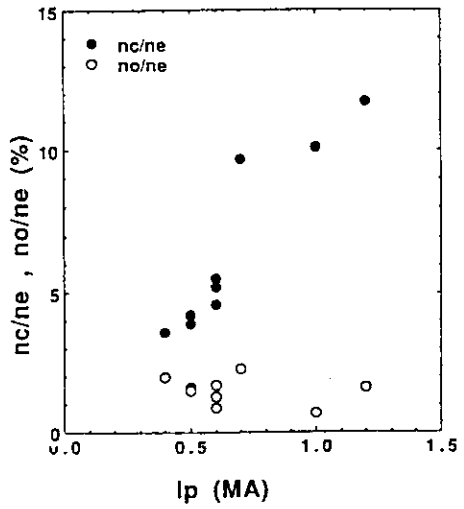

Fig. 4 *Ip dependence of concentrations of carbon and oxygen for discharges shown in fig. 3.*
●: *carbon concentration, (n_c /n_e)*
○: *oxygen concentration, (n_o /n_e)*

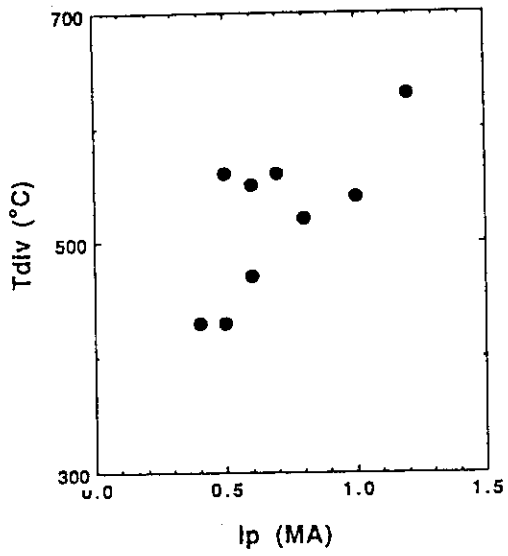

fig.5 Correlation between the maximum temperature of the divertor plate (T_{Div}) measured by IRTV and Ip for discharges shown in fig.3.

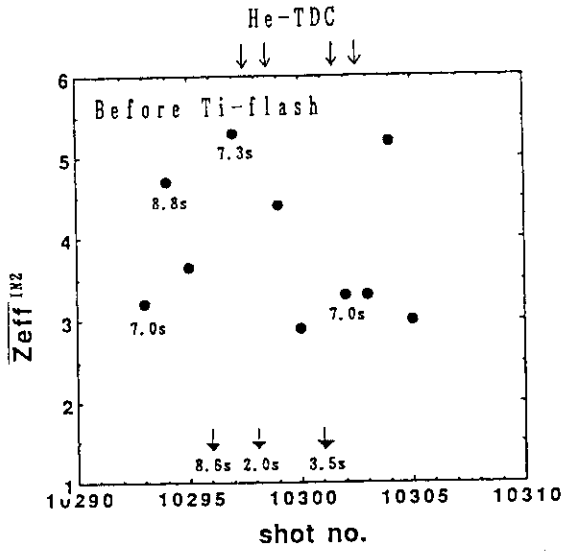

Fig.6 Variation of the $\overline{Zeff}^{IN2}$ value on a series of discharges before Ti-flash shown in fig.3. Timing of Disruptions are shown beneath the symbols, (●) and (↓). The symbol (↓) denotes shots which were not dealt.

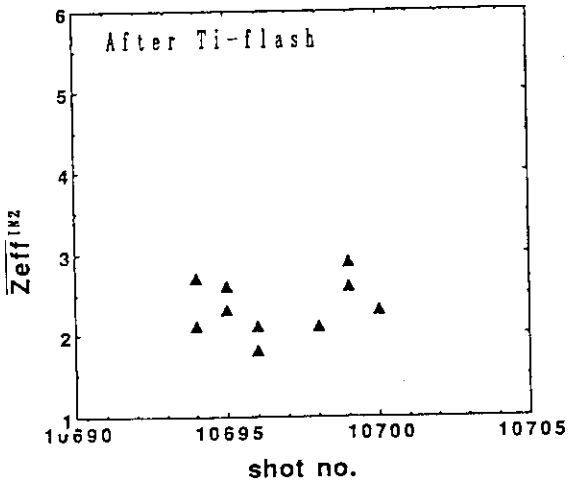

Fig.7 Variation of the $\overline{Zeff}^{IN2}$ value on a series of discharges after Ti-flash. Ip=0.5MA, Bt=4.5T, P_{NBI} = 17~19MW, $\overline{ne}^{U2.3}$ =1.6~2.4 ×10^{19} m^{-3}, evaluated at 0.6sec and 3.0sec after the beginning of NBI.

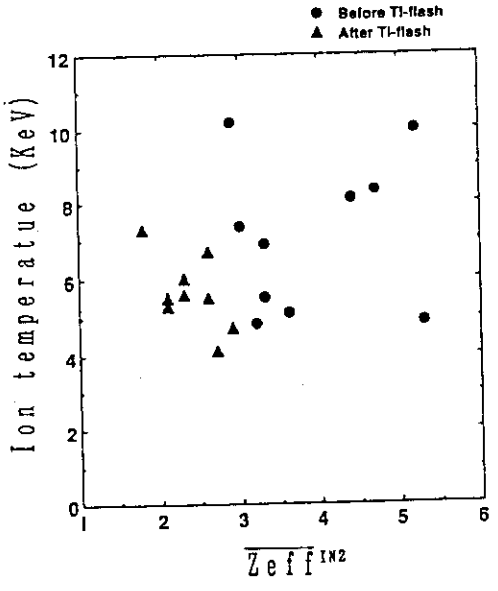

Fig.8 Correlation between the $\overline{Zeff}^{IN2}$ and the ion temperature.
●: before Ti-flash
▲: after Ti-flash

7. BOOTSTRAP CURRENT

7.1 THEORY OF NEOCLASSICAL BOOTSTRAP CURRENT DRIVEN BY ENERGETIC PARTICLES IN A TOKAMAK

M. Azumi, M. Kikuchi and K. Tani

ABSTRACT : Friction and viscous forces of fast ions are calculated under the assumption of isotropic energy distribution and small banana size. Derivation of these forces are presented in detail.

INTRODUCTION

Recent experiments in large tokamaks show the existence of the neoclassical bootstrap current . The theory of the neoclassical bootstrap current in a tokamak has been well developed and refined in the excellent formulation of the neoclassical transport theory [1]. Various numerical codes for evaluating the amount of the bootstrap current have been also developed. Most of theories, however, assume that a plasma consists of particles with Maxwellian velocity distribution. For the evaluation of the bootstrap current in a plasma intensively heated by NBI and IC, the contribution of energetic ions, or fast ions, should be included. Kim and Callen proposed the simple model that the bootstrap current coefficients for fast ions are the same as those for bulk ions[2]. However, the velocity distribution of fast ions largely deviates from the Mawellian one and we have no reason why fast ions play the same role as bulk ions. The neoclassical bootstrap current is caused by the balance between the friction force and the viscous force parallel to the magnetic field. These two forces for fast ions were derived by Hirshman and Sigmar in order to evaluate beam driven current. By using these expressions, Stacey and Mandrekas studied the toroidal current in the NBI current drive phase, including the beam driven bootstrap current[3]. The Hirshman-Sigmar expression of fast ion friction and viscous forces was derived by using the first Legendre harmonic component of the fast ion distribution function and the effect of the zeroth harmonic component, that is the isotropic component, was neglected. Therefore, these expressions are valid only for the beam current evaluation. Then we have derived friction and viscous coefficients of fast ions under the the assumption that they have the isotropic velocity distribution and the banana size is much smaller than the characteristic length [4]. In this paper, we give the detail derivation of these coefficients, following the formulation by Hirshman and Sigmar[1].

FRICTION AND VISCOUS FORCES OF FAST IONS

The basic equation is the steady state drift kinetic equation with Coulomb collision;

$$(v_{//} + v_D) \cdot \nabla f = C(f) + S(\psi)\, \delta(v - v_b)$$

where f is the distribution function, v_D the drift velocity, C the Coulomb collision operator, S the source and ψ the flux surface. Here, we have assumed that the source has the isotropic velocity distribution with velocity of v_b. In the following, we also assume that $\nu/v_b << \rho/a << 1$, where ν, v_b, ρ and a are the collision frequency, bounce frequency, larmor radius and characteristic length of a system, respectively. These assumptions ensure that the zeroth order pressure tensor of fast ion is diagonal and isotropic. Now we expand f for these small parameters;

$$f = f^0 + f^1 + \cdots ; f^1 = f_0^1 + f_1^1 + \cdots$$

where numbers of superscript and subscript of f denote order of ρ/a and v/v_b, respectively. Then the lowest order equation is

$$v_{//} \cdot \nabla f^0 = C(f^0) + S(\psi)\,\delta(v - v_b)$$

and, assuming $v_i << v << v_b$ (v_i is the thermal velocity of bulk ions), the lowest order solution is

$$f^0(\psi, v) = \frac{S\tau_s}{4\pi} \cdot \frac{1}{v^3 + v_c^3},$$

or,

$$f^0(\psi, v) = \frac{n_f}{4\pi} \cdot \frac{\tau_s}{\tau_{th}} \cdot \frac{1}{v^3 + v_c^3}$$

$$v_c^3 = \frac{3\sqrt{\pi}}{4} v_e^3 \sum_i \frac{Z_i^2 n_i}{n_e} \frac{m_e}{m_f}, \quad \tau_s = \frac{\tau_{ee}}{Z_f^2} \frac{m_e}{m_f}, \quad \tau_{th} = \frac{\tau_s}{3} \ln\left[\left(\frac{v_b}{v_c}\right)^{3/2} + 1 \right]$$

where τ_s,τ_{th} and v_c are the slowing down time, thermalization time and critical velocity of fast ions, respectively. The suffix f, e and i denote the fast ion, electron and bulk ion, respectively. The first order equation and the solution are

$$v_{//} \cdot \nabla \left[f_0^1 + \frac{I v_{//}}{\Omega} \frac{\partial f^0}{\partial \psi} \right] = 0,$$

$$f_0^1 = -\frac{I v_{//}}{\Omega} \frac{\partial f^0}{\partial \psi} + g(\psi, v, \zeta)$$

where Ω is a cyclotron frequency, $I = R B_\varphi$ and $\zeta = v_{//}/v$. The function g is determined from the solvability condition of the next order equation;

$$v_{//} \cdot \nabla f_1^1 = C(f_0^1).$$

Taking into account of only the pitch angle scattering, that is,

$$C(f) = \frac{\nu_D}{2} \frac{\partial}{\partial \zeta} (1 - \zeta^2) \frac{\partial f}{\partial \zeta}$$

we have

$$g = \frac{1}{2} \frac{IB}{\Omega} v \frac{\partial f^0}{\partial \psi} \int_\lambda^{\lambda_c} \frac{d\lambda}{\langle \zeta \rangle} H(\lambda_c - \lambda)$$

$$\langle \zeta \rangle = \oint \zeta \frac{dl}{B}; \quad \lambda = \frac{1 - \zeta^2}{B}; \quad H(x) = 1 \ (x > 0), 0 \ (x < 0)$$

At this point, we note that this expression of f^1 gives the parallel flow velocity

$$n_f \langle B u_{//f} \rangle = -\frac{4\pi}{3} f_t \frac{IB}{\Omega} \int dv \cdot v^4 \frac{\partial f^0}{\partial \psi}, \quad f_t = 1 - \frac{3}{4} \langle B^2 \rangle \int \frac{\lambda d\lambda}{\langle |\zeta| \rangle}$$

where f_t is the trapped particle fraction. This flow velocity is independent on the friction. The discrepancy comes from the neglect of the slowing-down and energy diffusion terms in the collision operator. More general form of g , proposed by Hirshman and Sigmar, is

$$g = \frac{\sigma v}{2}\sqrt{<B^2>}\, G(\psi, v) f^0 \int_\lambda^{\lambda_c} \frac{d\lambda}{<\zeta>} H(\lambda_c - \lambda) \ , \quad \sigma = \pm 1$$

Then, the parallel flows of particle and energy are given by

$$n_f < B\, u_{//f} > = n_f B\, V_{1f} + \frac{4\pi}{3} f_c \sqrt{<B^2>} \int dv\, v^4\, G f^0$$

$$< B\, q_{//f} > = \frac{5}{2} p_f B\, V_{2f} + \frac{4\pi}{3} f_c \sqrt{<B^2>} \int dv\, v^4\, G f^0 \left(\frac{m_f}{2} v^2 - \frac{5}{2}\frac{p_f}{n_f}\right)$$

where

$$V_{1f} = -\frac{I}{e_f n_f B}\left[\frac{\partial p_f}{\partial \psi} + e_f n_f \frac{\partial \phi}{\partial \psi}\right], \quad V_{2f} = -\frac{I}{e_f B}\left[\frac{2}{5}\frac{m_f}{p_f}\frac{\partial r_f}{\partial \psi} - \frac{\partial p_f}{\partial \psi}\right]$$

$$p_f = \frac{4\pi m_f}{3}\int dv\, v^4 f^0, \quad r_f = \frac{2\pi m_f}{3}\int dv\, v^6 f^0, \quad f_c = 1 - f_t$$

and ϕ is the electrostatic potential. Now we can evaluate the viscous force parallel to the magnetic field by using the following expression;

$$< \mathbf{B} \cdot \nabla \cdot \pi > = < m_f B \int d^3v\, v_{//}\, C(f^1) >$$

$$- < m_f B \int d^3v\, v_{//} \frac{v}{f_c}\frac{<B^2>}{B^2} \int_\lambda^{\lambda_c} \frac{d\lambda'}{<\zeta>} <\frac{B}{v_{//}} C(f^1) > >$$

Assuming that the pitch angle scattering is dominant for the viscous force,

$$< \mathbf{B} \cdot \nabla \cdot \pi > = \frac{2}{3} f_t\, 2\pi m_f \sqrt{<B^2>} \int dv\, \nu_D\, v^4\, G f^0$$

The function G is related to the flows of particle and energy in the poloidal direction. For the particles with Maxwellian velocity distribution, the functional form of G is determined by expanding it in a Laguerre polynomial series and by adjusting coefficients such that moments of G give the poloidal flows of particle and energy. For fast ions, this procedure breaks down because the series does not converge within a few terms because of the contribution of high energy component and we have to solve the full Fokker Planck equation in order to have the exact expression of G Instead of that, in the following, we simply assume G as the constant in the zeroth order approximation and consider only the friction-viscous balance for particle flow of fast ions. Then G is expressed as

$$G = \frac{1}{f_c \sqrt{<B^2>}} \frac{n_f m_f}{p_f} [<B u_{//f}> - B V_{1f}]$$

And finally we have

$$< \mathbf{B} \cdot \nabla \cdot \pi > = \frac{f_t}{f_c}\frac{n_e m_e}{\tau_{ee}}\frac{Z_f^2 n_f}{n_e}\frac{\hat{Z} v_c^3}{\hat{v}_c^3} [<B u_{//f}> - B V_{1f}]$$

$$\text{where } \frac{1}{\hat{v}_c^3} = \frac{\tau_s}{3\tau_{th}}\frac{n_f m_f}{2 p_f}\int_0^{v_b} \frac{v\, dv}{v^3 + v_c^3} \ , \quad \hat{Z} = \sum Z_i^2 n_i \Big/ \sum Z_i^2 n_i \frac{m_f}{m_i} .$$

The parallel friction force can be easily calculated from

$$< \mathbf{B} \cdot \mathbf{F}^{e,i} > = < m_f B\,(u_{//} - u_{//}^{e,i}) \int d^3v\, \nu_s(v)\, v_{//} \frac{\partial f^0}{\partial v_{//}} >$$

and straightforward calculations give the following results;

$$< \mathbf{B} \cdot \mathbf{F}^{e} > = - \frac{n_e m_e}{\tau_{ee}} \frac{Z_f^2 n_f}{n_e} < B\,(u_{//} - u_{//}^{e}) >$$

$$< \mathbf{B} \cdot \mathbf{F}^{i} > = - \frac{3\sqrt{\pi}}{4} \frac{n_i m_i}{\tau_{ii}} \frac{Z_f^2 n_f}{Z_i^2 n_i} \left(1 + \frac{m_i}{m_f}\right) \frac{v_i^3}{\hat{v}_b^3} < B\,(u_{//} - u_{//}^{j}) >$$

$$\text{where } \frac{1}{\hat{v}_b^3} = \frac{\tau_s}{3\tau_{th}} \frac{1}{v_c^3}$$

SUMMARY

We have derived the friction and viscous forces of fast ions under the assumptions that the fast ion source has the isotropic velocity distribution and the banana size of fast ion is much smaller than the characteristic length of the system. Friction and viscous coefficients of fast ions are summarized as follows;

$$l_{11}^{fe} = \frac{n_e m_e}{\tau_{ee}} \frac{Z_f^2 n_f}{n_e}$$

$$l_{11}^{fi} = \frac{3\sqrt{\pi}}{4} \frac{n_i m_i}{\tau_{ii}} \frac{Z_f^2 n_f}{Z_i^2 n_i} \left(1 + \frac{m_i}{m_f}\right) \frac{v_i^3}{\hat{v}_b^3}$$

$$\mu_f = \frac{f_t}{f_c} \frac{n_e m_e}{\tau_{ee}} \frac{Z_f^2 n_f}{n_e} \frac{\hat{Z} v_c^3}{\hat{v}_c^3}$$

These expressions have the similar forms as those derived by Hirshman and Sigmar, where $\hat{v}_b$ and $\hat{v}_c$ are replaced by $\overline{v_b^3} = \int v_{//} f dv / \int (v_{//}/v^3) f dv$,which is evaluated from the first Legendre moment of fast ion distribution function, instead of the zeroth one. By using the friction and viscous coefficients of fast ions derived in this paper and neglecting parallel flows of electron and bulk ions, the cross field particle flux of fast ions can be computed as;

$$\Gamma = - \frac{2\rho_{pf}^2}{n_f m_f} \frac{\mu_f\,(l_{11}^{fe} + l_{11}^{fi})}{\mu_f + l_{11}^{fe} + l_{11}^{fi}} \frac{\partial n_f}{\partial r}$$

$$= - f_t \frac{2\rho_{pf}^2}{\tau_{ee}} \frac{m_e}{m_f} Z_f^2 \hat{Z} \frac{v_c^3}{\hat{v}_c^3} \frac{1 + (1+\hat{Z}) v_c^3/\hat{v}_b^3}{1 + (1+\hat{Z}) v_c^3/\hat{v}_b^3 1 + f_t \hat{Z} v_c^3/\hat{v}_c^3} \frac{\partial n_f}{\partial r}$$

We note that this particle flux is the diffusive one, not the convective one which was evaluated by Cordey[5] and Hirshman and Sigmar[1] in the case of the directed neutral beam injection. The diffusion coefficient derived above is in agreement with the numerical result of Monte Calro simulation within a factor of two.

REFERENCES

[1] S.P. Hirshman and D.J. Sigmar, Nucl. Fusion 21(1981)1079
[2] Y.B. Kim, J.D. Callen and H. Hamnen, submitted in Nucl. Fusion
[3] W.M. Stacey, J. Mandrekas, Georgia Institute of Technology, USA, Report No. GTFR-83(1988)
[4] M. Azumi, M. Kikuchi, K. Tani, JAERI-M 89-033 (1989); we have found some mistakes in friction coefficients due to the incorrect boundary condition. Revised values are listed in the summary of this paper.
[5] J.G. Cordey, Nucl. Fusion 16(1976)499

7.2 Numerical Analysis of Self-Consistent Non-Inductive Plasma Currents in Tokamaks

K. Tani and M. Azumi

Abstract

We have developed a numerical code to investigate neutral-beam-driven, Ohmic and bootstrap currents which are consistent with MHD equilibrium. The code can describe the effects of mirror trapping, energy diffusion and bounce motion of fast ions on the beam-driven current. The bootstrap current is evaluated for multi-species ions including impurity and unthermalized fast ions. An iterative algorithm is employed to obtain a self-consistent current and MHD equilibrium.

1. Introduction

Recent observations of substantial plasma-current driven by neutral beam injection [1,2,3] ,lower hybrid waves [4,5] and neoclassical current [3,6] suggest the posibile development of steady-state tokamak reactors. These experimental results motivate us to analyse 2-D MHD equilibrium with these non-inductive plasma currents. These currents and the MHD equilibrium, however, strongly depend on each other. Therefore, for an accurate treatment, a self-consistent analysis of 2-D MHD equilibrium and the current distribution is necessary. Accordingly, we have developed a code, ACCOME (Analyzer for Current drive COnsistent with MHD Equilibrium), version I. ACCOME employs an iterative method to deduce non-inductive currents which are consistent with MHD equilibrium.

2. Calculation procedure

In ACCOME plasma densities and temperatures are assumed to be given by fixed functional forms of a normalized effective minor radius ρ. The variable ρ is defined as $\rho = \sqrt{V(\psi)/V_{tot}}$ where $V(\psi)$ is the plasma volume within ψ and V_{tot} is the value of V at the plasma surface. Consequently, the pressure of bulk plasma p^{th} is also given by a function of ρ. In the

presence of tritons and deuterons, the pressure of unthermalized alpha particles p^{α} is calculated by using an analytical solution of Fokker-Planck equation and the local fusion reaction rate.

The MHD equilibrium is solved with a restriction that the total plasma current I_p is kept constant at every iteration step. ACCOME has two options to keep the total plasma current constant: one is to regulate one-turn voltage U_o with given neutral-beam-power input P_{NBI} and the other is to regulate P_{NBI} with fixed U_o.

From the geometric properties of the desired solution, i.e., plasma elongation κ, triangularity δ, major radius R_t, minor radius a and plasma current I_p, we set up a Solov'ev model equilibrium. With the old MHD equilibrium of the i^{th} iteration ψ_i, the flux-surface-averaged beam driven current $\langle j_{\parallel}^{f} B\rangle_i$, $\langle j_{\parallel}^{BD} B\rangle_i$ [7], bootstrap current $\langle j_{\parallel}^{BS} B\rangle_i$ [8], and Ohmic current $\langle j_{\parallel}^{OH} B\rangle_i$ are calculated. During the calculation process for beam-driven current, the additional pressure due to unthermalized fast ions p^f is also calculated. Since we employ a Monte-Carlo method to evaluate the birth profile of fast ions, the solution of $\langle j_{\parallel}^{BD} B\rangle_i$ involves Monte-Carlo noise. In order to reduce the error bar, we use an averaging technique in the iterative procedure. The beam driven current at the i^{th} iteration is given as

$$[\langle j_{\parallel}^{BD} B\rangle]_i = \frac{1}{i}\langle j_{\parallel}^{BD} B\rangle_i + \frac{i-1}{i}[\langle j_{\parallel}^{BD} B\rangle]_{i-1}$$

where $[X]_i$ denotes

$$\frac{1}{i}\sum_{j}^{i} X_j .$$

The same technique is adopted to the bootstrap current and the total plasma pressure

$$[\langle j_{\parallel}^{BS} B\rangle]_i = \frac{1}{i}\langle j_{\parallel}^{BS} B\rangle_i + \frac{i-1}{i}[\langle j_{\parallel}^{BS} B\rangle]_{i-1},$$

$$[p]_i = \frac{1}{i} p_i + \frac{i-1}{i}[p]_{i-1},$$

where $p = p^{th} + p^{\alpha} + p^{f}$. Then the total plasma current is given by

$$\langle j_{\parallel} B \rangle_i = [\langle j_{\parallel}^{BD} B \rangle]_i + [\langle j_{\parallel}^{BS} B \rangle]_i + \langle j_{\parallel}^{OH} B \rangle_i .$$

From these quantities and the old values of the toroidal field function F_i and $\langle B^2 \rangle_i$, we can compute the first derivative of the plasma pressure $[p]_i'$ and the quantity

$$F_i F_i' = -\mu_o (F_i^2 [p]_i' + F_i \langle j_{\parallel} B \rangle_i) / \langle B^2 \rangle_i .$$

and use them to solve the Grad-Shavranov equation

$$\Delta^* \psi_{i+1} = -\mu_o R^2 [p]_i' - F_i F_i' .$$

All components of plasma current are calculated again with the new MHD equilibrium. These calculation of plasma current and MHD equilibrium are executed iteratively until both results converge. With the converged values of $\langle j_{\parallel} B \rangle$, the respective toroidal current densities are given by

$$j_\varphi = \frac{1}{2\pi} \frac{F}{\langle B^2 \rangle} \left\langle \frac{1}{R^2} \right\rangle \langle j_{\parallel} B \rangle \frac{dV}{dA} ,$$

$$j_\varphi^\alpha = \frac{1}{2\pi} \frac{F}{\langle B^2 \rangle} \left\langle \frac{1}{R^2} \right\rangle \langle j_{\parallel}^\alpha B \rangle \frac{dV}{dA} \quad for \quad \alpha = 'OH', 'BD' \; and \; 'BS',$$

where A is the area of poloidal cross section within ψ. The above mentioned calculation procedure is summarized in Fig.1.

References

1. R.J. HAWRYLUK, *et al.*, in Plsama Physics and Controlled Nuclear Fusion Research 1986 (Proc. 11th Int. Conf. Kyoto 1986) Vol.1 IAEA Vienna (1987) 51.
2. T.C. SIMONEN, *et al.*, Phys. Rev. Lett. 61 (1988) 1720.
3. C.D. CHALLIS, *et al.*, Nucl. Fusion 29 (1988) 563.
4. J.E. STEVENS, *et al.*, Nucl. Fusion 28 (1988) 217.
5. K. USHIGUSA, *et al.*, Nucl. Fusion 29 (1989) 1052.
6. M.C. ZARANSTORFF, *et al.*, Phys. Rev. Lett. 60 (1988) 1306.
7. K. TANI, M. SUZUKI, S. YAMAMOTO and M. AZUMI, JAERI-M 88-042 (1988).
8. JT-60 Team JAERI-M 89-033 p.231

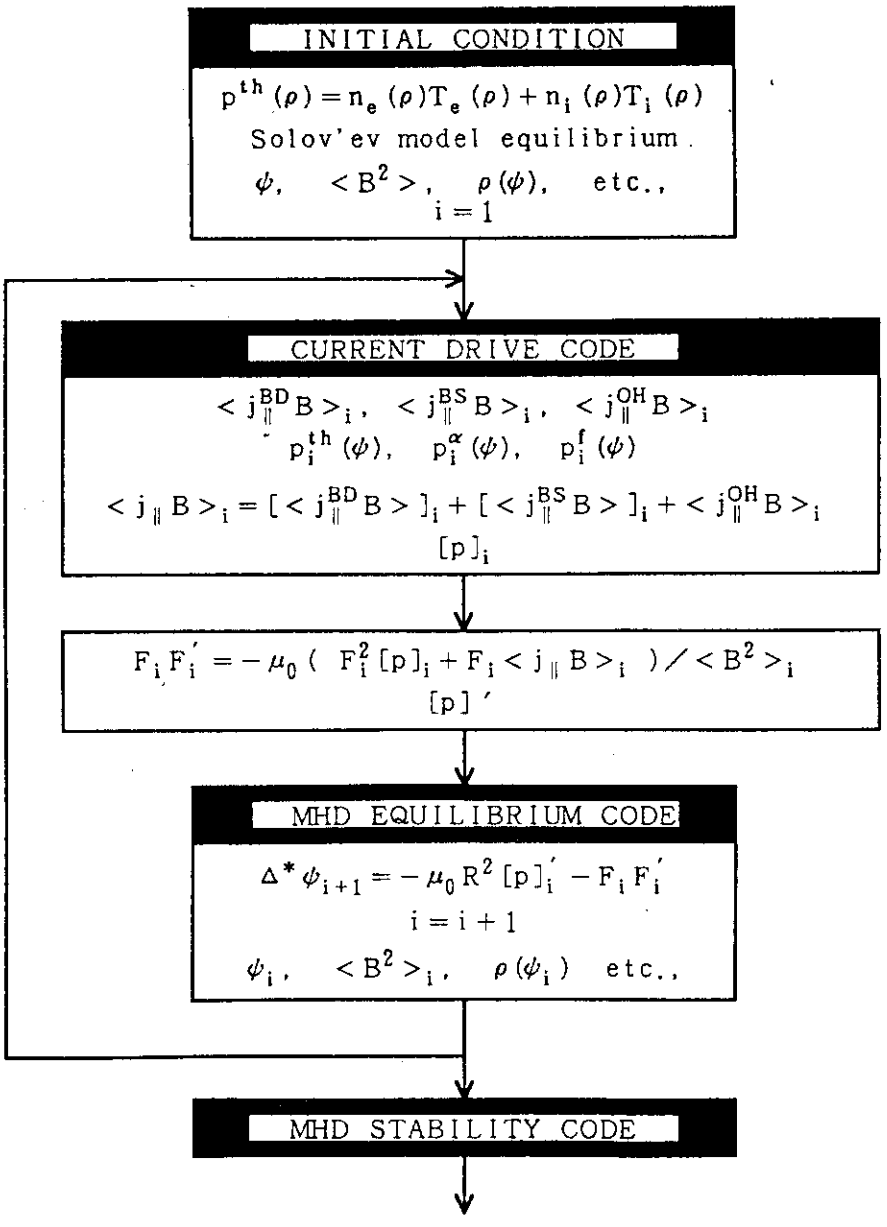

Fig. 1 Calculation procedure to obtain non-inductively driven currents which are consistent with MHD equilibrium.

7.3 ATTAINMENT OF THE DISCHARGES DOMINATED BY THE BOOTSTRAP CURRENT IN JT-60

M. KIKUCHI, M. AZUMI, K. TANI, S. TSUJI and S. ISHIDA

The neoclassical bootstrap current is studied in the JT-60 tokamak. It is shown that up to 80% of total plasma current is driven by the bootstrap current in extremely high β_p regime ($\beta_p = 3.2$) and the current drive product $I_{p(bootstrap)}\overline{n_e}R_p$ up to 4.4 x 10^{19} MAm^{-2} has been attained with the bootstrap current. The experimental resistive loop voltages are compared with the calculations using the neoclassical resistivity with and without the bootstrap current. The calculated resistive loop voltage is consistent with the neoclassical prediction including the bootstrap current.

1. INTRODUCTION

Non-inductive current drive is one of the most important subjects for the tokamak system. Since Bickerton pointed out the importance of the bootstrap current in a tokamak [1], nineteen years passed before its existence in a tokamak was confirmed. This was partly due to the difficulty of attaining low collisionality in a high β_p regime. Recent observation of the bootstrap current in TFTR [2] stimulated a renewed interest in the transport process parallel to the magnetic field. The JT-60 tokamak can produce highly collisionless plasmas by both ohmic heating and high power neutral beam heating up to 24MW. Since JT-60 is the only large tokamak device equipped with nearly perpendicular NBI heating, the plasma pressure can be increased without introducing significant beam driven current.

2. EXPERIMENTAL CONDITIONS

High power neutral beams are injected into these plasmas from the 14 upper and lower slant ports tilted in the toroidal direction. Eight units are in the coinjection direction and others are in the counter injection direction. The experimental and diagnostics set-up for lower side divertor is shown in Fig. 1. In order to validate stationary analysis, discharges with the inductive loop voltage $|V_I|$ (= $|0.25\ \mu_0 R_p I_p dl_i/dt|$),estimated from the diamagnetic β_p and the Shafranov Λ less than 0.1 V are chosen for the analysis. For the highest β_p discharge in the lower side divertor, the internal inductance li is evaluated for some time slices by the magnetic analysis to check its stationality. Sawtooth are observed in most of the discharges. The radial profile of the electron temperature is measured with the six-point Thomson scattering system. The radial profile of the electron density is also measured with this system calibrated with the FIR interferometer. The line-averaged effective ionic charge Z_{eff} is measured with the visible bremsstrahlung at λ = 5232.6 A. The measured Z_{eff} ranges from 1.1 to 4.0. The ion temperature profile is measured by the 8 channel charge-exchange-recombination spectroscopy (CXRS).

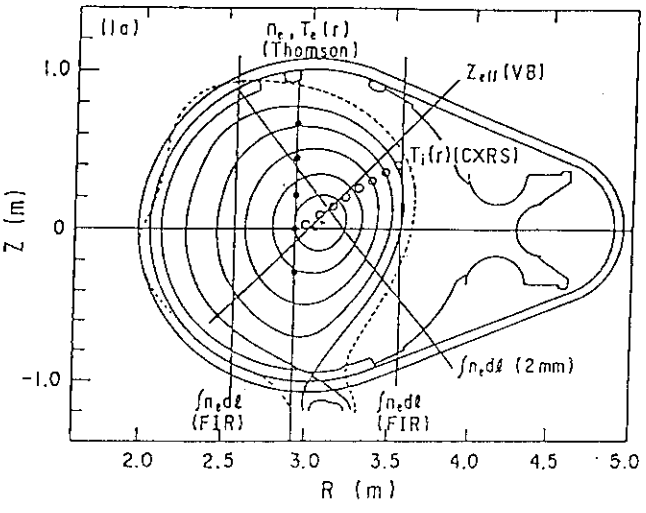

Fig. 1 The equilibrium configurations and the diagnostics set-up for the bootstrap current studyin the lower side diverter configuration.

3. COLLISIONALITY

The measured central electron temperature ranges from 2 - 5 keV and the ion temperature ranges from 3 - 12 keV. The plasma transport regime via classical coulomb collision is characterized by the collisionality parameter ν^* and is devided into three regimes, i.e., collisional (or MHD) regime ($\nu^* > (R/r)^{1.5}$), plateau regime ($1 < \nu^* < (R/r)^{1.5}$) and collisionless regime ($\nu^* < 1$). The bootstrap current becomes significant in a collisionless plasma. The electron and ion collisionality parameters (ν_e^* and ν_i^*) are defined by $Rq\nu_{ee}(R/r)^{1.5}/V_{Te}$ and $Rq\nu_{ii}(R/r)^{1.5}/V_{Ti}$, respectively where ν_{ee} and ν_{ii} are electron

and ion Braginskii collision times, respectively. The transport regime characterized by $0.1 < \nu^* < 1$ is called by banana-plateau transition regime in some cases. The electron and ion collisionalities are typically 0.2 and 0.05, respectively.
The ion is in the collisionless regime while the electron is in the banana-plateau transition regime. In this regime , particles can follow their orbits without frequent collision.

4. TYPICAL RESULTS

The time evolution of the discharge parameters are shown in Fig.2 for a typical high poloidal beta discharge. The difference between the diamagnetic βp ($=\beta_{p\perp}$) and the Shafranov Λ ($=\beta_{peq}+l_i/2$) generally decreases at the beginning of the beam pulse due to the change of the internal inductance and the development of the pressure anisotropy and becomes nearly stationary at about 1 second after the onset of the beam pulse. High β_p ($=3.2$) state is maintained for almost 1 s. The equilibrium poloidal beta β_{peq} and the internal inductance l_i are separated with the magnetics measurement. The equilibrium β_{peq} and the plasma internal inductance li at t = 5.0 s are 2.9 and 0.85, respectively. The equilibrium poloidal beta and the internal inductance at t = 5.5 s are 2.85 and 0.84, respectively. Thus the Poynting energy flux across the plasma surface is almost consumed by the resistive dissipation and the inductive correction is only 10%. The surface voltage calculated from the time variation of the surface flux calculated by the 6 filament magnetic fitting code stays constant at 60 mV during the period which is close to the loop voltage. The resistive loop voltage calculated using the neoclassical resistivity and measured T_e profile and Z_{eff} from the visible spectroscopy is 260mV which is extremely higher than the measurement. The measured profiles at t = 5.5 s are shown in Fig.3 . The ion temperature profile is fairly peaked near the center accompanied by the disappearance of the sawtooth activity unlike the usual L-mode. The calculated bootstrap current profile is peaked except near the center and the calculated internal inductance is 0.88 which is fairly good agreement with the measurement. The calculated current profile is shown in Fig.4. The calculated bootstrap current is 447 kA of the total plasma current of 481 kA while the bootstrap current estimated from the experimental resistive loop voltage and the

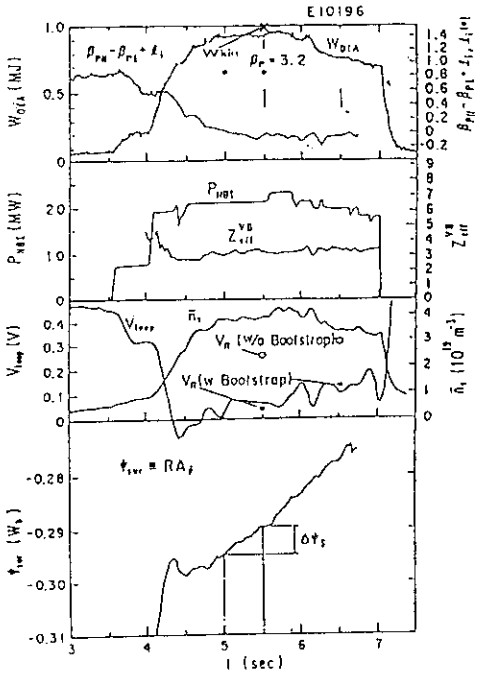

Fig. 2 Temporal evolution of the discharge parameters

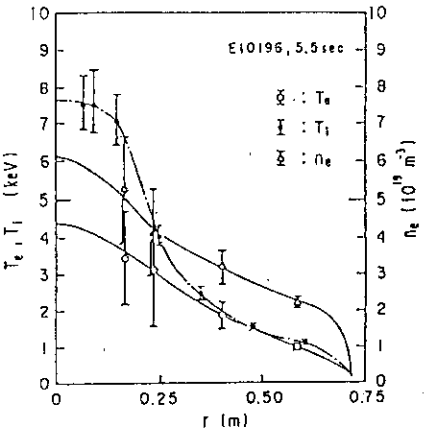

Fig. 3 The electron temperature, the ion temperature and the electron density profiles for a high βp discharge.

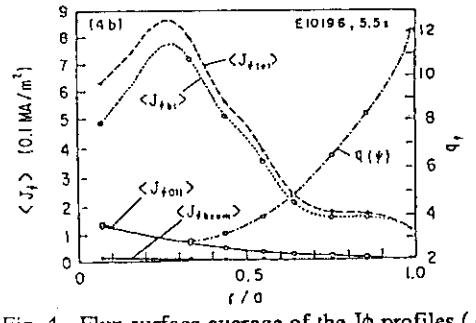

Fig. 4 Flux surface average of the Jϕ profiles (<Jϕ>) as a function of the minor radius, namely the total current, the bootstrap current, the ohmic current and the beam driven current, respectively.

neoclassical resistivity is 370kA (77%). The current drive product $I_p(\text{bootstrap})\overline{n_e}R_p$ in this discharge is 4.4 x 10^{19} MAm^{-2} with the bootstrap current

5. POLOIDAL BETA DEPENDENCE

The fraction of the bootstrap current to the total plasma current is a function of the inverse aspect ratio ε and the poloidal beta β_p. Most important dependence expected from the theory is the proportionality to β_p. In order to confirm the existence of the bootstrap current, we have checked the proportionality of the measured driven current to the poloidal beta β_p. The resistive loop voltage is expressed by, $V_R=\Omega_{NC}(I_p-I_{bootstrap})$ where Ω_{NC} i s the plasma resistance expected from the neoclassical theory which is found to be effective in JT-60. The experimental study of the plasma resistance is shown in section 7.5. The experimental comparison of the resistive voltage with the theories during the neutral beam heating is shown in Figure 5. As is clear from the figure, the experimental loop voltage is quite consistent with the neoclassical prediction including bootstrap current. Defining the neoclassical loop voltage V_R^{NC} by $\Omega_{NC}I_p$, the normalized resistive loop voltage decreases with increasing bootstrap current as $V_R/V_R(NC) = 1-I_{bootstrap}/I_p$. Fig.6 shows the ratios of the measured resistive loop voltage and the neoclassical calculation including the bootstrap current to the neoclassical calculation without the bootstrap current as a function of the poloidal beta β_p. If we take into account that $I_{bootstrap} \sim \beta_p$, the normalized voltage must decrease with increasing poloidal beta β_p. The experimental normalized voltage decreases with increasing β_p which is consistent with the bootstrap current theory. The normalized resistive voltage is also calculated using the measured T and n profiles which also gives good agreement the experimental result. The required β_p to realize full current drive with the bootstrap current is fairly large ($\beta_p \sim 4$) due to the inefficient bootstrap current drive by the fast ion.

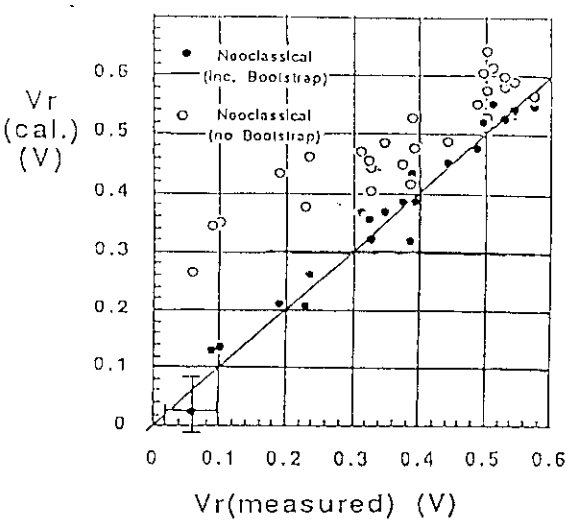

Fig. 5 Comparison of measured and calculated resistive loop voltages open circle ; using neoclassical resistivity without bootstrap current closed circle; using neoclassical resistivity with bootstrap current

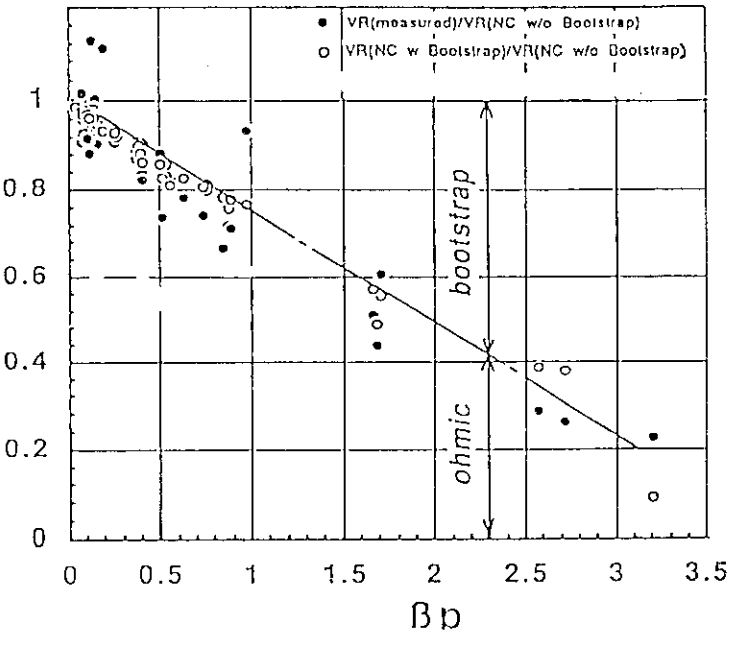

Fig. 6 A comparison of the ratios of the resistive loop voltages as a function of the diamagnetic β_p. The closed circle (o) is the ratio of the measured resistive loop voltage to the calculated resistive loop voltage using the neoclassical resistivity without the bootstrap current (V_{RNC}). The open circle (o) is the ratio of the calculated neoclassical resistive loop voltage including the bootstrap current to the V_{RNC} .

6. DISCUSSION AND CONCLUSION

The neoclassical bootstrap current is investigated for discharges with perpendicular neutral injection in the JT-60 tokamak. The experimental comparison of the resistive loop voltage with calculations using the neoclassical resistivity with and without the bootstrap current demonstrates the

existence of the bootstrap current. Up to 80 % current-drive with the bootstrap current is attained for high β_p discharge ($\beta_p = 3.2$). The comparison has been made for a wide range of plasma parameters $I_p = 0.5$-2.0 MA , $\beta_p = 0.1$-3.2. The driven plasma current reaches up to 400kA with the average plasma density of 3.8×10^{19} m^{-3}. The current drive product up to 4.4×10^{19}MA/m^2 are attained.

However, it seems surprising to us to observe such a classical behaviour for the "diffusion-driven" current. It may be very instructive to enjoy a simplified discussion on the origin of the bootstrap current in a tokamak. The momentum balance equation along the magnetic field line for the electron is given by,

$$0 = \vec{B}.(-en_e(\vec{E}+\vec{V}x\vec{B})-\nabla P_e-\nabla.\vec{\Pi}_e+\vec{F_{1e}}) \qquad (1)$$

Flux surface average of equation (1) gives

$$<\vec{B}.\vec{F_{1e}}> = <e\vec{B}.\vec{E}> + <\vec{B}.\nabla.\vec{\Pi}_e> \qquad (2)$$

where, left hand side represents the electron-ion friction force parallel to the magnetic field. The first term of the right hand side represents the electric field force and the second term represents the parallel viscous force driven by the parallel drift of the trapped particles. The parallel viscous force originates from the radial pressure gradient of the trapped particles. The large radial excursion of the trapped particle (or banana width) produces the strong parallel drift velocity of $u_{//e} = \Delta_t v_{//}\,(dn/dr)/n$ (Δ_t; banana width) similar to the diamagnetic drift. This parallel drift of the trapped particle produces the net parallel force on the passing electrons through the electron-electron collision. This viscous force is the primary driving force of the bootstrap current and the " diffusion " is not essential but the existence of the pressure gradient is essential. The parallel viscous and friction forces are obtained by the kinetic equation as follows,

$$<\vec{B}.\nabla.\vec{\Pi}_e> = <(P_{//e}-P_{\perp e})(\vec{b}.\nabla)B> = \frac{n_e m_e}{\tau_{ee}}<B^2>\mu_1^{ee}u_{\theta e} \qquad (3)$$

$$<\vec{B}.\vec{F}_{1e}> = -\frac{n_e m_e}{\tau_{ee}}f_{11}^e<B>(u_{//e}-u_{//i}) \qquad (4)$$

where $u_{\theta e}$, μ_1^{ee} and f_{11}^e are normalized poloidal flow, electron viscosity coefficient (= 1.53 f_T/f_c, f_T; trapped electron fraction) and friction coefficient (= 1.0), respectively. The poloidal flow is a combination of the diamagnetic flow and the perpendicular projection of the parallel flow as $Bu_{\theta e} = u_{//e}-\frac{I}{e}T_e(\ln P_e)'$. Substitution of the equation (3) and (4) into equation (2) gives a relation of the parallel electron flow to the diamagnetic (thermodynamic) force and electric force. The generalized ohm's law is thus obtained as follows,

$$J_{//e} = -en_e u_{//e} = -en_e[\frac{\mu_1^{ee}}{1+\mu_1^{ee}}\frac{I}{e}T_e(\ln P_e)' - \frac{e\tau_{ee}}{m_e(1+\mu_1^{ee})}E_{//}] \qquad (5)$$

The first term of the right hand side of equation (5) is the bootstrap current driven by the pressure gradient and is independent of collision frequency because both viscous and friction forces are proportional to the collision frequency (see (3),(4)) and the bootstrap current converges to a finite value in the collisionless limit. On the other hand, the ohmic current is proportional to the electron collision time and the electrical conductivity is modified from the spitzer conductivity as,

$$\sigma = e^2 n_e \tau_{ee}/(m_e(1+\mu_1^{ee})) \qquad (6)$$

Here, it should be noted that the viscosity coefficient μ_1^{ee} appears for both bootstrap current term and the neoclassical resistivity term. Thus it is natural to expect the bootstrap current if the viscosity works on the electrical conductivity in a tokamak. From such a point of view, it may be natural to get a classical bootstrap current when the parallel electrical conductivity follows the classical value (instability induced anomalous resistivity is negligibly small).

REFERENCES

[1] BICKERTON, R. J., CONNOR, J.W., TAYLOR, J. B. , Nat. Phys. Sci. 229 (1971) 110. ; GALEEV, A. A., Sov. Phys.- JETP 32 (1971) 752.
[2] ZARNSTORFF, M. C., BELL, M.G.,BITTER, et al., Phys. Rev. Lett. 60 (1988) 1306.
[3] BICKERTON, R.J. and the JET team, IAEA-CN-50/A-I-3 (1989,Nice).
[4] KIKUCHI,M., JAERI-M 89-164 , to be published in Nuclear Fusion.
[5] KIKUCHI, M., ANDO, T., ARAKI, M., et al., Proc. 15-th Symp. Fusion Tech. vol.15(1989)287.

7.4 CURRENT SUSTAIN WITH THE BOOTSTRAP CURRENT

M. KIKUCHI, K. USHIGUSA, M. NAGAMI and M. AZUMI

The current sustain with the bootstrap current has been attempted in high βp discharge by keeping the ohmic circuit current constant at the onset of the high power beam heating. An enhancement of the L/R time constant has been observed much larger than those expected from the electrical conductivity. A comparison with the ohmic case (hence low βp) clearly demonstrates the existence of the non-inductive current in high βp regime. This enhancement of the L/R time constant is close to that expected from the neoclassical theory including bootstrap current.

1. CURRENT SUSTAIN EXPERIMENT

In order to study the effect of the bootstrap current on the plasma current sustainment, the feedback control of the plasma current with the ohmic circuit is shut off during the high power neutral beam heating. The decay of the plasma current represents the L/R time constant due to ohmic dissipation. Fig. 1 shows a comparison of the decay of the plasma current for ohmic and neutral beam heated discharges in which OH circuit is shut off at ~4 second. The plasma current decays following the L/R time constant. In the low β_p OH discharges, the plasma current decays with the L/R time constant $\tau \sim 6.2$ seconds. When high power neutral beam power is injected into the plasma, plasma pressure is increased and the decay of the plasma current is significantly suppressed in such a high β_p discharge (the decay time of 27 second at t = 7 second).

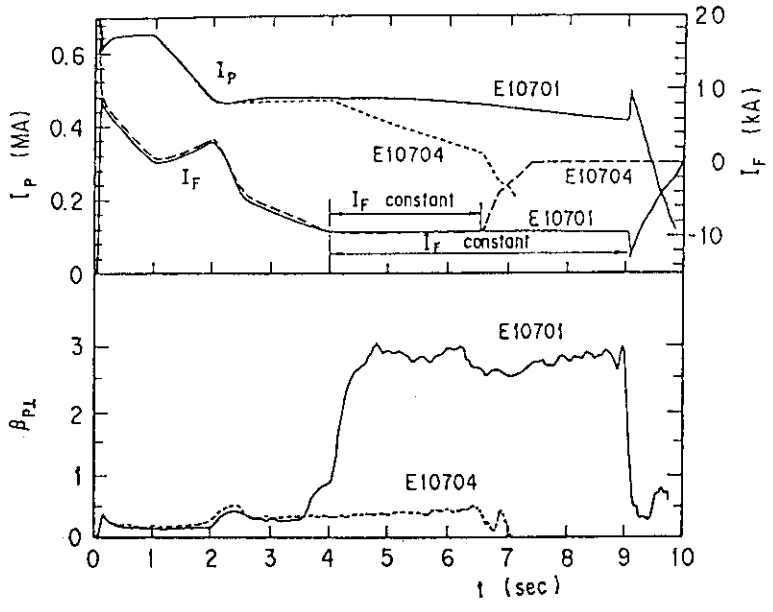

Fig. 1 The current decay characteristics of the ohmic and high βp discharges. The feedback control of the plasma current is terminated at 4 second. The plasma current decays following the L/R decay time.

Fig. 2 shows a comparison of the plasma equilibrium and the temperature profiles for ohmic and high β_p beam heated discharges. The comparison of the plasma resistance without bootstrap current predicts 1.75 times difference in the L/R decay time (E10701,7s and E10704,4.6s) which is fairly different from the measurement (L/R decay time ratio of 4). The current profile is calculated by using the measured T_e, n_e and T_i profiles under the assumption of uniform electric field although the discharges are not stationary. The bootstrap current is expected to increase L/R time constant significantly. The expected L/R time constant is expressed by,

$$\tau = \frac{L_p}{2R_p\left(1-\frac{I_{p(\text{bootstrap})}}{I_p}\right)} \int dr^2/\eta^{NC} \qquad (1)$$

The enhancement factor $(1-I_p(\text{bootstrap})/I_p)$ of the L/R time constant comes from the passive current drive with the bootstrap current. For the ohmic discharge (low βp discharge; E10704,4.6 sec), the expected L/R decay time using equ. (1) is 6.2 second while measured decay time is 6.8 second. For the high βp discharge (E10701, 7sec, βp=2.53) , the L/R decay time is significantly affected by the bootstrap current.

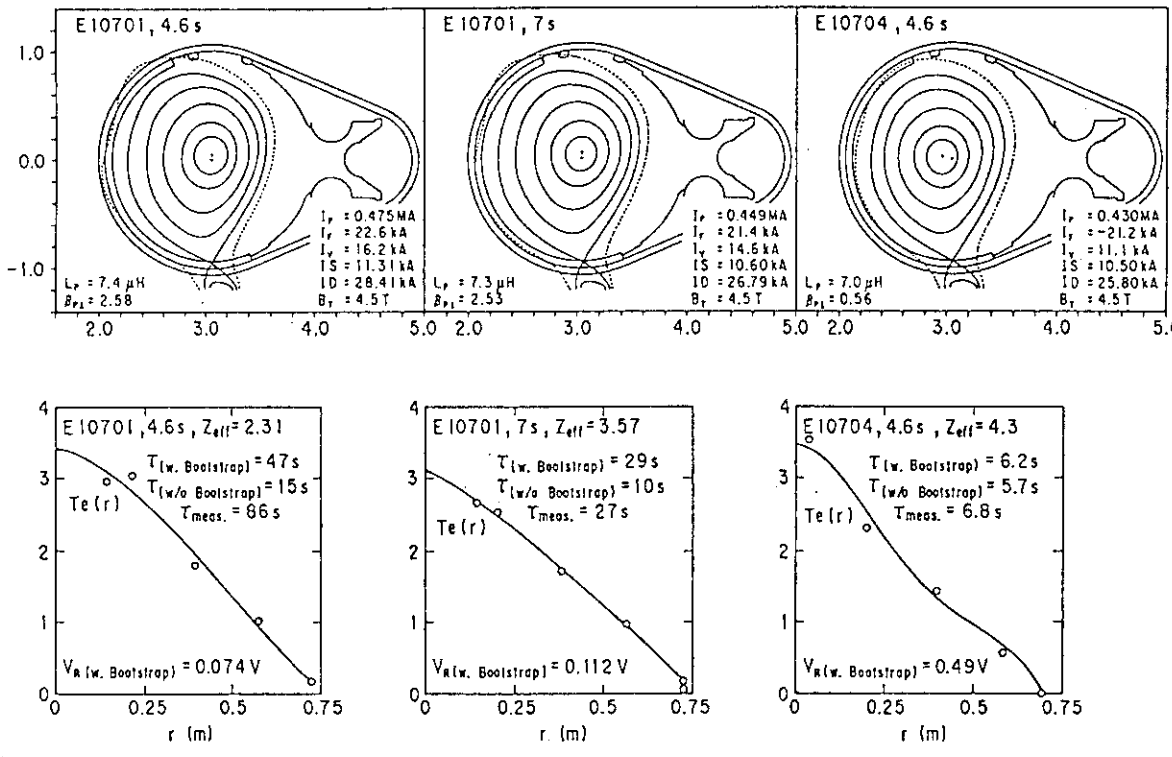

Fig. 2 The equilibrium and the temperaure profiles for ohmic and high βp discharges. The measured current decay time τ (= L_p/R) is compared with the calculations with and without the bootstrap current. The decay time is consistent with the calculation including the bootstrap current except the case of E10701,4.6s.

The bootstrap current profile is calculated by using the measured T_e, n_e and T_i profiles. The calculation is shown in Figure 3 together with the pressure profiles and ballooning stability analysis. The calculated bootstrap current is 2/3 times the total plasma current for the high βp discharge (E10701,7sec,βp=2.53). This large bootstrap current fraction indicates 3 times enlargement of the L/R decay time. The L/R decay time without bootstrap current is only 10 second while L/R decay time including bootstrap current is 29 second. The experimental result (L/R decay time of 27 second) is fairly close to the theoretical prediction (equation 1) including bootstrap current.

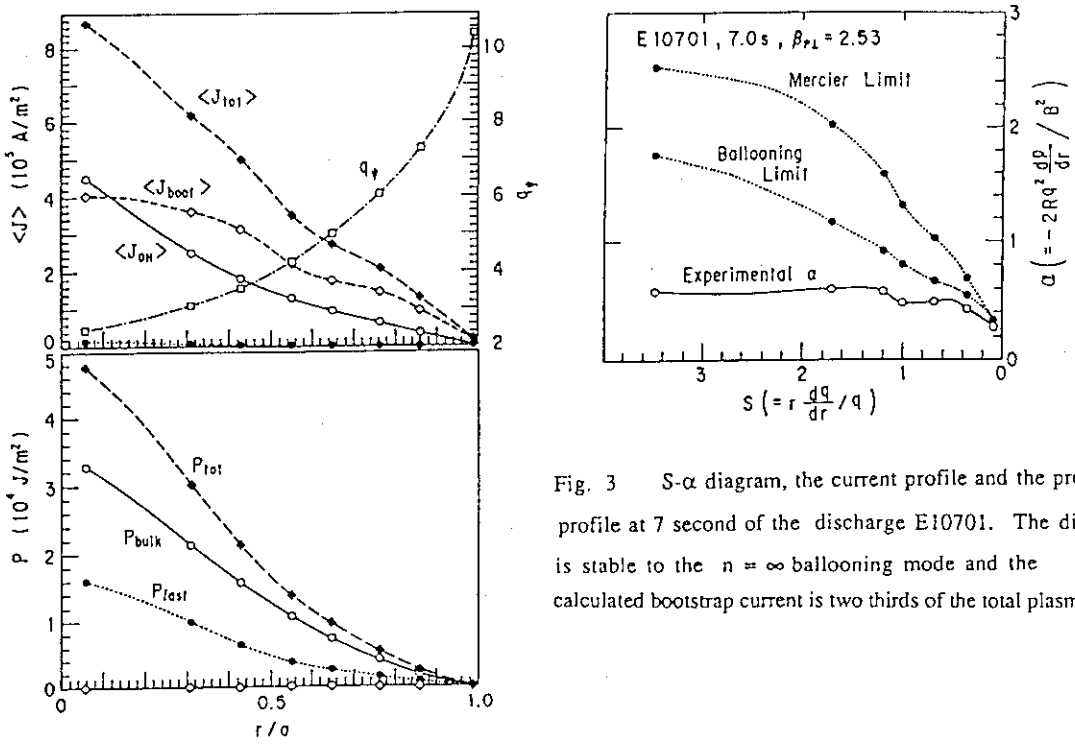

Fig. 3 S-α diagram, the current profile and the pressure profile at 7 second of the discharge E10701. The discharge is stable to the n = ∞ ballooning mode and the calculated bootstrap current is two thirds of the total plasma current.

2. CONCLUSION

The current sustain with the bootstrap current has been attempted to demonstrate the existence of the bootstrap current in a tokamak. The experimental comparison of the L/R decay time between high and low βp discharges clearly supports the existence of the non-inductive current close to that expected from the neoclassical theory (bootstrap current).

7.5 ELECTRICAL CONDUCTIVITY OF THE JT-60 TOKAMAK IN THE COLLISIONLESS REGIME

M. KIKUCHI, H. KUBO and M. AZUMI

A careful investigation of the plasma conductivity has been conducted in the JT-60 tokamak in the collisionless regime. The resulting electrical conductivity is found to agree with that expected from the neoclassical theory.

1. INTRODUCTION

The plasma conductivity in the collisionless regime is strongly influenced by the existence of the trapped particles. However the experimental investigation in the medium size tokamaks [1] indicated some departures from the electrical conductivity of the neoclassical theory. Even in the JT-60 tokamak, preliminary investigation gave Z_{eff} (calculated from neoclassical conductivity and measured T_e and V_{loop}) < 1.0 in high density ohmic discharges[2]. Here we have examined fairly steady ohmic discharges in more collisionless regime with improved diagnostics capability. The theoretical electrical conductivity is given in the following section. The experimental and diagnostic conditions are given in section 3. The experimental comparison between the theoretical resistive loop voltage and the measured resistive loop voltage is given in section 4. Current profile is discussed between those expected from the neoclassical theory and from simple Spitzer resistivity in section 5. The conclusion is given in section 6.

2. ELECTRICAL CONDUCTIVITY OF A TOKAMAK

The neoclassical conductivity relates the parallel current density to the electric field averaged over a magnetic surface; $\langle\langle j_{//}.B\rangle = \sigma_{//}\langle\vec{E}.\vec{B}\rangle$ where $\langle A\rangle$ denotes the flux surface average of A. The parallel electrical conductivity σ can be obtained either by solving the parallel momentum balance equation[3] or using the approximate formula. An analytic formula is given by Hirshman, Hawryluk and Birge [4] which gives fairly good agreement with numerical results as follows,

$$\sigma_{//}=\sigma_{sp}\left(1-\frac{f_T}{1+\xi\nu_{*e}}\right)\left(1-\frac{C_R(Z_{eff})f_T}{1+\xi\nu_{*e}}\right) \qquad (1)$$

$$Z_{eff}=\sum_{i\neq e}\frac{n_i Z_i^2}{n_e},\quad \sigma_{sp}=\frac{n_e e^2}{G(Z_{eff})m_e\nu_{ee}},\quad G(z)=\frac{z(2.67+z)}{3.4(1.13+z)},\quad \nu_{ee}=\frac{16\sqrt{\pi}n_e e^4\ln\Lambda}{3m_e^2\left(\frac{2T_e}{m_e}\right)^{1.5}},$$

$$f_T=1-\frac{(1-\varepsilon)^2}{\sqrt{1-\varepsilon^2}(1+1.46\sqrt{\varepsilon})},\quad C_R(z)=\frac{0.56(3-Z)}{Z(3+Z)},\quad \xi(z)=0.58+0.20Z,\quad \nu_{*e}=\frac{Rq\nu_{ee}}{\varepsilon^{1.5}\sqrt{T_e/m_e}}$$

This approximate formula gives slightly (~5%) higher resistivity in the collisionless regime ν_{*e} <1.0 as is shown in Fig.2 of the ref.[4].

The coulomb logarithm $\ln\Lambda$ for the electron-proton collision with Te = Ti including impurity effect in the Debye length is given by[5] with intrinsic uncertainty up to 5%,

$$\ln\Lambda=8.724+\ln\frac{T_e(ev)}{\sqrt{(Z_{eff}+1)n_e(10^{20}m^{-3})}} \qquad (2)$$

This trapped particle correction is related to the parallel viscosity (see section 7.3 eq.6). Therefore the experimental confirmation of the neoclassical resistivity is equivalent to the confirmation of the neoclassical parallel viscosity. The trapped electron fraction f_T is shown as a function of the inverse aspect ratio in Figure 1.

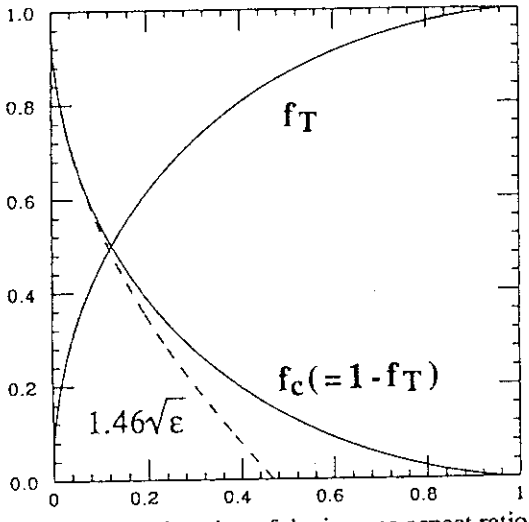

Fig. 1 Trapped particle fraction as a function of the inverse aspect ratio

3. EXPERIMENTAL AND DIAGNOSTIC CONDITIONS

Two types of experimental approaches are used to study neoclassical effect on the plasma conductivity in JT-60. One is to compare the resistive loop voltage between experiment and theory. The neoclassical correction gives roughly two times larger loop voltage compared with that calculated by simple Spitzer conductivity. Another is to see current profile (or the location of q=1 surface compared with that deduced from sawtooth) and to compare calculated internal inductance with the measurement.

Typical experimental configuration and the diagnostics setup is shown in Fig.2. The electron temperature profile is measured with the Thomson scattering system. A small temperature correction up to 3% has been made to compensate the darkening of the viewing window. The line averaged Z_{eff} has been measured with the visible bremmstrahlung at λ = 5232.6 ± 5.9 Å. By a multichannel spectrometer, CIII 5244.7Å was identified as the nearest line to the wavelength band, and it was confirmed that the bremsstrahlung signal did not affected by any line emission. A schematic diagram of the Z_{eff} measurement system is given in Fig.3. The absolute calibration of the visible bremmstrahlung has been made by using a tungsten ribbon lamp calibrated at the National Institute of Standards and Technology, USA. Because the reflectance of a fine graphite surface is less than 20 %, the reflectance of the real surface of the graphite tile is estimated to be much less than 20%. Therefore, the effect of signal reflected by the first wall would not be significant.

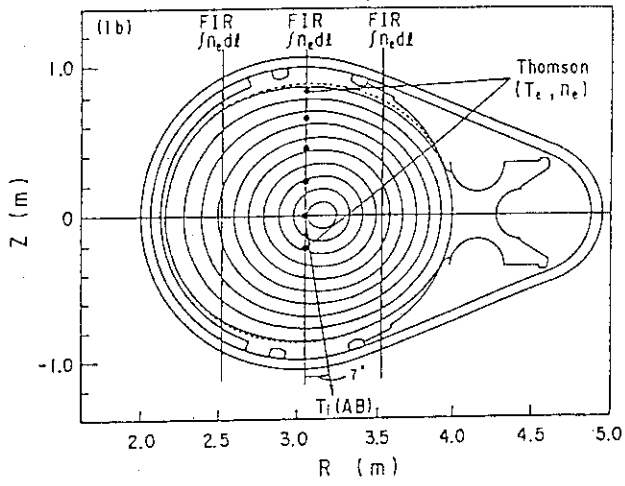

Fig. 2 Typical equilibrium configuration and the diagnostic setup

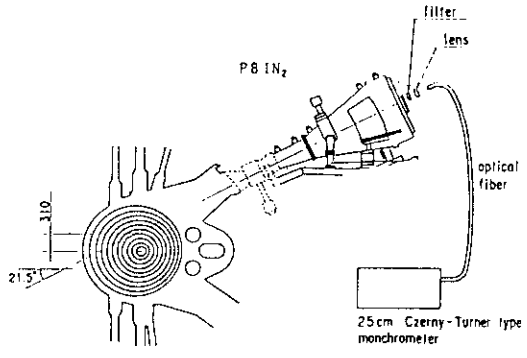

Fig. 3 Schematic diagram of the Z_{eff} measurement system

4.EXPERIMENTAL COMPARISON OF RESISTIVE VOLTAGE

The time evolution of the discharge parameters I_p, n_e,V_{loop} , Shafranov Λ, β_p and l_i are shown in Fig.4 for a typical low β_p ohmic discharge. The discharge becomes fairly stational at the time shown by the arrow. The experimental resistive loop voltage is evaluated from the loop voltage measurement and the dl_i/dt (calculated from β_{pdia} and Λ). The equilibrium flux surface is shown in Fig.2. Figure 5 shows the measured T_e and n_e profiles together with the electron

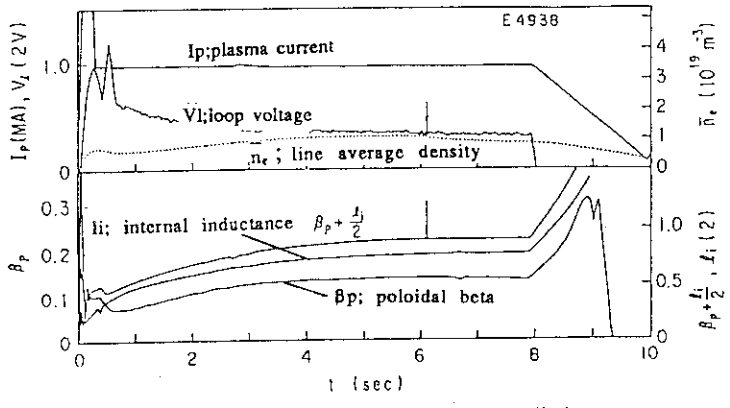

Fig. 4 Time evolution of the low density ohmic discharge

collisionality parameter. The electron collisionality parameter ν_e^* is very low (<0.1) but the bootstrap current of this discharge is very small due to low poloidal beta value (β_p = 0.14). The resistive loop voltage V_R is calculated using the stationary condition E_ϕ (r) = constant as follows,

$$V_R = 2R_p I_p^{OH} / \int dr^2/\eta^{NC} \quad (1)$$

where $I_p^{OH} = I_p - I_{bt}$ and I_{bt} is the total neoclassical bootstrap current. This resistive loop voltage is calculated using the measured T_e, n_e profiles and the line averaged Z_{eff}. Discharges are restricted to low βp ohmic discharges where the bootstrap current is negligibly small. We also restrict our analysis to the discharges where the electron collisionality parameter ν_e^* ranges from 0.02 to 0.1. The resistive loop voltage in the ohmic discharges ranges from 0.6 V to 1.0 V. The restriction of the discharges to the inductive loop voltage $|V_I| < 0.1$ V validates the stationary analysis. When we neglect the trapped electron correction to the plasma resistivity (Spitzer resistivity), the calculated resistive loop voltage is fairly lower than the measurement. Thus the experimental results seem to support the existence of the trapped electron correction to the plasma resistivity. The comparison of the measured resistive loop voltage and the calculations for various shots are shown in Fig.6. As is clear from the figure, the resistive loop voltage calculated without the trapped particle correction (shown by the symbol Δ) is significantly lower than the measurement in contrast to the previous analysis[2] where more collisional high density ohmic discharges are analyzed and the bootstrap current is not negligible for the resistivity study.

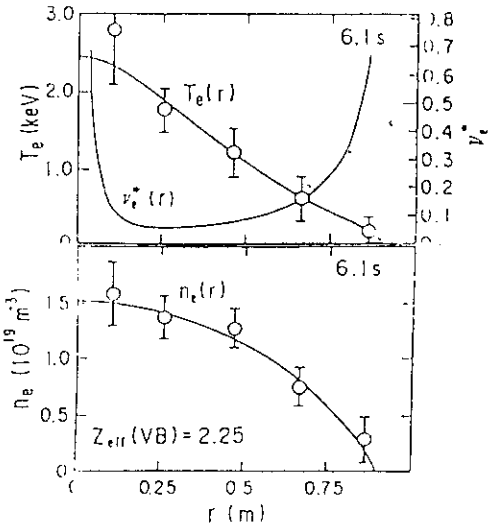

Fig. 5 Typical temperature and density profile measurement The electron collisionality parameter is also shown.

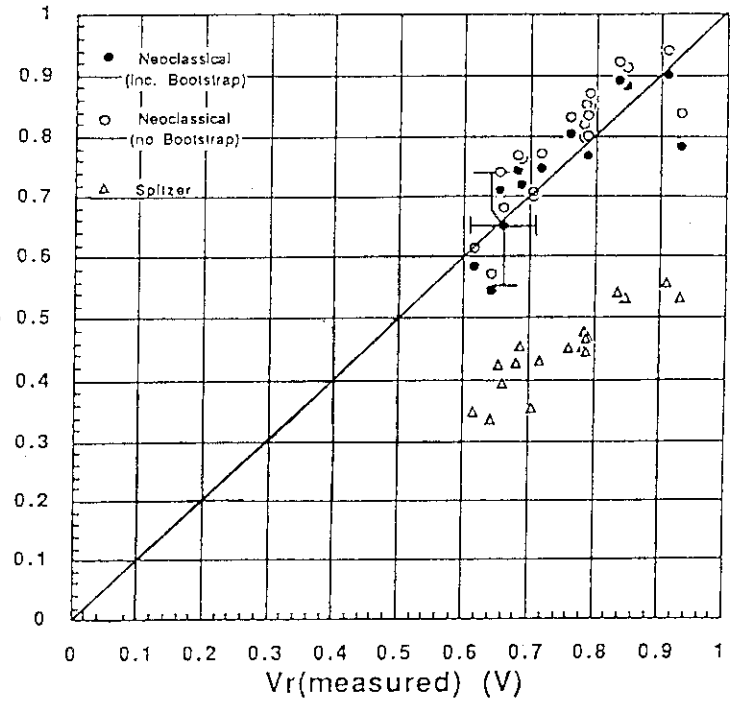

Fig. 6 Comparison of the resistive loop voltage between theory and experiment
open circle ; resistive voltage calculated with neoclassical resistivity without bootstrap current
closed circle; resistive voltage calculated with neoclassical resistivity including bootstrap current
open triangle; resistive loop voltage calculated with simple Spitzer resistivity

5.CURRENT PROFILE AND q=1 SURFACE

There are many arguments on the temperature profile shape concerning so-called temperature profile consistency. Waltz [6] discussed the relation between temperature profile and current profile using the Spitzer resistivity with the assumption of q(0)=1. He proposed a lower and upper bounds for the temperature peakedness parameter $q_a^{2/3} < T_{e0}/\langle T_e \rangle < q_a$. However, as is clear from the experiments, the existence of the trapped particle correction to the electrical conductivity completely denies such an argument. Figure 7 shows the safety factor dependence of the temperature profile peakedness parameter $T_{e0}/\langle T_e \rangle$ as a function of the safety factor q_a. The upper and lower bounds proposed by Waltz are also shown in the figure. The electron temperature peakedness deviates significantly in high q regime. Figure 8 shows the current profiles calculated with and without trapped particle correction to the electrical conductivity. As is clear from the figure, the central safety factor q(0) calculated without trapped particle correction becomes more than 1 which contradicts with the experimental observation of the sawtooth acticity.

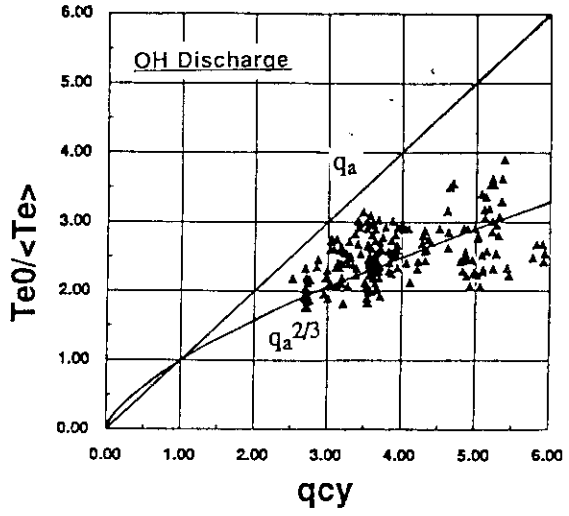

Fig. 7 Temperature peakedness parameter as a function of cylindrical safety factor

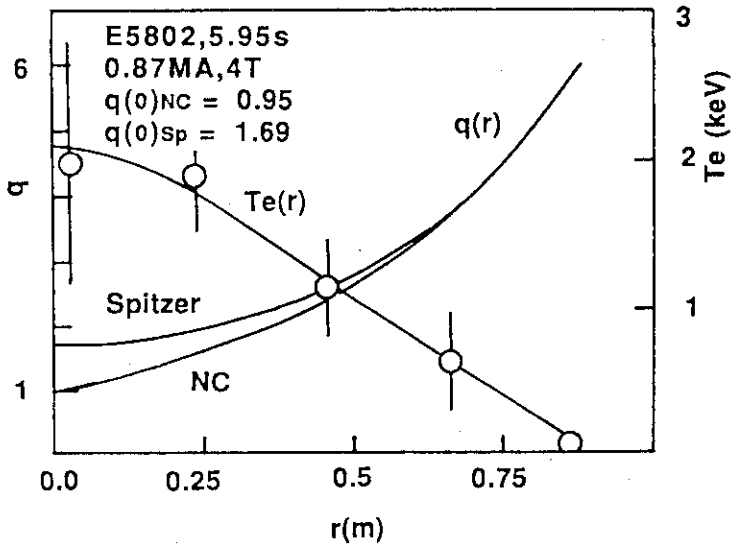

Fig. 8 Current profiles calculated with and without trapped electron correction to the electrical conductivity

6.CONCLUSION

The electrical conductivity is examined in JT-60 to see whether the trapped electron correction to the plasma conductivity exists or not. The experimental resistive loop voltage in low βp regime agrees with that calculated using the neoclassical conductivity. The use of the neoclassical resistivity is consistent with the observation of the sawtooth activity in high q regime. These experimental evidences clearly supports the existence of the trapped electron correction (or viscosity coefficient) to the plasma conductivity.

REFERENCES

[1] EJIMA,S.,PETRIE,T.W.,RIVIERE,A.C., et al., Nuclear Fusion 22(1982) 1627
[2] HIRAYAMA,T.,SHIMIZU,K.,SHIRAI,H., et al., Proc. 15-th Europ. Conf. Plasma Phys. Contr. Fusion and Plasma Physics 3(1988)1065
[3] KUKUCHI,M., AZUMI,M.,TANI,K.,TSUJI,S.,KUBO,H., Nuclear Fusion30(1990)343.
[4] HIRSHMAN,S.P.HAWRYLUK,R.,J.,BIRGE,B, Nuclear Fusion 17(1977)611.
[5] SIVUKHIN,D.V., in Reviews of Plasma Physics 4 page109.
[6] WALTZ,R.E., S.K.WONG,GREEN,J.M.,DOMINGUEZ,R.R., Nucl. Fusion26(1986)1729.

8. Transport Analysis

8.1 Ion Temperature Profile Measurement

Y. Koide, A. Sakasai

1. Introduction

Charge exchange recombination spectroscopy (CXRS) has been put into operation in June, 1988. Its hardware and data analysis algorithms are described in ref [1]. This paper deals with the reliability of deduced ion temperature and toroidal rotation velocity, which must be took into account in using these data. Some problems left to be solved are also presented.

2. Evaluation of excess impurity temperature

Our ion temperature measurement by CXRS is based on the Doppler broadening of carbon line because of its enough intensity. So we must evaluate the preferential heating of impurity (scaling as Z^2/m_z). Deviation from a Maxwellian in the impurity velocity distribution might also be important especially in the case of high injection power into low density plasma. The following discussion is somewhat preliminary based on the stationary solution of Fokker-Plank equation with isotropic background distribution function,

$$f_i = f_i^0 + f_b$$

, where f_i^0 is Maxwellian bulk and f_b is the beam part. Generally, distribution function of impurity is determined by took into account collisions between protons, electrons and impurities themselves as follows;

$$\frac{\partial f_z}{\partial t} = L_{zi}[f_z] + L_{zz}[f_z] + L_{ze}[f_z]$$

. L_{zi} and L_{zz} are collision operators describing collisions of impurities with ions and electrons, respectively. L_{ze} is for self-collisions of impurities. Here we assume that collisions with electrons and self-collisions are negligible for the simplicity. The first neglect is not so bad approximation because impurity energy exchange between electron is much smaller than that with proton (scaling as $\sqrt{m_e/m_z}$). The next neglect is valid if the following condition is realized:

$$\frac{n_z}{n_i} \leq \frac{1}{Z^2}\sqrt{\frac{128 m_i}{m_z}}$$

In usual experiments under full power injection, $Z_{eff} \geq 2$ (Cleanest plasma is realized by titanium flush). So the neglect of $L_{ze}[f_z]$ is over-neglection in

usual case. Including this effect and analysis for particular discharges are now in progress. Here we show a result of present calculation for the following parameters;

$n_e=6\times10^{19}$ m^{-3}
$T_e=5$ keV
$T_i=5$ keV
$Z_{eff}=2$
$P_{NBI}=1.5$MW/m^3
$E_{beam}=70$ keV

The resulting distorted distribution function of carbon ion is shown in Fig.1. Maxellian distribution with T_i of proton temperature is also plotted in the same figure. In this case, distortion of f_z gives rise to the over-estimation of T_i by ~8 %. As mentioned before, we neglected the self-collisions of impurities. If we include this effect, excess temperature will became smaller because slow speed of impurity tends to pull back to from the drag due to fast protons. So our present result gives the least upper bound of excess temperature.

3. Beam modulation for background estimation

Measured signal consists of charge-exchange induced component and background component, and these must be separately estimated. As shown in Fig. 2, modulation in #14 unit is applied for background estimation. The validity of this method depends on the assumption that background spectrum can be linearly interpolated from the two background spectra at the beginning- and the end-phases of injection. In usual cases, this approximation seems to be satisfied, which is confirmed from the result that signal drops to the interpolated level when diagnostic beam (#14 unit) instantaneously breaks down. Another evidence supporting its justification is that the CXR spectra of NeX line, which is almost free from background component, shows the similar deduced ion temperature (Fig.3). In the case with abrupt increase in background signal, which may be due to carbon influx or etc..., ion temperature will be under-estimated.

4. Cross-check of deduced Ti with other systems

JT-60 has two other ion temperature diagnostics, i.e. crystal spectrometer (T_iXXI Kα line is usually used.) and active beam scattering. Fig. 4 shows the cross-check of (a)T_i^{CXR} with T_i^{XXI} and (b)T_i^{AB}. In these figures, three of these show good agreement. We must check the effect of high energy

ion,as mentioned in the previous section, and chord-integral measurement.

5. Toroidal rotation velocity

Because the optics looks at the diagnostic beam (#14 unit) almost tangentially, toroidal rotation is deduced from the Doppler shift of the CXR-induced spectrum. The basis of rotation velocity is determined from the central wavelength of ohmic spectrum on the assumption that the line emission in the ohmic phase,which comes from the very edge region of plasma, is not Doppler-shifted. This assumption is checked by the comparison of location of ohmic spectrum in changing the direction of plasma current. These two cases are corresponding to the change from co- to counter-injection. The maximum difference in velocity,among 8 spatial chs., deduced from the two cases is $<2\times10^4$ m/s So the ambiguity may be within this range.

6. Problems in present CXRS measurement

Time resolution is restricted to be > 50 msec due to insufficient S/N ratio.

Necessity of beam modulation means the difficulty in measuring fast phenomena.

Beam attenuation is severe in high density plasma ($n_e(0) > 10^{20}$ m^{-3}).

Sufficient clearance (~8 cm) must be kept between plasma boundary and first wall on lower field side; otherwise deduced T_i is low (The reason for it is not clear at present.).

Reference

[1] Koide, Y., Sakasai, A., et al., Rep. JAERI-M 89-033, Japan Atomic Energy Research Institute, Ibaraki (1982) 243.

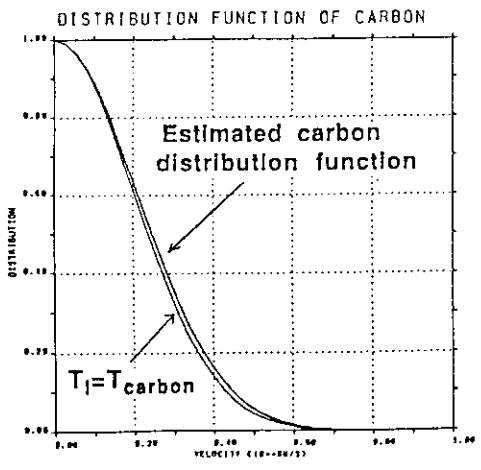

Fig. 1 Calculated carbon distribution function. The effect of high energy proton works on the expansion for it. So deduced temperature is little higher than proton temperature. The self-collisions of impurities are not included. The following parameters are assumed; $n_e=6\times10^{19}$ m^{-3}, $T_e=5$ *keV*, $T_i=5$*keV*, $Z_{eff}=2$, $P_{NBI}=1.5$ *MW/m* ^{3} *and* $E_{beam}=70$ *keV.*

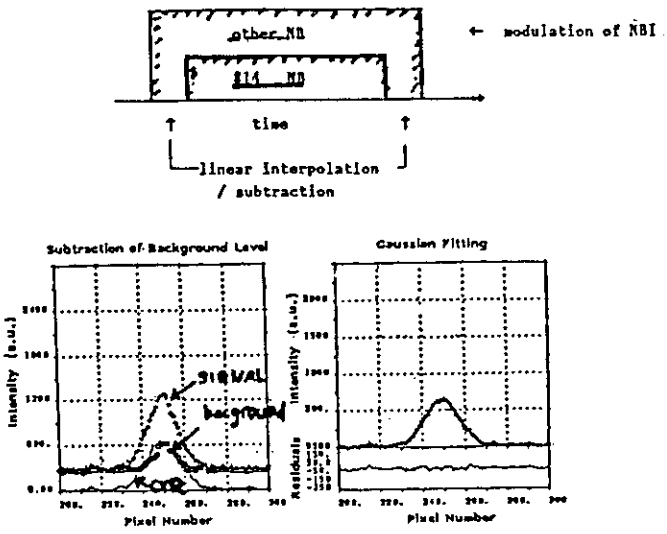

Fig. 2 Beam modulation for background evaluation. Diagnostic beam (#14 unit) injected later and turned off earlier than other units. Background spectrum is linearly interpolated by this method.

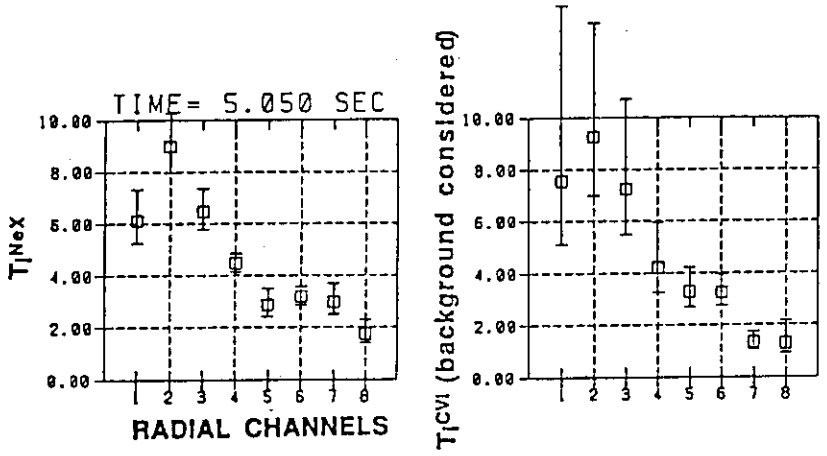

Fig. 3 Comparison of deduced Ti from lines of CVI and NeX. The latter accompanies negligible background spectrum. This agreement of deduced temperature roughly supports the justification of beam modulation.

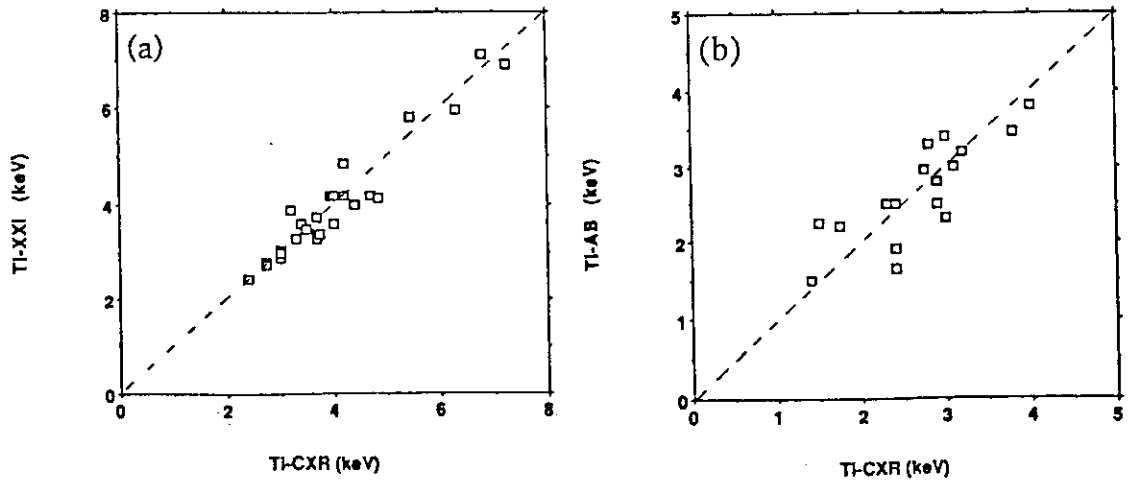

Fig. 4 Cross check of deduced Ti with other systems, T_i^{AB} and T_i^{XXI}.

8.2 Zeff Profile Measurement

Y. Kawano, H. Kubo, T. Sugie, T. Hirayama, M. Kikuchi, K. Itami,
A. Nagashima, T. Matoba and JT-60 team

1. Introduction

The Zeff profile has been evaluated from the visible bremsstrahlung intensity profile observed by a multi-chordal spectrometer for JT-60 plasmas, compared with other results from two spectrometers. Both Zeff values have a good agreement, while sensitivities of the former and the latter are calibrated independently. And evaluated Zeff values show flat profiles except the plasma edge region.

2. Zeff profiles for divertor plasmas

Figure 1 shows viewing chords of three spectrometers. Two single-chordal spectrometers are located at the U6 port (A4e) and the upper IN2 port (A41), respectively. They measure the visible bremsstrahlung (Vis. Brems.) intensity at 5232.6 ±5.0 Å and 5232.6 ±5.5 Å, respectively. The multi-chordal spectrometer with a rotating mirror (A6d) [1] is located at the lower IN2 port and observes Vis. Brems. intensity at 5232 ±3.5 Å. The sensitivity calibration of A6d is decided independently from those of A4e and A41. Profiles of the electron density (n_e) and the electron temperature (T_e) measured by Thomson scattering are used for the evaluation of Zeff values. The electron density by Thomson scattering was compared with the line-averaged electron density from FIR interferometers, and calibrated.

Figure 2 shows profiles of the chord averaged Zeff value ($\overline{Zeff}$) for lower divertor JT-60 plasmas with neutral beam heatings of 3MW and 11MW. In fig. 2, the horizontal axis is the flux co-ordinate along the plasma minor radius. Here, plasma minor radii; a_p =0.7m, plasma current; Ip=1.0MA, toroidal magnetic field; Bt=4.5T, respectively. In fig. 2, Zeff values show flat profile at $\rho \leqq 0.5$m, and Zeff values for P_{NBI} =11MW are about 40% greater than those for P_{NBI} =3MW. It is supposed that the increase in Zeff values near the plasma boundary is due to emissions from the plasma near the X-point (see section 4).

3. Comparison between Zeff values evaluated by A6d and evaluated by A4e

Figure 3 shows the comparison between Zeff values evaluated by A6d and evaluated by A4e at their equivalent chords. In fig. 3, shown values are evaluated from plasmas of various conditions as follows; limiter plasmas with pellet injection (H_2 prefilled, Ip/Bt=2.1MA/4.5T, before Ti-flash), limiter plasmas with NBI (H_2 prefilled, Ip/Bt=1.0MA/3.0T, 1.0MA/4.5T and 2.0MA/4.5T, after Ti-flash) and divertor plasmas with NBI (H_2 prefilled Ip/Bt=1.0MA/3.3T and H_e prefilled, Ip/Bt=1.4MA/4.5T, after Ti-flash). For such various plasmas, Zeff values evaluated by A6d have a good agreement with Zeff values evaluated by A4e.

4. Comment on the increase in Zeff value near the plasma boundary

We have $\overline{Zeff}$ profiles increasing near the plasma boundary for not only divertor plasmas but also limiter plasmas. Figure 4(a) shows the chord

averaged Zeff profile for the limiter plasma with pellet injection (a_p = 0.86m, H_2 prefilled, Ip/Bt=2.1MA/4.5T, $P_{NBI} \sim$ 9MW and evaluated at 0.2sec after the injection of 3 pellets. The plasma is limited by the lower inside wall as shown in ref.2). The Zeff profile is almost flat at $\rho \leqq 0.7$m (Zeff$\sim$1.8). On the other hand, Zeff values tend to increase steeply as ρ increases at the outer region ($\rho \geqq 0.7$m) (the indicated error bar is estimated from error bars of n_e and T_e). Figure 4(b) shows the profile of Vis.Brems. intensity observed and profiles calculated for cases Zeff=1.0 and 1.83 with using profiles of n_e and T_e measured by Thomson scattering. It is noted that calculated profiles of Vis.Brems. intensity smoothly decrease to towards the plasma boundary. While the observed profile has certain values even near the boundary. As shown in fig.4(c), the difference between observed and calculated (for Zeff=1.83) values increases at the outer region, and resulted in the increase in Zeff values. The reason is not yet clear. We are considering of a number of causes as follows.

1) emissions from the scrape off layer
The scrape off layer of several tens millimeter thickness was observed for small a_p limiter plasmas. Their contributions were not accounted in fig.4.

2) emissions from the plasma near the limiter (and near the X-point)
Strong emissions were often observed at viewing chords near the limiter (like a weak marfe) and the X-point.

3) stray lights reflected by the inner wall
It is supposed that lights reflected by the inner wall can not affect the observed profile of Vis.Brems. intensity seriously due to the viewing dump on it, and this is supported by results from the monitor TV.

4) line spectra of impurities
No strong impurity line spectrum was observed at the wavelength range for the observation of Vis.Brems. intensities.

5) accuracies of profiles of n_e and T_e
Error bars of n_e and T_e were not small near the plasma boundary resulted in large error bars of calculated Vis.Brems. intensities (see fig.4(a) for the case of Zeff value).

6) accumulations of impurities near the plasma boundary (the Zeff value increases truly).
It is suggested that there are no obvious accumulations of impurities near the plasma boundary by results from the numerical simulation with observed plasma radiation profiles. [3]

So, we suppose that the increase in the difference between observed and calculated Vis.Brems. intensities near the boundary is mainly attributed to 1), 2) and 5) mentioned above. But more quantitative examinations including other factors are required to evaluate more accurate profiles of Zeff values.

References

[1] Y.Yamashita et al.,"KAKUYUGO KENKYU",59 Supplement(1989)289.
[2] Y.Kawano et al.,this report,section 2.9.
[3] T.Hirayama et al.,private communication.

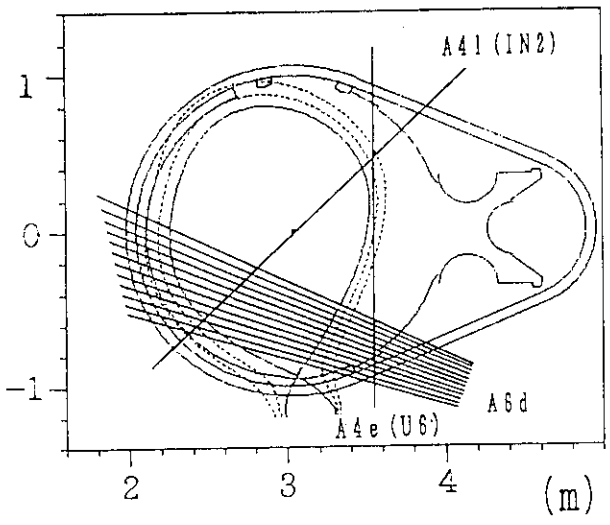

Fig.1 Viewing chords for three spectrometers.

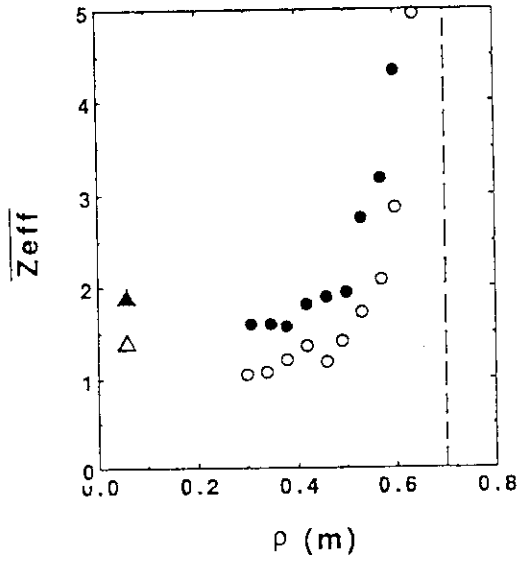

Fig.2 Chord averaged Zeff profiles for lower divertor plasmas, minor radius; a_p =0.7m, Ip=1.0MA, Bt=4.5T, $\overline{ne}^{U23}$ = ～3.1 ×10^{19} m^{-3}, respectively.
● ▲ : P_{NBI} ～11MW
○ △ : P_{NBI} ～ 3MW

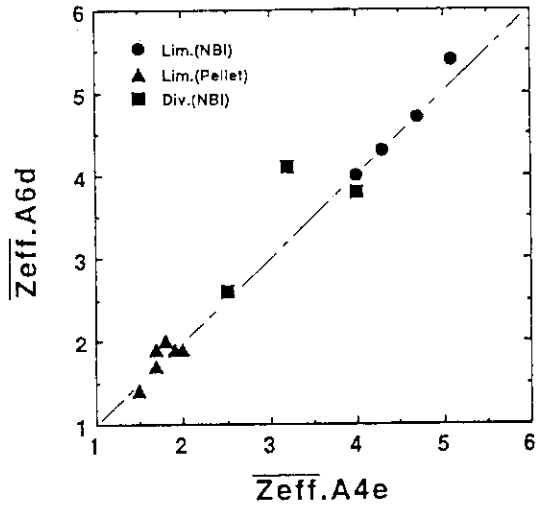

Fig.3 Comparison between Zeff values evaluated by A6d ($\overline{Zeff}$.A6d) and Zeff values evaluated by A4e ($\overline{Zeff}$.A4e).
● : limiter plasmas with NBI
▲ : limiter plasmas with pellets
■ : divertor plasmas with NBI

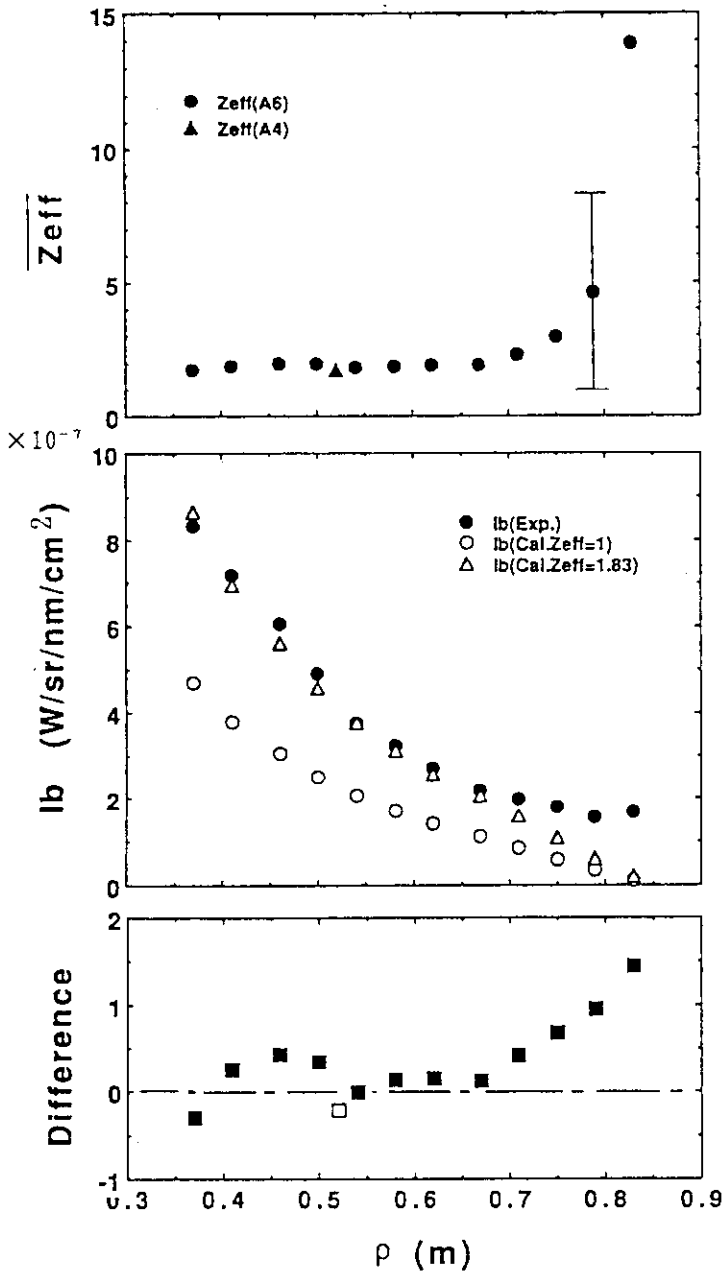

Fig. 4 *(a)chord averaged Zeff profile for a limiter plasma with 3 pellets injection, minor radius; a_p =0.86m, Ip=2.1MA, Bt=4.5T, P_{NBI} ~9MW, respectively. Zeff values are evaluated at 0.2sec after the injection of pellets.*

- ● : $\overline{Zeff}$. *A6d*
- ▲ : $\overline{Zeff}$. *A4e*

(b)profiles of visible bremsstrahlung intensity.

- ● : *observed by A6d*
- ○ : *calculated from profiles of n_e and T_e for Zeff=1.0*
- △ : *calculated from profiles of n_e and T_e for Zeff=1.8*

(c)difference between the observed visible bremsstrahlung intensity and the calculated one (Zeff=1.83).

8.3 Radiation Profile Measurement

T. Nishitani, K. Nagashima, T. Kondo and T. Kaneko

INTRODUCTION

Radiation losses, charge-exchanged neutral particles and heat load on the divertor plates or limiter are main mechanism of the energy loss from the plasma. Measurement of the radiation losses is important not only for the power balance study but also for impurity behavior and transport study. The results of the global power balance study by the bolometric measurements are described in Ref. [1].

STATUS OF THE HARDWARE

After the installation of new divertor coils for lower X-point configuration, the radiation profile of the main plasma was measured by two fan arrays of bolometer and the radiated power that from the divertor region was measured by single bolometer as shown in Fig. 1. The lower array consisted of 15 channel metal-resistor bolometers [2]. The upper array had consisted of 16 channel thermistor-bolometers. Thermistor bolometer [3] was a one of most popular detector due to its large sensitivity. The solid angle of the upper array was about tenth of that of lower array, so that we had employed thermistor bolometers for upper array. However, thermistor bolometer had been affected by electromagnetic noises more than metal resistor bolometer, because resistant of thermistor bolometer is about 2 order larger then that of metal resistor bolometer. And it had been difficult to calibrate the relative sensitivities of upper and lower arrays. So the all thermistor bolometers of upper array were replaced by the metal resistor bolometers in May 1989. After June 1989, more than half of the amplifiers in the lower array became out of order one by one, which were repaired in September 1989. Thus, both upper and lower array were available in only in October 1989.

COMMENTS ON RADIATION PROFILE

Generally, an Abel transformation is used to obtain the radiation profile from the chord-integrated radiated power. However, an Abel transformation is valid only for a poloidally symmetric radiation profile. It was estimated from the raw data of the bolometer array that the radiation profile had a poloidal asymmetry near the X-point in the divertor discharges and around touched limiter in limiter discharges. So an Abel inversion was not available

to obtain the radiation profiles. In TiC molybdenum wall period, additional three channel vertically-viewing-bolometers and one channel bolometer viewing near the X-point were available, so that the radiation profile was estimated by the reconstruction using asymmetric Abel inversion. The result showed the intense asymmetric radiation around the outer X-point.

The overlap region of the upper and lower arrays was not so large that the reconstruction needed horizontal array. The three vertical bolometers and one viewing near the outer X-point were taken off for install of lower divertor coils. Therefore the reconstruction of the radiation profile became difficult after the modification for lower X-point divertor.

The chord integrated radiation loss decreases with the distance between the X-point and the viewing chord, which indicates the poloidal asymmetric radiation profile in lower X-point discharges. However, INDAT system provides the radiation profile assuming that the radiation loss is uniform in the magnetic surface. Therefore INDAT system is not suitable to obtain the radiation profile from the chord integrated radiation losses.

REFERENCES

[1] T. Nishitani, et al. , submitted to Nucl. Fusion.

[10] T. Nishitani, K. Nagashima, T. Sugiyama, M. Hara, H. Takeuchi and JT-60 Team, Rev. Sci. Instrum. 59 (1988) 1866.

[11] T. Nishitani, K. Nagashima, T. Sugiyama, S. Koide and H. Takeuchi, Kakuyugo Kenkyu 59 Suppl. (1987) 243.

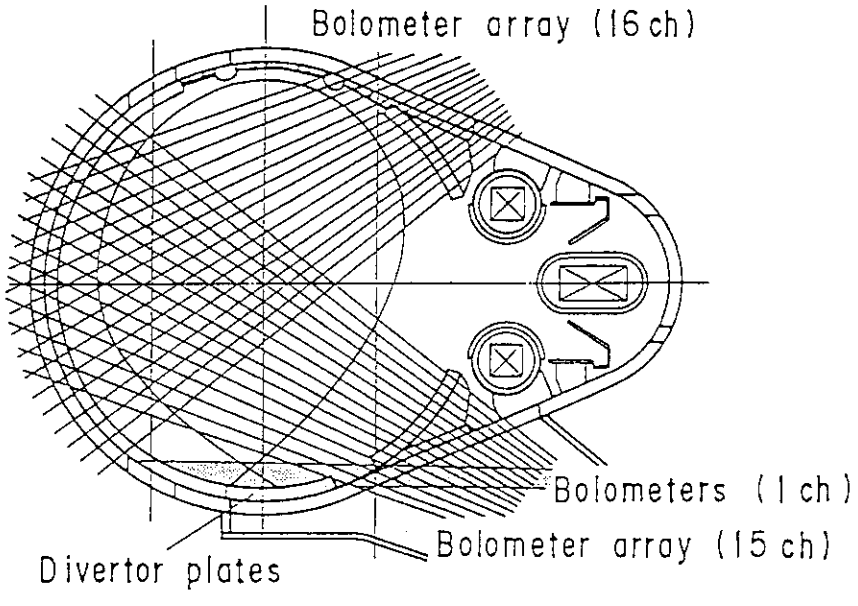

Fig. 1 Sightlines of the bolometers in the period May 1987 - October 1989.

8.4 OHMIC ENERGY CONFINEMENT

M. KIKUCHI, K. TOBITA, Y. KUSAMA, K. NAGASHIMA
and T. HIRAYAMA

Ion heat conduction in ohmic discharges is analyzed using Ti(0) measured by the Rutherford scattering of the He beam (AB). The ion transport loss becomes dominant with increasing plasma density while the electron thermal conduction coefficient follows Neo-Alcator like dependence $\chi_e \sim 1/(n_e q)$ even near the saturated ohmic confinement regime. The ion thermal conduction coefficient is found to be fairly large compared with the neoclassical value. The gross electron energy confinement time stays constant from $n_e = 2 - 8 \times 10^{19} m^{-3}$ (SOC). In order to explain such a saturated ohmic confinement, the ion transport anomaly is considered. The ion transport coefficient is evaluated assuming electron transport still follows Neo Alcator dependence in the saturated ohmic confinement regime. The calculated ion thermal conduction coefficient is fairly higher than the neoclassical value.

1. ION TRANSPORT ANOMALY IN LOW DENSITY OHMIC PLASMAS

The energy confinement in low density regime is studied using the T_e and n_e profiles, $T_i(0)$ with AB and the line-averaged Z_{eff} from the visible brems.. Fig. 1 shows a typical example of the measurement for a low density ohmic discharge. The central ion temperature is fairly smaller than that expected from the neoclassical theory. The ion temperature profile is calculated using neoclassical multiplier for the ion thermal conduction coefficient (χ_i) under the constraint that the central ion temperature matches the measurement. The resulting χ_i is larger than the χ_e by a factor of two. The χ_i is 20 times neoclassical ion thermal conduction coefficient given by Chang-Hinton[1]. The χ_i and χ_e at 2/3 of minor radius are plotted as a function n_e and I_p in Fig.2. This figure clearly indicates that the electron transport follows the Neo Alcator dependence ($\chi_e \sim 1/(qn_e)$) while the ion transport shows large departure from the neoclassical theory. The χ_i is an increasing function of the density and becomes larger than the χ_e in relatively low density regime. The global energy confinement time tends to saturate at relatively low density as is shown in Fig.3.

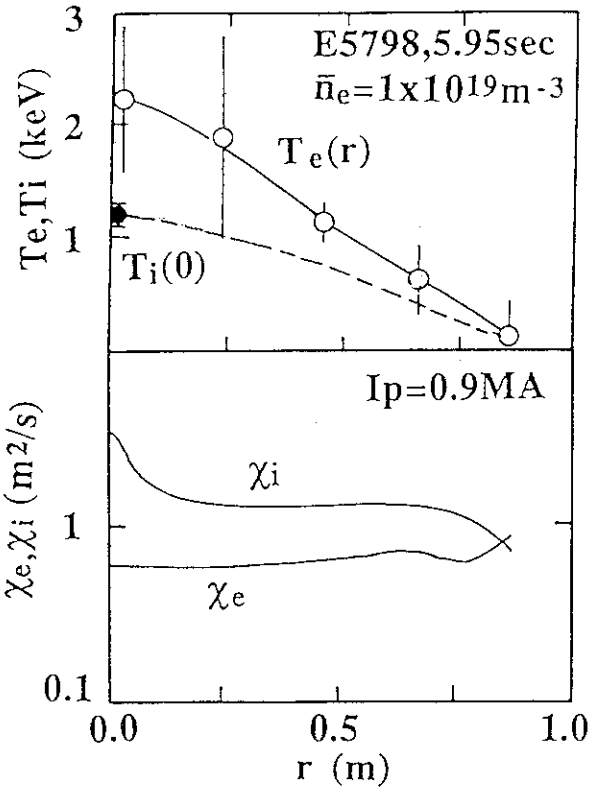

Fig. 1 Te profile measured by the Thomson scattering and Ti(0) measured by the active scattering of the He beam. The electron and ion thermal conduction coefficients are also shown.

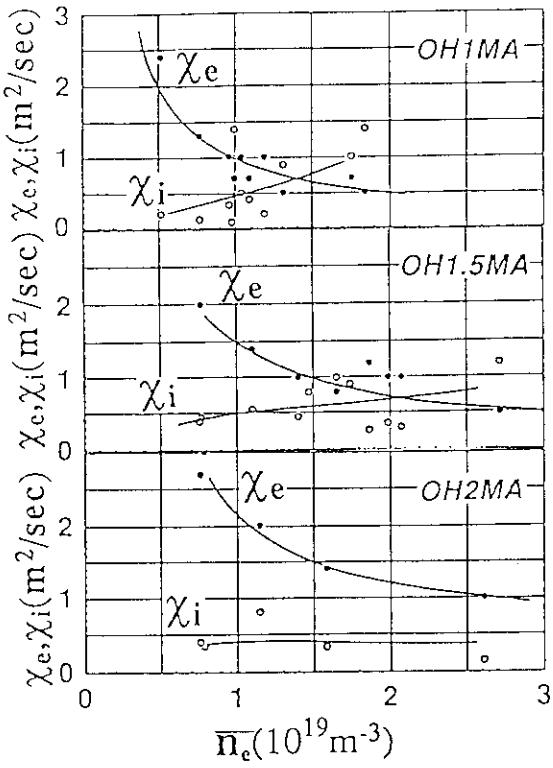

Fig. 2 χe and χi at 2/3a as a function of $\bar{n}_e$ for various plasma currents.

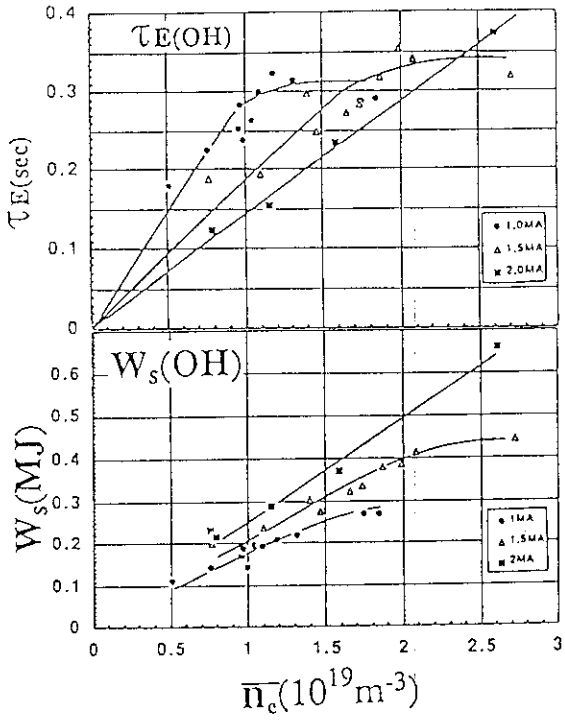

Fig. 3 Energy confinement time and the total stored energy as a function of $\bar{n}_e$.

2. SATURATION OF THE GROSS ELECTRON CONFINEMENT TIME

The kinetic profile data base has been accumulated during the 5 years of JT-60 experiments. The available data set is shown in the Ip-ne diagram in Fig.4. This dataset contains relatively high density ohmic discharges up to $8 \times 10^{19} m^{-3}$. In such a high density plasma, we could not observe the energy confinement time proportional to the line average electron density expected from the neo Alcator transport of the electron ($\chi_e \sim 1/(qn_e)$). The electron temperature in SOC regime is limited by the strong electron-ion energy equipartition. The gross electron energy confinement time τ_E^G ($=W_e/P_{OH}$) is plotted as a function of $\bar{n}_e$ in Fig.5. The τ_E^G quickly saturates at about $\bar{n}_e = 1 \times 10^{19}\ m^{-3}$.

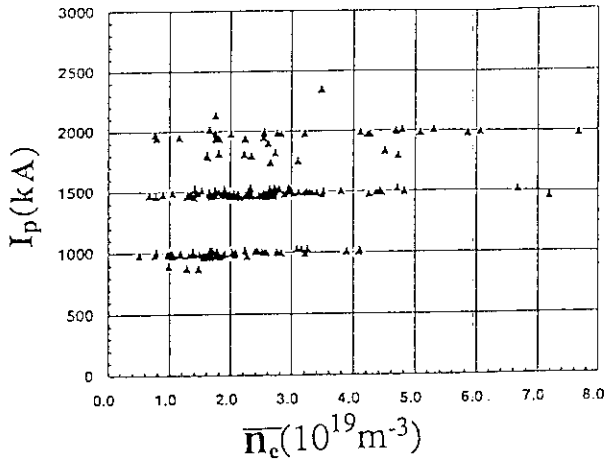

Fig. 4 Operational diagram of the ohmic discharges in (n_e, I_p) plane.

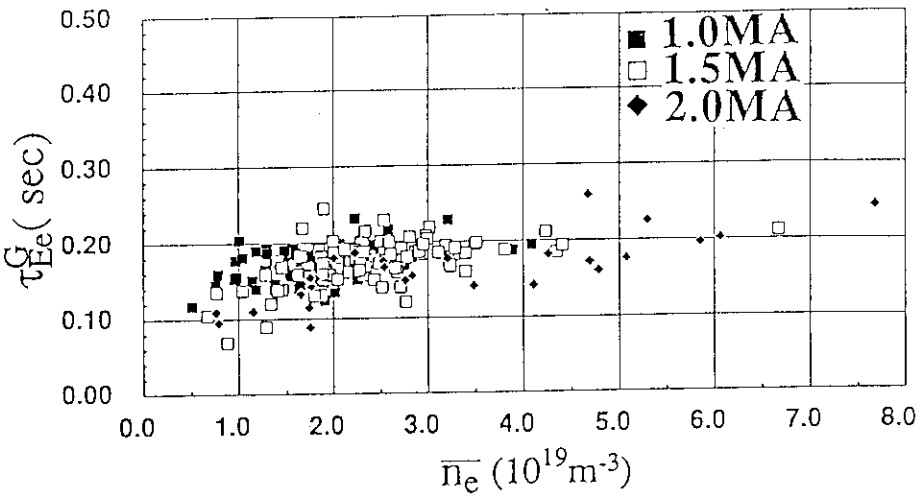

Fig. 5 Gross electron energy confinement time as a function of $\bar{n}_e$. Saturation is earlier in low Ip cases.

3. INTERPRETATION OF THE SATURARED OHMIC CONFINEMENT (SOC) WITH ION TRANSPORT ANOMALY

If the ion transport is the cause of the saturation of the energy confinement in high density ohmic plasmas, the ion thermal conduction coefficient can be obtained using the electron temperature profile because of the strong electron-ion coupling. In such a coupled plasma, the ion temperature can be calculated by using the electron energy balance by assuming the transport scaling for the electron. Here we analyze the experimental data assuming that the electron follows Neo Alcator transport.

$$T_i = T_e - \frac{2\tau_{ei}^{eq}}{3n_e}\left[\frac{1}{r}\frac{\partial}{\partial r} r q_e - P_{OH} + P_{rad}\right] \qquad (1)$$

where,
$$q_e = -n_e\chi_e\frac{\partial T_e}{\partial r} + \frac{3}{2}\Gamma_e T_e \qquad (2)$$

The ion thermal conduction coefficient χ_i can be deduced by solving the ion energy balance equation as follows,

$$-\frac{1}{r}\frac{\partial}{\partial r} r q_i - \frac{3}{2} n_e \frac{T_e - T_i}{\tau_{ei}^{eq}} - P_{cx} = 0 \qquad (3)$$

where,
$$q_i = -n_i\chi_i\frac{\partial T_i}{\partial r} + \frac{3}{2}\Gamma_i T_i \qquad (4)$$

The electron thermal conduction coefficient $\chi_e(m^2/sec) = 1.25\times10^{19}/n_e$ is used to analyze the 1MA , $q_{cy} = 4.2$ density scan. The χ_i profiles are shown for various density in Fig.6. The $\chi_i(2a/3)$ is given as a function of n_e for various plasma current in Fig.6 together with the neoclassical values. The ion thermal conduction coefficient seems to be independent of Ip and ne in the saturated ohmic confinement regime.

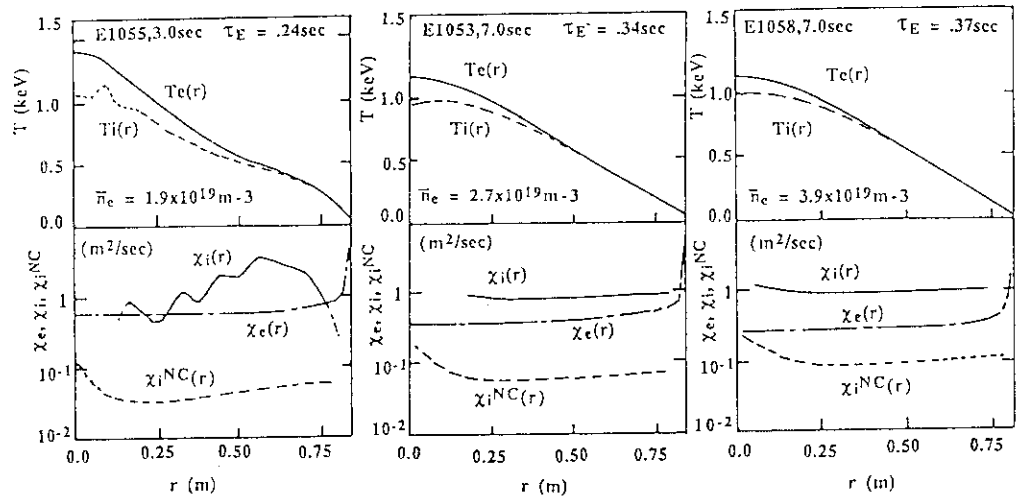

Fig. 6 Calculated radial ion thermal conduction coefficients for various density.

4. Bt DEPENDENCE OF SOC CONFINEMENT

The SOC energy confinement properties is checked by the diamagnetic measurement. Shimomura proposed a scaling of the SOC confinement as follows,

$$\tau_E^{SOC} = 0.045R(m)a(m)B_t(T)\sqrt{\kappa A_i}$$

This confinement scaling is supported by JFT-2M, DIII-D etc. Figure 7 shows the SOC energy confinement time as a function of Bt for He limiter discharges. The SOC confinement time does not show clear B_t dependence. For the divertor Bt scan, we see some improvement with B_t (~ $B_t^{0.5}$). The cause of the discrepancy is not well understood at present.

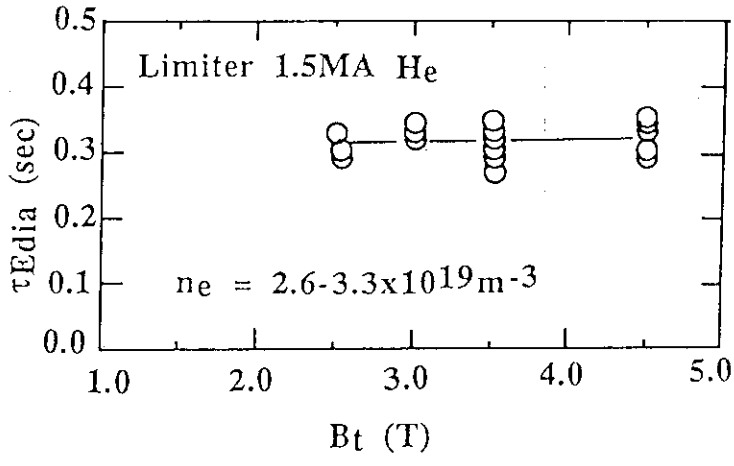

Fig. 7 SOC energy confinement time by the diamagnetic measurement. $\bar{n}e$ = 2.6-3.3 x10^{19}m^{-3} for the B_t scan.

5. CONCLUSION

The energy confinement properties during ohmic heating in the JT-60 tokamak is analyzed using the measured central ion temperature in low density regime and the existence of the enhanced ion transport is confirmed. The ion thermal conduction coefficient evaluated assuming the Neo Alcator transport for the electron has been evaluated. The Bt scan experiment do not show clear Bt dependence of the SOC confinement in He discharge which contradicts with Shimomura scaling.

8.5 Comments on Heat Pulse Propagation Analysis

K. Nagashima, M. Kikuchi and T. Hirayama

The application of the perturbation method for the sawtooth induced heat pulse propagation study has been employed as the successful method for the estimation of electron thermal diffusivity in the several tokamaks [1-3]. But the obtained values were systematically larger than the values calculated using the power balance analysis in the many cases. In this subsection, we consider the problem and limitation of sawtooth induced heat pulse propagation study.

In JT-60 the heat pulse propagation study has been performed using the soft x-ray detector array. So the measured data is chord-integrated and complicated due to the overlaps of heat and density pulses, because the cut off energy of absorbing filter is set to be nearly equal to the plasma electron temperature and the measured soft x-ray intensity is comparably sensitive to both the electron temperature and electron density perturbations. Moreover, the several intrinsic problems exist in the electron temperature perturbation equation,

$$\frac{3}{2}\frac{\partial \tilde{T}_e}{\partial t} = \frac{1}{r}\frac{\partial}{\partial r}\left(r\chi_e \frac{\partial \tilde{T}_e}{\partial r}\right) + \frac{\chi_e}{L_n}\frac{\partial \tilde{T}_e}{\partial r} - \frac{1}{n_e r}\frac{\partial}{\partial r}\left(\frac{5}{2} r\tilde{T}_e\Gamma_e\right) - \frac{3}{2}\frac{\tilde{T}_e - \tilde{T}_i}{\tau'} + \frac{\partial P_e}{\partial T_e}\tilde{T}_e \quad (1)$$

$$\frac{1}{\tau'} = \frac{1}{\tau_{eq}}\left(\frac{3}{2}\frac{T_{i,0}}{T_{e,0}} - \frac{1}{2}\right) \quad (2)$$

where $T_j(r,t)=T_{j,0}(r)+\tilde{T}_j(r,t)$ (j=e, i represent electron and ion, respectively.) and the density perturbation is neglected. χ_e, L_n, Γ_e, P_e and τ_{eq} represent electron thermal diffusivity, density gradient scale length, electron particle flux, energy source to electron and electron-ion energy equipartition time, respectively. In the usual heat pulse propagation study, only the first term in the right hand side of eq.(1) is considered as the basic diffusion equation, but the energy

equipartition and the source terms become considerable in the reallistic condition. The second and third terms, which are due to the bulk density gradient and the particle flux, are considered to be negligible compared to the other terms except in the edge region.

As easily understood in eq.(1), the equipartition term becomes dominant in the high density and low temperature plasma, and the energy source term becomes considerable only in the high power heating case. Firstly, using the assumption that the heating power is deposited spatially constant and P_e has the temperature dependence of $T_e^{-3/2}$, the energy source term is estimated as,

$$\frac{\partial P_e}{\partial T_e} \approx -\frac{3}{2}\frac{P_e}{T_e} \approx -\frac{3}{2}\frac{16\,\varepsilon_e P_{in}[MW]}{n_e/E+19[m^{-3}]\ T_e[keV]} \equiv -\frac{3}{2}\tau_s^{-1} \qquad (3)$$

where ε_e and P_{in} represent the electron heating ratio and the total input power, respectively. In the case of full NBI power(Pin≈20MW) and low density in JT-60, τ_s is estimated to be 20-40 msec. As the interested time interval for the heat pulse propagation in JT-60 is about 10 to 20 msec, this energy source term does not become dominat but it can't be neglected in the high power heating case. Secondly, the equipartition term is estimated using eq.(1) including the first and fourth term. For example, the peaking time of electron temperature perturbation at $r/a_p=0.58$ are plotted as a function of electron density in Fig.1. In the calculation, the parameters are set to be $n_e(r)=n_e(0)(1-(r/a_p)^2)^{0.5}$ [m^{-3}], $T_e(r)=2.0(1-(r/a_p)^2)^{1.5}$ [keV], effective ionic charge $Z_{eff}=1.0+3.0/n_e(0)$, $\chi_e=1.5/n_e(0)$ [m^2/sec], the sawtooth inversion radius $r_s=27$ cm, and the ion temperature experiences no sawtooth oscillation. These parameters approximately correspond to the case of ohmic discharge in JT-60. In the figure the acceralation of heat pulse due to the equipartition term can be seen and its effect results in the increasing of the estimated thermal diffusivity.

As above mentioned, it must be paid a caution for the estimation of thermal diffusivity from the heat pulse propagation, except for the *fortunate* case of low density and low heating power where the basic

diffusion eqution is not invalid. In Fig.2 the peaking times of soft x-ray intensity(chord-integrated) are shown as a function of line-averaged electron density. These points are obtained from the discharges of I_p=1.0 MA, B_t=3.5 T, hydrogen species, limiter configuration and ohmic heating, where the electron density perturbation is small relative to the temperature perturbation. The peaking times saturate in high density region as can be seen in Fig.1, but it is indeterminable whether the saturation is due to the effect of equipartition term or not. In the low density region of Fig.2 (which are *fortunate* cases), it is easy to see that the thermal diffusivity is improving with electron density and it consistents with the results of power balance analysis and the ohmic energy confinement scaling.

References

[1] SOLER, M., CALLEN, J.D., Nucl. Fusion 19 (1979) 703
[2] FREDRICKSON, E.D., et al., Nucl. Fusion 26 (1986) 849
[3] LOPES CARDOZO, N.J., et al., Nucl. Fusion 28 (1988) 1173

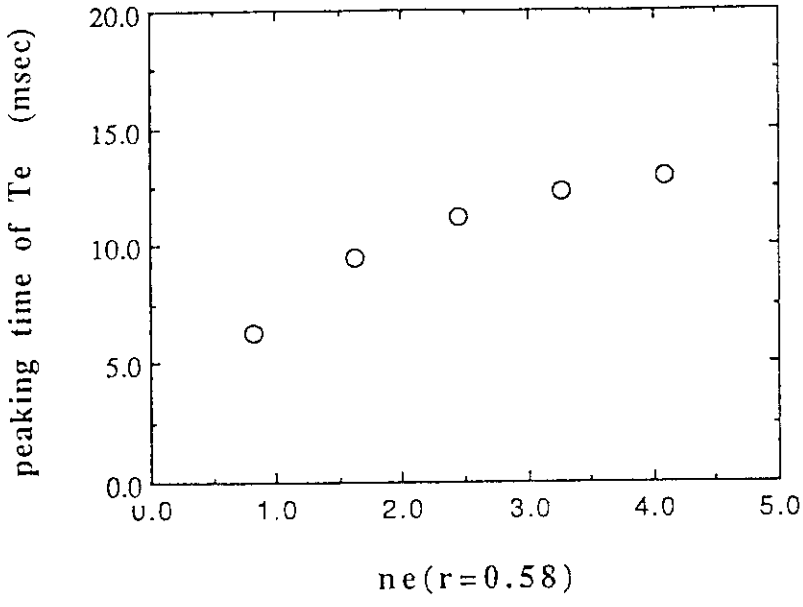

Fig.1 A electron density dependence of the peaking time of electron temperature perturbation as a example of the effect of equipartition term in eq.(1).

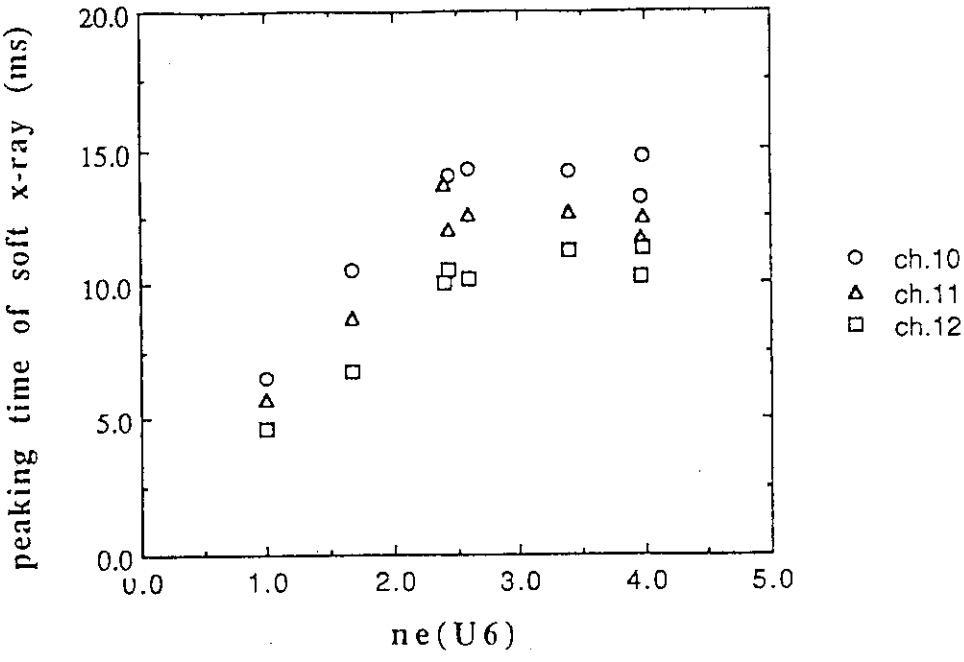

Fig.2 The measured peaking time of soft x-ray intensity as a function of line-averaged electron density.

8.6 L-mode Transport Analysis I
- Transport Analysis of JT-60 Plasmas with L-mode Characteristics -

T. Hirayama, M. Kikuchi, H. Shirai, K. Shimizu, and Y. Koide

Local heat transport in L-mode plasmas has been studied, using interpretive code and set of consistent experimental data. Effective heat diffusivities χ_{eff} estimated at plasma radii of a/2 and 2a/3 present the same parameter dependencies of $P_{abs}^{0.5}$ as the L-mode, Goldston scaling. χ_{eff} also has a clear density dependence.

1. Introduction

Understanding transport process is a key issue of tokamak research. In order to obtain an energy confinement scaling extrapolated into the reactor regime, we have been studying the physics of transport process, working on the global and local confinement behavior of L-mode plasmas.

Local heat transport properties have been analyzed in L-mode phases of divertor (single null X-point), and limiter discharges with hydrogen neutral beam heating into hydrogen plasmas, based on sets of consistent experimental data including ion temperature profiles by CXRS measurement[1]. Parameter dependencies of effective heat diffusivities locally determined are compared with those of global confinement scaling on the L-mode. Total kinetic stored energy is divided into three parts of electrons, ions and beam components, and parameter dependencies of each energy content are studied for comparison with a global energy confinement characteristics.

2. Experiments and Analysis

For limiter and divertor discharges, plasma configuration are slightly shifted inside (major radius of 2.9 m), so that diagnostic measurement works as close as to the central region of plasmas. Profile data used for transport analysis, are electron temperature from Thomson scattering and ECE[2] measurements, electron density from 8 ch Thomson scattering and 2 ch FIR, radiation profile from 16ch borometric measurements[3], and Zeff from visible Bremss[4]. However, particle confinement time needed to estimate particle flux is given by a scaling from a previous work[5].

Global Confinement Characteristics

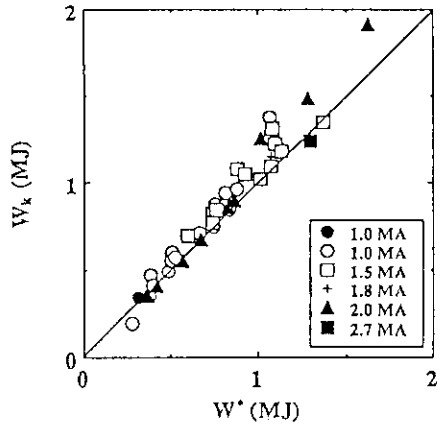

Fig. 1 Comparison between diamagnetic measured energy content W^* and kinetic, total stored energy including beam component.

For sets of consistent experimental data, the total kinetic stored energy including beam components calculated by OFMC code shows good agreement with the diamagnetic measured stored energy within 15% errors (Fig. 1). In order to distinguish from contributions of electrons and ions to the stored energy, estimated total kinetic stored energy is divided into three parts of electron, ion and unthermalized fast ions, and shown as a function of the plasma current in Fig. 2; at the region of $3.0\times10^{19} \leq \bar{n}_e \leq 4.0\times10^{19}$ m^{-3} and $9.6 \leq P_{abs} \leq 10.1$ MW. For divertor discharges with 1 MA, the electron stored energy increases with the rise in the plasma current. On the other hand, the ion stored energy exhibits no any increment with the plasma current. The beam components are also constant, because of fixed electron density and constant, net

input power. This experimental evidence suggests that the ion stored energy is reduced not only by serious dilution of ion density, but also might have relative weak current dependence.

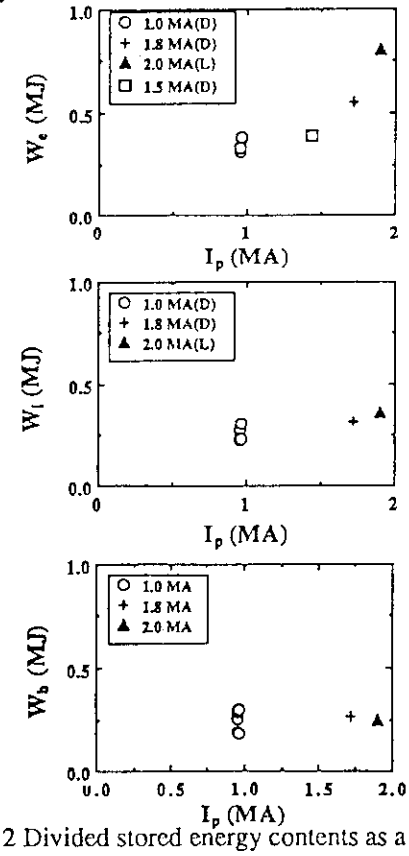

Fig. 2 Divided stored energy contents as a function of Ip, for rigorous data set; $2.8 \leq \bar{n}_e \leq 3.9\times10^{19}$, $9.6 \leq P_{abs} \leq 10.1$MW. Open symbols show divertor discharge and closed one limiter discharge:a) electron stored energy;b) ion stored energy;c)unthermalized beam energy content.

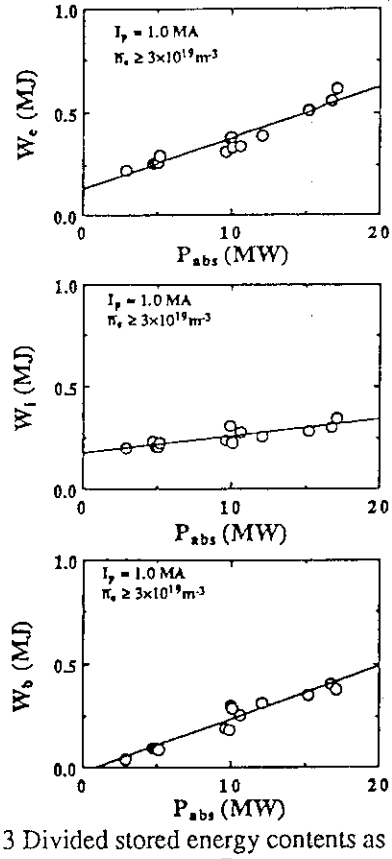

Fig. 3 Divided stored energy contents as a function of total input power P_{abs} for 1MA, divertor discharges, at $\bar{n}_e \geq 3.0\times10^{19}m^{-3}$:a)electron stored energy;b) ion stored energy;c)unthermalized beam energy.

Next, the P_{abs} dependencies of distributed kinetic energies are shown in Figs.3, for divertor discharge with I_p=1.0 MA. The electron stored energy increases by a factor of three, whereas the ion only by 50 %. The beam components increase with input powers. Since the slope of each kinetic stored energy against the absorbed power can be defined as the incremental time of each energy, the components of stored energy are presented by using the incremental tine, as follows,

$$W_e = W_e^p + \tau_e^{inc} P_{abs},$$

$$W_i = W_i^p\ (+ \tau_i^{inc} P_{abs}),$$

$$W_b = \tau_b^{inc}(P_{abs} - P_{OH}) \cong \tau_b^{inc} P_{abs}.$$

Using above relations, the energy confinement time is reduced to

$$\tau_E = \frac{W_e^p + W_i^p}{P_{abs}} + \tau_e^{inc} + \tau_b^{inc}\ (+ \tau_b^{inc})$$

Accordingly, the summation of each incremental time $\tau_e^{inc} + \tau_b^{inc}$ $(+ \tau_b^{inc})$ is strictly same as the incremental energy confinement time τ_E^{inc}. The incremental confinement time for 1MA, lower X-point discharges has been reported to be 45±5 ms[6]. In Figure 3, it is found that the incremental times for electron, ion and beam component are 26±2 ms, 8±3 ms and 25±2 ms, respectively. The summed incremental time results in 59±7 ms. Both incremental times are almost the same, within their error bars. Therefore, the incremental energy confinement time,

τ_E^{inc} is sufficiently attributed to the incremental energy of electrons and beam components, and there is a little contribution of ions to τ_E^{inc}. This slight contribution of ions is part of the evidence supporting the idea that power degradation of global confinement is mainly due to degradation in ion transport. Again, the situation is much complicated, because Zeff increases with heating power.

Local Transport Analysis

In a data set for relative lower density $\bar{n}_e \leq 3.0\times10^{19}m^{-3}$ and up to moderate heating power ($P_{abs} \leq 10$ MW), we can separately determine electron thermal conductivity, κ_e and ion thermal conductivity, κ_i. In Fig. 4, thermal conductivities at r=a/2 are shown as a function of total input power, P_{abs} for discharges with I_p=1.0MA and 2.0MA. Figure 1-a shows that for I_p=1.0MA, κ_i significantly increases in proportion to P_{abs} and is about three times κ_e at P_{abs}~9MW. However, κ_e slowly grows with input powers. As for discharges with I_p=2.0MA (Fig. 4-b), κ_i also rises and becomes comparable to κ_e with increasing P_{abs}, although κ_e is larger than κ_i at low power level of 4MW. The large value of κ_e may be attributed to the remained, ohmic confinement characteristic that becomes worse with higher current in low density regimes. From Figs. 4-a and -b, it is found that κ_i has clear I_p dependence; $\kappa_i^{1MA} \sim 2\kappa_i^{2MA}$ at P_{abs}~6MW. Against to that, κ_e has no-I_p dependence. Therefore, as for relative, low density regimes, we can conclude that the power degradation of global confinement is mainly due to degradation in ion transport.

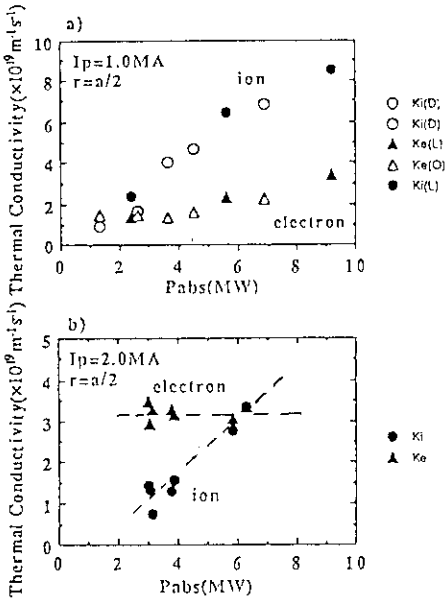

Fig. 4 Power dependencies of thermal conductivities (r=a/2), in which circles show κ_i and triangles κ_e. Open and closed symbols present divertor and limiter discharges, respectively: a) I_p=1.0MA ; b) I_p=2.0MA.

Next, we have analyzed a data set for relatively higher density ($\bar{n}_e \geq 3\times10^{19}m^{-3}$). In such density regimes, it is very hard to separately determine the electron heat diffusivity, χ_e and the ion heat diffusivity, χ_i, because the uncertainty in the electron-ion energy exchange term becomes too large. Therefore, in the following, we will discuss the effective heat diffusivity as a local transport parameter.

The effective heat diffusivity, averaged over both species of electron and ion, is defined by

$$\chi_{eff}(\rho) = \frac{\frac{3}{2}(T_e\Gamma_e+T_i\Gamma_i) + \frac{1}{\rho\langle|\nabla\rho|^2\rangle}\int_0^\rho (P_J+P_{NB}-P_R)\rho d\rho}{-(n_e\frac{\partial T_e}{\partial\rho} + n_i\frac{\partial T_i}{\partial\rho})}$$

in which fast ions from neutral beams are excluded from ion density, n_i. Figure 5 shows spatial profiles of χ_{eff} for 1.5 MA, divertor discharge scanning total input power from 4.6 MW to 16.7 MW, in which electron densities are rigorously fixed to $(4.3\sim4.9)\times10^{19}m^{-3}$. It is found that χ_{eff} grows across the radius with increasing total input power.

Figure 6 shows the dependence of $\chi_{eff}(a/2)$ on the total input power, P_{abs}. The results show that $\chi_{eff}(a/2)$ roughly increases in proportion to the function of $P_{abs}^{0.5}$ and is systematically re-

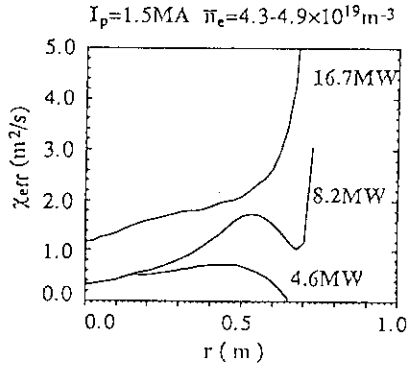

Fig.5 Spatial profiles of χ_{eff} as a function of total input power.

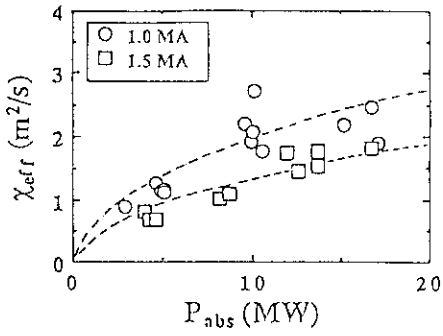

Fig.6 $\chi_{eff}(a/2)$ as a function of total input power.

duced to smaller values with higher current. These parameter dependencies are consistent with the global confinement, L-mode scaling (Goldston scaling). The current dependence of $\chi_{eff}(a/2)$, however, seems to be lost in higher power region (~17MW). This is related to a density dependence of χ_{eff}. Figure 7 shows $\chi_{eff}(a/2)$ as a function of electron density. For constant input powers, χ_{eff} significantly decreases with increasing electron density, whiles a global confinement characteristics has no or weak density dependence.

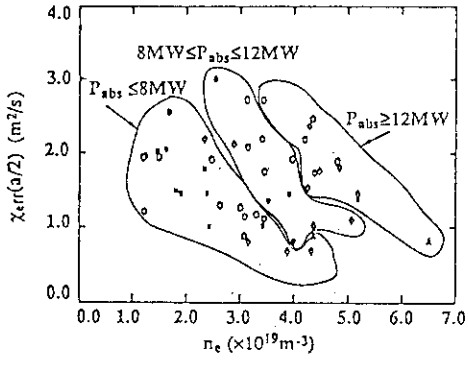

Fig. 7 The density dependence of $\chi_{eff}(a/2)$ for a fixed input power.

Summary

In divertor discharges with Ip=1.0 and 1.5 MA, global confinement characteristics have been studied on the dependencies of the kinetic stored energy contents divided into three components of electrons, ions, and unthermalized fast ions. The ion stored energy has no any dependencies on the plasma current and the total input power. This results suggest that the deterioration in energy confinement for diverted discharges with q<3 might be ascribed to ion transport characteristics. Really, the incremental confinement time, τ_E^{inc} is decided by the increments of electron and beam energy components. The ion stored energy has no or weak contribution to the τ_E^{inc}.

As for relatively, low density regimes, the power degradation of global confinement is mainly due to degradation in ion transport. The results of local transport analysis show that the spatial profile of χ_{eff} grows across the radius with increasing input power. In addition, χ_{eff} roughly has the standard L-mode dependence ($P_{abs}^{0.5}$).

References

[1] Y. Koide, et al. , see section 8.1 in this report.
[2] N. Isei, et al., see 9. in this report.
[3] T. Nishitani, et al., see 8.3 in this report.
[4] Y. Kawano, et al., see 8.2 in this report.
[5] K. Yamada, et al., Nucl. Fusion, 27, (1987), 1203.
[6] O. Naito, et al., to be published in Nucl Fusion.

8.7 L-mode Transport-II(Ion Transport Anomaly)

M. Kikuchi, T. Hirayama, Y. Koide, H. Yoshida and H. Shirai

Abstract Ion transport properties are studied during the high power neutral beam injection using the profile data base obtained in the L-mode transport experiments. Ion transport loss is found to be a dominant loss channel except high Ip low power limiter discharges. The ion conduction loss is significantly reduced for the divertor configuration compared with the limiter configuration. These data suggest that the ion transport coefficient is a decreasing function of the poloidal field. The electron thermal conduction coefficient seems to be a decreasing function of the electron density even in the high power regime with some power degradation (ie. positive temperatue dependence) .

1. ENERGY LOSS CHANNEL OF THE L MODE DISCHARGES

Typical example of the profile measurement in a low density limiter discharge is shown in Fig.1. The measured ion temperature stays low although more than half of the heating power goes to the ion. The total kinetic energy including beam component agrees with the diamagnetic measurement. If we assume the neoclassical ion thermal conduction, the calculated ion temperature and the total kinetic stored energy significantly deviate from the measurement. The calculated ion thermal conduction coefficient is significantly larger than that of the electron. Figure 2 shows the power loss partitioning at r= 2/3a for various loss channels, electron and ion conduction losses and convection and radiation losses. As is clear from the figure, the ion conduction loss plays major role in the limiter 1MA L-mode case. Such a property is also observed in the divertor low plasma current cases (Ip < 1.5 MA). On the other hand, the conduction loss of the electron is found to be larger than that of the ion for the high current limiter discharges at relatively low power (2MA, Pabs<10MW) as is shown in Figure 3.

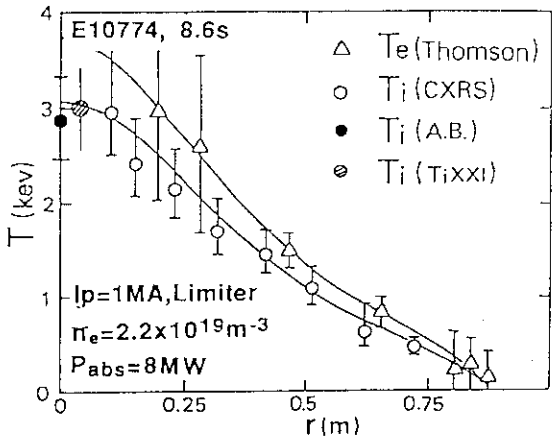

Fig. 1 Typical example of Te and Ti profiles. The CXRS measurement matches to the other measurements(active beam, Titanium XXI).

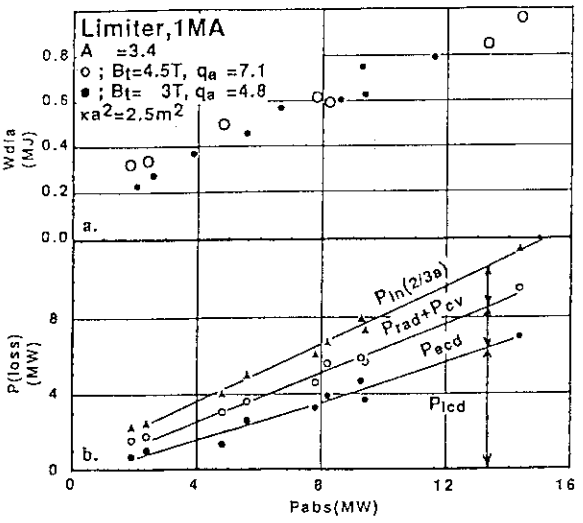

Fig. 2 The energy confinement and power losses from various loss channels evaluated at 2/3 of plasma minor radius. Pin;absorbed power, Prad+Pcv;radiation and convection, Pecd; electron conduction, Picd;ion conduction

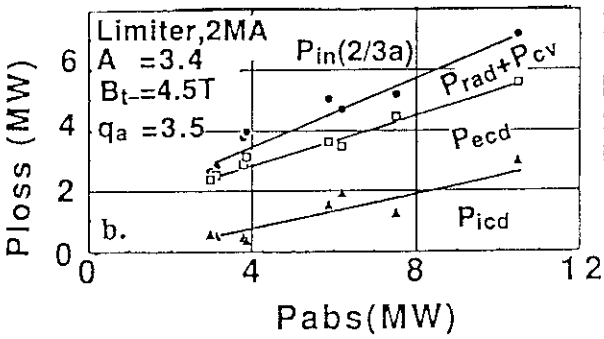

Fig. 3 The power losses for 2MA discharges

2. ELECTRON AND ION THERMAL CONDUCTION COEFFICIENTS

The electron and ion thermal conduction coefficients (χ_e and χ_i) are evaluated at 1/2 of the plasma minor radius for various discharges. Figure 4 shows χ_e and χ_i as a function the absorbed power for 1MA limiter discharges (see Fig.1). The ion thermal conduction coefficient is significantly higher than the electron thermal conduction coefficient. The χ_i increases with heating power. On the other hand,the χ_e shows little or no power degradation. It should be noted that the line average electron density is not kept constant for this power scan. The electron density increases with the absorbed power ($\bar{n}_e$~ (0.9-2.4) x $10^{19}m^{-3}$ increases with P_{abs} (2-15MW)). This observation will be discussed in section 3 in more detail. On the other hand, the transport process in high current limiter discharges (Ip = 2MA) is fairly different from the low Ip (1MA) case. The electron conduction loss shares a significant fraction of the power flow as shown in Fig. 3 and the ion thermal conduction coefficient is reduced significantly compared with 1MA case by a factor of 2-3. However, it is more than 10 times the neoclassical value. Figure 5 shows the power dependence of the thermal conduction coefficients for the 2MA limiter discharges. The ion thermal conduction coefficient tends to increase with the absorbed power. But the electron conduction coefficient stays relatively constant or slightly decreasing. In this power scan, the electron density increases with power , $\bar{n}_e$ ~ (1.5 - 3.7) x $10^{19}m^{-3}$.

Although we have tried to obtain 2.7MA limiter data set, the strong equipartition between electron and ion prohibits to separate electron and ion transports.

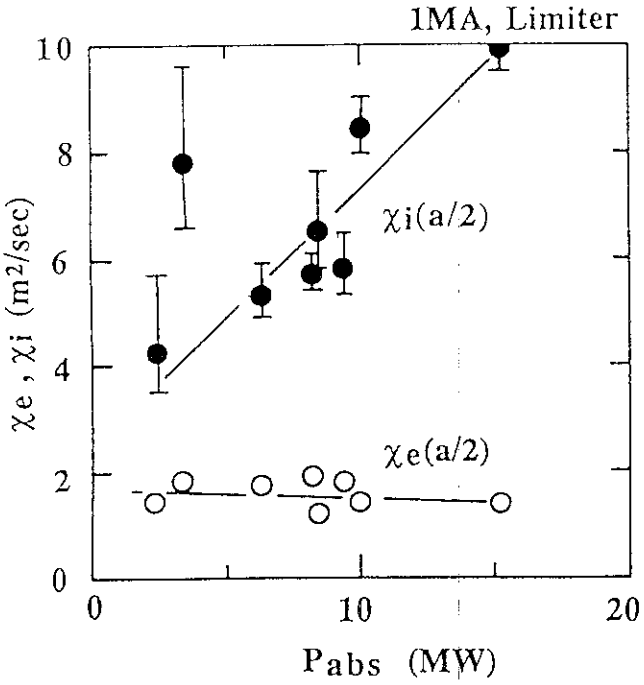

Fig. 4 Electron and ion thermal conduction coefficients at r=a/2 for 1MA limiter power scan. The error bar stands for the χ_i error by the assumption of the main impurity(carbon and oxygen).

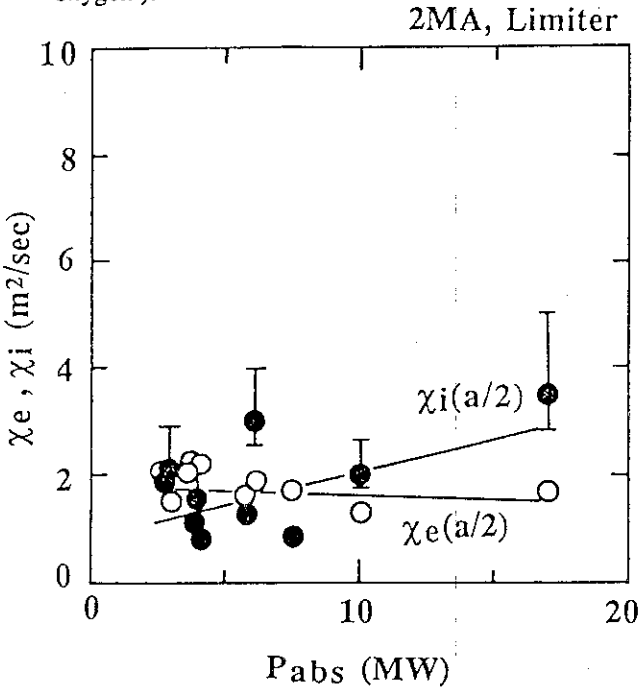

Fig. 5 Electron and ion thermal conduction coefficients at r=a/2 for 2MA limiter power scan.

For the divertor discharges, we have made power scans with relatively constant density operation. Figure 6 and 7 shows the power dependences of the thermal conduction coefficients. Both electron and ion thermal conduction coefficients are significantly reduced compared with the limiter 1MA case. This is relatively trivial reason for the observation of almost same confinement times in limiter and divertor 1MA discharges. As is seen in the figure, the χ_e stays constant or increases weakly with heating power while the χ_i increases strongly with heating power.

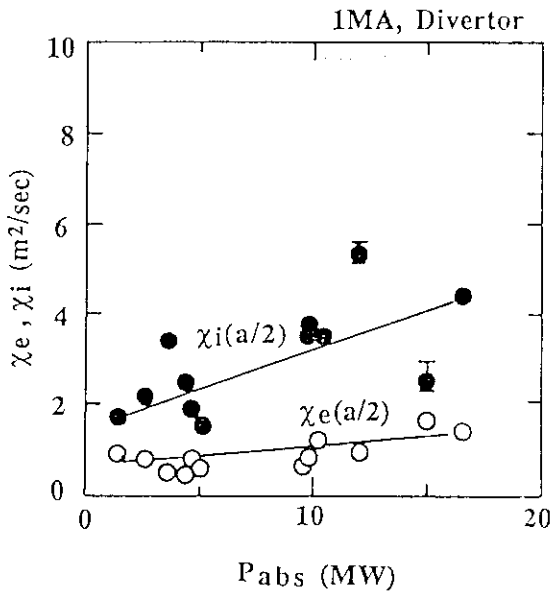

Fig. 6 Electron and ion thermal conduction coefficients at r=a/2 for 1MA divertor power scan.

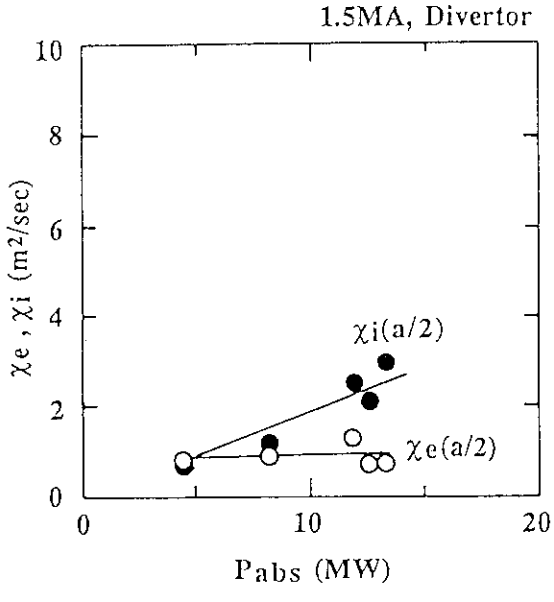

Fig. 7 Electron and ion thermal conduction coefficients at r=a/2 for 1.5MA divertor power scan.

3. n_e AND T_e DEPENDENCES OF χ_e

As is clear from Figures 4 - 7, the χ_e is relatively constant in the power scan for both divertor and limiter configurations. Fig. 8 shows the operational diagram of the kinetic data set in (P_{abs}, n_e) plane. As is given in section 8.4 (Ohmic Energy Confinement), the χ_e is inversely proportional to the electron density at least in the linear regime. Therefore, it is natural to expect n_e dependence of χ_e even during the high power heating.

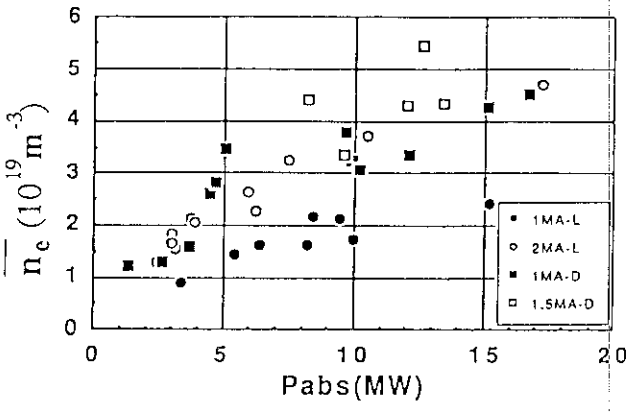

Fig. 8 Operational diagram for the L mode transport experiments.

Fig. 9 shows the n_e dependence of the for the limiter power scan in which n_e and P_{abs} are linked following the operational diagram shown in Fig. 8. The χ_e shows weaker n_e dependence compared with ohmic discharges possibly due to the increased electron temperature by the NBI heating. The correlation with the local T_e is also shown in Fig. 10.

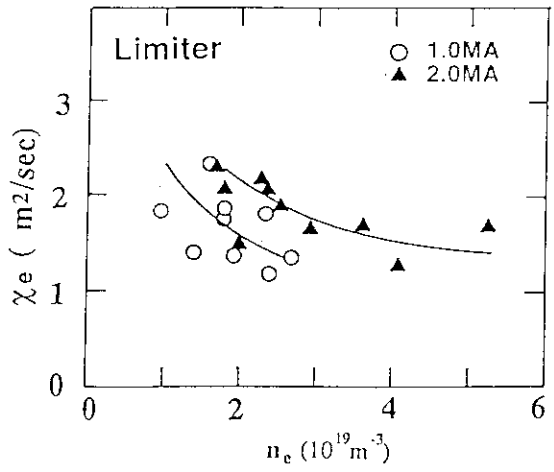

Fig. 9 The electron thermal conduction coefficient as a function of local electron density for the limiter power scan (r = a/2).

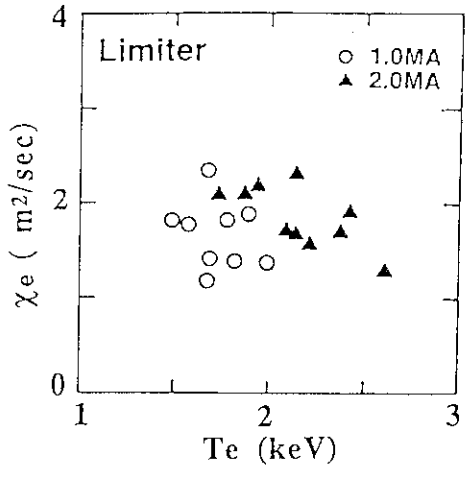

Fig. 10 The electron thermal conduction coefficient as a function of local electron temperature for the limiter power scan (r = a/2).

For the divertor discharges, the χ_e does not show clear n_e dependence as is shown in Fig. 11 and the T_e dependence is more enhanced as is shown in Fig.12.

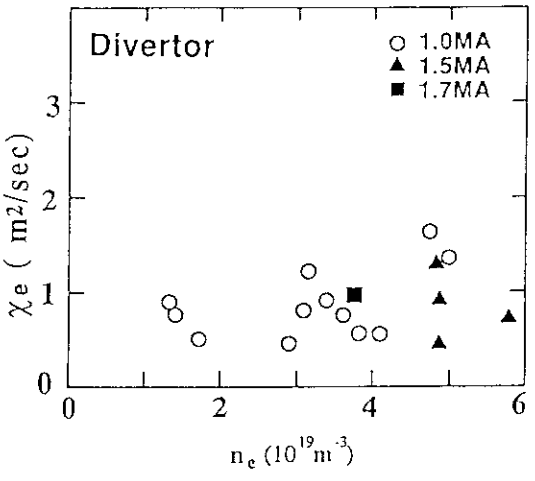

Fig. 11 The electron thermal conduction coefficient as a function of local electron density for the divertor power scan (r = a/2).

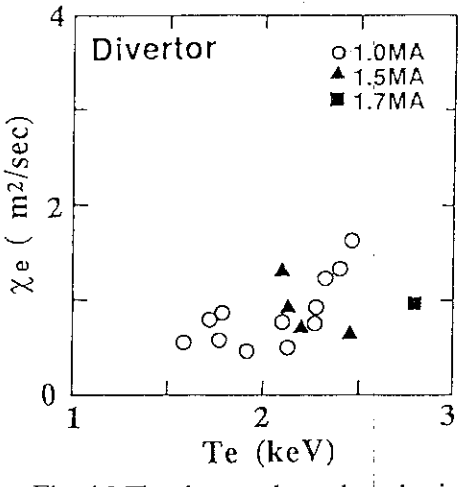

Fig. 12 The electron thermal conduction coefficient as a function of local electron temperature for the divertor power scan (r = a/2).

4. CONCLUSIONS

The parametric dependences of the thermal conduction coefficients χ_e and χ_i are evaluated using the kinetic data set obtained during the L mode transport experiments. The ion conduction loss is found to be a major loss channel except high current low power limiter discharges. The power degradation of the χ_i is extremely large compared with the χ_e. Almost no power degradation of the χ_e is related to the favourable dependence of χ_e on the density.

8.8 L-MODE TRANSPORT III

ION TEMPERATRE PROFILE ANALYSIS OF JT-60 PLASMA BY ION TEMPERATRE GRADIENT MODE

Hiroshi SHIRAI, Toshio HIRAYAMA, Masafumi AZUMI

Abstract

Ion temperature profiles of neutral beam heated plasmas in JT-60 have been studied by using thermal diffusivities based on the ion temperature gradient mode (η_i mode) turbulence proposed by Dominguez. The calculated ion temperature profile is compared with the experimental data measured by charge exchange recombination reaction. They show considerably good agreement in the divertor plasmas with I_P = 1.0 ~ 1.8 MA, P_{abs} = 1.3 ~ 16.7 MW , $\overline{n_e}$ = 1.2 ~ 5.0 × 10^{19} m^{-3} and in the limiter plasmas with I_P = 2.0 ~ 2.7 MA, P_{abs} = 3.0 ~ 17.4 MW, $\overline{n_e}$ = 1.5 ~ 6.5 × 10^{19} m^{-3}. In the 1.0 MA limiter plasmas, however, the calculated ion temperature becomes much higher than that of experimental data. High ion temperature shots with low plasma current cannot be reproduced by this model, either.

Ion temperature profiles of neutral beam heated L-mode plasmas in both limiter and divertor configurations in JT-60 have been analyzed in the wide range of plasma parameters; I_P = 1.0 ~ 2.7 MA, P_{abs} = 1.3 ~ 17.4 MW, $\overline{n_e}$ = 1.2 ~ 6.5 × 10^{19} m^{-3}. In the analysis of ion temperature profile, we assume the ion thermal diffusivity to be written as the following formula;

$$\chi_i = C^{\eta_i}\,\chi_i^{\eta_i} + C^{TE/CE}\,\chi_i^{TE/CE} + \chi_i^{Neoclassical} \tag{1}$$

where the thermal diffusivity based on the ion temperature gradient mode (η_i mode) turbulence proposed by Dominguez [1], $\chi_i^{\eta_i}$, and the η_i mode threshold value proposed by Romanelli [2], η_{ic} , are

$$\chi_i^{\eta_i} = \frac{5}{2}\frac{\omega_{*e}}{k_\theta^2}\left(\frac{2T_iL_n\eta_i}{T_eR}\right)^{1/2}\frac{1}{1+\exp(-6(\eta_i-\eta_{ic}))} \tag{2}$$

$$\eta_{ic} = \eta_{ic}(\varepsilon_n) = \begin{cases} 1 & (\varepsilon_n \le 0.2) \\ 1 + 2.5\,(\varepsilon_n - 0.2) & (\varepsilon_n \ge 0.2) \end{cases} \tag{3}$$

Other parameters are defined as follows;

$$\eta_i = \frac{d\ln T_i}{dr} \Big/ \frac{d\ln n_e}{dr}, \quad L_n = n \Big/ \frac{dn}{dr}, \quad L_{Ti} = T_i \Big/ \frac{dT_i}{dr}, \quad \omega_{te} = \left(\frac{2T_e}{m_e}\right)^{1/2}\frac{1}{qR},$$

$$\omega_{*e} = \frac{k_\theta T_e}{L_n e B_t}, \quad \rho_s = \frac{(m_i T_e)^{1/2}}{eB_t}, \quad k_\theta = 0.3\,\rho_s^{-1}, \quad \varepsilon_n = L_n/R$$

The second term of the RHS of equation (1) is contribution from the trapped electron mode and the circulating electron mode [1],

$$\chi_i^{TE/CE} = \frac{5}{2}\frac{\omega_{*e}}{k_\theta^2}\left\{\varepsilon^{1/2}\min\left(1, \frac{\omega_{*e}\varepsilon}{\nu_{ei}}\right) + \frac{\omega_{*e}}{\omega_{te}}\max\left(1, \frac{\nu_{ei}}{\omega_{te}}\right)\right\} \tag{4}$$

which is added to the χ_i formula to reproduce the enhancement of edge transport. The third term is Chang-Hinton's neoclassical diffusion coefficient [3]. Coefficients are set $C^{\eta_i} = 0.5$ and $C^{TE/CE} = 0.2$ for every shot.

The ion temperature profile is calculated by the ion energy balance equation. The profile of n_e, n_i, T_e, J_z, Z_{eff}, P^e_{NBI}, P^i_{NBI}, P_{rad} are fixed. As for the current profile, we set $J(\rho) = J(0)\,(1-\rho^2)^{q(1)-1}$ assuming q(0) = 1. The calculated ion temperature profile is compared with that of experimental data measured by charge exchange recombination reaction.

Figure 1(a) is the profile of thermal diffusivity of 1.5 MA divertor shot (E10737, P_{abs} = 11.1 MW, $\overline{n_e} = 2.9 \times 10^{19}$ m^{-3}). The thin solid line, the broken line and the dotted line are contribution from the η_i mode, the trapped electron mode and the neoclassical diffusion respectively. The thick solid line is the sum of them. Except for the very near to the magnetic axis and the plasma edge region, where the neoclassical diffusivity or the trapped electron mode becomes large, η_i mode is the dominant in the bulk plasma region. Figure 1(b) is the comparison of thermal diffusivity by the model above (solid line) and that calculated by the steady state analysis with both electron and ion temperature profiles fixed (broken line). The comparison of the calculated ion temperature and the experimental data is shown in Fig.1(c). They show good agreement.

Figure 2 shows the comparison of ion temperature profiles by the calculation and experimental data with different plasma current, (a) 1.0 MA, (b) 1.8 MA, (c) 2.0 MA and (d) 2.7 MA (P_{abs} = 9.7 ~ 12.1 MW). The case (a), (b) and (c), (d) are divertor and limiter shots respectively. Good agreement between calculation results and experimental data can be seen with fixed coefficients of C^{η_i} and $C^{TE/CE}$. The ion stored energy obtained by the calculation and that of experimental data is compared in Fig. 3. Divertor shots with I_p = 1.0 ~ 1.8 MA and limiter shots with I_p = 2.0 ~ 2.7 MA are included. They show good agreement

We have got almost the same result by using the χ_i model based on η_i mode proposed by Lee & Diamond [4], which has strong η_i dependence but has weak I_p dependence; shear parameter dependence and the χ_i model model proposed by Romanelli [1], which has no I_p dependence. Their formula of χ_i have the same temperature dependence, which is proportional to $T^{1.5}$.

Even if the second term of RHS of equation (1) is replaced by the Intor type scaling; $C^{Intor}\ 5 \times 10^{19} / n_e$ where we set C^{Intor} = 0.3, the calculated ion temperature profiles agree well with the experimental data. This indicates that the ion temperature profile is weakly depends on the edge transport model if it is not dominant in the bulk plasma region. It can be said that η_i mode is a plausible candidate for the ion conduction loss mechanism in the bulk plasma in the plasma parameter region mentioned above, although some mechanism of the thermal diffusivity enhancement in the plasma peripheral region must be considered.

In the 1.0 MA limiter discharges, however, the χ_i model mentioned above alone cannot reproduce the ion temperature profiles in the experiment. Figure 4 is the profile of (a) thermal diffusivity and (b) ion temperature (E10774, P_{abs} = 9.2 MW, $\overline{n_e} = 2.5 \times 10^{19}$ m^{-3}). Apparently ion temperature in the experiment is much lower than the result of calculation. We have only two more 1.0 MA limiter shots which are available for the ion transport analysis but they also show the disagreement of calculation and experiment. This may be results from the fact that the ion stored energy has strong I_p dependence in limiter discharges, whereas weak I_p dependence in divertor discharges [5].

As for the high ion temperature plasmas with low plasma current (less than 0.5 MA) and large neutral beam heating power (more than 15 MW), the bulk plasma transport cannot explained only by this model, either. Figure 5 is the result of calculation. The comparison of χ_i profile between the calculation (solid line) and the steady state analysis (broken line) (Fig.5(a)) shows the fairly difference. In the steady state analysis, the value of χ_i is small in the plasma center region and large in the plasma edge region, while in the calculation χ_i value is almost the same in the plasma. This results in the less peaked ion temperature profile by the calculation than experimental data (Fig.5(b)).

In summary, χ_i model based on the η_i mode turbulence is partially successful in explaining the ion temperature profile in the experiment. We must still more investigate the transport model for the low current limiter shots and high ion temperature shots.

References

[1] R.R.Dominguez, R.E.Waltz, Nucl.Fusion, **27** (1987) 65.
[2] F.Romanelli, Phys. Fluids, B **1** (1989) 1018.
[3] C.S.Chang, F.L.Hinton, Phys. Fluids, **29** (1986) 3314
[4] G.S.Lee, P.H.Diamond, Phys. Fluids, **29** (1986) 3291.
[5] O.Naito, submitted to Nucl.Fusion

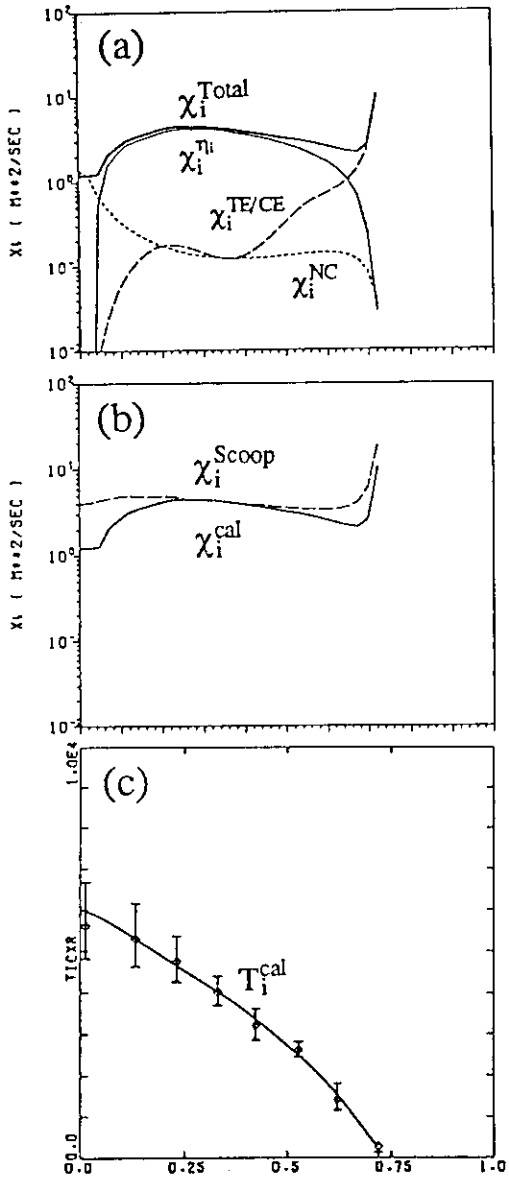

Fig.1 χ_i and T_i profile of I_p = 1.5 MA shot (E010737)

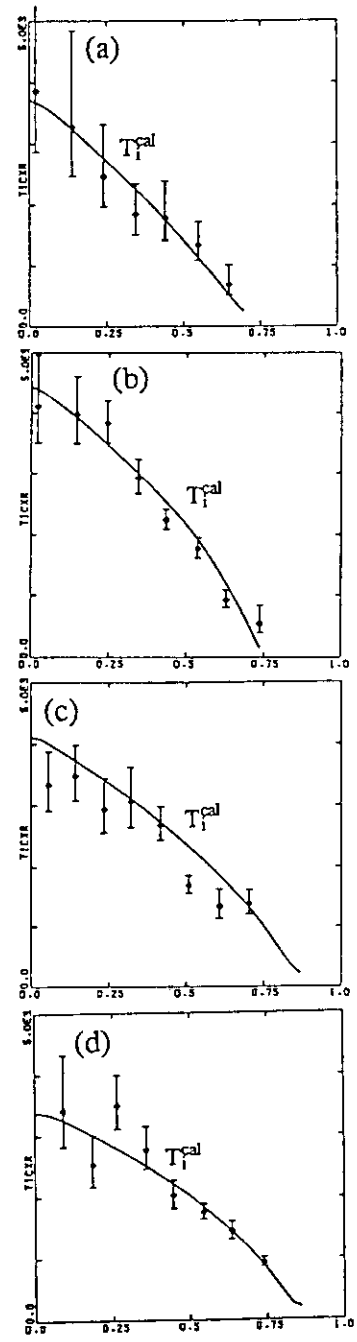

Fig.2 T_i profile comparison with different I_p shots.
(P_{abs} = 9.7 ~ 12.1 MW)

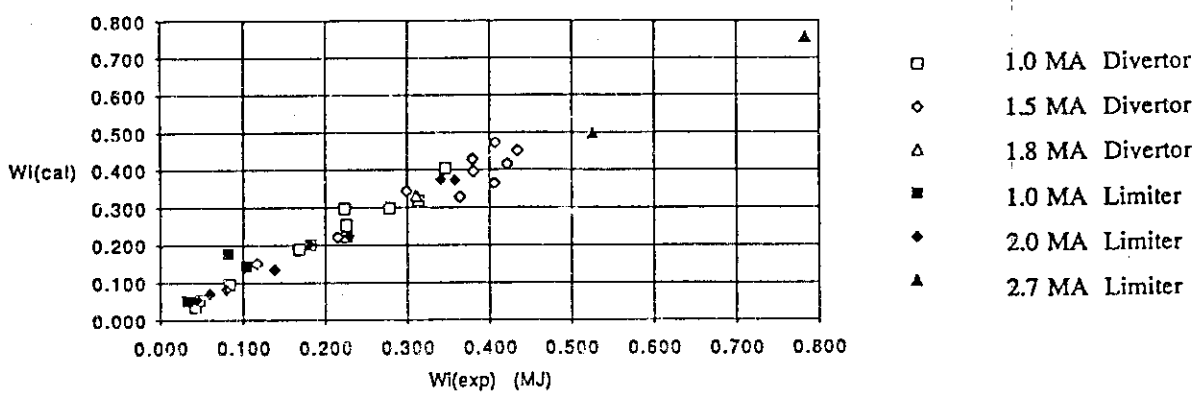

Fig.3 Comparison of ion stored energy of experimental data and results of calculation

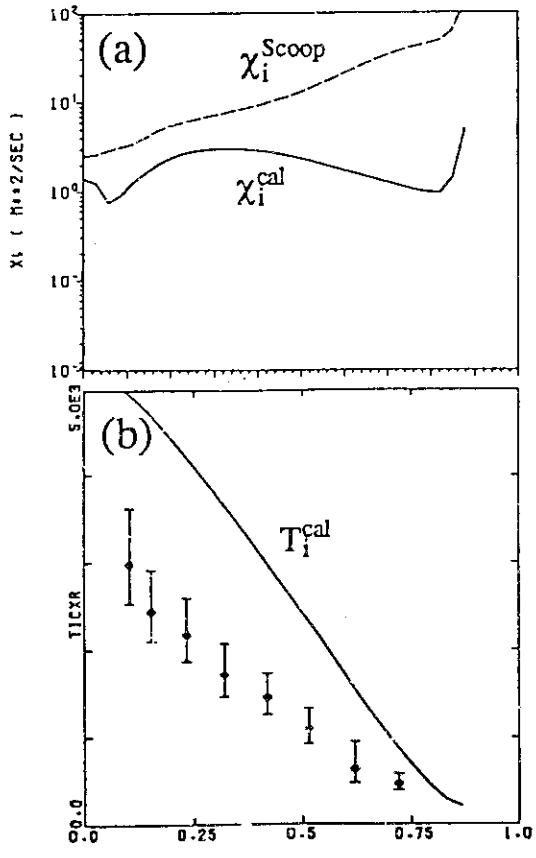

Fig.4 χ_i and T_i profile of 1.0 MA limiter shot (E010774)

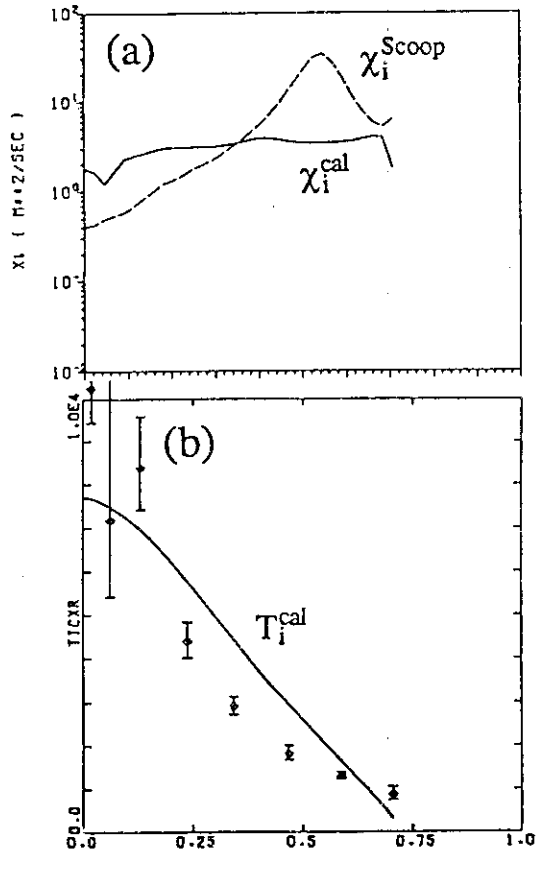

Fig.5 χ_i and T_i profile of high T_i shot (E010300)

8.9 High-Ti Transport Analysis

T. Hirayama, Y. Koide, S. Ishida, M. Kikuchi, H, Shirai, and N. Isei

High ion temperature ($T_i(0)$=8~12keV) was observed at high β_p(=2~3) plasmas, with peaked profiles of ion temperature and electron density. This enhancement is mainly due to improvement in ion transport. The electron transport shows no change between discharges with L- and high-Ti modes. The improved transport is restricted only to a central regime inside a/2. At peripheral region (2a/3), the heat diffusivity increases up to the L-mode.

1.Introduction

Extremely peaked ion temperature profiles and well peaked electron density profiles have been observed in diverted, high poloidal beta plasmas (β_p=2~3) with near-perpendicular hydrogen neutral beam injection. In such high T_i modes, the central ion temperature is about two times the electron temperature. There are many types of MHD activities observed, especially in relation to the degradation of confinement. MHD characteristics of high-Ti plasmas are described in the section of 6. Here, the discussion will be limited only to an improved transport property observed in high-Ti phase. The electron thermal transport and ion thermal transport are compared in both discharges of L- and high-Ti phases for a single null X-point, medium density, NBI heated discharges.

2. Experiments and Transport Analysis

Transport analysis procedures are described in the session of 8.6 and discharge operation for high-Ti mode in the session of 6.

In Fig. 1, typical profile data of high-Ti plasma with I_p=0.5MA, P_{abs}=17MW, and B_t=4.5 T, are presented, compared with profiles of L-mode. The most remarkable features are peaked profiles of ion temperature and electron density. The difference in birth profiles of neutral beams (Fig. 1-b) is a little and heating powers deposited to electrons and ions are almost the same inside a half radius. Therefore, the feature of peaked profiles could not be ascribed to differences in heating profiles but to substantially improved confinement.

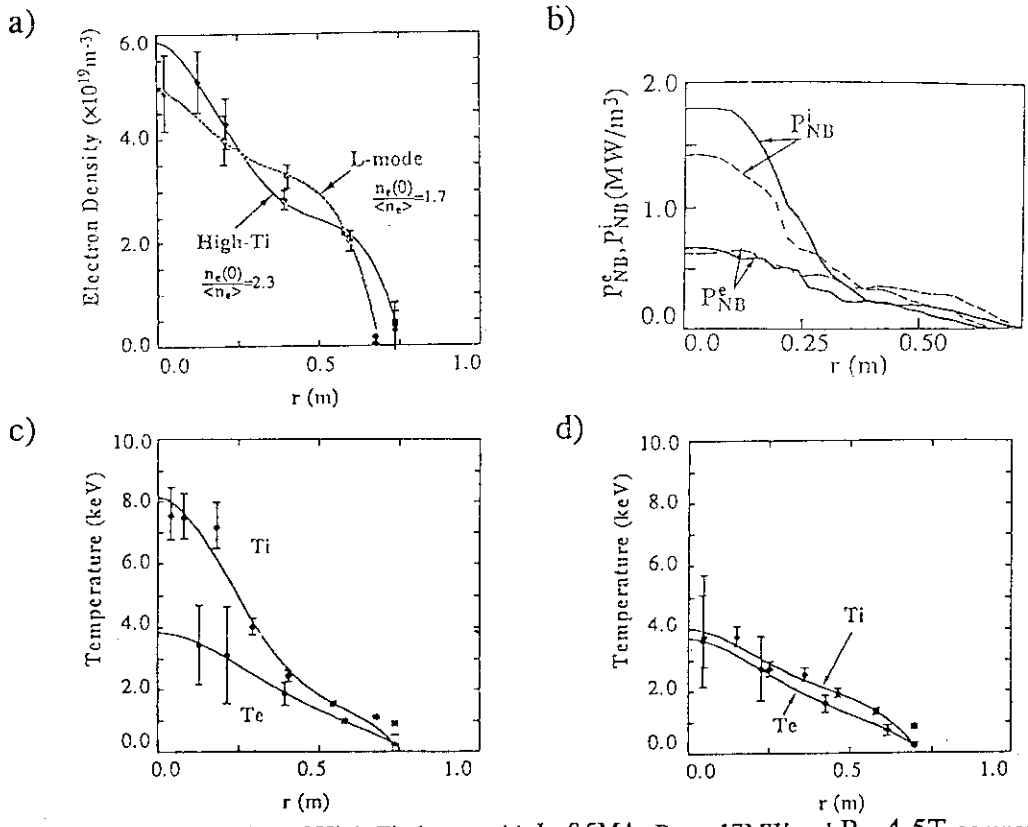

Fig. 1 Typical profile data of High-Ti plasma with I_p=0.5MA, P_{abs}=17MW and B_t=4.5T, compared with L-mode plasma with I_p=0.7MA, P_{abs}=17MW and B_t=4.5T; a) electron density profiles; b) beam deposition profiles; c) radial temperature profiles of electron and ion in High-Ti phase; d) radial temperature profiles of electron and ion in L-mode phase.

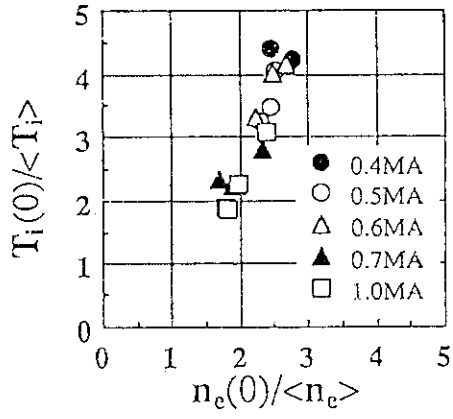

Fig.2 Comparison between peaking factors of ion temperature profiles and electron density profile.

A peaking factor of ion temperature, $T_i(0)/\langle T_i\rangle$, is shown in Fig. 2 as a function of a peaking factor of electron density, $n_e(0)/\langle n_e\rangle$. In spite of the large uncertainty in profiles, the clear relation between both peaking factors is sufficient that we can still conclude that the ion temperature profiles are peaked more than the electron density profiles and become more steeper with decreasing plasma current.

The local transport analysis, using sets of experimental data including the ion temperature profile measurements, indicate that at a central region inside a half radius the

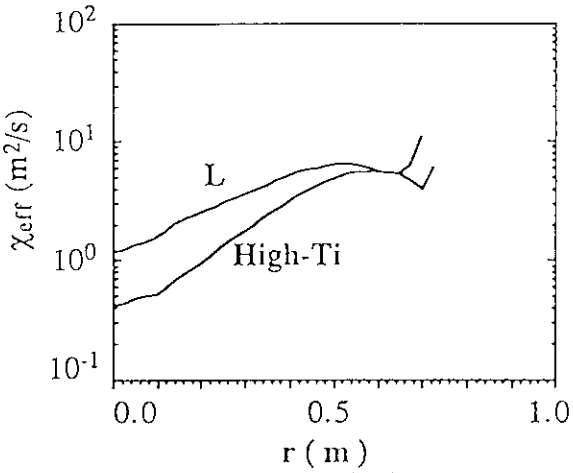

Fig. 3 Radial profiles of effective heat diffusivities in High-Ti mode, compared with in L-mode.

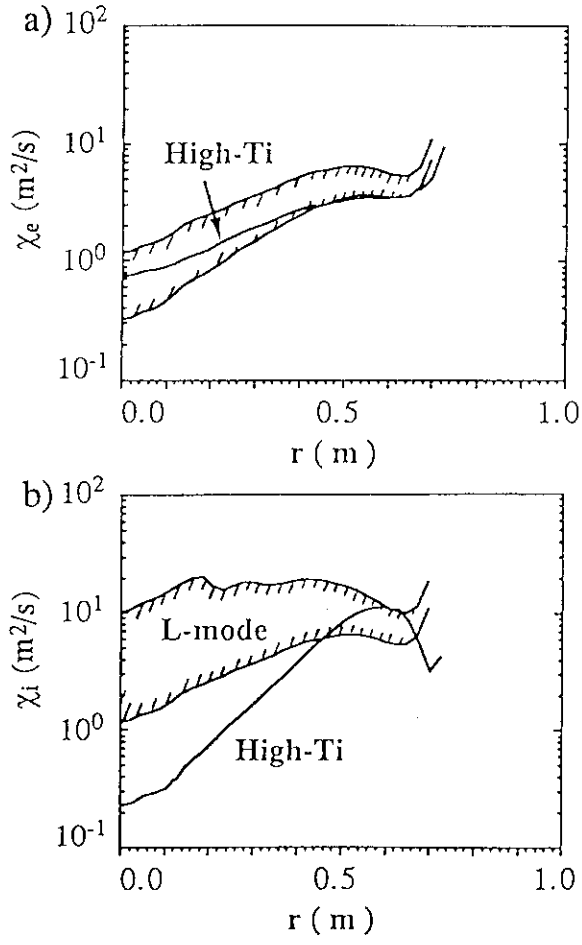

Fig.4 Comparison of spatial profile of heat diffusivities of electron and ion in High-Ti and L-modese; a) profiles of electron heat diffusivities; b) profiles of ion heat diffusivities.

effective heat diffusivity is apparently reduced to a smaller value by factor of 2-5 than in the L-mode (Fig. 3). At a peripheral region (>2a/3), the effective heat diffusivities increase up to a L-mode, which is responsible for relatively low confinement time about 50ms, although hot temperature modes with $T_i(0)$=8keV and $T_e(0)$=4keV are produced at a central region.

With a large difference in electron and ion temperatures, we can separately determine electron heat diffusivity, χ_e and ion heat diffusivity, χ_i. Figures 4-a and -b show spatial profiles of each heat diffusivity, in comparison with those of L-mode discharge. (Of course, since we cannot separately determine χ_e and χ_i in L-mode discharge, the values of χ_e and χ_i are shown in a region lied between χ_{eff} and χ_e/χ_i.) The results show that χ_i in high-Ti mode is significantly improved inside a half radius than in L-mode. Really, χ_i is close to neoclassical at r<a/3. On the other hand, the improvement in χ_e is small across over radius, but is , however, subject to large uncertainty. In spite of the larger error bars, the decrease in the ion heat diffusivities allows determination that the enhanced ion temperature is mainly due to improvement in ion transport.

3. Discussion and Summary

Since small contribution of ions to the increment of total stored energy is found in the divertor, L-mode discharges, as increases the heating power, it is reasonable that the reduction of χ_i is responsible for the improved transport observed in high-Ti mode. The improved transport is strongly related to the peakedness of electron density profiles. It has been pointed that χ_i decreases with increasing density and that particle and ion heat transport might be related [1]. It seems possible to consider that the enhanced confinement regimes observed in the presence of peaked density profiles are related to ion temperature gradient mode (η_i mode) induced transport. However, the analysis[2] show that the anomalous ion transport induced by the η_i mode in combination with the trapped electron mode results in broader ion temperature profiles due to growing trapped electron mode instead of the stablized η_i mode.

Peaked profiles of ion temperature and electron density are observed, followed by a large difference between electron and ion temperatures. The heat diffusivities of ion are significantly reduced to smaller values by a factor of about two to five in high-Ti mode than in L-mode. The central ion heat diffusivity (<a/3) is equal to neoclassical. However, the improved confinement is restricted to a central regime inside a/2. At peripheral region (2a/3), the heat diffusivity increases up to the L-mode.

References

[1] M.L. Watkins, et al.,Plasma Phys. and Cont. Fusion. **31**, pp. 1713-1724, 1989.

[2] H. Shirai, et al., see 8.8 in this report.

9. Helium Ash Experiments

9.1 NBI System for Central Helium Fueling

Masaaki Kuriyama and NBI group

1. Introduction

On purpose to simulate a helium ash exhaustion in a fusion reactor, a neutral helium beam was injected into the JT-60 plasma by using NBI one beamline unit out of 14 units. Since the JT-60 NBI[1] was designed as a neutral hydrogen beam injector, a few modification were required to operate helium beam. Those are a magnet intensity to bend a residual ion beam because of the difference of the mass weights between hydrogen and helium ions, and a pumping system to evacuate a large amount of helium gas in a beamline chamber since the present cryopump be cooled down to liquid helium temperature cannot evacuate the helium gas.

In this report, the operation, the beam characteristics of the helium beam and the pumping system for helium gas by using the JT-60 NBI are presented.

2. Operation and beam characteristics of helium beam

Since the mass weight of helium ion is four times heavier than the hydrogen ion which is regularly operated in the JT-60 NBI, the intensity of magnetic field at the bending magnet must be increased to maintain the same orbits of helium ions as those of hydrogen ones. The maximum current of the power supply for bending magnet coils on the JT-60 NBI is limited to 1500 A, and the maximum magnetic field generated is about 1.7 kG at the center of the magnet. Thus, the maximum acceleration voltage with the helium beam is limited to below 35 kV. And furthermore, the acceleration power supply for the JT-60 NBI is limited to the acceleration voltage of oner 30 keV.

In the helium beam accelerations by the JT-60 NBI ion source, the one stage acceleration system[2] which could extracted a large amount of ions in a lower beam energy level was used, because the helium beam operation range with the JT-60 NBI is limited to such a low beam energy of 30 - 35 keV described above. It can be altered easily from the original two stage acceleration by changing the connection of the power supply cables to the ion sources.

Previous to the helium beam injection into the JT-60, the helium beam characteristics including neutral beam power has been measured with the proto-type unit for JT-60 NBI. The beam extracted was 18 - 23 A per source at the acceleration voltage of 30 - 31 kV for 5 sec. The arc voltage and arc current were roughly 100 V and 400 A, respectively. The arc efficiency,defined by the amount of the acceleration current divided by arc power,was 0.5 A/kW. It was about 60 % compared with the case of hydrogen beam of 0.8 -0.9 A/kW with the same ion source. The beam current more than 23 A could not be extracted due to the unbalanced arc discharge, though the beam current of 23 A did not reach an optimum divergence judging from decreasing of the heat loads to the beamline

components with increasing beam current as shown in Fig.1. The acceleration voltage could not be raised up higher than 31 kV because the beam divergence is a change for the worse. The neutral beam power injected into a target tank is about 200 kW with an ion source as shown in Fig.2.

After the beam extraction tests on the proto-type unit, the helium beam injection into the JT-60 was performed using one unit out of 14 units. The wave forms of the acceleration voltage and current with a helium beam operation are shown in Fig.2. In this case,the helium beam of 38.9 A was extracted from two sources at the acceleration voltage of 31.5 kV, and injection power was about 400 kW. The maximum beam pulse length on the helium beam injection into the JT-60 was 3 sec.

3. Pumping system for helium gas

In the helium beam operation, a special gas pumping system which could evacuate a large amount of the helium gas was required. The present cryopump system of the JT-60 NBI can not pump out the helium gas. A cryo-sorption pump[3] was adopted to pump out the helium gas. The SF6 gas was condensed on the surface of the present cryopanels which are cooled down to below 4 K ahead of pumping the helium gas. The condensed surface layer of SF6 gas has a capabilty of helium gas pumping at a liquid helium temperature range. The layer does not have pumping capability at the temperature of liquid nitrogen, though the SF6 gas will condense at the temperature range below -50 degree centigrade. Thus, the SF6 gas have no need to be condensed to the shevron buffles which are cooled down to the liquid nitrogen temperature. The SF6 gas feeder tubes made of stainless steel were set up between the cryopanel and the shevron buffle in the cryopump inorder to condense the gas onto the cryopanel only. The SF6 gas is spouted out to the cryopanel from a lot of tiny holes of 0.3 mm in diameter with a pitch of 20 mm. The tubes are heated up over the temperature of freezing point of SF6 gas by flowing directly the electric current.

Prior to helium gas pumping operation, the SF6 gas of about 80000 $Pa.m^3$ was fed onto the large size pump(1 m in width x 4 m in height x 4 panels) and about 6000 $Pa.m^3$ onto small size pump(0.6 m x 1 m x 2 panels). The wave forms of the beamline pressure with beam injection are shown in Fig.3. The total pumping speed achived with six panels (total pumping area: 15 m^2) of the cryo-sorption pumps was about 800 m^3/s for helium gas at the pressure of the order of 10^{-3} Pa. The cryo-sorption pump was operated well with long pulse helium beam injection up to 3 sec, and any problem was not found.

4. Summary

1) The helium beam injection for investigating fusion alpha particles exhaustion was performed using one unit of the JT-60 NBI. The helium beam current extracted was 40 - 45 A with two sources at the energy of 31 keV, the neutral helium beam power obtained was about 400 kW.

2) A large amount of helium gas pumping was confirmed by using SF6 gas condensed cryo-sorption pump. The pumping speed for helium gas achieved was about 800 m^3/S.

References

[1] S.Matsuda,et al.,"The JT-60 Neutral Beam Injecton System" Fusion Engng. and Design 5(1987) pp85-100
[2] M.Mizuno, et al.,"Operation of The JT-60 Neutral Beam Injection System" in Proceeding of the 12th Symp. on Fusion Engng, Monterey,Oct.12-16 (1987) pp281-284
[3] K.Shibanuma,et al.,"Experiment on Helium Evacuation by Cryosorption pump",J.of Vacuum Soc.of Japan,31-5 (1988) 311(in Japanese)

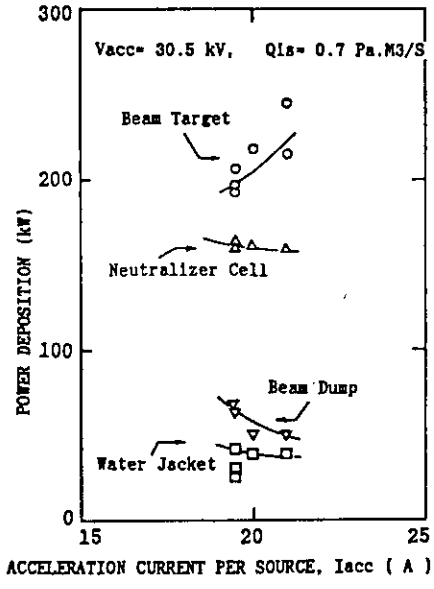

Fig.1 Heat loads to the beamline components with helium beam

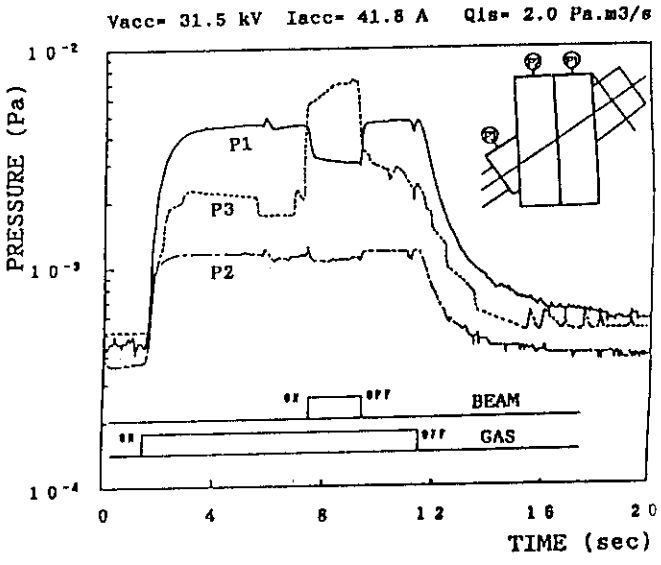

Fig.3 Pressures in the beamline with helium beam

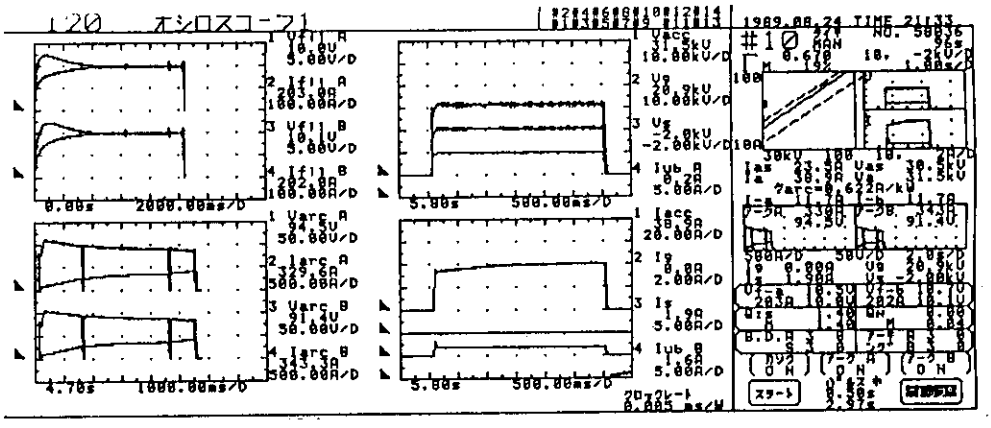

Fig.2 Wave forms with helium beam

9.2 Divertor Residual Gas Mass Analyzer System in Helium Ash Experiments

T. Arai, A. Kaminaga and JT-60 Team

1. Introduction

For tokamak reactor design, characteristics of helium ash produced by DT reaction is one of the key issues. Therefore, experiments on helium ash exhaust is important in existing mashine. In helium ash experiments, measurements of neutral pressures of hydrogen and helium in divertor region is one the important items for evaluations of neutral pressure build-up and helium enrichment factor. For this purpose, in JT-60 lower divertor experiments, the neutral pressures of helium and hydrogen near inner divertor region were measure by a magnetically shielded residual gas mass analyzer. In this paper, description of the RGA system and typical experimental results are described.

2. Description of RGA System

Figure 1 shows overview of the RGA system in this study. RGA used in this study is MSQ 150 produced by ULVAC Co. (Japan). This RGA was attached to lower port and lacated on floor of torus hall. Vertical and horizontal components of magnetic field at the location of the RGA are 200 Gauss in flat-top of Ip=2.2 MA discharge. To reduce these magnetic field to acceptable level, magnetic shield was used. Delay time of this system is about 0.4 s. Minimum scanning time is 0.1 s. Scanning range of mass can be selected by digital switch. Signal from the RGA was transfered to central control room by optical fiber through a CAMAC system in the torus hall. In the control room, RGA signal was stored in hard disc memory of personal computer (PC9801E, NEC). After completition of data acquisition, wave form of the RGA mass spectrum was displayed.

3. Results

3.1 Caliburation of RGA

To obtain absolute neutral pressures of helium and hydrogen, caliburation experiment was done in JT-60 machine. Helium or hydrogen gas was injected during 30 to 60s to obtain steady state condition inside vacuum vessel. Absolute neutral pressures were measured by caliburated ionization gauge of torus main pumping system. Relation between the RGA signal and the absolute neutral pressure was obatined. Using sensivities of the ionization gauge as 0.491 for hydrogen and 0.022 for helium, sensivities of the RGA are 0.014 Pa/A for hydrogen and 0.022 Pa/A for helium.

3.2 Divertor Experiment

Figure 2 shows typical wave form of RGA mass spectrum in 1 MA divertor discharge. In this case, scanning range of the RGA was m/e=1 to 6. Hygrogen NB was injected in t= 4 s to 8.5 s. Helium NB was injected in t=4.5 s to 6 s. After a start of the hydrogen NB, increase of hydrogen neutral pressure was obserbed. Also, helium neutral pressure increase. In the NB heated divertor discharges with helium NB fuelling, both neutral pressures increase with ne^3 . This characteristics is promising for helium ash exhaust with open divertor. High density operation is necessary for efficient ash exhaust.

4. Summary

In JT-60 lower divertor experiments, magneticaly shielded RGA was used. Results are summarized as follows;

- Magnetically shielded RGA can be used in JT-60 lower divertor experiments.
- Neutral pressures of hydrogen and helium were measured with a scanning time of 0.1 s in the range of m/e=1 to 6.
- Density dependences of the neutral pressures show hydrogen and helium pressures increase with ne^3 .

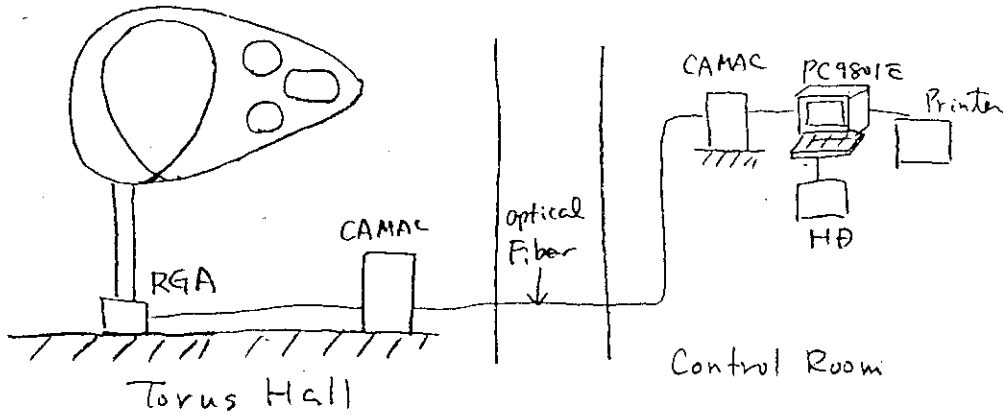

Fig. 1 Overview of divertor RGA system and data aquisition system in helium ash experiment.

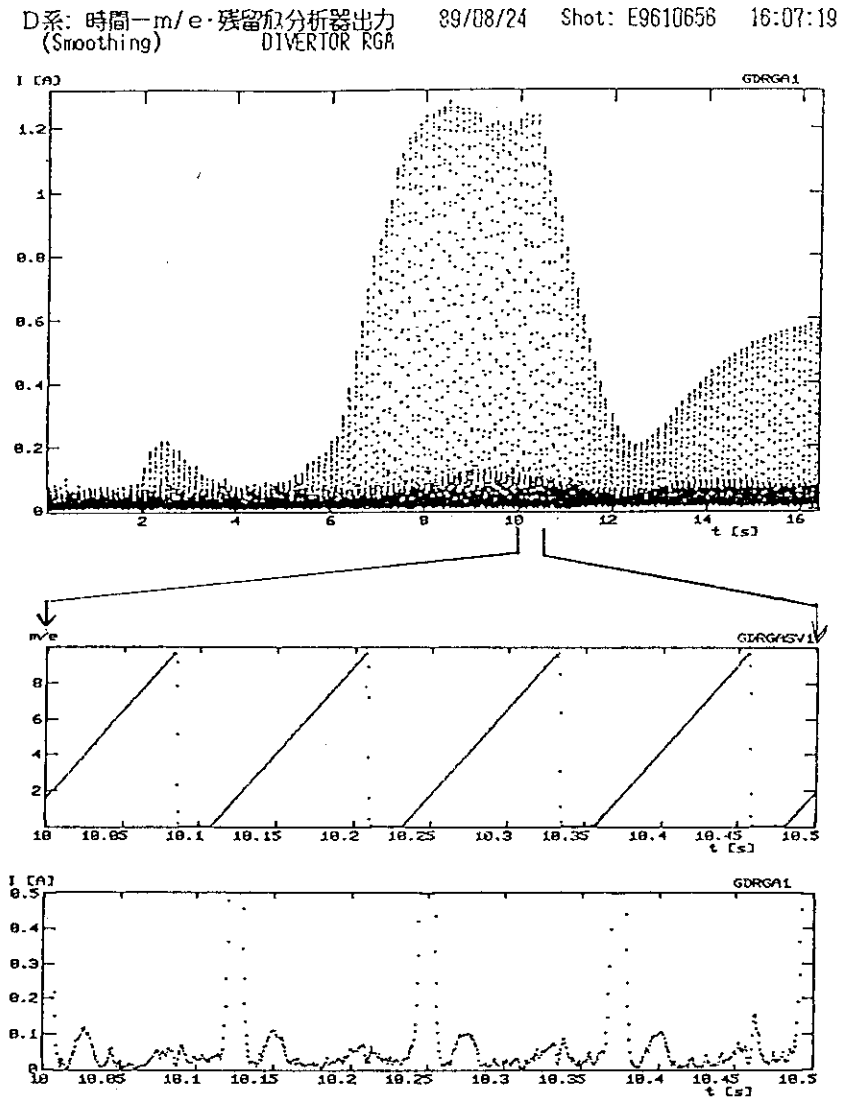

Fig. 2 Typical waveforms of neutral pressures of hydrogen and helium in divertor discharge of Ip= 1 MA and P_{NB}=8 MW.

9.3 Helium Ash Exhaust Experiments in Lower Divertor

H. Nakamura, K. Tobita, Y. Koide, T. Hirayama, T. Arai
T. Itoh, A. Kaminaga, K. Kikuchi, H. Kubo, M. Kuriyama
Y. Kusama, M. Mizuno, T. Sugie, K. Tani, Y. Tsukahara

1. Introduction

To realize quasi-steady DT burning plasma, control of helium ash produced by DT reaction is one of key issues. For this purpose, investigations on helium ash exhaust and transport are important. In previous experiments, helium ash exhaust was studied in ohmically heated discharges[1], [2] and helium ash transport in additionally heated one with Pabs=1.2 MW[3]. But, in these experiments, the heating powers are not enough high to simulate a reactor-grade plasma. Also, in these experiments, helium was injected by gas puffing. But, in the helium ash produced in DT reaction, helium ash has centraly peaked profile. Therefore, to study the helium ash characteristics in the conditions of high heating power and central helium fuelling, the helium ash simulation experiments have been done with 10 MW to 20 MW of the hydrogen neutral beam injection heating and central fuelling by 30 keV helium neutral beam. Characteristics of helium ash exhaust on neutral build-up and enrichment factor have been studied.

2. Experimental Apparatus

Fig. 1 shows the major diagnostics in the helium ash exhaust experiments. He^0 fuelling beam is injected with beam energy of 30 kev and fuelling rate of 0.2Pam^3/s. Fig. 2 shows calculated deposition profile of helium beam. The line integral electron density of the main plasma was measured by a 3 channel sub-milimeter FIR interferlmeter. Neutral partial pressures of hydrogen and helium are measured by magnetically shielded residual gas mass analyzer with time delay of 0.4 s in the inner divertor side. Scanning time from m/e=1 to m/e=6 is 0.1 s. In the divertor region, Hβ and HeII intensities were measured by spectrometer with view angle around the X-point and the divertor plate. Helium particle density in the central region was measured by injecting He probe beam with the beam energy of 160 keV to 200 keV.

3. Results

Enrichment factor η is defined with the equation of $\eta = (n_{He}/n_H)^{DIV} / (n_{He}/n_H)^{MAIN}$, where n_{He} and n_H are particle densities of helium and hydrogen in divertor and

main plasmas. In this study, η was calculated by the modified equation of $(P_{He}/2P_{H2})^{DIV}/(\Delta ne/2ne)^{MAIN}$, where Δne is increment of the density afterthe helium gas puff, ne is the electron density, P_{He} is partial pressure of helium, P_{H2} is partial pressure of hydrogen.

(1) NB heated discharge with helium gas puff[4]

In neutral beam heated discharges, the helium gas was fuelled by two different fuelling modes. In short pulse mode, helium gas was injected with fuelling rate of 2.5 Pam^3/s x 0.2 s before or during the NB heating. In long pulse mode, fuelling rate of helium gas was of 0.5 Pam^3/s x 0.2 s during the NB heating. P_{NB} is 5 MW to 18 MW, ne is (2~6) x10^{19} m^{-3}, Ip is 1 MA and Bt is 3 T to 4.5 T. Fig. 3 shows density dependence of the hydrogen and helium pressures in short pulse fuelling mode. Although exact density dependence is not obtained, both pressures increase with similar density dependence. Fig. 4 shows density dependence of the enrichment factor in short pulse mode and long pulse one. In the short pulse mode, η is 0.1 to 0.3 in ne= (2 ~ 5.5) x10^{19} m^{-3}. On the other hand, in the long pulse mode, η is 0.7 to 0.8. This high enrichment factor is considered to be caused by shielding of the fuelled helium in edge plasma.

(2) NB heated discharge with helium NB injection

To simulate helium ash in plasma core region, helium neutral beam was injected with beam energy of 30 keV and fuelling rate of 0.2 Pam^3/s in 2 s during the hydrogen NB heating. Discharge parameters are Ip=1 MA, Bt=4.5 T, P_{NB}= 10 MW to 18 MW, and ne= (3~5) x10^{19}m^{-3}. Figs. 5 shows density dependences of the hydrogen and helium partial pressures. Both pressures increase in proportion to ne^3, although fuelling rate of helium beam is constant. Helium build-up is induced by enhanced recycling in the divertor plasma. Fig. 6 shows the density dependence of the enrichment factor η. Enrichment factor is 0.3 to 0.6 and increases with ne. This linear dependence of the enrichment factor on ne can be explained by parameter dependences of $P_{He}, P_{H2} \propto ne^3$ and constant helium fuelling rate. These results suggest that high density operation can reduce required pumping speed of helium ash in divertor region.

4. Discussion

To explain characteristics of helium ash exhaust in JT-60 lower divertor, simple zero point mode has been applied. Particle balance equations are as follows;

$$\frac{dNm}{dt} = Q - (1-R)\frac{Nm}{\tau p} \qquad \text{---------- (1)}$$

$$(Pdiv - Pmain)\,C = R\,\frac{Nm}{\tau p} \quad \text{---------- (2)}$$

$$Pdiv\,Sp = (1-R)\,\frac{Nm}{\tau p} = Q \quad \text{---------- (3)}$$

where definitions of each parameter are

Nm ; Total Number of Helium in Main Plasma
Q ; Fuelling Rate or Generation Rate of Helium
τp ; Particle Confinement Time of Helium
Pmain ; Neutral Pressure around Main Plasma
Pdiv ; Neutral Pressure in Divertor Region
R ; Recycling Coefficient
C ; Conductance between Plasma and Divertor
Sp ; Pumping Speed

For steady state conditions, neutral pressure in the divertor region is calculated by $Pdiv = Nm/(C\tau_p)$ assuming $C \gg Sp$. In case of $ne=1\times10^{20}$ m^{-3}, $Nm=8.4\times10^{19}$, τ_p is 26 ms and C is 260 m^3/s, calculated neutral pressure in divertor region is 0.025 Pa. This value is by a factor 4 small to the value estimated by the experimental result, which is 0.1 Pa. This difference is caused by ambiguities in particle confinement time and conductance between main plasma and divertor region.

5. Summary

In helium ash experiment with JT-60 lower divertor discharges, the following results are obtained.

- In NB heated discharges with helium gas puff, enrichment factors are 0.1-0.3 in short pulse helium puff and 0.7-0.8 in long pulse helium puff.
- In NB heated discahrges with He beam fuelling, He and H_2 neutral pressures increase with ne^3. Enrichment factor is 0.3-0.6 and increase with ne.

These results show that helium ash exhaust is promising in open divertor of fusion reactor. In future, experiment on helium transport is necessary.

References

[1] M. Shimada, et al., Phys. Rev. Lett. 47 (1981) 796.
[2] J. C. Deboo, et al., Nucl. Fusion 22 (1982) 572.
[3] R. J. Fonck, et al., PPPL-2068 (1984).
[4] H. Nakamura, et al., in Proc. of IAEA TCM on α particle confinement and heating, Kiev, Oct. 1989. (to be published in Special issue of Fusion Technology)
[5] H. Nakamura, et al., to be submitted to Phys. Rev. Lett.

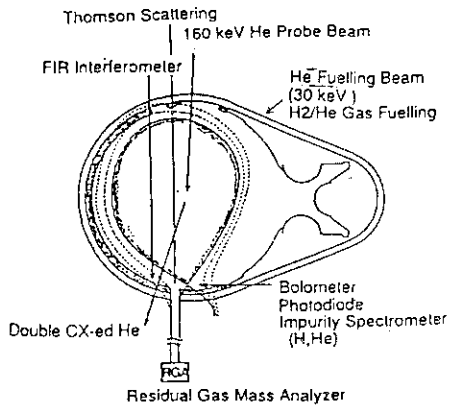

Fig. 1 Major diagnostics in helium ash experiment.

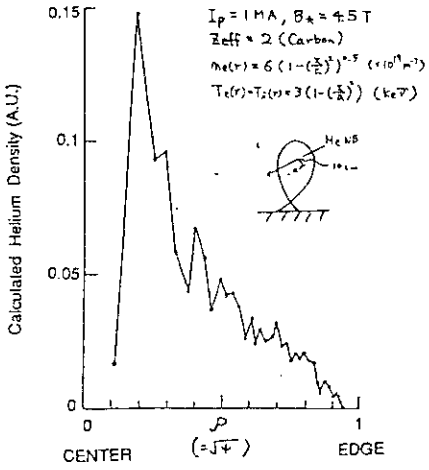

Fig. 2 Calculated deposition profile of helium beam.

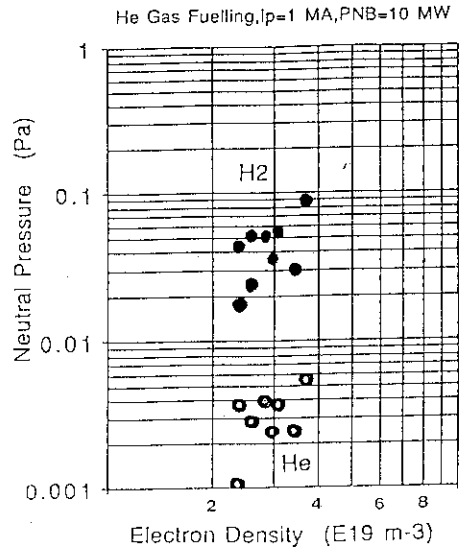

Fig. 3 Density dependence of neutral pressures of H2 and He in NB heated discharges with He gas fuelling.

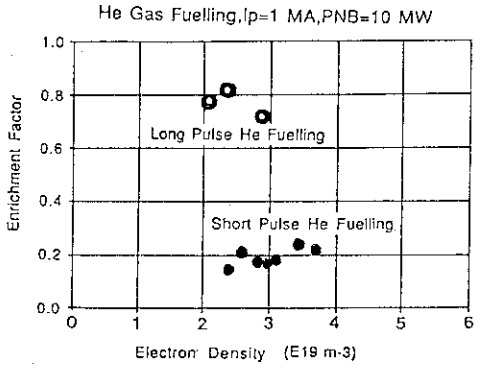

Fig. 4 Density dependence of enrichment factor in short and long pulse He fuelling.

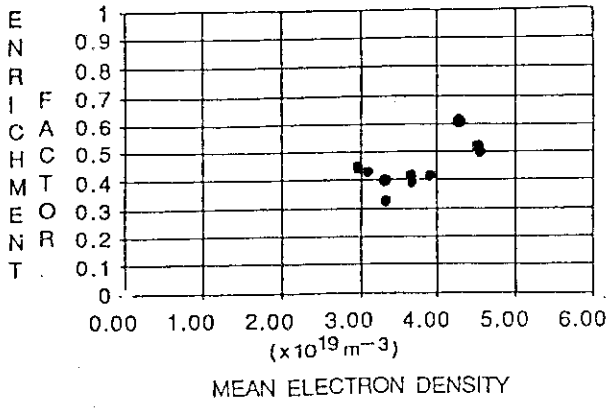

Fig. 6 Density dependence of enrichment factor in He NB fuelling.

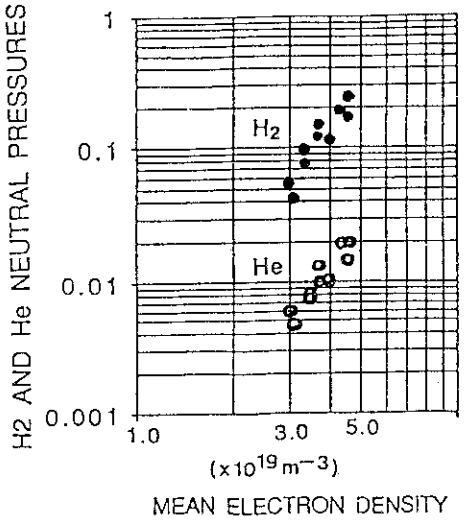

Fig. 5 Density dependence of neutral pressures of H2 and He in NB heated discharges with He NB fuelling.

9.4 Central helium density measurement

K. Tobita, Y. Kusama, T. Itoh, H. Nakamura, Y. Tsukahara, M. Nemoto
and H. Takeuchi

Radial alpha density profile is one of keys to understanding the transport of alpha ash in a fusion plasma. The alpha density is one of the most difficult quantities to be measured. Possible methods for measuring it are charge exchange recombination spectroscopy[1], and nuclear techniques which make use of the $d(d,n)^3He$, $^3He(d,p)\alpha$ and $t(d,n)\alpha$ fusion reactions[2]. In this section we describes the helium density measurement using double-electron transfer reaction, $He_{th}^{2+} + He_b^0$ -----> $He_{th}^0 + He_b^{2+}$, where He_{th}^{2+} and He_b^0 represent thermal alpha and probing atomic helium, respectively. The cross section of this reaction is over 10^{-16} cm^2 below a reduced energy of 50 keV/amu. This technique is applicable to the alpha velocity distribution measurement[3] as well as the density measurement. The number of He^0 detected within a velocity of v and v+dv is given as follows:

$$n_{det}(v)\,dv = n_b\, n_\alpha\, f_\alpha(v)\, \sigma_{20}(|\vec{v} - \vec{v}_b|)\,|\vec{v} - \vec{v}_b|\,(1-A_1)\,(1-A_2)\,\eta_D \frac{\Delta\Omega}{4\pi}\,\Delta V\,dv \quad (1)$$

where n_b, n_α, $f_\alpha(v)$, $\vec{v}$ and $\vec{v}_b$ are the number density of the probing beam entering the plasma, the alpha density and the velocity distribution function of alphas, the velocity of a neutralized alpha and the velocity of the probing beam, respectively. The detection efficiency of the particle detection system, the observing solid angle of the system and the observation volume in the plasma are represented by η_D, $\Delta\Omega$ and ΔV, respectively. The transmission of the beam from the plasma boundary to the plasma center and that of the produced He^0 from the center to the boundary are denoted by $(1-A_1)$ and $(1-A_2)$, respectively, and the cross section for double-electron transfer is represented by σ_{20}. Integrating eq.(1) over v from 0 to ∞, we can determine n_α when the efficiencies of the diagnostic beam and the detecting system are known.

Measuring system consists of a 100-200 keV He diagnostic beam and a calibrated E//B type neutral particle analyzer (Fig.1). The diagnostic beam typically

injects 0.2-0.35 A of ground-state and 0.06-0.11A of metastable atoms. The metastables are of no use in the measurement because almost all of them disappears in the edge plasma because of their short mean free path. The line-of-sight of the analyzer intersects the beam line at the plasma center at an angle of 5.3°. The analyzer selectively detects helium atoms.

Figure 2 shows time evolutions of the electron line density ($n_e l$), the injected beam power (P_{NB}), the flow quantity of puffed gas (Q), HeII emissivity ($HeII^{div}$) in the divertor and the central alpha density ($n_{\alpha 0}$) hydrogen discharges with and without He gas puffing. Existence of alpha in the no gas puffing shot is due to release of He gas from the first wall. Difference in $n_{\alpha 0}$ in both the shots is 4.5×10^{12} cm^{-3} at t = 7.0 s. This value is comparable with the alpha density inferred from the electron density difference ($\Delta\bar{n}_e/2 = 3.5\times10^{12}$ cm^{-3}). Time evolution of them for a long He puffing shot is shown in Fig.3. In the period of t = 5.0-6.0 s, the alpha density increment $\Delta n_{\alpha 0}/\Delta t$ (= 1.5×10^{12} cm^{-3}/s) agrees well with the value estimated from $\Delta\bar{n}_e/2\Delta t$ (= 1.5×10^{12} cm^{-3} /s). Although He gas is fed at a constant Q and the emissivity of HeII from the divertor plasma rises linearly with time, the density increment of $n_{\alpha 0}$ decreases with $n_e l$. This result shows that the ratio of central helium density to the electron temperature saturates at 6% in this case. Excessive accumulation of helium in the central region is not observed.

References

[1] R.J.Fonck, and R. A. Hulse, Phys. Rev. Lett. **52** (1984) 530.

[2] J.D.Strachan, R.E.Chrien, and W.W.Heidbrink, J. Vac. Sci. Technol. **A1** (1983) 811.

[3] D.E.Post, D.R.Mikkelsen, R.A.Hulse *et al.*, Journal of Fusion Energy **1** (1981) 129.

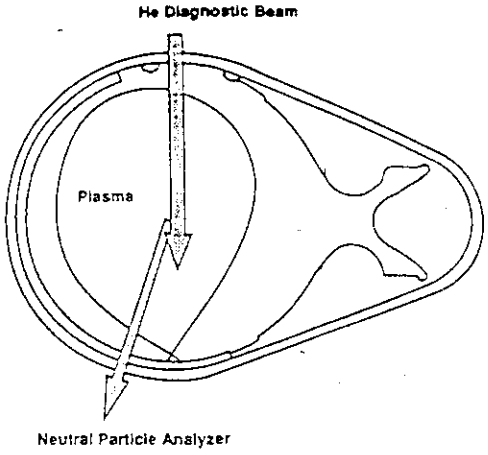

Fig. 1 Experimental arrangement for the central alpha density measurement

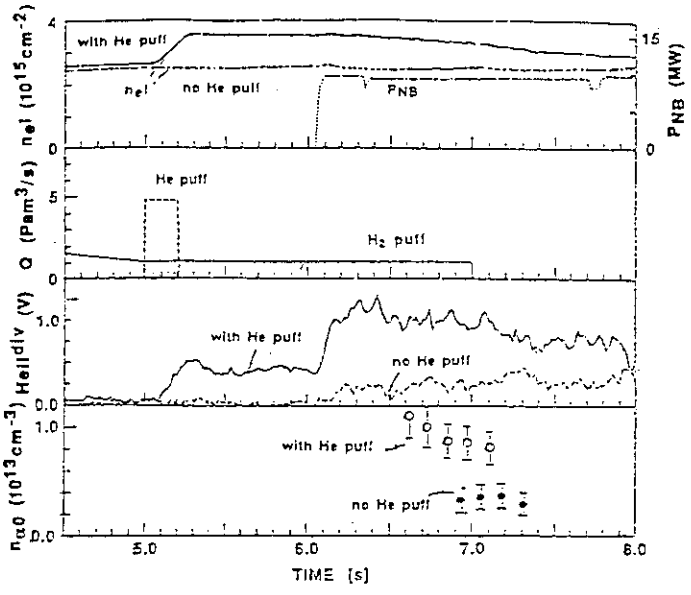

Fig. 2 Time evolution of $n_e l$, P_{NB}, Q, $HeII^{div}$ and $n_{\alpha 0}$ in shots with and without He gas puffing

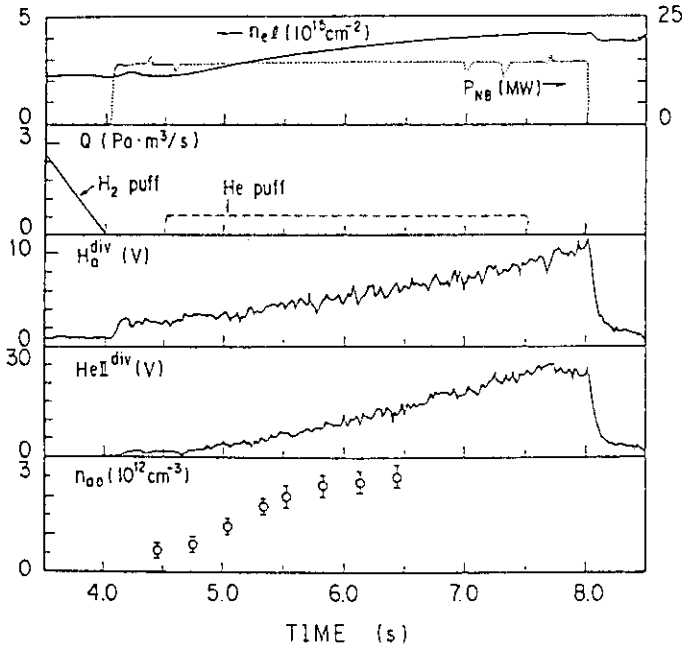

Fig.3 Time evolution of $n_e l$, P_{NB}, Q, $H\alpha^{div}$, $HeII^{div}$ and $n_{\alpha 0}$ in a long He puffing shot

10. Disruptions

10.1 STATISTICAL ANALYSIS OF DISRUPTIONS

I. Yonekawa, T. Kimura and the JT-60 team

1. INTRODUCTION

Clarification of the disruption phenomena in tokamak operation is one of the important issues for nuclear fusion development. For obtaining some qualitative explanations of the disruptions, we have investigated statistically the characterisics of the disruptions, and their relations to the operation conditions at JT-60. The statistical survey was reported in ref.[1] of the disruptions in the JT-60 operation before the development of the lower X-point divertor configuration. This paper describes the survey of the disruptions occurred in the past five-year operation from the first plasma to the lower X-point divertor operation.

2. RESULTS AND DISCUSSIONS

The disruption shots, which are picked up among about 9000 shots from the first plasma in April, 1985 to the end of the advanced experiment(I) in October, 1989, are statistically investigated on the following items; the frequency, the discharge phase occurred, the decay speed of the plasma current, their features in the NB injected heating experiments, etc.

(1) Frequency of disruptions

As shown in Table 1, the average frequency of the disruptions occurred in the whole period of JT-60 is about 30%. A lot of disruptions took place at the operation phases for step-up of plasma current after the first plasma and just after the replacement of the first wall of TiC coated molybdenum to graphite in 1987, and in the duct cleaning shots for NB injection system after the long discharge cleaning. Table 2 shows that the disruption frequency depends on the additional heating method. The average frequencies in the NB heated discharge shots and the RF wave heated ones are 36% and 18% respectively. This difference suggests that one of the main causes of the disruptions may be the density limit. The frequency in the operation for the plasma heating combined with NB and RF waves is 28%, which corresponds to the average in the individual heating operation.

(2) Decay speed of the plasma current

The decay speed of the plasma current dIp/dt in all of the JT-60

disruption shots is summarized in Fig. 1. The maximum value of the decay speed of the plasma current increases linearly with increasing the plasma current. The minimum value of the plasma current quench time is about 6 msec. The decay rate of the fastest disruption is 470 MA/sec, which was observed just after turning the NB power off in the 3 MA limiter discharge (E5841). The number of the disruption shots where the decy speed exceeds the design value of 270 MA/sec amounts to about 4 % of the total disruption shots in the operation before the modification for the lower X-point divertor operation. On the other hand, the numer of the disruption shot with the Ip decay speed over the design value is only one. As shown in Figs. 2 and 3, there is no significant differnce between the maximum values of the Ip decay speed in the limiter and divertor operations after the modificaion for the lower X-point divertor.

As shown in Fig. 4, the maximum value of the Ip decay rate is related linearly with increasing Ip in the limiter discharges before the modification for the lower X-point divertor. In the limiter operation after the modification, however, the maximum Ip decay rate saturates with increasing Ip over 2 MA as shown in Fig. 3. This fact suggests that the coupling of the plasma current to the poloidal field coil current may change due to the modification of the poloidal field coils.

(3)Features of the disruptions in the neutral beam heating experiments

As shown in Table 2, in the NB heating experiments about two third of the disruptions took place after its input power off and no disruptions were observed at the start phase of the power input. The number of disruption shots during the power input amounts to about 7 % of the total NB heated shots. Most of the above disruptions occurred in the operation for the duct cleaning and in the operation combined with NB heating and pellet injection after the divertor modification. The rest of the disruptions occrred in the low-q, the reverse of the toroidal field direction and the Ne injection operations.

3. SUMMARY

The disruptions in the JT-60 operation from the first plasma to the end of the advanced experiment (1) are statistically investigated on the frequency, the discharge phase occurred, the decay speed of the plasma current, the features of the disruplons in the operation of NB heating, etc. These results must be help of further investigations for the explanation of the disruption mechanism in the tokamak.

REFERENCES

[1] Kimura, T., Yonekawa, I., et al., JAERI-M 89-033 (1989) 34.

Table 1 Disruption frequencies at JT-60

FY / First Wall / Configuration	1985,1986 TiC(Mo) (C)	1987 Graphite Before (D) Modification for LX Divertor	1988,1989 Graphite After (E) Modification for LX Divertor	Whole Period (C)+(D)+(E)
Limiter (A)	152/374 (40.6%)	350/912 (38.4%)	736/2433 (30.3%)	1238/3719 (33.3%)
Divertor(B)	370/1902 (19.5%)	222/639 (34.7%)	785/2521 (31.2%)	1377/5062 (27.2%)
Total Number (A)+(B)	522/2276 (22.9%)	572/1551 (36.9%)	1521/4954 (30.7%)	2615/8781 (29.8%)

LX Divertor: Lower X-point Divertor

Table 2 Disruption Analysis of NB Heating shots

OH	NBI	RF	NBI+RF
1296/3800 (33.3%)	669/1872 (35.7%)	331/1858 (17.8%)	319/1155 (27.6%)

Just power on	On power	During power down	After power off
0 (0%)	136 (20.3%)	82 (12.3%)	451 (67.4%)

FY	L/D	NB only	NB with Pellet	cleaning shots
'85 ~ '87	L:14	13	0	1
	D:20	20	0	0
'88 ~ '89	L:76	29	25	22
	D:26	19	2	5

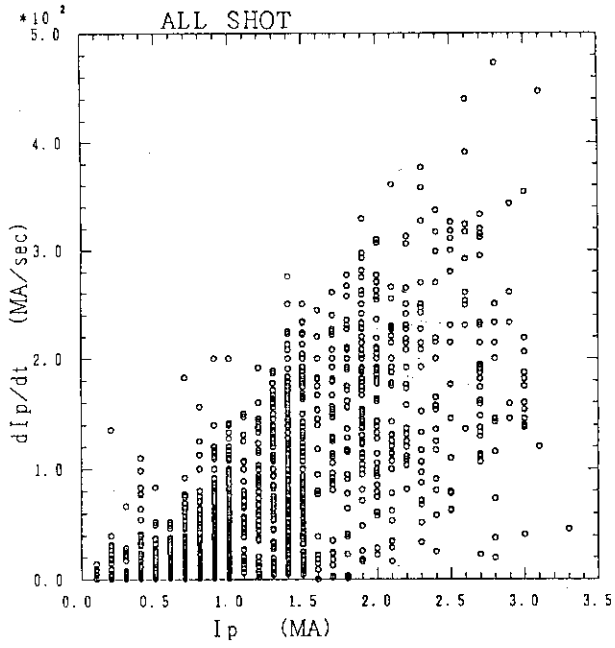

Fig.1 Ip decay speed of all the disruption shots.

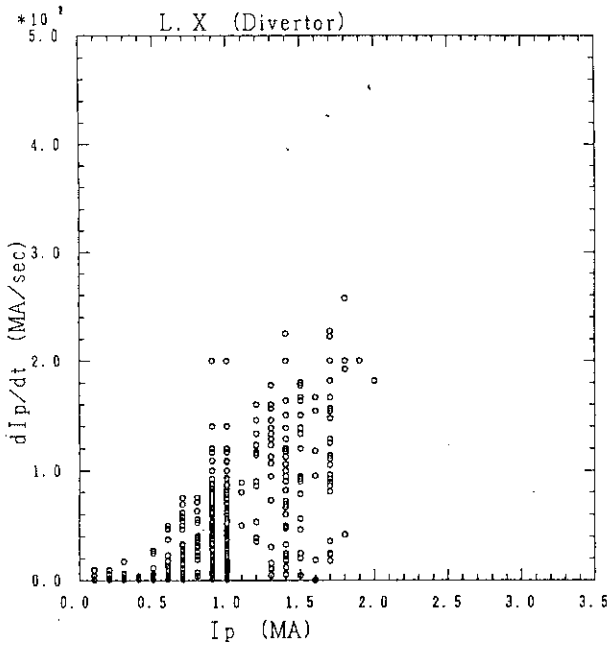

Fig.2 Ip decay speed of the disruptions in the divertor operation after the LX divertor modification

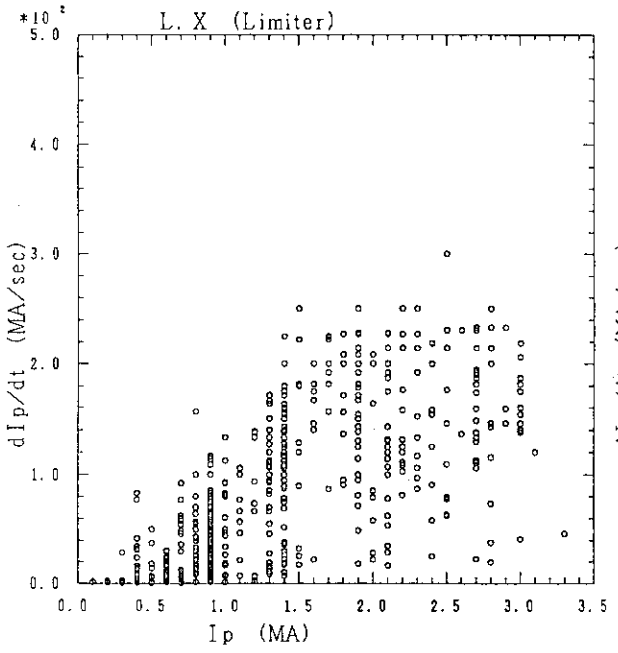

Fig.3 Ip decay speed of the disruptions in the limiter operation after the LX divertor modification

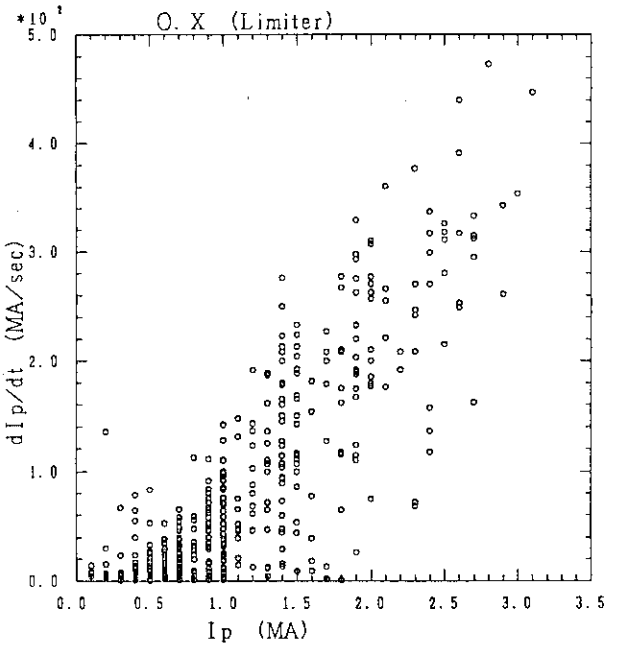

Fig.4 Ip decay speed of the disruptions in the limiter operation before the LX divertor modification

10.2 Magnetic Energy Loss During Major Disruptions

N.Hosogane

1. Introduction

There are two phases for energy loss in a disrutpion; heat quench phase and current quench phase. In the heat quench phase, thermal energy of plasma is released very fast through the ergotic magnetic structure caused by the MHD activities. The plasma is rapidly cooled in this phase, and the plasma resistance increases by an order of 100-1000. As a result, the plasma current decays very rapidly. In the current quench phase, the magnetic energy of the plasma and the poloidal magnetic field coils is lost. Some of the magnetic energy is dissipated due to the plasma resistance, some is lost through the induction of the vessel current and the generation of runaway electrons. The magnetic energy loss is much larger than the thermal energy loss in JT-60. The energy loss in disruptions is critical for designing large tokamaks. It is, therefore, important to evaluate the energy loss in each branch, and to understand the energy loss mechanism. Here, the magnetic energy loss is discussed.

2. Evaluation of magnetic energy loss for disruptions

The magnetic energy dissipated in the plasma is expressed as

$$\Delta W_{diss.} \equiv \int_t^{t+\Delta t} R_p I_p^2 dt = -\Delta\left(\sum_{i=1}^{N}\sum_{j=1}^{N}\frac{1}{2}M_{ij}I_iI_j\right) - \sum_{i=1}^{N}\int_t^{t+\Delta t} R_iI_i^2dt + \sum_{k=1}^{N-1}\int_t^{t+\Delta t} V_kI_kdt \qquad (1)$$

where I_p and I_i's are plasma current and poloidal magnetic field coil (P/S coil) currents, M_{ij}'s are self-inductances (i=j) and mutual-inductances ($i\neq j$) between them, R_p and R_i's are their resistances, respectively. V_k is applied voltage of P/S coils. Δt is disruption time. The energy loss given by the left hand side of Eq.(1) includes the energy loss not only due to the plasma resistance, but also due to the generation of runaway electrons. Here, the vessel current induced by the disruption is neglected. The energy loss through the induction of the vessel current is discussed in section 3. Assuming that the plasma inductance is constant during a disruption, the right hand side of Eq.(1) can be calculated. For lower X-point divertor plasmas, outer X-point divertor plasmas and limiter plasmas, L_p's (=M_{11}) are assumed to be 7.8 μH, 7.1 μH and 7.1μH, respectively.

Figure 1 shows a typical disruption of lower X-point divertor discharge. The plasma current is 1.7 MA. The major disruption occurs at 7.05 sec. The current quench time is about 15 msec. The variation of magnetic energy before and after the disruption is 12 MJ, and the dissipated energy loss is 10.5 MJ. The ohmic input energy during the disrutpion is

small (0.1 MJ). The average dissipated power is about 700 MW. The dissipated energy is roughly equal to the magnetic energy of plasma current stored in the space between plasma and the P/S coils including the inside of the plasma. This is because the resistance of the vessel current is so large that the vessel does not decouple the plasma current with the P/S coils even in the fast phenomenon.

Figure 2 shows the dissipated energy loss as a function of plasma current. The dissipated energy is proportional to the square of plasma current, and increases up to about 24 MJ for a disruption of 3.1 MA limiter discharge. At the same plasma current, the dissipated energies for lower X-point divertor discharges are large compared with those of other limiter and outer X-point divertor discharges since self-inductances of plasmas are large.

3. Measurement of Induced Vessel Current

The vessel current induced by disruptions was measured with two Rogowski coils installed inside and outside the vessel. The induced vessel current at its peak is shown in Fig.3 as a function of plasma current $I_p(0)$ just before disruptions. The sampling time of the measurement is 5 msec, so that there may be errors of about 25 %. For 3 MA disruptions, the induced vessel current is about 0.3-0.4 MA. The induced vessel current I_{VV} depends on the disruption speed. Figure 4 shows the ratio $I_{VV}/I_p(0)$ as a function of dI_p/dt. The ratio $I_{VV}/I_p(0)$ is about 10 %. The variation of $I_{VV}/I_p(0)$ is weak compared with dI_p/dt although the induced loop voltage is proportional to dI_p/dt. This is considered to be due to the skin effect for the fast disruption.

Since the vessel current is not uniform, the dissipated energy loss through the vessel current is estimated using the simulation of the induction described in section 4.

4. Simulation of the induction of the vessel current

To check the measurement of the vessel current and to estimate the dissipated energy loss through it, simple simulation of the induction of the P/S coil current and the vessel current by disruptions was carried out. In this calculation, the vessel is divided into 18 blocks, and is replaced with 18 filament coils having resistances equivalent to those of the blocks.

A typical calculation result is shown in Fig.5. In Fig.5(a), the plasma resistances before the disruption is 0.5 $\mu\Omega$, and increases up to 0.5 mΩ in 0.1 msec and 2.5 mΩ exponentially so as to quench the plasma current as observed in the experiment. The resistance of 1 mΩ corresponds to that of plasma with electron temperature of about 10 eV. Such low temperature is reasonable since plasma should be significantly cooled in the hard disruption. In the calculation, the disruption speed is about 500 MA/sec, and

the induced vessel current is 0.4 MA. This disruption speed is almost the maximum speed observed in the experiment (450 MA/sec) , and the calculated vessel current is almost the same level as measured in the disruption. Therefore, it is considered that the calculation result is not far from the experiment. The variation of magnetic energy is shown in Fig.5(b). The magnetic energy drops from 34 MJ to 12 MJ during the disruption. The energies dissipated through the plasma resistance and the vessel resistance are respectively 20 MJ and 1.7 MJ. The ratio is almost independent of the disruption speed, and is about 10 %.

To compare the result of JT-60 with other machine having the vessel with low resistance, for example, JT-60U, ITER etc., the same calculation was made under the condition that only the resistances of the filament coils were changed. The results are shown in Fig.6(a), (b) and (c), where $R_{VV}/R_{VV}(0)$ indicates the ratio of the resistance of the vessel. From these figure, the followings are found. (1) The vessel of JT-60 is resistive, and the most of the magnetic energy stored in the space between plasma (including plasma itself) and the P/S coils are dissipated in the plasma (W_{joul}). (2) As the vessel resistance becomes small, W_{joul} becomes small and saturates at a certain level. This level corresponds to the magnetic energy of plasma inside the vessel. (3) If the plasma resistance rises up to 1 mΩ, the disruption speed becomes fast. This is because the inductance of plasma becomes effectively small due to the decoupling by the conductive vessel.

5. Conclusion

The dissipated energy in the plasma during the disruption is proportional to the square of the plasma current, irrespective of the disruption speed, and is 24 MJ at 3.1 MA. The induced vessel current in JT-60 is roughly 10 % of the plasma current before disruptions. The energy loss through the vessel current is order of 10 % of the total magnetic energy loss. The vessel of JT-60 is resistive, so that the effect of the vessel is small on the energy loss in disruptions.

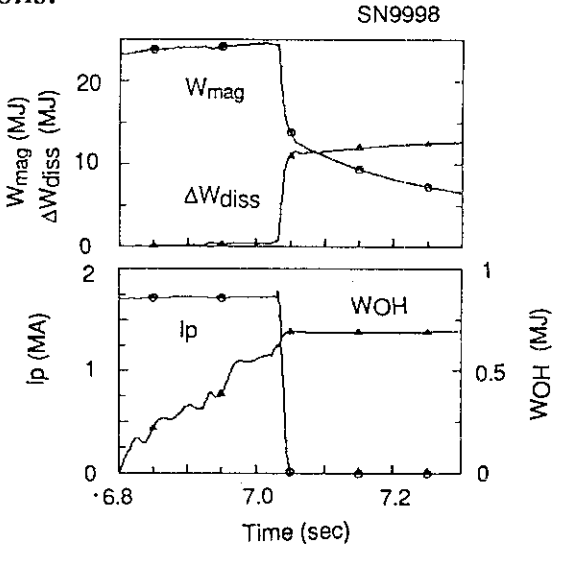

Fig.1 Variation of magnetic energy and dissipated energy in the plasma for a disruption of lower X-point divertor discharge.

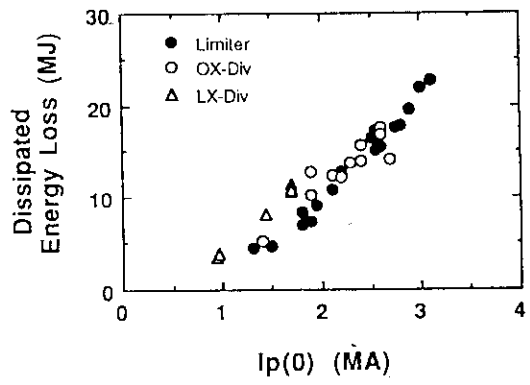

Fig.2 Dissipated energy loss as a function of plasma current

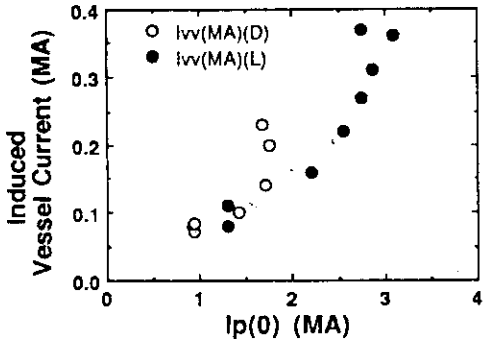

Fig.3 Measured vessel current induced by disruptions as a function of plasma current

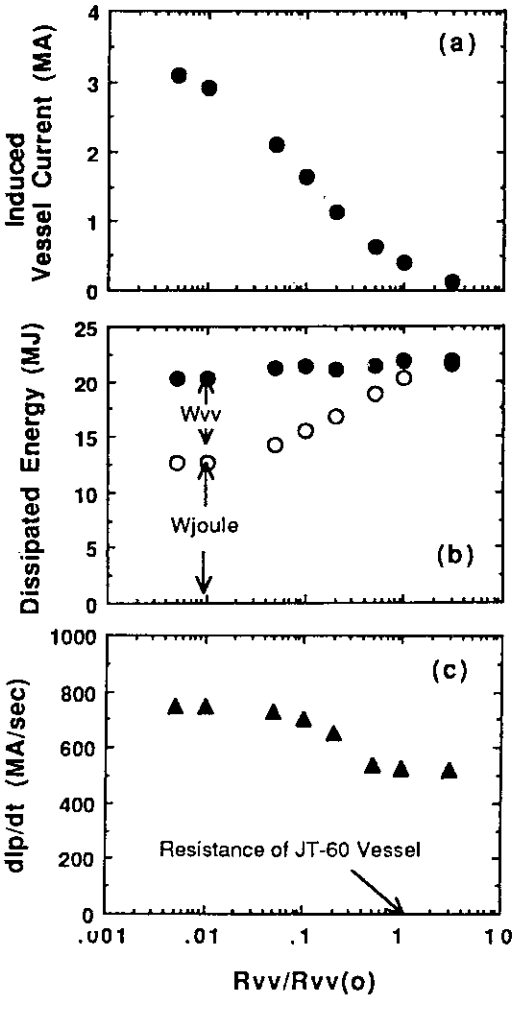

Fig.6 Effect of the vessel resistance on the induction of vessel current (a),the ratio of magnetic energy loss (b) and the disruption speed (c).

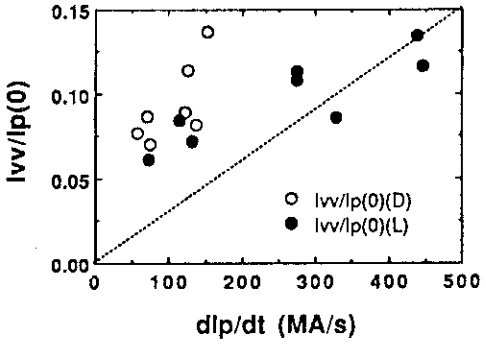

Fig.4 Ratio Ivv/Ip(0) as a function of dIp/dt

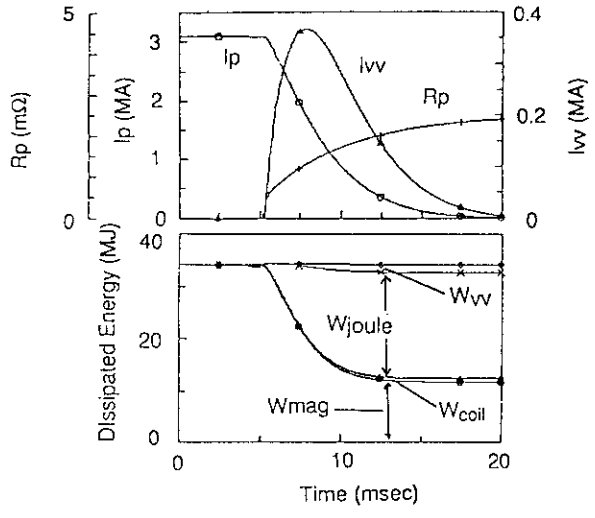

Fig.5 Calculation of the induction of vessel current and the magnetic energy loss
(a) Plasma current, Vessel current and Plasma resistance
(b) Magnetic energy loss

10.3 Radiation Loss in Major Disruptions

N.Hosogane and T.Nishitani

1. Introduction

Radiation loss is a favorable energy loss channel in major disruptions. Energy loss through radiation is distributed to the wide area of the first wall, so that it does not damage locally the first wall. In the specification of designing ITER, radiation loss is treated as a main energy loss channel in the current quench phase[1]. However, there is few presentation indicating that radiation loss is a dominant one in this phase[2]. Therefore, it is very important to confirm it experimentally in large tokamaks.

2. Radiation loss of limiter and outer X-point divertor plasmas in disruptions

Radiation loss of limiter and outer X-point divertor plasmas was measured with a 15 channel bolometer array installed at the lower side port[3]. Since the time resolution is not good enough to study the time evolution of radiation during a disruption, time integral of radiation loss during the current quench phase is discussed.

Figure 1 shows typical profiles of chord integral of radiation loss integrated during the current quench phase. The profiles indicate that there is strong asymmetric radiation near the inner wall. Abel inversion cannot be used to evaluate the total energy for such asymmetrically distributed radiation. Instead, a method of profile fitting is used. The radiation distribution is assumed to be a following function with parameters of C_1,C_2,C_3,α, β and γ.

$$P(x,y)=P_0[(1-C_1)(\frac{1-x/a}{2})^{\alpha}+C_1][(1-C_2)(\frac{\sqrt{x^2+y^2}}{a})^{\beta}+C_2][(1-C_3)(\frac{1+\cos\theta}{2})^{\gamma}+C_3)],$$

where a is minor radius and $\theta=\tan^{-1}(x/y)$. These parameters are adjusted so as to fit the chord integral of radiation loss obtained from the assumed distribution to the measured profiles. An example is shown in Fig.2(a) and (b). The total radiated energy loss is not sensitive to the assumed distribution as long as it is an asymmetric one with a maximum near the inner wall as shown in Fig.2(b). The error due to the uncertainty of distribution is ± 5%. Figure 3 shows the total radiated energy loss as a function of the dissipated energy in the current quench phase. Here, the radiation is assumed to be uniform in the toroidal direction, and the dissipated energy is obtained in the way described in [4]. This figure indicates that the radiated energy loss is almost equal the dissipated energy loss. The energy loss through the vessel current is about 10 %. The energy

loss through the generation of runaway electron is not certain. In ITER, it is estimated to be 0.1×(dissipated energy loss). Taking into account these energy loss, the radiated energy loss is somewhat overestimated, but is still a dominant energy loss channel in the current quench phase.

3.Radiation loss of lower X-point divertor plasmas in disruptions

Radiated energy loss during disruptions of lower X-point divertor plasmas were studied in the same way as limiter and outer X-point divertor plasmas. For the measurements, both the upper(ch.16-30) and lower(ch.1-15) bolometer arrays[3] were used. Figure 4(a),(b) and (c) show the profiles of radiated energy. As shown in these figure, different profiles were observed shot by shot. The Hα intensities measured from three vertical ports(R=2.5, 3.0 3.5 m) were saturated during the disruptions, but the order of their recovery informs us that the plasmas are finally pulled toward the inner wall for the horizontal direction. It is clear that the profile shown in Fig.4(a) corresponds to the plasma pulled toward the divertor plates. The profile in Fig.4(b) is considered to touch the inner wall although the chord integral profile of radiated energy is not sufficiently reconstructed from the assumed radiation distribution. As for the profile in Fig.4(c), it is impossible to reconstruct it, supposing that the radiation is dominant near the inner wall. Another radiation loss seems to exist near the limiters at 30 degree of poloidal angle. In this discharge, the plasma surface is kept to be close to the LHRF launcher for the application of the LHRF power. The launcher is located just at the 30-degree limiters. This may results in the time evolution of the radiation loss which brings the profile measured in the experiments.

Figure 5 shows shows the total radiated energy loss as a function of the dissipated loss of magnetic energy in the current quench phase. As shown in this figure, the proportion of the radiated energy loss is about 70% for the high current disruption(1.5-1.7 MA). For the low current disruption(1 MA), the proportion is small less than 40 %. Compared with the result of limiter and outer X-point divertor, the proportion of radiated energy loss is small, but is still dominant.

4. Discussion and conclusions

In a disruption of 3.1 MA limiter plasma, it was observed that the radiated energy reached 22 MJ in the period of 19 msec until the plasma current disappeared. The averaged radiation power is 1.2 GW in this period. Is it possible to realize such large radiation power?

Suppose a plasma with the following parameters; plasma volume $V=45\ m^3$, $\overline{n_e}=5\times10^{19}m^3$, $Z_{eff}=5$ (carbon 13 %). To obtain radiation power of 1.2 GW for this plasma, radiation power parameter Q given by $P_{rad}/(n_e n_z V)$ is required to be $8.2\times10^{-32}W/m^3$. This corresponds to

the maximum value obtained at electron temperature of 8 eV in the coronal model. In case of disruptions, the radiation power parameter is not sensitive to electron temperature because the effect of increase in particle recycling raises it in the higher temperature[5]. Therefore, radiation power of 1.2 GW can be obtained if plasma parameters are close to the above ones. Note that this is an estimation for the radiation power averaged on the time and space. To more strictly check it, it is necessary to use space and time resolved parameters, and to know the degree of toroidal uniformity of the measurement.

In conclusion, radiation loss is a dominant energy loss channel for magnetic energy in the current quench phase. The proportion of measured radiated energy is almost 100% of dissipated loss of magnetic energy for disruptions of limiter and outer X-point divertor plasmas, and is about 70% for disruptions of lower X-point divertor plasmas.

[1] Status of work on disruptions (ITER-IL-PH-8-9-1,March 1989)
[2] J.A.Wesson et al. , Nuclear Fusion 29(1989)641
[3] JT-60 Team, JAERI-M 89-033, Section 2.4
[4] N.Hosogane, Section 10.2
[5] M.Shimada et al., Nuclear Fusion 22(1982)643

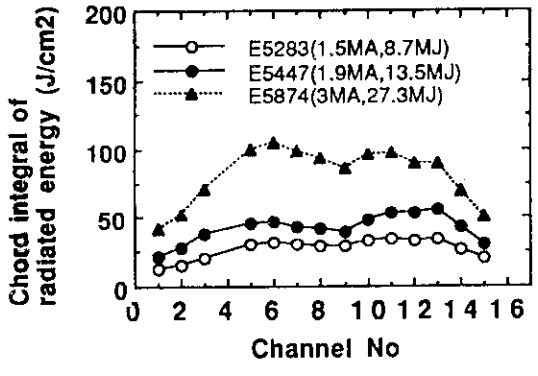

Fig.1 Profiles of chord integral radiation loss integrated during the current quench phase.

Fig.2(a)

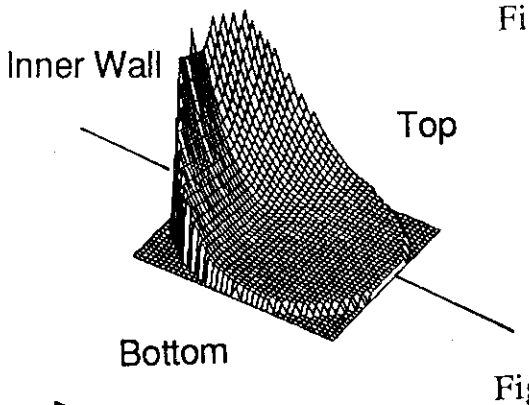

Fig.2(b)

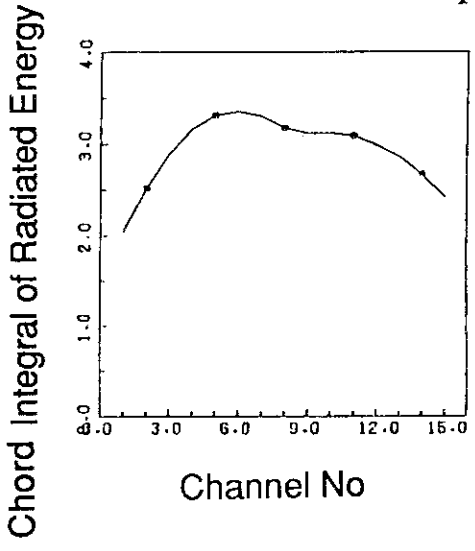

Fig.2 An example of profile fitting.
(a) Radiation distribution
(b) Calculated profile of chord integral of radiated energy

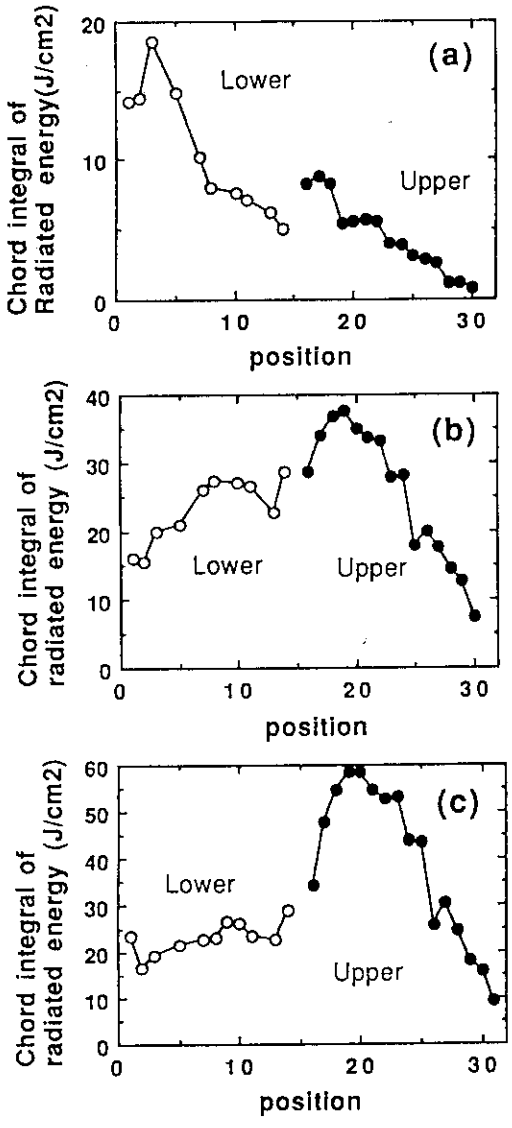

Fig.4 Profiles of chord integral of radiated energy for lower X-point divertor plasmas. Profiles(a) and (b) indicate that plasma touches
(a) divertor plates,
(b) inner walls
and profile(c) is explainable with a radiation source near the limiters around 30 degrees.

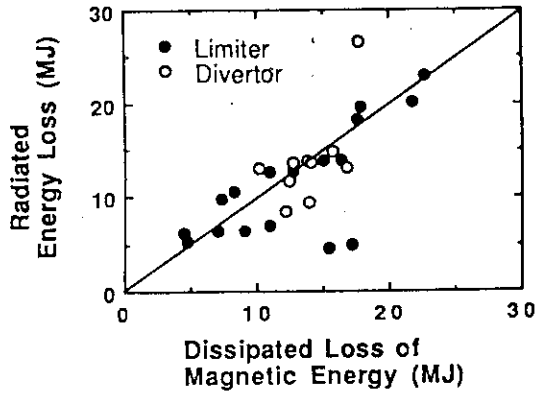

Fig.3 Total radiated energy loss as a function of dissipated loss of magnetic energy for limiter and outer X-point divertor plasmas.

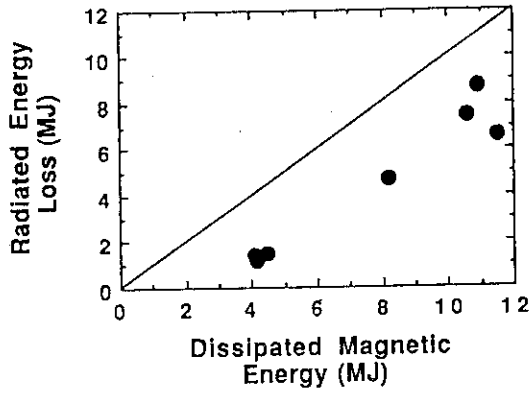

Fig.5 Total radiated energy loss as a function of dissipated loss of magnetic energy for lower X-point divertor plasmas.

10.4 Heat Flow to Divertor Plates and Energy Balance in Disruptions

N.Hosogane, K.Itami and R.Yoshino

1. Introduction

Thermal and magnetic energy of plasma is lost very fast in disruptions. The heat flux to the plasma-facing components is very large, and is a serious problem for designing tokamaks. However, there is few information on the characteristics of heat energy loss; heat deposition places, proportion of heat flow to each place, deposition profile, etc. It is an urgent matter to answer these questions in large tokamaks.

In JT-60, heat flux to divertor plates was measured with a fast scanning IRTV camera($\Delta\tau$=0.4 msec) for disruptions of lower X-point divertor plasmas[1]. In this paper, the experimental results are described from the above view points. In addition, incorporating the radiation loss and the magnetic energy loss discussed in sections 10.2 and 10.3, energy balance in disruptions is presented.

2. Heat flow to divertor plates in disruptions

Figure 1 shows a disruption of 1.7 MA discharge. LHRF power is applied until 7 sec. Disruptions occur at 7.022 sec(minor disruption) and 7.030 sec(major disruption). At the heat quench phase of the major disruption, sudden temperature rise up to larger than 1100°C(saturated) was observed at inside divertor plates. The temperature rise was asymmetric at inside and outside divertor plates, which may depend on the helical magnetic structure of plasmas. The heat flow reached up to larger than 1000 MW at the major disruption. The heat pulse is within 0.8 msec(two scans of TV camera).

Figures 2(a),(b) and (c) show temperature profiles of the divertor plates, heat flux profiles in the heat quench phase and magnetic surfaces at the divertor. The numbers 1, 2 and 3 in Fig.2(c) respectively indicate scrape off layers which are 1, 2 and 3 cm apart from the separatrix surface(solid line) at the mid-plane of the torus.

The temperature profile before the disruptions has a peak at the place of R=3.19 m where the steady LHRF power flows. The heat flux to the inside divertor plates rises up to larger than 350 MW/m^2(saturated). The half width of the heat flow is about 5 cm at 7.0304 sec. It is found that peaks of temperature and heat flux due to the disruptions appear at about 5 cm outside of the steady peak position, which corresponds to the scrape off layer of 3 cm for the steady divertor equilibrium. Such heat deposition patterns have also been found for disruptions of NB heated plasmas from the photographic observation using the IRTV cameras shown in Photo.1. The magnetic fitting results from 7.030 sec to 7.032 sec show that the plasma column is pulled inward and downward during this phase by order of 1-2 cm, which may include errors due to the eddy current, but the magnetic configuration near the X-point remains almost unchanged. The outward shift of the heat flux may be explained as follows. The plasma particles expand outward during the disruption, while the plasma column shrinks at the same time. So that, when the plasma particles released flow along the magnetic lines, they possibly move to the outside magnetic lines, and flow to the divertor plates outside of the peaks of the steady heat flow. It should be noted from these results that the peak temperature of divertor plates in disruptions is appreciably lowered, and the divertor plates damaged by the heat flow of disruptions are different from the places of steady heat flow.

It is also investigated by the photographic observation as shown in Photo.1 at which legs of the separatrix lines at the divertor the heat flow appears. Figure 3 shows a statics of the places where large heat flow is observed in major disruptions for different discharges conditions. It is found that there is a tendency that the heat flow appears at the inside leg when Ip is positive, and vice versa when Ip is negative. This tendency may be explained by the helical structure of plasmas in disruptions. This result is considered to

indicate that the damage in divertor plates will tend to be one-side if the plasma discharge is operated under the condition of the same direction of plasma current. The more data is necessary to confirm it.

3. Energy balance in disruptions

Figure 4 shows time evolutions of the dissipated magnetic energy discussed in [2], ohmic input energy, diamgnetic stored energy, soft X-ray signal from the plasma center, heat energy loss to divertor plates, radiated energy loss in the disruption. The ohmic input energy is estimated from the external coil currents and voltages of the power supplies. The detailed time evolutions of the heat energy during the minor and major disruptions are respectively shown in Fig.5(a) and (b).

In the minor disruption, the heat loss rises up to 0.25 MJ in 0.8 msec as shown in Fig.5(a). The heat loss in this period corresponds to the release of thermal energy in the region where the m=2/n=1 and m=3/n=2 mode grow[3]. The heat energy loss successively rises up to 0.65 MJ in 5 msec until the soft X-ray signal of the central channel(CH24) stop decreasing. The decrease in stored energy is estimated to be 0.12-0.18 MJ including errors due to the oscillation caused by the vertical displacement. The ohmic input energy during disruptions is about 0.1 MJ. The dissipation loss of the magnetic energy of the plasma is considered to be negligible, because the appearance of positive loop voltage suggests that there is no decrease in internal inductance which is a energy source of the dissipation. The total energy released during the minor disruption is roughly 0.2- 0.3 MJ. This value explains half the heat energy loss observed in the experiment although the radiation loss is neglected.

In the heat quench phase of the major disruption, the heat energy loss rapidly rises up to about 1 MJ in 1 msec as shown in Fig.5(b). The heat energy loss increases up to about 3 MJ at the end of the current quench phase. From the bolometric measurements[4], the plasma seems to touch the walls in the current quench phase, so that the heat flow to the divertor is considered to be partially obstructed. The stored energy of 0.3-0.35 MJ is released in the heat quench phase. The ohmic input energy from the external coil system is 0.1 MJ. The other source for the heat energy loss is the dissipation of the magnetic energy. If the negative spike observed in the heat quench phase is caused by the decrease in internal inductance, the magnetic energy to be dissipated is given by $1/2\mu_0 R\Delta l_i I_p^2$. Assuming $\Delta l_i=0.2$, the dissipated energy of 0.54 MJ is expected. Thus, to be balanced to the heat energy loss of 1 MJ, the dissipation of magnetic energy corresponding to $\Delta l_i=0.2$ is required.

The energy balance in the current quench phase is obtained by comparing the dissipation of the magnetic energy, the joule input energy from the external coil system and the thermal energy with the heat flow to the divertor plates and the radiated energy loss. Figure 6 shows the balance of these energy inputs and losses, where the dissipated energy loss through the vessel current is neglected. This energy loss is about 10 %[2]. It is found from this figure that the energy loss in the current quench phase is balanced by the heat flow to the divertor plates and the radiation loss, and the radiation loss is a dominant loss channel. This result is obtained under the assumption of the toroidal uniformity of the energy loss. The validity should be checked in the future.

4. Conclusion

Large temperature rise larger than 1100°C is observed in the heat quench phase of disruption of a 1.7 MA discharge. The heat flow to the divertor plates appears at about 5 cm outside of the peaks of the steady heat flow. There is a tendency that the heat flow appears at the one-side leg of separatrix line at the divertor under the condition of the one-side direction of plasma current. In the heat quench phase, the heat energy observed is larger than the thermal energy of the plasma. The energy loss in the current quench phase is

balanced by the heat flow to the divertor plates and the radiation loss, and the radiation loss is a dominant loss channel.

[1] K.Itami et al., section 10.6 in this review.
[2,3,4,5] N.Hosogane et al., sections 2, 5, and 3 respectively.

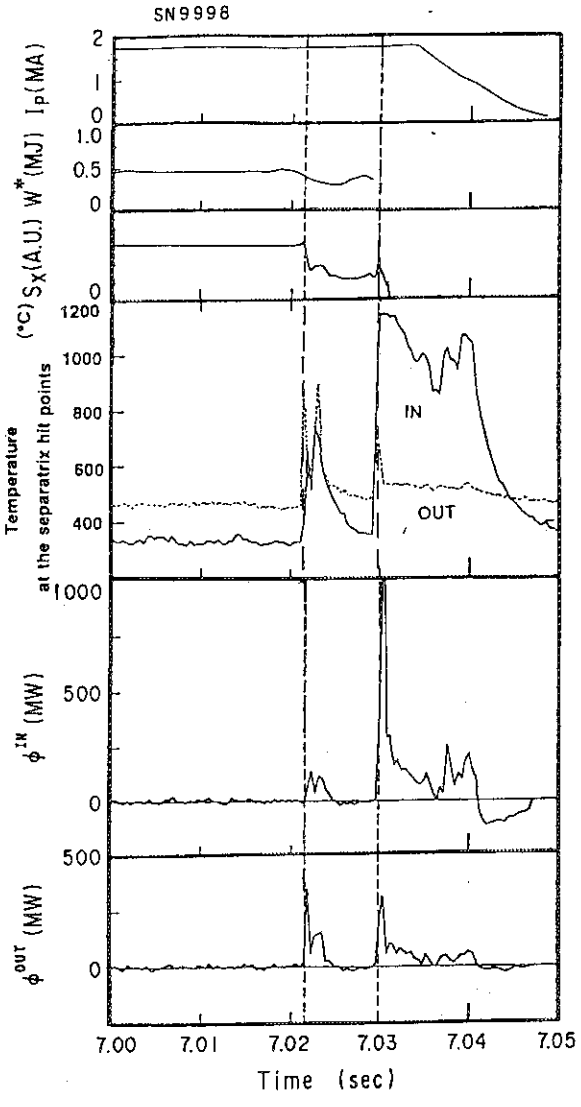

Fig.1 Time evolution of temperatures of divertor plates and heat flows to them in a disruption

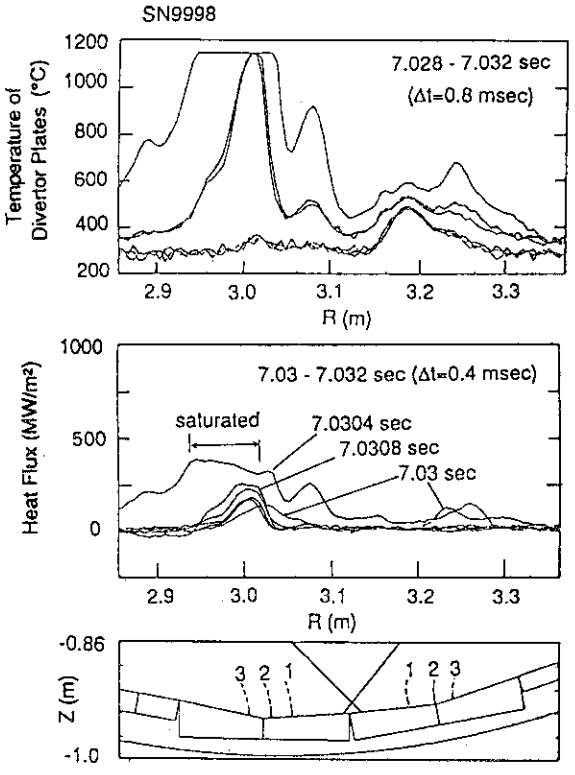

Fig.2 Time evolutions of
(a) temperature profiles of the divertor plates,
(b) heat flux profiles and
(c) scrape-off layers at the divertor.
The numbers 1, 2 and 3 stand for the scrape-off layers corresponding to those which are 1, 2 and 3 cm apart from the separatrix at the mid-plane.

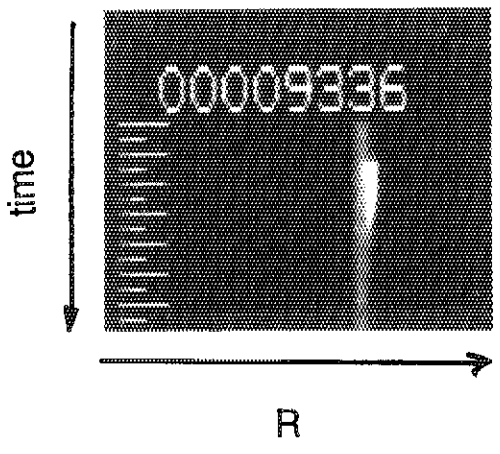

Photo.1 Photograph of the heat flux obtained with the IRTV camera. The faint line indicates the steady heat flow during NB heating,.The bright spot stands for the heat flow during the disrutpion.
The only steady heat flow to the outside plates is seen.

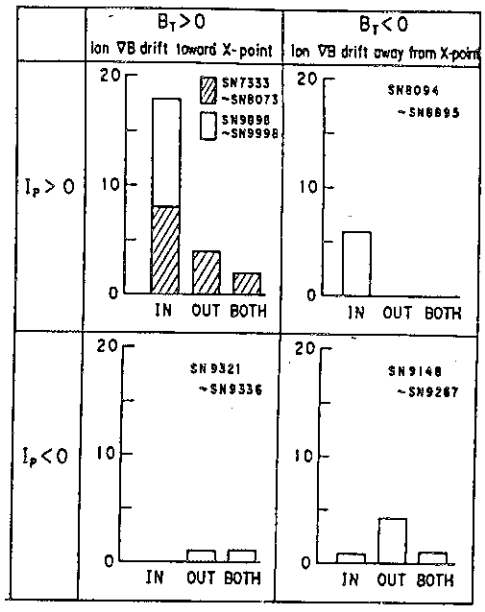

Fig. 3 Statics of the places where large heat flow is observed in disruptions.

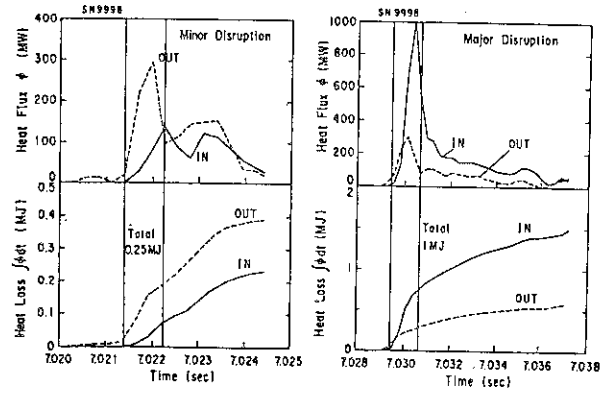

Fig.5 Detailed time evolutions of the heat flows in a minor (a) and a major disruption (b).

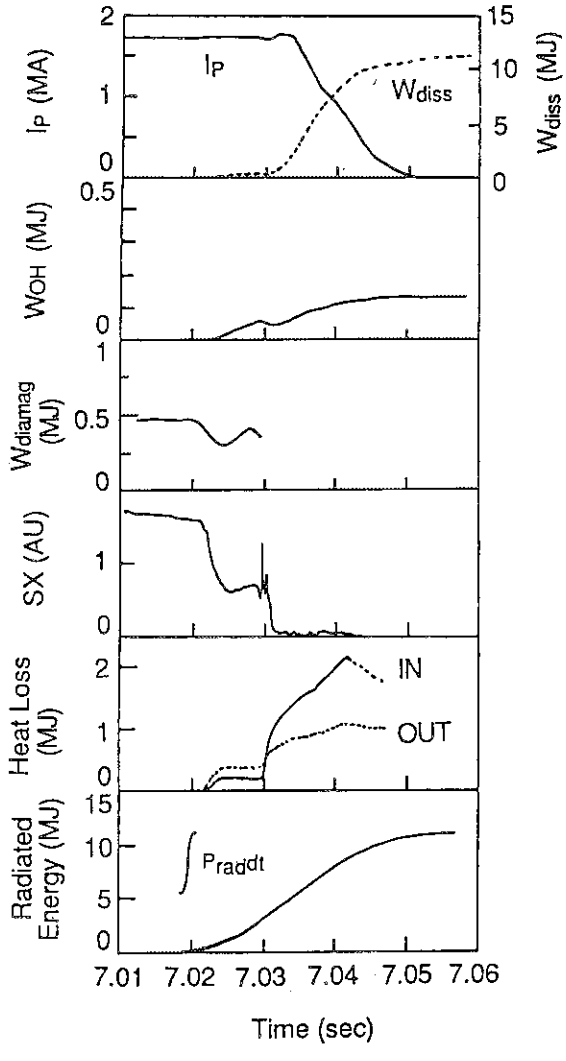

Fig.4 Time evolutions on energy flow in a disruption.

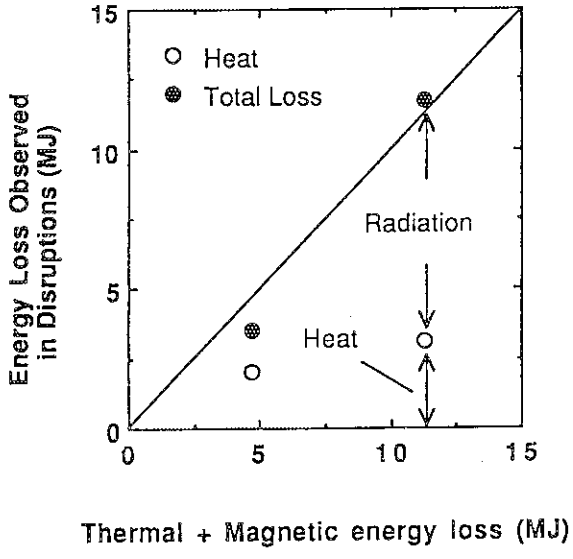

Fig.6 Energy balance in disruptions.

10. 5 Collapse of Magnetic Structures and Thermal Energy Release in Disruptions

N.Hosogane and K.Itami

1.Introduction

In general, m=2/n=1 tearing mode grows before major disruptions and causes minor disruptions. The m=2/n=1 mode couples with the m=3/n=2 mode , which results in the collapse of the magnetic structure, and the release of the thermal energy of plasma. To understand how the thermal energy is released, it is important to study the correlation with the magnetic structure of disruptive plasmas.

2. Soft X-ray profiles in minor disruptions

Figure 1 shows the arrangement of two soft X-ray arrays and an IRTV camera for measurement of heat flux to divertor plates. The two measurement system is 140 degree apart each other in the toroidal direction. Figure 2(a) and (b) show soft X-ray profiles before and after a minor disruption for different discharges (a) q_{eff}=2.4, pellet, limiter and (b) q_{eff}=3.9, OH, divertor, and amplitudes of soft X-ray oscillations of m=2 mode just before them. It is found from these figures that the soft X-ray profiles outside of the region shown by arrows are scraped out by minor disruptions, while the shapes of the profiles inside them remain almost unchanged. Such characteristics of soft X-ray profiles are found in common for various disruptions (density limit, pellet, integer q_{eff}, divertor, limiter etc.) Figure 3 shows a relationship between $1/q_{eff}$ and channel numbers for sawtooth inversion, indication of arrows and the maximum amplitude of m=2 mode shown in Fig.2. The channel numbers indicated by arrows are between the above channels. This suggests that the m=2/n=1 mode couples with the m=3/n=2 mode, and the thermal energy in the coupling region is rapidly released, but is kept in the core region.

3.Correlation of thermal energy release and collapse of magnetic structures

Figures 4(a) and (b) show time evolution of heat flow to divertor plates and soft X-ray signals for a disruption of lower X-point divertor discharge. The equilibrium configuration at 7.030 sec is shown in Fig.1, which almost does not change from 7.020 sec to 7.032 sec. The profiles of soft X-ray during the minor disruption are shown in Fig.5. As described above, the soft X-ray profile are scraped out in the region outside of a certain surface corresponding to the the channel number 13 in the first stage from 7.021 sec to 7.022 sec. While, the central part remains

unchanged in this period. The decay of the central part is observed in the next stage from 7.022 sec and 7.024 sec, and is slow compared with the first stage. Such a change in soft X-ray profile is well correspondent to the time evolution of the heat flow shown in Fig.4(a). In the first stage, the heat flow to inner divertor plates rapidly increases and decreases in about 1 msec, while the heat flow in the next stage, which appears to both sides, seems to increase after 7.0225 sec and continues until 7.025 sec. Therefore, it may be considered that in minor disruptions, the thermal energy is firstly released due to the collapse of the magnetic structure where the the m=2/n=1 and m=3/n=2 modes grow, and is successively released from the central region of plasma maintained.

Figure 6 shows time evolutions of the heat flow to the divertor plates and the soft X-ray signals measured with the upper and lower PIN arrays in the major disruption. The heat quench starts at 7.0292 sec. The soft X-ray signals suddenly increases at 7.0296-7.0298 sec, and oscillate in large amplitude until 7.0305 sec. The behavior of the heat flow seems to correspond to those of the soft X-ray in two periods, 7.0292-7.0295 sec and 7.0296-7.0305 sec, although it is impossible to check the exact correspondences because the time resolution of the IRTV measurement is 0.4 msec. In the first period, the heat flow begins to increase. The heat flow suddenly increases up to larger than 500 MW in the second period, and decays in 1 msec. The detailed behavior and correlation between them are discussed in the following.

The changes in soft X-ray profiles measured with the upper and lower PIN arrays are shown in Fig.7. The profiles measured with the upper PIN array seem to indicate that the hot core shifts upward from 7.0295 sec to 7.0297 sec. At 7.0298 sec, the soft X-ray signals of the upper PIN array decrease, and on the other hand those of the lower PIN array increase. This seems to indicate the the hot core moves clockwise in the configuration shown in Fig.1, and moves to the region below the mid-plain at 7.0298 sec. It should be noted that the edge profile from CH.1 to CH.10 of the lower PIN array continuously increases when the hot core does not rotate to the lower side of the plasma yet. The heat flow to the divertor plates measured at the other toroidal section 140 degrees apart the soft X-ray measurement suddenly increases in this period, so that it possibly generates influx of carbon impurities. The effect of impurities from the divertor plates is considered to be observed by the PIN array from CH.1 to CH.10 which view the region up to about 20 cm from the divertor plates, and raises the edge profile of the soft X-ray. Also, the impurity influx explains the increase in intensities of all the soft X-ray signals in disruptions although there is other possibilities of increase in electron density and the effect of the helical structure of the plasma caused by the

MHD instabilities. The further detailed discussion on the effect of the MHD instabilities on the heat flow is given in section 10.5.

4.Conclusion

In minor disruptions, collapse of magnetic structures where the m=2/n=1 and m=3/n=2 modes grow occurs and thermal energy in this region is released. In the study of a major disruption, it was observed that the thermal energy was released when the hot core rotates. The increase in the edge of the soft X-ray profile was observed which suggested the impurity influx from the divertor plates due to the high heat load.

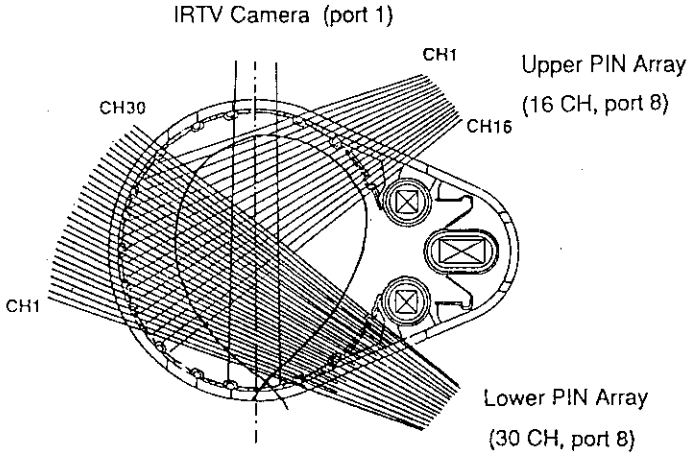

Fig.1 Arrangement of upper and lower PIN array systems and IRTV system. The PIN array systems and the IRTV system are 140 degree apart from each other in the toroidal direction.

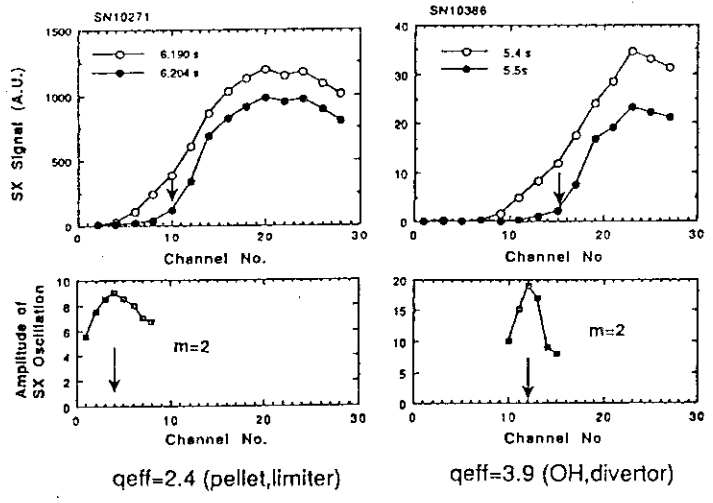

Fig.2 Soft X-ray profiles before and after minor disruptions and amplitude of m=2 mode.

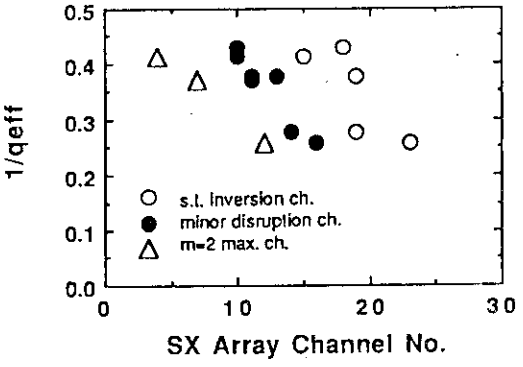

Fig.3 Relationship between $1/q_{eff}$ and PIN array channels for sawtooth inversion, location of the arrow and the maximum of m=2 mode. Minor disruption ch. stands for the location of the arrow.

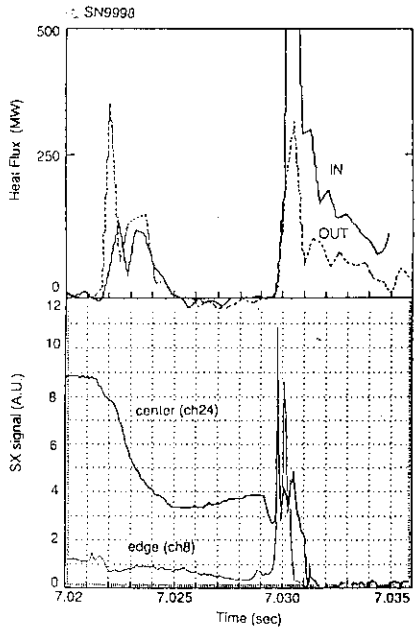

Fig.4 Time evolution of heat flow to divertor plates and soft X-ray signals in a disruption of lower X-point discharge.

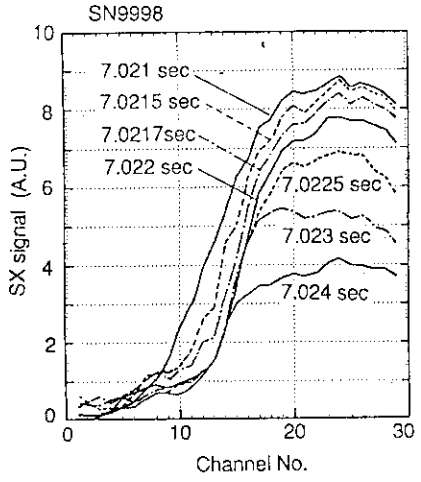

Fig.5 Soft X-ray profiles in the minor disruption

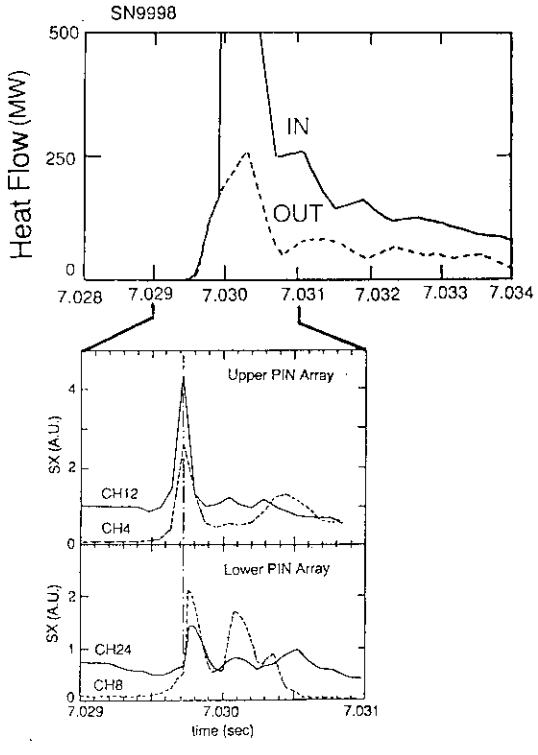

Fig.6 Time evolution of heat flow to divertor plates and soft X-ray signals measured with the upper and lower PIN arrays.

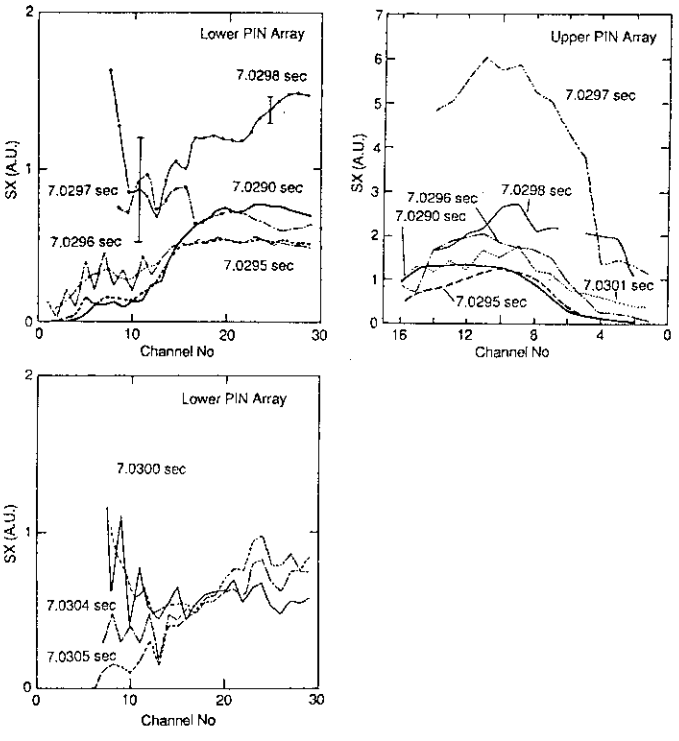

Fig.7 Time evolution of the soft X-ray profiles measured with the upper and lower PIN arrays.

10.6 Study of the energy release to the divertor at the disruptive instabilities

K.Itami, N.Hosogane, K. Nagashima

Transient heat load at disruptions is a major unknown to be resolved for designing fusion reactors in future. The first measurement of the energy release to the divertor has been carried out by using thermographic technique with a time scale of few hundreds of microseconds. The results including several new findings are presented in this paper.

The heat load at the disruptions has been studied for LHRF heated discharges and OH discharges. The quantitative analysis is only obtained by the data acquisition of digitized data of IRTV camera with the fastest possible sampling rate. Since the temperature easily exceed the highest measurable temperature, it was impossible to measure the behaviors in beam heated discharges.

The precise measurement of the time evolution of the heat flux has revealed that the large portion of the stored energy is carried to the divertor plates by the MHD instability (probably island) structure in a time scale of a few milliseconds and that the abrupt loss of the thermal energy is strongly correlated with a growth of MHD instabilities. The shot 9998 demonstrates a lot of features which are typical for the thermal quench at the disruption. Thus we follow the disruption phenomenon in the shot 9998. Figure 1 shows the time evolution of the maximum temperature at the inner half of the divertor and at the outer half respectively. Figure 2 shows the soft-X ray signal on the chord viewing the edge and middle of the plasma and the magnetic fluctuations from the Mirnov coil in the shot 9998.

An important common feature is that a major disruption is preceded by minor disruptions. The maximum value of heat flux observed at the minor disruption ranges from several tens to 300 MW/m^2. The disruption phase starts with the growth of m/n=2/1 or 3/1 tearing modes. A clear growth of the instability is only seen at the first minor disruption. At the shot 9998 a m/n=2/1 tearing mode grows up before the first disruption and the phase of the mode locks for 40 ms. Although the a large portion of stored energy is lost before the first disruption and the magnetic signal shows the irregular fluctuations, the plasma survives and reheats. It is found that the saturated MHD modes survives until the termination of the discharge from the analysis of the mode.

As shown in these figures, the minor disruptions associated with the thermal quench occur at t=6.74 sec , 6.76 sec , 6.815 sec , 6.92 sec

and 7.02 sec. It is not straight forward to estimate the energy deposition at minor disruptions , because the toroidal symmetry shouldn't be valid. From the measurement of the heat deposition during the quasi-steady mode, it was found that the peak value of the heat flux is four times as large as the averaged heat flux over the period of the mode [1]. Thus the calculation based on the toroidal symmetry may overestimate (or underestimate) the real value. In case we assume a toroidal symmetry, it is estimated that 50 to 300kJ of the stored energy is lost with MHD instabilities in few milliseconds at minor disruptions. In this shot 200kJ to 300 kJ is lost at the each minor disruptions. Since the diamagnetic calculation indicates the energy loss at the each minor disruptions is 100kJ to 200kJ, the energy balance may be explained. After the first minor disruption the nonlinearly grown-up MHD instabilities survive until the major disruptions. These are usually identified as the combination of $m=2$ and $m=3$ component. Compared with low q discharges(such as the shot 9998) , higher safety factor q discharges need a wider island to expand from the rational surface (q = 2 surface) to the edge of the plasma. Thus it is observed the magnetic fluctuations at the energy release in high q discharges are up to twice (~2% of equilibrium poloidal field) as large as those in low q discharges.

Heat flux profile during the major and minor disruption shows a great variety of behaviors, such as oscillating , mode locked etc. These behaviors correlate with the growth of the nonlinearly saturated mode. Fig 3 and 4 show the fluctuating heat flux during the major disruption in the shot 9998 and the shot 9961.

The heat flux profile at the disruption is different from the profile at the steady state. It is found that the heat flux due to the disruption is deposited outside the steady state heat flux. This deposition imply the the heat flux is carried along the outer flux tube. These feature is common to the minor and major disruption. Figure 5 show the temperature rise due to the minor disruption. As shown in this figure, heat flux due to the LHRF heating is deposited around the separatrix, the transient heat flux due to the minor disruption is deposited more than 5cm out of the steady heat flux both at the inner divertor and outer divertor.

After the rapid release of the stored energy in the thermal quench phase, the plasma current start to decrease rapidly in the current quench phase. The release of the energy after the last minor disruption is shown in the Figure 6. In the current quench phase additional few MJ of the energy is deposited at the divertor in a time scale of a current decay (typically ten to twenty milliseconds). The

total power deposited at the divertor plates may exceeds stored energy because of the increased resistive ohmic input power during the disruption phase. The energy balance during this period will be discussed elsewhere [2]. One point to note is that the heat load is preferentially large at the inner divertor during the current quench phase, while such a asymmetry is rather weak in the thermal quench phase.

Summary

The first measurement of the energy release to the divertor is carried out by using thermographic technique with a time scale of 400 microseconds. It has revealed that the large portion of the stored energy is carried to the divertor plates by the MHD instability (probably island) structure in a time scale of a few milliseconds and the abrupt loss of the thermal energy is strongly correlated with a growth of MHD instabilities. A major disruption is preceded by minor disruptions and it cause the huge feat flux (more than 400 MW/cm^2 at maximum) and the energy deposition of several hundreds of kilo joule at the divertor.

Reference

[1] JAERI-M 89-033 Section 12.4.
[2] N. Hosogane et al. this review

Figure Captions

Fig.1 Time evolution of the maximum temperature at the inner half of the divertor and at the outer half respectively.
Fig.2 Soft-X ray signal on the chord viewing the edge and middle of the plasma and the magnetic fluctuations from the Mirnov coil in the shot 9998.
Fig.3 Heat flux during the major disruption in the shot 9998 .
Fig.4 heat flux during the major disruption in the shot 9961.
Fig.5 Temperature rise due to the minor disruption.
Fig.6 Integrated power deposited at the divertor after the last minor disruption. The rapid release of the stored energy in the thermal quench phase and the current quench phase.

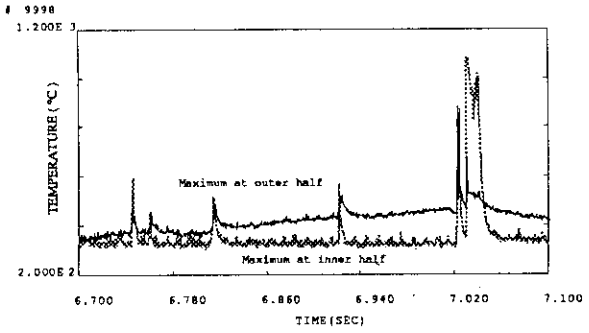

Fig.1

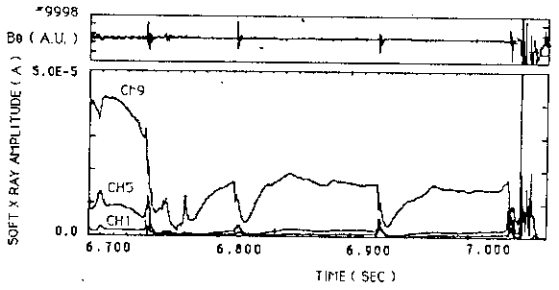

Fig.2

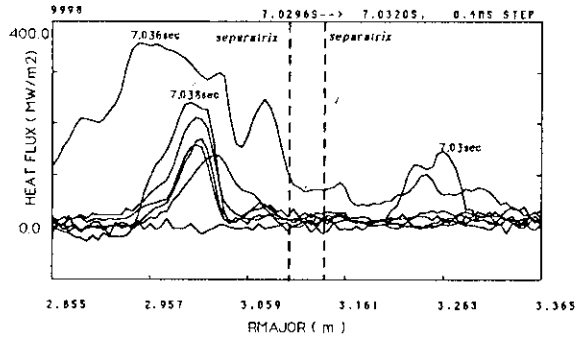

Fig.3

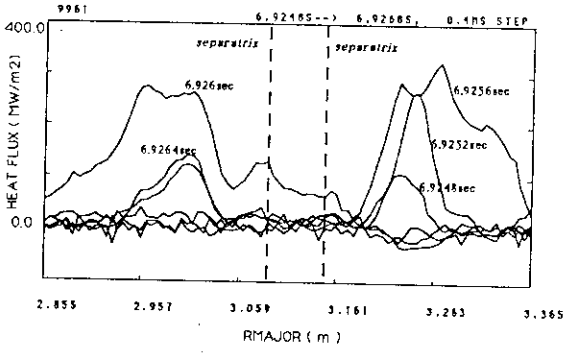

Fig.4

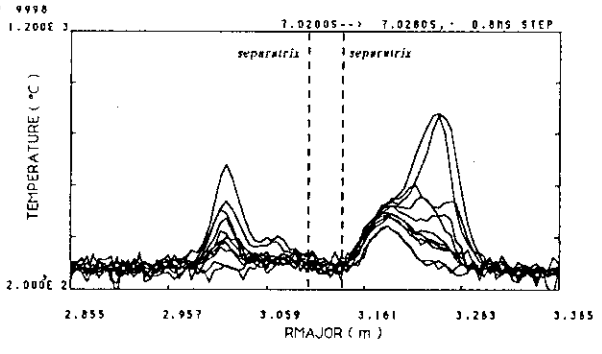

Fig.5

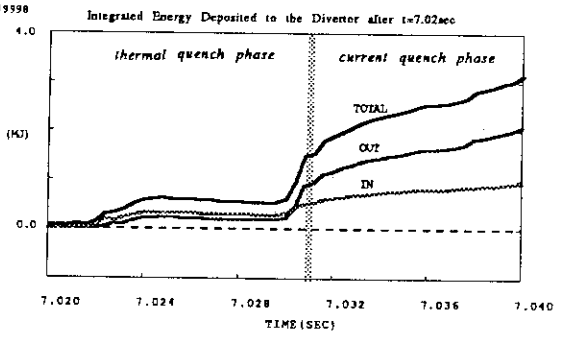

Fig.6

11. Diagnostics

11.1 20-Channel Grating Polychromator Diagnostic System

S. Ishida, M. Sato, N. Isei and A. Nagasima

A twenty-channel grating polychromator diagnostic system has been built to measure electron temperature profiles and electron temperature fluctuations in JT-60[1]. As details of the used diffraction grating spectrometer, based on a cross Czerny-Turner type of grating instrument, are described in the reference of [2], this paper presents the subsequent progress in this diagnostic system. The schematic of this system is indicated in Fig.1.

In Fig.2, the characteristic frequencies as a function of the major radius for the JT-60 plasma is shown together with the fundamental electron cyclotron frequency and the harmonics; ω_U indicates the upper cut off frequency, ω_{UH} the upper hybrid resonance frequency, ω_{pe} the plasma frequency, and ω_L the lower cut off frequency. The electron temperature can be measured in the region without overlaps of the second and third harmonics as shown in this figure. Second harmonic emissions with extraordinary modes for the plasma over 90-300 GHz is utilized, corresponding to B_t=2.0-4.8 T.

We have measured the instrument function of the grating polychromator by rotating the grating with a grating constant of d=3.0 mm as shown in Fig.3; in this case, millimeter waves with 137 GHz are injected into the entrance aperture of the spectrometer from a monochromatic microwave source. This result shown in Fig.3 manifests that all the channels have almost the same frequency resolution of $\lambda/\Delta\lambda$~130.

By turning over the grating plate grooving both sides, this grating polychromator is able to cover a wide range of frequency corresponding to that of the toroidal field maintaining high grating efficiency of 0.7-1.0. Figure 4 shows the covering ranges of λ/d (λ is the wavelength) without the harmonic overlaps as a function of the central toroidal field (B_0); in the range of $0.7 \leq \lambda \leq 1.0$, grating efficiencies higher than ~0.7 are achieved. Therefore, a grating plate with d=2.0 mm and d=3.0 mm is available for the toroidal fields of ~2.0 T to ~4.5 T. The grating angle is automatically set up between the discharges following an algorithm based on the grating equation and the geometry of the spectrometer.

Tall S-band waveguides (WRJ-3; 34.0x72.1 mm) with ~38 m long are installed to guide the millimeter waves emitted from the plasma over the biological shield wall to the grating instrument located in Diagnostic Regulation Room I; the electric vector is set to be parallel to the long side of the waveguide. The horn antenna is installed at the diagnostic port of P16-S4-U in the torus hall with the viewing angle of +7.6° to the equatorial plane. The waveguide bends in the transmission line are

composed of seven H-plane bends and two E-plane bends; including seven grating bends with 90° bending. The total losses for the waveguides are measured to be ~7.1 dB at 137 GHz. Measured transmissivities for each transmission component are listed in Table 1, showing that the total transmissivity of this system comes to be ~0.01. The observed signal levels of emissions are consistent with the levels estimated from this transmissivity, taking account for the sensitivity of ~4 kV/W for the InSb detector.

Figure 5. shows the initial result to measure the electron temperature fluctuations at R~3.10 m and R~3.16 m in pellet experiments with injection of neutral beams and lower hybrid frequency waves. In this figure, a rapid decrease of electron temperatures followed by pellet injection is observed along with sawtooth oscillations. At present, the system has some initial problems as to electrical noses picked up at the detectors and the preamplifiers and softwares for the signal processing. Therefore, after settling these problems during the long shut down period in JT-60, this system will be completed in the JT-60U experiment in 1991.

REFERENCE:

[1] M.Sato, S. Ishida, N. Isei et al., 14th Int. Conf. on Infrared and Millimeter Waves, Wurzburg, Germany, 1989.

[2] S. Ishida, M. Sato and T. Matoba, JAERI-M 89-033, p239.

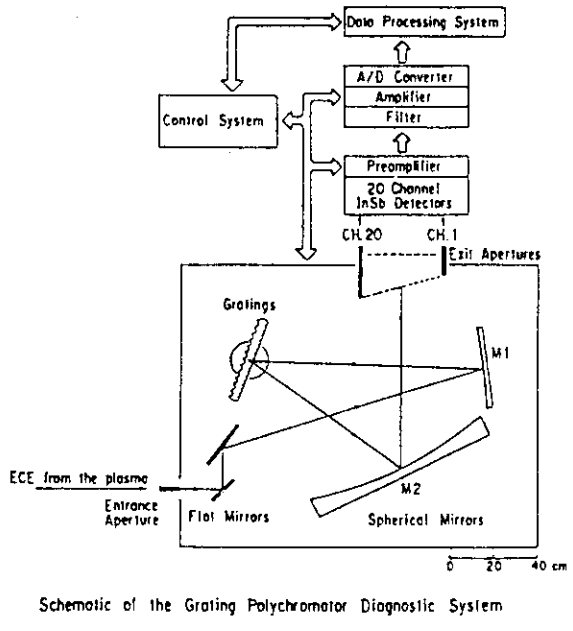

Schematic of the Grating Polychromator Diagnostic System

Fig. 1

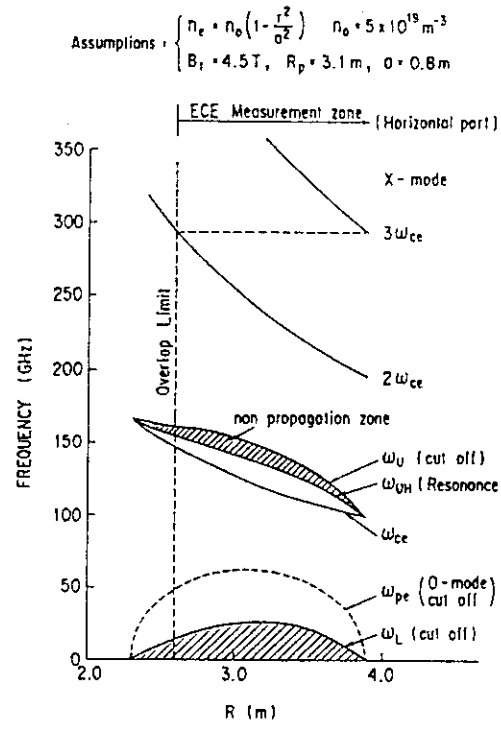

Fig. 2

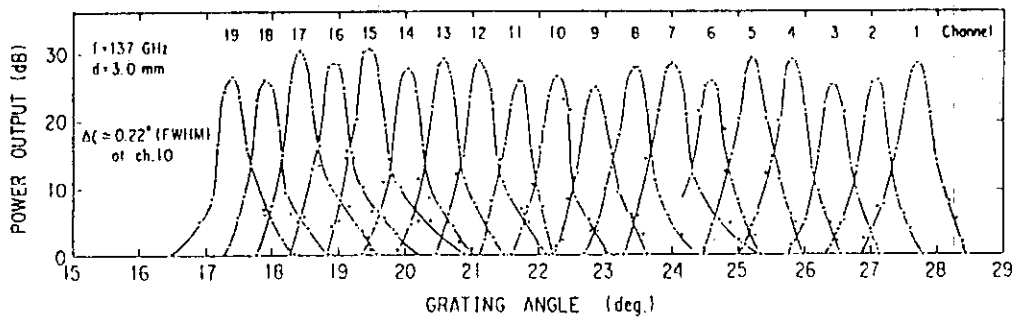

Fig. 3

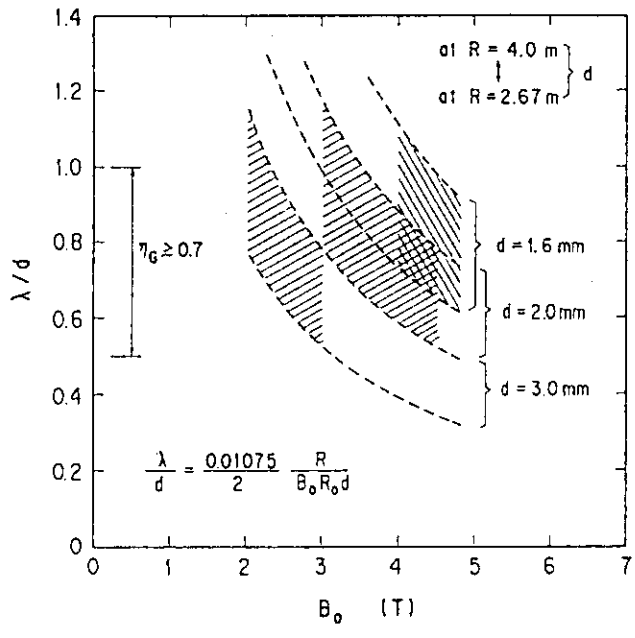

Fig. 4

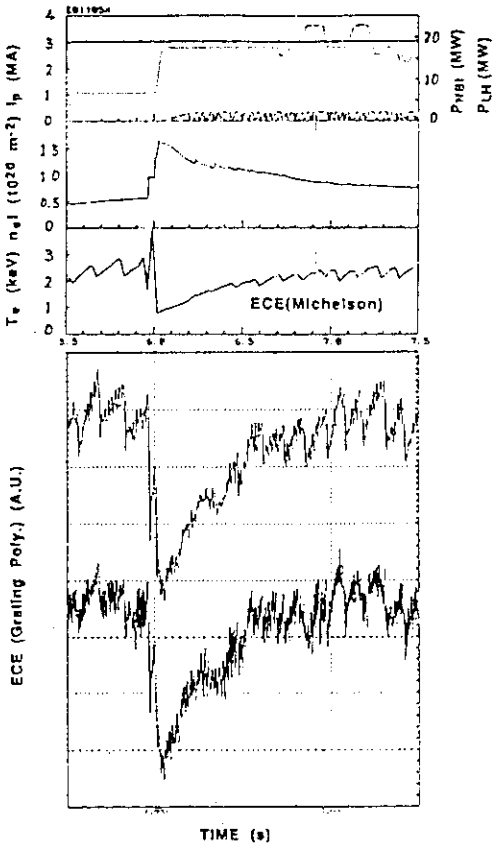

Fig. 5

Table 1

Measured transmissivity

Window	0.58
Waveguide	0.20
Grating spectrometer	0.26
Exit aperture	0.89
Detector (including optical filters)	0.39
--->Total transmissivity	~0.01

11.2 ECE Calibration for Fourier Transform Spectrometer

N. Isei, S. Ishida, M. Sato, A. Nagashima and T. Matoba

INTRODUCTION: In order to obtain absolute values of the electron temperature from electron cyclotron emission (ECE) measurements, the sensitivity calibration of a system is indispensable. Normally, this is done using a calibration source which has a known radiation, such as a black body using a microwave absorber (ECCOSORB). However, calibration sources were hard to be located in the vacuum vessel in JT-60. Therefore the frequency dependence of the sensitivity for our Fourier transform spectrometer system[1] (FTS) is obtained on the basis of electron temperatures obtained from the Thomson scattering system (TS). While the statistical calibration (SC) method has been used so far, the obtained temperature profiles involve some problems. Recently we have newly developed the fitting normalization (FN) method in order to obtain a more accurate profile of electron temperature. In the followings, first, the SC method and the problems are discussed. Next, the FN method and some examples of its application are presented. Finally, conclusions and our future plan are presented.

STATISTICAL CALIBRATION METHOD: The SC method is used to obtain electron temperatures except for peripheral region of the plasma. Figure 1 shows a typical electron temperature profile obtained by this method. In this method, the ratios of electron temperatures measured by the TS to non-calibrated values measured by the FTS are calculated. Calibration factors are obtained from these ratios. Measuring positions of the TS are eight points. Electron temperatures at center region of the plasma are not measured by the TS, because the laser beam path of the TS is situated off axis. So, the ratios of TS value to FTS value are averaged on each frequency over the many discharges at several toroidal magnetic fields (B_t), in order to obtain the calibration factors for each frequency at all the needed frequency region. Figure 2 shows the frequency dependence of the ratio of TS value to FTS value for several B_t values. In this figure, the dotted lines stand for the region where electron temperatures are not measured by the TS. Since the data corresponding to the peripheral region of the plasma are not used, the calibration factors are obtained without much influence of reflection. This influence is thought to be caused by the viewing angle of 46.7° to the equatorial plane. Many data on the ratio are averaged so as to reduce the influence of statistical errors involved in the TS data.

There are the following problems involved in this SC method. Firstly peripheral electron temperatures are overestimated, because influence of reflection is not taken into account in the calibration factors. Secondly electron temperature profiles have some systematic dips or humps, because the ratio of TS value to FTS value has a little scattering according to the plasma parameters such as configuration, current and B_t. Figure 2 shows that the ratio seems to decrease with decreasing B_t.

FITTING NORMALIZATION METHOD: The FN method aims at improving the SC method, and providing more accurate profiles of electron temperatures. This method has the following features and ways of calculation. Normalization factors are obtained for each B_t in order to reduce the scattering according to B_t. The TS data fitted to a function are adopted in order to increase points of the ratio, because the TS values themselves do not cover all the needed frequency region as shown in Fig.2. In this method, the TS fitting data which have little dips or humps and small error bars must be selected. Normalization factors are calculated at each experimental condition of configuration and plasma current in addition to the B_t values. Figure 3(a) and (b) show typical electron temperature profiles obtained by this method. Profiles obtained by this method have no systematic dips or humps as shown in Fig.3(a) and (b), and have normal values even at peripheral region of the plasma as shown in Fig.3(b). It is considered from Fig.3(b) that the FTS data are in good agreement with the TS data. Figure 4 shows comparison with the TS data for many discharges. In this figure, electron temperatures at half a minor radius of the plasma are used to compare the FTS value by this method directly with the TS value, because a direct comparison at center of the plasma can not be done due to the lack of the TS data. By using the FN method, we calculated the peakedness of electron temperature profiles. These results are presented in section 6.8 .

Problems of the FN method are as follows. Firstly the FTS data by this method do not eliminate the influence of errors of the TS data, because normalization factors are calculated from one TS fitting data. Secondly normalization factors have to be calculated at each B_t, configuration and current of the plasma. Thirdly this method requires good quality of the TS data.

CONCLUSIONS AND FUTURE PLAN: The FN method has newly developed, and appropriate profiles of electron temperatures are obtained by using the TS data without using a calibration source.

The influence of reflection of ECE should be considerably reduced on JT-60U because of the use of the horizontal diagnostic port. Since it will be still hard to take calibration sources into the vacuum vessel owing to increasing radio activity, we have a plan of developing the calibration system which has simulated apparatuses such as an observation window. Although the calibration is done sufficiently using a calibration source, measured electron temperatures have to be cross-checked against values obtained by other measurement systems. Thus the FN method is useful for.

REFERENCE

1) M. Sato et al. , Kakuyugo Kenkyu Vol.59 Supplement (1988) 47.

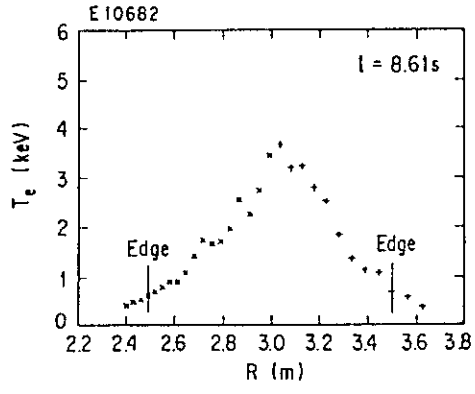

Fig.1 Typical T_e profile obtained by the SC method.

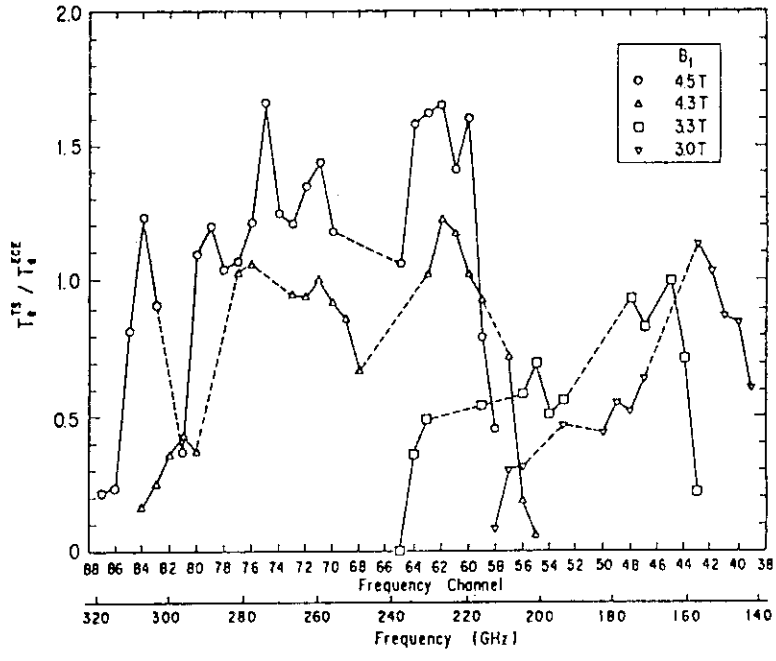

Fig.2 Frequency dependence of the ratio (T_e^{TS}/T_e^{ECE}).

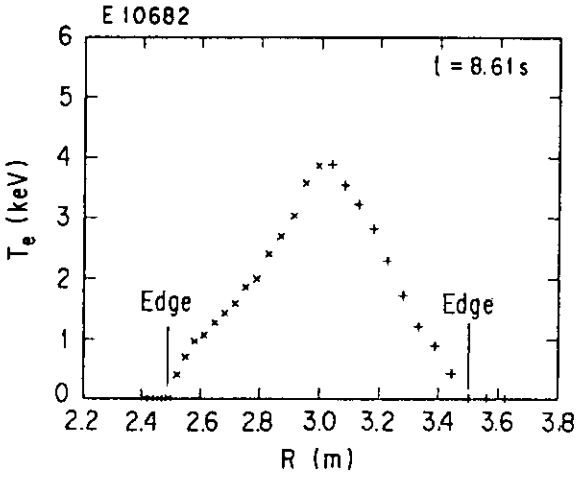

Fig.3(a) Typical T_e profile obtained by the fitting normalization method.

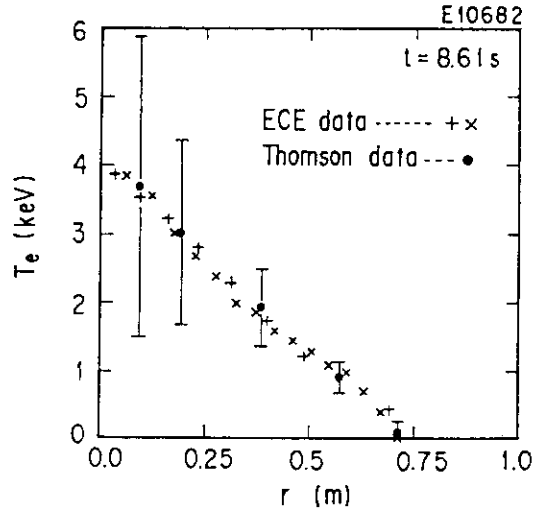

Fig.3(b) Typical T_e profiles obtained by the FTS (FN method) and the TS.

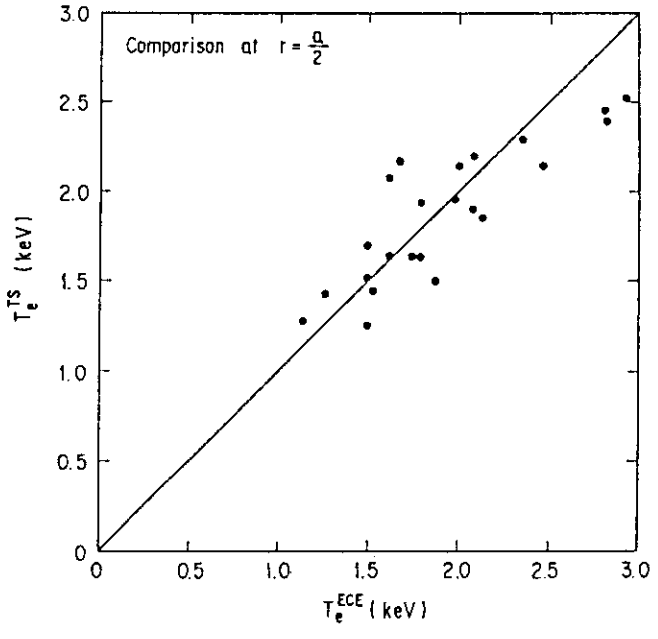

Fig.4 Comparison between the FTS data (FN method) and the TS data at half a minor radius of the plasma.

11.3 Millimeter-wave plasma radar system

T. Fukuda, S. Konoshima, and T. Matoba

Naka Fusion Research Establishment, Japan Atomic Energy Research Institute, Naka-machi, Naka-gun, Ibaraki-ken, Japan

ABSTRACT. A broadband reflectometric system in O-mode operation has been developed on the JT-60 tokamak. For the density profile determination, full Ka-Q band frequencies of BWOs have been swept for the continuous measurement of the group delay of reflected waves. The system also comprises a fixed frequency reflectometer with 24 and 34 GHz Gunn oscillators for the density fluctuation measurements. A description of the system and the preliminary test results are presented.

1. INTRODUCTION

The limited viewing access and asymmetric D-shaped plasmas on JT-60 make millimeter-wave reflectometry an attractive diagnostic for density profile measurements[1-3]. For a reflectometer the Abel inversion of the phase information is performed along the line of sight, so only a single viewing chord, and no symmetry assumption, is required. From the dispersion relation of the O-mode wave, the phase delay ϕ of a reflected wave is written in the form:

$$\phi = \frac{2\omega(x)}{c}\int_0^x \sqrt{1 - n(x)/n_c}\, dx - \frac{\pi}{2},$$

where n_c and $\omega(x)$ are the cutoff density and cutoff frequency, respectively. Position of the reflecting layer x can therefore be determined by the following integral equation[4].

$$x = \frac{c}{\pi}\int_0^{\omega(x)} \frac{d\phi}{d\omega}[\{\omega(x)\}^2 - \omega^2]^{-\frac{1}{2}}\, d\omega.$$

The required quantity to measure is the group delay $[\tau=(1/2\pi)(d\phi/d\omega)]$ of the propagating wave to the cutoff layer and back. Therefore, the incident frequency must be swept over a range, corresponding to the expected plasma densities.

2. DESCRIPTION OF THE SYSTEM

The reflectometric system for JT-60 is composed of two independent reflectometers; a broadband reflectometer for density profile measurements and fixed frequency reflectometer for density fluctuation measurements. The schematic diagram of the system is depicted in Fig. 1. In its final form, the broadband reflectometer will be composed of fast-sweep (>20 GHz/ms) YIG/BWO oscillators in a frequency range 2-110 GHz (corresponding to the critical density of 5.0×10^{16} -1.5×10^{20} m^{-3}). A novel feature of this system is that the group delay is measured *continuously*, while multichannel narrowband sweep reflectometers [Ref. 2] require the interpolating process for the estimate of group delay profiles. 23-75 GHz radiation is combined into a single X-band wave-guide, and it is launched into JT-60 through Brewster windows for the improvement of VSWR. The transmitting and receiving horn antennas are separated and their beam width is 2.2°. 2-18 and 75-110 GHz outputs are launched by different set of antennas. The addition of the 2-18 GHz band is aimed to improve the resolution for the profile determination, calculated by the above integration formula. Modified Ridge-type directional coupler has been employed for the preliminary experiment with Ka/Q-band BWOs, and it will be replaced with a three-guide hybrid[5] coupler to extend the frequency range up to 75 GHz. In order to suppress the mode conversion, oversized waveguides are 2-dimensionally arranged, and the reduced-height corner bends have been employed on all the oversized corners. The reflected wave is mixed with the local oscillator power generated at a directional coupler for the homodyne detection. The homodyne beat signals are processed with digitizers and a time-interval analyzer (HP5371A).

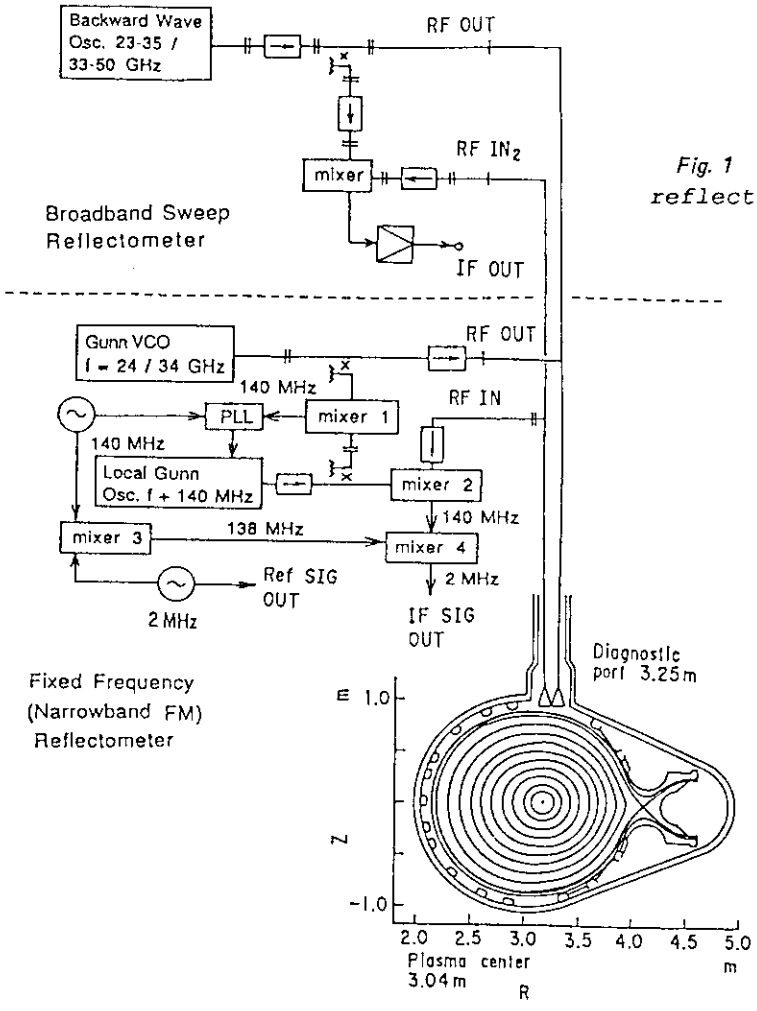

Fig. 1 Schematic diagram of the JT-60 reflectometer.

For fixed frequency reflectometry, the system also comprises 24 and 34 GHz (corresponding to 0.6×10^{19} and 1.3×10^{19} m^{-3}) phase-locked Gunn oscillators. The frequencies of the reflected signal are double-converted to 2 MHz, and the amount of phase shift is monitored by fringe counting electronics. Gunn oscillators can also be swept in a narrowband (340 MHz/5 ms) frequency to yield the local value of the group delay, which functions to corroborate the broadband data.

3. TEST RESULTS

In the present diagnostic layout, the incident wave is injected vertically down into the plasma. Therefore, notwithstanding the expected signal-to-noise ratio of 15 dB (including the estimated reflection loss of 20 dB at the critical density layer), intensity of the reflected wave experiences severe deterioration, according to the relative position of the magnetic axis and anntenna radiation pattern. The appropriate position of the plasma center has been deduced to be $0.15 < \Delta R < 0.25$ m by the result of ray tracing calculations and the result of experiment which shifts the horizontal plasma position. Fig. 2 shows the intensity of the reflected wave (lower figure) as a function of the plasma position (upper figure). In this experiment, the plasma position has been shifted by 0.35 m in 5.5 s, and the intensity of the reflected wave peaks at the axis of the diagnostic port. Examples of ray tracing calculation are shown in Fig. 3, which indicate the severe refraction of the propagating beam.

According to the laboratory test with a reflection plate for the broadband reflectometer, where BWOs were swept at 0.5 GHz/ms, the resolution is estimated to be 12.5 mm; however, the homodyne beat spectrum is broad (Δf =

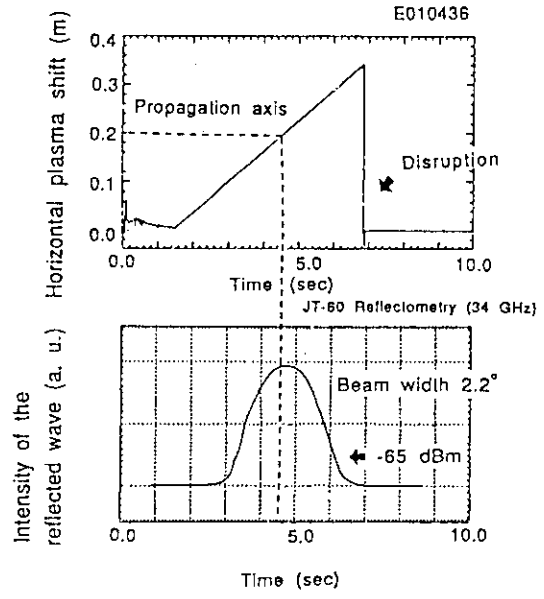

Fig. 2 Intensity of the reflected wave (lower figure) as a function of the plasma position (upper figure).

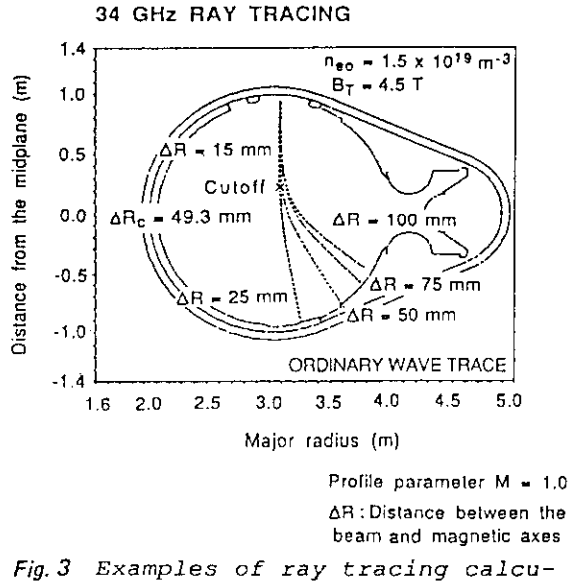

Fig. 3 Examples of ray tracing calculation.

2.5 kHz for the center frequency of 30 kHz), seemingly due to the low frequency stability of the BWO (Fig. 4),

The instrumental resolution of the fixed frequency reflectometer is 1 μs and less than 0.3 mm as shown in Fig. 5. The practical spatial resolution, however, is determined by the incident frequency and the density gradient, and it is estimated to be 10-50 mm. So far we have obtained information on the positional fluctuation of the reflection layer which correspond to the penetration of the pellets and sawtooth activities observed on soft X-ray signals. In Fig. 6(a) The movement of the $0.6x10^{19}$ m^{-3} layer is shown for the pellet injection experiment. The position of the reflection layer has been deduced to be r/a = 0.98 by the Thomson scattering measurement. It can be seen that the penetration of pellets only induces the temporal shift of the reflecting position, and it does not significantly raise the edge plasma density. As for the case with the $1.3x10^{19}$ m^{-3} layer, the periodical shift of the reflecting position (r/a = 0.53) due to the density pulse induced by sawteeth is clearly observed in Fig. 6(b).

Although, in the present diagnostics, the absolute position of the reflecting layer can not be determined by the broadband sweep reflectometer system, a preliminary result on the continuous density profile measurement has been obtained as shown in Fig. 7. However, broadband sweep IF signal suffers occasional frequency shifts, seemingly due to the doppler shift at the reflection layer. For this point, appropriate filters should possibly enlarge the diagnostic capabilities.

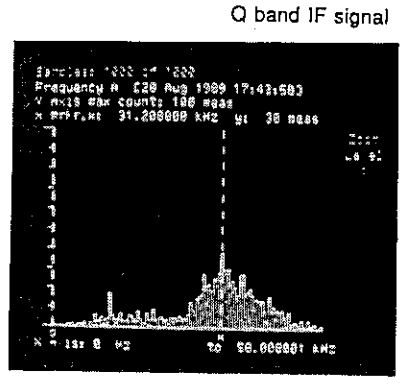

Fig. 4 Resolution of the broadband sweep reflectometer

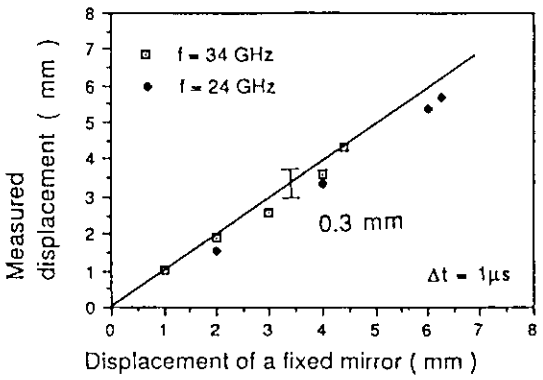

Fig. 5 Resolution of the fixed frequency reflectometer

4. CONCLUSION

It has been made clear that the incident wave should preferably be injected into a plasma horizontally, aiming the plasma center, in order to sustain the intensity of the reflected wave. The result of fluctuation measurements and the preliminary result on the continuous profile measurement encourage the local determination of the transport parameters.

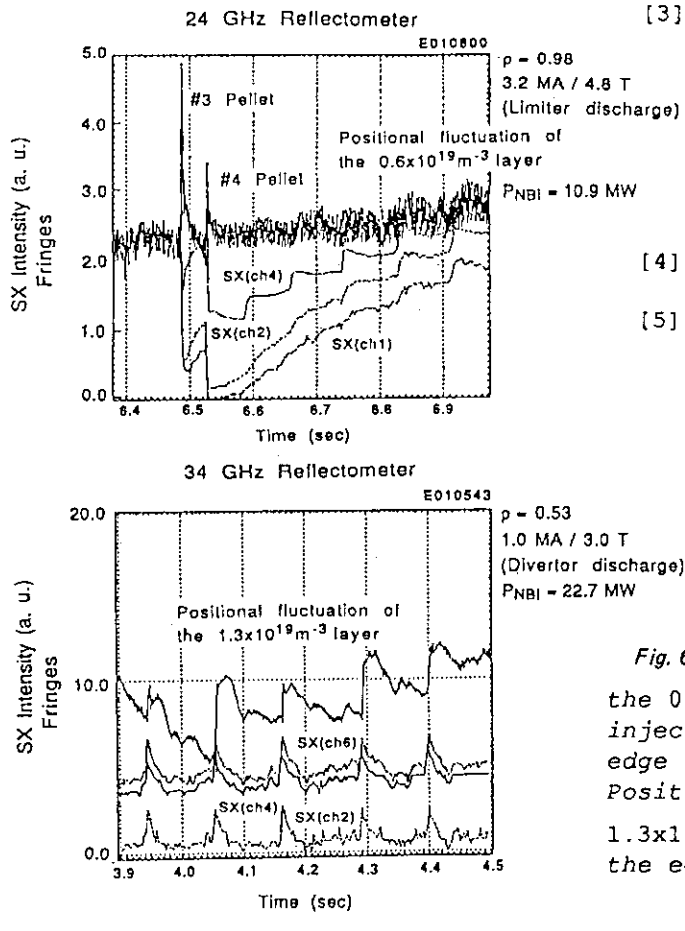

Fig. 6 (a) Positional fluctuation of the 0.6×10^{19} m^{-3} layer for the pellet injection experiment shown with the edge soft X-ray signals. (b) Positional fluctuation of the 1.3×10^{19} m^{-3} layer, correlating with the edge soft X-ray signals.

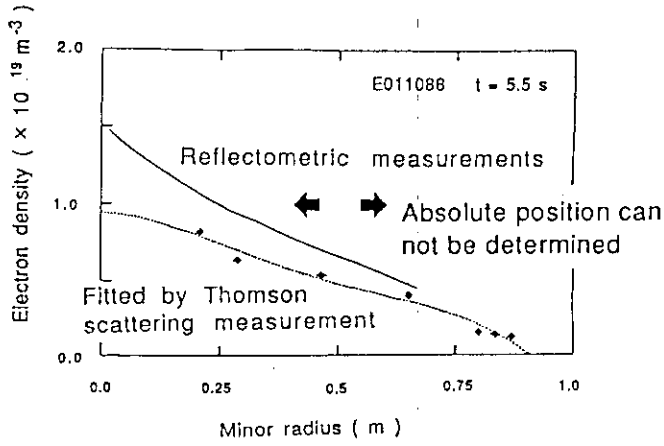

Fig. 7 Preliminary result of the profile measurement.

REFERENCES

[1] F. Simonet, Rev. Sci. Instrum, 56, 664(1985).

[2] A. Prentice, A. E. Costley, J. A. Fessey, and A. E. Hubbard, Course and Workshop on Basic and Advanced Diagnostic Technique for Fusion Plasmas, Varenna, Italy, EU19797, Vol.2, 451 (1986).

[3] R. Lehecka, E. J. Doyle, R. Philipona, N. C. Luhmann, Jr., W. A. Peebles, C. L. Hsieh, T. N. Carlstrom, R. P. Seraydarian, and the DIII-D group, GA-A19566(1989).

[4] R. J. Colchin, ORMAK Technical Memo No. 93(1973).

[5] F. Medeiros and N. Williams, Proc. 12 th Int. Conf. on IR and MM waves, Florida, USA(1987).

11.4 Tangential charge-exchange neutral particle analyzer with wide energy range

M.Nemoto, Y.Kusama, K.Tobita, H.Takeuchi and JT-60 Team

Charge-exchange (CX) measurement is an important method to study behaviors of ions in NB and/or RF heated plasmas. Remarkable beam ion acceleration phenomena had observed in previous experiments on JT-60. One of them was that ICRF waves were driven by higher power NB injection and interacted with beam ions[1)-3)]. The other was that LHRF wave accelerated hydrogen beam ions perpendiculaly up to 400keV[4)].

Since all of them had been measured by perpendiculaly installed CX neutral particle analyzers, tangential CX measurement was required to establish features of ion energy distributions of additionaly heated plasmas. From previous experimental results, an tangential CX neutral praticle analyzer was required to have a wide energy range up to 500keV for H^0. In addition, a size of that had to be compact in order to install in a limitted space for a measurement system. The developed analyzer is E//B type and uses the acceleration method which an acceleration tube between a stripping cell and a magnetic pole is equipped. Therefore, wide energy range from 1keV to 500keV is available to H^0 energy distribution measurement. An arrangement of MCP detectors was modified in limitted space for H^0/D^0 or H^0/He^0 energy distributions measurements. The energy resolution was developped from range of 8.8%-2.6% in previous detectors to that of 6.5%-2.0%.

The newly developped analyzer called NPA-a(3) is installed on JT-60 and views plasma with the sight-line shown in Fig.1. Fig.2 shows typical energy spectra measured by the analyzer and the other perpendicular analyzers on NB heated plasmas with and without the acceleration by beam driven ICRF wave. From a comparison with those spectra, it resulted that beam driven ICRF wave accelerated beam ions perpendiculaly.

The analyzer is successfully operated and useful data are acquired routinely.

References

1) JT-60 Team, JAERI-M 88-063 (1988)381.

2) Nemoto,et al., JAERI-M 89-033 (1989)215.

3) Seki,et al., Phys.Rev.Lett. 24(1989)1989.

4) JT-60 Team, JAERI-M 87-113 (1987)293.

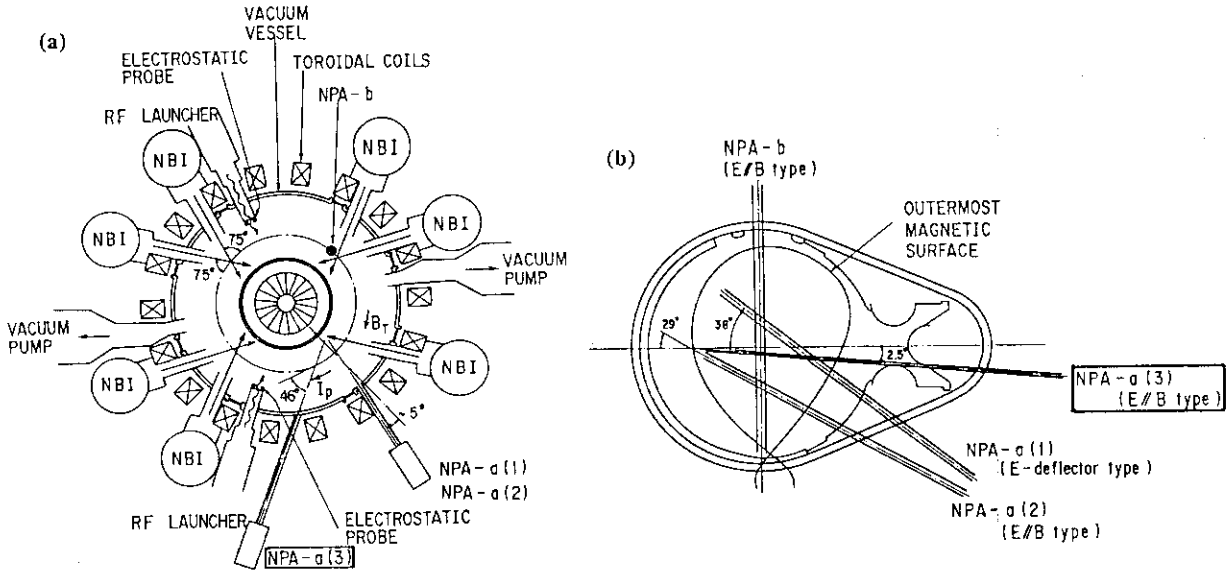

Fig.1 Arrangement of the tangential CX neutral particle analyzer NPA-a(3) ; (a) Top view : (b) Cross sectional sight-lines of CX analyzers.

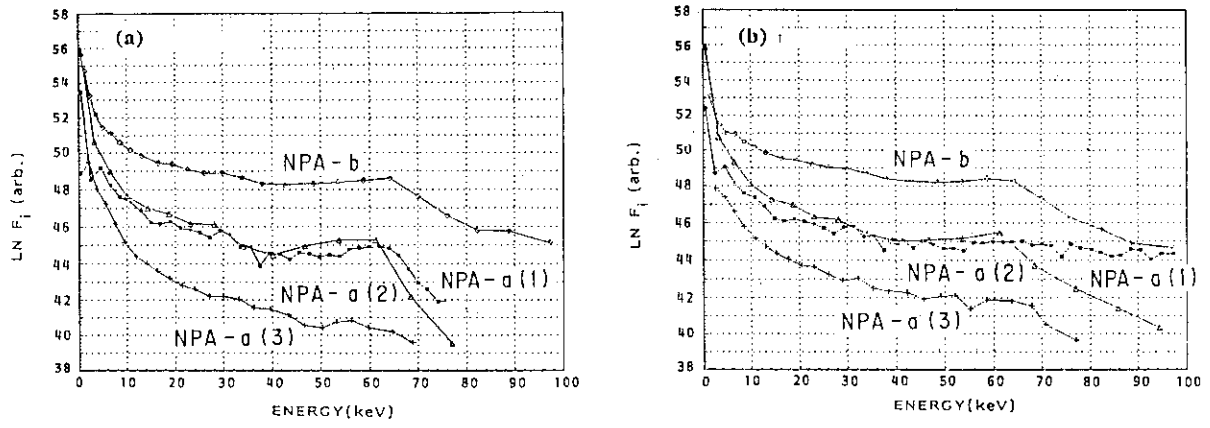

Fig.2 Typical ion energy distributions measured by CX analyzers on NB heated plasmas ; (a) without the beam ion acceleration by beam driven ICRF wave : (b) with the acceleration. Injected NB energy is 65keV on both cases.

11.5 Spatial Resolved Hard X-ray Measurement

K. Nagashima, T. Nishitani and H. Takeuchi

To measure the hard x-ray spatial and energy distributions, 4 channel NaI(Tl) scintillation detectors were installed on JT-60 as shown in Fig.1. This system consists of NaI(Tl) scintillator, photo-multiplier and pulse height analyser, and its measurable energy range was set to be about 50 keV to 1 MeV. The spatial and energy resolutions are about 8 cm and 10%, respectively. Due to the limitation of the floor space, the enough radiation shield could not be installed around the detectors, so the signal includes not only the incoming x-ray through the lead aperture but also the scattered back ground signal. To reject the effect of the latter, we employed one detector viewing the plasma peripheral region as the back ground monitor, which was blinded with the lead plate (see Fig.1).

The typical energy spectra are shown in Fig.2, which was measured in the lower hybrid current drive discharge. The measured energy spectrum is characterized by its intensity and declination. In a series of current drive experiments where the injected power spectra of LHRF were varied using the newly installed multi-junction launcher [1] ($N_{//}$ scan experiment), the characteristic behavior of hard x-ray spectra could be observed. Increasing the $N_{//}$ of injected RF spectrum, the central intensity of hard x-ray decreased and its spatial profile became broadening. It indicates that the RF power was absorbed in the more peripheral region with increasing $N_{//}$, and that the current profile became broader with increasing $N_{//}$. The latter fact was confirmed by that the internal inductance l_i became smaller with increasing $N_{//}$.

The declination of the x-ray energy spectrum corresponds to a temperature in a case of maxwellian distribution. But in the case of hard x-ray, the high energy electron tail is far away from a maxwellian and the measured energy spectrum in a perpendicular direction to the electron current is complicated due to the parallel and perpendicular components in the electron velocity space [2]. So, the declination is only the indication of the spread of electron

velocity distribution. In the above mentioned $N_{||}$ scan experiment, the declination became steeper with increasing $N_{||}$, and it indicates that the spread of electron velocity distribution corresponds to the phase velocity of injected RF spectrum.

In order to acquire the more useful information for the high energy electrons, the measurement in a tangential direction is necessary. For JT-60U, we are ready for the same type of hard x-ray measurement systems with 8 channel in perpendicular direction and both in co- and counter-direction.

References

[1] IKEDA, Y., et al., Nucl. Fusion 29 (1989) 1815
[2] VON GOELER, S., et al., Rev. Sci. Instrum. 57 (1986) 2130

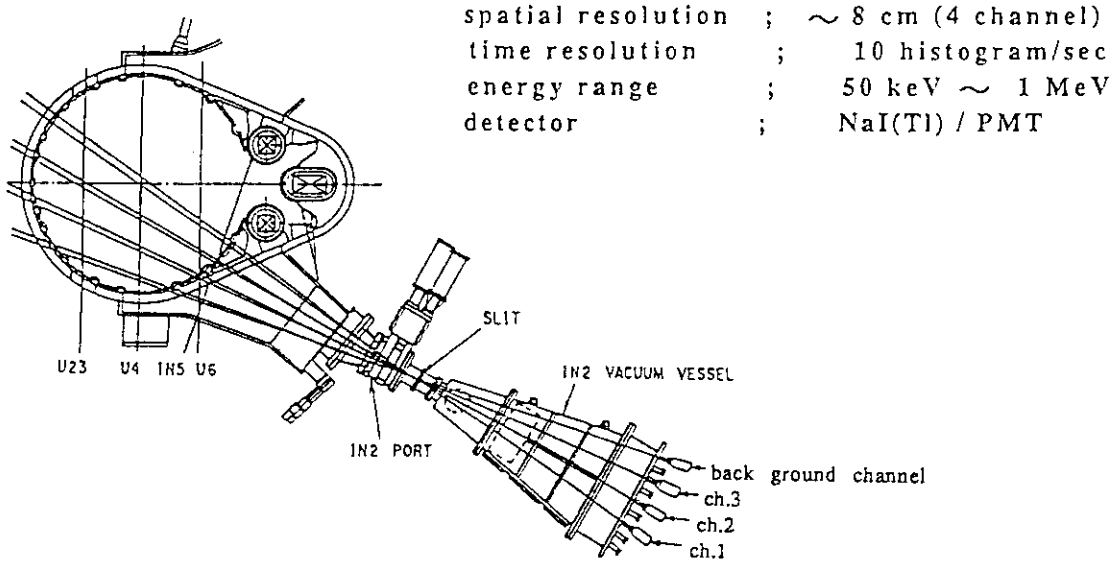

Fig.1 Schematic view of the spatial resolved hard x-ray PHA system.

E09383

divertor/H
I_p=1.0MA
B_t=4.0T
$\overline{n}_e$=0.9E+19
T_{e0}=2.34keV

B/2GHz
$\Delta\phi$=180°
P_{LH}=1.4MW

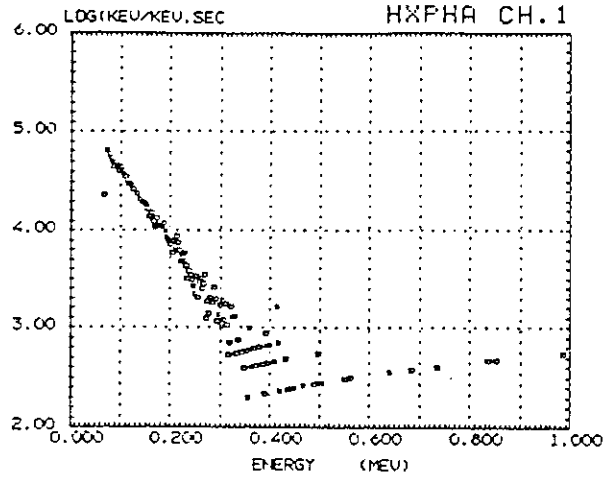

r/a = 0.02

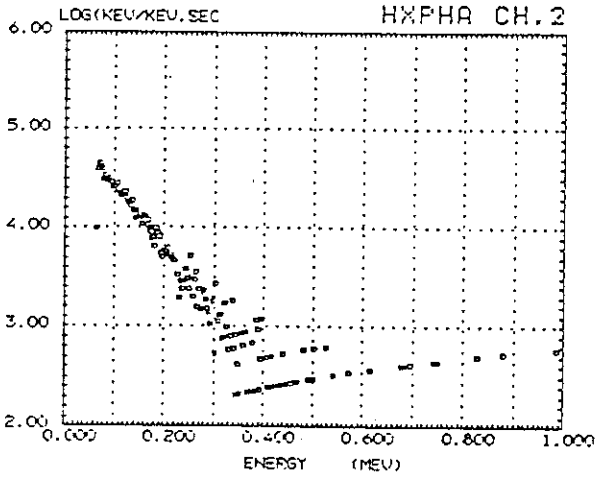

r/a = 0.34

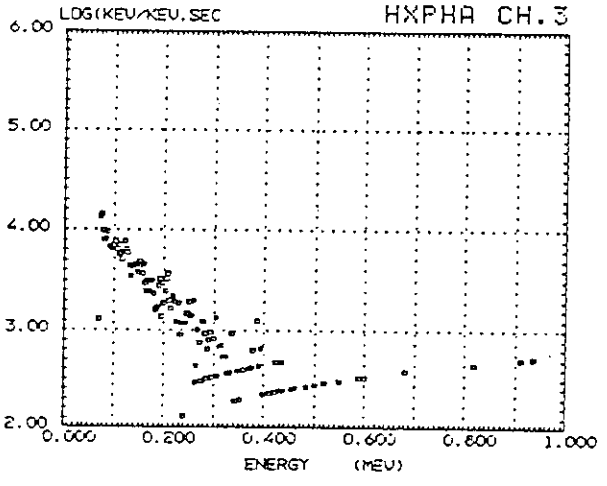

r/a = 0.67

Fig.2 Typical hard x-ray energy spectra measured in the lower hybrid current drive discharge.

11.6 Zeeman polarimeter

N.Nishino,H.Kubo, A.Sakasai, Y.Koide, N.Akaoka, T.Sugie
Y. Tsukahara, T.Ito and H.Takeuchi

A diagnostic technique for poloidal field measurement utilized He^0 beam probe[1] is developed in JT-60. He spectra is split to π and σ component by Zeeman effect due to the magnetic field. Viewing from normal direction to the magnetic field, the unshifted π component is polarized to the magnetic field direction. Therefore, if the direction of the toroidal magnetic field is known, we can calculate the poloidal field to measure the polarized angle of the π component. He 2s-3p (5015.7Å) line is a suitable line for this purpose because the polarizer can be used in visible wavelength region.

1. Active Beam and Optical System

The beam energy and its deviation are 200 keV and smaller than 0.2%. This energy is decided to enlarge the beam penetration in a plasma and to obtain Ti(0) by Rutherford scattering method[2]. The intensity of the beam is 0.6A. The diameter and the divergence are ϕ50 and smaller than 0.18°, respectively. Three pulse can be injected per shot. The total optical system is shown in fig. 1. The He light is gathered by condensing lens, and is focused an image of the beam. The light from an image is collimated by second lens. The direction of polarization of this light is rotated 45° by $\lambda/2$ plate, and the light passed through the wollaston prism is split two polarized components. Two $\lambda/4$ plates are to make the polarization light to circularly polarized light. Each component is focused just on the up or down side of entrance slit of the spectrometer by condensing lens, relay lens, and an image rotator. The transmittance and the resolution of the wavelength are important, because He light intensity is smaller than two order of magnitude typical line spectra of tokamak plasma and the splitting width of π and σ components are below than 1Å. Therefore, the littrow type spectrometers are used to meet this condition. The characteristics of spectrometers is shown in table 1. The entrance and exit slit consist of up and down side for measuring two polarization component and center part for wavelength calibration. The exit optical system is set to guide the light of the polarization component into the detector, which passed through the up or down side of the exit slit. The exit optical system consists of focusing lenses and a band-pass filter. The free spectral range of this spectrometer is narrow, therefore the exit optical system has a band-pass filter. It is necessary to use the detectors of which the quantum efficiency is high. The quantum efficiency of the photomultiplier is usually lower than 0.25. Therefore, APD is selected, because the quantum efficiency of APD is higher than 0.3 at 500 nm. APD is about 0.5 mm in diameter, and a detector has a pair of APD to measure the each component of polarization. The maximum count rate under Geiger mode is higher than 10^5 cps. The characteristics of APD is depend on the temperature, thus, the electric cooling system (perze element) is used to get stable gain. The usual temperature of the APD and the error of temperature is -50° and within 0.2°C, respectively. TMP (50 l/s) is used to make vacuum inside the detectors for avoiding ice of the surface of the APD. To measure He spectra accuracy, absolute wavelength calibration is needed. Therefore, the wavelength calibration by Ar laser are designed to be able to carry out in situ wavelength calibration any time. Four optical fiber are guided to the center of the entrance slit of each spectrometer. The light of Ar laser entered into entrance slit is focused at the center of the exit slit and detected by PD. The error of the wavelength calibration is below than 0.001nm and the reproducibility of the wavelength is good.

Total transmittance is represented by the product of the transmittance of the each assembly.

$T_{total}= T_p x T_s x T_e$

$Q_{total}=Q_d x T_{total}$

where T_p, T_s, T_e are the transmittance of the pre-optical system, spectrometer, exit optical system, respectively. Q_d is the quantum efficiency of the APD.

$T_p=0.9$, $T_s=0.4$, $T_e=0.6$ and $Q_d=0.3$ then $Q_{total}=0.064$.

2. Experimental Results and Discussion

The angle θ between the horizontal axis and the direction of the magnetic force line is obtained to deduce the ratio of two APD signal which are represented by the horizontal and vertical direction of the He light, respectively.

$$\theta_M=\mathrm{Atan}\left(\sqrt{\frac{I_x}{I_y}}\right) \qquad (1)$$

Fig. 2 shows the angle of the magnetic force line viewing from this system in L- and H-mode discharge by LH. This angle is decided the average of the several pulses. The angle of channel 4 (plasma periphery) in H-mode is larger than that of L-mode, and the angle of channel 1 (near plasma center) in H-mode is smaller than that of L-mode. Thus, it is seemed that the current distribution in H-mode is more flattened than L-mode. However, the angle obtained is larger than that of prediction by EQSEL code[3]. It seems that the error of the angle consist of the setting error of optical assembly, the mixing of π and σ component and the statistical error. The optical axis of the λ/2 plate is declined 22.5° to the horizontal direction intended to rotate the horizontal direction of polarization of light by 45°. If the axis is declined 22.5°+δθ to the horizontal axis, then the horizontal direction of polarization of light will change 45°+2δθ. The wollaston prism is installed of which axis is vertical. If the axis is declined $\delta\theta_\omega$ to the vertical axis, then the horizontal direction of polarization of light will change $\delta\theta_\omega$. The split width of π and two σ component are 0.4Å, 0.8Å, and the doppler broadening is 0.3Å typically. Therefore the APD signal is contained not only π component light but also the σ component light. The wavelength of the spectrometer is set down to 0.2Å from the center of the π component to eliminate the σ component light. As a result, the ratio of the intensity of π component light and total light is 0.85. The π and σ ratio is 0.2 (=0.15/0.85). Then, the relationship between the true θ and the measured θ_M is represented as follows.

$$\Delta\theta=\theta_M-\theta, \qquad \theta_M=\tan^{-1}\left(\sqrt{\frac{1+A\cdot\tan^2\theta}{\tan^2\theta+A}}\right) \qquad (2)$$

The largest error in this measurement is the statistical error by photon number because the photon number per pulse is several hundreds. The angle error due to the statistical error reaches several degrees, therefore, several pulses are used to determine the angle of the magnetic force line of plasma discharge. The error bar is already shown in fig.2

3. Summary

We have just started to measure the current distribution in JT-60. However, JT-60 was shut down after this period, no more date have been gotten. The data is qualitatively good, but the quantity is poor. That is future problem. In conclusion,

new diagnostic technique for the local poloidal field measurement is developed in JT-60. This apparatus consist of pre-optical system, spectrometers, and detectors. The transmittance of this optics is 0.2 and the quantum efficiency of APD is higher than 0.3.

References

1. T. Ito *et al* ; JAERI-M 86-114
2. K.Tobita *et al* ; Nucl. Fusion 28 10 (1988) 1719
3. S.Tuji *et al* ; JAERI-M 86-006

Table 1 Specification of Spectrometers

Type		Littrow type
Wavelength Region		495nm~675nm
Resolution		< 0.01nm at 500nm < 0.02nm at 670nm
Lens	ϕ	100mm
	f	1194mm
F-number		12
grating	ruling	79 g/mm
	blaze	75.58°
	size	102mmx254mm
	coating	Al coating

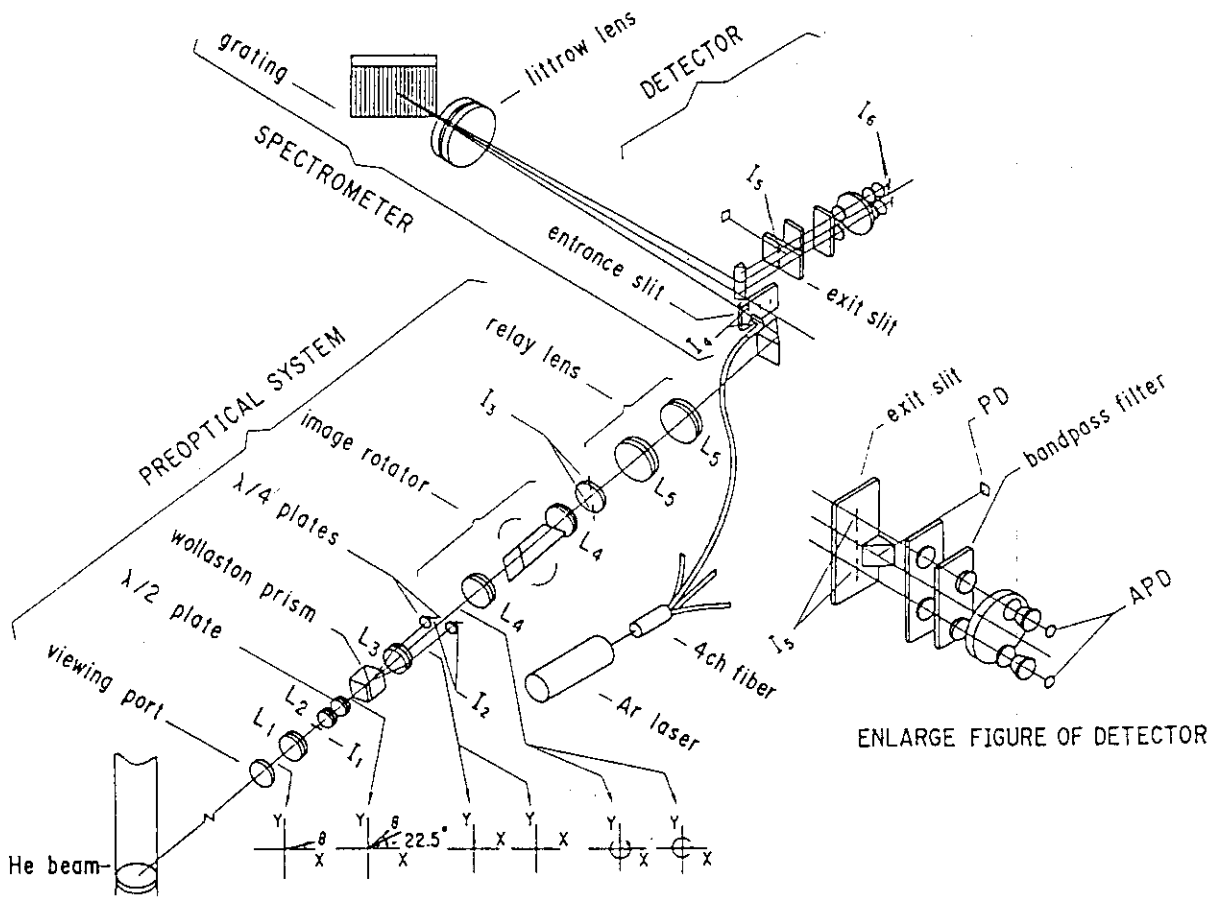

Fig.1 One channel of the optical system is shown. Ar laser system is installed for in situ absolute wavelength calbration.

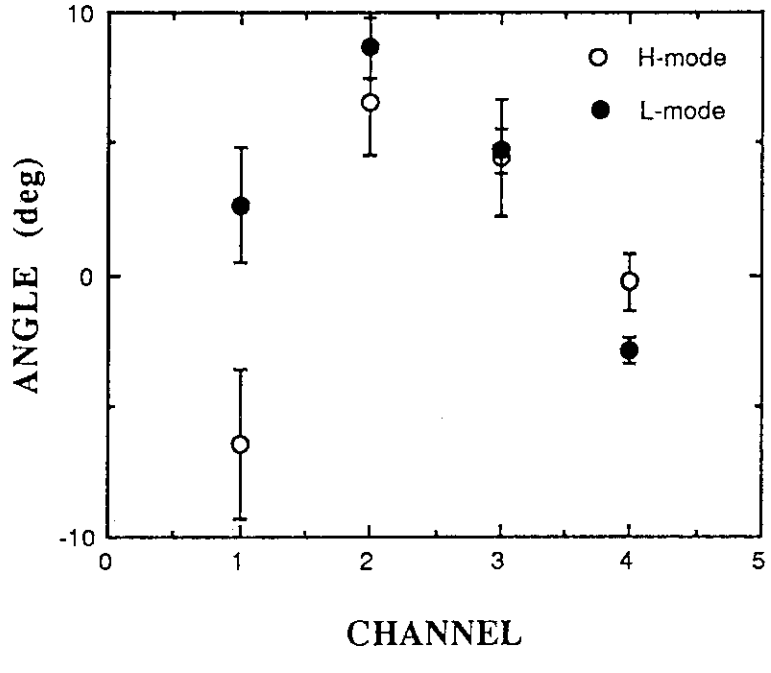

Fig.2 Angle of magnetic force line obtained by zeeman polarimeter in L- and H-mode are shown.

11.7 Multichordal charge-exchange recombination spectroscopy on JT-60U (Plan)

Y. Koide, A. Sakasai, H. Kubo,
N. Akaoka, T. Sugie, H. Takeuchi

1. Introduction

Charge exchange recombination spectroscopy (CXRS) will play an important role also in JT-60U experiments. This paper deals with the plan of CXRS system on JT-60U. As written in paper 8.2, some problems are left to be solved. A new system is designed so that these difficulties are overcome and higher time and spatial resolutions are expected.

2. Hardware

Figure 1 shows a schematic view of the planned CXRS system. For the simultaneous measurements of background components along chords which do not view beam lines, two sets of optical head are equipped, which method has been successful in JIPP T-IIU and JFT-2M [1,2]. If toroidal symmetry is satisfied, estimation of background is improved and the basis of rotation can be precise.

Outline of viewing optics is shown in Fig. 2. Optical head consists of quartz lens and quartz fibers, the core-radius of which is 200μm. Aluminum is adopted as coating material for the fiber, which is fit for high wall temperature operation such as bake out. A rotating shutter is equipped in front of the vacuum window, which prevents degradation of transparency due to carbon coating during discharge cleaning. The back of the shutter plate faced on the fiber is mirror-finished, which is used for in-situ calibration of the optical system. Figure 3 shows the projection of fiber images for (a) tangential and (b) perpendicular systems. The numbers of fibers are 110 for each tangential and 250 for perpendicular systems, respectively, where such many fibers are effective for raising S/N ratio, simultaneous measurements of other species and testing with other different types of detectors . Spatial resolution is ~7 cm for the tangential array, and ~1 cm (edge) and ~6 cm (around half radius) for the perpendicular array, respectively. Time resolution depends strongly on the signal strength. The minimum resolution is 16.7 msec for the CCD camera. For the perpendicular array, there are 10 fibers for each spatial point. Because the pixel size of the PCD array is large enough to detect all of these light, higher time-resolution is expected.

References

[1] Ida, K., Hidekuma, S., Rev. of Sci. Instrum. 60(1989) 867.
[2] Ida, K., Hidekuma, S., Miura, Y., JT-60/JFT-2M Workshop, JAERI Naka Japan, 1989.

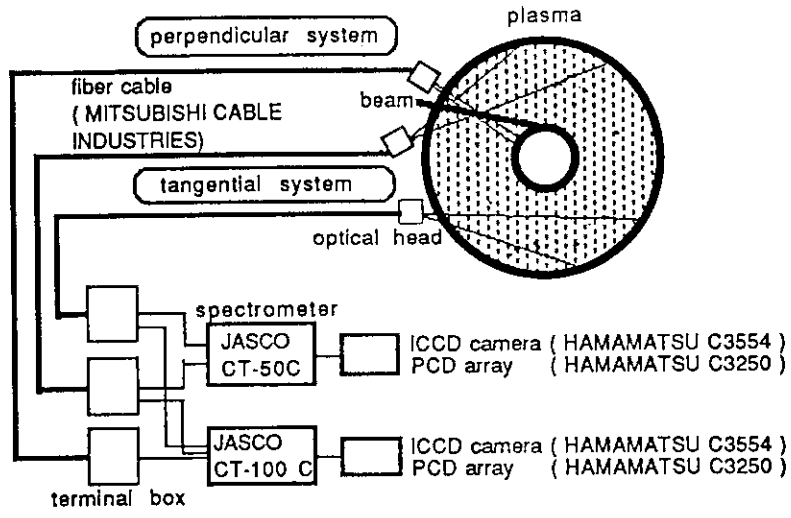

Fig.1 Schematic view of CXRS system.

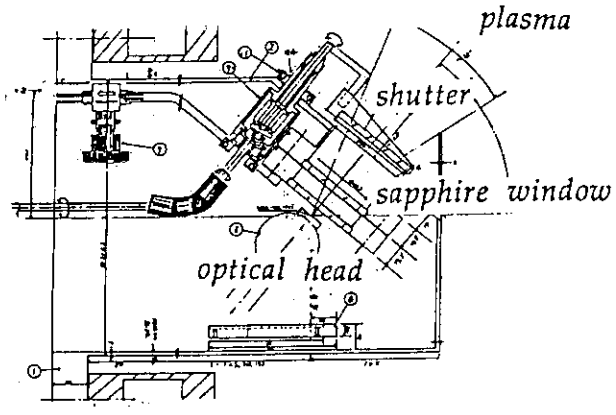

Fig. 2 Structure of viewing optics.

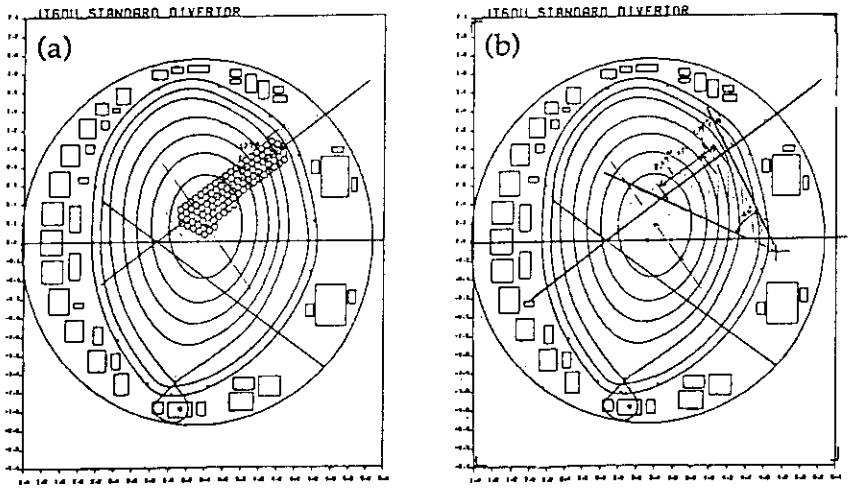

Fig. 3 Field of view of CXRS system.
(a) tangential (b) perpendicular.

12. First Wall

12.1 Post-experiment Observation of First Wall

T.Ando, H. Takatsu, M. Yamamoto, K. Kodama, T. Arai,
A. Kaminaga, T. Sasajima, H. Horiike

1. INTRODUCTION

Material behavior of graphite divertor plates and limiters during ten-month operation in 1989 is described in this section.

During shutdown period in late 1988, heavily damaged graphite tiles were replaced with new ones. Especially, edge tiles placed on bellows-overhanging sections of the divertor plates were changed to C/C composite (carbon fiber reinforced graphite) to improve thermal shock performance against enhanced heat load due to a toroidal gap (~30 mm). Besides, in order to carry out an inpile material test for JT-60U divertor plates, several grades of C/C composites with high thermal conductivity were placed on the divertor region during this period.

Damages and integrity of the divertor plates and limiters were examined within the vacuum vessel during the venting period in May and at the beginning of November after all experiments on JT-60 were finished.

2. OPERATION HISTORY AND DAMAGE OF FIRST WALL

Main operation parameters and shot data in this period are summarized in Table 1. High power and long pulse heating experiments were performed and total absorbed heating energy per discharge was approximately 100 MJ. Percentage of the number of disruption shots was approximately 25 %.

Typical views of divertor plates and limiters after use in all JT-60 operations are shown in Figs. 1 and 2, respectively. Overall integrity of divertor plates and limiters was maintained admirably as in the previous operation in 1988. The behavior of damaged graphite tiles was similar to that reported in ref. 1. Numbers of damaged tiles examined by visual inspections are listed in Table 2. Shallow erosion was observed on the edge region of a large number of divertor tiles with a slight level difference between adjacent tiles. Erosion depth was less than 1 mm. The rest of the top surface of divertor plates was not eroded, but covered with glossy-looking redeposited carbon layer along inboard and outboard high flux zones. Cracks were observed in some of the eroded tiles. Three graphite divertor tiles next to a toroidal gap (~30 mm) located at the bellows section and an opening for diagnostic port were broken.

Almost all of the damaged graphite limiters were edge tiles located at bellows sections with a gap, 500 mm long in the toroidal direction. Cracks were observed on the heavily eroded tiles. The observed cracking pattern was several straight-line cracks initiating at the eroded edge and propagating in the toroidal direction. On the contrary, the inboard midplane limiter tiles placed on the rigid sector were eroded flatways on the plasma-side surface and tortoise shell-shaped cracks were observed.

Erosion induced by arcing between tiles was observed on the inboard limiter tiles which were attached to different backing plates and contacting with each other due to a screw loose during operations.

The number of broken protection tiles attached to the outboard area of the vacuum vessel was relatively large compared to those in the previous operations, which was probably resulted from excessive heat load on the edge

region during LH experiments because these graphite tiles were placed discretely in the toroidal direction to keep big opening for various ports.

Figure 3 shows the C/C composite divertor tiles (CC-312) placed on the edge of the bellows section, where the graphite tiles installed previously were heavily eroded and broken by locally concentrated heat load. This material is 2-D felt-type carbon fiber composite with relatively high thermal conductivity (perpendicular to lamination) and superior mechanical strength compared to those of the isotropic graphite used in JT-60. The edge C/C tile on the outboard separatrix zone (electron-drift side) was heavily eroded with a depth of 3-4 mm, but cracking was not observed, which was a great contrast to the damage behavior of the graphite tiles. This result indicates that C/C composite has superior thermal shock properties and is suitable for armors in enhanced heat load region.

3. INPILE TEST OF C/C COMPOSITE FOR JT-60U DIVERTOR PLATES

Five grades of advanced C/C composites (PCC-2S, MCIfelt II, MFC-1, CX-2002U, CC-312) and a pyrolitic graphite were installed in the divertor region and exposed to the actual divertor plasma. These tiles were attached to two test sections at different toroidal position (#1 & #5 sectors) from Jan. to Apr. and removed in May. Similar test was continued with new tiles,placing at #4 & #5 sectors from June to Oct.. Figure 2 shows these C/C tiles after exposure in divertor operations. The plane of lamination of these tiles was identical with poloidal direction, except for tile G. Slight erosion was observed on the edge in some of the tiles, which was due to slight level difference between tiles. Considerable erosion was observed on tile B with the largest level difference as shown in (b). Thermocouples were inserted in tiles of grade B to measure temperature during operations. The observed maximum temperature of tile B shown in (a) and (b) were around 1000 °C and 600 °C, respectively (base temperature: ~250 °C). All of these C/C composites performed admirably without cracking or breaking. Difference in damage behavior among these materials was not clearly seen in this test.

REFERENCE

[1] JT-60 Team: JAERI-M 89-033, section 11.1 by H. Takatsu, et al. (March 1989).

Table 1 Operation history of JT-60 in 1989

	Jan.-Apr.	June-Oct.
Number of discharges	1351	1905
Number of disruptions	324	482
Number of additional heating shots (NB power>10 MW)	1091 (412)	1548 (502)
Absorbed heating power(MW)	<21.8	<23.2
Heating time(s)	<5.5	<6.0
Stored energy(MJ)	<2.6	<3.2
Plasma current(MA)	<3.2	<3.2
Divertor heat flux (MW/m^2)	<5	<5

Table 2 Number of damaged graphite tiles

Operation period / Grade of damage	Divertor plate: Bellows	Divertor plate: Rigid sector	Limiter	Protection tile
Jan.-Apr.				
(A)	48	many	47	6
(B)	1	10	78	
(C)	0	4	9	9(*)
(D)	0	0	1	10
June-Oct.				
(A)	46	many	-	-
(B)	5	30	143	26
(C)	2	8	2	1
(D)	2	1(**)	2	30
Number of tiles	640	750	~8000	

(A): Eroded, (B): Eroded with fine cracks,
(C): Eroded with macro cracks, (D) Broken.
(*): including grades (B) and (C).
(**): tile located at the opening of vertical port

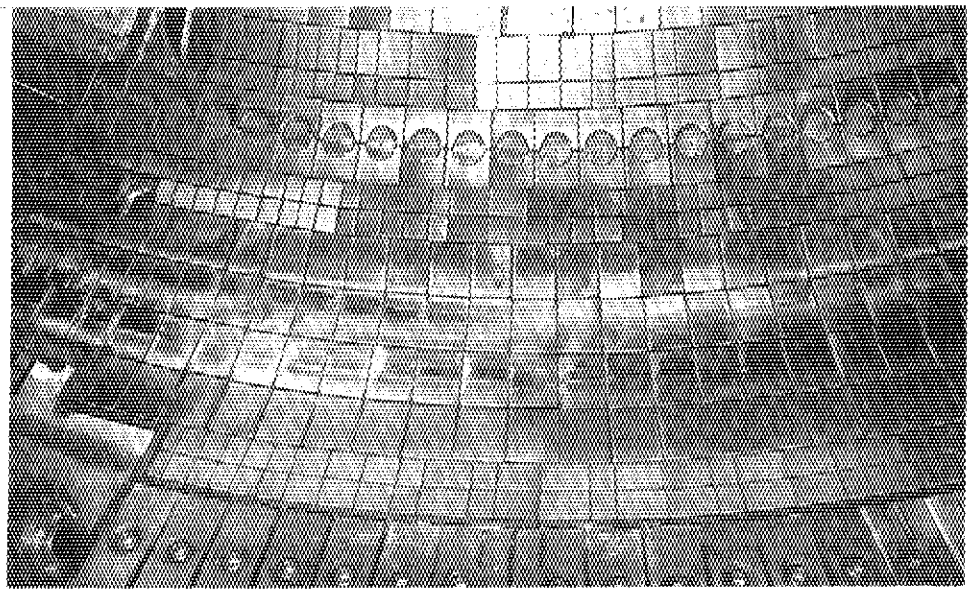

Fig. 1 Lower divertor plates after operation in 1989, showing inboard and outboard separatrix traces running in the toroidal direction. Tile edges are eroded due to slight level difference between adjacent tiles (<1 mm) and redeposited carbon is observed on the non-eroded surface along high flux zones.

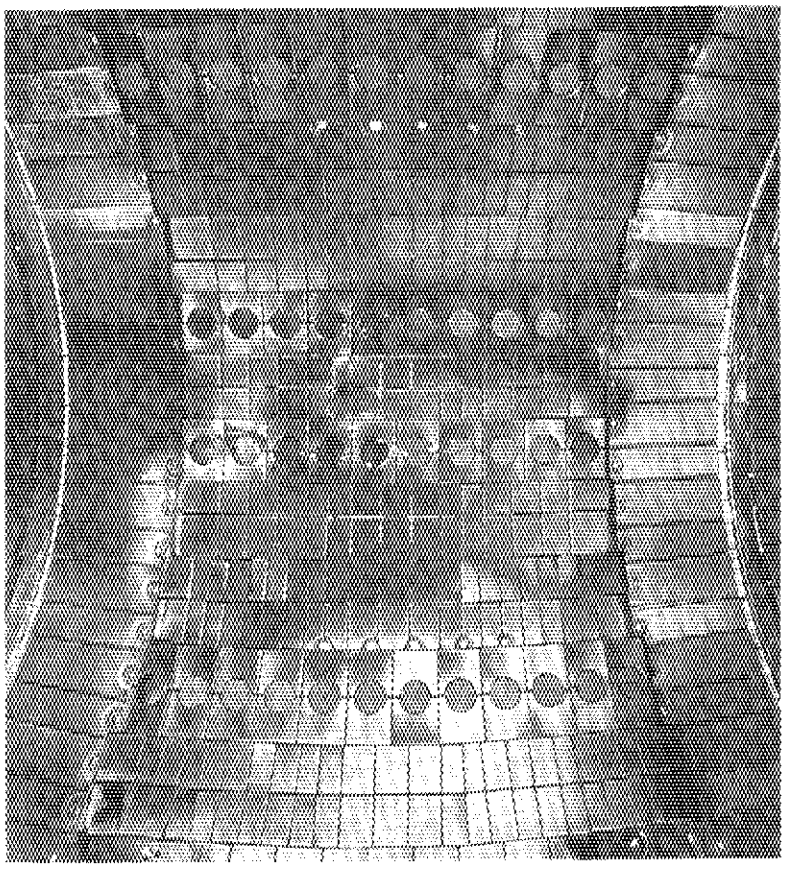

Fig. 2 Inboard limiters after operation in 1989 (#8 sector). Graphite tiles on the electron-drift side (left side) were slightly eroded, but serious failure of the tiles was avoided by adjusting the level of midplane tiles by 2 mm which were damaged in the previous operations.

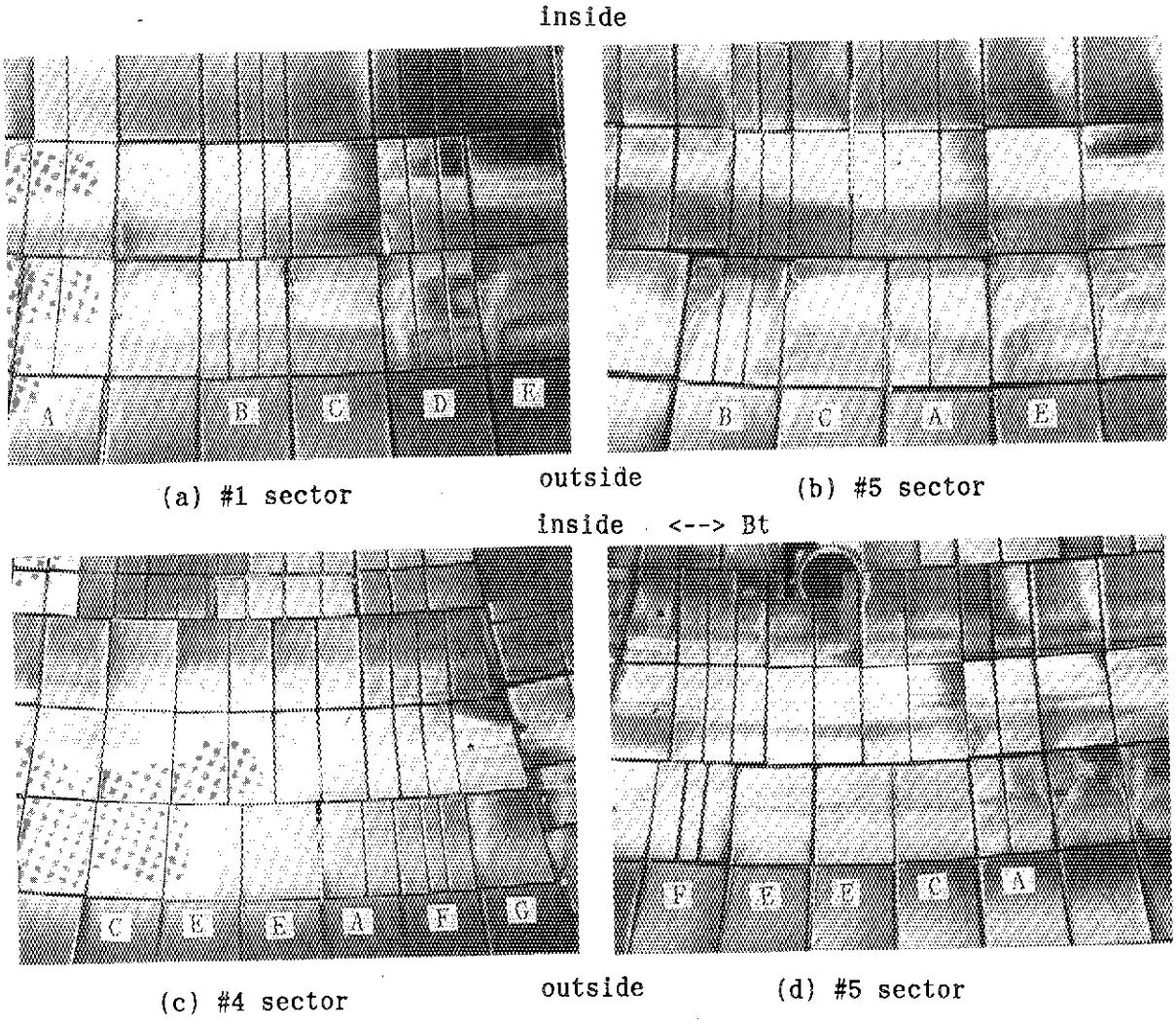

Fig. 4 C/C composite divertor tiles after use in JT-60 operation for inpile material test.
A:PCC-2S, B:CX-2002U, C:MFC-1,
D:Pyroid, E:MCIfelt II,
F:CC-312(//), G:CC-312(⊥)
(a)&(b):operation I(Jan.-Apr.)
(c)&(d):operation II(June-Oct.)

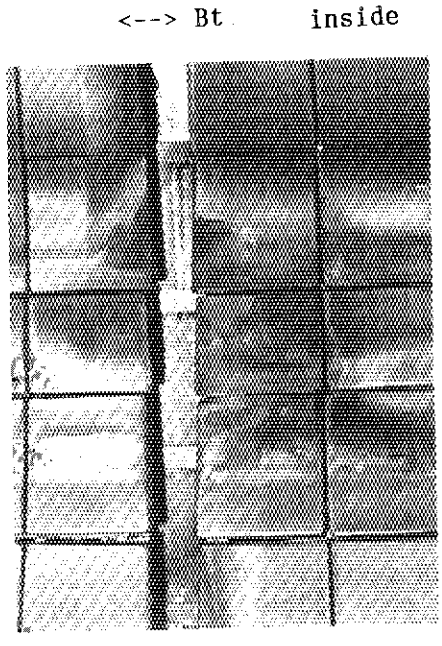

Fig. 3 C/C composite divertor tiles(CC-312(⊥)) after use in the operation from Jan. to Apr., placed at the edge of bellows section (#3-#4). Center tile is not broken in spite of considerable erosion due to locally concentrated heat load.

ACKNOWLEDGEMENT

The continuing support of Drs. M. Yoshikawa and M. Tanaka is gratefully acknowledged.